School of Molecular and Life Sciences

Luminescent Iridium Tetrazolato Markers for Live Cell Imaging

Chiara Caporale

This thesis is presented for the Degree of
Doctor of Philosophy
of
Curtin University

April 2018

Declaration

To the best of my knowledge this thesis contains no material previously published by any other person except where due acknowledgment has been made.

I declare that this thesis is my own account of my research and contains as its main content work which has not previously been submitted for a degree or diploma in any university.

Signature: 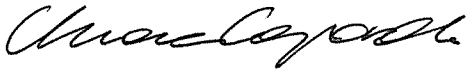

Date: 13.04.2018

Abstract

In this research, a series of iridium(III) tetrazolato complexes were synthesised and their photophysical and biological properties investigated. Both the cyclometalated and the ancillary ligands were systematically modified by substitution of functional groups or by increasing the extension of the π conjugation. This approach allowed a more systematic rationalisation of the structure-activity relationship, highlighting how variations in the chemical structure and charge might influence the biological behaviour of these complexes, especially in relation to cellular localisation and cytotoxicity.

A family of cyano and (iso)quinolyl-functionalised iridium(III) tetrazolato complexes was firstly investigated. Upon methylation of the tetrazolate ligand, positively charged complexes were synthesised from their neutral analogues, allowing specific comparison between isostructural complexes with different charge. The photophysical analyses were performed in dichloromethane, aqueous and lipophilic solvents, revealing a predominantly solvatochromic emission originating from mixed metal-to-ligand (MLCT) and ligand-to-ligand (LLCT) charge transfer excited state of triplet multiplicity. The behaviour of these complexes was then examined in live cells, showing localisation in the endoplasmic reticulum and lipid droplets for the neutral species, whereas the majority of the cationic complexes accumulated in mitochondria. Interestingly, the cytotoxicity of the charged species was extremely high in comparison to their neutral analogues, probably due to a combination of uptake and intracellular localisation. The mitochondrial accumulation of one of the methylated complex was also evaluated in fresh and fixed muscle tissue samples, extending the application of this probe to a field which relies mostly on immunochemistry.

The amino-functionalised iridium(III) tetrazolato series was then explored. The substitution of the nitrile with an amino group on the pyridyl tetrazolate ligand was conducted to investigate the protonation/deprotonation properties of these complexes,

aiming to the application in cellular pH-sensing. Lower emission intensity was recorded in all the solvents with respect to the previous series, due to the presence of a thermally available and dark metal-centred (^{3}MC) excited state. Moreover, solubility issues were also encountered. Nevertheless, the pH-sensing activity was recorded in organic solvent for one of the complexes, but the same trend was not reproducible in aqueous medium.

The amino complex [Ir(**ppy**)$_2$(**TzPyNH$_2$**)] was then combined with different fatty acids to form the fatty acid-functionalised iridium(III) family. The degree of unsaturation and the length of the fatty acid chains did not affect the photophysical properties of these complexes, which exhibit similar emission properties than their amino precursor. Moreover the low cytotoxicity and the accumulation of these probes in the area surrounding the nucleus was consistent along the whole series, but further investigations need to be performed in order to identify the specific stained organelle. On the other hand, different mechanisms of uptake were recorded, such as passive diffusion and mediated transport.

Supporting publications include:

Sorvina, A.; Bader, C.A.; Darby, J. R.T.; Lock, M. C.; Soo, J. Y.; Johnson, I. R.; Caporale, C.; Voelcker, N. H.; Stagni, S.; Massi, M.; Morrison, J. L.; Plush, S. E.; Brooks, D. A. *Sci. Rep.*, **2018**, *8*, 8191.

Caporale, C.; Massi, M. *Coord. Chem. Rev.*, **2018**, *363*, 71-91.

Caporale, C.; Bader, C. A.; Sorvina A.; MaGee, K. D. M.; Skelton, B. W.; Gillam, T. A.; Wright, P. J.; Raiteri, P.; Stagni, S.; Morrison, J. L.; Plush, S. E.; Brooks, D. A.; Massi, M. *Chem. Eur. J.*, **2017**, *23*, 15666-15679.

Acknowledgements

And here we are, trying to summarise three and an half years of PhD in a page of acknowledgements. A lot has happened since the day I walked in Building 500 for the first time, scared and excited at the same time.

Firstly, I would like to thank A/Prof Max Massi, for the opportunity to do this PhD and for the great project that I have been assigned to. It has been years of hard work, but your enthusiasm in my research study has help me to improve and become more and more passionate about this field. Also, I would like to thank Prof Mark Ogden for the co-supervision and for being encouraging and supportive during my all PhD.

I would like to acknowledge Dr Alexandra Sorvina, Dr Christie Bader, Dr Sally Plush and Prof Douglas Brooks for the fruitful collaboration during my project. Thank you for the knowledge and the experience in biological imaging you have shared with me. A particular thank to Christie, especially in the last phase of the writing process, for being available for last-minute explanations and clarifications.

I would like to thank Dr Ching Goh and Peter "Chappy" Chapman for the endless times they promptly help me out. Curtin would run way less smoothly without your precious knowledge and willingness.

To the Empire group, past and present, a big thank. It has been a pleasure to share these years with you. I have learnt a lot and, hopefully, I did not drive anybody too crazy.

To the other founder member of Little Italy, thanks Anna. You have been sometimes a friend, sometimes an Origin expert, sometimes my co-supervisor. Thanks to have been there to ride this rollercoaster with me. Although, we should probably write another thesis about the lab and general life-back stage!

To Nursha and Jason, thanks for the technical and grammatical support during my write-up phase. I would have probably ended up writing my thesis in Italian and with a typewriter without you two.

Thanks Shifaza, to have been my Aussie-Maldivian mum since you have moved in Perth. I think I have been officially adopted!
Also, thanks Fede for your patience and positivity, which made the last six months of PhD way more enjoyable.
A huge thanks to my family. Long time has passed since those four days of crying because I got a PhD offer 13000 km away from home and I did not know what to do. Thanks for that initial and really needed incentive, for the endless support and for the patience. I hope I made you proud of me.
Finally, thanks Matt. You have managed to stick by me in this last stressful and busy period of my life. I am not sure how you did it, but you did great!

Dedication

For Mum, Dad and Ale.

Commonly used Abbreviations and Symbols

τ	Excited state lifetime
ν	Wavenumber
Φ	Quantum yield
Φ_r	Quantum yield standard
λ_{abs}	Absorption wavelength
λ_{em}	Emission wavelength
λ_{ex}	Excitation wavelength
δ	Nuclear magnetic resonance chemical shift
ε	Molar absorptivity
AIE	Aggregation-induced emission
app.	Apparent
BODIPY	4,4-difluoro-4-bora-3a,4a-diaza-s-indacene
bpy	2,2'-bipyridine
br	Broad (IR)
BSA	Bovine serum albumin
bzq	Benzo[*h*]quinoline
ca.	Circa/approximately
CT	Computed tomography
d	Doublet (NMR)
DCM	Dichloromethane
dec	Decomposition
DMEM	Dulbecco's modified eagle medium
DMF	Dimethylformamide
DMSO	Dimethylsulfoxide
EPESS	Phosphorescence emission in the solid state
ER	Endoplasmic reticulum
F_2ppy	2-(2,4-difluorophenyl)pyridine

FCCP	Carbonyl cyanide-p-trifluoromethoxyphenylhydrazone
GS	Ground state
HOMO	Highest occupied molecular orbital
IC	Internal conversion
IC_{50}	Half maximal inhibitory concentration
ICP-MS	Inductively coupled plasma mass spectrometry
IL	Intra-ligand
ILCT	Intra-ligand charge transfer
IR	Infrared
ISC	Intersystem crossing
J	Coupling constant (NMR)
k_{ISC}	Intersystem crossing rate constant
k_{nr}	Non-radiative decay rate constant
k_{obs}	Observed rate constant
k_r	Radiative decay rate constant
LC	Ligand-centred
LEECs	Light-emitting electrochemical cells
LLCT	Ligand-to-ligand charge transfer
LUMO	Lowest unoccupied molecular orbital
Lys. fluid	Lysosomal pH= 4.5 fluid solution
m	Multiplet (NMR signal splitting), medium (IR)
M.P.	Melting point
MC	Metal-centred
MLCT	Metal-to-ligand charge transfer
MLLCT	Metal-ligand-to-ligand charge transfer
MRI	Magnetic resonance imaging
MTS	[3-(4,5-dimethylthiazol-2-yl)-5-(3-carboxymethoxyphenyl)-2-(4-sulfophenyl)-2H-tetrazolium bromide
MTT	3-(4,5-Dimethylthiazol-2-yl)-2,5-diphenyltetrazolium bromide
NAD(P)H	Nicotinamide adenine dinucleotide phosphate (reduced form)
NIR	Near-infrared
NMR	Nuclear magnetic resonance

OLEDs	Organic light-emitting devices
PBS	Phosphate buffered saline
PDT	Photodynamic therapy
PEG	Polyethylene glycol
PEI	Polyethylenimine
PET	Positron emission tomography
PeT	Photoinduced electron-transfer
PFA	Paraformaldehyde
phen	1,10-phenanthroline
ppy	2-phenylpyridine
pq	2-phenylquinoline
r.t.	Room temperature
ROS	Reactive oxygen species
RPMI	Roswell park memorial institute medium
s	Singlet (NMR signal splitting), sharp (IR)
S	Spin multiplicity
SPECT	Single photon emission computed tomography
t	Triplet (NMR signal splitting)
TD-DFT	Time-dependant density functional theory
UV	Ultraviolet
Vis	Visible
VR	Vibrational relaxation
w	Weak (IR)

Commonly used Abbreviations of Compounds

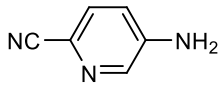	CN**PyNH$_2$**
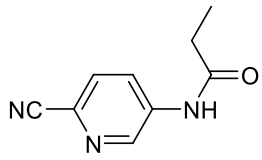	CN**PyNHC$_{3sat}$**
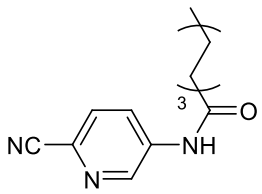	CN**PyNHC$_{8sat}$**
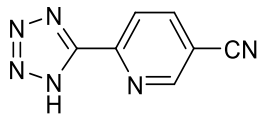	H**TzPyCN**
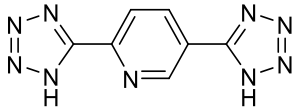	H**TzPyTz**
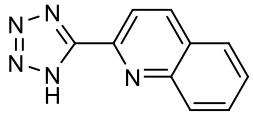	H**TzQn**
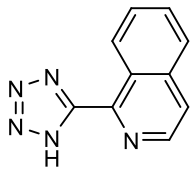	H**TziQn**
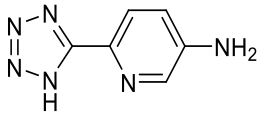	H**TzPyNH$_2$**

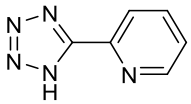

H**TzPy**

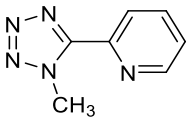

N4-Me**TzPy**

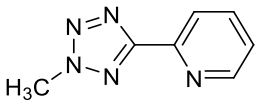

N3-Me**TzPy**

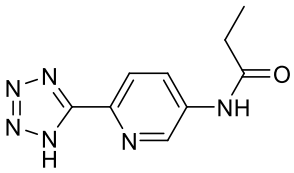

H**TzPyNHC$_{3sat}$**

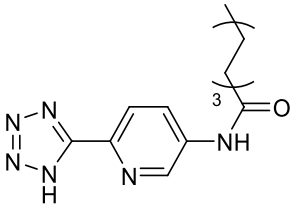

H**TzPyNHC$_{8sat}$**

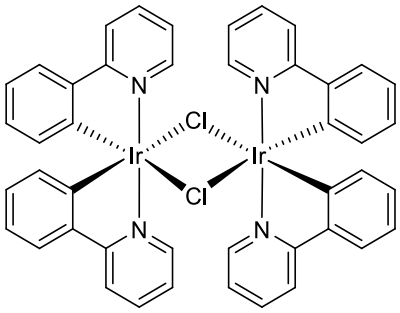

[Ir(**ppy**)$_2$(μ-Cl)]$_2$

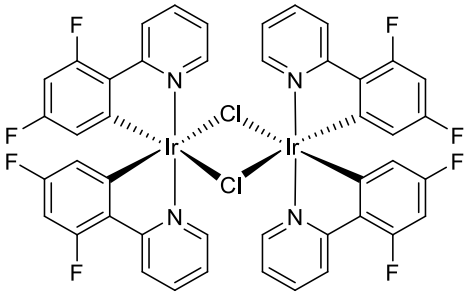

[Ir(**F$_2$ppy**)$_2$(μ-Cl)]$_2$

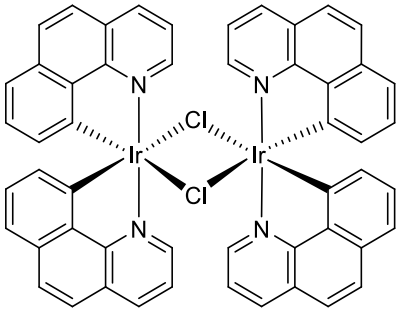

[Ir(**bzq**)$_2$(μ-Cl)]$_2$

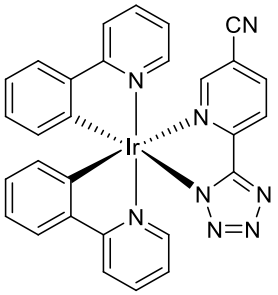

[Ir(**ppy**)$_2$(**TzPyCN**)]

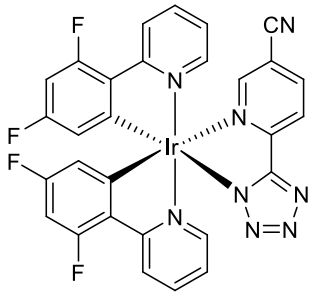

[Ir(**F$_2$ppy**)$_2$(**TzPyCN**)]

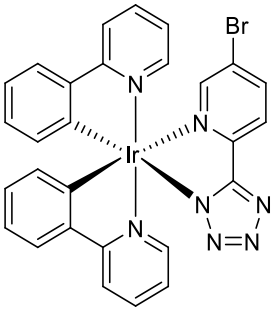

[Ir(**ppy**)$_2$(**TzPyBr**)]

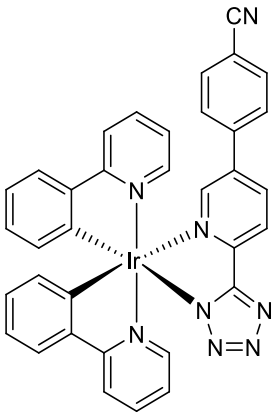

[Ir(**ppy**)$_2$(**TzPyPhCN**)]

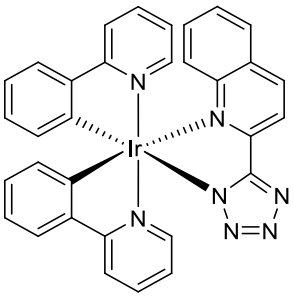

[Ir(**ppy**)$_2$(**TzQn**)]

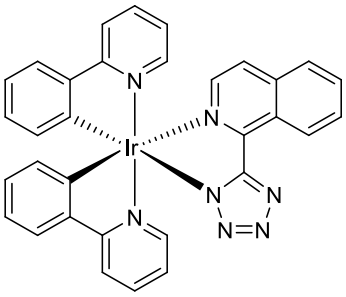

[Ir(**ppy**)$_2$(**TziQn**)]

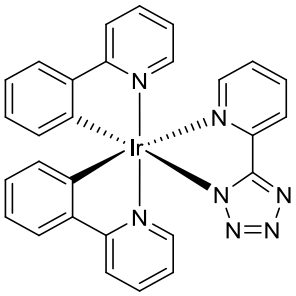

[Ir(**ppy**)$_2$(**TzPy**)]

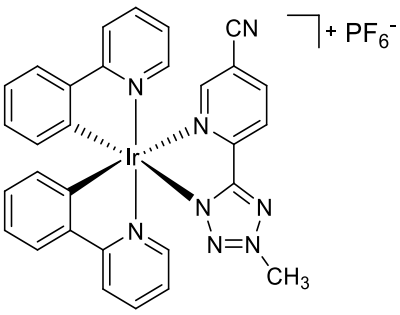

[Ir(**ppy**)$_2$(Me**TzPyCN**)][PF_6]

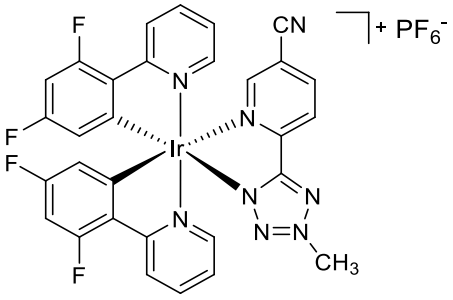

[Ir(**F$_2$ppy**)$_2$(Me**TzPyCN**)][PF_6]

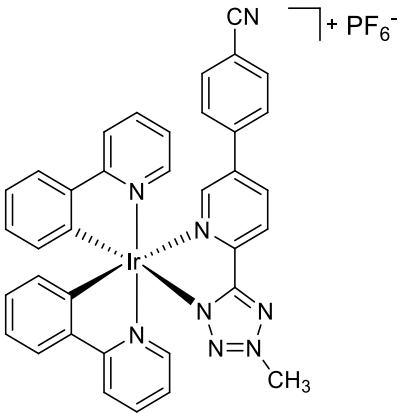

[Ir(**ppy**)$_2$(Me**TzPyPhCN**)][PF_6]

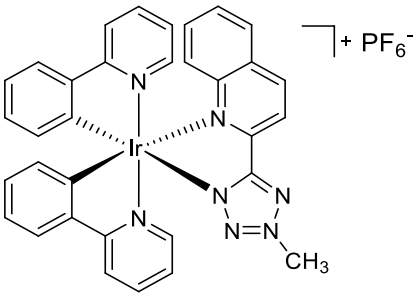

[Ir(**ppy**)$_2$(Me**TzQn**)][PF_6]

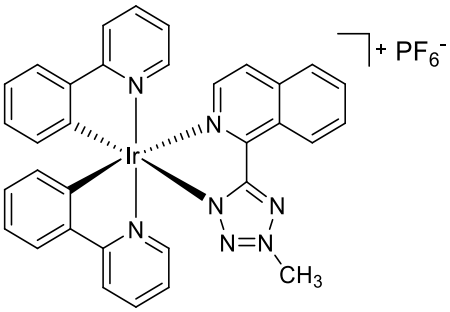

[Ir(**ppy**)$_2$(Me**TziQn**)][PF_6]

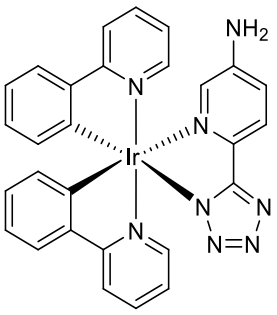

[Ir(**ppy**)$_2$(**TzPyNH$_2$**)]

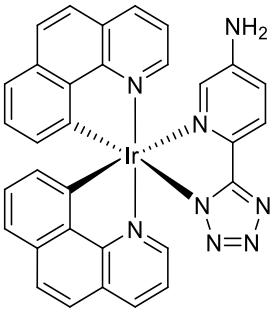

[Ir(**bzq**)$_2$(**TzPyNH$_2$**)]

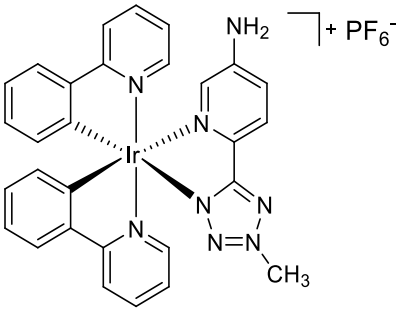

[Ir(**ppy**)$_2$(Me**TzPyNH$_2$**)][PF_6]

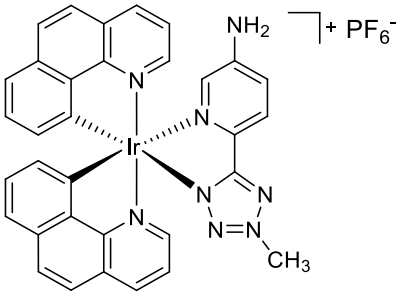

[Ir(**bzq**)$_2$(Me**TzPyNH$_2$**)][PF_6]

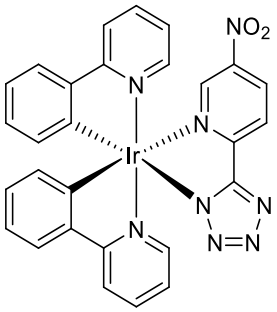

[Ir(**ppy**)$_2$(**TzPyNO$_2$**)]

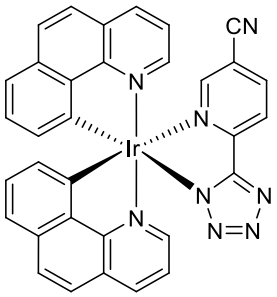

[Ir(**bzq**)$_2$(**TzPyCN**)]

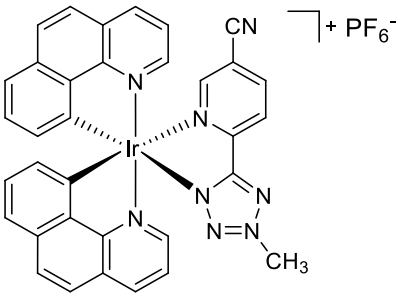

[Ir(**bzq**)$_2$(Me**TzPyCN**)][PF_6]

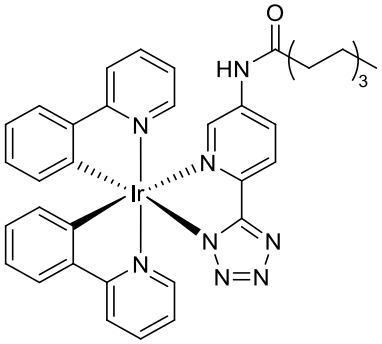

[Ir(**ppy**)$_2$(**TzPyNHC$_{8sat}$**)]

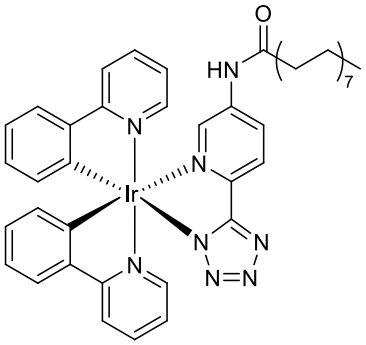

[Ir(**ppy**)$_2$(**TzPyNHC$_{16sat}$**)]

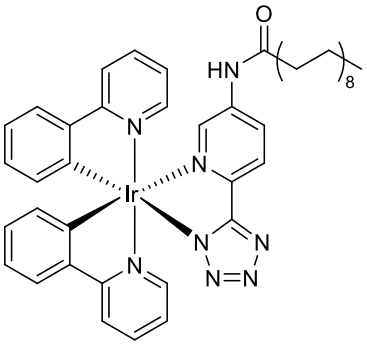

[Ir(**ppy**)$_2$(**TzPyNHC$_{18sat}$**)]

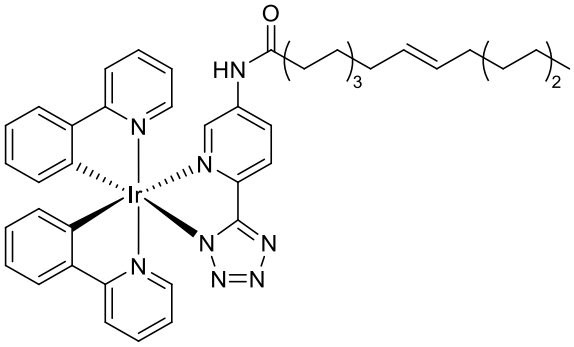

[Ir(**ppy**)$_2$(**TzPyNHC$_{16cis}$**)]

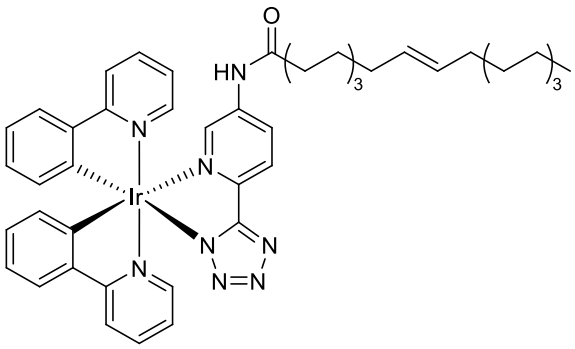

[Ir(**ppy**)$_2$(**TzPyNHC$_{18cis}$**)]

Table of Contents

Chapter 1

Introduction

Part of the content of this chapter has been published in:

Coordination Chemistry Reviews (2018) with the title "Cyclometalated Iridium(III) Complexes For Life Science".[1]

1.1 Biomedical Imaging

Biomedical imaging is the technique of producing visual representation of cells, tissues, organs or body parts for the use in clinical diagnosis, treatment and desease monitoring. The development of medical imaging techniques can be considered a milestone in medicine since Wilhelm Röntgen discovered X-rays in 1895 and was able to visualise the bones of a hand (**Figure 1.1** - A).

In the early 1970s, computed tomography (CT) enabled to collect for the first time cross-sessional images of human body (**Figure 1.1** - B). Although this technique can improve diagnoses, limit unneeded medical procedures and enhance treatments, major concerns are related to the exposure of patients to ionisation radiations.[2,3]

In the 1980s, magnetic resonance (MRI) revolutionised the medical diagnosis and biomedical research, allowing highly resolved and accurate discrimination of internal organs and tissues (**Figure 1.1** - C). Unlike X-ray and CT, MRI is a non-invasive technique which detects the energy released by protons in the body (most commonly found in water) after they have been excited by a radio frequency pulse in a strong magnetic field. Contrast in tissues is achieved by the different relaxation time of these protons, depending on their location. The improvement of the MRI image

output can be enhanced by the use of contrast agents, which are paramagnetic substances such as Gd^{3+} complexes.[4–6]

Highly sensitive methods such as positron emission tomography (PET) and single photon emission computed tomography (SPECT) have been emerging as complementary to CT and MRI techniques. Both PET and SPECT use small amount of radioactive markers (usually ^{18}F and ^{99m}Tc) to monitor biological activity, for example, the spatial distribution of blood flow and receptor concentrations, or even to detect tumours (**Figure 1.1** – D, E). PET provides higher spatial resolution imaging than SPECT, due to the detection of two positrons in opposite direction emitted by the radioactive tracer. On the other hand, SPECT measures directly the emitted gamma radiation, making this technique significantly less expensive and more widely available than PET.[7–10]

More recently, optical imaging has become a rapidly emerging area in the medical imaging field, with widespread applications ranging from clinical diagnosis to molecular biology. Noteworthy, optical imaging cannot be employed as whole body technique on humans as the previously discussed methods, due to limitations on the level of light penetration achievable and the overall contrast produced. Nevertheless, whole body *in vivo* imaging on small animals is commonly used, along with fluorescent image-guided surgery.[11] Optical imaging is non-invasive, utilises non-ionising radiation and can produce high resolution images at sub-cellular level.[12–14] This technique uses ultraviolet (UV) to near infrared (NIR) wavelength of light to excite fluorescent and phosphorescent dyes and, based on their specific emission, visualised molecule and biological moieties (**Figure 1.1** - F). On the other hand, label-free methods have also been developed, which allow the detection of autofluorescence arising from endogenous species.[15–19] In this chapter, the use of phosphorescent probes, their advantages over fluorescent dyes for specific applications and their main properties will be discussed.

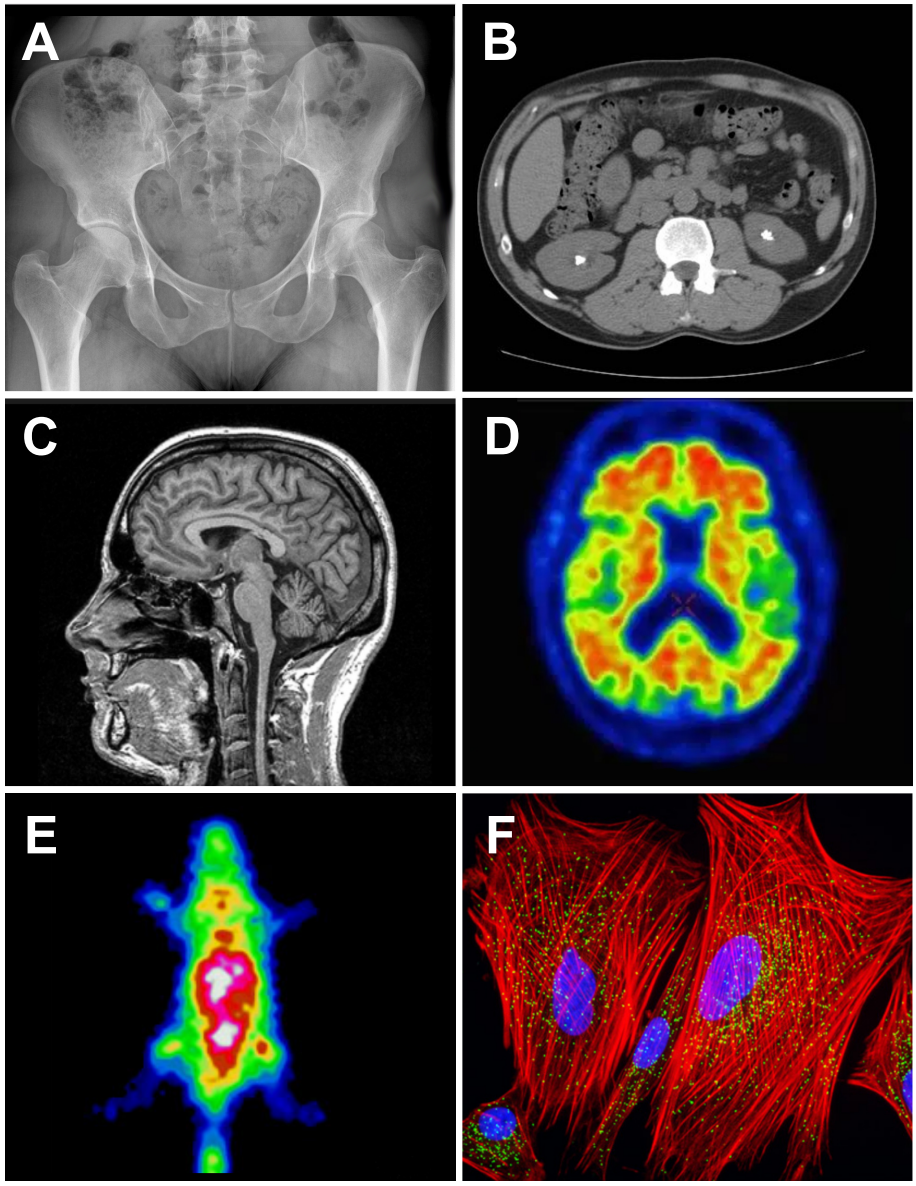

Figure 1.1 Examples of biomedical imaging techniques. A) X-ray; B) CT; C) MRI; D) PET; E) SPECT; F) Optical imaging. Adapted from ref[20–25].

1.1.1 Cellular and Tissue Optical Imaging

Optical imaging techniques have contributed to important discoveries in molecular and cell biology based on studies of single cells or *in vitro* tissue sections.[26,27] However, the use of optical methods in deep tissues has been limited by low penetration depth and strong light-scattering in the biological system, the latter being responsible for blurred and distorted optical signals.[12,13,28–31] The development of advanced confocal microscopes, along with a new generation of probes (in particular for the application in the NIR region of the spectrum) has allowed a remarkably deeper tissue penetration, lower autofluorescent interference and minimal damage to the samples.[32–37]

Both cells and tissues can be analysed *in vivo* or after a fixation process. This procedure can be achieved by chemical (immersion and perfusion methods) or physical (heat, microwave, and cryopreservation) means and aims to preserve cell and tissue components in an ideal "life-like state", preventing or arresting the natural degenerative processes.[38,39] Depending on the fixation process, different artefacts can be produced, due to the permeabilisation of the cellular membrane, denaturation and precipitation *in situ* of proteins, as well as, covalent cross-linking between molecules. On the other hand, fixed samples are necessary in the case of staining techniques as immunochemistry,[40,41] which requires the permeabilisation of cells, or in the case of large number of tissue samples, which cannot be analysed in short amount of time.

In vivo analyses, under certain situations, appear to be superior to those offered by the study of fixed samples. In fact, live optical imaging avoids the use of substances that strongly interfere with the cell or tissue structure and provides the opportunity to observe and track several biological functions and reactions taking place in real-time.[1,13,31,42] For this reason, luminescent probes for application in live optical imaging possess different properties (refer to section 1.4 of this chapter) in comparison to the dyes used in fixed cells or tissues, for example low cytotoxicity.

1.2 Probes for Optical Imaging

1.2.1 Organic Fluorophores

The area of organic fluorophores for cellular imaging is certainly well advanced and in continuous evolution, and many probes that are now of fundamental importance for optical imaging have been developed for various applications within a cellular environment.[43–48] The most common organic probes can be grouped in four main representative platforms. Rhodamine (**1**) and fluorescein (**2**) derivatives were the first dyes to be reported in the end of the nineteenth century, followed by BODIPY (**3**) and cyanine dyes (**4**) (refer to **Figure 1.2**).[45,49–52]

While these markers are indeed well established and essential in the field, for specific imaging conditions they might be associated with drawbacks that are intimately linked to the organic nature of these compounds.

Typically, luminescent organic molecules have rather small Stokes shifts, often resulting in a significant overlap between the absorption and emission spectral profiles.[37,50] Therefore, as the probe accumulates within a specific cellular compartment and its local concentration effectively increases, its brightness (defined as the product of molar absorptivity and photoluminescent quantum yield) can be reduced due to concentration quenching phenomena.

Noteworthy, cells are inherently fluorescent due to the presence of photoactive endogenous compounds such as flavins, nicotinamides, and indole side groups of tryptophan amino acids, for example.[53–58] If the excitation and emission profiles of the marker in use are in the same region as those of autofluorescent endogenous species, it might be difficult to discriminate between the two signals.

Lastly, but potentially one of the most limiting drawbacks, is represented by the tendency of some organic molecules to undergo photobleaching.[59–61] This process occurs once the compound is excited to higher energy states, from which unwanted reactivity can occur destroying the emissive properties of the marker. It should be noted that some molecular probes can undergo extensive photobleaching within a very short amount of time (less than one minute), limiting their usefulness for longer-time experiments in live cells.

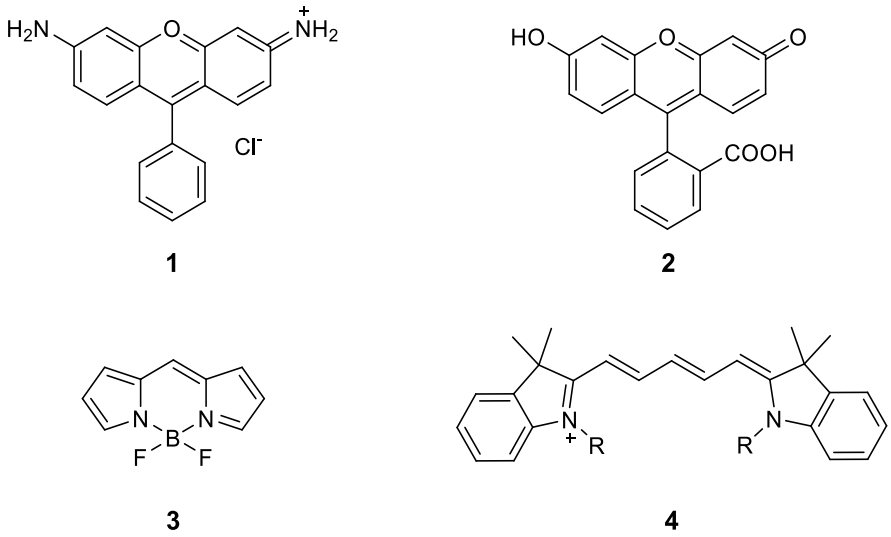

Figure 1.2 Examples of organic fluorophores used in optical imaging; 1) Rhodamine; 2) Fluorescein; 3) BODIPY core; 4) Cyanine.

1.2.2 Transition Metal Complexes

Photoluminescent transition metal complexes of low spin d^6 electronic configuration such a ruthenium(II), rhenium(I), and iridium(III), or d^8 electronic configuration such as gold(I) and platinum(II),[62–65] have been investigated to overcome some of the drawbacks associated with organic probes, as described in section 1.2.1 of this chapter. All these complexes display favourable chemical characteristics and advantageous photophysical properties (refer to section 1.3 and section 1.4) that make them ideal candidates for the development of probes complementary to organic fluorophores for applications in cellular imaging.[66] Some examples of transition metal probes of Ru(II) (**5**),[67] Ir(III) (**6**),[68] Re(I) (**7**),[69] Au(I) (**8**)[70] and Pt(II) (**9**)[71] developed as imaging agents have been depicted in **Figure 1.3**

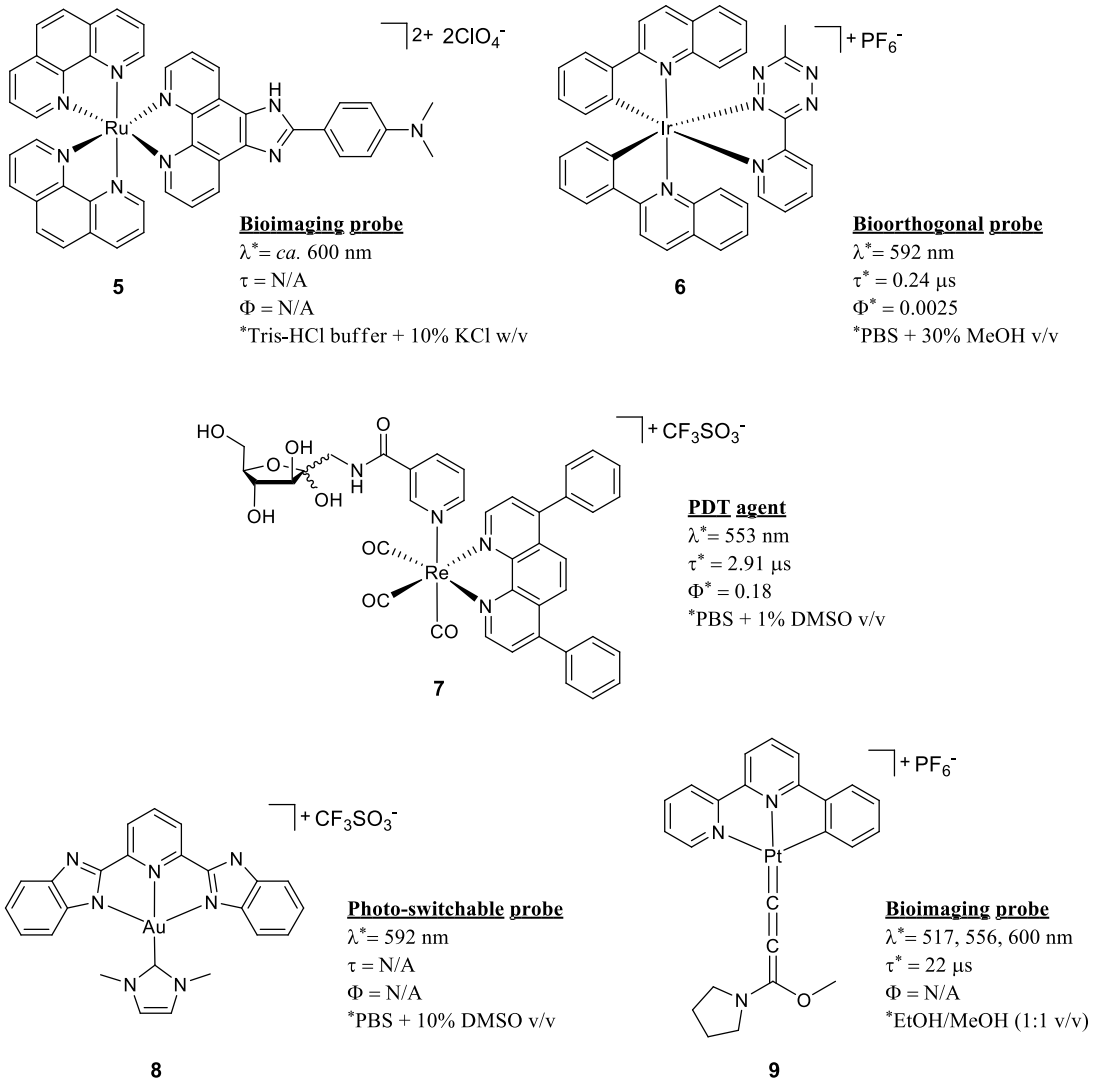

Figure 1.3 Examples of transition metal probes for biological imaging. Their photophysical properties and specific applications have been reported.

1.3 Photophysical Properties of Transition d^6 Metal Complexes

1.3.1 Fundamental Concepts

Photoluminescence is the emission of light from molecules, after the absorption of a photon. The absorption of light by a molecule dissolved in a diluted solution can be described by the Lambert-Beer law (**Equation 1.1**):

$$I = I_0 \times 10^{\varepsilon bc} \quad \textbf{(1.1)}$$

where I and I_0 are the intensity of the transmitted and incident radiation at a given wavelength, respectively, ε is the molar absorptivity coefficient, b is the path length and c is the concentration. The molar absorptivity coefficient describes the ability of a compound to absorb a specific wavelength of light.

The simplified Jablonski diagram depicted in **Figure 1.4** illustrates the processes taking place when a molecule interacts with light (hν).

The absorption of a photon allows the promotion of the molecule from its ground state (S_0) to an electronically excited states (e.g.: S_1, S_2). For each excited state, many vibrational levels can be populated and vibrational relaxation (VR) can occurred between them. This event consists in the redistribution of the vibrational energy gained during the electronic transition, which allows the molecule to move to the lowest vibrational level of the excited state.[72] Transitions between vibrational levels of different excited states with the same multiplicity can be also present. This process is known as internal conversion (IC) and, along with VR, is a rapid radiationless event occurring in the order of 10^{-13} - 10^{-14} seconds.[73] In the presence of a metal centre, from the excited state S_1, the molecule can undertake intersystem crossing (ISC), which is the transition from a singlet excited state to a more stable triplet state (T_1). This process is spin forbidden, but the spin orbit-coupling of metal complexes allows the relaxation of the spin selective rule (section 1.3.2) and the transition can take place.[74,75]

Decay processes from the lowest excited state (e.g.: S_1 or T_1) can be divided into two types. The non-radiative decay is directed by the overlap of the lowest vibrational level of the excited state and the levels of the ground state (S_0). The energy gap law (**Equation 1.2**) describes the relationship between the energy of this overlapping and the k_{nr}:

$$k_{nr} = Ae^{-\alpha \Delta E} \qquad (1.2)$$

where k_{nr} is the non-radiative decay constant, A is the pre-exponential coefficient, α is a proportionality constant and ΔE is the energy gap between the two states. **Equation 1.2** states that the greater is the energy gap between the excited and the ground state, the slower the non-radiative decay rate.[76]

The second type of process is named radiative decay and consists in the transition to the ground state by spontaneous emission of a photon. In the case of radiative decay between states of the same multiplicity, the phenomenom is described as *fluorescence*. On the other hand, a radiative transition involving a change in spin is known as *phosphorescence*, and is typical of metal complexes (**Figure 1.4**).

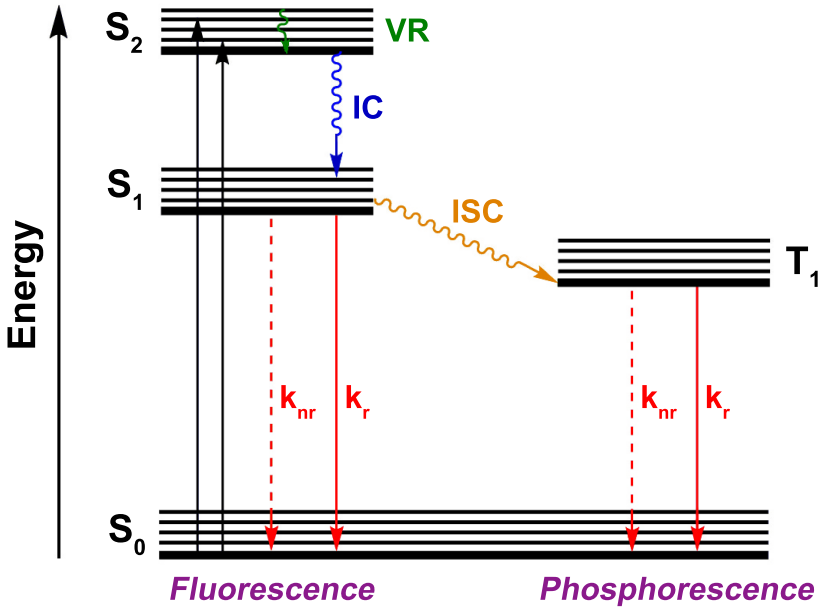

Figure 1.4 Simplified Jablonski diagram illustrating fluorescence and phosphorescence (solid red arrows).

The rate of the radiative decay process can be expressed by the radiative decay constants k_r, as previously shown for the non-radiative decay process (**Equation 1.2**). The overall decay rate of a molecule will be then described as the sum of the decay rates, and the excited state lifetime (τ) can be calculated as the inverse of this sum (**Equation 1.3**):

$$\tau = \frac{1}{k_r + k_{nr}} \quad (\mathbf{1.3})$$

Therefore, the lifetime can be defined by the time the molecule spends in the excited state prior to return to the ground state.

The emission quantum yield (Φ) is the ratio between the number of photons the molecule emits and the number of photons absorbed. It is therefore a proportion of the rate of radiative decay to the overall decay from the lowest excited state (**Equation 1.4**):

$$\Phi = \frac{k_r}{k_r + k_{nr}} \quad (\mathbf{1.4})$$

The radiative (k_r) and non-radiative (k_{nr}) decay constants can then be described by **Equation 1.5** and **Equation 1.6**, respectively:

$$k_r = \frac{\Phi}{\tau} \quad (\mathbf{1.5})$$

$$k_{nr} = \frac{1 - \Phi}{\tau} \quad (\mathbf{1.6})$$

1.3.2 Selection Rules

The probability of an electron transition to occur is directed by selection rules, which are associated with electronic wavefunction symmetry, overlap and multiplicity of the ground and excited states. Based on these rules, a transition is considered allowed or forbidden.

Laporte selection rule

The Laporte selection rule is applied to centrosymmetric species and states that transition between states of the same parity (gerade, *g* or ungerade, *u*) are forbidden. However this selection rule can be relaxed by a "vibronic coupling" process, which removes the centre of inversion of the molecule by asymmetric vibrations of the latter. As consequence, forbidden transitions can be observed, for example *d*-*d* transitions in octahedral metal complexes.

Spin conservation rule

The spin conservation rule states that transitions including a change in spin multiplicity (S) are forbidden. Therefore a singlet (S = 0) to singlet transition is allowed ($\Delta S = 0$), whereas a singlet cannot undergo transition to a triplet (S = 1) state. Once again, the rule can be relaxed if the molecule contains a heavy atom. Metal complexes possess a strong spin-orbit coupling, which favours the mixing of states with different multiplicity and increases the probability of transitions that would be otherwise forbidden.

1.3.3 Electronic Structure and Transitions

The photophysical properties of a molecule can be determined by examining its electronic structure. A simplified molecular orbital diagram for a low spin d^6 octahedral complex is depicted in **Figure 1.5**, showing some of the possible electronic transitions.

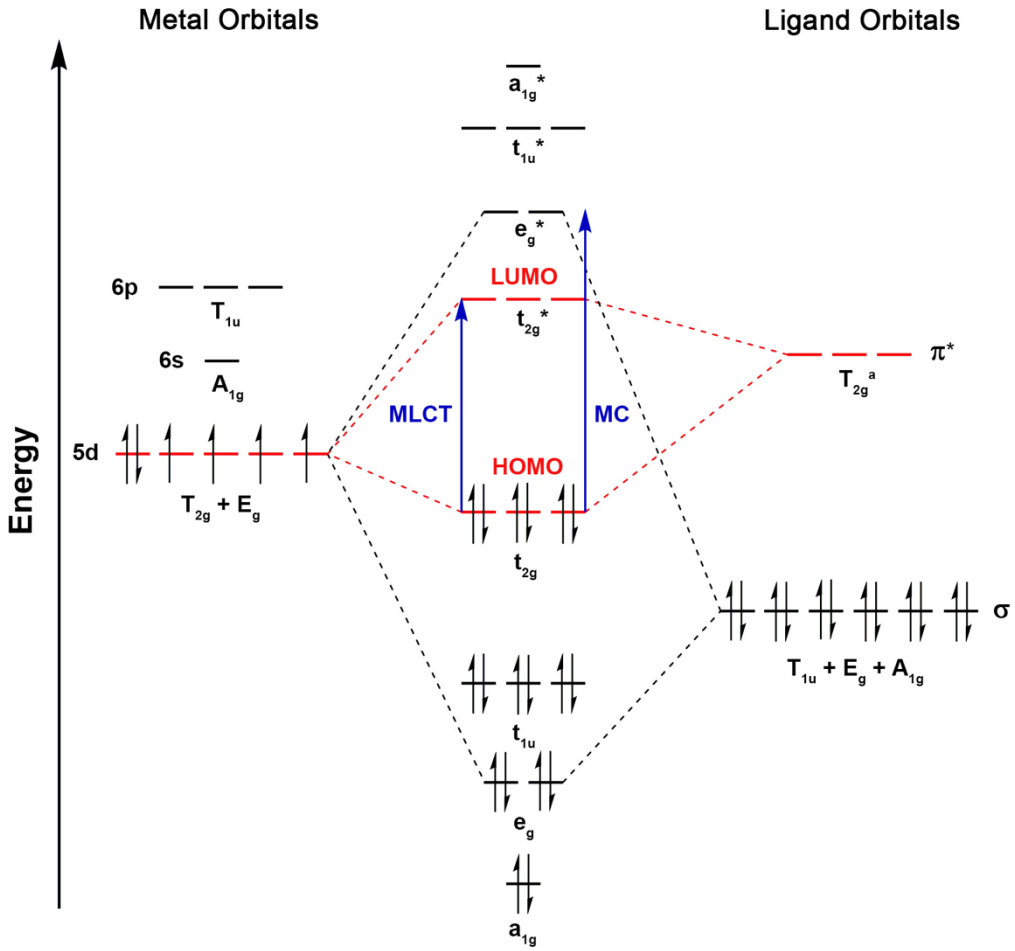

Figure 1.5 Simplified molecular orbital diagram for a low spin d^6 metal complex coordinated to 6 equivalent π-accepting ligands. This case represents a situation in which the metal centre is a second or third row transition metal and the surrounding ligands have low lying π* orbitals. The formation of t_{2g} (HOMO) and t_{2g}^* (LUMO) has been highlighted in red. MLCT and MC transitions are noted in blue. [a]Only the T_{2g} combination is considered for simplicity.

The molecular orbital diagram depicted in **Figure 1.5** is representative of complexes containing second or third row transition metal surrounded by π-accepting ligands, which cause a strong crystal field. For simplicity, in the construction of the diagram all of the ligands are assumed to be equivalent.

If the complex can be approximated to an octahedral symmetry, the metal centre can contribute to the formation of bonds with the *5d*, *6s* and *6p* orbitals. These orbitals are classified according to their symmetry in the octahedral point group. The *5d* orbitals are represented by symmetry labels T_{2g} and E_g, the *6s* orbitals is represented as A_{1g}, whereas the *6p* is represented as T_{1u}, as reported in **Figure 1.5**. For further simplify the diagram, only the π^* ligand orbitals of T_{2g} symmetry are showed to form molecular orbitals with the metal. The stability of low spin d^6 metal complexes is highlighted in **Figure 1.5** by the presence of totally filled bonding orbitals (a_{1g}, e_g, t_{1u} and t_{2g}) and empty anti-bonding orbitals (a_{1g}^*, e_g^*, t_{1u}^* and t_{2g}^*). Due to the strong crystal field of the ligands, which increase the metal-ligand interaction, the e_g^* is positioned at higher energy than t_{2g}^*. The higher energy of e_g^* is required for a metal complex to avoid the non-radiative decay pathways from a dark metal-centre state and thus guarantee a good emission intensity. The highest occupied molecular orbital (HOMO) and the lowest unoccupied molecular orbital (LUMO) corresponds to t_{2g} and t_{2g}^*, respectively, and the relative position of t_{2g} is determined by the presence and specific energies of the π^* orbitals of the ligands.

The absorption of a photon can induce different types of transitions for a metal complex, depending on the arrangement of electrons in the involved molecular orbitals. Some of the more common transitions for an octahedral metal complex have been highlighted in the simplified Jablonski diagram in **Figure 1.6**.

The transition of an electron from the predominantly metal-based t_{2g} (HOMO) to the predominantly ligand-based t_{2g}^* (LUMO) is known as metal-to-ligand charge transfer (MLCT). As mentioned above, in order to maximise the emission intensity of a metal complex, the MLCT and the dark MC state must possess sufficiently different energies, to avoid the thermal population of the latter.

The promotion of an electron from the t_{2g} orbitals to the empty antibonding e_g^* orbitals is defined as metal-centred (MC) transition. Due to the large ligand field splitting in octahedral metal complexes, the MC state usually lies at high energies and does not affect their emission properties.

Another possible transition occurs on the ligands themselves, and is known as ligand-centred (LC), intra-ligand (IL) or π-π^* transition. In this case, an electron is transferred from the occupied π orbitals to the empty π^* orbitals on the same ligand. Finally, if the coordinated ligands are not all equivalent, a transition of an electron from the π orbitals of a ligand to the empty π^* orbitals of a different ligand can occur. This transition is called ligand-to-ligand charge transfer (LLCT), and it is not illustrate in **Figure 1.6**.

In an illustrated representation, as showed in **Figure 1.6**, the absorption of a photon can excite the metal complex to the ^{1}MLCT, ^{1}LC or ^{1}MC, depending of its energy.[72,73] The complex can undergo vibrational relaxation (VR) and internal conversion (IC) to the lowest excited state ^{1}MLCT, in concordance with Kasha's rule.[73] Due to the heavy atom effect, intersystem crossing (ISC) can occur between states of different multiplicity, allowing the transfer of the complex from ^{1}MLCT to ^{3}MLCT. The complex then decay to the ground state ^{1}GS through radiative (k_r) or non-radiative decays (k_{nr}).

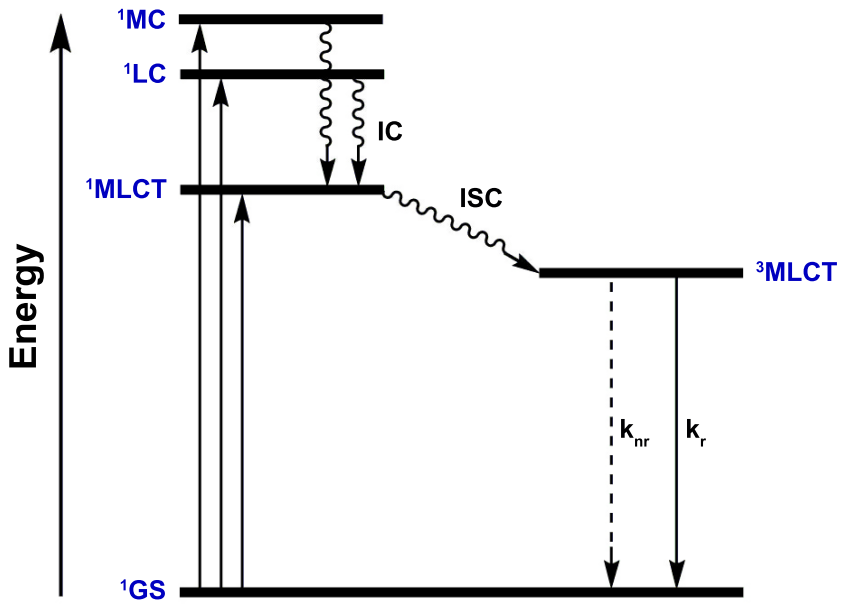

Figure 1.6 Simplified Jablonski diagram for an octahedral d^6 metal complex with lowest MLCT excited state. The radiative (k_r) and non-radiative (k_{nr}) rate constants have been reported. VR and the LLCT excited state are omitted for simplicity.

1.4 Properties and Requirements for Optical Imaging Metal Probes

1.4.1 Stokes Shift

The transition metal complexes listed in section 1.2.2 are triplet state emitters, which makes them phosphorescent, given that their ground state is of singlet spin multiplicity.[77,78] The energy stabilisation on passing from a singlet to a triplet excited state, promoted by the strong spin-orbit coupling of the metal centre, ensures that the Stokes shift is much larger compared to fluorescent molecules. This larger shift results in a lack of overlap between the absorption and emission profiles, therefore limiting the extent of concentration quenching.[79,80]

1.4.2 Excited State Lifetime

As the radiative decay of transition metal complexes is forbidden by the spin selection rule, given the fact that there is a change in spin multiplicity on decaying from a triplet excited state to a singlet ground state, the characteristic excited state lifetime of these species is typically longer compared to organic fluorophores.[81,82] Transition metal complexes usually decay within a time range between hundreds of nanoseconds up to microseconds, whereas spin-allowed fluorescence from organic species typically occurs within few nanoseconds. A long excited state lifetime can be exploited to significantly reduce unwanted background autofluorescence using time-gated detection associated with microscopy techniques (**Figure 1.7**).[83,84] In fact, a time delay of few hundreds of nanoseconds would ensure that the luminescence signal coming from the cells is exclusively belonging to the metal probe, because autofluorescence processes are already fully completed. This aspect is especially useful when the excitation and emission profiles of the probe overlap with those of endogenous fluorescent species.

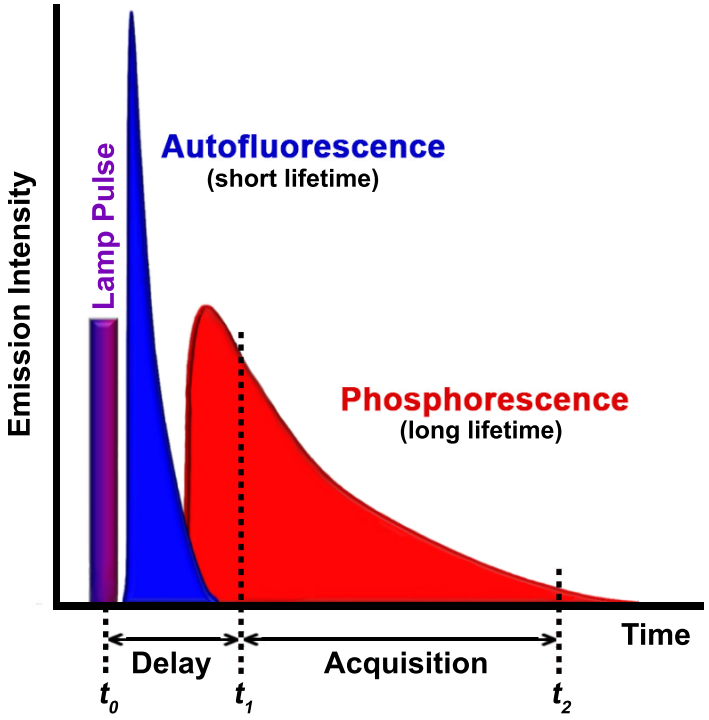

Figure 1.7 Diagram illustrating the lifetime of endogenous species (blue) in comparison to the lifetime of phosphorescent metal probes (red) during time-gated detection associated with macroscopy techniques. Adapted from ref[85].

1.4.3 Kinetic Inertness and Photostability

Depending on the specific chemical nature of the coordinated ligands, metal complexes of ruthenium(II), rhenium(I), iridium(III), gold(I) and platinum(II) can be kinetically inert, which favours lack of reactivity through ligand exchange that can potentially lead to cytotoxicity. These design factors can also indeed aid in reducing photobleaching, thus making metal complexes viable molecular probes for longer timescale imaging with live cells without significant loss of photoluminescence.[65,82,85,86]

1.4.4 Lipophilicity and Solubility

Lipophilicity is a physicochemical property of principal importance in drug discovery and development. In fact, the affinity for a lipophilic environment facilitates the transport of chemicals through membranes in a biological system and the formation of bonds between the studied probe or drug and the receptor binding site.[87] On the other

hand, high values of lipophilicity can affect negatively the solubility of the probe in aqueous environment, specifically the cellular medium employed in the analysis. Hence a good balance between solubility and lipophilicity must be carefully considered during the molecular design of a probe.[82]

1.4.5 Tissue Penetration

Near-infrared (NIR) light (*ca.* 700 – 2500 nm) can penetrate biological tissues more efficiently than visible light, due to the reduction of scattering and absorption by biological moieties at longer wavelengths.[88] The use of UV radiation should be also avoided due to the damage caused to live tissues.[89] Optimal excitation of the applied dye at different depths is therefore one of the requirements for the application of the probe in biological imaging. Three optical windows have been discovered to maximise the efficient excitation and detection of probes. The first and more conventionally used optical window is comprised between 650 and 950 nm (**Figure 1.8**),[90] but the penetration depth is still limited to 1 – 2 cm due to substantial background noise caused by autofluorescence. This signal-to-noise ratio can be highly improved in the second (1100 – 1350 nm) and third (1600 – 1870 nm) optical window (**Figure 1.8**),[88,91] however the use of these regions is limited by the lack of compatible probes.

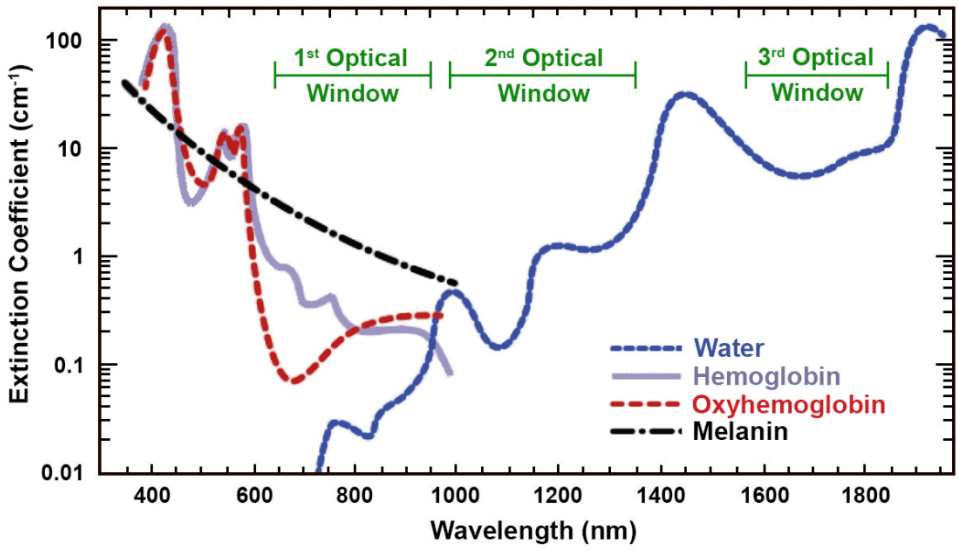

Figure 1.8 Graph illustrating the three optical windows. Adapted from ref[30].

1.4.6 Singlet Oxygen Production

While phosphorescent transition metal complexes certainly possess advantageous photophysical properties, it is essential to consider their ability to sensitise singlet oxygen. [92–94] Molecular oxygen has two low-lying singlet excited states ($^1\Delta_g$ and $^1\sum_g^+$) and a triplet ground state configuration ($^3\sum_g^-$).[95] Due to his small size, O_2 can easily diffuse in the cellular environment and quenched the long-lived triplet excited states of the metal complexes through intermolecular interactions.[93] The energy transfer (ET) between the triplet excited states of the metal complex and the triplet ground state of the molecular oxygen is spin-allowed, and therefore it occurs more rapidly than the radiative decay to the ground state of the metal (**Figure 1.9**). Interestingly, the emission of molecular oxygen from $^1\Delta_g$ can be easily detected in the NIR at around 1270 nm.[96]

Production of singlet oxygen within live cells can lead to extensive photocytotoxicity, even in cases when the metal complex is non cytotoxic when incubated within live cells that are kept in the dark. However, this very characteristic has sparked the investigation of many metal complexes from cellular markers to phototherapeutic agents in the field of photodynamic therapy (PDT).[97–101]

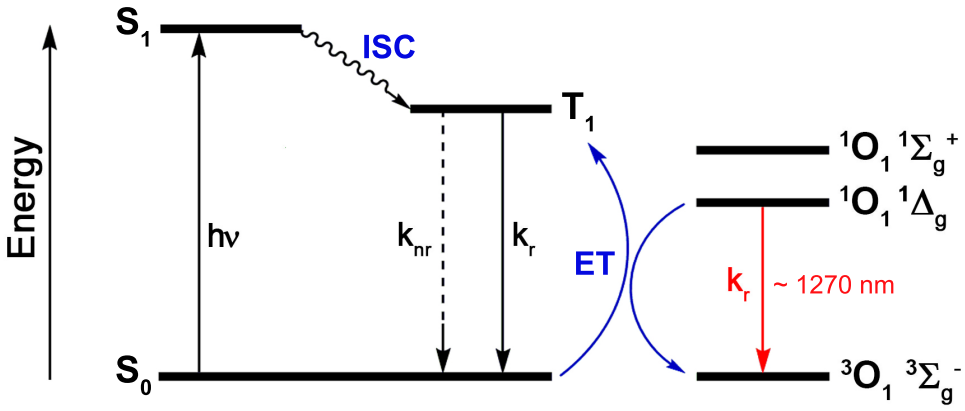

Figure 1.9 Simplified Jablonski diagram illustrating the generation of singlet oxygen by metal complexes.

1.5 Iridium(III) Complexes

Amongst the various metal complexes, cyclometalated iridium(III) species have received extensive investigation for applications in life science.[102–108]

Typically, these complexes comprise an iridium(III) centre bound to two cyclometalated ligands such as phenylpyridine (**ppy**), and one bidentate ligand such as a diimine (although it is not uncommon to find two monodentate ligands).

The chemical nature of this family of complexes can be readily tuned by chemical variations of the coordinated ligands, thus allowing tuning of properties such as charge, lipophilicity, and solubility, as well as photoluminescent characteristics. In fact, it is known that iridium complexes can be tuned to be emissive across the entire range of the visible spectrum, from blue to red, and further in the near-infrared region. Given this versatility, it is not surprising that a large number of iridium complexes have been investigated for their potential application as cellular markers and therapeutic agents.

A broad overview of the use of iridium complexes in life science has been reported.[1] Particular importance has been given not only to the specific chemical nature of the investigated cyclometalated iridium(III) complexes, but also to the various experimental conditions that have been used by the different research groups, all of which are summarised in **Table 1.1**.

In structuring this section, the complexes have been grouped according to their specific localisation, including cytoplasm, nucleus, lysosomes, endosomes, mitochondria, endoplasmic reticulum and Golgi apparatus.

Table 1.1 Summary of data and conditions for the cyclometalated iridium(III) complexes presented in this section.

Organelle	Probe	Charge	Application	Cell lines[a]	Lipophilicity	Incubation time[c,d,e]	Concentration	Viability dark	Phototoxic index	IC_{50}	Uptake mechanism (method of detection)	Ref.
CYTOPLASM	**10 – 11**	Cationic	Bioimaging	HeLa MCF-7 HCT-8	-	24 h	100 μM	>90%	-	-	- (Fluorescent intensity)	[109]
	12 – 15	Cationic	Bioimaging	HeLa MCF-7 HCT-8	-	24 h	100 μM	>90%	-	-	- (Fluorescent intensity)	[102]
	16	Neutral	Ratiometric probe	HeLa KB	-	24 h	100 μM	>90%	-	-	- (Fluorescent intensity)	[110]
	17	Neutral	Photo-switchable probe	KB	-	24 h	20 μM	>80%	-	-	- (Fluorescent intensity)	[111]
	18	Neutral	Bioimaging	KB	-	8 mins[d]	2 mg/mL[d]	-	-	-	- (Fluorescent intensity)	[112]
	19a - c **20a - b**	Neutral Cationic	Bioimaging	HeLa A549	1.28 - 1.57 0.56 - 0.89	24 h	20 μM[f]	-	-	73 - 200 50 - 120	Energy-dependent (flow cytometry)	[113]
	21	Cationic	Ratiometric	HeLa	-	48 h	600 mg/mL	>75%	-	-	Endocytosis (Fluorescent intensity)	[114]
	22 - 24	Cationic	Bioorthogonal probes	CHO-K1	-	1 h	5 μM[f]	-	-	50 - 100	- (ICP-MS)	[115]

NUCLEUS/ NUCLEOLUS	**25 - 27 (a - b)**	Cationic	Bioimaging	HeLa MDCK (live/ fixed)	0.90 – 3.95	48 h	5 μM[f]	-	-	1 - 25	- (Fluorescent intensity)	[116]
	28	Cationic	Bioimaging	HeLa KB FLS	-0.12	48 h	100 μM	>90%	-	-	Energy-dependent (ICP-AEC)	[117]
	29a - g	Cationic	Bioimaging	HeLa LO2	-0.09 - 2.12	24 h	20 μM	>90%	-	-	Energy-dependent (ICP-AEC)	[118]
	30 - 32	Cationic	Bioimaging	HeLa (fixed) MCF-7 (fixed)	-	24 h	10 – 20 μM[f]	-	-	25 – 56	- (Fluorescent intensity)	[118, 119]
LYSOSOMES/ENDOSOMES	**33** **34**	Neutral Cationic	Bioimaging	CHO	-	24 h	200 μM	-	-	>200	Energy-dependent (Flow cytometry)	[104]
	35a - i	Neutral	Bioimaging	4T1	-8.12 - 3.18[b]	1 h	0.1 μM	39 - 71%	-	-	- (Flow cytometry)	[121]
	36 - 39	Cationic	PDT agents	A549 LO2	1.97 – 2.12	15 mins (425 nm)[e]	20 μM[f]	-	25 - >833 3 - 23	-	Energy-dependent (Flow cytometry)	[105]
	40	Neutral	PDT agent	HeLA-S3	-	90 mins (377 nm)[e]	10 μM	-	10 - 30%[g]	-	Passive transport (ICP-AEC)	[122]
	41	Neutral	Bioimaging	HeLa	-	48 h	10 μM	>95%	-	-	Energy-independent (Fluorescent intensity)	[123]

	42	Cationic	Bioimaging	HeLa HEK293T	- 0.77	48 h	0.5 μM[f]	-	-	0.39 0.12	Energy – dependent (ICP-MS)	[124]
	43	Cationic	PDT agent	HeLa	0.62	1 h (365 nm)[e]	50 μM[f]	-	11.6	>200	Energy – dependent (ICP-MS)	[125]
MITOCHONDRIA	**44**	Neutral	Bioimaging	3T3 (live/fixed) HeLa RPE	-	12 h	10 μM	60%	-	-	Energy-dependent (Fluorescent intensity)	[126]
	45 – 46 (a – d) 47c	Cationic	Bioimaging	HeLa MCF-7	1.40 – 2.48	48 h	50 μM	-	-	1.4 - 3.8	Endocytosis (ICP-MS)	[127]
	48 - 49	Cationic	Bioorthogonal probes	CHO	5.69 – 7.14	6 h	50 μM	76 - 85%	-	-	Passive diffusion (Fluorescent intensity)	[128]
	50	Neutral	PDT agent	HeLa-S3	-	10 mins (465 nm)[e]	10 μM	-	>55%[g]	-	Passive transport (ICP-AEC)	[129]
	51 – 54	Cationic	Ratiometric probe	A549	-	12 h	10 μM	>80%	-	-	- (ICP-MS)	[130]
	55a - c	Cationic	PDT agents	HeLa	-	5 mins (365 nm)[e]	5 μM	-	3.6 – 9.2	-	- (ICP-MS)	[131]
	56a - e	Cationic	Bioimaging	HeLa	-	12 h	0.5 μM	>85%	-	-	Energy-dependent (ICP-MS)	[103]
	57 – 59	Cationic	PDT agents	HeLa LO2	0.77 – 1.42	- (405 nm)[e]	0.5 μM[f]	-	6.5 - 75 4.5 - 14	-	Endocytosis (ICP-MS)	[132]

	60a - c	Cationic	Bioimaging	HeLa	0.9 – 1.5	6 h	5 μM	-	>80%[g]	-	Energy-dependent (ICP-MS)	[133]
	61 – 62	Neutral	Bioimaging	HOS (live/fixed)	-	24 h	5 μM	>80%	-	-	- (Fluorescent intensity)	[134]
	63 – 64	Cationic	Anticancer agents	HeLa A549 (live/fixed) MDB-MA-231 PC3 LO2	0.23 – 2.12	48 h	10 μM[f]	-	-	0.5 - 10 0.2 - 24 0.3 - 28 1.0 - >100 1.5 - 27	Energy-dependent (ICP-MS)	[135]
	65 – 66	Cationic	Bioimaging	HeLa	-	24 h	20 μM	>70%	-	-	Energy-dependent (ICP-MS)	[32]
	67	Cationic	Anticancer agents	HeLa HepG2 BEL-7402 A549 LO2	-	48 h	0.5 μM[f]	-	-	0.5 1.1 1.5 0.8 2.6	Energy-dependent (ICP-MS)	[136]
	68	Cationic	PDT agent	HeLa	- 0.73	30 mins (365 nm)[e]	300 μM	-	>55.6	>300	- (ICP-MS)	[125]
	69	Cationic	PDT agent	HeLa	1.10	1 h (365 nm)[e]	10 μM[f]	-	17.2	8.6	Energy-dependent (ICP-MS)	[137]
ER/GOLGI APPARATUS	**70a - c** **71a - c**	Cationic Cationic	Bioimaging	HeLa	1.30 – 3.40	48 h	5 μM[f]	-	-	1.1 - 6.3	Endocytosis (Flow cytometry)	[138]
	72 - 74	Cationic	Bioimaging	HeLa	-	48 h	5 μM[f]	-	-	1.0 - 4.2	- (Fluorescent intensity)	[139]

	75	Cationic	Anticancer agent	HeLa A549 MCF-7	2.12	24 h	10 μM[f]	-	-	3.3 2.0 3.2	- (Fluorescent intensity)	[140]
	76	Neutral	Ratiometric	KB	-	24 h	200 μM	>98%	-	-	- (Fluorescent intensity)	[141]
	77 - 78	Cationic	Bioimaging	HeLa (live/fixed)	1.66 – 2.61	48 h	2 μM[f]	-	-	1.4 – 2.1	Energy – dependent (endocytosis) (ICP-MS)	[142]
	79	Cationic	Bioorthogonal probe	CHO-K1	-	20 h	20 μM	>80%	-	-	- (ICP-MS)	[143]
	80 - 81	Cationic	PDT agents	MCF-7 SKOV-3	-	10 sec[e]	2 μM	-	5.7 - 5.9 2.5 - 5.6	-	- (Fluorescent intensity)	[144]
	82	Cationic	Bioimaging	HeLa	-	48 h	10 μM[f]	-	-	565.9	- (ICP-MS)	[145]

[a] Incubated within live cell lines, unless otherwise stated.

[b] Theoretically calculated copying the ChemDraw structures into the structure builder on the web site http://intro.bio.umb.edu/111112/OLLM/111F98/newclogp.html.

[c] Incubation time and concentration are referred to the conditions of the cytotoxicity analysis.

[d] Incubation time and concentration are referred to the investigation by confocal luminescence microscopy.

[e] Irradiation time; in parenthesis the excitation wavelength is reported when available.

[f] Concentration is referred to the conditions of the internalisation analysis.

[g] Only the cytotoxicity upon exposure to light was index.

1.5.1 Cytoplasm Staining

The cytoplasm is the diffuse area enclosed between the cellular membrane and the nucleus. The cytoplasm hosts organelles and macromolecules, and many metabolic processes occur within this space, such glycolysis and protein folding.[146] The transport of materials between organelles also occurs in the cytoplasm, due to a process called cytoplasmic streaming.[147,148] The various interactions between organelles and biomolecules are highly regulated, and therefore imaging of the cytoplasm parameters and functions is a key component in life science.[146]

A library of photoactive iridium complexes displaying cytoplasmic localisation is shown in **Figure 1.10**. The majority of complexes are cationic, and only a small number of neutral iridium(III) complexes have reported showing accumulation within the cytoplasm. As a general trend, the cytotoxicity of these probes is quite low. On comparing analogous neutral and cationic complexes, the neutral complexes show lower cytotoxicity than their corresponding cationic analogues, albeit in only one illustrated study.

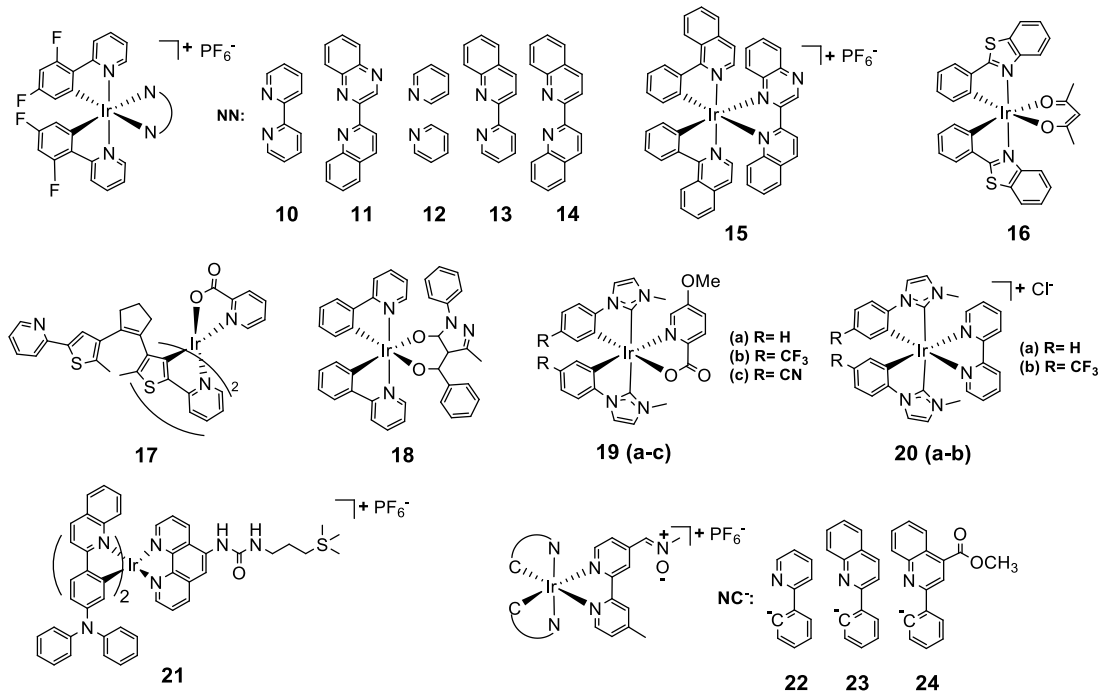

Figure 1.10 Examples of iridium(III) complexes with cytoplasmic localisation.

The first examples of cyclometalated iridium(III) probes for the staining of the cytoplasm in living cells were reported by Li in 2008.[109] Complexes **10** and **11** present the same fluorinated phenylpyridine moiety (**F_2ppy**) and different diimine ligands. The positive charge and the fluorination of the cyclometalated ligands, influencing the lipophilicity and aqueous solubility of the complexes, were argued to be the main factor for the internalisation of these probes within the cells. Confocal images of live HeLa cells incubated with **10** and **11** in DMSO/PBS (1 : 49 v/v), at a concentration of 20 μM and for an incubation time of 10 minutes, show intense intracellular luminescence with high signal-to-noise ratio between the cytoplasm (I_c) and the background (I_b), with $I_c/I_b \geq 50$. Moreover, the effect of the two complexes on the proliferation of MCF-7 and HCT-8 cell lines was determined by MTS assay over a period of 24 hour incubation, showing a cellular viability greater than 90% at the highest tested concentration (100 μM).

Few years later, the same group expanded on the previously presented work by preparing the cationic iridium(III) complexes **12**, **13**, and **14**, whose structures are analogous to those of **10** and **11**.[102] The group also reported complex **15**, where the two cyclometalated ligands are replaced by 2-phenylisoquinoline ligands and the diimine ligand is the neutral 2-(2-quinolyl)quinoxaline.[149] The new complexes **12-15** show similar biological properties in comparison to **10** and **11**, albeit different photophysical behaviour, as it might be expected by the variation of the π conjugation within the various ligands. Significant emission colour tuning from blue to deep red was obtained (λ_{emi} from 457 to 632 nm) due to the modification of the ancillary diimine ligands (**12-14**), which was attributed to the corresponding energy variations of the ^{3}MLCT [$d\pi(Ir) \rightarrow \pi^*_{diimine}$] and ^{3}LLCT [$\pi_{C\wedge N} \rightarrow \pi^*_{diimine}$] excited states. An increase in the conjugation of both cyclometalated and ancillary ligands further red-shifts the emission wavelength of **15** into the near-infrared region (λ_{emi} = 732 nm).[149] Emission in the near-infrared region is particularly appealing to biological imaging as it facilitates signal discrimination from autofluorescence, reduces scattering, and allows for deeper tissue penetration of biological samples.[34,150] Like the analogous complexes **10** and **11**, complexes **12-15** display predominant localisation within the cytoplasm. Consistently within the small library of iridium(III) complexes, for cells incubated with complexes **12-15**, the cellular viability after 24 hours incubation time at a relatively high concentration (100 μM) was again *ca.* 90%.

Complex **16** is the first example of neutral iridium(III) complex proposed for cellular imaging, which was reported by Zhao and Li. In this complex the two cyclometalated ligands are 2-phenylbenzothiazole and the remaining ligand is the bidentate anionic O-donor acetylacetonate.[110] The complex was proposed as a ratiometric luminescent sensor for the quantitation of cytoplasmic Hg(II) cations. In cuvette and upon addition of 1 equivalent of Hg(II), an acetonitrile solution of complex **16** shows a blue shift of *ca*. 40 nm that is evident in both the lowest energy absorption band and emission profile. The authors also illustrated how the shift is not affected by pH variations, within the range 2-12. When incubated within live HeLa and KB cells, complex **16** shows low cytotoxicity with values of viability ≥ 90% using 100 μM of **16** for 24 hours. The applicability of **16** in the ratiometric monitoring of intracellular Hg(II) was investigated by confocal microscopy using two optical windows: the green channel in the 515 ± 15 nm range, and the yellow channel in the 570 ± 10 nm range. KB cells were incubated with 10 μM of the complex **16** and 10 μM of Hg(II) for timeframes of 15 minutes, 1 hour and 8 hours. As it can be seen in **Figure 1.11**, the ratio between the emission intensity at 515 and 570 nm (I_{515nm}/I_{570nm}) is negligible (*ca.* 0.1) when KB cells are stained with only complex **16**. Upon addition of Hg(II), I_{515nm}/I_{570nm} increased up to 0.6, confirming the ratiometric behaviour of complex **16**.

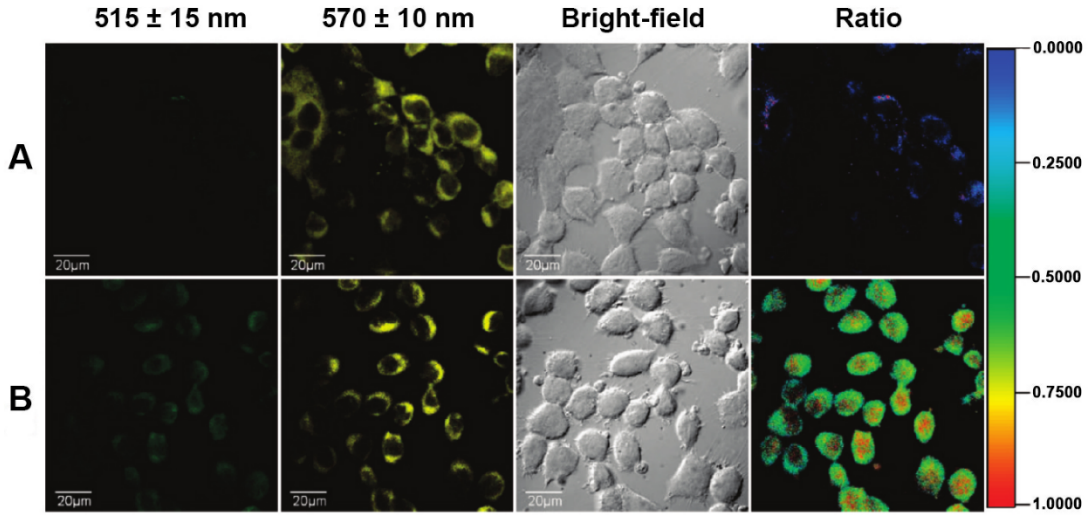

Figure 1.11 Ratiometric phosphorescent images of **16** incubated in KB cells at concentration of 10 μM for 15 minutes. (A) KB cells qstained with **16**. (B) KB cells incubated with **16** and then treated with 100 μM of Hg(II) for 1 hour. Reproduced with permission from ref[110].

The neutral iridium(III) complex **17** was reported by Yi and Tian.[111] The complex was designed to improve the water solubility of a previously published analogue, by replacing the acetylacetonato ligand with deprotonated 2-picolinic acid.[35] The MTT assay shows a cell viability greater than 80% with a concentration of 20 μM and 24 hour incubation time. By exploiting the reversible photoinduced ring opening/closing transformation of the diarylethene unit,[151] the complex was proposed as a photoswitchable probe for live cell imaging triggered by visible light. Upon excitation at 488 nm of a diluted tetrahydrofuran solution containing complex **17** with the ligands in their open form, a yellow/orange emission with λ_{emi} at 568 nm is detected. Upon continuous irradiation, the emission intensity of this band gradually decreases as the ligands undergo a photoinduced ring closing reaction, until no emission is detected. On the other hand, when the non-emissive closed form of complex **17** is continuously excited at wavelengths longer than 600 nm, the intensity of the emission band at 568 nm can be slowly recovered while the ligand reverses to its open form. Interestingly, a similar behaviour is detected from complex **17** when incubated within KB cells and irradiated with 458 nm of light for 2 minutes. The emissive open form is quenched and then recovered to the original state upon irradiation over 60 minutes at 633 nm. Unfortunately, cellular damage is detected with these experimental conditions, limiting the exploitation of the photoswitching properties of this probe in live cells.

Zhao and Li reported the neutral iridium(III) complex **18**, showing enhanced phosphorescent emission in the solid state (EPESS).[112] This complex exhibits very weak luminescence (Φ = 0.04%) in diluted solution, but the gradual addition of water causes an increase of the luminescent intensity that is ascribed to aggregation by the authors. Density functional theory (DFT) calculations illustrate the existence of π-π interactions involving the cyclometalated ligands, in support of the EPESS mechanism of **18**. To explore the biological application of this EPESS-active complex, **18** was embedded in water-dispersible polymer nanoparticles with an average diameter of *ca.* 190 nm and incubated in KB cells. These embedded **18**-PNPs particles internalise in only 8 minutes within the cells and exclusively stain the cytoplasm. No cytotoxicity data were reported by the authors.

Other neutral iridium(III) complexes (**19a-c**) were presented by Zhou,[113] together with two charged biscarbene complexes (**20a-b**). In both the neutral and cationic series, the introduction of the electron-withdrawing substituents CN and CF_3

into the biscarbene ligand affects the emission maxima by inducing a hypsochromic shift in organic solvents, but an analogous clear trend was more difficult to elucidate from aqueous solutions. The authors showed that the lipophilicity value log$P_{o/w}$ is mainly influenced by the overall charge of the complex, and the exchange of CN for CF_3 is not greatly affecting the lipophilicity. The neutral complexes **19a-c** exhibit higher log$P_{o/w}$ values (1.28 - 1.57) in comparison to **20a-b** (0.56 - 0.89), a trend that is expected on passing from a neutral to a cationic complex. The MTT assay towards HeLa and A549 cell lines also proved the lower toxicity of neutral **19a-c** versus charged **20a-b**, with average IC_{50} values of *ca.* 165 μM and *ca.* 85 μM for the neutral and charged complexes, respectively. All the complexes display cytoplasmic localisation and the authors determined that cellular internalisation occurred through energy-dependent uptake.

The iridium(III) complex **21** was proposed by Zhao, Li and Huang for hypoxia bioimaging.[114] Hypoxia is one of the most important features of many diseases such as solid tumours, inflammatory diseases and cardiac ischemia.[152–154] Hence, the monitoring of the oxygen level within cells is essential for the advancement of associated diagnostic and therapeutic techniques. Complex **21** was covalently attached to mesoporous silica-coated and lanthanoid-doped core-shell nanoparticles (UCNPs@$mSiO_2$). The use of a nanoparticle carrier for complex **21** was proposed in order to increase aqueous solubility and stability, as well as to facilitate the use of a continuous wave near-infrared (NIR) laser at 980 nm with low excitation power density (*ca.* 10^2 W cm^{-2}).[150] The use of this excitation source was sought to minimise autofluorescence and cellular photodamage. The embedded nanoparticles **21**-UCNPs@$mSiO_2$ cannot be efficiently excited at 980 nm within cells. Nonetheless, upon conventional excitation at 405 nm, the probe shows responsiveness when incubated within cells with a gradient of O_2. Additionally, the cytotoxicity was tested and the viability of HeLa cells results higher than 75% after 48 hours at high concentration (600 mg/mL). The authors showed that **21**-UCNPs@$mSiO_2$ stains the diffuse cytoplasm and cell membrane through a nonspecific endocytotic uptake.

Three charged iridium(III)-based fluorogenic (turn-ON) bioorthogonal probes (**22-24**) were reported by Lo. All these complexes carry a nitrone functional group appended to the diimine ligand.[115] The nitrone unit can selectively and rapidly react with modified proteins which possess the specific alkyne reaction partner.[155] Furthermore, the incorporation of the nitrone group quenches the emission of the probe

due to the photoisomerisation of the C=N bond, which provides a non-radiative deactivation pathway.[156,157] After bioconjugation with the labelled proteins (*bovine serum albumin* BSA, *human serum albumin* HSA and *holo-transferrin* HTf), the complexes **22**-**24** show a remarkable enhancement of the emission intensity (I/I_0 = 92.1 - 795.1). The intracellular distribution of the bioconjugated complexes **22**-**24** in CHO-K1 cell line highlights a cytoplasmic localisation. Additionally, MTT assay showed that the probes are essentially non-cytotoxic toward the same cell line for an incubation period of 1 hour (IC_{50} > 50 μM).

1.5.2 Nucleus and Nucleolus Staining

The nucleus is a highly specialised organelle with two main functions: storing of the cellular hereditary material in the form of DNA and coordination of many processes such as growth, intermediary metabolism, protein synthesis and cell division.[158,159] The nucleus is surrounded by a double-membrane envelope that exhibits a two-way traffic to proteins and nucleic acid between nucleus and cytoplasm.[160] The most prominent membrane-less substructure within the nucleus is the nucleolus, which is the site of rRNA transcription and processing, and also of ribosome assembly.[161,162]

A library of iridium complexes that have been reported for the staining of the nucleus or the nucleolus is illustrated in **Figure 1.12**. Of note, all the complexes described are cationic and there is no neutral iridium complex proposed as a nuclear stain.

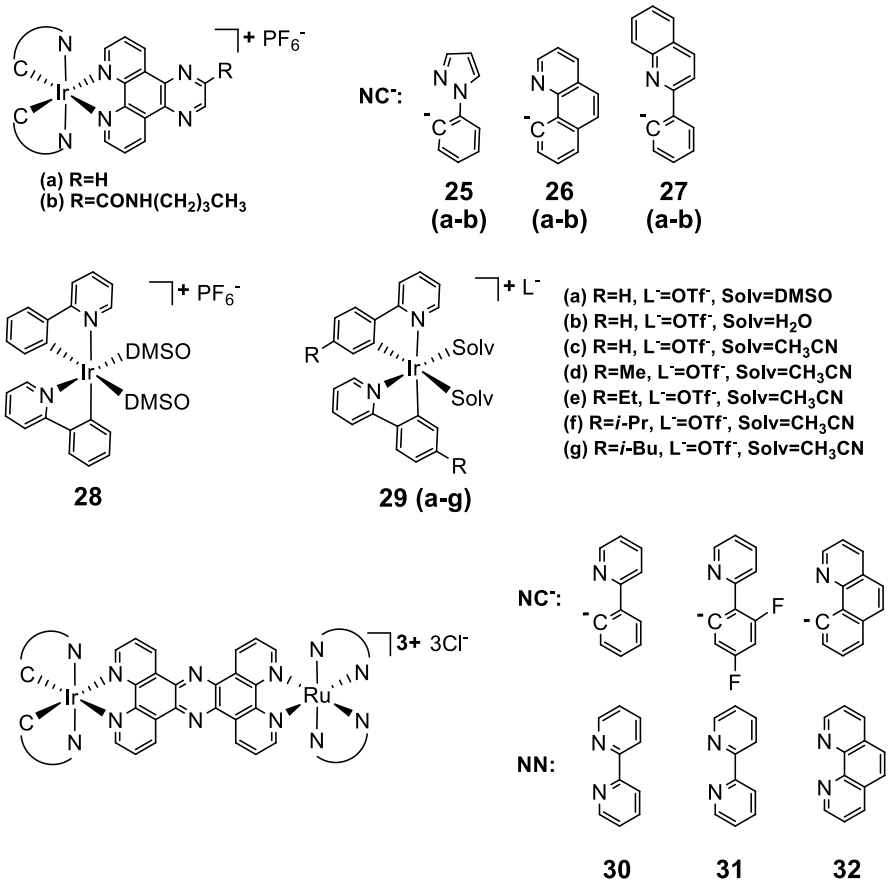

Figure 1.12 Examples of iridium(III) complexes with nuclear localisation.

One of the first examples of nucleolar staining in live cells was proposed by Lan and Lo, with a series of iridium(III) dipyridoquinoxaline complexes.[116] The modification of the chemical structure of the cyclometalated ligands (**25a**-**27a**) and the presence of a long chain on the dipyridoquinoxaline (**25b**-**27b**) modulates the lipophilicity and cytotoxicity of the complexes. Extending the conjugation of the ligands increases the value of $logP_{o/w}$ (**bzq**>**pq**>**ppy**)[138,142] and the addition of an alkyl chain on the two phenyl rings of the cyclometalated ligands also results in an increment of the lipophilicity, especially in the case of a *n*-butyl substituent. The IC_{50} values of all the complexes towards HeLa and MDCK cell lines are lower than that of cisplatin, indicating high cytotoxicity, especially for the more lipophilic **26a**-**26b** and **27a**-**27b**. Localisation studies within the MDCK cell line revealed accumulation in the nucleus after 90 minutes of incubation, followed by a more specific nucleolar uptake after 120 minutes. In particular, it was proven that the complexes bind to the hydrophobic pockets of proteins and intercalate with DNA.

The group of Li developed the non-emissive iridium(III) solvato complex **28**, bound to two molecules of DMSO in place of a diimine ligand. This complex can react selectively with free histidine and histidine-rich proteins with a 300-fold increase of its emission intensity in a fluorogenic turn-ON fashion.[117] The uptake in HeLa cell line of **28** (10 μM, 10 minute incubation time) reveals an exclusive staining of the nucleus, with an energy-dependent internalisation pathway. Moreover, the MTT assay toward HeLa, KB and FLS cell lines showed low toxicity for complex **28**, even after 48 hours, with values of viability greater than 90%.

Based on the previous results, the same research group synthesised a series of non-emissive iridium(III) complexes (**29a**-**g**) by varying the counter ions, the coordinated solvent and the substituent on the phenylpyridine ligands.[118] The structure-activity relationship studies showed how the nature of the counter ions and solvent ligands do not affect the behaviour of the probes within cells. On the other hand, the length of the appended carbon chain significantly influences the cellular uptake and accumulation in living cells, showing nuclei staining for the shorter chain **29d** and a diffused cytoplasmic accumulation for the longer **29f**-**g**.

Thomas and Smythe proposed two heterobimetallic iridium(III)-ruthenium(II) complexes **30**-**31** containing a tetrapyridophenazine unit as a bridging ligand.[119] The probes show good water-solubility, which is often the limiting factor of many cyclometalated systems.[163] Both complexes **30** and **31** display an unstructured red

emission (*ca*. 640 nm) and low quantum yield ($\Phi < 0.02\%$), which increases about 10 and 24 times upon addition of DNA, respectively (**Figure 1.13**). Interestingly, the binding affinity of **31** was lower than the non-fluorinated analogue **30**. This lower affinity for DNA was rationalised by the increased polarity of the probe. However, the increased lipophilicity of **31** enhances cellular uptake without loss of nuclear localisation (**Figure 1.13**). MTT assay demonstrated low cytotoxicity over a 24 hour incubation period for both **30** and **31** with IC_{50} values of 56 and 43 μM, respectively.

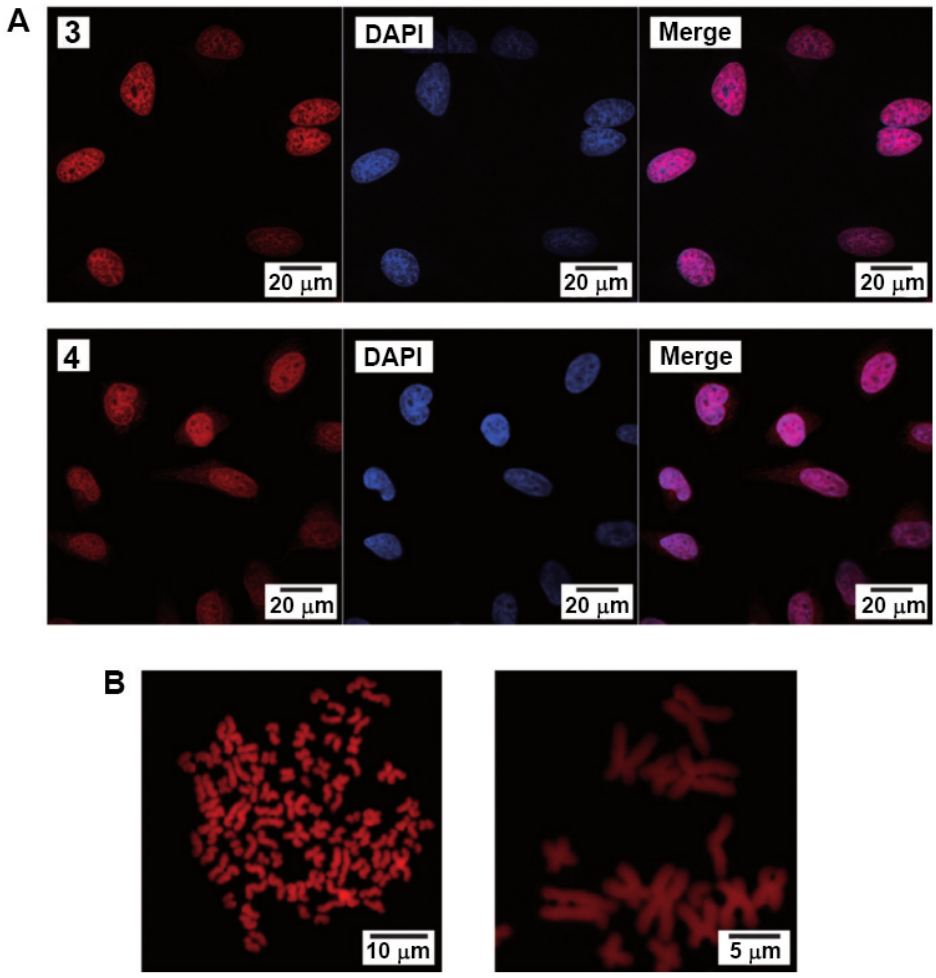

Figure 1.13 (A) Co-staining of **30** (3) and **31** (4) with the nuclear stain DAPI in fixed HeLa cells. (B) Isolated HeLa chromosomes stained with **30** (3). Reproduced with permission from ref[119].

The same authors reported complex **32**[120] as a more lipophilic analogue of the previously discussed complexes **30** and **31**. The authors could therefore compare the behaviour of these probes upon systematic increase in lipophilicity, providing evidence that increasing the lipophilic character can be counterproductive for the uptake and the specific localisation of the probe. In fact, the incubation of complex **32** in MCF-7 cells (10 μM, 24 hour incubation time) results in poor intracellular emission and lack of nuclear staining. Subsequent binding tests proved that complex **32** interacts more strongly with *bovine serum albumin* (BSA), which inhibits the targeted nuclear accumulation.

1.5.3 Lysosomal and Endosomal Staining

Lysosomes are acidic organelles containing a variety of hydrolytic enzymes capable of degrading biomacromolecules delivered by ways of phagocytosis, autophagy and endocytosis.[164,165] Moreover, lysosomes participate in various other cellular processes as cell migration, intracellular transport, plasma membrane repair, apoptosis and exosome release.[166–168] Lysosomal dysfunctions are associated with diverse neurodegenerative and muscular diseases, lysosomal storage disease and cancer.[169–171] In most eukaryotic cells the internalisation, recycling, transport and break down of cellular and extracellular components is mediated by the highly dynamic lysosome-endosome system.[172,173] The pH level in endosomes plays an important role during the endocytosis process, including the release of iron from transferrin, general cleavage of ligands from their receptor and, most importantly, the activation of lysosomal hydrolases.[174] As in the case of lysosomal dysfunctions, endosome regulation and development is altered in a surprising range of human disorders, including Alzheimer's disease, atherosclerosis and also lysosomal storage disease.[174,175] For these reasons, luminescent probes for the tracking of these organelles need to possess resistance to degradation, low toxicity, high photostability, great penetration depth, near-infrared or longer excitation wavelengths and, more importantly, long-term localisation.[29,176]

Examples of iridium(III) complexes reported for the staining of lysosomes and endosomes are shown in **Figure 1.14**. While both neutral and cationic complexes have been proposed for lysosomal and endosomal staining, the presence of protonatable basic substituent seems to be a common factor for this family of complexes. This is not surprising given the lower pH of the lysosomal and endosomal environment.

The group of Williams published the cyclometalated iridium(III) complex **33**, carrying a 2-pyridylbenzimidazole ligand, and its protonated analogue **34**.[104] Photophysical data in dichloromethane solution show a structured emission profile in the green region of the spectrum for **33**, and an expected red shift for **34**, with emission centred around 590 nm. Nevertheless, the emission profiles from CHO cells incubated with the probes at a concentration of 10 μM for 5 minutes are essentially identical. In fact, the protonation equilibrium between the two complexes is a function of the local pH, with **33** being the predominant form within the cellular environment, which is regulated at pH values around 7.4. A shift is observed in acidic lysosomes, as the

protonation equilibrium forms the cationic complex **34**. The MTT assay evidenced low cytotoxicity of these probes, with IC_{50} values > 200 μM (200 μM, 24 hour incubation) for both.

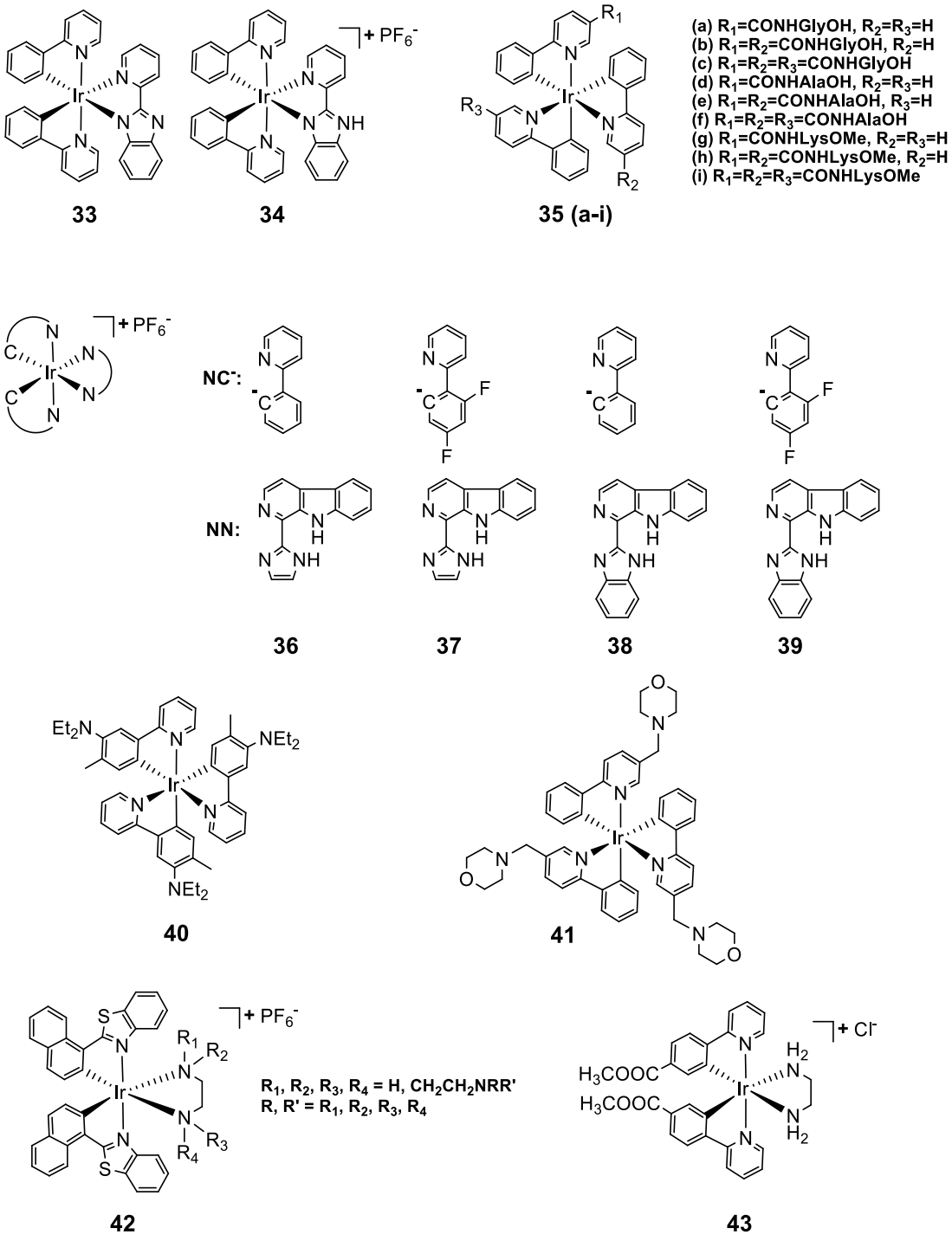

Figure 1.14 Examples of iridium complexes with lysosomal and endosomal localisation.

A family of nine neutral iridium(III) complexes (**35a-i**) was synthesised by Velders. The complexes are functionalised with a different number (mono-, di-, tri-) and type (glycine, alanine, lysine) of amino acids on the 2-phenylpyridine (**ppy**) ligands.[121] The monosubstituted complexes **35a**, **35d**, and **35g** show a remarkable 20-fold higher cellular uptake in 4T1 cells (10 μM, 1 hour incubation), a trend that was associated with the more lipophilic nature of the probes.[177] This result was supported by the authors with the determination of the theoretical lipophilicity (Clog*P*), which shows a distribution coefficient between 2.05 and 3.18, in comparison to the negative values of Clog*P* for the di- (**35b**, **35e** and **35h**) and tri-substituted (**35c**, **35f** and **35i**) complexes. Analysis by flow cytometry showed a substantial reduction of the cell viability for the lysine derivatives (**35a-c**), with higher toxicity for the more substituted complex **35c** (viability lower than 39%). The cellular distribution of complexes **35a-c** displays different localisation, depending of the number of lysine residues, with nuclear staining for mono-**35a**, endosomes staining for bis-**35b** and lysosome staining for tris-**35c**.

Four iridium(III) complexes with β-carboline ligands (**36-39**) were developed by Tan and Mao as pH-responsive tumour/lysosome-targeted photodynamic therapeutic (PDT) agents.[105] The pH-response can be achieved with the introduction of the protonation sites on the imidazole and benzimidazole groups.[178,179] On the other hand, the selectivity toward acidic environment can be enhanced by the presence of the β-carboline ligand.[180] The complexes show similar lipophilicity values (1.97 - 2.12), with a greater cellular penetration for the smaller imidazole-derivatives **36**-**37**. Upon irradiation, they show highly selective phototoxicity against A549 cancer cells. In particular, complex **37** displays a phototoxicity index greater than 833. Even if all the complexes localise within the lysosomes, **37** is the more promising to be used to track the lysosomal integrity during PDT, which provides a convenient method for *in situ* monitoring of therapeutic effects.

The group of Aoki developed a neutral iridium(III) probe **40** that can be used as luminescent pH-sensor and also as pH-dependent photosensitiser in live cells.[122] Photophysical analysis in degassed aqueous buffer has shown a blue-shifted emission maximum upon addition of 1 equivalent of acid, and an enhancement of the emission intensity induced by the second and third protonation of the diethylamino groups. As predicted, through a passive transport mechanism, complex **40** localises within the lysosomes of HeLa-S3 cells. Additionally, photoirradiation of **40** at 377 or 470 nm for

30 minutes induces necrosis-like death in HeLa-S3 cells, demonstrating the ability of the probe to generate $^1O_2$ in a pH-dependent manner.

An interesting neutral iridium(III) probe **41** for long-term lysosome tracking was designed by Chao.[123] The water-soluble triscyclometalated iridium(III) complex is functionalised by morpholine moieties, which can be protonated inside the lysosomes[181] and work as a "locker", allowing the accumulation of **41** in these acidic organelles (**Figure 1.15**). Additionally, the electron-rich morpholine quenches the iridium(III) phosphorescence by photoinduced electron transfer (PeT) in basic condition, but upon protonation this process is suppressed, leading to an enhancement of the emission intensity in acidic lysosomes. The uptake of complex **41** occurs through an energy-dependent pathway and the probe results non-toxic for HeLa cell lines (10 μM, 48 hour incubation). Moreover, **41** is able to track lysosomes for a period of 4 days, allowing imaging and observation of most physiological activities of the lysosomes.

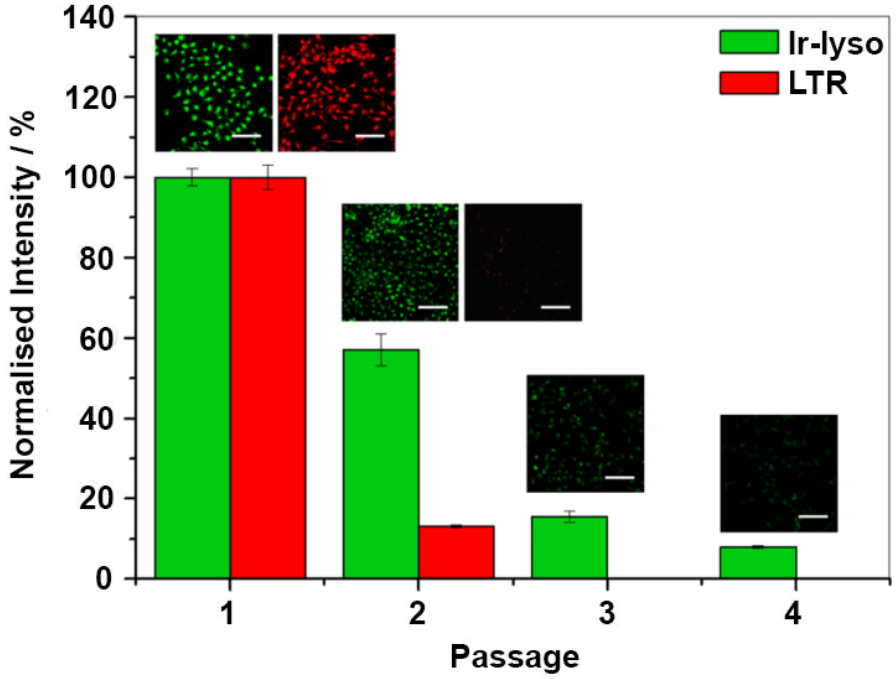

Figure 1.15 Normalised emission intensities and images of living HeLa cells stained with 2 μM of **41** (Ir-lyso) and 2 μM of LysoTracker Red DND-99 (LTR) at different passages. Scale bar = 100 μm. Reproduced with permission from ref[123].

A cyclometalated iridium(III) polyamine complex (**42**) was developed by Lo's group.[124] Poly(ethyleneimine) (PEI) ligands have been commonly used as DNA-condensing and gene-delivery vectors due to their highly positive charge density and high proton buffer capacity over a wide range of pH.[182–184] The PEI moiety plays a dominant role in the lipophilicity of **42**, which shows a negative value of -0.73, to benefits its water-solubility. Moreover, the presence of the polymer doubled the uptake of this probe in comparison to the non-polymeric analogue, also causing an increase of the cytotoxicity (IC_{50} = 0.39 and 3.2 μM). The higher IC_{50} value can be probably due to the disruption of the cytomembrane and the mitochondrial membranes of the cells, as previously shown in similar PEI derivatives.[185,186] Nevertheless, upon internalisation through an energy-requiring process, such as endocytosis, **42** accumulated in lysosomes (0.5 μM, 2 hours).

The same group reported an ethylenediamine iridium complex functionalised with polar ester substituents on the cyclometalated ligands (**43**)[125] in order to increase the specificity of the probe for *bovin serum albumin* (BSA). Unfortunately, protein-binding studies have highlighted minimum emission profile changes of **43** upon titration with BSA. However, **43** showed a marked cytotoxicity enhancement ($IC_{50\text{-dark}}$ > 200 μM, $IC_{50\text{-light}}$ = 17.3 μM) in HeLa cells upon irradiation at 365 nm for 1 hour, which allowed this probe to be eligible for PDT applications. After internalisation inside living cells through an energy-requiring mechanism, **43** accumulates in endosomes, as evidenced by colocalisation studies with Alexa Fluor 633-conjugated transferrin (Pearson's coefficient = 0.88).

1.5.4 Mitochondrial Staining

Mitochondria are rod-shaped organelles performing diverse functions, involving energy production via oxidative phosphorylation, calcium modulation, redox signalling, and apoptosis.[187,188] Furthermore, mitochondria are dynamic organelles that frequently change their number, size, shape and distribution within the cytoplasm in response to metabolic and environmental stress.[189] It is therefore not surprising that mitochondrial dysfunction has emerged as a key factor in a range of diseases, including metabolic disorders, cancer and neurodegenerative diseases, such as Alzheimer and Parkinson.[190]

Figure 1.16 illustrates various iridium(III) complexes reported to localise within the mitochondria. The majority of the complexes are positively charged, with very limited examples of neutral species developed for the staining of mitochondria. In general, the presence of a positive charge facilitates mitochondrial localisation as a result of the mitochondrial membrane electrical potential.

A charged iridium(III) complex carrying a phenanthroline ligand and functionalised with an isothiocyanate group (**44**) was developed to target specific mitochondrial proteins.[126] As a previous study showed,[139] the isothiocyanate unit allows the probe to covalently bind to amine-containing biomolecules such as lysine and the N-terminal of proteins, yielding luminescent bioconjugates. Interestingly, complex **44** accumulates only in the mitochondria of living 3T3, HeLa and RPE cells, while a diffuse staining is present with prefixed 3T3 cells, indicating that the process requires active cellular metabolism. The binding of complex **44** to mitochondrial proteins interferes with the function and the morphology of this organelle, as showed in the MTT assay. The viability of 3T3 cells decreases to 60% with concentration higher than 10 μM and an incubation time of 12 hours.

Another series of bioconjugated iridium(III) complexes was proposed by Lo.[127] In this case, the complexes are appended with a β-D-glucose (**45a-d**) or a D-galactose unit (**46a-d)** via a polyethylene glycol (PEG) linker to the diimine ligand, while the degree of π conjugation was varied on the cyclometalated ligands. The general idea is to increase the specific cellular uptake of these sugar-appended probes in cancer cells, which usually show an elevated expression of glucose transporters (GLUTs) and hexokinases to support higher metabolic functions.[191,192]

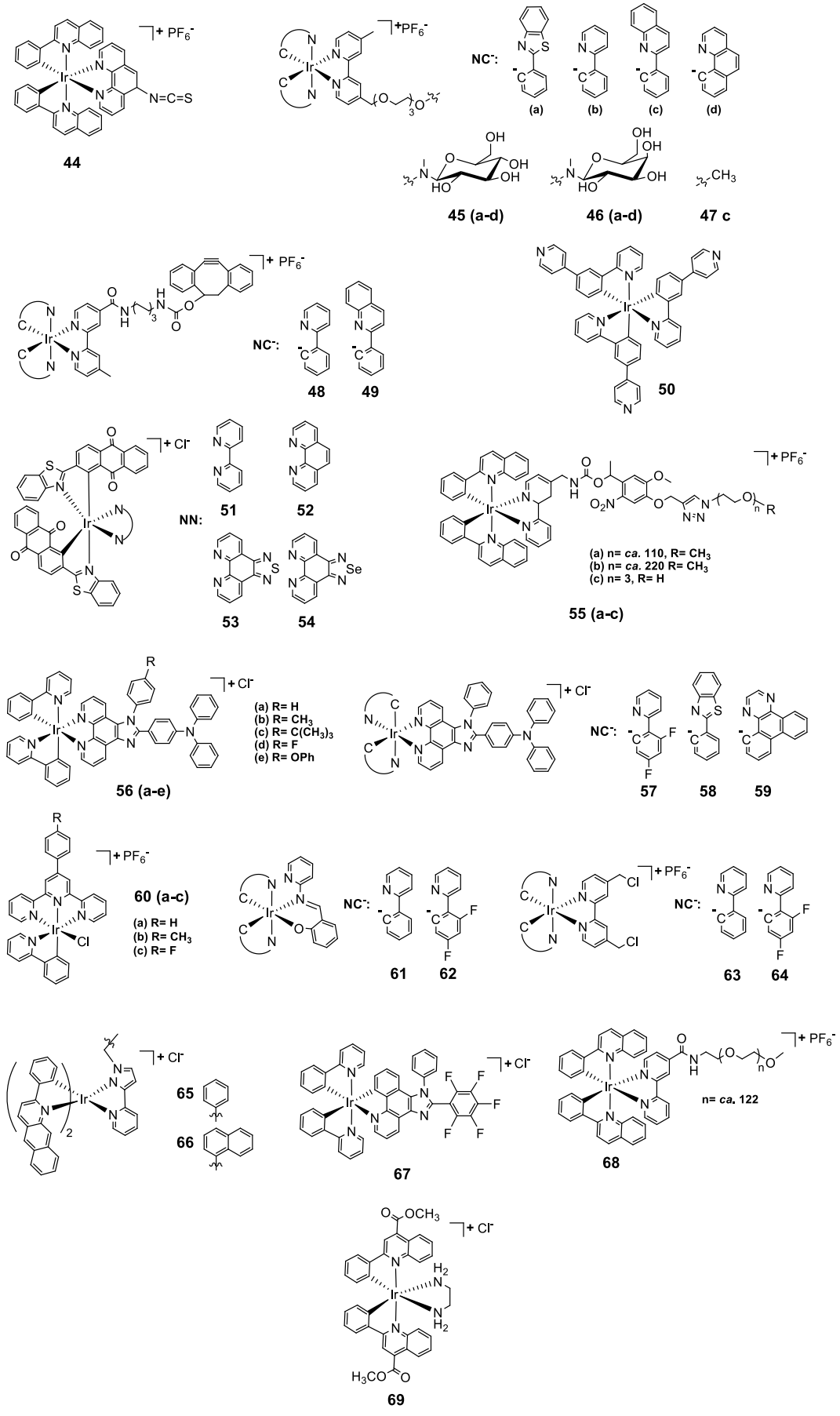

Figure 1.16 Examples of iridium(III) complexes with mitochondrial localisation.

The lipophilicity was tested, highlighting that the main contributing factor was the nature of the cyclometalated ligands (**a**, **c**, **d**>>**b**). In fact, the complexes of the groups **45** and **46** show similar values of lipophilicity when the cyclometalated ligands are the same. Overall, the lipophilicity characters of **45(a-d)** and **46(a-d)** are slightly lower than **47c**, illustrating the effect of the polar carbohydrate groups. Additionally, the cytotoxicity toward HeLa cells (50 μM, 48 hour incubation) displays lower IC_{50} values in comparison to cisplatin for almost all the probes. Both **45a** and **46a** localise within mitochondria through an energy-dependent pathway, but only complex **45a** enters the cells using a GLUT-mediated mechanism.

Two charged bioorthogonal iridium(III) probes (**48**-**49**) were reported by Lo. The complexes are appended with a dibenzocyclooctyne moiety,[128] which is capable of targeting different azide-labelled biomolecules.[193] Lipophilicity studies of **48** and **49** revealed very high values of 5.69 and 7.14, respectively. Both complexes exhibit mitochondrial localisation in CHO cells achieved through passive diffusion. Regardless of the higher lipophilicity of **49**, complex **48** enters the cells more efficiently, suggesting that the smaller molecular size plays a critical role in the uptake of the probe. Both complexes exhibit a moderate cytotoxicity with a percentage of surviving CHO cell of 75.6% and 84.9%, at concentration of 50 μM for an incubation time of 6 hours.

After their previous publication on pH-responsive probes,[122] the group of Aoki synthesised a further neutral iridium(III) analogue containing three pyridyl groups at the 4'-position of the phenylpyridine ligand (**50**).[129] Complex **50** exhibits a reversible pH-dependent emission profile based on protonation and deprotonation of the pyridine rings, with an intense green emission in neutral and basic conditions and a weaker red emission in acidic pH. Upon incubation in HeLa-S3 cells, complex **50** accumulates within mitochondria, potentially through a passive transport mechanism. Moreover, after photoirradiation at 465 nm for 10 minutes, **50** generates much more $^1O_2$ in comparison to the previously published iridium(III) probe,[122] thus inducing necrosis-like cell death.

The group of Chao developed four iridium(III) anthraquinone complexes (**51**-**54**) that can be excited *via* two-photon absorption, as hypoxia-sensitive imaging probes.[130] The anthraquinone unit is an efficient quencher of the iridium luminescence. However, in hypoxic conditions, it can be converted into the hydroquinone form, thus restoring the emission of the probe.[194] In cells, the ligand can be reduced by the

coenzyme nicotinamide adenine reductase phosphate (NAD(P)H) in the presence of cellular reductase.[195] Interestingly as shown in **Figure 1.17**, the emission intensity of the complexes **51-54** internalised within A549 cells rapidly increases (11- to 19-fold) after enzymatic reactions with NAD(P)H in hypoxic condition, without interference from other biological reductants. Moreover, the probes display different sensitivity toward oxygen, with an increment of phosphorescence at $[O_2] \leq 5\%$ for **51**, and 1% or less for **52-54**. All the probes localise in the mitochondria of A549 cells and show quite low cytotoxicity with viability values greater than 80% under both normoxic and hypoxic conditions, after 12 hour incubation at a concentration of 10 μM.

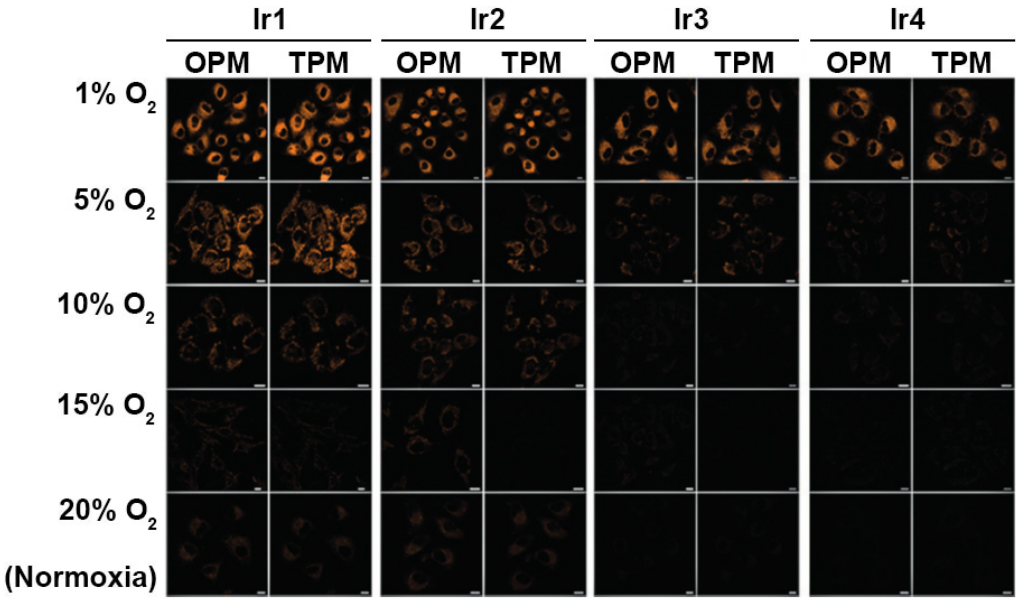

Figure 1.17 Confocal images of adherent A549 cells treated with 5 μM of **51-54** (Ir1-Ir4) under normoxic (20% O_2) and different hypoxic (15, 10, 5 and 1% O_2) conditions. Scale bar = 10 μm. Reproduced with permission from ref[130].

A series of photoactive iridium(III) complexes (**55a-c**) functionalised with a nitroveratryl photolabile protecting group and polyethylene glycol (PEG) chains of various lengths were designed by Lo.[131] The PEG chain increases the water solubility,[196] and also reduces the toxicity as the chain increases in length. In fact, despite similar uptake efficiency within this small family of complexes, the viability in the dark of HeLa cells incubated with **55a** and **55b** (> 80%) is higher than for **55c** (> 60%), due to the greater biocompatibility of the longer PEG chain. Upon irradiation

for 5 minutes, the nitroveratryl group is cleaved and the cytotoxic iridium(III) core is released, showing a significant decrease of the percentage of cell survival. The complexes **55a-b** display good accumulation within the mitochondria.

The group of Chao synthesised five iridium(III) complexes (**56a-e**)[103] with aggregation-induced emission (AIE) characteristics, showing almost no fluorescence in solution and high emission in the aggregated state.[197] All the complexes exhibit low toxicity (viability > 85%) upon incubation at 500 nM for a period of 12 hours. The uptake in the mitochondria of HeLa cells follows a non-endocytic energy-dependent process. Remarkably, **56a** was employed to successfully monitor a mitophagy process in living cells.[198]

The same research group recently published a similar series of AIE-active iridium(III) probes (**57-59**), which are analogous to the family of complexes **56a-e** with variations in the cyclometalated ligands. In line with the previously reported complexes, these species can also be used as two-photon absorbing agents for photodynamic therapy (PDT).[132] In particular, complex **57** displays a significant two-photon absorption cross-section, a high ROS (reactive oxygen species) generation capacity and a significant lethality at low concentration upon aggregation within mitochondria.

Another family of terpyridyl iridium(III) complexes (**60a-c**) for the real-time dynamic tracking of mitophagy[198] with two-photon excitation was proposed by Chao.[133] These probes exhibit lipophilicity values $\log D_{7.4}$ in a range between 0.9 and 1.5 and moderate cytotoxicity in HeLa cells, with a viability greater than 80% after 6 hour incubation at concentration of 5 μM. Interestingly, complexes **60a-c** are capable of localising within the mitochondria independently of the membrane potential, an advantageous characteristic over the commercially available mitochondrial stain MitoTracker™ Red (which in the absence of membrane potential distributes within the cytoplasm and other organelles). Moreover, complexes **60a-c** show deep tissue penetration under two-photon excitation, enabling the visualisation of the inner structure of tridimensional multicellular tumour spheroids.[199]

Laskar and Chowdhury designed two of the few examples of neutral iridium(III) probes (**61-62**) for the staining of mitochondria.[134] As Chao's probes,[103,132] **61** and **62** exhibit aggregation induced emission with an increment of the emission intensity in the solid state 60 and 34 times higher than in solution, respectively. Additionally, these complexes show low toxicity at concentration lower than 5 μM

(viability > 80%) for an incubation time of 24 hours in HOS cells and specific mitochondrial staining.

Mao and Tan synthesised two iridium(III) complexes (**63**-**64**) with chloromethyl-functionalised bipyridine as diimine ligands.[135] These complexes are designed to react with thiol functional groups present in various mitochondrial proteins and immobilise the complexes inside this organelle.[200] The cytotoxicity of **63**-**64** was tested against a series of cancer cell lines, showing very low IC_{50} values (0.2 - 27 μM) after treatment for 48 hours. Additionally, **63** shows a 11-fold higher selectivity for cancerous A459 cells over non-cancerous LO2 cells, inducing a caspase-dependent and ROS-mediated apoptotic cell death.[201]

Complexes **65** and **66** are some of the few examples of NIR iridium(III) probes,[32] due to the presence of phenylbenzo[g]quinoline as cyclometalated ligands.[34] These complexes display a strong emission band around *ca.* 750 nm, superior photostability and reduced pH-dependence of the phosphorescent intensity. Those properties, in addition to a low cytotoxicity with viability greater than 70% after 24 hour incubation at 20 μM in HeLa cells, have allowed to track changes in the mitochondrial morphology during the early stage of apoptosis (**Figure 1.18**).

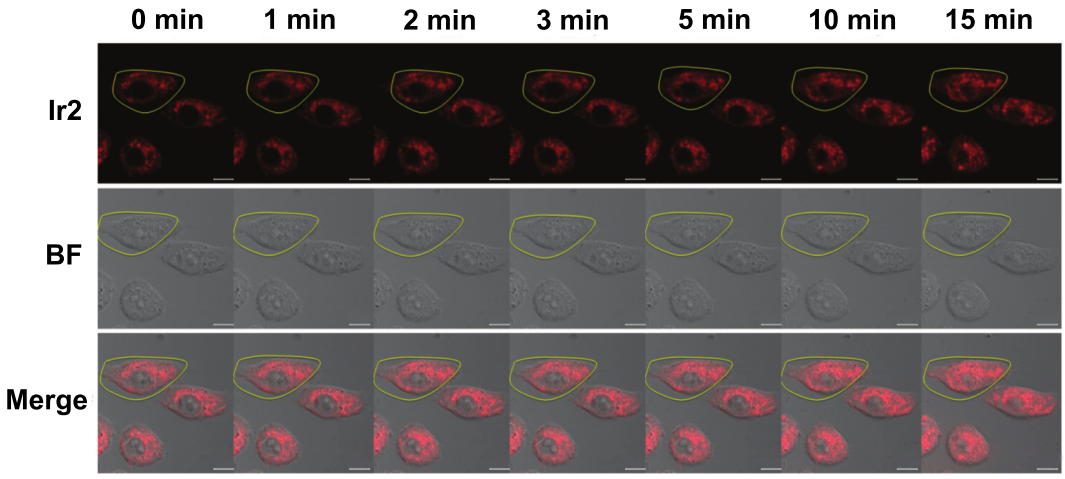

Figure 1.18 Phosphorescent images of CCCP (carbonyl cyanide m-chlorophenyl hydrazone) (10 μM) treated living HeLa cells stained with 20 μM of **66** (Ir2), during an increasing scan time. The upper panels are the luminescence images of **66** (Ir2), the middle panels are the bright field (BF) images, whereas the lower panels are the merged images. Reproduced with permission from ref[32].

Based on the structure of previously reported iridium(III) derivatives,[103,202] the group of Chao synthesised a family of complexes to assess the effect of various degrees of fluorination on anti-proliferation.[136] In particular, the complex with the highest degree of fluorination (**67**) shows high cytotoxicity against 5 different human cancer cell lines (IC_{50} values: 0.5 - 2.6 μM) with also the highest selectivity for the cisplatin-resistant cell line A549R.

Polyethylene glycol (PEG) moieties have shown to increase the biocompatibility of complexes within cells and their solubility in aqueous media.[66,131,203] For this reason, an iridium(III) complex appended with a PEG unit (**68**) was developed by Lo's group for application in photodynamic therapy (PDT).[137] Interestingly, **68** demonstrated to be non-toxic after incubation in HeLa cells (300 μM, 12 hours), but its cytotoxicity was triggered by irradiation at 365 nm for 30 minutes (PI > 55.6). The mitochondrial accumulation of **68** facilitates efficient oxidative damage to these organelles, causing necrotic cell death upon photoexcitation.

Another iridium(III) PDT agent, bearing a methyl ester substituent on the cyclometalated ligands was reported by the same research group.[125] Complex **69** shares a similar chemical structure with **43**, but the higher degree of conjugation of the quinoline ligands increases its lipophilicity (from 0.62 for **43** to 1.10 for **69**) and it also shows a mitochondrial accumulation instead that an endosomal localisation. Moreover, the photoinduced cytotoxicity of **43** and **69** is comparable, but probably due to the mitochondrial localisation of the latter, its cytotoxicity in the dark is an order of magnitude higher (IC_{50} = 8.6 μM), making this probe less promising than **43** for photodynamic therapy application.

1.5.5 Endoplasmic Reticulum and Golgi Apparatus Staining

The endoplasmic reticulum (ER) is the largest membrane-bound organelle in eukaryotic cells and it consists of multiple structural domains that are interconnected and contiguous.[204] The ER serves different roles within the cell such as protein folding, lipid and steroid synthesis, carbohydrate metabolism as well as calcium storage and release.[205] Importantly, a number of physiological and pathological conditions are known to disturb proper ER function and thereby cause ER stress, which can lead to unfolded protein response (UPR) or the release of calcium in the cytoplasm, followed by mitochondria-mediated apoptosis .[206,207] Together with the ER, the Golgi apparatus is a central organelle in the secretory pathway, sustaining the delivery of proteins from their site of synthesis in the ER to their final cellular destination.[208,209] During transit to the Golgi complex, key modifications are made to most proteins, including changes to their glycosylation profile, sulfation, phosphorylation and also proteolytic cleavage.[208,210] Structural and functional alteration of this organelle have been recognised as a constant pathological hallmark of various neurodegenerative diseases, such as amyotrophic lateral sclerosis, Parkinson, Alzheimer, Huntington and prion diseases.[209,211]

A family of iridium(III) complexes that display localisation within the endoplasmic reticulum and Golgi apparatus is shown in **Figure 1.19**. A look over these complexes highlights that the majority of them are cationic and exhibit acute cytotoxicity. On the other hand, neutral complexes with accumulation within the endoplasmic reticulum appear to exhibit lower cytotoxicity, even at longer incubation time.

One of the first examples of ER probes was a series of charged iridium(III) complexes appended with an indole moiety (**70a-c**/**71a-c**).[138] The binding properties of the indole unit with proteins such as serum albumin, which contains six specific substrate-binding sites,[212,213] are well known. Lipophilicity measurements show slightly higher values for the probes with a longer spacer (**70a-c**), compared with their analogues (**71a-c**), and increased $\log D_{7.4}$ with higher conjugation of the two cyclometalated ligands (**c**>**b**>**a**). Additionally, all the probes display high levels of cytotoxicity toward HeLa cell, with IC_{50} values ranging from 1.1 to 6.3 μM at 48 hour

incubation time. Through an energy-requiring process such as endocytosis, **71a** localised in the perinuclear area of cells.

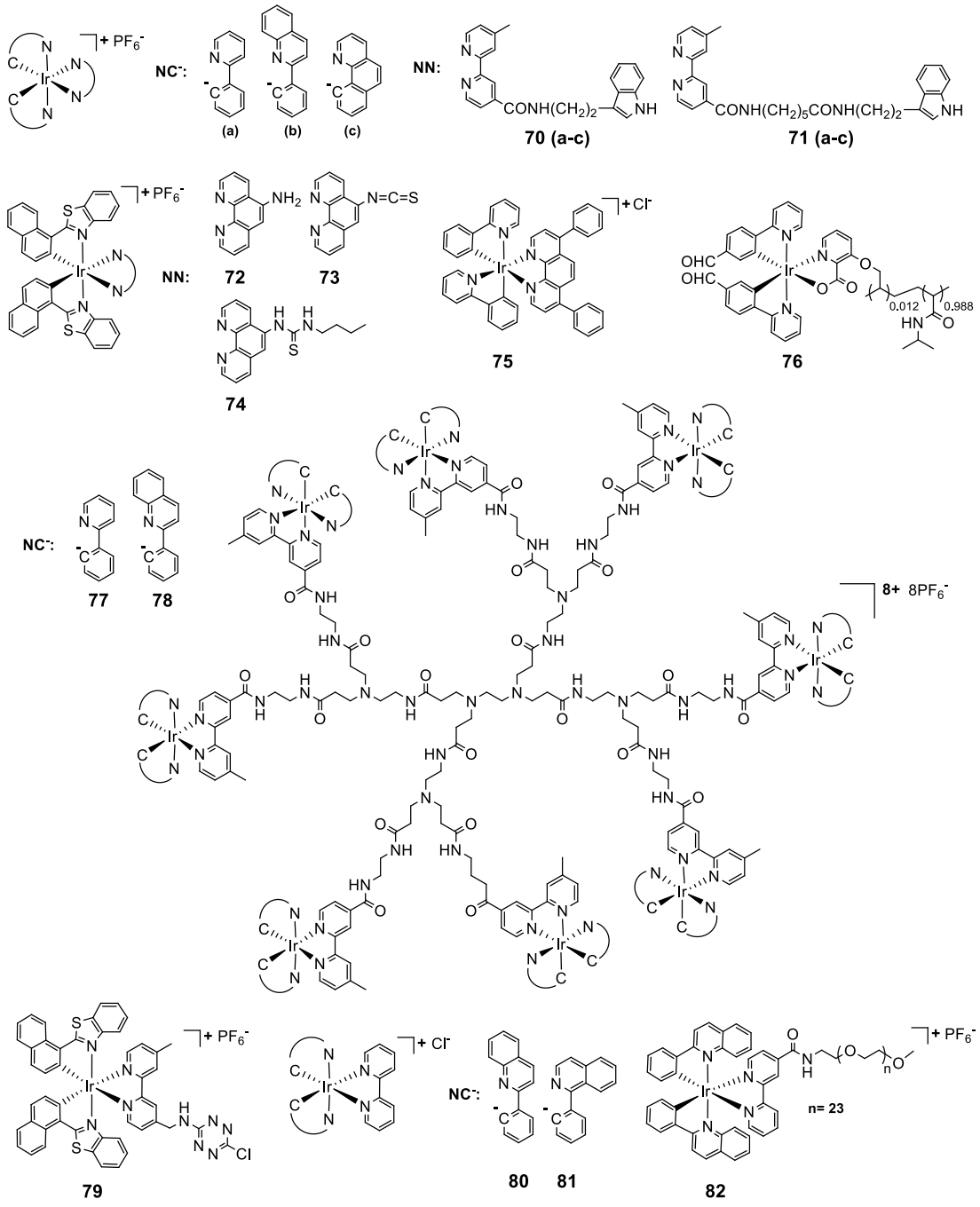

Figure 1.19 Iridium(III) complexes proposed for the staining of the endoplasmic reticulum and the Golgi apparatus.

A family of three iridium(III) complexes bound to functionalized 1,10-phenanthroline ligands (**72-74**) was studied by the group of Lo.[139] Complex **74** was the only probe in the series that can undergo bioconjugation with proteins, such as *bovine serum albumin* or *human serum albumin*. Surprisingly, the intracellular distribution of **72-74** in HeLa cells was the same, with the formation of a luminescent ring surrounding the nucleus. Additionally, cytotoxicity data show similar IC_{50} values (1.0 – 4.2 μM), revealing the high toxicity of these probes.

The bathophenanthroline iridium(III) probe **75** was discovered by Fei and Zhou.[140] The size and conjugation degree of the diimine ligand increases the lipophilicity and cytotoxicity of complex **75** in comparison to a previous published analogue.[214] The greater lipophilicity causes the localisation of the probe in the membrane of the endoplasmic reticulum (**Figure 1.20** - B), inducing ER stress and initiating an intrinsic apoptotic pathway,[206,207] characterised by mitochondria fragmentation (**Figure 1.20** - A). Additionally, the high cytotoxicity against HeLa, A549 and MCF-7 cell lines has highlighted the antitumor potential of **75**, with IC_{50} values of 3.3, 2.0 and 3.2 μM, respectively.

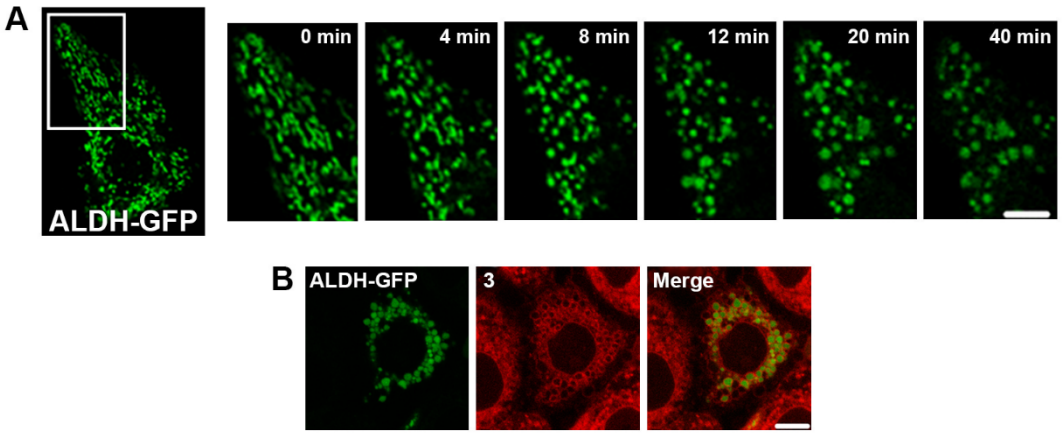

Figure 1.20 Mitochondrial fragmentation and onset of apoptosis. (A) In the time-lapse confocal images of **75** (3) treated HeLa cells, ALDH-GFP (aldehyde dehydrogenase fused with green fluorescent proteins) labelled mitochondria became fragmented, resulting in small and rounded organelles. (B) Representative image of ALDH-GFP stained mitochondria (green) and membrane localised **75** (3, red). Scale bar = 20 μm. Adapted and reproduced with permission from ref[140].

The poly(*N*-isopropylacrylamide) iridium(III) probe **76** was reported by Zhao and Huang as cellular sensor for homocysteine (Hcy) and cysteine (Cys).[141] The chemical structure of **76** is characterised by a water-soluble polymeric moiety, which increases the solubility of the probe in biological environment, and two aldehyde groups, which are responsible to selectively react with thiol groups in Hcy and Cys.[215,216] Upon reaction with Hcy and Cys, with consequential formation of thiazolidine and thiazinane groups respectively, a blue shift in the absorption spectrum and increase in the emission intensity was recorded. Moreover, upon incubation in KB cells (200 μM, 24 hours), **76** localised in the perinuclear region of the cells, showing a viability ≥ 98%.

Two examples of dendritic iridium(III) polypyridine probes (**77-78**) were designed and compared to their monomeric analogues.[142] As expected, due to the hydrophobic nature of the dendritic skeleton moiety, the lipophilicity of **77-78** was higher compared to the monomeric probe (1.66 - 2.61 vs 0.44 - 2.01, respectively). However the cellular uptake resulted similar. Upon efficient internalisation (2 μM, 2 hours) by an energy-requiring mechanism such as endocytosis, **77** and **78** localised in the perinuclear area of HeLa cells. Costaining studies with fluorescent antibodies confirmed the localisation of these probes in the Golgi apparatus. The accumulation in this organelle seems to contribute to the higher cytotoxicity of the dendritic probes (IC_{50} = 1.4 - 2.1 μM) with respect to their monomeric species (IC_{50} = 5.5 - 26.4 μM).

The bioorthogonal iridium(III) complex **79** containing a 1,2,4,5-tetrazine moiety is almost non-emissive, but its emission highly enhances upon selective coordination with modified *bovine serum albumin* (I/I_0 = 1113.7).[143] The cytotoxicity of the probe was tested by MTT assay on CHO-K1 cells and shows viability greater than 80% after 20 hour incubation at concentration up to 20 μM. The localisation of complex **79** shows a perinuclear and sharp granular cytoplasmic staining, due to the dynamic recycling of the probe from the endoplasmic reticulum to subcellular organelles for enzymatic processing.[217]

Kwon, Rhee and Lim reported two bipyridine iridium(III) complexes (**80-81**) which can be used as photodynamic therapy (PDT) agents, due to their high efficiency in the production of ROS.[144] In fact, at really low concentration (2 μM) the probes can be photoactivated (10 second irradiation time, 100 J cm^{-2} light) and reduce significantly the viability of SKOV-3 cancer cells, with IC_{50} values of 4.89/0.83 μM (**80**) and 3.61/0.63 μM (**81**) in the absence/presence of light. Interestingly, the

localisation of the probes was mainly in the endoplasmic reticulum, but the $^1O_2$ produced might be diffused through the ER membrane and also modify some mitochondrial proteins, by protein-protein cross-linking and protein oxidation mechanisms.

The biological properties of PEG-appended iridium complexes can be modulated by changing the length of the polymeric chain.[218–220] The group of Lo developed a new iridium(III) appended with a shorter PEG moiety (23 units)[145] with respect to the previously discussed probe **68** (*ca.* 122 units). As its analogue **68**, probe **82** showed low cytotoxicity in HeLa cells (IC_{50}= 565.9 μM) even for long period of time (48 hours). Moreover, **82** accumulates in the perinuclear region of the cells, likely binding to hydrophobic organelles such as endoplasmic reticulum or Golgi apparatus.

1.5.6 State of the Art

This section surveyed the research area of cyclometalated iridium(III) complexes and their use in life science.[1] It is evident that this area is still incredibly active and it has been diversified over the years. While phosphorescent iridium(III) complexes were initially screened as cellular markers for optical imaging, their versatility has expended potential use in broader areas including therapy. Despite the large body of work that has appeared in the literature to date, a full rationalisation of structure-activity relationship is still difficult to achieve.

Most of the design of new iridium probes and/or therapeutic agents starts with considerations of chemical nature such as charge, lipophilicity, solubility and bioconjugation to specific biological vectors. However, as illustrated in the various examples within this section, a systematic investigation related to a biological context is lacking. In fact, the various research groups have tested the iridium complexes in very different conditions including diverse cell lines, concentration and incubation time. The area, in its multidisciplinary feature bridging chemistry and biology, would certainly benefit for the establishment of a set of conditions to assess newly synthesised iridium(III) complexes and to revise currently available ones.

1.6 Tetrazoles and Tetrazolato Metal Complexes

Tetrazoles are a class of five-member N-heterocyclic compounds. They are carboxylic acid isosteres and possess similar acidity (pKa ~ 5).[221] However, tetrazoles result more metabolically stable in comparison to their carboxylic analogues. Hence, they are commonly applied in medicinal chemistry as isosteric substituents of various carboxylic groups in biologically active molecules. Tetrazoles and their derivatives have been used in a wide variety of applications as antibacterial, anti-inflammatory, antifungal, antiviral, antitubercolours, cyclo-oxygenase inhibitors, hypoglycemic and anticancer agents.[222–224]

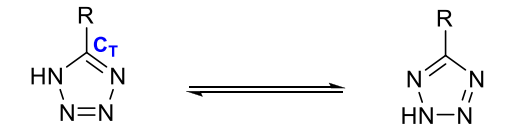

N1 tautomer **N2** tautomer

Figure 1.21 N1 and N2 tautomers of protonated tetrazoles. The tetrazolic carbon ($\mathbf{C_T}$) is highlighted in blue.

Protonated tetrazoles exist in two tautomeric forms, with the tetrazolic proton residing on either the N1 or N2 atom, as showed in **Figure 1.21**. These two tautomeric forms can be identified by ^{13}C NMR, as previously described by Butler *et al.*.[225–227] Chemical shifts of the tetrazolic carbon ($\mathbf{C_T}$) ranging from 152 - 156 ppm, indicate the predominant presence of the N1 tautomer, whereas values of 162 - 165 ppm are indicative of the N2 one.

Tetrazoles have been coordinated to transition metal atom such as Ru(II),[228–230] Re(I),[231–235] Ir(III),[236–241] Cu(I)[242–244] and Pt(II).[245–248] In the metal coordination sphere, the tetrazole can behave as an ancillary, chelating, or bridging ligand between two different metal centres, as well as a substituent group on other ligands.

These metal complexes has been utilised in a multitude of fields (**Figure 1.22**). Noteworthy, the majority of these species have found application as OLEDs (Organic Light Emitting Devices) or in the fabrication of LEECs (Light Emitting Electrochemical Cells). For example, the Ru(II) complex **83** has been developed for non-doped NIR light electrochemical cells,[229] whereas the combination of the anionic (**88a**) and cationic (**88b**) Ir(III) species allowed the formation of a soft salt characterised by an almost pure white light emission.[241] Surprisingly, tetrazolato metal

complexes have not been used in biological applications until 2014, when the Re(I) complex **89** was successfully incubated in *Drosophila* fat body tissue and 3T3-L1 cells for the staining of lipid droplets.[233,249]

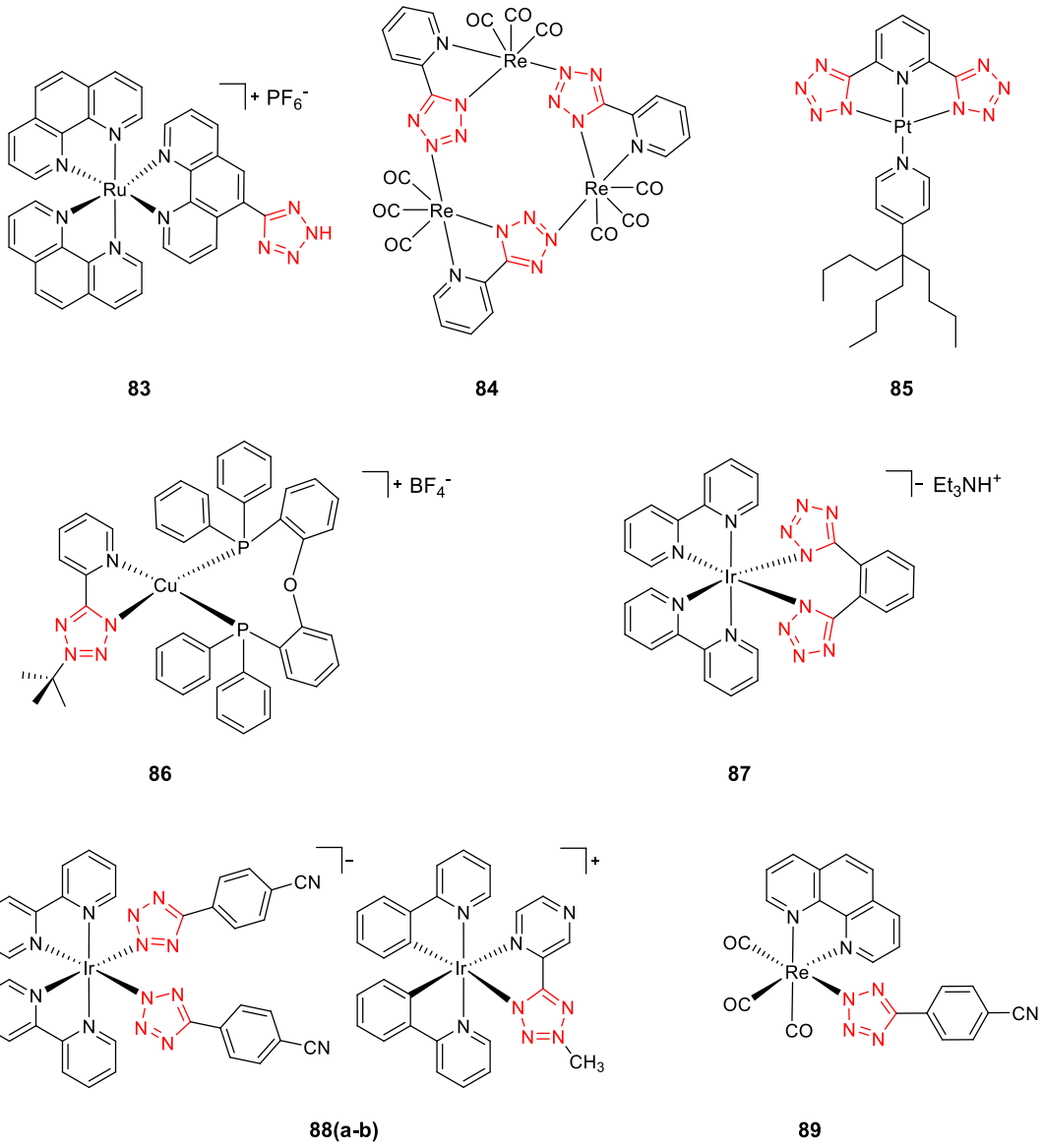

83 **84** **85**

86 **87**

88(a-b) **89**

Figure 1.22 Examples of previously reported transition metal complexes functionalised with tetrazolate ligands. The tetrazolate moiety has been highlighted in red.

1.7 This Investigation and Scope

In the last decades transition metal complexes of iridium(III), ruthenium(II), rhenium(II), platinum(II) and gold(I) have been investigated for biological applications, as previously highlighted in this chapter. Modulations in the chemical structure of these metal probes have showed to influence not only the photophysical properties but also the uptake mechanism, localisation and cytotoxicity within live and fixed cells. However, a structure-activity rationalisation has appeared to be challenging due to the variety of factors involved in the design of the probes.

To further expand the knowledge in this field, this study investigates a series of iridium(III) complexes bearing a tetrazolate moiety as ancillary ligand (**Figure 1.23**).

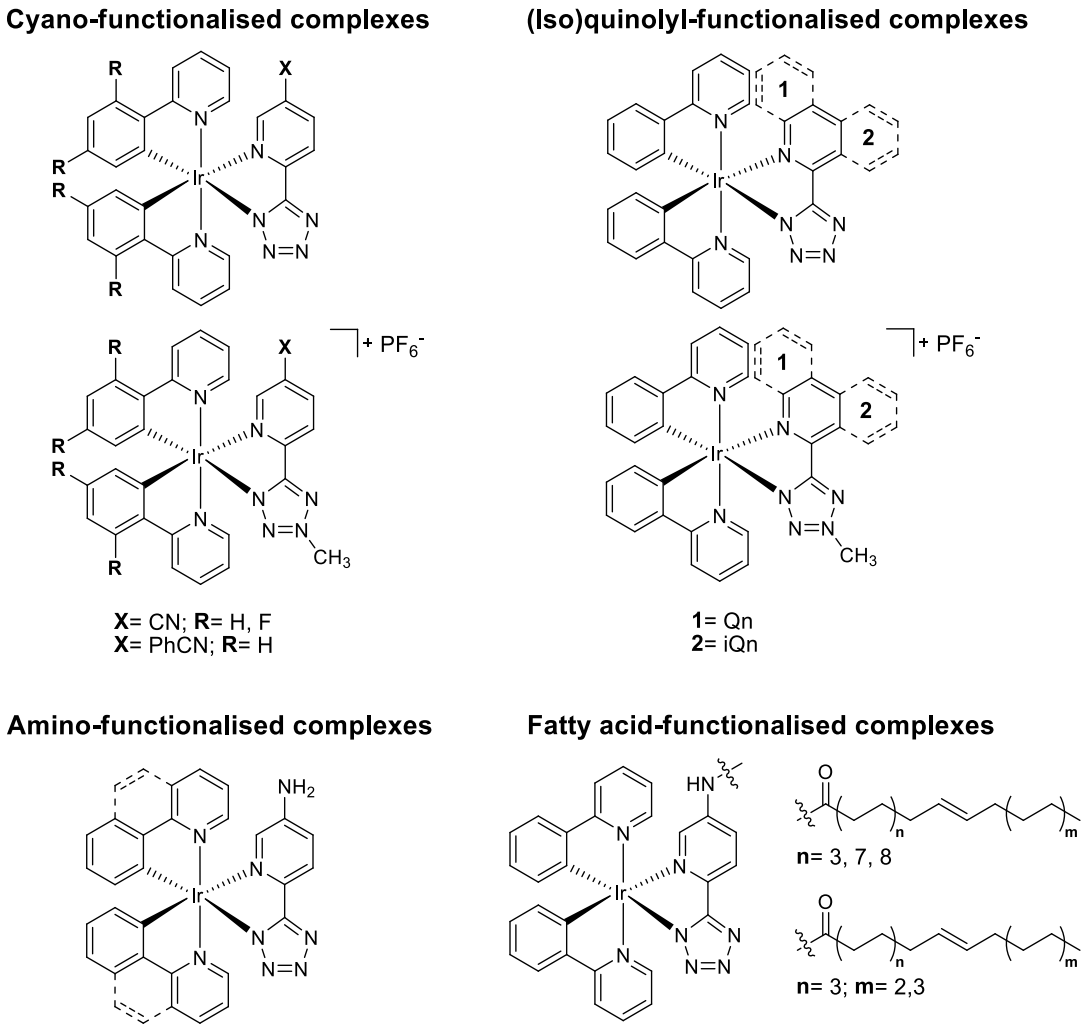

Figure 1.23 Structure of the target iridium(III) tetrazolato complexes in this thesis.

Interestingly, despite the favourable properties (antibacterial, analgesic, anti-inflammatory, antifungal, anticonvulsant and anticancer activity)[222–224,250] exhibited by tetrazoles, the use of tetrazolato metal complex in biology was not investigated until 2014 (refer to complex **89** - **Figure 1.22**).[233] Moreover, no reports of iridium(III) tetrazolato complexes for biological applications have been published until 2017.[239]

Hence, the aim of this multidisciplinary research is to rationalise the relationship between the chemical structure of a family of iridium(III) tetrazolato complexes and the effect that modifications on both cyclometalated and ancillary ligands produce on solubility, lipophilicity, uptake mechanism, cytotoxicity and localisation of the probes in live cells and fresh/fixed tissues.

Chapter 2

Synthesis and Photophysical Investigation of Cyano and (Iso)Quinolyl-Functionalised Iridium Tetrazolato Complexes

The content of this chapter has been published in:

Chemistry – A European Journal (2017) with the title "Investigating intracellular localisation and cytotoxicity trends for neutral and cationic iridium tetrazolato complexes in live cells".[239]

2.1 Introduction

The interest in cyclometalated iridium(III) complexes has increased over the years since the discovery of the luminescent *fac*-Ir(**ppy**)$_3$, initially found as a side product of the dichloro-bridged dimer [Ir(**ppy**)$_2$(μ-Cl)]$_2$ (**Figure 2.1**).[251–253] Many studies have been published on iridium complexes with formula [Ir(N^C)$_2$(N^N)]$^{0/+}$, in which N^C represents monoanionic cyclometalated ligands and N^N is usually a diimine unit.[254–256] A large number of [Ir(N^C)$_2$(N^N)]$^{0/+}$ complexes have been reported with application as light-emitting materials [Organic Light Emitting Diodes (OLEDs) or Light Emitting Electrochemical Cells (LEECs)],[257–259] sensitisers for dye-sensitised solar cells,[260–262] chemosensors[263–265] and, more recently, as luminescent markers for biological imaging.[32,123,144] Along with many transition metal complexes of Ru(II), Re(I), Au(I) and Pt(II),[62,63,65] Ir(III) complexes have specific photophysical properties that can potentially solve many of the drawbacks associated with commonly studied organic fluorophores, such as enhanced photostability, large Stokes shifts and relatively long excited state lifetimes.[66] Additionally, the chemical and photophysical

properties can be readily modified by altering the ancillary or cyclometalated ligands around the metal centre.

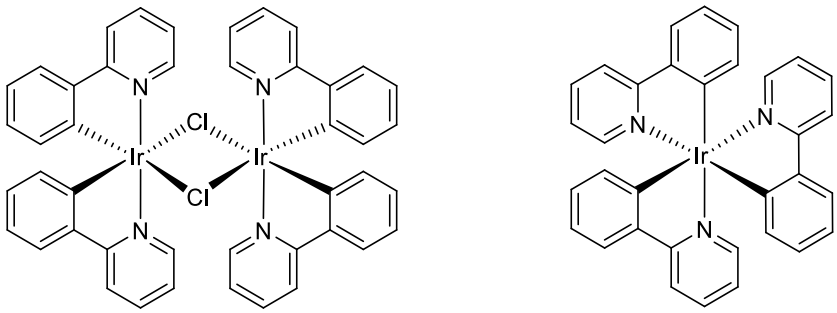

$[Ir(\mathbf{ppy})_2(\mu\text{-Cl})]_2$ *fac*-$Ir(\mathbf{ppy})_3$

Figure 2.1 Structure of the dichloro-bridged dimer $[Ir(\mathbf{ppy})_2(\mu\text{-Cl})]_2$ (left) and *fac*-$Ir(\mathbf{ppy})_3$ (right).

In this work, tetrazolate moieties have been chosen as ancillary ligands due to the intrinsic reactivity towards electrophiles,[232,237,266] which can allow an easy methylation reaction to achieve charged analogues starting from neutral species. A family of five neutral complexes and five methylated analogues has been synthesised by modifying the functional groups on the ligands and by the extension of the π conjugation (**Figure 2.2**). A systematic investigation of the relationship between chemical structure and photophysical behaviour has been carried out, recording the emission properties of the complexes in organic, lipophilic and aqueous media, in order to consider their applicability in biological environment.[239]

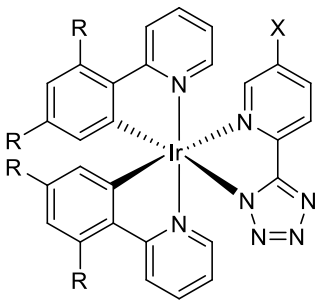

R= H; X= CN [Ir(**ppy**)$_2$(**TzPyCN**)]
R= F; X= CN [Ir(**F$_2$ppy**)$_2$(**TzPyCN**)]
R= H; X= C_6H_4CN [Ir(**ppy**)$_2$(**TzPyPhCN**)]

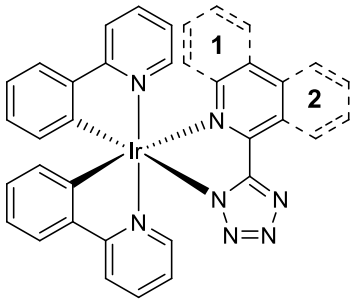

1 [Ir(**ppy**)$_2$(**TzQn**)]
2 [Ir(**ppy**)$_2$(**TziQn**)]

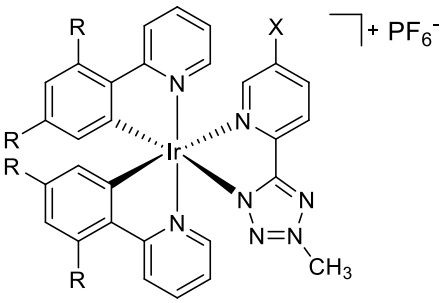

R= H; X= CN [Ir(**ppy**)$_2$(Me**TzPyCN**)]$^+$
R= F; X= CN [Ir(**F$_2$ppy**)$_2$(Me**TzPyCN**)]$^+$
R= H; X= C_6H_4CN [Ir(**ppy**)$_2$(Me**TzPyPhCN**)]$^+$

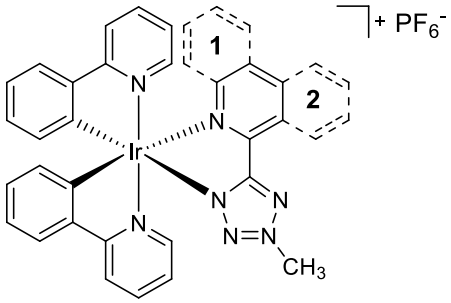

1 [Ir(**ppy**)$_2$(Me**TzQn**)]$^+$
2 [Ir(**ppy**)$_2$(Me**TziQn**)]$^+$

Figure 2.2 Structure of target complexes in this investigation, illustrating neutral species (top) and charged analogues (bottom).

2.2 Synthesis of the Tetrazolato Ligands

2.2.1 Pyridyl-Tetrazole Synthesis and Characterisation

H**TzPyCN** was synthesised following the literature procedure showed in **Figure 2.2**. The ligand precursor was obtained in three steps starting from the commercially available 2,5-pyridinecarboxylic acid. Following a Fisher esterification to form the corresponding methyl ester groups,[267] aminolysis with aqueous ammonia gave the corresponding primary amides.[268] Lastly, dehydration of the amide groups yielded the desired nitrile moieties.[269] The synthesis of H**TzPyCN** was carried out following a methodology developed by Sharpless *et al.*,[270] in which the nitrile was reacted with sodium azide in presence of zinc bromide and in water at reflux.

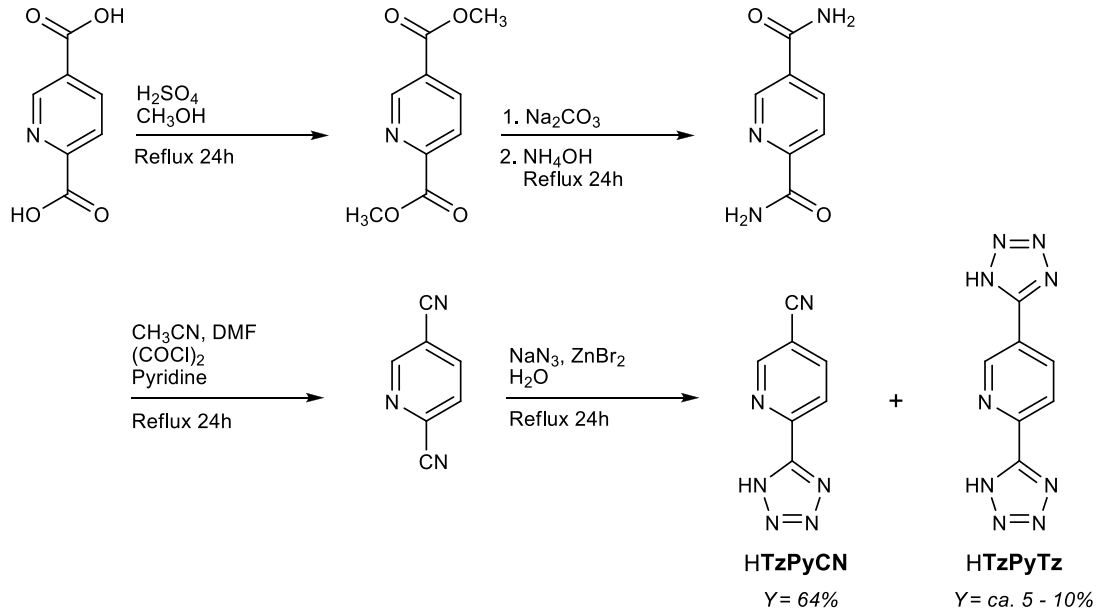

Figure 2.2 Scheme of the synthetic procedure for H**TzPyCN**.

Complete separation of H**TzPyCN** from the ditetrazole byproduct H**TzPyTz** (present in 5 – 10% molar amount determined by NMR analysis) by selective protonation was challenging, and the impure H**TzPyCN** was used as recovered for complexation with iridium. The purification of the final complexes was easily achieved *via* column chromatography, as described in details in section 2.3.1.

The main IR bands indicative of the tetrazole formation are the C=N and N–H stretching, observed at 1604 and 3071 cm^{-1}, respectively.

As mentioned above, ^{1}H NMR characterisation in DMSO-d_6 shows the presence of a small percentage of H**TzPyTz**. Characteristic peaks are found at 9.42, 8.67 and 8.44 ppm, which resonate at higher chemical shifts in comparison to those of the tetrazolate product (**Figure 2.3**).

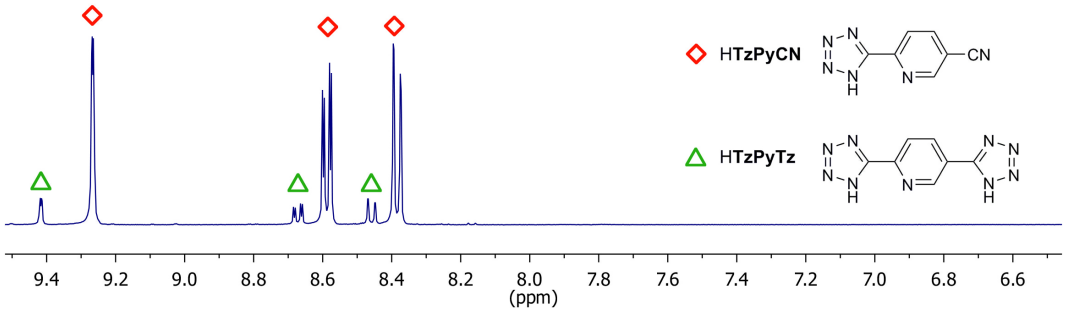

Figure 2.3 ^{1}H NMR in DMSO-d_6 for H**TzPyCN** (red diamond) with the byproduct H**TzPyTz** (green triangle). The peaks have been assigned for the two species.

The presence of the H**TzPyTz** is not visible in the ^{13}C NMR spectrum, probably due to the negligible amount in the sample solution. On the other hand, the resonance of the tetrazolic carbon $\mathbf{C_T}$ is well visible at 153.5 ppm, confirming again the formation of the desired final product.

2.2.2 Quinolyl and Isoquinolyl-Tetrazole Synthesis and Characterisation

The ligands H**TzQn** and H**TziQn** were synthesised following the procedure developed by Koguro *et al.*,[271] shown in **Figure 2.4**, where the nitrile was combined with the azide in presence of triethylammonium chloride in toluene at reflux to yield the desired product.

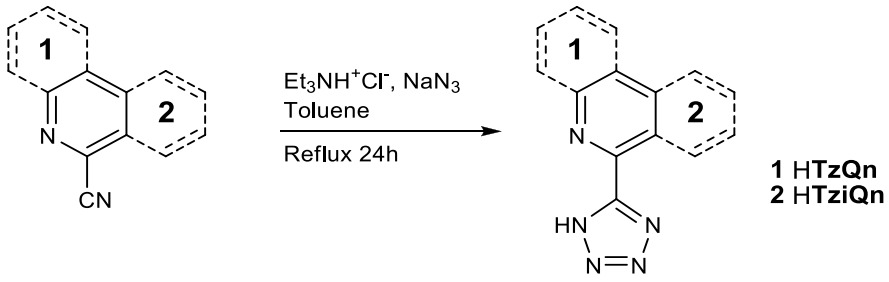

Figure 2.4 Scheme of the synthetic procedure for H**TzQn** and H**TziQn**.

H**TzQn** and H**TziQn** were characterised by IR, ^{1}H NMR and ^{13}C NMR spectroscopy. The IR bands present at 1600 and 1613 cm^{-1}, for H**TzQn** and H**TziQn** respectively, are associated with the stretching of the C=N, whereas the bands at 3058 and 3063 cm^{-1} derive from the stretching of N–H bond. These two sets of bands are demonstrating the formation of the desired species. Moreover, the lack of the sharp nitrile band at *ca*. 2240 cm^{-1} suggests the absence of starting material.

The spectroscopic characterisation of H**TzQn** and H**TziQn** by ^{1}H NMR and ^{13}C NMR in DMSO-d_6 is consistent with previous reports of these compounds.[234,269,271] The ^{13}C NMR of both H**TzQn** and H**TziQn** shows the characteristic $\mathbf{C_T}$ peak at 155.2 and 155.0 ppm, respectively, and supports the predominant formation of the N1 tautomer, in agreement with Butler's studies (refer to Chapter 1 – section 1.6).[225,226]

2.3 Synthesis of the Iridium(III) Complexes

2.3.1 Synthesis and Characterisation of Neutral Iridium(III) Complexes

The neutral iridium(III) complexes have been synthesised following a previously reported procedure.[236] [Ir(**ppy**)$_2$(**TzPyCN**)], [Ir(**ppy**)$_2$(**TzQn**)] and [Ir(**ppy**)$_2$(**TziQn**)] were prepared by reaction between [Ir(**ppy**)$_2$(μ-Cl)]$_2$ and the corresponding pyridyl or (iso)quinolyl tetrazolate species, as showed in **Figure 2.5**. In the case of [Ir(**F$_2$ppy**)$_2$(**TzPyCN**)], the starting material was bearing 2-(2,4-difluorophenyl)pyridine (**F$_2$ppy**) as cyclometalated ligands, in place of **ppy**.

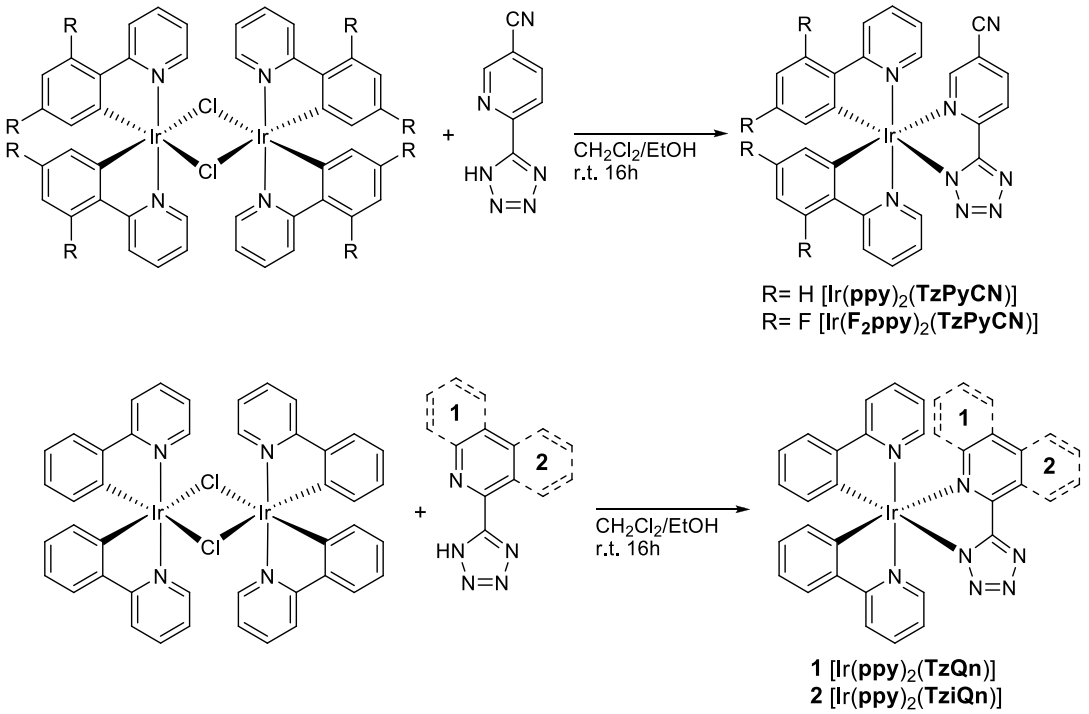

Figure 2.5 Scheme of the synthetic procedures for [Ir(**ppy**)$_2$(**TzPyCN**)], [Ir(**F$_2$ppy**)$_2$(**TzPyCN**)], [Ir(**ppy**)$_2$(**TzQn**)] and [Ir(**ppy**)$_2$(**TziQn**)].

The complex [Ir(**ppy**)$_2$(**TzPyPhCN**)] was prepared *via* a different route, involving a Suzuki coupling[272] of the previously reported [Ir(**ppy**)$_2$(**TzPyBr**)][236] with 4-cyanoboronic acid (**Figure 2.6**). Previous attempts to react [Ir(**ppy**)$_2$(μ-Cl)]$_2$ with the pre-formed corresponding tetrazolate ligand were unsuccessful, as an inseparable mixture of products was obtained.

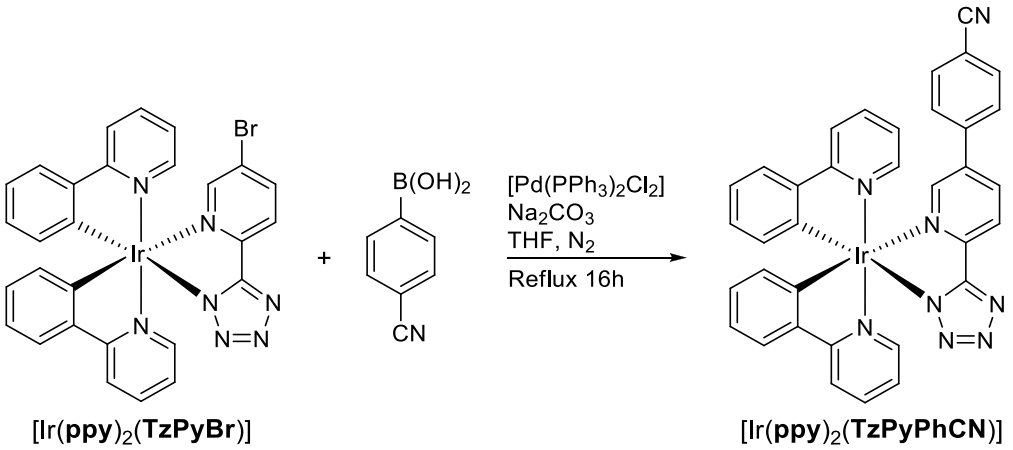

Figure 2.6 Scheme of the synthetic procedure for [Ir(**ppy**)$_2$(**TzPyPhCN**)].

Chromatographic separation on neutral alumina as stationary phase was required for all the neutral iridium(III) complexes, in order to obtain pure final products with average yields around 75%. Only [Ir(**ppy**)$_2$(**TzQn**)] was isolated with a slightly lower yield of 53%.

The IR spectra display the characteristic C≡N peak around 2230 cm^{-1} for [Ir(**ppy**)$_2$(**TzPyCN**)], [Ir(**F$_2$ppy**)$_2$(**TzPyCN**)] and [Ir(**ppy**)$_2$(**TzPyPhCN**)], in addition to the aromatic stretching of the tetrazolic C=N at *ca.* 1600 cm^{-1} for the whole neutral family. The coordination of the tetrazolate ligand to the metal centre was also supported by the absence of the N–H band around 3100 cm^{-1}.

Spectroscopic characterisation by ^{1}H NMR shows two doublet peaks in the range 6.5 – 5.5 ppm (**Figure 2.7**), which are assigned to the protons in *meta* position with respect to the pyridine ring of **ppy** (or **F$_2$ppy)** and are characteristic of cyclometalated iridium(III) complexes.[126,133,273] In ^{13}C NMR spectra the tetrazolic carbon **C$_T$** resonating around 163.5 ppm indicates a coplanar arrangement adopted by the rings in the tetrazole moiety, suggestive of chelation of the ancillary ligand.[236] Consequently, the downfield shift of the **C$_T$** resonance shows that the coordination occurred through N1 position of the tetrazolato ring.

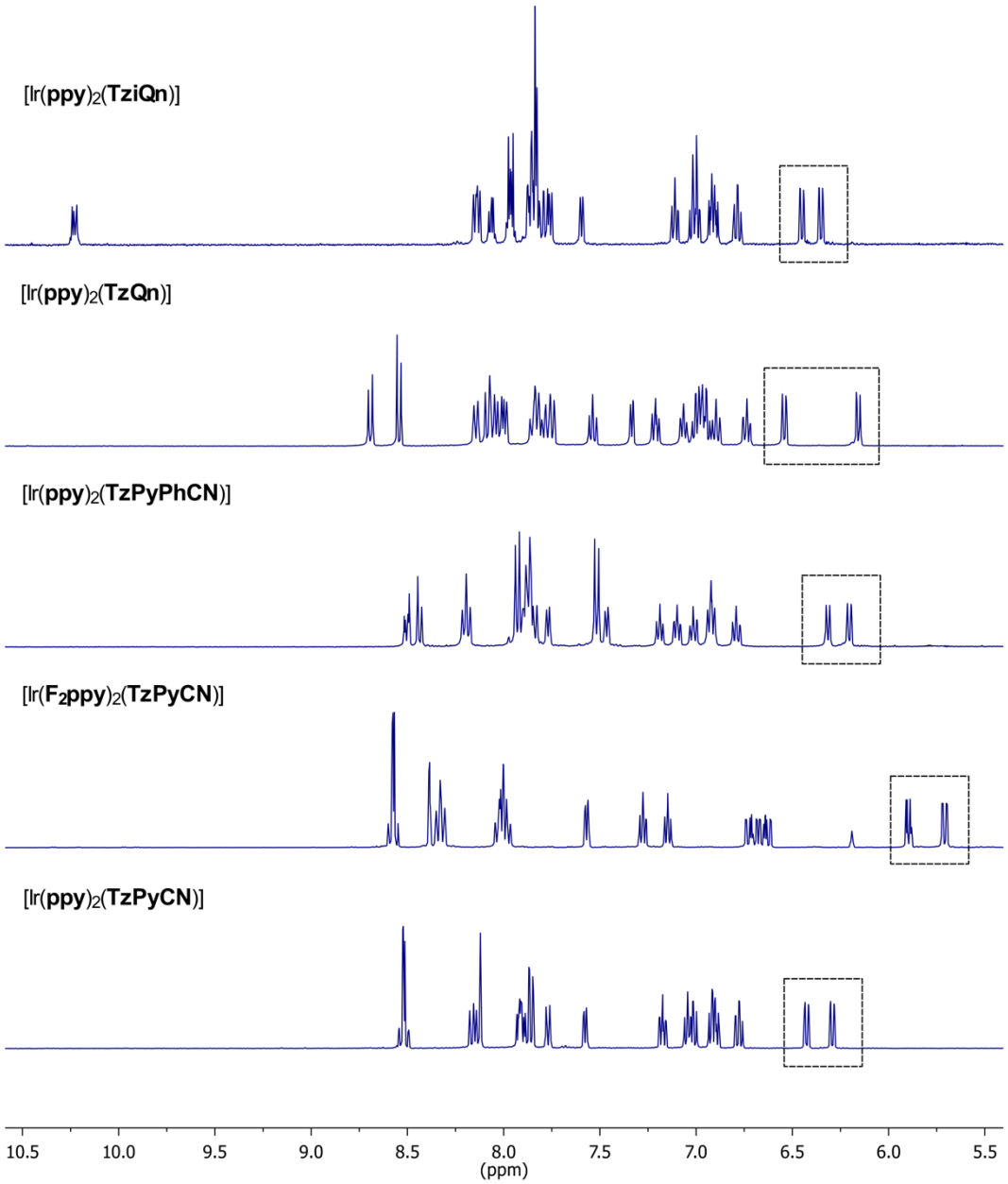

Figure 2.7 ^{1}H NMR in acetone-d_6 for [Ir(**ppy**)$_2$(**TzPyCN**)], [Ir(**F$_2$ppy**)$_2$(**TzPyCN**)], [Ir(**ppy**)$_2$(**TzQn**)] and [Ir(**ppy**)$_2$(**TziQn**)]. ^{1}H NMR of [Ir(**ppy**)$_2$(**TzPyPhCN**)] was recorded in DMSO-d_6. In the spectra, the two characteristic doublet peaks of cyclometalated iridium complexes have been highlighted in boxes.

Single crystals suitable for X-ray diffraction were obtained for the neutral [Ir(**F$_2$ppy**)$_2$(**TzPyCN**)] complex. This species crystallised in the monoclinic space group *I*2/*a* (**Figure 2.8**). The coordination arrangement presents the two pyridine rings of the phenylpyridine ligands adopting a *trans* configuration, while the two cyclometalated phenyl rings being arranged in *cis* configuration. The rest of the coordination sphere is occupied by the two nitrogen atoms of the tetrazole and pyridine rings. The crystallographic data can be found in Appendix A, **Table A.1** – **Table A.2**.

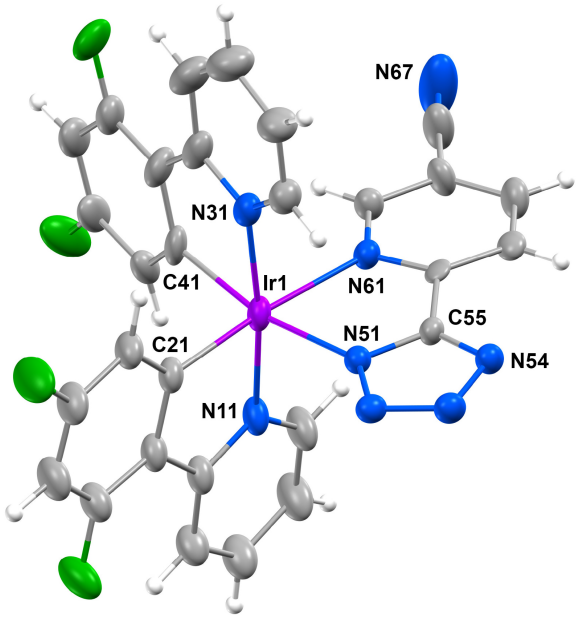

Figure 2.8 X-ray crystal structure of [Ir(**F$_2$ppy**)$_2$(**TzPyCN**)], with displacement ellipsoids drawn at the 50% probability level.

2.3.2 Synthesis and Characterisation of Cationic Iridium(III) Complexes

The cationic iridium(III) complexes $[Ir(\mathbf{ppy})_2(Me\mathbf{TzPyCN})]^+$, $[Ir(\mathbf{F_2ppy})_2(Me\mathbf{TzPyCN})]^+$, $[Ir(\mathbf{ppy})_2(Me\mathbf{TzPyPhCN})]^+$, $[Ir(\mathbf{ppy})_2(Me\mathbf{TzQn})]^+$ and $[Ir(\mathbf{ppy})_2(Me\mathbf{TziQn})]^+$ were synthesised from their neutral analogues. Methylation of all the neutral species was performed by treatment with methyl trifluoromethanesulphonate, followed by metathesis with ammonium hexafluorophosphate (**Figure 2.9**).

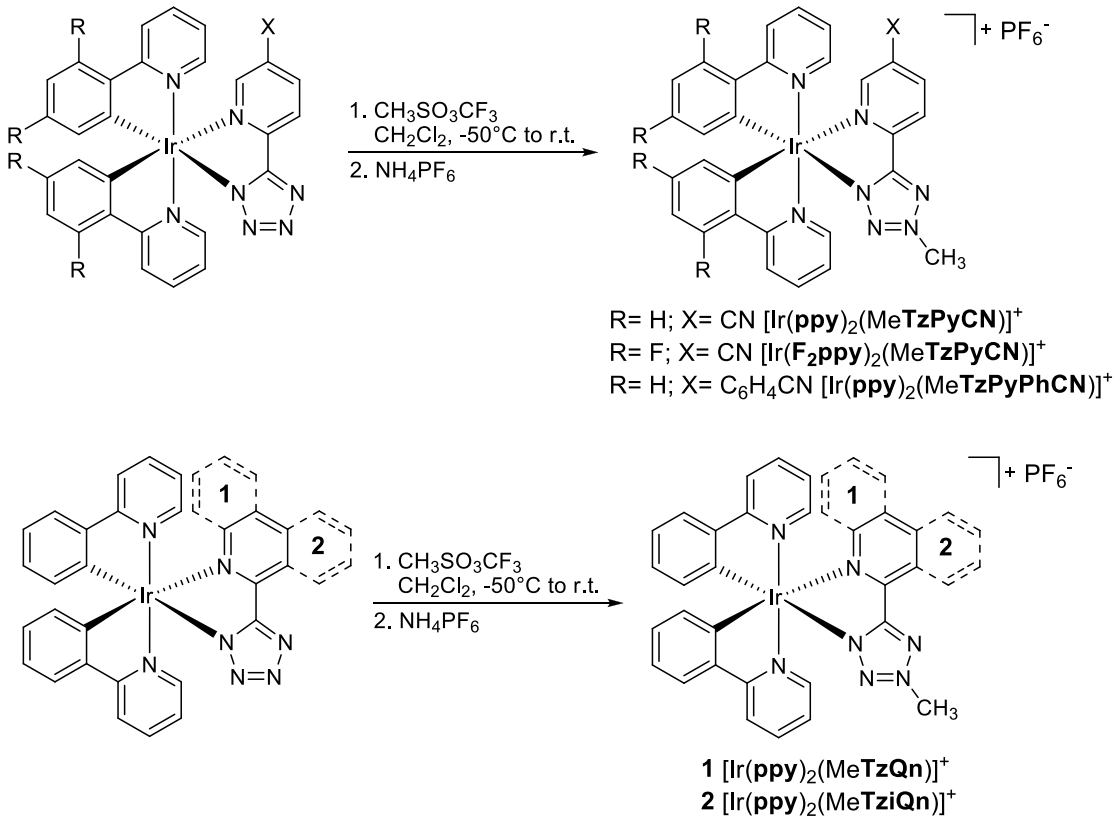

Figure 2.9 Scheme of the synthetic procedures for $[Ir(\mathbf{ppy})_2(Me\mathbf{TzPyCN})]^+$, $[Ir(\mathbf{F_2ppy})_2(Me\mathbf{TzPyCN})]^+$, $[Ir(\mathbf{ppy})_2(Me\mathbf{TzPyPhCN})]^+$, $[Ir(\mathbf{ppy})_2(Me\mathbf{TzQn})]^+$ and $[Ir(\mathbf{ppy})_2(Me\mathbf{TziQn})]^+$.

The regioselective methylation at the N3 position of the tetrazolato ring was achieved by using low temperature (-50 °C), avoiding the formation of a mixture of N2, N3 and N4 isomers. The use of a slightly excess of methyl trifluoromethanesulphonate ensured the complete conversion of the neutral starting materials into the cationic products. All the methylated complexes could be isolated with acceptable purity and high yield by simple extraction from the crude mixture and no column chromatography work-up was required.

The ^{1}H NMR and ^{13}C NMR spectra clearly indicate the presence of one methyl group which resonates around 4.55 and 42.5 ppm, respectively. In addition, the downfield shift of the tetrazolic carbon $\mathbf{C_T}$ from *ca.* 163.5 ppm for neutral [Ir(**ppy**)$_2$(**TzPyCN**)], [Ir(**F$_2$ppy**)$_2$(**TzPyCN**)] and [Ir(**ppy**)$_2$(**TzPyPhCN**)] to *ca.* 166.7 ppm for cationic [Ir(**ppy**)$_2$(Me**TzPyCN**)]$^+$, [Ir(**F$_2$ppy**)$_2$(Me**TzPyCN**)]$^+$ and [Ir(**ppy**)$_2$(Me**TzPyPhCN**)]$^+$ (**Figure 2.10**) supports the hypothesis of methylation in N3 position, as previously demonstrated by Stagni *et al.*.[236] In the case of [Ir(**ppy**)$_2$(**TzQn**)] and [Ir(**ppy**)$_2$(**TziQn**)] the same phenomenon is observed, but due to the higher degree of conjugation of the tetrazolate ligand, the $\mathbf{C_T}$ signal was at slightly higher resonance, shifting from *ca.* 166.0 ppm to *ca.* 168.0 ppm (**Figure 2.11**).

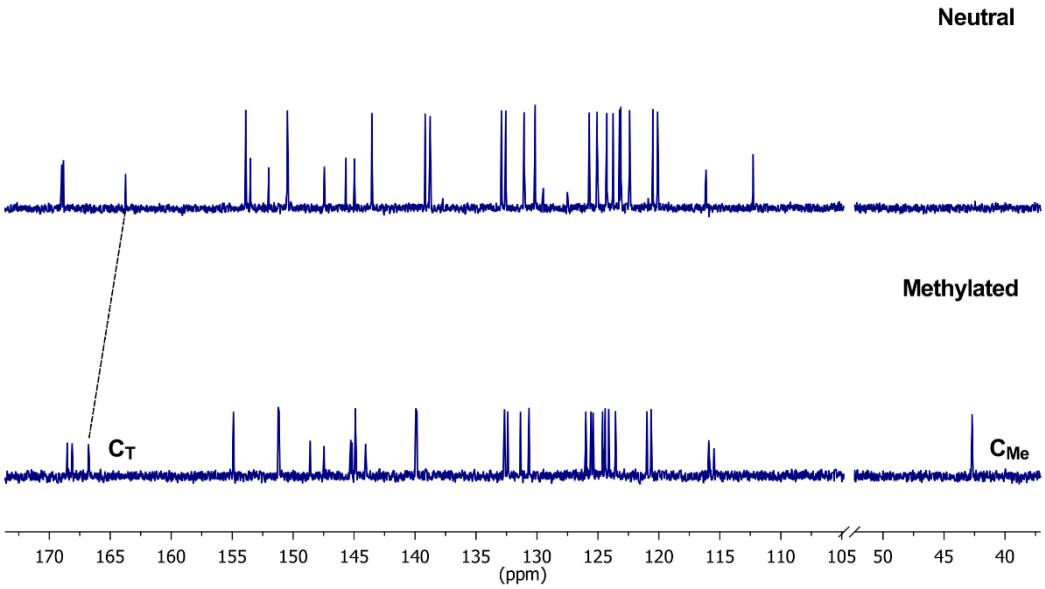

Figure 2.10 ^{13}C NMR in acetone-d_6 for the neutral complex [Ir(**ppy**)$_2$(**TzPyCN**)] (top) compared to the methylated analogous [Ir(**ppy**)$_2$(Me**TzPyCN**)]$^+$ (bottom).

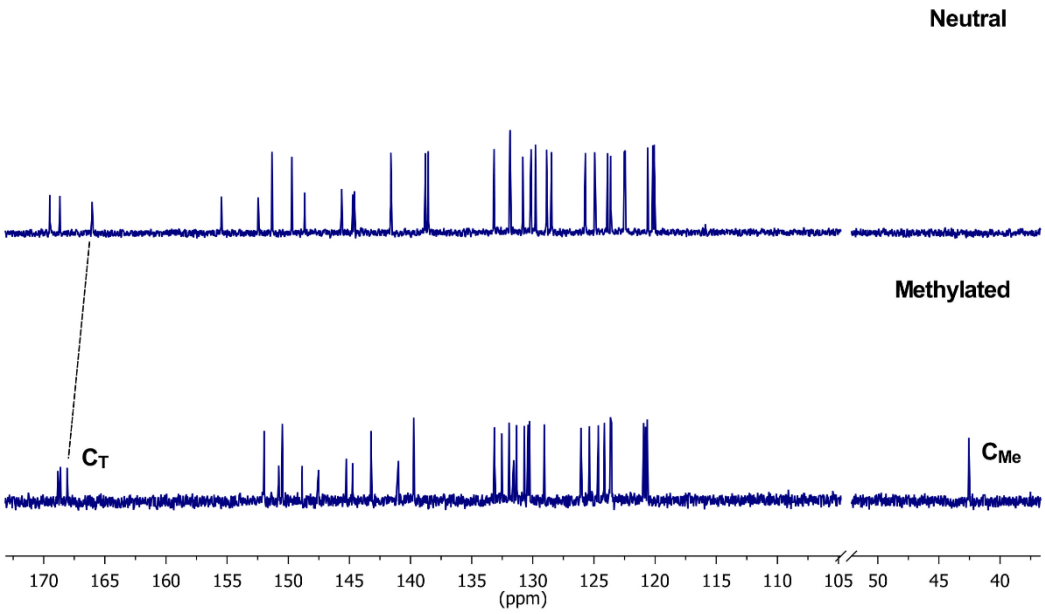

Figure 2.11 ^{13}C NMR in acetone-d_6 for the neutral complex [Ir(**ppy**)$_2$(**TzQn**)] (top) compared to the methylated analogous [Ir(**ppy**)$_2$(Me**TzQn**)]$^+$ (bottom).

The crystallographic analysis on [Ir(**ppy**)$_2$(Me**TzPyPhCN**)]$^+$ highlights again the tetrazolic N3 nitrogen as specific site for methylation to occur. The complex crystallised in monocline space group *P*2/*n*, as visible in **Figure 2.12**. The coordination sphere around the metal centre is consistent with the one obtained for the neutral [Ir(**F$_2$ppy**)$_2$(**TzPyCN**)]. The crystallographic data can be found in Appendix A, **Table A.3** – **Table A.4**.

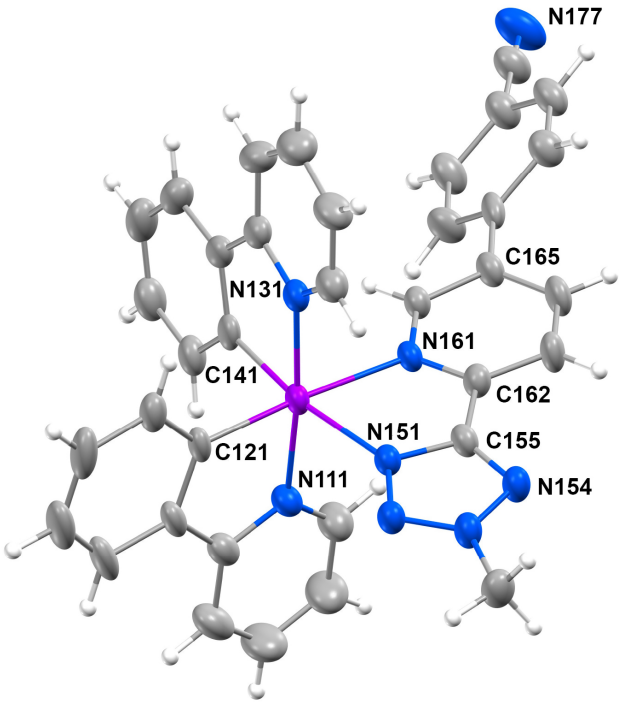

Figure 2.12 X-ray crystal structure of [Ir(**ppy**)$_2$(Me**TzPyCN**)]$^+$, with displacement ellipsoids drawn at the 50% probability level. The counter anion (PF_6^-) is omitted for clarity.

2.4 Photophysical Investigation

2.4.1 Absorption in Dichloromethane

A summary of the absorption properties of the iridium(III) complexes in diluted dichloromethane solutions is listed in **Table 2.1**.

Table 2.1 Absorption data of dichloromethane solutions (10^{-5} M) of the reported complexes.

Complex	λ_{abs} [nm] (10^4 ε [$M^{-1}cm^{-1}$])
[Ir(**ppy**)$_2$(**TzPyCN**)]	263 (6.57), 339 (1.59), 382 (1.09), 420 (0.58)
[Ir(**F$_2$ppy**)$_2$(**TzPyCN**)]	256 (5.20), 364 (0.95)
[Ir(**ppy**)$_2$(**TzPyPhCN**)]	268 (3.95), 290 (3.64), 345 (0.58), 423 (0.27)
[Ir(**ppy**)$_2$(Me**TzPyCN**)]$^+$	266 (8.93), 376 (1.44)
[Ir(**F$_2$ppy**)$_2$(Me**TzPyCN**)]$^+$	250 (3.56), 316 (1.28), 356 (0.58)
[Ir(**ppy**)$_2$(Me**TzPyPhCN**)]$^+$	267 (3.39), 290 (3.14), 378 (0.40)
[Ir(**ppy**)$_2$(**TzQn**)]	263 (8.44), 345 (1.97), 428 (0.42)
[Ir(**ppy**)$_2$(**TziQn**)]	260 (9.77), 340 (3.13), 424 (0.75)
[Ir(**ppy**)$_2$(Me**TzQn**)]$^+$	257 (9.29), 376 (0.95)
[Ir(**ppy**)$_2$(Me**TziQn**)]$^+$	253 (6.96), 303 (2.45), 371 (1.24)

The absorption spectra from air-equilibrated dichloromethane solutions are presented from **Figure 2.13** to **Figure 2.16**. All the iridium complexes show intense absorption bands in the UV region between 250 – 300 nm, which are associated with ligand-centred (LC) π-π* transitions, involving the cyclometalated **ppy** and **F$_2$ppy** ligands. On the other hand, the weaker and broader bands tailing off into the visible region of the spectra are ascribed to ligand-to-ligand (LLCT) and metal-to-ligand charge transfer (MLCT) transitions.[236] Since the iridium metal centre possesses high spin-orbit coupling constant (ξ = 3909 cm^{-1}),[76] these bands are attributed to singlet-to-singlet and singlet-to-triplet LLCT/MLCT transitions, with the latter being red-shifted in the spectrum due to its lower energy.

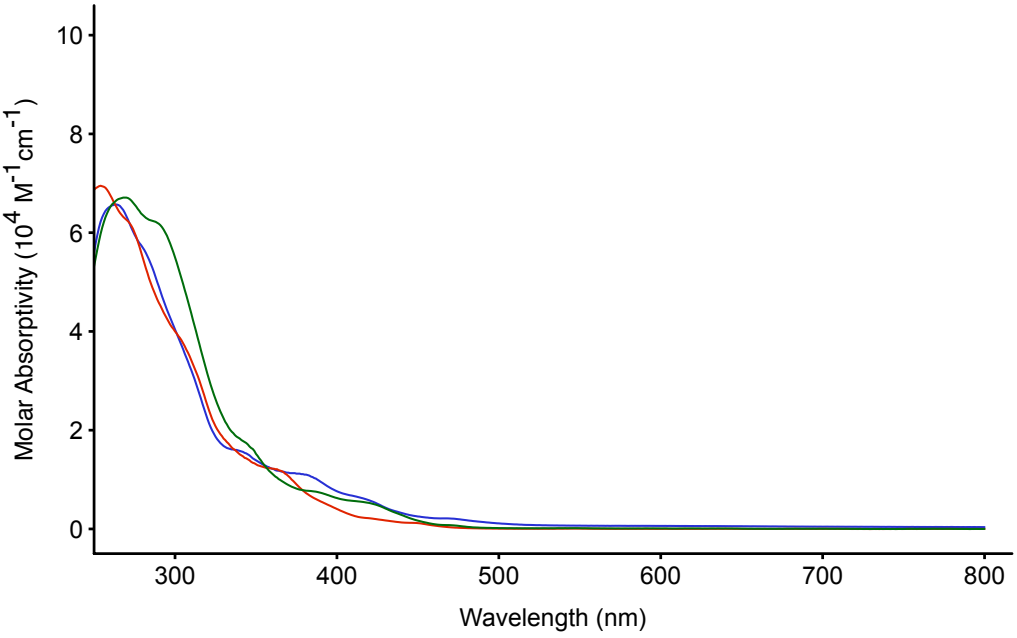

Figure 2.13 Absorption profiles of [Ir(**ppy**)$_2$(**TzPyCN**)] (blue), [Ir(**F$_2$ppy**)$_2$(**TzPyCN**)] (red) and [Ir(**ppy**)$_2$(**TzPyPhCN**)] (green) in dichloromethane.

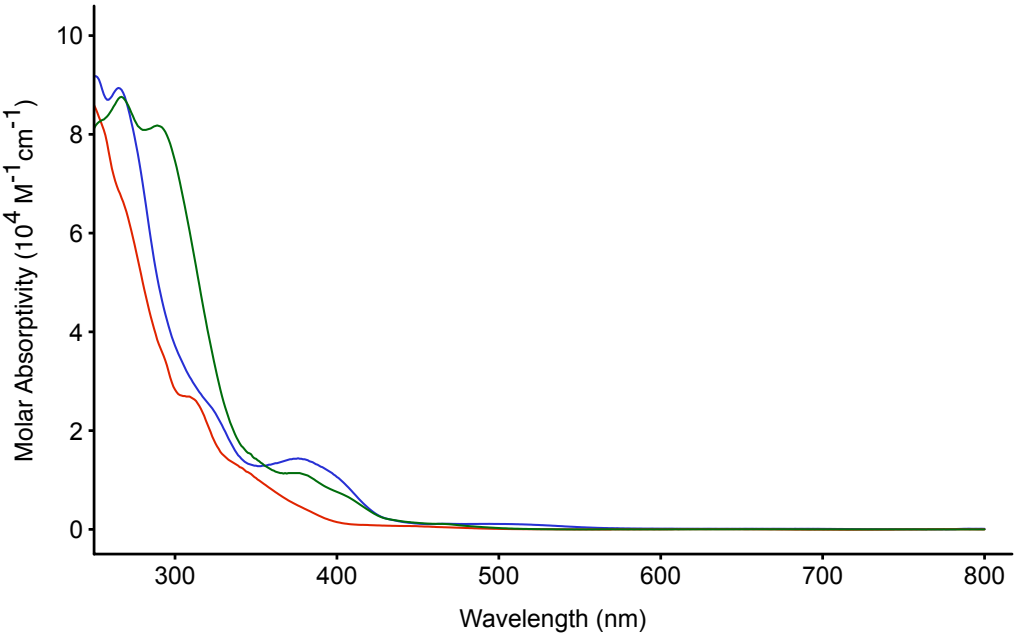

Figure 2.14 Absorption profiles of [Ir(**ppy**)$_2$(Me**TzPyCN**)]$^+$ (blue), [Ir(**F$_2$ppy**)$_2$(Me**TzPyCN**)]$^+$ (red) and [Ir(**ppy**)$_2$(Me**TzPyPhCN**)]$^+$ (green) in dichloromethane.

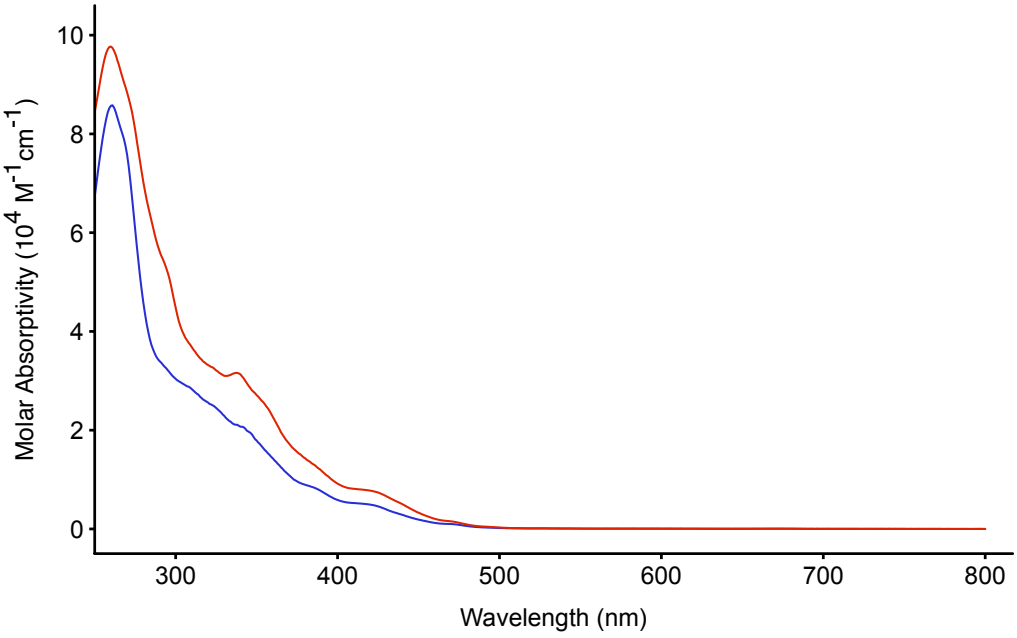

Figure 2.15 Absorption profiles of [Ir(**ppy**)$_2$(**TzQn**)] (blue) and [Ir(**ppy**)$_2$(**TziQn**)] (red) in dichloromethane.

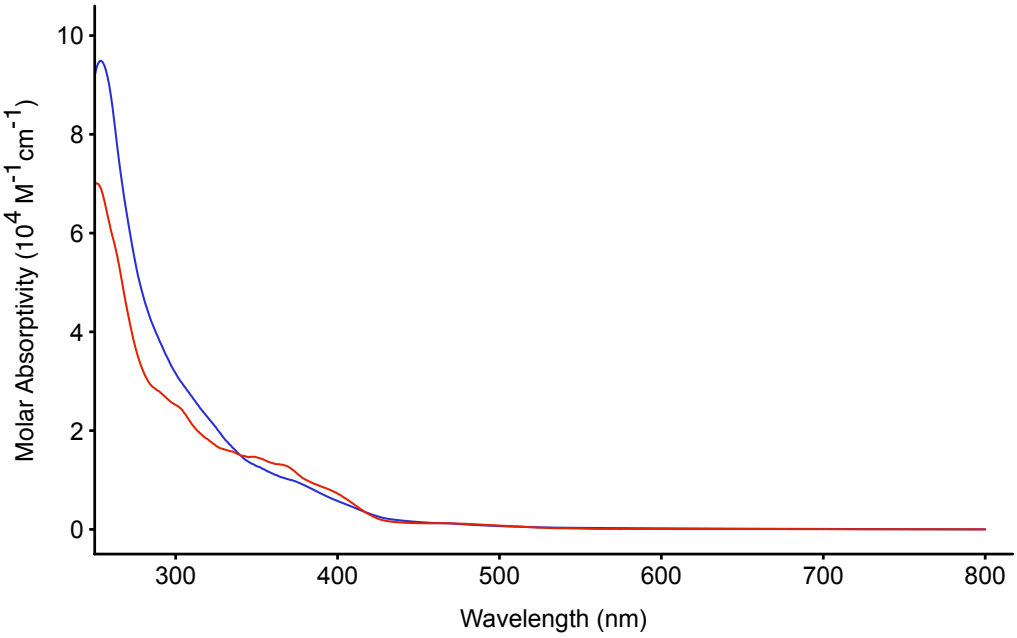

Figure 2.16 Absorption profiles of [Ir(**ppy**)$_2$(Me**TzQn**)]$^+$ (blue) and [Ir(**ppy**)$_2$(Me**TziQn**)]$^+$ (red) in dichloromethane.

2.4.2 Emission Properties in Dichloromethane

All the emission properties of the iridium(III) family are summarised in **Table 2.2**. Excitation of the iridium complexes at 375 nm results in orange to red emission in air-equilibrated dichloromethane solutions, and the emission spectra measured at 298 K are shown from **Figure 2.17** to **Figure 2.20**.

Table 2.2 Photophysical data of dichloromethane solutions (10^{-5} M) of the reported complexes.

Complex	λ_{em} [nm]	τ_{aer} [ns][a]	τ_{deaer} [ns][a]	Φ_{aer}[b]	Φ_{deaer}[b]
[Ir(**ppy**)$_2$(**TzPyCN**)]	618	131	529	0.055	0.397
[Ir(**F$_2$ppy**)$_2$(**TzPyCN**)]	542	140	697	0.042	0.406
[Ir(**ppy**)$_2$(**TzPyPhCN**)]	560	114	880	0.023	0.149
[Ir(**ppy**)$_2$(Me**TzPyCN**)]$^+$	680	31 (79), 168 (21)	35(61), 362 (39)	0.012	0.014
[Ir(**F$_2$ppy**)$_2$(Me**TzPyCN**)]$^+$	600	287	551	0.057	0.118
[Ir(**ppy**)$_2$(Me**TzPyPhCN**)]$^+$	600	184	434	0.057	0.093
[Ir(**ppy**)$_2$(**TzQn**)]	580	153	831	0.021	0.065
[Ir(**ppy**)$_2$(**TziQn**)]	535, 575, 620	497	6713	0.036	0.114
[Ir(**ppy**)$_2$(Me**TzQn**)]$^+$	635	218	546	0.028	0.043
[Ir(**ppy**)$_2$(Me**TziQn**)]$^+$	640	208	485	0.049	0.063

[a] For the biexponential excited state lifetime (τ), the relative weights of the exponential curves are reported in parentheses. [b] Measured versus [Ru(**bpy**)$_3$]$^{2+}$ in H_2O (Φ_r = 0.028).[274]

The neutral complexes [Ir(**ppy**)$_2$(**TzPyCN**)], [Ir(**F$_2$ppy**)$_2$(**TzPyCN**)], and [Ir(**ppy**)$_2$(**TzPyPhCN**)] are characterised by broad and featureless emission bands, that are typical for radiative decays from excited states of charge transfer character (**Figure 2.17**).[76] The [Ir(**ppy**)$_2$(**TzPyCN**)] complex presents a red-shifted maximum at 618 nm, which is ascribed to a stabilisation of the unoccupied π^* orbitals localised on the **TzPyCN**$^-$ ligand caused by the electron-withdrawing nature of the nitrile functional

group.[236] As expected, the addition of electron-withdrawing fluoride substituents on the **ppy** ligands causes a blue shift of the emission maximum for [Ir(**F$_2$ppy**)$_2$(**TzPyCN**)] (λ_{em} = 542 nm), as a consequence of the stabilisation of the occupied π orbitals of the ligands and iridium *5d* orbitals composing the mixed LLCT(**F$_2$ppy**→**TzPyCN**) and MLCT(Ir→**TzPyCN**) transition.[236] The emission maximum of [Ir(**ppy**)$_2$(**TzPyPhCN**)] at 560 nm is again blue-shifted with respect to [Ir(**ppy**)$_2$(**TzPyCN**)], albeit to a lesser extent when compared to [Ir(**F$_2$ppy**)$_2$(**TzPyCN**)]. This trend is ascribed to the fact that the electron-withdrawing effect of the nitrile group on the pyridyltetrazole π* system is decreased by the addition of a phenyl ring spacer.

The emission profiles of the methylated complexes [Ir(**ppy**)$_2$(Me**TzPyCN**)]$^+$ (λ_{em} = 680 nm), [Ir(**F$_2$ppy**)$_2$(Me**TzPyCN**)]$^+$ (λ_{em} = 600 nm), and [Ir(**ppy**)$_2$(Me**TzPyPhCN**)]$^+$ (λ_{em} = 600 nm) are red-shifted compared to their corresponding neutral complexes (**Figure 2.18**). Once more, this red shift demonstrates that the π* system of the pyridyltetrazole ligand acts as an electron acceptor in the charge transfer transitions.[236,237] When comparing the emission maxima of these three methylated iridium complexes, the trend for the emission properties is analogous to that observed for their neutral counterparts, with the most red-shifted emission originating from [Ir(**ppy**)$_2$(Me**TzPyCN**)]$^+$.

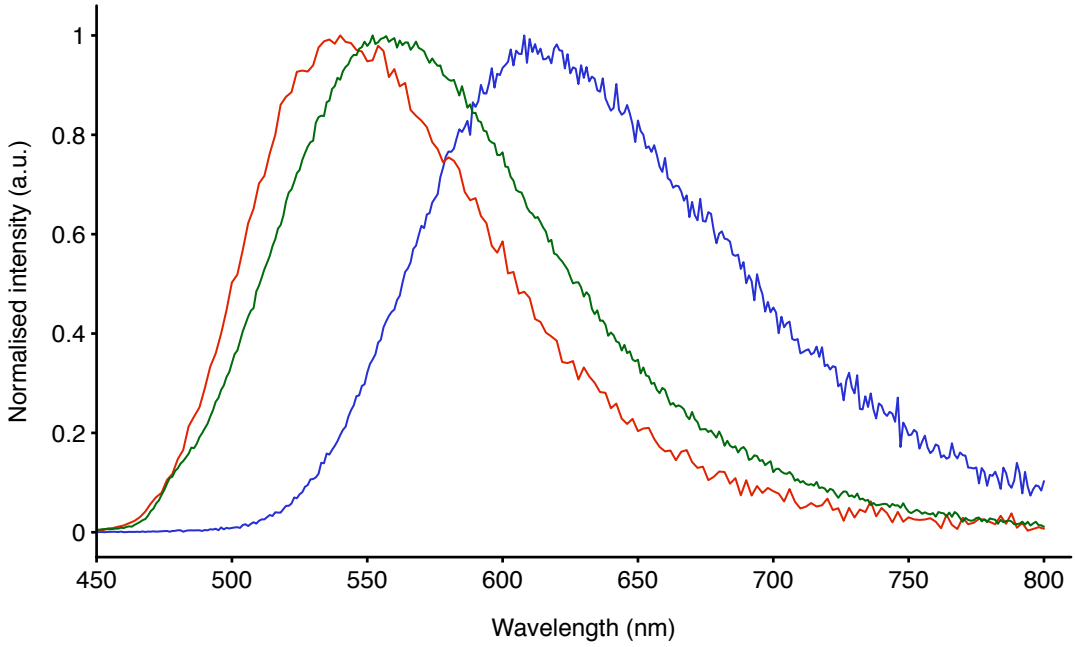

Figure 2.17 Normalised emission profiles of [Ir(**ppy**)$_2$(**TzPyCN**)] (blue), [Ir(**F$_2$ppy**)$_2$(**TzPyCN**)] (red) and [Ir(**ppy**)$_2$(**TzPyPhCN**)] (green) in dichloromethane.

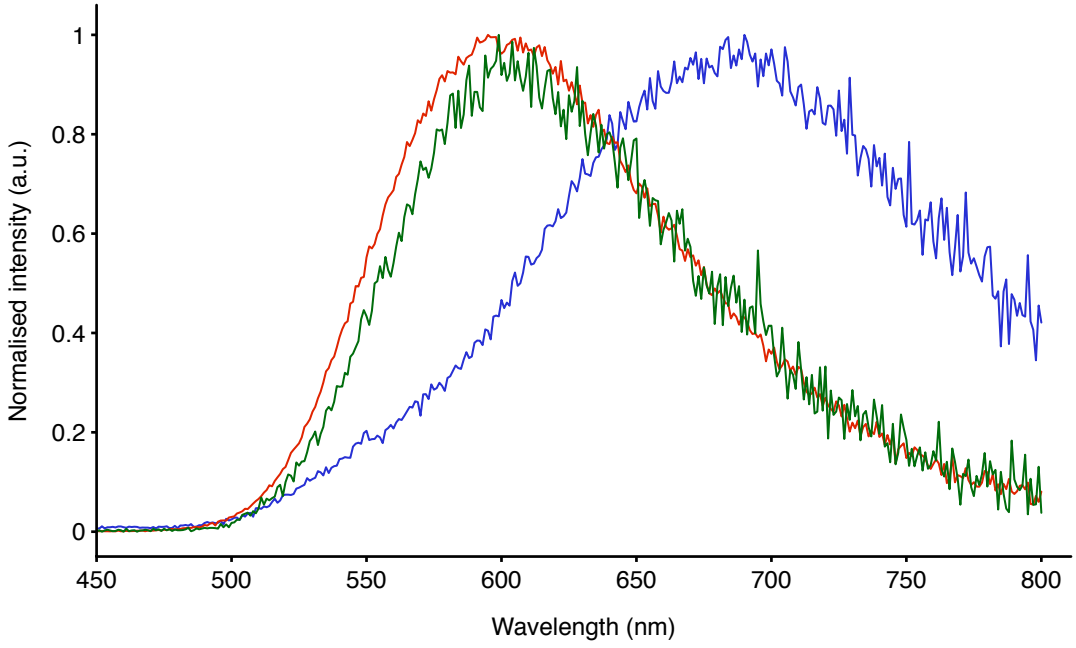

Figure 2.18 Normalised emission profiles of [Ir(**ppy**)$_2$(Me**TzPyCN**)]$^+$ (blue), [Ir(**F$_2$ppy**)$_2$(Me**TzPyCN**)]$^+$ (red) and [Ir(**ppy**)$_2$(Me**TzPyPhCN**)]$^+$ (green) in dichloromethane.

The iridium complexes containing quinolyl and isoquinolyl-functionalised tetrazolate ligands, [Ir(**ppy**)$_2$(**TzQn**)] and [Ir(**ppy**)$_2$(**TziQn**)], reveal emission bands that are similarly ranging between 500 and 750 nm (**Figure 2.19**). Compared to the previously published complex [Ir(**ppy**)$_2$(**TzPy**)],[236] where **TzPy**$^-$ is 5-(2'-pyridyl)tetrazolate, displaying a structured emission band with peaks at 481 and 510 nm, the complexes [Ir(**ppy**)$_2$(**TzQn**)] and [Ir(**ppy**)$_2$(**TziQn**)] present a red-shifted emission that is rationalised by the increased π conjugation on passing from a phenyl to a quinolyl or isoquinolyl substituent. The structures of these two bands appear to be quite different. The emission profile of [Ir(**ppy**)$_2$(**TzQn**)] is broad and structureless, whereas that of [Ir(**ppy**)$_2$(**TziQn**)] appears to be structured with a vibronic progression spaced around 1,300 cm^{-1}. Furthermore, the excited state lifetime of [Ir(**ppy**)$_2$(**TziQn**)] in air-equilibrated solution is significantly longer than that of [Ir(**ppy**)$_2$(**TzQn**)], with even a more prominent elongation in deaerated solution, with values of 831 and 6713 ns, respectively (**Table 2.2**). These results suggest the presence of a more dominating charge transfer character for the emission of [Ir(**ppy**)$_2$(**TzQn**)].[256] On the other hand, the excited state of [Ir(**ppy**)$_2$(**TziQn**)] seems to be strongly influenced by the LC character, as indicated by the long excited state decay lifetime in degassed dichloromethane solution.[256,275] For a better understanding of the different behaviour of these two complexes, time-dependent density functional theory (TD-DFT) analysis has been performed and will be discussed in section 2.4.3.

As expected, the emission profiles of the methylated [Ir(**ppy**)$_2$(Me**TzQn**)]$^+$ and [Ir(**ppy**)$_2$(Me**TziQn**)]$^+$ complexes appear red-shifted, broad, and structureless, as depicted in **Figure 2.20**.

For all the complexes, an elongation of the excited state lifetime decay (τ) and increase of photoluminescence quantum yield (Φ) values is observed upon degassing. This behaviour is indicative of the triplet spin multiplicity of the excited state.[76,77]

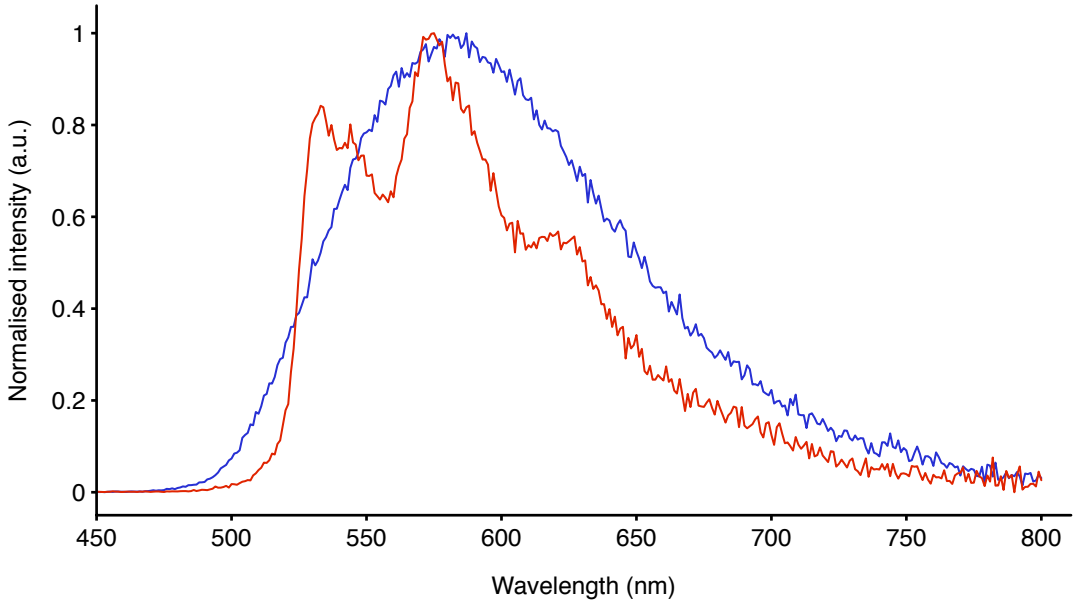

Figure 2.19 Normalised emission profiles of [Ir(**ppy**)$_2$(**TzQn**)] (blue) and [Ir(**ppy**)$_2$(**TziQn**)] (red) in dichloromethane.

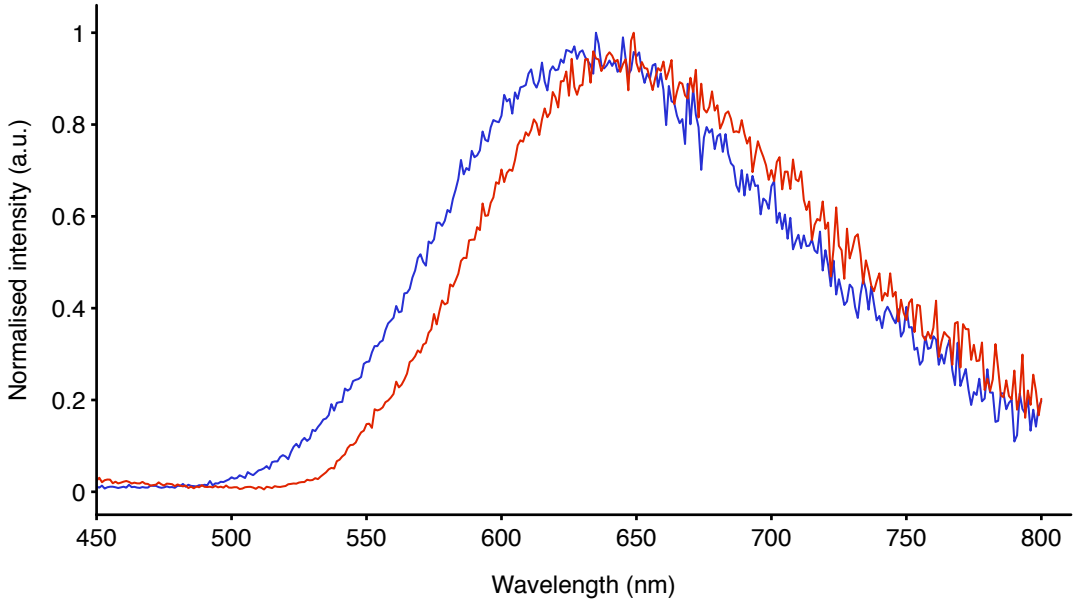

Figure 2.20 Normalised emission profiles of [Ir(**ppy**)$_2$(Me**TzQn**)]$^+$ (blue) and [Ir(**ppy**)$_2$(Me**TziQn**)]$^+$ (red) in dichloromethane.

The radiative (k_r) and non-radiative (k_{nr}) decay constants of the majority of the investigated iridium(III) complexes were calculated for degassed dichloromethane solutions and reported in **Table 2.3**. Unfortunately, the k_r and k_{nr} values of [Ir(**ppy**)$_2$(Me**TzPyCN**)]$^+$ could not have been evaluated due to the biexponential nature of the excited state lifetime of the latter.

Table 2.3 Radiative (k_r) and non-radiative (k_{nr}) decay constants in degassed dichloromethane solutions.

Complex	k_r $10^6[s^{-1}]$[a]	k_{nr} $10^6[s^{-1}]$[b]
[Ir(**ppy**)$_2$(**TzPyCN**)]	0.751	1.140
[Ir(**F$_2$ppy**)$_2$(**TzPyCN**)]	0.583	0.852
[Ir(**ppy**)$_2$(**TzPyPhCN**)]	0.169	0.967
[Ir(**ppy**)$_2$(Me**TzPyCN**)]$^+$	-[c]	-[c]
[Ir(**F$_2$ppy**)$_2$(Me**TzPyCN**)]$^+$	0.214	1.601
[Ir(**ppy**)$_2$(Me**TzPyPhCN**)]$^+$	0.214	2.090
[Ir(**ppy**)$_2$(**TzQn**)]	0.078	1.125
[Ir(**ppy**)$_2$(**TziQn**)]	0.021	0.128
[Ir(**ppy**)$_2$(Me**TzQn**)]$^+$	0.079	1.753
[Ir(**ppy**)$_2$(Me**TziQn**)]$^+$	0.130	1.923

[a] Calculated as [Φ/τ] using measurements from deaerated dichloromethane solutions. [b] Calculated as [$(1-\Phi)/\tau$] using measurements from deaerated dichloromethane solutions. [c] The lifetime shows a biexponential nature and so did not allowed the calculation of k_r and k_{nr}.

In general, the neutral [Ir(**ppy**)$_2$(**TzPyCN**)], [Ir(**F$_2$ppy**)$_2$(**TzPyCN**)] and [Ir(**ppy**)$_2$(**TzPyPhCN**)] display higher k_r constants with respect to [Ir(**ppy**)$_2$(**TzQn**)] and [Ir(**ppy**)$_2$(**TziQn**)], which are associated with a less conjugation degree of the pyridyl-tetrazolate ligand in comparison to the (iso)quinolyl-tetrazolate moieties. Previous studies have shown how a more conjugated ligand can minimise the spin-orbit coupling effect of the metal centre, reducing the intersystem crossing rate constant (k_{ISC}), and lowering the k_r.[230,276] This effect can also be highlighted by comparing the smaller radiative decay constant of [Ir(**ppy**)$_2$(**TzPyPhCN**)], which

carries a phenyl spacer in the tetrazolate ligand, with the ones of [Ir(**ppy**)$_2$(**TzPyCN**)] and [Ir(**F$_2$ppy**)$_2$(**TzPyCN**)], where no spacer is present.

The cationic [Ir(**F$_2$ppy**)$_2$(Me**TzPyCN**)]$^+$, [Ir(**ppy**)$_2$(Me**TzPyPhCN**)]$^+$, [Ir(**ppy**)$_2$(Me**TzQn**)]$^+$ and [Ir(**ppy**)$_2$(Me**TziQn**)]$^+$ show the same trend that their neutral analogues, with one order of magnitude of k_r greater for the cyano-functionalised complexes in comparison to the quinolyl and isoquinolyl-functionalised species.

Furthermore, the non-radiative constants (k_{nr}) are smaller than the radiative decay values for almost all the complexes, with higher values for the cationic species. This result explains the better luminescent properties, such as higher quantum yield and longer excited state lifetime, for the neutral complexes with respect to their methylated analogues.

2.4.3 TD-DFT Analysis

TD-DFT analysis have been performed on [Ir(**ppy**)$_2$(**TzQn**)] and [Ir(**ppy**)$_2$(**TziQn**)] to better explain the difference in the photophysical properties of these complexes.
The computational calculations highlight that for [Ir(**ppy**)$_2$(**TzQn**)] in the single state, the HOMO-type orbitals are mainly localised on the phenyl ring of the **ppy** ligands and the iridium metal centre, while the LUMO-type orbitals are on the quinoline ring (LUMO) and also delocalised on the entire cyclometalated **ppy** ligands (LUMO+N; N = 1 – 5), as showed in **Figure 2.21**.

In the case of [Ir(**ppy**)$_2$(**TziQn**)], the localisation of the HOMO and LUMO orbitals is similar to the one of [Ir(**ppy**)$_2$(**TziQn**)], but there is also a contribution from the tetrazolate ligand in the case of HOMO-4 (**Figure 2.22**). The HOMO-4→LUMO transition corresponding to a LC transition localised on the **TziQn**$^-$ ligand. Additionally, the computational calculations also confirm that the lower energy bands for both the complexes are mainly composed of MLCT and LLCT transitions. The full TD-DFT data can be found in Appendix A, **Table A.5** – **Table A.6**.

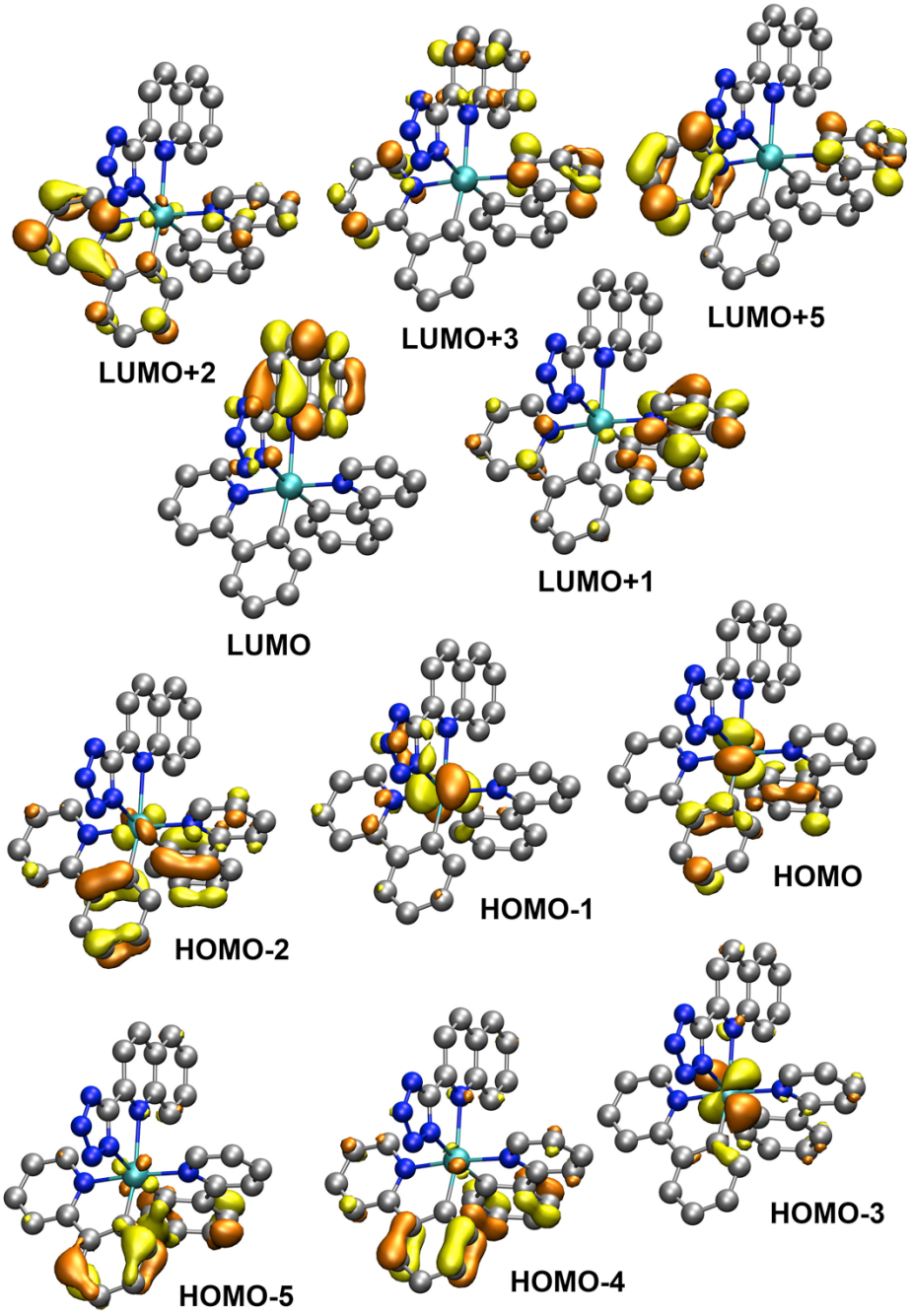

Figure 2.21 Localisation of the HOMO-5 to the LUMO+5 for [Ir(**ppy**)$_2$(**TzQn**)]. The simulated orbitals are spaced vertically relative to their energy.

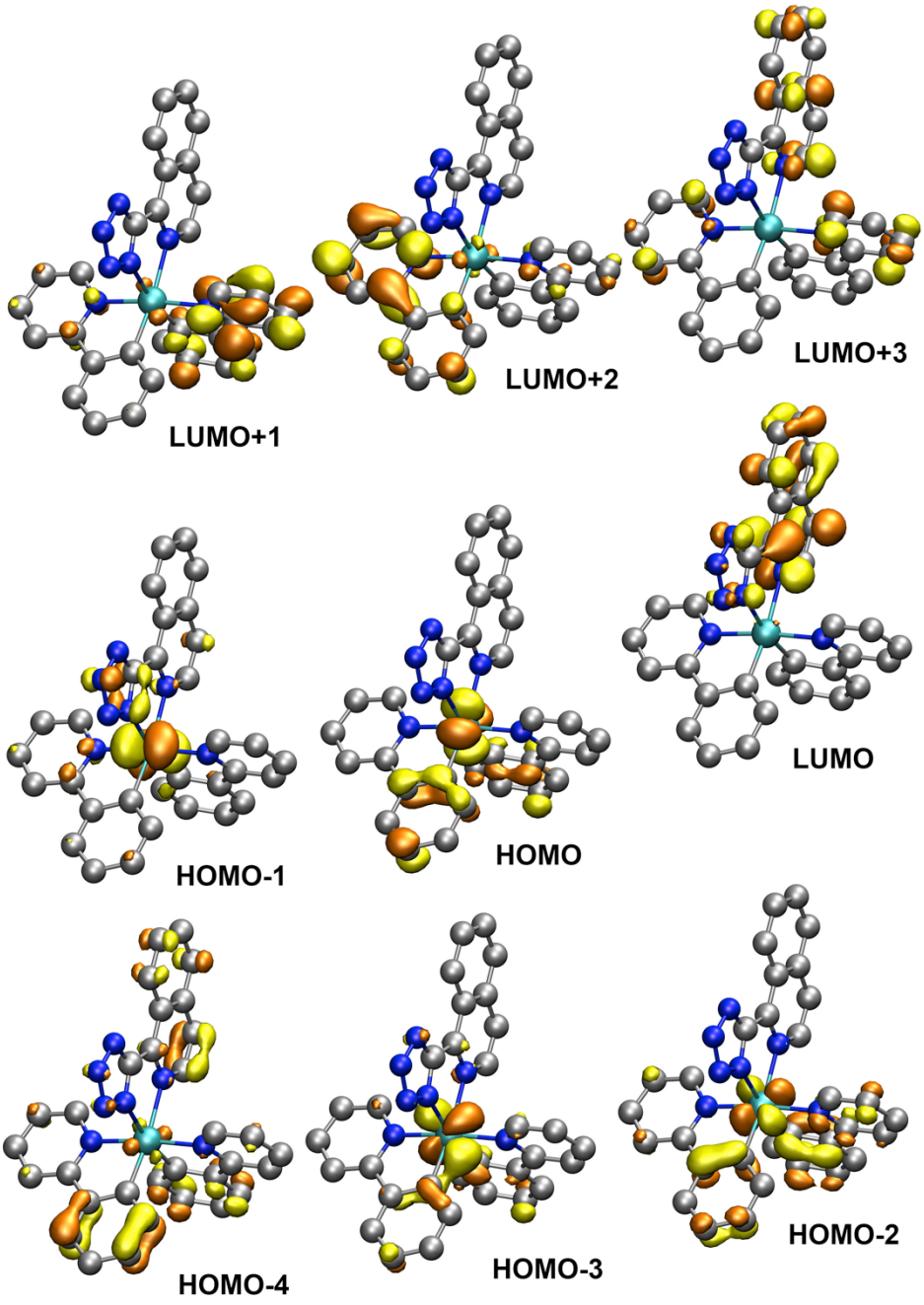

Figure 2.22 Localisation of HOMO-4 to the LUMO+3 for [Ir(**ppy**)$_2$(**TziQn**)]. The simulated orbitals are spaced vertically relative to their energy.

2.4.4 Absorption in Aqueous and Lipophilic Solvents

The photophysical behaviour in aqueous and lipophilic solvents has been investigated to assess the applicability of the iridium(III) tetrazolato complexes in a biological environment.

The aqueous media contained 0.2% DMSO to favour the solubilisation of the iridium complexes. These solvents have been chosen to highlight possible modulations of the photophysical properties of the probes in different cellular organelles. In particular, lysosomal pH fluid solution was used to mimic the acidic lysosomes, whereas PBS would resemble the cytoplasmic conditions. Moreover the choice of ethyl laurate was driven by the necessity to explore the photophysical properties of the iridium complexes in lipid-rich compartments, such as membranes, endoplasmic reticulum and lipid droplets.

All the absorption data have been summarised in **Table 2.4** and **Table 2.5** for the cyano and (iso)quinolyl-substituted tetrazolato complexes, respectively.
The absorption profiles follow the same trend that the ones presented in section 2.4.1, **Table 2.1**. All the iridium complexes display a more intense spin-allowed ligand-centred (LC) π-π* transitions in the UV region (250 – 300 nm) and a combination of spin-allowed and spin-forbidden ligand-to-ligand (LLCT) and metal-to-ligand charged transfer (MLCT) absorption shoulders or bands in the visible region (350 – 440 nm) of the spectra.[236]

The molar absorptivity (ε) of the complexes in the different solvent systems does not follow a well-defined trend. In general, for aqueous media, methylated complexes show higher molar absorptivity coefficients in comparison to the ones in the lipophilic ethyl laurate. The opposite trend has been found for the neutral species, which display higher lipophilicity and are more likely to slightly aggregate in aqueous solutions.

Absorption spectra of the neutral [Ir(**F$_2$ppy**)$_2$(**TzPyCN**)] and [Ir(**ppy**)$_2$(**TziQn**)] and the charged [Ir(**F$_2$ppy**)$_2$(Me**TzPyCN**)]$^+$ and [Ir(**ppy**)$_2$(Me**TziQn**)]$^+$ complexes have been reported, as example, from **Figure 2.23** to **Figure 2.26**. The absorption profiles of all the other iridium(III) complexes can be found in Appendix A, **Figure A.1** – **Figure A.6**.

Table 2.4 Absorption data of aqueous and lipophilic solutions (10^{-5} M) of the reported cyano-substituted complexes.

Complex	Solvent[a]	λ_{abs} [nm] (10^4 ε [$M^{-1}cm^{-1}$])
[Ir(**ppy**)$_2$ (**TzPyCN**)]	H_2O	253 (3.52), 377 (0.69)
	Lys. Fluid	254 (4.59), 380 (1.15)
	PBS	260 (5.21), 372 (1.47)
	Ethyl Laurate	258 (7.67), 271 (7.35), 341 (1.98), 378 (1.23)
[Ir(**F$_2$ppy**)$_2$ (**TzPyCN**)]	H_2O	256 (4.83), 302 (3.36), 366 (1.16)
	Lys. Fluid	259 (3.62), 300 (2.64), 362 (1.10)
	PBS	258 (3.84), 306 (2.80), 366 (1.33)
	Ethyl Laurate	262 (9.18), 307 (5.17), 371 (1.44)
[Ir(**ppy**)$_2$ (**TzPyPhCN**)]	H_2O	286 (1.87), 350 (0.86), 421 (0.34)
	Lys. Fluid	262 (1.24), 319 (1.11), 372 (0.55)
	PBS	291 (1.31), 420 (0.38)
	Ethyl Laurate	266 (3.26), 355 (0.22)
[Ir(**ppy**)$_2$ (Me**TzPyCN**)]$^+$	H_2O	260 (4.44), 373 (0.59)
	Lys. Fluid	260 (6.08), 309 (2.01), 357 (0.96)
	PBS	261 (6.03), 308 (1.98), 357 (0.93)
	Ethyl Laurate	265 (2.45), 379 (0.18)
[Ir(**F$_2$ppy**)$_2$ (Me**TzPyCN**)]$^+$	H_2O	260 (4.12), 309 (1.55), 353 (0.66)
	Lys. Fluid	296 (1.84), 315 (1.49), 350 (0.70)
	PBS	260 (4.88), 309 (1.69), 353 (0.72)
	Ethyl Laurate	262 (3.27), 310 (1.19), 365 (0.42)
[Ir(**ppy**)$_2$ (Me**TzPyPhCN**)]$^+$	H_2O	264 (3.82), 390 (0.35)
	Lys. Fluid	264 (4.34), 373 (0.49)
	PBS	265 (4.35), 374 (0.54)
	Ethyl Laurate	270 (4.95), 289 (4.54), 345 (0.91), 387 (0.56)

[a] Aqueous solvents contain 0.2% DMSO.

Table 2.5 Absorption data of aqueous and lipophilic solutions (10^{-5} M) of the reported (iso)quinolyl-substituted complexes.

Complex	**Solvent**[a]	**λ_{abs} [nm] (10^4 ε [$M^{-1}cm^{-1}$])**
[Ir(**ppy**)$_2$ (**TzQn**)]	H_2O	266 (4.41), 350 (2.35), 425 (0.97)
	Lys. Fluid	265 (3.18), 350 (1.76), 430 (0.75)
	PBS	261 (3.19), 350 (2.07), 439 (0.89)
	Ethyl Laurate	265 (4.75), 343 (1.36), 433 (0.33)
[Ir(**ppy**)$_2$ (**TziQn**)]	H_2O	268 (3.42), 350 (2.00), 435 (0.80)
	Lys. Fluid	270 (3.53), 345 (2.35), 427 (1.08)
	PBS	257 (1.74), 293 (1.82), 352 (1.50), 4.27 (0.93)
	Ethyl Laurate	257 (8.09), 274 (7.78), 342 (3.21), 431 (0.77)
[Ir(**ppy**)$_2$ (Me**TzQn**)]$^+$	H_2O	251 (8.30), 307 (2.52), 364 (1.09)
	Lys. Fluid	251 (8.91), 310 (3.16), 365 (1.55)
	PBS	251 (8.53), 310 (3.00), 358 (1.56)
	Ethyl Laurate	255 (4.76), 306 (1.69), 350 (0.95)
[Ir(**ppy**)$_2$ (Me**TziQn**)]$^+$	H_2O	251 (6.64), 291 (2.60), 355 (1.36)
	Lys. Fluid	251 (6.38), 295 (2.42), 350 (1.41)
	PBS	251 (5.29), 295 (2.05), 350 (1.23)
	Ethyl Laurate	255 (6.15), 298 (2.69), 355 (1.52)

[a] Aqueous solvents contain 0.2% DMSO.

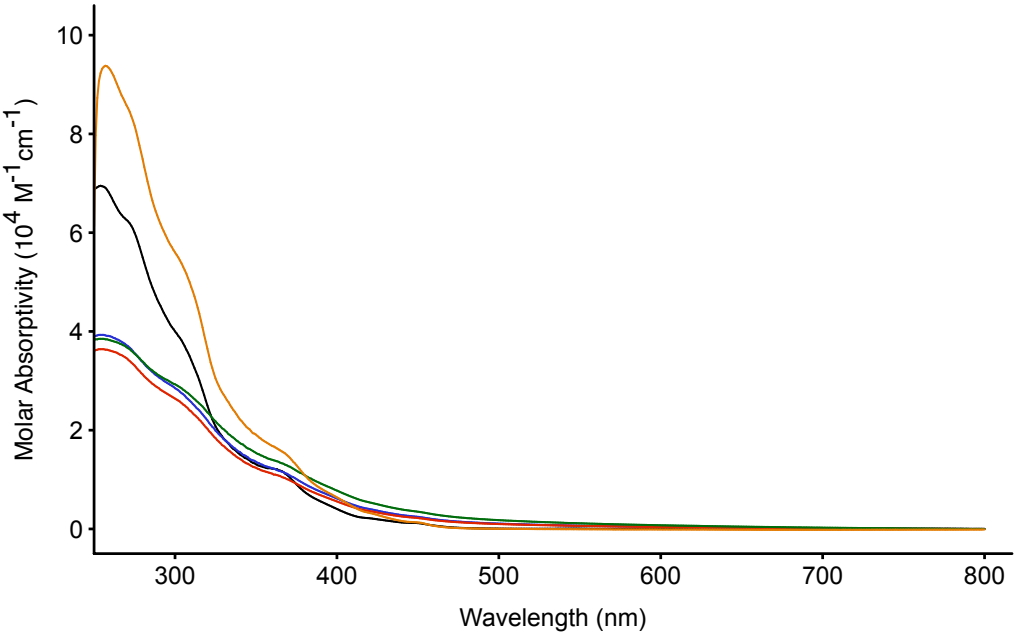

Figure 2.23 Absorption profiles of [Ir(**F$_2$ppy**)$_2$(**TzPyCN**)] in dichloromethane (black), H_2O (blue), lys. fluid (red), PBS (green) and ethyl laurate (orange).

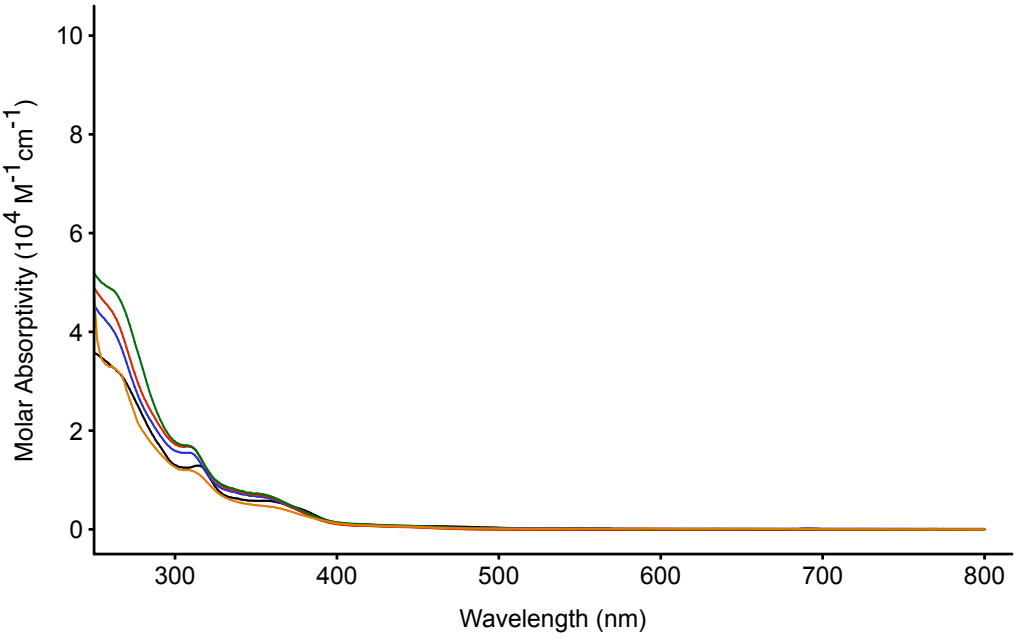

Figure 2.24 Absorption profiles of [Ir(**F$_2$ppy**)$_2$(Me**TzPyCN**)]$^+$ in dichloromethane (black), H_2O (blue), lys. fluid (red), PBS (green) and ethyl laurate (orange).

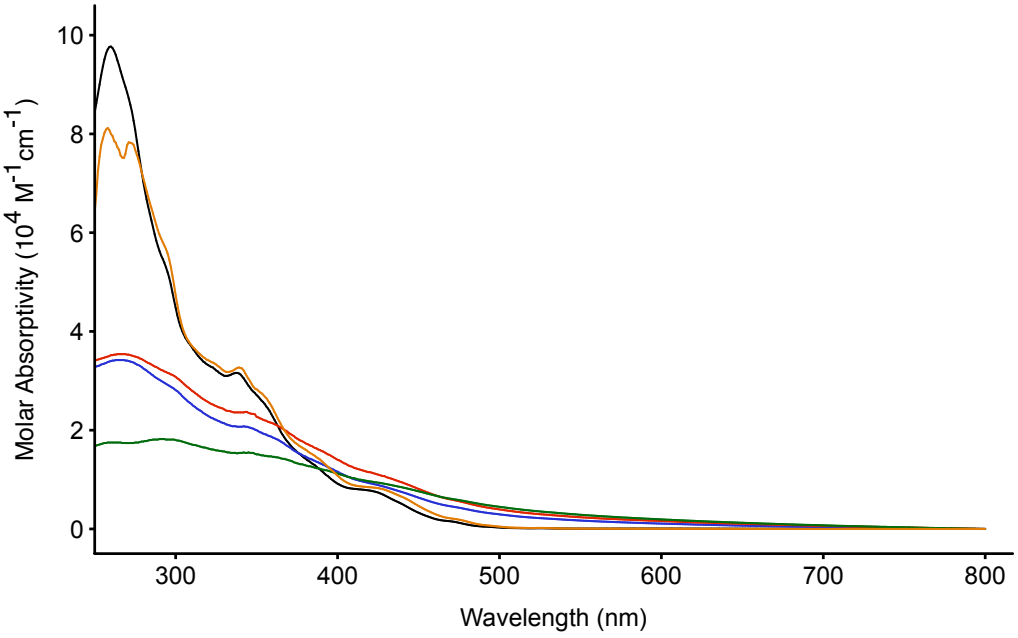

Figure 2.25 Absorption profiles of [Ir(**ppy**)$_2$(**TziQn**)] in dichloromethane (black), H_2O (blue), lys. fluid (red), PBS (green) and ethyl laurate (orange).

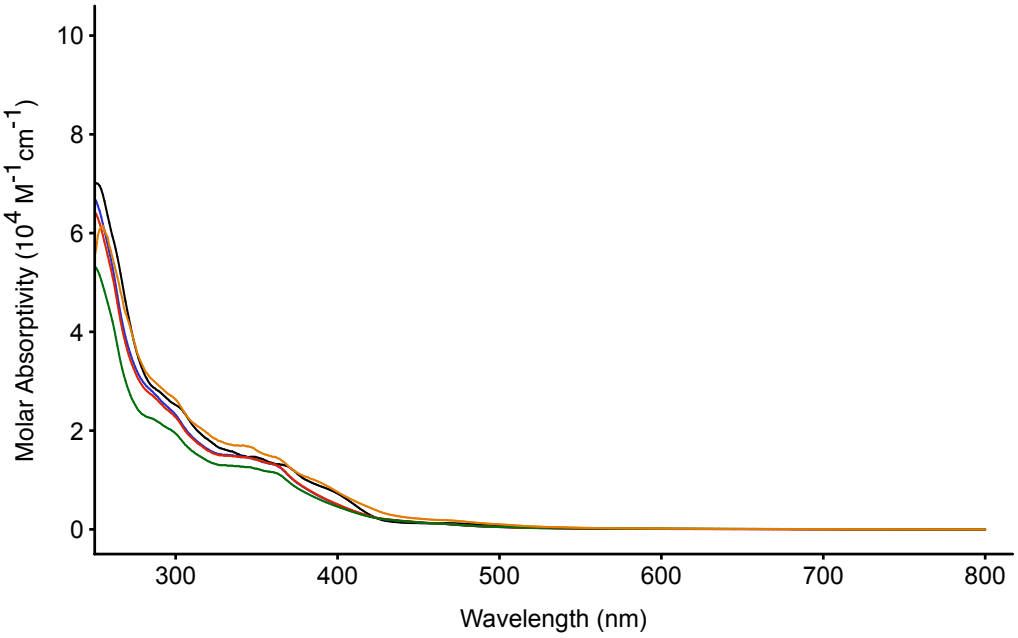

Figure 2.26 Absorption profiles of [Ir(**ppy**)$_2$(Me**TziQn**)]$^+$ in dichloromethane (black), H_2O (blue), lys. fluid (red), PBS (green) and ethyl laurate (orange).

2.4.5 Emission Properties in Aqueous and Lipophilic Solvents

The emission properties in aqueous and lipophilic solvents has been listed in **Table 2.6** and **Table 2.7** for cyano and (iso)quinolyl-functionalised complexes, respectively. The emission spectra of the neutral [Ir(**F$_2$ppy**)$_2$(**TzPyCN**)] and [Ir(**ppy**)$_2$(**TziQn**)] and the charged [Ir(**F$_2$ppy**)$_2$(Me**TzPyCN**)]$^+$ and [Ir(**ppy**)$_2$(Me**TziQn**)]$^+$ complexes are showed as reference from **Figure 2.27** to **Figure 2.30**. The emission profiles of all the other iridium(III) complexes can be found in Appendix A, **Figure A.7** – **Figure A.11**.

The analysis of the emission bands in various solvents reveals solvatochromic behaviour, with a red shift of the emission maxima upon increasing the polarity of the solvent. The most blue-shifted emission is recorded in ethyl laurate, while the emission red shifts by *ca.* 20 – 30 nm in dichloromethane, with the exception of [Ir(**ppy**)$_2$(Me**TzPyPhCN**)]$^+$ and [Ir(**ppy**)$_2$(Me**TziQn**)]$^+$ for which almost no shift is observed. The emission bands further shift (*ca.* 10 – 30 nm) towards longer wavelength in aqueous media. There are no significant differences in the various aqueous solvents, apart from [Ir(**ppy**)$_2$(Me**TzPyPhCN**)]$^+$ that shows a 22 nm red shift on passing from PBS to a lysosomal pH fluid solution. The methylated complex [Ir(**ppy**)$_2$(Me**TzPyCN**)]$^+$ is found to have appreciable emission only in dichloromethane solution, as the complex is virtually non-emissive in aqueous and lipophilic solvents. In general, the methylated complexes highlight a greater degree of quenching in aqueous solvents with respect to their neutral analogues. While conclusive explanations cannot be drawn from these data, potential causes could be ascribed to increased non-radiative decays due to energy gap law and the higher solubility of the cationic complexes in aqueous solvents. In fact, a similar behaviour has been observed for neutral rhenium complexes, where a decrease of solubility in aqueous media showed an enhanced quantum yield and elongated excited state lifetime.[232]

The majority of the iridium complexes show greater quantum yield in ethyl laurate, with higher emission intensity for the more lipophilic neutral species in comparison with their methylated analogues (refer to Chapter 3 – section 3.2.1 - **Table 3.1**). [Ir(**ppy**)$_2$(**TzQn**)] and [Ir(**ppy**)$_2$(**TziQn**)] are exceptions, displaying comparable quantum yields in the lipophilic solvent with the cationic [Ir(**ppy**)$_2$(Me**TzQn**)]$^+$ and [Ir(**ppy**)$_2$(Me**TziQn**)]$^+$.

Table 2.6 Photophysical data of diluted (10^{-5} M) aqueous and lipophilic solutions of the reported cyano-substituted complexes.

Complex	Solvent[a]	λ_{em} [nm]	τ_{aer} [ns][b]	Φ_{aer}[c]
[Ir(**ppy**)$_2$ (**TzPyCN**)]	H_2O	618	123 (25), 440 (75)	0.047
	Lys. Fluid	616	152 (32), 447 (68)	0.057
	PBS	618	144 (25), 470 (75)	0.085
	Ethyl Laurate	588	156	0.209
[Ir(**F$_2$ppy**)$_2$ (**TzPyCN**)]	H_2O	552	189 (41), 628 (59)	0.057
	Lys. Fluid	560	81 (34), 384 (66)	0.049
	PBS	552	179 (39), 616 (61)	0.087
	Ethyl Laurate	520	100 (92), 216 (8)	0.159
[Ir(**ppy**)$_2$ (**TzPyPhCN**)]	H_2O	580	200 (31), 728 (69)	0.055
	Lys. Fluid	580	156 (44), 605 (56)	0.039
	PBS	580	188 (39), 657 (61)	0.033
	Ethyl Laurate	540	83 (61), 371 (39)	0.100
[Ir(**ppy**)$_2$ (Me**TzPyCN**)]$^+$	H_2O	-[d]	-[d]	-[d]
	Lys. Fluid	-[d]	-[d]	-[d]
	PBS	-[d]	-[d]	-[d]
	Ethyl Laurate	-[d]	-[d]	-[d]
[Ir(**F$_2$ppy**)$_2$ (Me**TzPyCN**)]$^+$	H_2O	636	11 (76), 56 (24)	0.005
	Lys. Fluid	636	10 (71), 57 (29)	0.007
	PBS	636	11 (66), 88 (34)	0.006
	Ethyl Laurate	580	260	0.067
[Ir(**ppy**)$_2$ (Me**TzPyPhCN**)]$^+$	H_2O	605	17 (22), 320 (88)	0.005
	Lys. Fluid	640	15 (84), 123 (16)	0.002
	PBS	618	16 (28), 320 (72)	0.002
	Ethyl Laurate	600	151 (55), 287 (45)	0.002

[a] Aqueous solvents contain 0.2% DMSO. [b] For the biexponential excited state lifetime (τ), the relative weights of the exponential curves are reported in parentheses. [c] Measured versus [Ru(**bpy**)$_3$]$^{2+}$ in H_2O ($\Phi_r = 0.028$).[274] [d] Not emissive.

Table 2.7 Photophysical data of dilute (10^{-5} M) aqueous and lipophilic solutions of (iso)quinolyl-substituted complexes.

Complex	Solvent	λ_{em} [nm]	τ_{aer} [ns][a]	Φ_{aer}[b]
[Ir(**ppy**)$_2$ (**TzQn**)]	H_2O	600	305 (25), 928 (75)	0.039
	Lys. Fluid	600	255 (25), 820 (75)	0.033
	PBS	600	279 (27), 865 (73)	0.033
	Ethyl Laurate	566	126 (70), 258 (30)	0.027
[Ir(**ppy**)$_2$ (**TziQn**)]	H_2O	590	217 (33), 531 (67)	0.018
	Lys. Fluid	590	222 (53), 652 (47)	0.008
	PBS	590	254 (45), 638 (55)	0.020
	Ethyl Laurate	532, 572, 622	397	0.032
[Ir(**ppy**)$_2$ (Me**TzQn**)]$^+$	H_2O	630	17 (39), 134 (61)	0.004
	Lys. Fluid	630	18 (40), 153 (60)	0.029
	PBS	635	22 (30), 160 (70)	0.024
	Ethyl Laurate	628	224	0.068
[Ir(**ppy**)$_2$ (Me**TziQn**)]$^+$	H_2O	660	9 (53), 93 (47)	0.004
	Lys. Fluid	660	9 (59), 120 (41)	0.005
	PBS	670	9 (62), 85 (37)	0.005
	Ethyl Laurate	640	223	0.054

[a] Aqueous solvents contain 0.2% DMSO. [b] For the biexponential excited state lifetime (τ), the relative weights of the exponential curves are reported in parentheses. [c] Measured versus [Ru(**bpy**)$_3$]$^{2+}$ in H_2O ($\Phi_r = 0.028$).

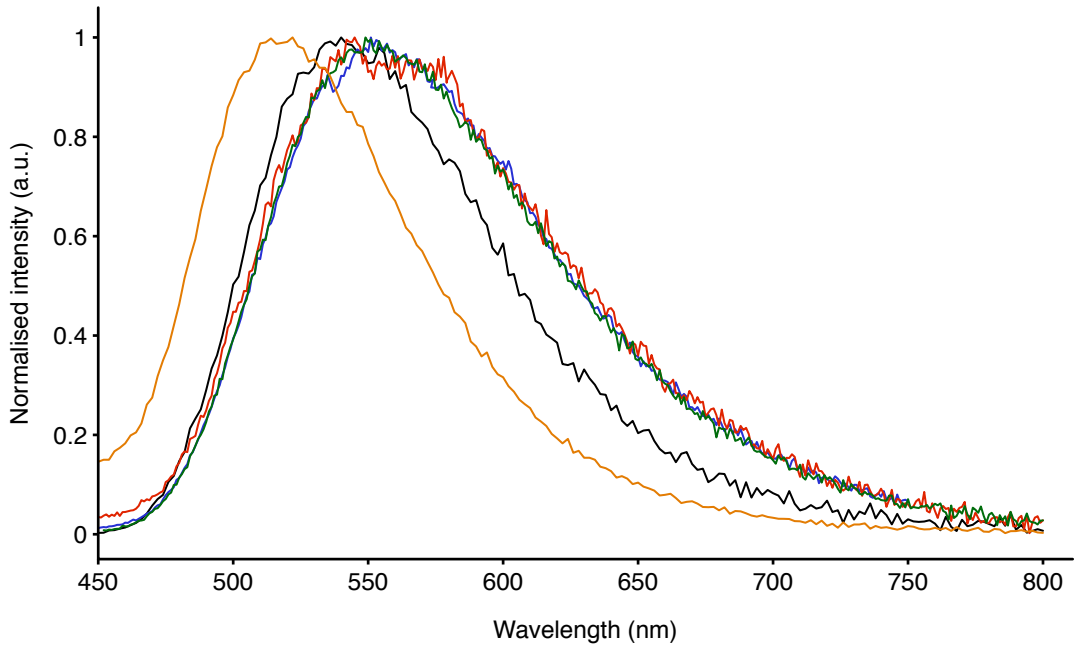

Figure 2.27 Normalised emission profiles of [Ir(**F$_2$ppy**)$_2$(**TzPyCN**)] in dichloromethane (black), H_2O (blue), lys. fluid (red), PBS (green) and ethyl laurate (orange).

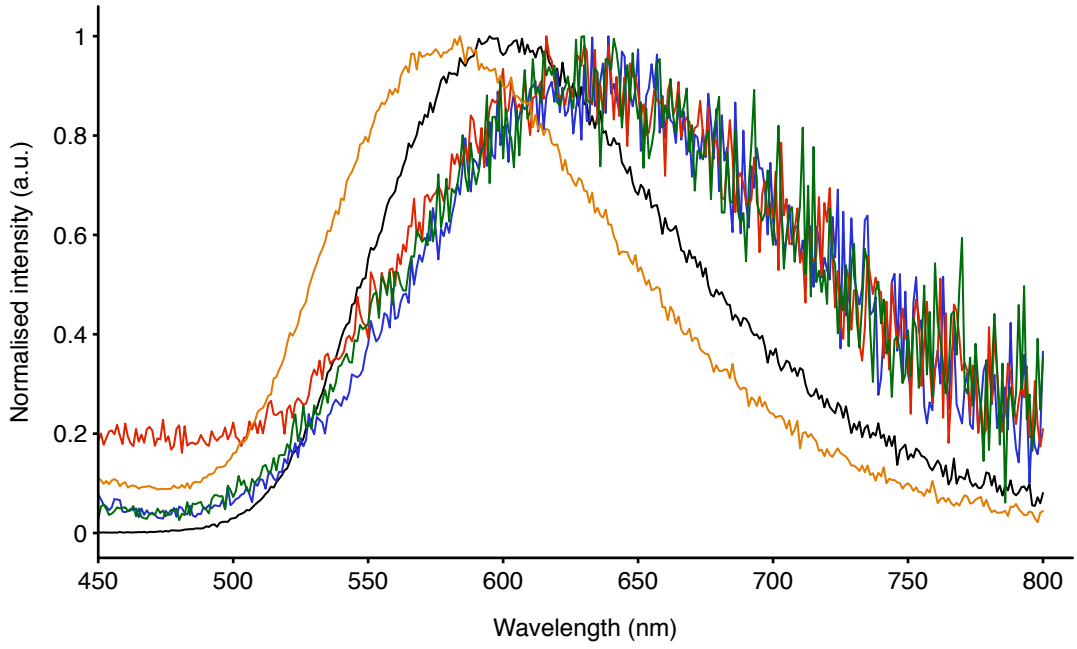

Figure 2.28 Normalised emission profiles of [Ir(**F$_2$ppy**)$_2$(Me**TzPyCN**)]$^+$ in dichloromethane (black), H_2O (blue), lys. fluid (red), PBS (green) and ethyl laurate (orange).

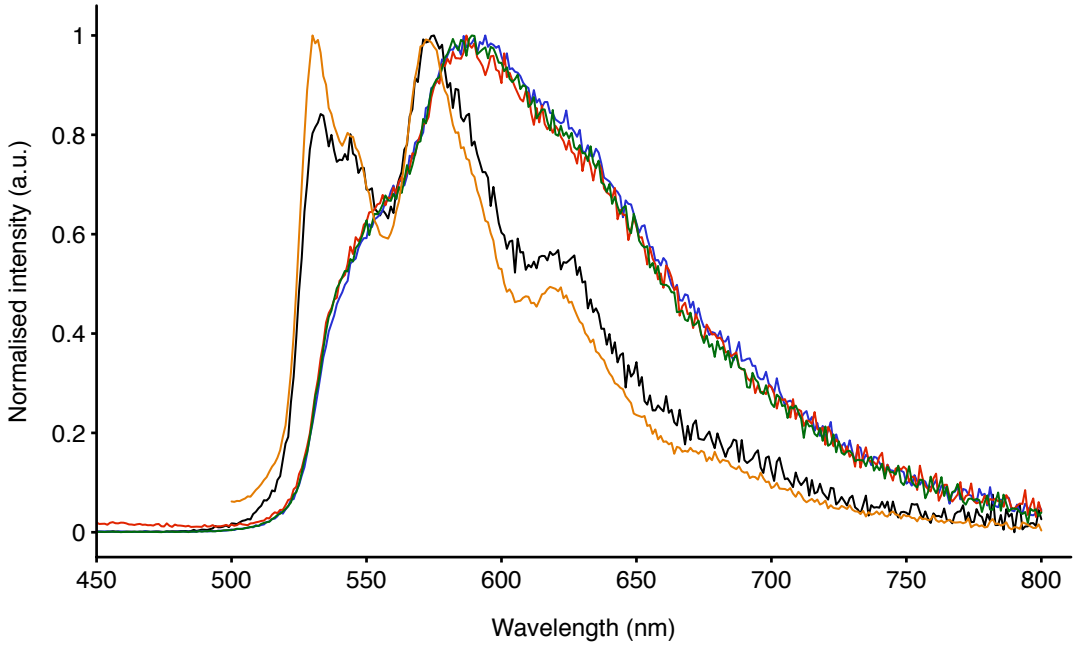

Figure 2.29 Normalised emission profiles of [Ir(**ppy**)$_2$(**TziQn**)] in dichloromethane (black), H_2O (blue), lys. fluid (red), PBS (green) and ethyl laurate (orange).

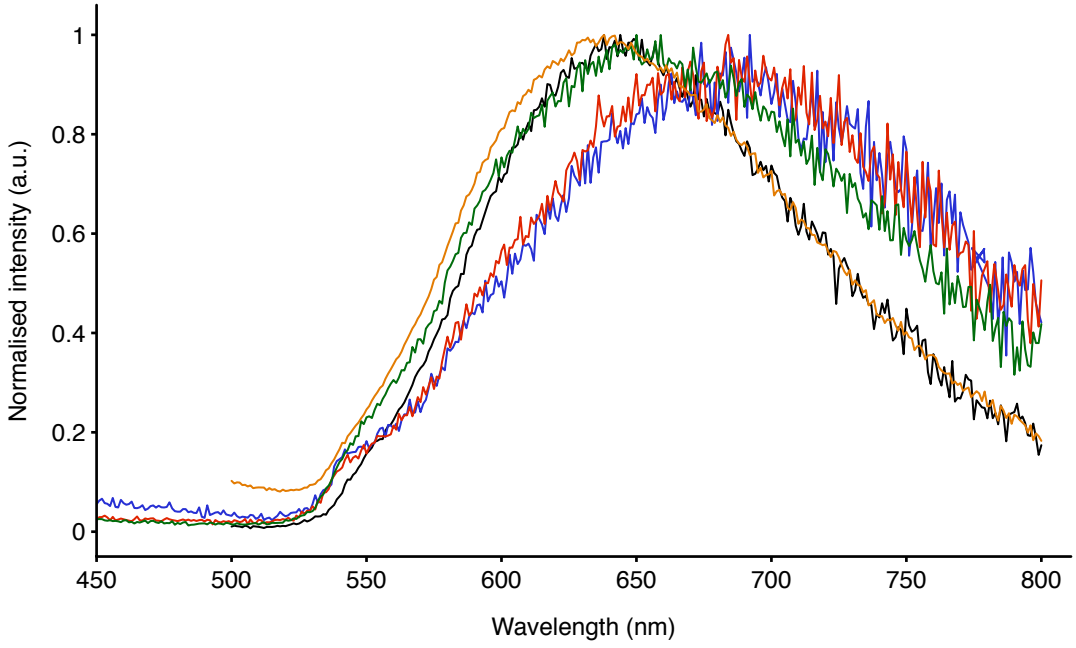

Figure 2.30 Normalised emission profiles of [Ir(**ppy**)$_2$(Me**TziQn**)]$^+$ in dichloromethane (black), H_2O (blue), lys. fluid (red), PBS (green) and ethyl laurate (orange).

2.5 Conclusions

In this chapter, a library of neutral iridium(III) tetrazolato complexes has been synthesised, displaying chemical variations in the cyclometalated phenylpyridine and tetrazolate ligands. Furthermore, methylation of these species has allowed facile access to the cationic analogues, so that a correlation between the chemical structure and the photophysical properties of the complexes could have been more systematically investigated.

NMR and X-ray crystallography studies have confirmed the formation of only one isomer of the complexes, with nitrogens of the phenylpyridine in *trans* with respect to the metal centre, and the cyclometalated carbons occupying *cis* positions. Moreover, the methylation site for the charged complexes was proved to be the N3 position on the tetrazolato ligand, in accordance with previously reported studies.[231,236]

The photophysical properties have revealed typical phosphorescent emission from excited state of charged transfer nature, as a mixture of ^{3}MLCT and ^{3}LLCT. The emission of the complexes was found to be general solvatochromic, with red shift occurring upon increase of the medium polarity.

Based on the photophysical data summarised in this chapter, discrimination between organelles cannot be achieved by monitoring the shift of the emission maximum of this family of iridium probes. Moreover, the variation in the pH between the lysosomial fluid (pH = 7.4) and the PBS (pH = 4.5) highlighted the lack of pH-sensing activities of these probes.

Nevertheless, the photophysical investigations in aqueous and lipophilic media have showed that the complexes are suitable for biological investigation, with the exception of [Ir(**ppy**)$_2$(Me**TzPyCN**)]$^+$, which displayed appreciable emission only in organic solvent.

2.6 Experimental

2.6.1 General Procedures

Unless otherwise stated, all reagents and solvents were purchased from Sigma Aldrich or Alfa Aesar and used as received without further purification. The species [Ir(**ppy**)$_2$(μ-Cl)]$_2$,[277] [Ir(**F$_2$ppy**)$_2$(μ-Cl)]$_2$[277] and [Ir(**ppy**)$_2$(**TzPyBr**)][236] were prepared according to previously published procedures.

Nuclear magnetic resonance spectra were recorded using a Bruker Avance 400 spectrometer (400 MHz for ^{1}H NMR; 100 MHz for ^{13}C NMR) at 300 K. All NMR spectra were calibrated to residual solvent signals. For the NMR characterisation, proton and carbon of all the iridium(III) tetrazolato complexes were assigned as pyridinic (A), phenylic (B) and tetrazolic (T), according to **Figure 2.31**.

Infrared spectra were recorded using an attenuated total reflectance Perkin Elmer Spectrum 100 FT-IR with a diamond stage. IR spectra were recorded from 4000–650 cm^{-1}. The intensity of the band is reported as strong (s), medium (m), or weak (w), with broad (br) bands also specified.

Melting points were determined using a BI Barnsted Electrotermal 9100 apparatus.

Elemental analyses were carried out on bulk samples using a Thermo Finning EA 1112 Series Flash; the presence of solvents was further confirmed by ^{1}H NMR. Elemental analyses were performed by Robert Herman at the School of Molecular and Life Sciences (Curtin University) or by Dr Thomas Rodemann at the Central Science Laboraty (University of Tasmania).

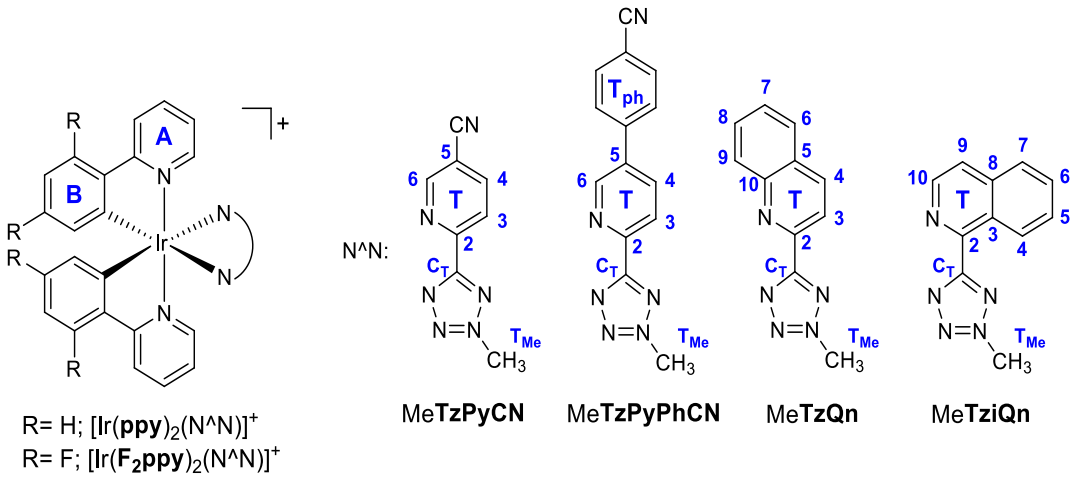

Figure 2.31 NMR referencing layout.

2.6.2 Photophysical Measurements

Absorption spectra were recorded at room temperature using a Cary 4000 UV/Vis spectrometer. Uncorrected steady state emission and excitation spectra were recorded on an Edinburgh FLSP980-S2S2-stm spectrometer equipped with: i) a temperature-monitored cuvette holder; ii) 450 W Xenon arc lamp; iii) double excitation and emission monochromators; iv) a Peltier cooled Hamamatsu R928P photomultiplier tube (spectral range 200-870 nm). Emission and excitation spectra were corrected for source intensity (lamp and grating) and emission spectral response (detector and grating) by a calibration curve supplied with the instrument. According to the approach described by Demas and Crosby,[278] luminescence quantum yields (Φ_{em}) were measured in optically dilute solutions (O.D. < 0.1 at excitation wavelength) obtained from absorption spectra on a wavelength scale [nm] and compared to the reference emitter by the following **Equation 2.1**:

$$\Phi_x = \Phi_r \left[\frac{A_r(\lambda_r)}{A_x(\lambda_x)} \frac{I_r(\lambda_r)}{I_x(\lambda_x)} \frac{n_x^2}{n_r^2} \frac{D_x}{D_r}\right] \qquad (2.1)$$

where A is the absorbance at the excitation wavelength (λ), I is the intensity of the excitation light at the excitation wavelength (λ), n is the refractive index of the solvent, D is the integrated intensity of the luminescence and Φ is the quantum yield. The subscripts r and x refer to the reference and the sample, respectively. The quantum yield determinations were performed at identical excitation wavelength for the sample and the reference, therefore cancelling the $I(\lambda_r)/I(\lambda_x)$ term in the equation. The

quantum yields of complexes were measured against an aqueous solution of [Ru(**bipy**)$_3$]Cl$_2$ (**bipy** = 2,2'-bipyridine; Φ_r = 0.028).[274] Emission lifetimes (τ) were determined with the time correlated single photon counting technique (TCSPC) with the same Edinburgh FLSP980-S2S2-stm spectrometer using either a pulsed picosecond LED (EPLED/EPL 377 nm, FHWM < 800 ps). The goodness of fit was assessed by minimising the reduced χ^2 function and by visual inspection of the weighted residuals. The solvents used for the preparation of the solutions for the photophysical investigations were of LR grade and the water was deionised. Degassing of the dichloromethane solutions was performed using the freeze-pump-thaw method. Experimental uncertainties are estimated to be ±8% for lifetime determinations, ±20% for quantum yields, ±2 nm and ±5 nm for absorption and emission peaks, respectively.

2.6.3 Computational Method

Time-dependent density functional theory (TD-DFT) calculations were performed with GAUSSIAN 09[279] by Dr Phillip J. Wright at the Department of Chemistry, Curtin University. Prior to these calculations, the structures were relaxed at the B3LYP level of theory.[280,281] The Ir atoms were treated with the Stuttgart-Dresden effective core potential,[268] the Pople 6-311G** basis set was used for all the other atoms, and the effect of the solvent was mimicked with the PCM solvation model,[282] with parameters adequate for dichloromethane. The low-lying singlet–singlet excitation energies were calculated at the same level of theory, and the spectra were reproduced as the superposition of Gaussian functions with heights proportional to calculated intensities and a variance of 11 nm.

2.6.4 Synthesis

HTzPyCN

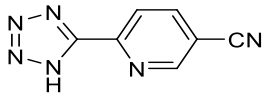

2,5-dicyanopyridine (0.100 g, 0.774 mmol), sodium azide (0.050 g, 0.769 mmol) and zinc bromide (0.192 g, 0.853 mmol) were dissolved in 10 mL of water. The resulting suspension was vigorously stirred and heated at reflux overnight. The milky reaction

mixture was then made basic by addition of a 0.25 M sodium hydroxide solution (7.76 mL, 1.938 mmol) and the formed yellow precipitate was filtered. The filtrate was acidified to pH≈1 with 3 M hydrochloric acid. The formed white precipitate was then filtered and dried in air. Yield: 0.085 g (64%), M.P. 234 °C (dec). IR (ν / cm^{-1}): 3071 w (tetrazole N–H), 2235 w (C≡N), 1604 w (tetrazole C=N). ^{1}H NMR (δ / ppm, DMSO-*d*$_6$): 9.27 (s, 1H, **H$_{T6}$**), 8.59 (d, 1H, **H$_{T4}$**, J = 8.2 Hz), 8.38 (d, 1H, **H$_{T3}$**, J = 8.2 Hz). ^{13}C NMR (δ / ppm, DMSO-*d*$_6$): 154.4 (**C$_{T}$**), 153.0 (**CH$_{6}$**), 146.6 (**C**N), 142.1 (**CH$_{T4}$**), 122.4 (**CH$_{3}$**), 116.5 (**C$_{T5}$**), 110.6 (**C$_{T2}$**).

H**TzQn**

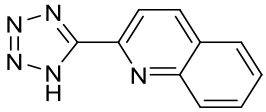

Triethylamine (1.9 mL, 0.030 mol) was added to toluene (25 mL) and the solution was cooled to 0 ºC. HCl 32% (1.6 mL, 0.030 mol) was added to the reaction mixture and stirred until fuming subsided. 2-quinolinecarbonitrile (0.600 g, 0.004 mol) and sodium azide (0.868 g, 0.018 mol) were added and heated at reflux overnight. After cooling down to room temperature, the mixture was extracted with water (2 × 15 mL) and the aqueous phase was collected and acidified to pH≈3 with HCl 32%. The formed off-white precipitate was then filtered and dried in air. Yield: 0.722 g (94%). M.P. 197 – 198 °C. IR (ν / cm^{-1}): 3057 w (tetrazole N–H), 1600 w (tetrazole C=N). ^{1}H NMR (δ / ppm, DMSO-d_6): 8.67 (d, 1H, $\mathbf{H_{T4}}$, J = 8.5 Hz), 8.33 (d, 1H, $\mathbf{H_{T3}}$, J = 8.5 Hz), 8.19 (d, 1H, $\mathbf{H_{T9}}$, J = 8.5 Hz), 8.13 (d, 1H, $\mathbf{H_{T6}}$, J = 8.2 Hz), 7.91 (t, 1H, $\mathbf{H_{T8}}$, J = 7.7 Hz), 7.75 (t, 1H, $\mathbf{H_{T7}}$, J = 7.7 Hz). ^{13}C NMR (δ / ppm, DMSO-d_6): 155.2 ($\mathbf{C_T}$), 147.2 ($\mathbf{C_{T2}}$), 144.1 ($\mathbf{C_{T10}}$), 138.4 ($\mathbf{C}H_{T4}$), 130.9 ($\mathbf{C}H_{T8}$), 128.9 ($\mathbf{C}H_{T9}$), 128.3 ($\mathbf{C}H_{T6}$), 128.2 ($\mathbf{C}H_{T7}$), 119.2 ($\mathbf{C}H_{T3}$), 114.5 ($\mathbf{C_{T5}}$).

H**TziQn**

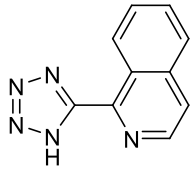

Triethylamine (1.9 mL, 0.030 mol) was added to toluene (25 mL) and the solution was cooled to 0 ºC. HCl 32% (1.6 mL, 0.030 mol) was added to the reaction mixture and stirred until fuming subsided. 2-quinolinecarbonitrile (0.600 g, 0.004 mol) and sodium azide (0.868 g, 0.018 mol) were added and heated at reflux overnight. After cooling down to room temperature, the mixture was extracted with water (2 × 15 mL) and the aqueous phase was collected and acidified to pH≈3 with HCl 32%. The formed white precipitate was then filtered and dried in air. Yield: 0.528 g (69%). M.P. 237 – 238 °C. IR (ν / cm^{-1}): 3063 w (tetrazole N–H), 1613 w (tetrazole C=N). ^{1}H NMR (δ / ppm, DMSO-d_6): 9.37 (d, 1H, $\mathbf{H_{T10}}$, J = 8.3 Hz), 8.74 (d, 1H, $\mathbf{H_{T9}}$, J = 5.5 Hz), 8.16 – 8.13 (m, 2H, $\mathbf{H_{T4}}$, $\mathbf{H_{T7}}$), 7.94 – 7.86 (m, 2H, $\mathbf{H_{T5}}$, $\mathbf{H_{T6}}$). ^{13}C NMR (δ / ppm, DMSO-d_6):

155.0 (**C**$_{T}$), 143.0 (**C**$_{T2}$), 141.8 (**C**H$_{T9}$), 136.6 (**C**$_{T3}$), 131.3 (**C**H$_{T5}$), 129.3 (**C**H$_{T6}$), 127.5 (**C**H$_{T4}$), 126.3 (**C**H$_{T10}$), 125.7 (**C**$_{T8}$), 123.6 (**C**H$_{T7}$).

[Ir(ppy)$_2$(TzPyCN)]

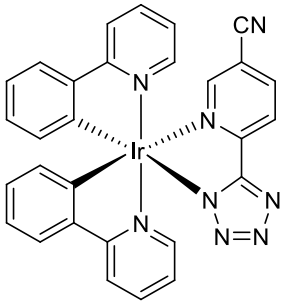

[Ir(**ppy**)$_2$(μ-Cl)]$_2$ (0.226 g, 0.211 mmol) was combined with H**TzPyCN** (0.080 g, 0.465 mmol) and dissolved in 13 mL of a dichloromethane/ethanol mixture (10:3 v/v). The resulting suspension was stirred at room temperature overnight. The solvents were concentrated and the product was purified *via* column chromatography using Brockmann I grade neutral alumina-filled as stationary phase and a dichloromethane/acetone (9:1 v/v) solvent system as eluent. The targeted complex eluted as the second fraction (yellow). Yield: 0.215 g (76%). M.P. 210 °C (dec). IR (ν / cm^{-1}): 2235 w (C≡N), 1606 w (tetrazole C=N). ^{1}H NMR (δ / ppm, acetone-*d*$_6$): 8.55 – 8.49 (m, 2H, **H**$_{T4}$, **H**$_{T3}$), 8.18 – 8.12 (m, 2H, **2H**$_{A}$), 8.12 (s, 1H, **H**$_{T6}$), 7.93 – 7.88 (m, 2H, **2H**$_{A}$), 7.86 (d, 2H, **2H**$_{A}$, J = 8.0 Hz), 7.77 (d, 1H, **H**$_{B}$, J = 7.6 Hz), 7.58 (d, 1H, **H**$_{B}$, J = 5.8 Hz), 7.17 (app. t., 1H, **H**$_{B}$, splitting = 7.3 Hz), 7.06 – 6.99 (m, 2H, **2H**$_{A}$), 6.93 – 6.88 (m, 2H, **2H**$_{B}$), 6.78 (app. t., 1H, **H**$_{B}$, splitting = 7.4 Hz), 6.43 (d, 1H, **H**$_{B}$, J = 7.5 Hz), 6.29 (d, 1H, **H**$_{B}$, J = 7.7 Hz). ^{13}C NMR (δ / ppm, acetone-*d*$_6$): 168.9 (**C**$_{A}$), 168.8 (**C**$_{A}$), 163.7 (**C**$_{T}$), 153.9 (**C**H$_{T6}$), 153.5 (**C**N), 152.0 (**C**$_{B}$), 150.4 (**C**H$_{A}$), 147.4 (**C**$_{B}$), 145.7 (**C**$_{B}$), 145.0 (**C**$_{B}$), 143.5 (**C**H$_{T4}$), 139.2 (**C**H$_{A}$), 138.8 (**C**H$_{A}$), 132.9 (**C**H$_{B}$), 132.5 (**C**H$_{B}$), 131.0 (**C**H$_{B}$), 130.1 (**C**H$_{B}$), 125.7 (**C**H$_{A}$), 125.1 (**C**H$_{B}$), 124.3 (**C**H$_{B}$), 123.8 (**C**H$_{B}$), 123.2 (**2C**H$_{A}$), 123.1 (**C**H$_{T3}$), 122.4 (**C**H$_{B}$), 120.5 (**C**H$_{A}$), 120.1 (**C**H$_{A}$), 116.1 (**C**$_{T2}$), 112.3 (**C**$_{T5}$). Anal. Calcd for [Ir(**ppy**)$_2$(**TzPyCN**)]·0.8(acetone): C, 52.47; H, 3.31; N, 15.67. Found: C, 52.79; H, 2.95; N, 15.71.

[Ir(F$_2$ppy)$_2$(TzPyCN)]

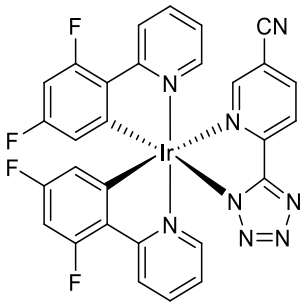

[Ir(**F$_2$ppy**)$_2$(μ-Cl)]$_2$ (0.129 g, 0.113 mmol) was combined with H**TzPyCN** (0.040 g, 0.232 mmol) and dissolved in 13 mL of a dichloromethane/ethanol mixture (10:3 v/v). The resulting suspension was stirred at room temperature overnight. The solvents were concentrated and the product was purified *via* column chromatography using Brockmann I grade neutral alumina-filled as stationary phase and a dichloromethane/acetone (9:1 v/v) solvent system as eluent. The targeted complex eluted as the second fraction (yellow). Yield: 0.120 g (71%). M.P. 252 °C (dec). IR (ν / cm^{-1}): 2232 w (C≡N), 1601 w (tetrazole C=N). ^{1}H NMR (δ / ppm, acetone-*d$_6$*): 8.61 – 8.57 (m, 2H, **H$_{T4}$**, **H$_{T3}$**), 8.33 (s, 1H, **H$_{T6}$**), 8.28 (app. t., 2H, **2H$_A$**, splitting = 8.5 Hz), 8.00 – 7.91 (m, 3H, **3H$_A$**), 7.51 (d, 1H, **H$_A$**, J = 5.8 Hz), 7.23 (app. t., 1H, **H$_A$**, splitting = 7.4 Hz), 7.10 (app. t., 1H, **H$_A$**, splitting = 7.4 Hz), 6.66 (app. t., 1H, **H$_B$**, splitting = 12.4 Hz), 6.59 (app. t., 1H, **H$_B$**, splitting = 12.4 Hz), 5.84 (d, 1H, **H$_B$**, J = 8.6 Hz), 5.66 (d, 1H, **H$_B$**, J = 8.9 Hz). ^{13}C NMR (δ, ppm, acetone-*d$_6$*): 165.7 (d, **2C$_B$**, J$_{CF}$ = 50.4 Hz), 165.2 (d, **C$_B$**, J$_{CF}$ = 28.8 Hz), 165.0 (d, **C$_B$**, J$_{CF}$ = 28.8 Hz), 163.6 (**2C$_A$**), 163.2 (**2C$_B$**), 163.1 (d, **2C$_B$**, J$_{CF}$ = 20.0 Hz), 154.7 (**CH$_{T6}$**), 152.8 (**C**N), 151.6 (d, **2C**H$_A$, J$_{CF}$ = 28.0 Hz), 150.8 (d, **C**H$_A$, J$_{CF}$ = 107.2 Hz), 144.3 (**CH$_{T4}$**), 140.2 (d, **C**H$_A$, J$_{CF}$ = 111.6 Hz), 129.5 (d, **C**H$_B$, J$_{CF}$ = 15.2 Hz), 128.9 (d, **C**H$_B$, J$_{CF}$ = 17.6 Hz), 124.8 (**CH$_A$**), 124.4 (**CH$_A$**), 124.0 (dd, **C**H$_A$, J$_{CF}$ = 97.2 Hz), 123.4 (**CH$_{T3}$**), 115.9 (**C$_{T2}$**), 114.9 (dd, **C**H$_B$, J$_{CF}$ = 72.0 Hz), 112.8 (**C$_{T5}$**), 99.5 (dd, **C**H$_B$, J$_{CF}$ = 108 Hz), 98.7 (dd, **C**H$_B$, J$_{CF}$ = 108 Hz); quaternary tetrazolic C peak was not visible in the spectrum. Crystals suitable for X-ray analysis were obtained by slow diffusion of hexane into a solution of the complex in dichloromethane. Anal. Calcd for [Ir(**F$_2$ppy**)$_2$(**TzPyCN**)]·0.2(CH_2Cl_2): C, 46.39; H, 2.13; N, 14.62. Found: C, 46.36; H, 1.75; N, 14.68.

[Ir(ppy)$_2$(TzPyPhCN)]

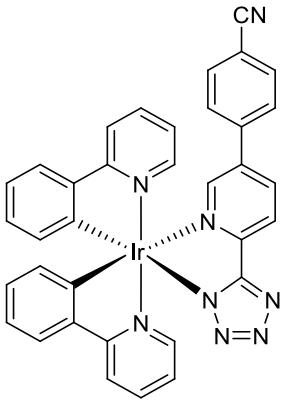

[Ir(**ppy**)$_2$(**TzPyBr**)] (0.150 g, 0.207 mmol), 4-cyanophenylboronic acid (0.036 g, 0.248 mmol), and bis(triphenylphosphine)palladium(II) dichloride (0.005 g, 0.006 mmol) were combined and dissolved in 10 mL of dry THF. The solution was stirred under nitrogen for 15 minutes and 1 M aqueous Na_2CO_3 (15 mL, 0.290 mmol) was added and refluxed overnight. The cooled crude mixture was washed with water and extracted with dichloromethane (3 × 15 mL). The combined organic phase was dried over $MgSO_4$ and filtered. The product was purified *via* column chromatography using Brockmann I grade neutral alumina-filled as stationary phase and a dichloromethane/acetone (9:1 v/v) solvent system as eluent. The targeted complex eluted as the second fraction (yellow). Yield: 0.134 g (87%). M.P. 234 – 236 °C. IR (ν / cm^{-1}): 2232 w (C≡N), 1606 w (tetrazole C=N). ^{1}H NMR (δ / ppm, DMSO-*d*$_6$): 8.51 (d, 1H, $\mathbf{H_{T4}}$, J = 8.2 Hz), 8.44 (d, 1H, $\mathbf{H_{T3}}$, J = 8.2 Hz), 8.20 (app. t., 2H, $\mathbf{2H_A}$, splitting = 8.4 Hz), 7.94 – 7.83 (m, 6H, $\mathbf{2H_{Tph}}$, $\mathbf{3H_B}$, $\mathbf{H_A}$), 7.77 (d, 1H, $\mathbf{H_A}$, J = 7.6 Hz), 7.64 – 7.60 (m, 1H, $\mathbf{H_{T6}}$), 7.52 (d, 2H, $\mathbf{2H_{Tph}}$, J = 8.4 Hz), 7.46 (d, 1H, $\mathbf{H_A}$, J = 7.6 Hz), 7.19 (app. t., 1H, $\mathbf{H_A}$, splitting = 7.2 Hz), 7.10 (app. t., 1H, $\mathbf{H_A}$, splitting = 7.2 Hz), 7.02 (app. t., 1H, $\mathbf{H_A}$, splitting = 8.2 Hz), 6.93 (app. t., 2H, $\mathbf{2H_B}$, splitting = 7.4 Hz), 6.79 (app. t., 1H, $\mathbf{H_B}$, splitting = 7.6 Hz), 6.32 (d, 1H, $\mathbf{H_B}$, J = 6.4 Hz), 6.20 (d, 1H, $\mathbf{H_B}$, J = 6.4 Hz). ^{13}C NMR (δ / ppm, acetone-*d*$_6$): 167.2 ($\mathbf{C_A}$), 167.0 ($\mathbf{C_A}$), 163.1 ($\mathbf{C_T}$), 151.5 ($\mathbf{C_B}$), 149.2 ($\mathbf{CH_A}$), 148.9 ($\mathbf{CH_A}$), 147.9 (**C**N), 147.4 ($\mathbf{CH_B}$), 147.2 ($\mathbf{CH_B}$), 144.5 ($\mathbf{C_B}$), 144.1 ($\mathbf{C_B}$), 139.4 ($\mathbf{C_{Tph}}$), 138.5 ($\mathbf{CH_A}$), 138.2 ($\mathbf{CH_A}$), 138.0 ($\mathbf{CH_{T4}}$), 136.2 ($\mathbf{C_{T2}}$), 133.2 ($\mathbf{CH_{Tph}}$), 131.4 ($\mathbf{CH_{T6}}$), 131.5 ($\mathbf{CH_B}$), 130.0 ($\mathbf{CH_B}$), 129.1 ($\mathbf{CH_B}$), 128.8 ($\mathbf{CH_B}$), 128.7 ($\mathbf{CH_B}$), 127.4 ($\mathbf{CH_{Tph}}$), 124.9 ($\mathbf{C_B}$), 124.4 ($\mathbf{CH_{Tph}}$), 123.7 ($\mathbf{CH_A}$), 123.4 ($\mathbf{CH_A}$), 122.4 ($\mathbf{CH_{Tph}}$), 122.0 ($\mathbf{CH_{T3}}$), 121.2 ($\mathbf{CH_B}$), 119.8 ($\mathbf{CH_A}$), 119.3 ($\mathbf{CH_A}$), 118.3 ($\mathbf{C_{T5}}$), 111.7

(**C**$_{\mathbf{Tph}}$). Anal.Calcd for [Ir(**ppy**)$_2$(**TzPyPhCN**)]·(CH_2Cl_2)·0.3(acetone): C, 52.15; H, 3.19; N, 13.15. Found: C, 51.99; H, 2.82; N, 13.37.

[Ir(ppy)$_2$(MeTzPyCN)][PF$_6$]

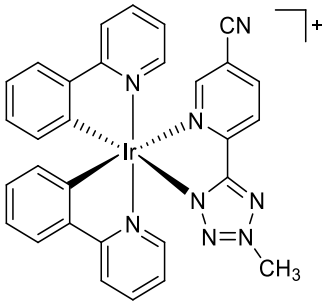

[Ir(**ppy**)$_2$(**TzPyCN**)] (0.060 g, 0.089 mmol) was dissolved in dichloromethane (10 mL) and cooled down to –50 °C using an ethyl acetate/liquid nitrogen cool bath. Thereafter, a 0.1 M methyl trifluoromethanesulfonate solution in dichloromethane (0.022 g, 0.133 mmol) was added dropwise to the vigorously stirred solution. After being maintained at –50 °C for 30 minutes, the solution was warmed up at room temperature and left to stirred overnight. An excess of ammonium hexafluorophosphate (0.029 g, 0.178 mmol) was added and stirred for 45 minutes. The crude mixture was washed with water and extracted with dichloromethane (3 × 15 mL) and the combined organic phase was dried on $MgSO_4$. The targeted complex was then collected after filtration and removal of the solvent as a red solid. Yield: 0.063 g (85%). M.P. 242 – 243 °C. IR (ν / cm^{-1}): 2240 w (C≡N), 1609 w (tetrazole C=N). ^{1}H NMR (δ / ppm, acetone-*d*$_6$): 8.79 (d, 1H, **H$_{T4}$**, J = 8.2 Hz), 8.73 (d, 1H, **H$_{T3}$**, J = 8.2 Hz), 8.32 (s, 1H, **H$_{T6}$**), 8.22 (d, 2H, **2H$_A$**, J = 8.0 Hz), 8.03 – 7.96 (m, 4H, **4H$_A$**), 7.89 (d, 1H, **H$_B$**, J = 7.7 Hz), 7.83 (d, 1H, **H$_B$**, J = 7.7 Hz), 7.03 – 6.98 (m, 2H, **2H$_A$**), 7.06 (app. t, 1H, **H$_B$**, splitting = 7.8 Hz), 6.87 – 6.80 (m, 2H, **2H$_B$**), 6.85 (app. t., 1H, **H$_B$**, splitting = 7.5 Hz), 6.34 (d, 1H, **H$_B$**, J = 7.6 Hz), 6.28 (d, 1H, **H$_B$**, J = 7.7 Hz), 4.57 (s, 3H, **3H$_{TMe}$**). ^{13}C NMR (δ / ppm, acetone-*d*$_6$): 168.5 (**C$_A$**), 168.1 (**C$_A$**), 166.8 (**C$_T$**), 154.9 (**CH$_{T6}$**), 151.2 (**CH$_A$**), 151.1 (**CH$_A$**), 148.6 (**C**N), 147.5 (**C$_B$**), 145.3 (**C$_B$**), 145.2 (**C$_B$**), 144.9 (**CH$_{T3}$**), 144.0 (**C$_B$**), 139.9 (**CH$_A$**), 139.8 (**CH$_A$**), 132.7 (**CH$_B$**), 132.4 (**CH$_B$**), 131.3 (**CH$_B$**), 130.6 (**CH$_B$**), 126.0 (**CH$_B$**), 125.6 (**CH$_B$**), 125.4 (**CH$_{T4}$**), 124.6 (**CH$_A$**), 124.4 (**CH$_A$**), 124.1 (**CH$_B$**), 123.5 (**CH$_B$**), 121.0 (**CH$_A$**), 120.6 (**CH$_A$**), 115.9 (**C$_{T2}$**), 115.5 (**C$_{T5}$**), 42.7 (**CH$_{TMe}$**). Crystals were formed in the NMR tube and have been used for

the elemental analysis. Anal.Calcd for [Ir(**ppy**)$_2$(Me**TzPyCN**)][PF_6]·0.3(CH_2Cl_2) ·0.3(acetone): C, 43.26; H, 2.88; N, 12.81. Found: C, 43.21; H, 2.57; N, 12.77.

[Ir(F$_2$ppy)$_2$(MeTzPyCN)][PF$_6$]

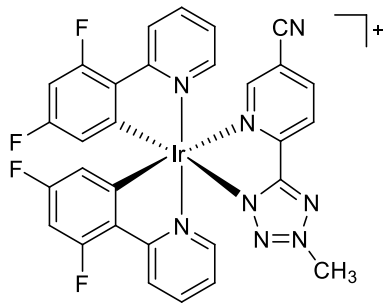

[Ir(**F$_2$ppy**)$_2$(**TzPyCN**)] (0.060 g, 0.081 mmol) was dissolved in dichloromethane (10 mL) and cooled down to –50 °C using an ethyl acetate/liquid nitrogen cool bath. A 0.1 M methyl trifluoromethanesulfonate solution in dichloromethane (0.020 g, 0.121 mmol) was added dropwise to the vigorously stirred solution. After being maintained at –50 °C for 30 minutes, the solution was warmed up at room temperature and left to stir overnight. An excess of ammonium hexafluorophosphate (0.026 g, 0.162 mmol) was added and stirred for 45 minutes. The crude mixture was washed with water and extracted with dichloromethane (3 × 15 mL) and the combined organic phase was dried on $MgSO_4$. The targeted complex was then collected after filtration and removal of the solvent as a red solid. Yield: 0.092 g (88%). M.P. 293 °C (dec). IR (ν / cm^{-1}): 2243 w (C≡N), 1599 w (tetrazole C=N). ^{1}H NMR (δ / ppm, acetone-d_6): 8.84 (m, 2H, **H$_{T4}$, H$_{T3}$**), 8.63 (s, 1H, **H$_{T6}$**), 8.37 (d, 2H, **2H$_A$**, J = 8.8 Hz), 8.11 – 8.06 (m, 4H, **4H$_A$**), 7.26 – 7.21 (m, 4H, **2H$_A$**), 6.81 – 6.71 (m, 2H, **2H$_B$**), 5.79 (d, 1H, **H$_B$**, J = 8.6 Hz), 5.71 (d, 1H, **H$_B$**, J = 8.7 Hz), 4.61 (s, 3H, **3H$_{TMe}$**). ^{13}C NMR (δ / ppm, acetone-d_6): 166.7 (**C$_T$**), 165.5 (d, **C$_B$**, J_{CF} = 12.8 Hz), 165.0 (d, **C$_B$**, J_{CF} = 12.6 Hz), 163.4 (d, **C$_A$**, J_{CF} = 13.1 Hz), 163.0 (d, **C$_B$**, J_{CF} = 20.8 Hz), 162.9 (d, **C$_B$**, J_{CF} = 21.2 Hz), 162.4 (d, **C$_B$**, J_{CF} = 12.5 Hz), 160.9 (d, **C$_B$**, J_{CF} = 12.9 Hz), 160.3 (d, **C$_B$**, J_{CF} = 52.0 Hz), 155.8 (**C**H$_{T6}$), 151.7 (**C**H$_A$), 151.5 (**C**H$_A$), 151.2 (d, **C$_A$**, J_{CF} = 27.6 Hz), 148.0 (**C**N), 145.7 (**C**H$_{T4}$), 141.0 (**2C**H$_A$), 129.2 (d, **C$_B$**, J_{CF} = 74.0 Hz), 125.8 (**C**H$_{T3}$), 125.1 (d, **2C**H$_A$, J_{CF} = 30.8 Hz), 124.7 (d, **C**H$_A$, J_{CF} = 78.8 Hz), 124.3 (d, **C**H$_A$, J_{CF} = 80.4 Hz), 116.3 (**C$_{T2}$**), 115.3 (**C$_{T5}$**), 114.9 (dd, **C**H$_B$, J_{CF} = 14.8 Hz), 114.8 (dd, **C**H$_B$, J_{CF} = 12.8 Hz), 100.4 (dd, **C**H$_B$, J_{CF} = 107.6 Hz), 99.9 (dd, **C**H$_B$, J_{CF} = 92.0 Hz), 42.9 (**C**H$_{TMe}$). Anal.Calcd for

[Ir(**F$_2$ppy**)$_2$(Me**TzPyCN**)][PF_6]·0.3(diethyl ether): C, 40.37; H, 2.24; N, 12.15. Found: C, 40.20; H, 1.95; N, 11.91.

[Ir(ppy)$_2$(MeTzPyMeCN)][PF_6]

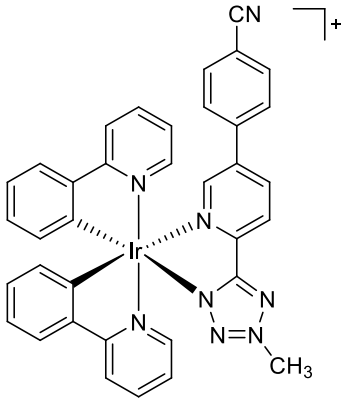

[Ir(**ppy**)$_2$(**TzPyPhCN**)] (0.050 g, 0.067 mmol) was dissolved in dichloromethane (10 mL) and cooled down to –50 °C using ethyl acetate/liquid nitrogen cool bath. A 0.1M methyl trifluoromethanesulfonate solution in dichloromethane (0.016 g, 0.100 mmol) was added dropwise to the vigorously stirred solution. After being maintained at –50 °C for 30 minutes, the solution was warmed up at room temperature and left to stir overnight. An excess of ammonium hexafluorophosphate (0.022 g, 0.134 mmol) was added and stirred for 45 minutes. The crude mixture was washed with water and extracted with dichloromethane (3 × 15 mL) and the combined organic phase was dried on $MgSO_4$. The targeted complex was then collected after filtration and removal of the solvent as a yellow solid. Yield: 0.044 g (73%). M.P. 222 – 224 °C. IR (ν / cm^{-1}): 2229 w (C≡N), 1608 w (tetrazole C=N). ^{1}H NMR (δ / ppm, DMSO-d_6): 8.70 – 8.65 (m, 2H, $\mathbf{H_{T4}}$, $\mathbf{H_{T3}}$), 8.24 (d, 2H, $\mathbf{2H_A}$, J = 9.2 Hz), 8.00 – 7.85 (m, 8H, $\mathbf{H_{T6}}$, $\mathbf{4H_{Tph}}$, $\mathbf{3H_A}$), 7.58 (d, 3H, $\mathbf{3H_B}$, J = 8.8 Hz), 7.21 – 7.14 (m, 2H, $\mathbf{2H_A}$), 7.06 (app. t., 1H, $\mathbf{H_A}$, splitting = 7.6 Hz), 6.99 – 6.93 (m, 2H, $\mathbf{2H_B}$), 6.83 (app. t., 1H, $\mathbf{H_B}$, splitting = 7.6 Hz), 6.23 (d, 1H, $\mathbf{H_B}$, J = 4.2 Hz), 6.16 (d, 1H, $\mathbf{H_B}$, J = 4.2 Hz), 4.54 (s, 3H, $\mathbf{3H_{TMe}}$). ^{13}C NMR (δ / ppm, DMSO-d_6): 166.8 ($\mathbf{C_T}$), 166.2 ($\mathbf{C_{Tph}}$), 165.6 ($\mathbf{C_{Tph}}$), 150.3 ($\mathbf{CH_A}$), 150.1 ($\mathbf{CH_A}$), 148.3 ($\mathbf{CH_{T6}}$), 147.6 ($\mathbf{C_B}$), 144.2 ($\mathbf{C_A}$), 144.1 ($\mathbf{C_A}$), 144.0 (**C**N), 143.5 ($\mathbf{C_{T2}}$), 139.1 ($\mathbf{CH_{Tph}}$), 139.0 ($\mathbf{CH_{Tph}}$), 138.9 ($\mathbf{CH_{Tph}}$), 138.8 ($\mathbf{CH_{Tph}}$), 133.3 ($\mathbf{CH_A}$), 132.0 ($\mathbf{CH_B}$), 131.5 ($\mathbf{CH_B}$), 131.4 ($\mathbf{CH_B}$), 130.9 ($\mathbf{CH_B}$), 130.3 ($\mathbf{CH_B}$), 129.5 ($\mathbf{CH_B}$), 128.8 ($\mathbf{C_B}$), 128.7 ($\mathbf{C_B}$), 127.8 ($\mathbf{CH_B}$), 125.1 ($\mathbf{CH_{T4}}$), 124.6 ($\mathbf{CH_{T3}}$), 124.0 ($\mathbf{CH_A}$), 123.9 ($\mathbf{CH_A}$), 122.8 ($\mathbf{CH_A}$), 122.2 ($\mathbf{CH_B}$), 120.1 ($\mathbf{CH_A}$), 119.8 ($\mathbf{CH_A}$), 118.2 ($\mathbf{C_{T5}}$), 112.3 ($\mathbf{C_B}$), 42.1

(**C**H_{TMe}). Crystals suitable for X-ray analysis were obtained by slow diffusion of hexane into a solution of the complex in dichloromethane. Anal.Calcd for [Ir(**ppy**)$_2$(Me**TzPyMeCN**)][PF_6]·0.2(CH_2Cl_2): C, 47.01; H, 2.88; N, 12.12. Found: C, 47.14; H, 3.04; N, 12.07.

[Ir(ppy)$_2$(TzQn)]

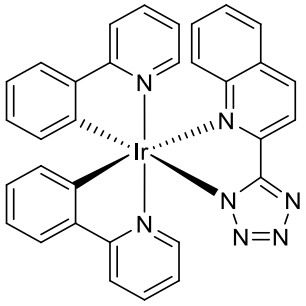

[Ir(**ppy**)$_2$(μ-Cl)]$_2$ (0.250 g, 0.233 mmol) was combined with H**TzQn** (0.115 g, 0.583 mmol) and dissolved in 13 mL of a dichloromethane/ethanol mixture (10:3 v/v). The resulting suspension was stirred at room temperature overnight. The solvents were concentrated and the product was purified *via* column chromatography using Brockmann I grade neutral alumina-filled as stationary phase and a dichloromethane/acetone (8:2 v/v) solvent system as eluent. The targeted complex eluted as the second fraction (yellow). Yield: 0.172 g (53%). M.P. 314 – 317 °C. IR (ν / cm^{-1}): 1602 w (tetrazole C=N). ^{1}H NMR (δ / ppm, acetone-d_6): 8.69 (d, 1H, $\mathbf{H_{T4}}$, J = 8.2 Hz), 8.54 (d, 1H, $\mathbf{H_{T3}}$, J = 8.5 Hz), 8.14 (d, 1H, $\mathbf{H_{T9}}$, J = 8.0 Hz), 8.10 – 7.98 (m, 4H, **4H$_A$**), 7.86 – 7.73 (m, 4H, **4H$_B$**), 7.54 (app. t., 1H, $\mathbf{H_A}$, splitting = 7.4 Hz), 7.33 (d, 1H, $\mathbf{H_A}$, J = 6.0 Hz), 7.21 (app. t., 1H, $\mathbf{H_A}$, splitting = 8.0 Hz), 7.06 (app. t., 1H, $\mathbf{H_A}$, splitting = 6.8 Hz), 7.02 – 6.97 (m, 4H, $\mathbf{H_{T6}}$, $\mathbf{H_{T7}}$, $\mathbf{H_{T8}}$, $\mathbf{H_B}$), 6.73 (app. t., 1H, $\mathbf{H_B}$, splitting = 7.5 Hz), 6.54 (d, 1H, $\mathbf{H_B}$, J = 7.6 Hz), 6.16 (d, 1H, $\mathbf{H_B}$, J = 7.6 Hz). ^{13}C NMR (δ / ppm, acetone-d_6): 169.5 ($\mathbf{C_A}$), 168.7 ($\mathbf{C_A}$), 166.0 ($\mathbf{C_T}$), 155.5 ($\mathbf{C_B}$), 152.5 ($\mathbf{C_{T5}}$), 151.3 (**C**H$_A$), 149.7 (**C**H$_A$), 148.7 ($\mathbf{C_{T10}}$), 145.6 ($\mathbf{C_B}$), 144.7 ($\mathbf{C_B}$), 144.6 ($\mathbf{C_B}$), 141.6 (**C**H$_{T4}$), 138.8 (**C**H$_B$), 138.5 (**C**H$_B$), 133.2 (**C**H$_B$), 131.9 (**C**H$_B$), 130.8 (**C**H$_A$), 130.2 (**C**H$_{T7}$), 130.1 (**C**H$_{T6}$), 129.8 (**C**H$_B$), 128.9 (**C**H$_A$), 128.5 (**C**H$_A$), 125.7 (**C**H$_B$), 124.9 (**C**H$_B$), 123.9 (**C**H$_A$), 123.6 (**C**H$_A$), 122.5 (**C**H$_{T8}$), 122.4 (**C**H$_B$), 120.6 (**C**H$_{T3}$), 120.2 (**C**H$_{T9}$), 120.1 (**C**H$_A$); quaternary tetrazolic C peak was not visible in the spectrum. Anal. Calcd for [Ir(**ppy**)$_2$(**TzQn**)]·(CH_2Cl_2)·0.2(acetone): C, 54.78; H, 3.71; N, 12.70. Found: C, 54.81; H, 3.86; N, 12.67.

[Ir(ppy)$_2$(TziQn)]

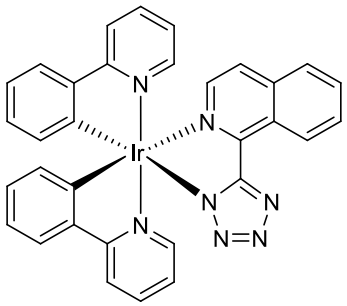

[Ir(**ppy**)$_2$(μ-Cl)]$_2$ (0.250 g, 0.233 mmol) was combined with H**TzQn** (0.115 g, 0.583 mmol) and dissolved in 13 mL of a dichloromethane/ethanol mixture (10:3 v/v). The resulting suspension was stirred at room temperature overnight. The solvents were concentrated and the product was purified *via* column chromatography using Brockmann I grade neutral alumina-filled as stationary phase and a dichloromethane/acetone (8:2 v/v) solvent system as eluent. The targeted complex eluted as the second fraction (yellow). Yield: 0.235 g (72%). M.P. 272 – 275 °C. IR (ν / cm^{-1}): 1606 w (tetrazole C=N). ^{1}H NMR (δ / ppm, acetone-*d*$_6$): 10.25 – 10.21 (m, 1H, **H$_{T9}$**), 8.16 – 8.12 (m, 2H, **2H$_A$**), 8.10 – 8.04 (m, 1H, **H$_{T10}$**), 7.97 – 7.94 (m, 2H, **H$_{T6}$**, **H$_{T7}$**), 7.88 – 7.81 (m, 5H, **3H$_A$**, **H$_{T4}$**, **H$_{T5}$**), 7.79 – 7.75 (m, 2H, **H$_A$**, **H$_B$**), 7.59 (d, 1H, **H$_B$**, J = 6.0 Hz), 7.11 (app. t., 1H, **H$_B$**, splitting = 6.8 Hz), 7.04 – 6.98 (m, 2H, **2H$_A$**), 6.94 – 6.89 (m, 2H, **2H$_B$**), 6.78 (app. t., 1H, **H$_B$**, splitting = 7.4 Hz), 6.67 (d, 1H, **H$_B$**, J = 7.6 Hz), 6.35 (d, 1H, **H$_B$**, J = 7.6 Hz). ^{13}C NMR (δ / ppm, acetone-*d*$_6$): 169.3 (**C$_A$**), 169.1 (**C$_A$**), 166.0 (**C$_T$**), 154.7 (**C$_{T8}$**), 150.4 (**CH$_B$**), 150.1 (**CH$_B$**), 149.6 (**C$_B$**), 145.6 (**C$_B$**), 145.1 (**C$_B$**), 142.5 (**CH$_{T4}$**), 138.8 (**CH$_A$**), 138.5 (**CH$_A$**), 137.7 (**C$_{T3}$**), 133.5 (**CH$_{T6}$**), 132.8 (**CH$_B$**), 132.7 (**CH$_B$**), 131.0 (**CH$_B$**), 130.4 (**CH$_B$**), 130.1 (**CH$_{T7}$**), 128.9 (**CH$_{T9}$**), 128.1 (**CH$_{T10}$**), 127.3 (**C$_B$**), 125.6 (**CH$_{T5}$**), 125.1 (**CH$_A$**), 125.0 (**CH$_A$**), 124.1 (**CH$_B$**), 123.7 (**CH$_A$**), 122.8 (**CH$_A$**), 122.1 (**CH$_B$**), 120.2 (**CH$_A$**), 120.1 (**CH$_A$**); quaternary tetrazolic C peak was not visible in the spectrum. Anal. Calcd for [Ir(**ppy**)$_2$(**TziQn**)]·0.7(CH_2Cl_2): C, 52.08; H, 3.12; N, 13.01. Found: C, 52.26; H, 2.94; N, 13.04.

[Ir(ppy)$_2$(MeTzQn)][PF$_6$]

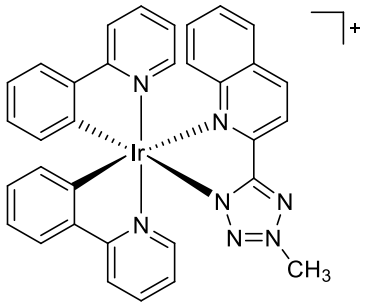

[Ir(**ppy**)$_2$(**TzQn**)] (0.050 g, 0.072 mmol) was dissolved in dichloromethane (10 mL) and cooled down to –50 °C using an ethyl acetate/liquid nitrogen cool bath. Thereafter, a 0.1 M methyl trifluoromethanesulfonate solution in dichloromethane (0.018 g, 0.108 mmol) was added dropwise to the vigorously stirred solution. After being maintained at –50°C for 30 minutes, the solution was warmed up at room temperature and left to stirred overnight. An excess of ammonium hexafluorophosphate (0.025 g, 0.144 mmol) was added and stirred for 45 minutes. The crude mixture was washed with water and extracted with dichloromethane (3 × 15 mL) and the combined organic phase was dried on $MgSO_4$. The targeted complex was then collected after filtration and removal of the solvent as an orange solid. Yield: 0.050 g (81%). M.P. 242 – 246 °C. IR (ν / cm^{-1}): 1607 w (tetrazole C=N). ^{1}H NMR (δ / ppm, acetone-d_6): 8.97 (d, 1H, **H$_{T4}$**, J = 8.4 Hz), 8.66 (d, 1H, **H$_{T3}$**, J = 8.5 Hz), 8.26 (d, 1H, **H$_{T6}$**, J = 8.1 Hz), 8.19 – 8.07 (m, 4H, **4H$_A$**), 7.99 (app. t., 1H, **H$_{T7}$**, splitting = 8.2 Hz), 7.94 – 7.83 (m, 4H, **2H$_A$**, **2H$_B$**), 7.71 (app. t., 1H, **H$_A$**, splitting = 7.6 Hz), 7.35 (app. t., 1H, **H$_A$**, splitting = 8.0 Hz), 7.10 – 6.98 (m, 5H, **3H$_B$**, **H$_{T8}$**, **H$_{T9}$**), 6.84 (app. t., 1H, **H$_B$**, splitting = 7.5 Hz), 6.43 (d, 1H, **H$_B$**, J = 7.6 Hz), 6.17 (d, 1H, **H$_B$**, J = 7.7 Hz), 4.59 (s, 3H, **3H$_{TMe}$**). ^{13}C NMR (δ / ppm, acetone-d_6): 168.8 (**C$_A$**), 168.6 (**C$_A$**), 168.1 (**C$_T$**), 152.0 (**CH$_A$**), 150.8 (**C$_B$**), 150.5 (**CH$_A$**), 148.9 (**C$_B$**), 147.5 (**C$_{T2}$**), 145.2 (**C$_B$**), 144.7 (**C$_B$**), 143.2 (**CH$_{T4}$**), 141.0 (**C$_{T10}$**), 139.7 (**CH$_A$**), 139.6 (**CH$_{T7}$**), 133.1 (**CH$_B$**), 132.5 (**CH$_B$**), 131.9 (**CH$_B$**), 131.6 (**C$_{T5}$**), 131.3 (**CH$_{T8}$**), 130.7 (**CH$_A$**), 130.4 (**CH$_A$**), 130.3 (**CH$_A$**), 129.0 (**CH$_A$**), 126.1 (**CH$_B$**), 125.4 (**CH$_B$**), 124.6 (**CH$_{T9}$**), 124.1 (**CH$_B$**), 123.7 (**CH$_B$**), 123.6 (**CH$_B$**), 120.9 (**CH$_{T3}$**), 120.8 (**CH$_{T6}$**), 120.6 (**CH$_A$**), 42.6 (**CH$_{TMe}$**). Anal.Calcd for [Ir(**ppy**)$_2$(Me**TzQn**)][PF$_6$]·0.2(CH$_2$Cl$_2$): C, 45.74; H, 2.93; N, 11.26. Found: C, 45.71; H, 2.60; N, 11.13.

[Ir(ppy)$_2$(MeTziQn)][PF$_6$]

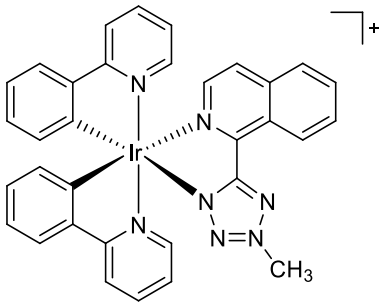

[Ir(**ppy**)$_2$(**TziQn**)] (0.060 g, 0.086 mmol) was dissolved in dichloromethane (10 mL) and cooled down to –50 °C using an ethyl acetate/liquid nitrogen cool bath. Thereafter, a 0.1 M methyl trifluoromethanesulfonate solution in dichloromethane (0.021 g, 0.129 mmol) was added dropwise to the vigorously stirred solution. After being maintained at –50°C for 30 minutes, the solution was warmed up at room temperature and left to stirred overnight. An excess of ammonium hexafluorophosphate (0.028 g, 0.163 mmol) was added and stirred for 45 minutes. The crude mixture was washed with water and extracted with dichloromethane (3 × 15 mL) and the combined organic phase was dried on $MgSO_4$. The targeted complex was then collected after filtration and removal of the solvent as an orange solid. Yield: 0.044 g (60%). M.P. 215 – 218 °C. IR (ν / cm^{-1}): 1607 w (tetrazole C=N). ^{1}H NMR (δ / ppm, acetone-*d*$_6$): 9.58 (d, 1H, **H$_{T9}$**, J = 9.8 Hz), 8.27 – 8.20 (m, 4H, **4H$_A$**), 8.15 – 8.10 (m, 2H, **H$_{T6}$**, **H$_{T7}$**), 8.05 (app. t., 2H, **H$_A$**, **H$_{T10}$**, splitting = 5.7 Hz), 7.99 – 7.92 (m, 3H, **3H$_A$**), 7.87 (d, 2H, **H$_{T4}$**, **H$_{T5}$**, J = 7.7 Hz), 7.10 – 7.06 (m, 3H, **2H$_A$**, **H$_B$**), 7.03 – 6.95 (m, 2H, **2H$_B$**), 6.88 (app. t., 1H, **H$_B$**, splitting = 7.6 Hz), 6.35 (app. t., 2H, **2H$_B$**, splitting = 7.6 Hz), 4.69 (s, 3H, **3H$_{TMe}$**). ^{13}C NMR (δ / ppm, acetone-*d*$_6$): 168.8 (**C$_A$**), 168.5 (**C$_A$**), 168.2 (**C$_T$**), 151.2 (**CH$_{T4}$**), 150.8 (**CH$_{T6}$**), 150.1 (**C$_B$**), 145.9 (**C$_{T8}$**), 145.5 (**C$_B$**), 145.2 (**C$_B$**), 145.1 (**C$_B$**), 143.0 (**CH$_A$**), 139.7 (**CH$_A$**), 139.6 (**CH$_A$**), 138.1 (**C$_{T3}$**), 134.4 (**CH$_{T10}$**), 132.8 (**2CH$_B$**), 132.2 (**CH$_{T7}$**), 131.4 (**CH$_B$**), 130.6 (**CH$_B$**), 129.1 (**CH$_A$**), 128.8 (**CH$_A$**), 127.8 (**C$_{T2}$**), 126.6 (**CH$_{T9}$**), 125.9 (**CH$_A$**), 125.4 (**CH$_{T5}$**), 124.5 (**CH$_B$**), 124.4 (**CH$_B$**), 123.8 (**CH$_B$**), 123.3 (**CH$_B$**), 120.7 (**CH$_A$**), 120.6 (**CH$_A$**), 42.7 (**CH$_{TMe}$**). Anal.Calcd for [Ir(**ppy**)$_2$(Me**TziQn**)][PF$_6$]·0.4(CH_2Cl_2)·0.2(H_2O): C, 44.85; H, 2.95; N, 10.96. Found: C, 44.84; H, 2.90; N, 10.65.

Chapter 3

Biological Investigation of Cyano and (Iso)Quinolyl-Functionalised Iridium Tetrazolato Complexes

The content of this chapter has been published in:

Chemistry – A European Journal (2017) with the title "Investigating intracellular localisation and cytotoxicity trends for neutral and cationic iridium tetrazolato complexes in live cells".[238]

Scientific Reports (2018) with the title "Mitochondria imaging in live cells and live or fixed tissues using a luminescent iridium complex".[283]

3.1 Introduction

The translucent nature of cells has made detailed cellular studies hard to achieve, until the development of differential cell stains. This process began in 1858 when Joseph von Gerlach established that a dilute solution of carmine could preferentially stain the nuclei of brain tissues.[284] However, classical dyes such as Gram or hematoxylin and eosin (H&E) stains (**Figure 3.1** - left), are generally not highly selective against specific biomolecules and their imaging process is based on the absorption of transmitted light, which does not allow 3D images.[285,286]

In contrast, the development of luminescent probes has provided a new tool for the study of cells at subcellular level with higher sensitivity and better spatial resolution. Initially, these probes were based on organic fluorophores[48,50] (**Figure 3.1** - centre), fluorescent proteins[287,288] or quantum dots.[289,290] Although they could efficiently localise within cells and accumulate in particular organelles, their

application was limited by inherently small Stokes shifts and short excited state lifetimes.[291]

As alternative to the organic probes, transition metal complexes [e.g.: Re(I), Ru(II), Os(II), Au(I), Ir(III) and Pt(II)][64,65,80,292,293] (**Figure 3.1** - right) and luminescent lanthanide species [e.g.: Eu(III), Tb(III) and Yb(III)][291,294,295] have been explored due to their alternative photophysical properties, which have allowed major improvements in the optical imaging techniques. In particular, luminescent iridium(III) complexes have showed to be exceptional systems for the application in live cells imaging. Two main approaches have been employed for the construction of these probes. In the first case, small complexes have been designed to internalise and accumulate within the cells based on the functional groups present on the coordinated ligands.[101–104,116,139,296,297] In the second group, iridium complexes have been conjugated with biologically relevant moieties such as carbohydrates,[126,298] biotin/avidin,[107,299–301] amino acids[120] and proteins[302] in an attempt to control their biospecificity.

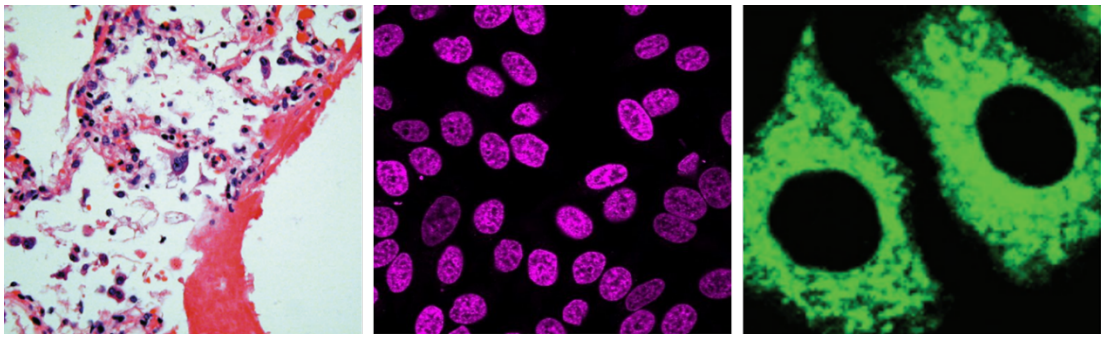

Figure 3.1 Different cells and tissues staining. (Left) H&E staining of lung tissue showing hyaline-membrane formation and pneumocyte desquamation with focal giant-cell formation (× 400). (Centre) Nuclei of live HeLa cells stained with NucSpot™ 650 (Biotium). (Right) Mitochondria of live A549 cells stained with an iridium(III) complex (scale bar = 10 μm). Reproduced with permission from ref [303,304].

In this chapter, the biological properties of the neutral and methylated iridium(III) complexes discussed in Chapter 2 are described, aiming to highlight the structure-activity relationship of these probes. The biological investigation has been carried out in live H9c2 rat cardiomyoblast cells, and the uptake mechanism, specific localisation and photostability of the iridium complexes has been assessed in detailed.

Interesting behaviour trends have been defined, in particular related to the accumulation of the neutral probes in the endoplasmic reticulum (ER) and lipid droplets. In fact only a few examples of iridium(III) complexes applied to the stain of ER have been reported, and the majority of them are highly toxic.[105,137–139,143,305–307] On the other hand, the cytotoxicity analyses on the neutral cyano and (iso)quinolyl-functionalised iridium probes have evidenced their applicability in live cells imaging. Moreover, only one rhenium phosphorescent dye has been developed for the specific localisation in lipid droplets.[232,248]

Some of the methylated complexes have shown good mitochondrial specificity, but also high toxicity against live H2c9 cells for long term experiment.

The staining of mitochondria in tissues relies primarily on immunochemistry due to the lack of probes which are able to localise in these organelles in the absence of membrane potential. Interestingly, the cationic $[Ir(\mathbf{ppy})_2(Me\mathbf{TzPyPhCN})]^+$, which had showed mitochondrial accumulation in live H9c2 cells, has also successfully stained mitochondria in both fresh and fixed tissues. Noteworthy, $[Ir(\mathbf{ppy})_2(Me\mathbf{TzPyPhCN})]^+$ represents the first example of metal probe with the ability of localised in these organelles in fixed tissues, suggesting a mechanism of uptake independent from the mitochondrial membrane potential.[283]

3.2 Biological Investigation in H9c2 cells

3.2.1 Lipophilicity and Cellular Uptake

Lipophilicity is one of the main factors to consider during the design of a new imaging probe, as previously discussed in Chapter 1, section 1.4.4. The lipophilicity of the investigated iridium complexes was measured by the shake-flask method described in this chapter (section 3.5.2), using a pH = 7.4 buffered PBS solution and *n*-octanol.[308] The calculated $logD_{7.4}$ values are listed in **Table 3.1**.

Table 3.1 Distribution coefficient values ($logD_{7.4}$) for neutral and charged iridium complexes.

Complex	$logD_{7.4}$	Amount of complex [a] (fmol)	Concentration[b] (μM)
[Ir(**ppy**)$_2$(**TzPyCN**)]	2.09 ± 0.06	0.042 ± 0.004	21.16 ± 1.85
[Ir(**F$_2$ppy**)$_2$(**TzPyCN**)]	2.01 ± 0.05	0.319 ± 0.049	159.71 ± 46.95
[Ir(**ppy**)$_2$(**TzPyPhCN**)]	2.68 ± 0.08	0.171 ± 0.042	85.46 ± 20.76
[Ir(**ppy**)$_2$(Me**TzPyCN**)]$^+$	0.64 ± 0.03	0.015 ± 0.002	7.35 ± 0.81
[Ir(**F$_2$ppy**)$_2$(Me**TzPyCN**)]$^+$	1.86 ± 0.02	0.025 ± 0.007	12.74 ± 3.26
[Ir(**ppy**)$_2$(Me**TzPyPhCN**)]$^+$	1.87 ± 0.08	0.045 ± 0.005	22.74 ± 2.48
[Ir(**ppy**)$_2$(**TzQn**)]	2.23 ± 0.04	0.346 ± 0.070	173.03 ± 35.20
[Ir(**ppy**)$_2$(**TziQn**)]	2.57 ± 0.05	0.063 ± 0.011	31.61 ± 5.60
[Ir(**ppy**)$_2$(Me**TzQn**)]$^+$	1.68 ± 0.05	0.372 ± 0.038	186.24 ± 18.92
[Ir(**ppy**)$_2$(Me**TziQn**)]$^+$	1.49 ± 0.06	0.515 ± 0.085	257.29 ± 42.64

[a] Average number of moles of iridium complex incubated within a H9c2 cell (see Experimental - section 3.5.5 for incubation conditions). [b] The relative concentration was calculated assuming an average volume of H9c2 cell equal to 2 pL.

The values obtained are within a range that is similar to those reported previously for cyclometalated iridium complexes.[104,112,115,126] In the case of the neutral species, the $logD_{7.4}$ was comparable to the BODIPY family (functionalised 4,4-difluoro-4-bora-3a,4a-diaza-s-indacene cores), which is known to localise in lipid droplets.[309]

The values for the five neutral probes fall in a range between 2.01 and 2.68. Methylation of the iridium complexes lowers the lipophilicity, which is ascribed to the introduction of the cationic charge, and results in $logD_{7.4}$ values occuring in the range 1.49 - 1.97. The lowest lipophilicity is observed for the complex $[Ir(\mathbf{ppy})_2(Me\mathbf{TzPyCN})]^+$ at 0.64. A comparison of the $logD_{7.4}$ values between $[Ir(\mathbf{ppy})_2(\mathbf{TzPyCN})]$, $[Ir(\mathbf{ppy})_2(\mathbf{TzPyPhCN})]$, $[Ir(\mathbf{ppy})_2(\mathbf{TzQn})]$, and $[Ir(\mathbf{ppy})_2(\mathbf{TziQn})]$, shows that extending the conjugation of the tetrazolato ligands increases lipophilicity. A similar trend also holds true for the methylated analogues, $[Ir(\mathbf{ppy})_2(Me\mathbf{TzPyCN})]^+$, $[Ir(\mathbf{ppy})_2(Me\mathbf{TzPyPhCN})]^+$, $[Ir(\mathbf{ppy})_2(Me\mathbf{TzQn})]^+$, and $[Ir(\mathbf{ppy})_2(Me\mathbf{TziQn})]^+$.

The introduction of fluoride substituents on aromatic moieties is often associated with an increase in $logD_{7.4}$ values.[131,134,310,311] However, this trend was only observed in the charged complexes, where $logD_{7.4}$ increased from 0.64 for $[Ir(\mathbf{ppy})_2(Me\mathbf{TzPyCN})]^+$ to 1.86 for $[Ir(\mathbf{F_2ppy})_2(Me\mathbf{TzPyCN})]^+$. In contrast, little change was observed in the $logD_{7.4}$ value between $[Ir(\mathbf{ppy})_2(\mathbf{TzPyCN})]$ and $[Ir(\mathbf{F_2ppy})_2(\mathbf{TzPyCN})]$, consistently with previously published cyclometalated iridium complexes with lipophilicity values around 2.[104]

The cellular uptake for the synthesised iridium complexes was studied by means of ICP-MS measurements, and the results are reported in **Table 3.1**. The H9c2 cells were incubated with complexes at 20 μM in cell culture medium (0.2% DMSO) for 30 minutes at 37 °C. The calculated cellular concentration values were obtained assuming an average volume of a single H9c2 cell equal to 2 pL.[312] The amount of iridium complex accumulated within the cells is comparable with other cyclometalated iridium systems,[127,144,296,313] even those bioconjugated with carbohydrate or biotin moieties, which possess lipophilicity values in a range of 2.5 and 8.2.[126,298,306]

The analysis of the data does not reveal a simple trend and it could potentially suggest that lipophilicity is not the only factor affecting the cellular uptake of probes. For example, three of the neutral complexes, $[Ir(\mathbf{F_2ppy})_2(\mathbf{TzPyCN})]$, $[Ir(\mathbf{ppy})_2(\mathbf{TzPyPhCN})]$, and $[Ir(\mathbf{ppy})_2(\mathbf{TzQn})]$ exhibit high iridium intracellular concentrations indicating good cellular internalisation. The remaining two complexes,

[Ir(**ppy**)$_2$(**TzPyCN**)] and [Ir(**ppy**)$_2$(**TziQn**)], exhibit lower intracellular iridium concentrations although their lipophilicity fell within the range of the aforementioned neutral complexes. On the other hand, only the cationic iridium complexes bound to the quinolyl and isoquinolyl tetrazolate ligands, [Ir(**ppy**)$_2$(Me**TzQn**)]$^+$ and [Ir(**ppy**)$_2$(Me**TziQn**)]$^+$, exhibit efficient cellular internalisation. The lack of straightforward trends suggests that the mechanism of internalisation might be different for the various complexes.

3.2.2 Localisation

The cellular localisation of the iridium complexes within H9c2 cells was investigated *via* confocal microscopy (refer to section 3.5.14). Following the same incubation protocol described for the ICP-MS measurements, complexes could be detected in cells by single photon excitation at 403 nm and were also shown to be compatible with two-photon imaging modalities, with optimal excitation in the range of 810 – 830 nm. Representative lambda stack micrographs and two-photon images of live H9c2 cells incubated with the iridium complexes are listed in Appedix B from **Figure B.1** to **Figure B.5**.

All the complexes could be readily detected within cells in an emission interval of 525 – 644 nm, which is consistent with the emission profiles recorded for aqueous solutions in cuvette and showed in Chapter 2, section 2.4.5, **Table 2.6** and **Table 2.7**. The $[Ir(\mathbf{ppy})_2(Me\mathbf{TzPyCN})]^+$ complex was the only exception as it had low detectability within the whole instrument range (420 – 740 nm), consistent with measurements taken in aqueous media. Thus it was omitted from co-localisation studies with commercially available organic dyes.

All the neutral complexes had similar staining patterns and evidenced a diffuse network emanating from the nucleus and extending into the cytoplasm (**Figure 3.2**), consistent with the endoplasmic reticulum. In addition, the methylated cationic complex $[Ir(\mathbf{ppy})_2(Me\mathbf{TzQn})]^+$ also detected this reticular network in the perinuclear region (**Figure 3.2**).

For a better understanding of the co-localisation of the iridium(III) tetrazolato probes with organic markers such as ER-Tracker™, BODIPY® 500/510 C_1,C_{12} and MitoTracker®, Pearson's correlation coefficient[314] was calculated for the endoplasmic reticulum (ER), lipid droplets and mitochondria respectively (**Table 3.2**). The absence of the data related to $[Ir(\mathbf{ppy})_2(Me\mathbf{TziQn})]^+$ is due to the interference of this complex with the normal staining pattern of the commercial organic probe, which were found in unusual cellular structures.

Co-staining with ER-Tracker™ revealed relatively high Pearson's correlation coefficients,[314] with values above 0.7, confirming that the neutral complexes and the methylated cationic complex $[Ir(\mathbf{ppy})_2(Me\mathbf{TzQn})]^+$ localise within the endoplasmic reticulum.

While these probes were predominately localised within the ER, their emission was also detected within compartments in the cytoplasm that were not labelled with ER-Tracker™. The morphology and localisation of these compartments resembled lipid droplets. Hence, BODIPY® 500/510 C_1,C_{12}, a fatty acid analogue that localises with lipid droplets and partially with the endoplasmic reticulum was employed for co-localisation studies and produced strong overlapping with these complexes (**Figure 3.3**). A high Pearson's correlation coefficients[314] (**Table 3.2**) was obtained for these probes and BODIPY® 500/510 C_1,C_{12} (ranging between 0.63 and 0.92), confirming that these compartments were lipid droplets.

Interestingly, it has been demonstrated that lipid droplets interact with organelles such as ER and mitochondria.[203] In particular the ER-lipid droplets connection involves important physiological functions including protein and lipid trafficking, response to ER stress and a role in ER-associated degradation.[315,316] Hence it can be hypothesised that part of the iridium probe that localised and accumulated in the ER, could have been enclosed in lipid droplets with other lipids, and then released in the cytoplasm.

Table 3.2 Pearson's correlation coefficients in live H9c2 cells.

Complex	ER-Tracker™	BODIPY® 500/510 C_1,C_{12}	MitoTracker®
[Ir(**ppy**)$_2$(**TzPyCN**)]	0.70 ± 0.02	0.91 ± 0.01	-
[Ir(**F$_2$ppy**)$_2$(**TzPyCN**)]	0.88 ± 0.03	0.85 ± 0.02	-
[Ir(**ppy**)$_2$(**TzPyPhCN**)]	0.79 ± 0.05	0.75 ± 0.03	-
[Ir(**F$_2$ppy**)$_2$(Me**TzPyCN**)]$^+$	N/A[a]	-	0.65 ± 0.04
[Ir(**ppy**)$_2$(Me**TzPyPhCN**)]$^+$	-	-	0.71 ± 0.05
[Ir(**ppy**)$_2$(**TzQn**)]	0.82 ± 0.01	0.63 ± 0.05	-
[Ir(**ppy**)$_2$(**TziQn**)]	0.70 ± 0.02	0.92 ± 0.01	-
[Ir(**ppy**)$_2$(Me**TzQn**)]$^+$	0.81 ± 0.01	0.81 ± 0.01	-

[a] Co-localisation experiments with ER-Tracker™ could not be performed, as the addition of ER-Tracker™ to cells stained with this complex caused the displacement of the iridium species from the ER.

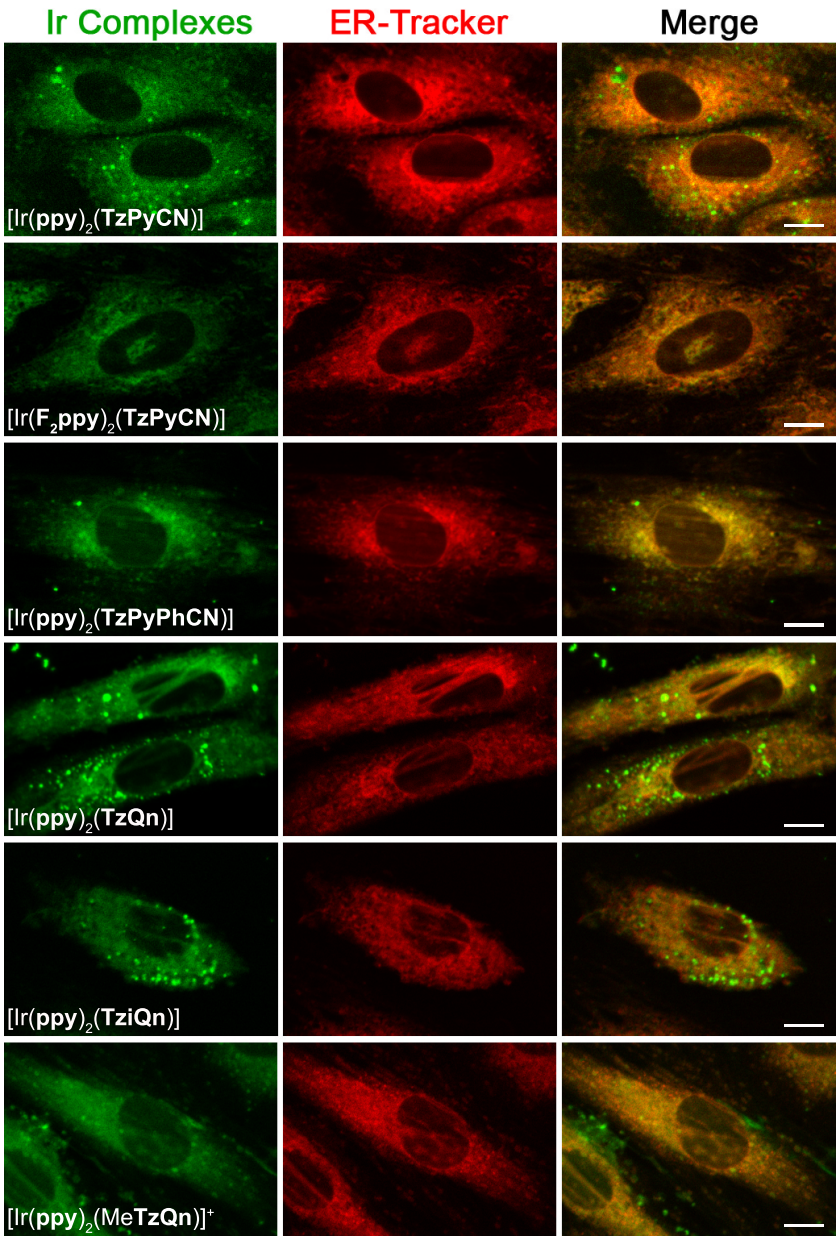

Figure 3.2 Iridium complexes interacting with endoplasmic reticulum (ER) in live H9c2 cells. Micrographs of H9c2 cells stained with the iridium complexes (green) and counter-stained with ER Tracker™ (red). Yellow/orange colour in the merge indicates marker co-localisation. Scale bars = 10 μm.

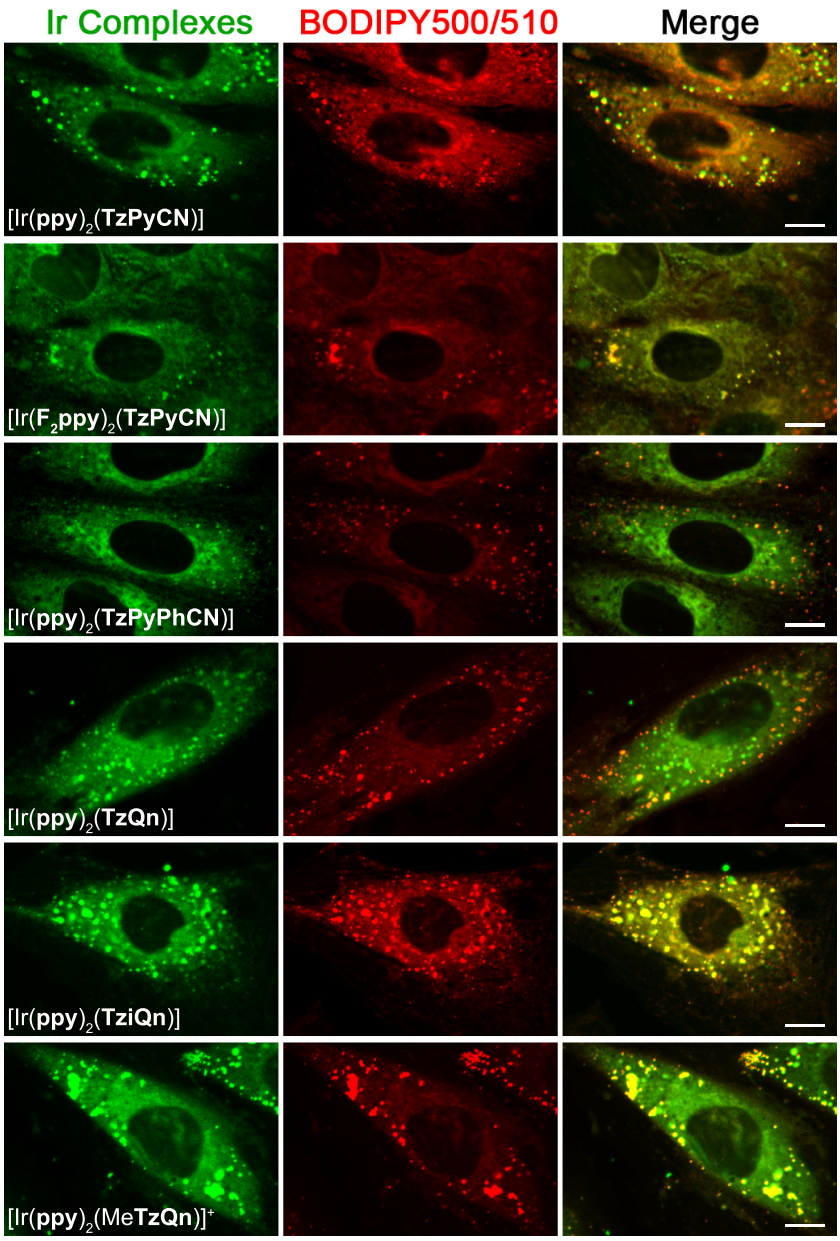

Figure 3.3 Iridium complexes localise with lipid droplets in live H9c2 cells. Micrographs of H9c2 cells stained with the iridium complexes (green) and counter-stained with BODIPY® 500/510 C_1,C_{12} fatty acid analogue (red). Yellow/orange colour in the merge indicates marker co-localisation. Scale bars = 10 μm.

The methylated complexes [Ir(**F$_2$ppy**)$_2$(Me**TzPyCN**)]$^+$ and [Ir(**ppy**)$_2$(Me**TzPyPhCN**)]$^+$ localised within elongated structures throughout the cytoplasm, a staining pattern that is characteristic of mitochondrial association (**Figure 3.4**). Co-staining with MitoTracker® Red CMXRos confirmed this interaction, with Pearson's correlation coefficient[314] between 0.65 and 0.71 (**Table 3.2**).

In general, the positive charge favours the transport of the dye across the mitochondrial membrane as a consequence of the intermembrane electrical potential gradient. For this reason, the majority of the complexes for the staining of this organelle are lipophilic cations.[317] Nevertheless, the uptake of [Ir(**ppy**)$_2$(Me**TzPyPhCN**)]$^+$ in H9c2 cells has been showed to be independent from the mitochondrial potential (refer to section 3.3.3 for the discussion).

It is interesting to note that the complex [Ir(**F$_2$ppy**)$_2$(Me**TzPyCN**)]$^+$ also stained what appears to be the ER along with the mitochondria, although co-staining between the complex and ER-Tracker™ could not be performed, due to displacement of the organic dye upon addition of the fluorinated iridium complex (**Table 3.2**). Despite the use of different staining protocols, the localisation of the fluorinated iridium probe within the cells was affected by the presence of the organic dye and resulted in dislocation from the ER.

While [Ir(**ppy**)$_2$(Me**TziQn**)]$^+$ also co-located with MitoTracker® Red CMXRos, this charged complex appeared to induce apoptosis, characterised by the formation of cellular vacuoles and rounding of the mitochondria (**Figure 3.4**). In this case, ER-Tracker™ was also observed to co-localise with these unusual cellular structures. An increase of caspase activity in H9c2 cells after incubation with [Ir(**ppy**)$_2$(Me**TziQn**)]$^+$ confirmed the induction of apoptosis[318] and will be discussed in details in section 3.2.4.

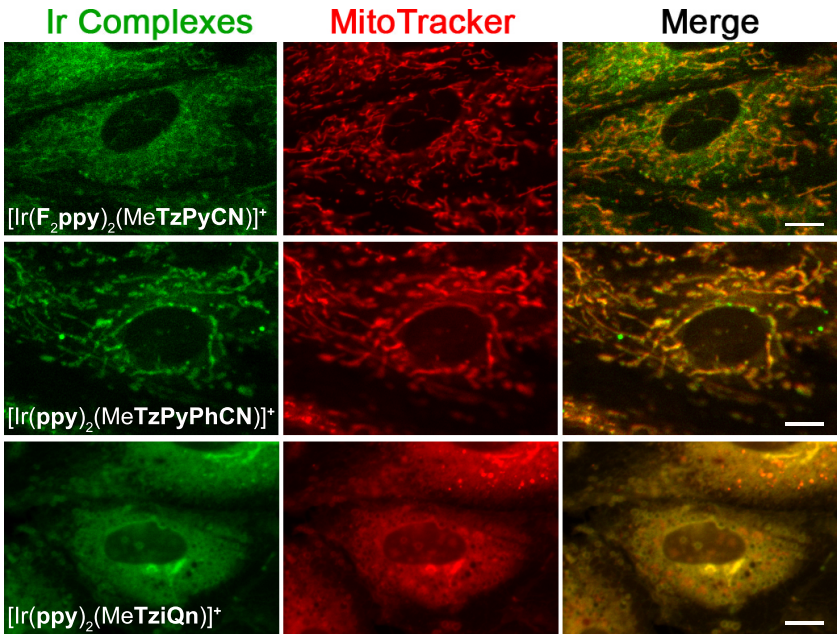

Figure 3.4 Iridium complexes interacting with mitochondria in live H9c2 cells. Micrographs of H9c2 cells stained with the iridium complexes (green) and counter-stained with MitoTracker®Red CMXRos (red). Yellow/orange colour in the merge indicates co-localisation between markers. Scale bars = 10 μm.

3.2.3 Mechanism of Cellular Internalisation

Confocal microscopy was also employed to assess the mechanism of cellular internalisation. The intensity of the emission from the iridium complexes was compared between cells incubated at 37 and 4 °C (**Figure 3.5**), the latter to suppress energy-mediated mechanisms of entrance.

The emission detected from each complex at 37 °C shows a good correlation with the average amount of iridium found in cells measured by ICP-MS (**Table 3.1**). Cells incubated with [Ir(**F$_2$ppy**)$_2$(**TzPyCN**)], [Ir(**ppy**)$_2$(**TzPyPhCN**)], [Ir(**ppy**)$_2$(**TzQn**)], [Ir(**ppy**)$_2$(Me**TzQn**)]$^+$ and [Ir(**ppy**)$_2$(Me**TziQn**)]$^+$ show the highest emission intensity, and also record the largest concentration of iridium per cell. The trend in emission intensity also correlates well with the quantum yield values in aqueous media (Chapter 2, section 2.4.5, **Table 2.6** and **Table 2.7**). For example, the emission detected from [Ir(**ppy**)$_2$(**TzPyPhCN**)] is comparable with [Ir(**ppy**)$_2$(Me**TzQn**)]$^+$ and [Ir(**ppy**)$_2$(Me**TziQn**)]$^+$, even though the former was detected at a lower concentration.

The emission detected from each of the cells following incubation at 4 °C was significantly reduced. This suggests that energy dependent pathways are predominantly involved in the cellular uptake of these complexes, a result that is consistent with previously studied cyclometalated iridium species incubated in various cell lines.[115,117,125,254,319] Again, the lack of clear trends in **Figure 3.5** suggests variable mechanism of entrance even for subtle chemical changes. For example, [Ir(**ppy**)$_2$(**TzQn**)] is detected well upon incubation at 4 °C, but [Ir(**ppy**)$_2$(**TziQn**)] is barely visible, even though the two complexes differ only by the orientation of the quinolyl substituents and have very similar lipophilicity values. These results reinforce previously reported views[80,292] that conclusions based exclusively on lipophilicity measurements might not be adequate, even for families of complexes with very similar chemical structures.

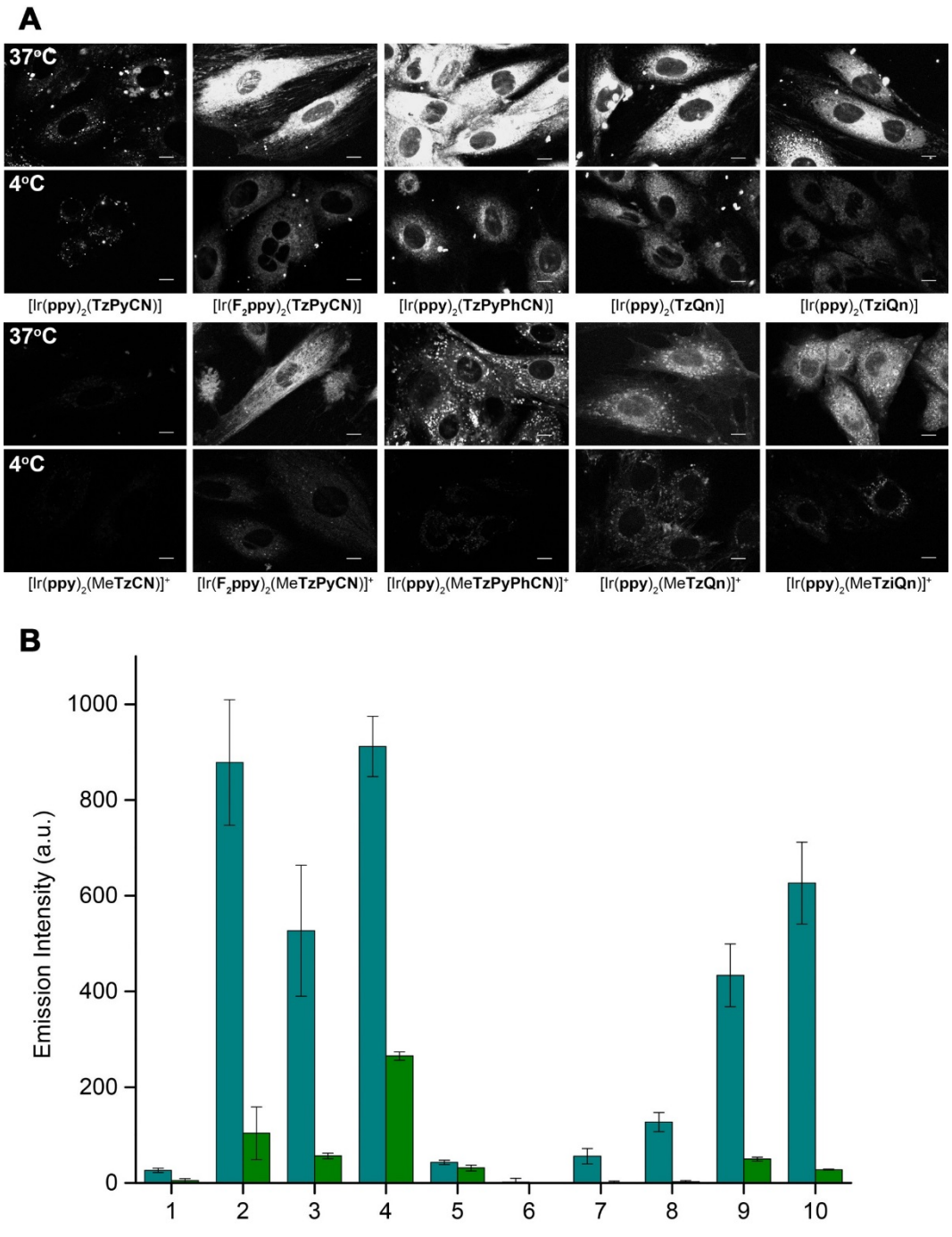

Figure 3.5 (A) Confocal micrographs of H9c2 cells incubated with iridium complexes at 37 °C or 4 °C. Scale bar = 5 μm. (B) Histogram showing the emission intensity of iridium complexes detected from H9c2 cells when incubated at 37 °C (turquoise) or 4 °C (green) to inhibit energy dependent cell entry. 1) [Ir(**ppy**)$_2$(**TzPyCN**)]; 2) [Ir(**F$_2$ppy**)$_2$(**TzPyCN**)]; 3) [Ir(**ppy**)$_2$(**TzPyPhCN**)]; 4) [Ir(**ppy**)$_2$(**TzQn**)]; 5) [Ir(**ppy**)$_2$(**TziQn**)]; 6) [Ir(**ppy**)$_2$(Me**TzPyCN**)]$^+$; 7) [Ir(**F$_2$ppy**)$_2$(Me**TzPyCN**)]$^+$; 8) [Ir(**ppy**)$_2$(Me**TzPyPhCN**)]$^+$; 9) [Ir(**ppy**)$_2$(Me**TzQn**)]$^+$; 10) [Ir(**ppy**)$_2$(Me**TziQn**)]$^+$.

3.2.4 Cytotoxicity

The cell viability was assessed via MTS assay to highlight cytotoxic effects of iridium probes in the darkness after internalisation in live cells. The MTS protocol is described in Experimental - section 3.5.6. The H9c2 cells were incubated for either 2 hours or 24 hours with the complexes at 20 μM or 40 μM.

An important trend emerges from the collected results (**Figure 3.6**), highlighting the fact that while the neutral complexes only exhibit slight cytotoxicity, cell viability is reduced upon incubation with the corresponding cationic complexes. On comparing the cytotoxicity and ICP-MS data from incubated cells (**Table 3.1**), it is clear that cytotoxic effects are not exclusively dependent on the relative amount of iridium complexes incubated within the cells. For example, the fluorinated complex [Ir(**F$_2$ppy**)$_2$(**TzPyCN**)] does not exhibit significant cytotoxicity compared to its methylated analogous [Ir(**F$_2$ppy**)$_2$(Me**TzPyCN**)]$^+$, even though the concentration of the latter is lower by an order of magnitude. These results suggest that cytotoxic effect for this family of iridium complexes might be strongly related to their relative cellular localisation.

The only exception to the cytotoxic effect of the cationic complexes seems to be related to [Ir(**ppy**)$_2$(Me**TzPyCN**)]$^+$, which from the ICP-MS results showed minimal accumulation within the cells (**Table 3.1**). Unfortunately however, the localisation of this compound could not be assessed due to its non-emissive nature in aqueous media.

These results demonstrate that the neutral series of iridium tetrazolato complexes possess very promising properties for the development of iridium-based markers for imaging of the ER in live cells. This is in contrast to other cationic iridium complexes that were previously shown to accumulate in the endoplasmic reticulum, but which were cytotoxic due to the triggering of Ca^{2+} release into the cytoplasm.[139]

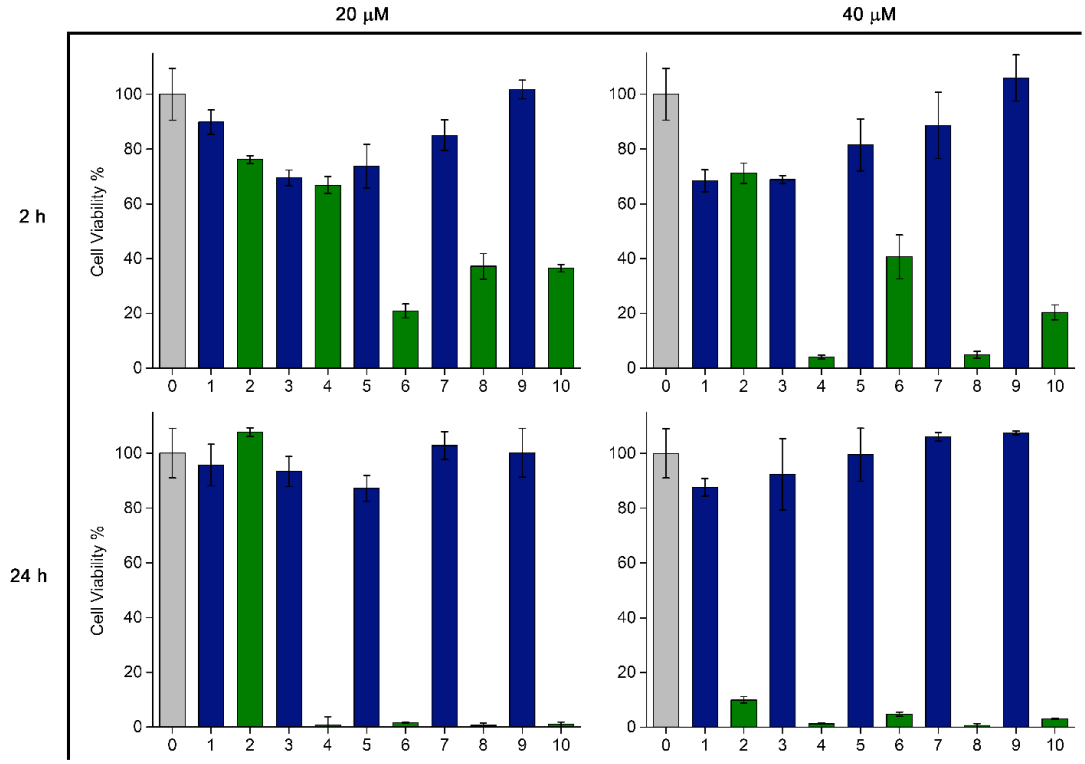

Figure 3.6 Cell viability after 2 and 24 h incubation with the iridium complexes at 20 and 40 μM. Neutral complexes are represented by blue bars, whereas cationic complexes are represented by green bars. 0) Control (0.2% DMSO in serum-free DMEM medium); 1) [Ir(**ppy**)$_2$(**TzPyCN**)]; 2) [Ir(**ppy**)$_2$(Me**TzPyCN**)]$^+$; 3) [Ir(**F$_2$ppy**)$_2$(**TzPyCN**)]; 4) [Ir(**F$_2$ppy**)$_2$(Me**TzPyCN**)]$^+$; 5) [Ir(**ppy**)$_2$(**TzPyPhCN**)]; 6) [Ir(**ppy**)$_2$(Me**TzPyPhCN**)]$^+$; 7) [Ir(**ppy**)$_2$(**TzQn**)]; 8) [Ir(**ppy**)$_2$(Me**TzQn**)]$^+$; 9) [Ir(**ppy**)$_2$(**TziQn**)]; 10) [Ir(**ppy**)$_2$(Me**TziQn**)]$^+$.

It is well known that phosphorescent metal complexes act as sensitisers for singlet oxygen.[93] Previous studies by Werrett *et al.*[230] have showed that during imaging *via* confocal microscopy, a resting time of 30 seconds reduced or eliminated the effect of reactive oxygen species in live cells.

Following this protocol and imaging cells incubated for 30 minutes with a 20 μM solution of the iridium complex, blebbing of the cell membrane was never observed. On the other hand, cells incubated under the same conditions (refer to section 3.5.7) and continuously illuminated, displayed signs of blebbing within a 30 minutes timeframe, as reported in **Table 3.3**, indicating the start of apoptotic pathways. This result futher confirms what previously observed by Werrett *et al.*[230] and highlights that the protocol has been used for the staining of live cells with these complexes was effectively optimised.

Table 3.3 Live H9c2 cell response to continuous irradiation at 403 nm.

Complex	Appearance of cell blebbing (min)
[Ir(**ppy**)$_2$(**TzPyCN**)]	29
[Ir(F$_2$**ppy**)$_2$(**TzPyCN**)]	9
[Ir(**ppy**)$_2$(**TzPyPhCN**)]	6
[Ir(F$_2$**ppy**)$_2$(Me**TzPyCN**)]$^+$	12
[Ir(**ppy**)$_2$(Me**TzPyPhCN**)]$^+$	17
[Ir(**ppy**)$_2$(**TzQn**)]	3
[Ir(**ppy**)$_2$(**TziQn**)]	3
[Ir(**ppy**)$_2$(Me**TzQn**)]$^+$	9
[Ir(**ppy**)$_2$(Me**TziQn**)]$^+$	2

During co-localisation analysis [Ir(**ppy**)$_2$(Me**TziQn**)]$^+$ has shown high cytotoxicity within the cells, expressed by changing in the morphology of mitochondria and formation of cellular vacuoles. In order to confirm the initiation of apoptotic pathways trigged by the iridium probe, a caspase assay has been performed (refer to section 3.5.8).[318] Caspases are enzymes that play a central role in various phases of apoptosis. Upon activation, caspases cleave specific substrates and thereby mediate many of the typical biochemical and morphological changes in apoptic cells, such as cell shrinkage, DNA fragmentation and plasma membrane blebbing.[200,320,321] For all these reasons, the detection of caspase activity can be used as a biochemical marker for apoptosis.

After incubation with 20 μM of [Ir(**ppy**)$_2$(Me**TziQn**)]$^+$ in H9c2 cells, the caspase activity was significantly increased ($P < 0.0001$) compared to the untreated control cells (**Figure 3.7**). This result demonstrated high toxicity of the iridium probe, however it is unclear why the isostructural [Ir(**ppy**)$_2$(Me**TzQn**)]$^+$ complex does not show a similar biological behaviour.

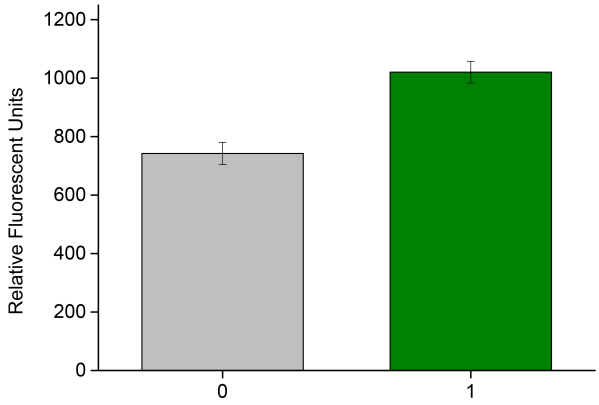

Figure 3.7 Caspase assay for the detection of apoptosis in H9c2 cells incubated with 20 μM of [Ir(**ppy**)$_2$(Me**TziQn**)]$^+$. The released Rhodamine-110 was excited at 499 nm and the emission was collected at 521 nm. 0) Control (0.2% DMSO in complete DMEM medium); 1) [Ir(**ppy**)$_2$(Me**TziQn**)]$^+$.

3.2.5 Photostability

Photobleaching is a severely limiting factor in biological imaging. In fact, upon continuous irradiation, a fluorophore can undergo irreversible conversion into a less or non-fluorescent species, affecting the optical studies over extended time periods.[284,322]

To assess the photostability of the iridium probes, photobleaching experiments were carried out on H9c2 cells incubated with the iridium complexes at 20 μM for 30 minutes (refer to section 3.5.9). The cells were illuminated continuously at 403 nm for 900 seconds, and the decrease in emission intensity was compared with that from cells incubated with ER-Tracker™. All the complexes evaluated in cells showed better photostability than ER-Tracker™, with the cationic complexes exhibiting emission intensity above 85% of the initial values after 900 seconds irradiation (**Figure 3.9**). The neutral iridium complexes revealed to be slightly more prone to photobleaching, but still displayed emission above 70% of the initial emission intensity after 900 seconds irradiation (**Figure 3.8**). The data clearly highlight how the cationic complexes exhibit better photostability than their neutral analogues.

Results from [Ir(**ppy**)$_2$(**TziQn**)] are not shown since the cells displayed tendency to detach, creating great variability in the intensity measurement. Moreover, [Ir(**ppy**)$_2$(Me**TzPyCN**)]$^+$ and [Ir(**ppy**)$_2$(Me**TziQn**)]$^+$ have not been tested due to low emission in aqueous medium and enhanced cytotoxicity in live cells, respectively.

Unfortunately, the lack of literature regarding photobleaching analysis on neutral iridium probes does not permit a comparison with the data obtained for this series of tetrazolato complexes. On the other hand, cationic iridium species have been largely studied and their final emission intensity falls in a range of 60% to 99% with continuous irradiation at 405 nm for 120 - 360 seconds.[102,127,201,323] Interestingly, the photobleaching analysis for the tetrazolato complexes was conducted for 900 seconds, highlighting the superior photostability of [Ir(**F$_2$ppy**)$_2$(Me**TzPyCN**)]$^+$, [Ir(**ppy**)$_2$(Me**TzPyPhCN**)]$^+$, [Ir(**ppy**)$_2$(Me**TzQn**)]$^+$.

The same general trend was also observed performing the photobleaching experiments in cuvette, using 10^{-5} M PBS solutions (0.2% DMSO), excited using a Pen-Ray Mercury Lamp source at 365 nm (refer to section 3.5.9).

Upon irradiation for 600 seconds, neutral iridium complexes (**Figure 3.10**) have shown a decrease of the initial intensity up to 55%, with only [Ir(**ppy**)$_2$(**TzPyPhCN**)]

which resulted more photobleached, with a final emission intensity of 30% with respect to the starting phosphorescence. On the other hand, methylated cationic complexes (**Figure 3.11**) displayed really high photostability, with emission above 85% of the initial emission intensity after 600 seconds of continuous irradiation.

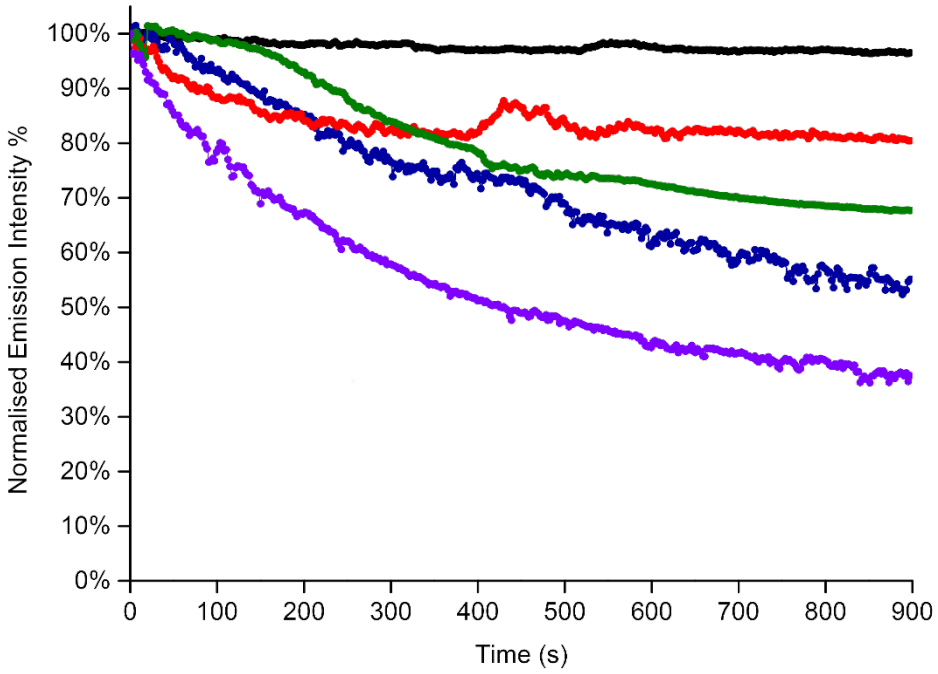

Figure 3.8 Photobleaching analysis in live H9c2 cells of [Ir(**ppy**)$_2$(**TzPyCN**)] (black), [Ir(**F$_2$ppy**)$_2$(**TzPyCN**)] (blue), [Ir(**ppy**)$_2$(**TzPyPhCN**)] (red), [Ir(**ppy**)$_2$(**TzQn**)] (green) and ER-Tracker™ (purple).

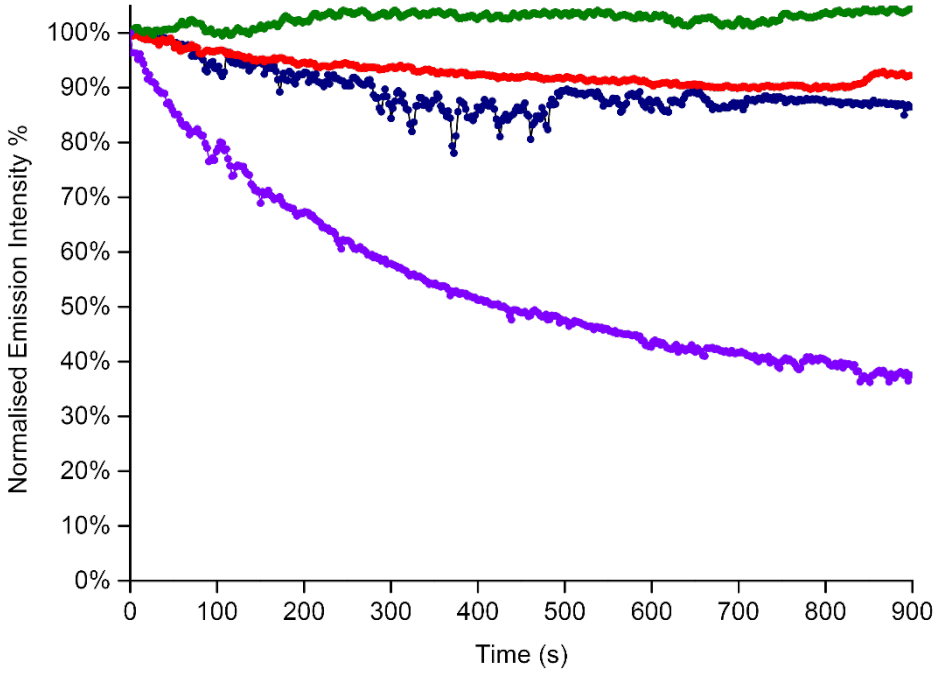

Figure 3.9 Photobleaching analysis in live H9c2 cells of [Ir(**F$_2$ppy**)$_2$(Me**TzPyCN**)]$^+$ (blue), [Ir(**ppy**)$_2$(Me**TzPyPhCN**)]$^+$ (red), [Ir(**ppy**)$_2$(Me**TzQn**)]$^+$ (green) and ER-Tracker™ (purple).

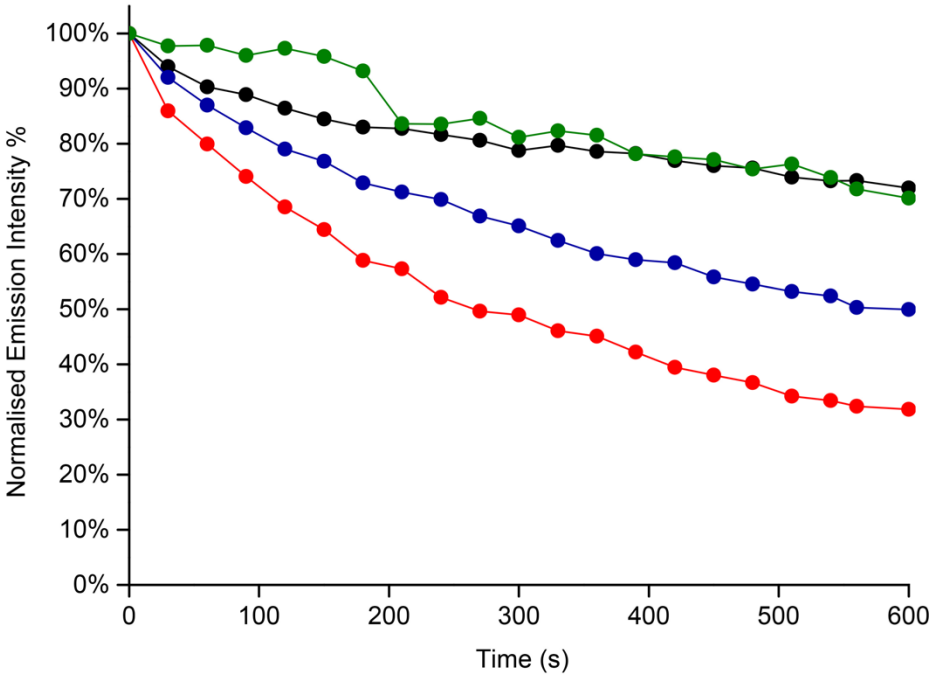

Figure 3.10 Photobleaching analysis in PBS (0.2% DMSO) of [Ir(**ppy**)$_2$(**TzPyCN**)] (black), [Ir(**F$_2$ppy**)$_2$(**TzPyCN**)] (blue), [Ir(**ppy**)$_2$(**TzPyPhCN**)] (red) and [Ir(**ppy**)$_2$(**TzQn**)] (green).

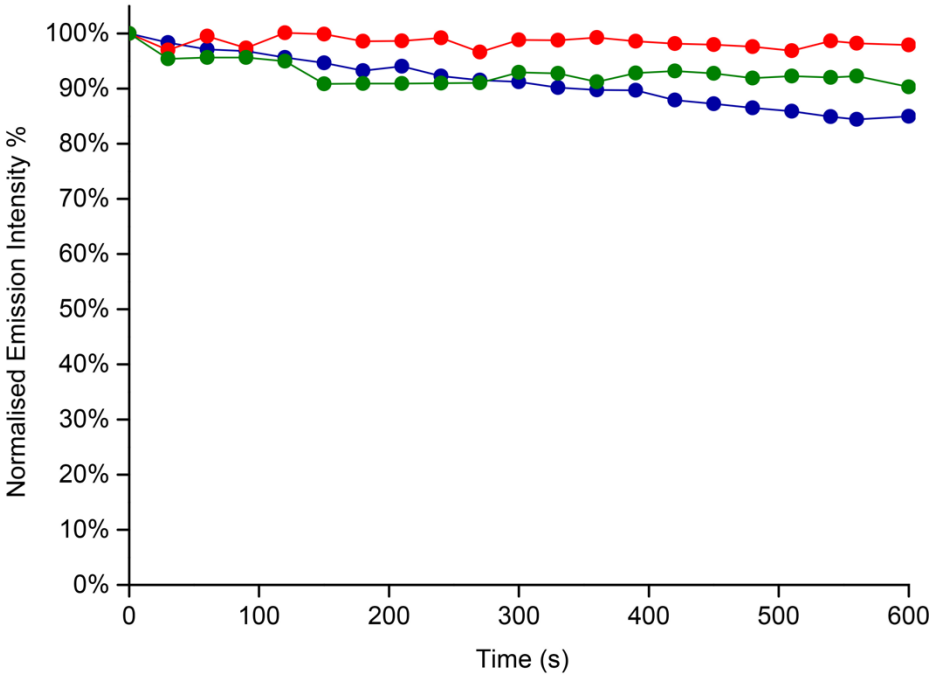

Figure 3.11 Photobleaching analysis in PBS (0.2% DMSO) of [Ir(**F$_2$ppy**)$_2$(Me**TzPyCN**)]$^+$ (blue), [Ir(**ppy**)$_2$(Me**TzPyPhCN**)]$^+$ (red) and [Ir(**ppy**)$_2$(Me**TzQn**)]$^+$ (green).

3.3 Biological Investigation in Tissue Samples

The normal function of muscle tissue is particularly reliant on mitochondria to fulfil high energy demand, to regulate calcium[324] and to control ROS production.[325] Mitochondrial morphology is directly linked to many important cell and tissue functions, and consequently significant organelle remodelling is observed in response to changes in energy demand and cellular environment.[326,327] Moreover, changes in mitochondrial morphology are also observed in a range of human pathologies, including cardiovascular diseases and neuromuscular disorders.[327–329] For this reason, understanding the role of mitochondria in disease pathogenesis has been greatly advanced by the visualisation of these organelles, using a variety of microscopy techniques to image affected tissues.[328,329] In particular, mitochondrial imaging by fluorescence microscopy is often utilised in medical research, but the currently available mitochondrial stains have mainly been limited to uses in live samples. This can be problematic for pathology testing, in clinical or in large cohort studies, where tissue samples cannot be immediately processed for assessment, and tissue preservation by fixation is highly preferable before imaging.

Mitochondrial imaging in tissue samples is primarily performed using fluorescence imaging by small fluorescent molecules or immunochemistry.[40] The majority of commercially available mitochondrial dyes are organic fluorophores that accumulate in the mitochondrial matrix due to the organelle transmembrane potential. These dyes are therefore only suited for use on live samples, for example, JC-1 and the MitoTrackers CMTMRos and CMXRos.[330,331] Commercial dyes that stain independently of mitochondrial polarisation tend to have an affinity for other mitochondrial-specific constituents (e.g. Mito-ID® Red, which specifically binds to cardiolipin in the inner mitochondrial membrane), but their cellular uptake is still often limited to live samples.[40] To date, the visualisation of mitochondria in fixed samples has relied on immunochemistry. While antibody detection is sensitive, it is time consuming and requires multiple processing steps that may introduce significant artefacts. Moreover, issues with antibody availability can limit their use in a range of model species. There is, therefore, a need for small molecule imaging tools that can quickly and effectively image mitochondria in both live and fixed tissue samples.

On the basis of the superior properties displayed in live cell imaging by the series of iridium(III) tetrazolato probes presented in this chapter, the application in the

staining of muscle tissues of [Ir(**ppy**)$_2$(Me**TzPyPhCN**)]$^+$, which has previously showed high specificity for mitochondria in live H9c2 rat cardiomyoblasts,[238] was explored as well. This iridium(III) probe is now also commercially available as IraZolve-Mito^{TM}.

3.3.1 Localisation in Live Tissues

The localisation of [Ir(**ppy**)$_2$(Me**TzPyPhCN**)]$^+$ was firstly assessed in live tissues. The samples were collected from the left ventricle of the heart (cardiac muscle) and the quadriceps (skeletal muscle) of adult ewes, and stained with 20 μM of the iridium complex, following the preparation and incubation protocol described in section 3.5.10 – section 3.5.12. The complex was excited at 403 nm and clearly detected, in both cardiac and skeletal muscles, in cylindrical-shaped organelles, which resemble mitochondria (**Figure 3.12** – a, a$^/$, c, c$^/$). These organelles were arranged in a regular network structure throughout the muscle fibres, in a distinctive distribution consistent with previous observations of mitochondrial in skeletal muscle.[332,333]

To further confirm the mitochondrial localisation of [Ir(**ppy**)$_2$(Me**TzPyPhCN**)]$^+$, the distribution of NAD(P)H, which is known to be associated with these organelle,[334] was detected by two-photon imaging microscopy. NAD(P)H produces a strong endogenous fluorescence at 489 nm, when exposed to two-photon illumination at 740 nm.[18] The distribution of NAD(P)H was compatible with the staining pattern of the iridium probe, as shown in **Figure 3.12** - b, b$^/$, d, d$^/$.

Moreover the live tissue samples were also co-stained with MitoTracker® Red CMXRos (**Figure 3.12** – e, e$^/$ cardiac and f, f$^/$ skeletal tissue), giving a significant high Pearson's correlation coefficient of 0.84 and 0.86 (**Table 3.4**) for cardiac and skeletal muscle, respectively.

Table 3.4 Pearson's correlation coefficients in live tissues.

Tissue	**MitoTracker®**
Live cardiac muscle	0.84 ± 0.01
Live skeletal muscle	0.86 ± 0.03

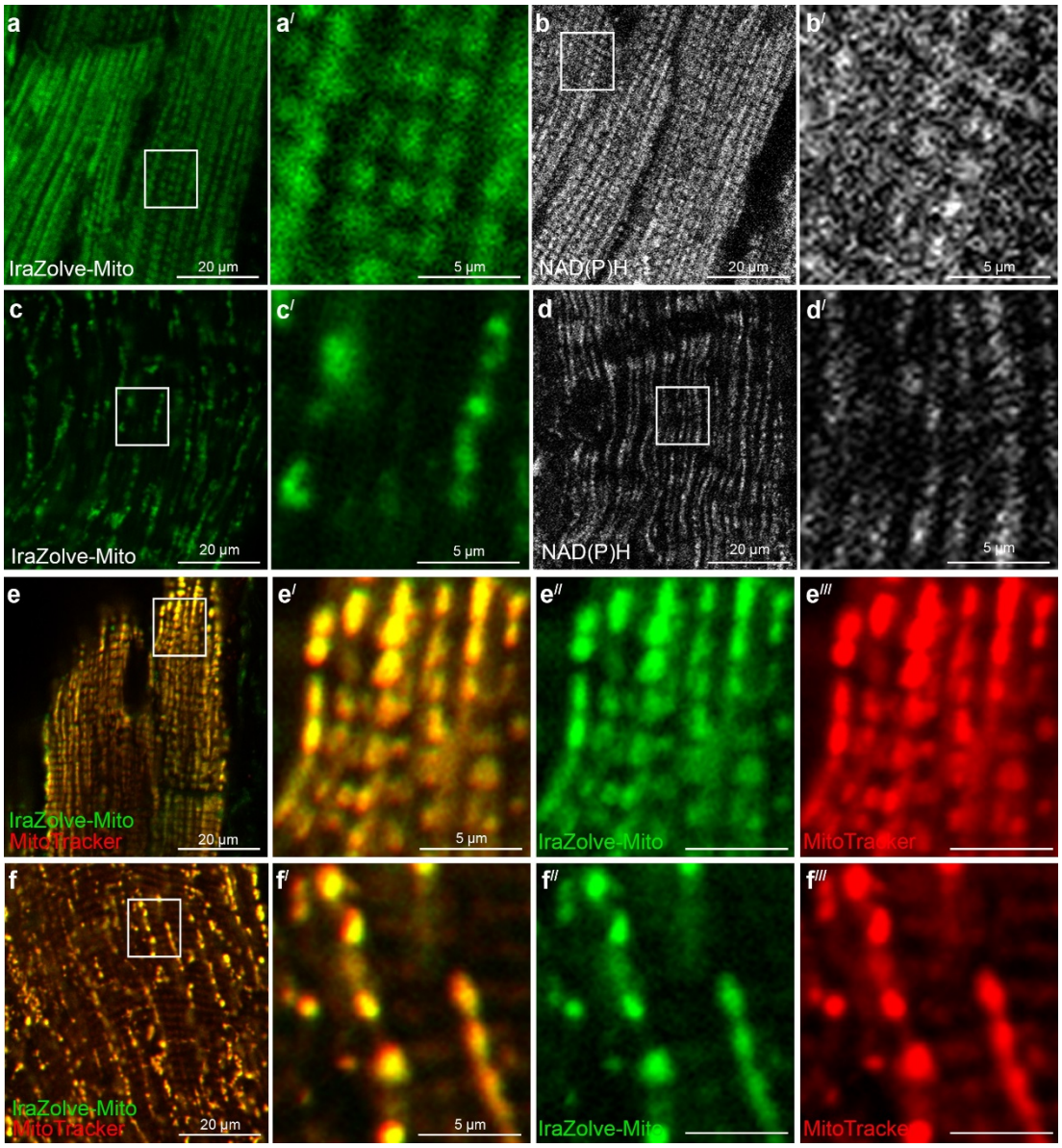

Figure 3.12 [Ir(**ppy**)$_2$(Me**TzPyPhCN**)]$^+$ (IraZolve-Mito^{TM}) detects mitochondria in fresh live cardiac and skeletal muscle samples. Micrographs showing mitochondria detected with [Ir(**ppy**)$_2$(Me**TzPyPhCN**)]$^+$ in cardiac (a; enlarged in a$^/$) and skeletal (c; enlarged in c$^/$) muscle samples. Endogenous NAD(P)H detected by two-photon microscopy in cardiac (b; enlarged in b$^/$) and skeletal (d; enlarged in d$^/$) muscle samples (excited at 740 nm and collected at 474-504 nm). Micrographs showing co-staining of mitochondria with [Ir(**ppy**)$_2$(Me**TzPyPhCN**)]$^+$ (green in e - e$^{//}$ and f - f$^{//}$) and MitoTracker® Red CMXRos (red in e, e$^/$, e$^{///}$ and f, f$^/$, f$^{///}$) in cardiac (e; enlarged in e$^/$-e$^{///}$) and skeletal (f; enlarged in f$^/$ - f$^{///}$) muscle samples. Scale bars = 20 µm (a - f) and 5 µm (a$^/$ - d$^/$, e$^/$ - e$^{///}$ and f$^/$ - f$^{///}$).

3.3.2 Localisation in Fixed Tissues

The localisation of [Ir(**ppy**)$_2$(Me**TzPyPhCN**)]$^+$ was investigated even in fixed tissue samples, adopting the same protocol optimised for live tissues. The cardiac and skeletal muscle samples were fixed in 4% paraformaldehyde for 20 hours and after a 30 minutes washing step, were stored in PBS at 4 °C (refer to section 3.5.11).

After incubation with the probe, the staining pattern of [Ir(**ppy**)$_2$(Me**TzPyPhCN**)]$^+$ in fixed tissues (**Figure 3.13** – a, a′, c, c′) was consistent with the one obtained for fresh live tissues (**Figure 3.12** – a, a′, c, c′) and similar to the mitochondrial detection obtained with antibody probing for cytochrome C protein, which localises to the inner membrane of mitochondria (**Figure 3.13** - b, b′, d, d′).

Unfortunately, it was impossible to perform co-staining studies with anti-Cytochrome C antibody due to the loss in mitochondrial accumulation of the iridium complex, probably derived from the use of permeabilising agents required for the immunochemistry protocol (refer to section 3.5.12).

Nevertheless, to confirm the localisation of [Ir(**ppy**)$_2$(Me**TzPyPhCN**)]$^+$, live tissue samples were incubated with MitoTracker® Red CMXRos and, after fixation in 4% paraformaldehyde, co-stained with the iridium probe. In this case, the fixation process was performed for only 1 hour to prevent the loss of MitoTracker® Red CMXRos. As observed for live tissues, co-staining with MitoTracker® Red CMXRos confirmed the interaction of [Ir(**ppy**)$_2$(Me**TzPyPhCN**)]$^+$ with mitochondria (**Figure 3.13** - e, e′ cardiac and f, f′ skeletal tissue), with Pearson's correlation coefficients of 0.89 for both cardiac and skeletal muscle (**Table 3.5**).

Table 3.5 Pearson's correlation coefficients in fixed tissues.

Tissue	**MitoTracker®**
Fixed cardiac muscle	0.89 ± 0.02
Fixed skeletal muscle	0.89 ± 0.02

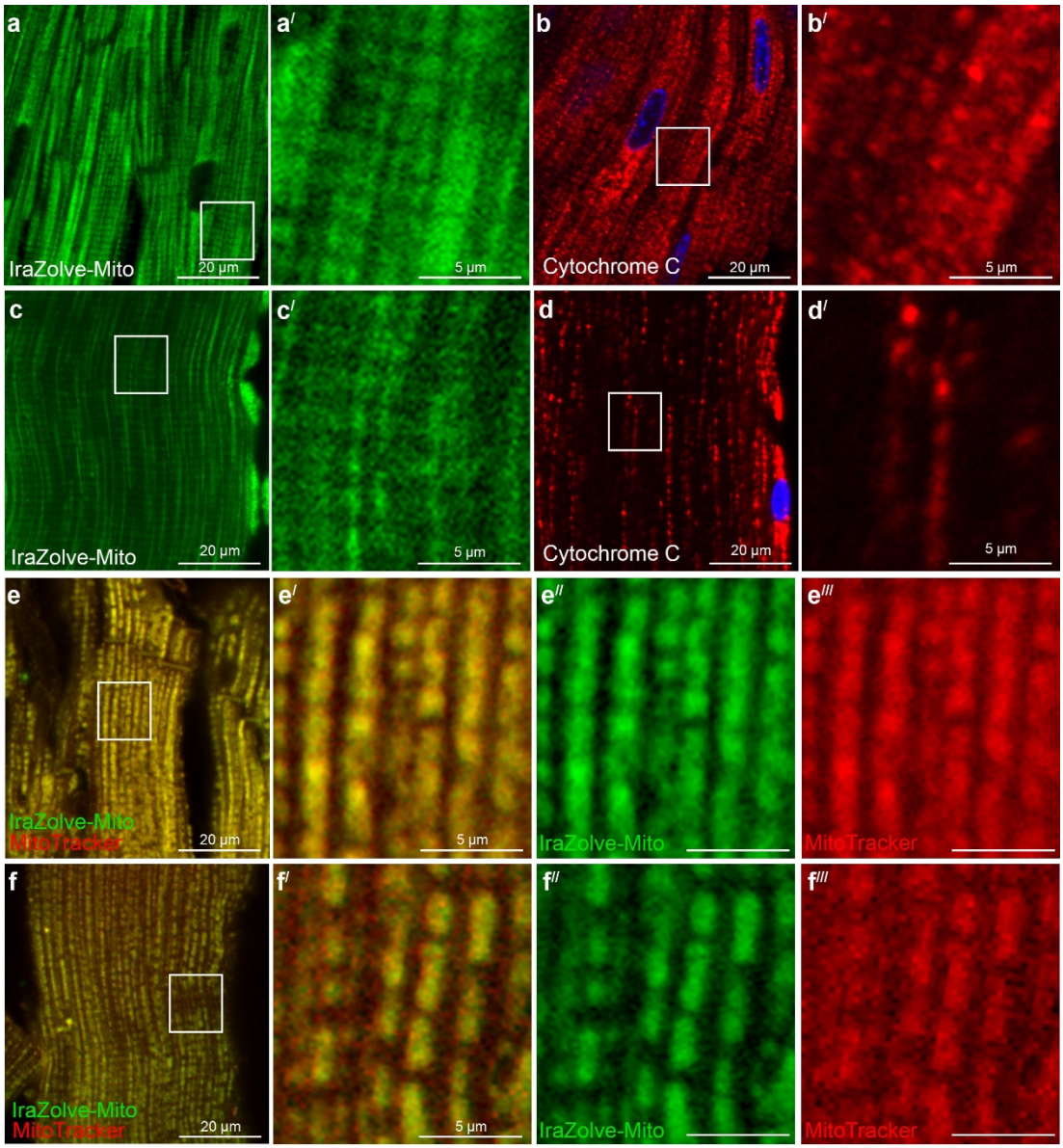

Figure 3.13 Staining pattern of [Ir(**ppy**)$_2$(Me**TzPyPhCN**)]$^+$ (IraZolve-Mito^{TM}) in fixed cardiac and skeletal muscle samples. Micrographs showing subcellular distribution of [Ir(**ppy**)$_2$(Me**TzPyPhCN**)]$^+$ in 4% PFA fixed cardiac (a; enlarged in a$^/$) and skeletal (c; enlarged in c$^/$) muscle samples. Micrographs showing localisation of Cytochrome C detected with an anti-Cytochrome C antibody in cardiac (b enlarged in b$^/$) and skeletal (d; enlarged in d$^/$) muscle samples. Micrographs showing co-staining of mitochondria with [Ir(**ppy**)$_2$(Me**TzPyPhCN**)]$^+$ (green in e - e$^{//}$ and f - f$^{//}$) and MitoTracker® Red CMXRos (red in e, e$^/$, e$^{///}$ and f, f$^/$, f$^{///}$) in cardiac (e; enlarged in e$^/$ - e$^{///}$) and skeletal (f; enlarged in f$^/$ - f$^{///}$) muscle samples. Scale bars = 20 µm (a - f) and 5 µm (a$^/$ - d$^/$, e$^/$ - e$^{///}$ and f$^/$ - f$^{///}$).

3.3.3 Mechanism of Internalisation

The compatibility of [Ir(**ppy**)$_2$(Me**TzPyPhCN**)]$^+$ for mitochondrial staining of fixed tissue suggests that the mechanism controlling the localisation is not solely based on its cationic nature. To confirm that the localisation of [Ir(**ppy**)$_2$(Me**TzPyPhCN**)]$^+$ with mitochondria was not dependent on membrane polarisation, the mitochondrial membrane potential was deregulated by using carbonyl cyanide-*p*-trifluoromethoxyphenylhydrazone (FCCP).[335] In H9c2 cells, FCCP treatment did not perturb [Ir(**ppy**)$_2$(Me**TzPyPhCN**)]$^+$ mitochondrial staining, as observed in **Figure 3.14** – c. By comparison MitoTracker®, which is dependent on mitochondrial membrane potential,[330,331] exhibited dispersed cytoplasmic staining in FCCP treated cells (**Figure 3.14** - e). Cytochrome C immunofluorescence confirmed that there were morphological changes in the mitochondria after FCCP treatment, which match [Ir(**ppy**)$_2$(Me**TzPyPhCN**)]$^+$ staining patterns (**Figure 3.14 –** f, g).

These results suggested that unlike the majority of mitochondrial dyes, the localisation of [Ir(**ppy**)$_2$(Me**TzPyPhCN**)]$^+$ in these organelles is independent from the mitochondrial membrane potential, which likely accounts for its compatibility with fixed tissue staining. This behaviour allows the visualisation of mitochondria during stress conditions in live cells and tissues, which may be induced by, for example, drug treatments or pathological processes, as well as its ability to stain fixed tissues.

Noteworthy, a number of similar cationic iridium complexes have shown membrane potential independent localisation into mitochondria (**Figure 3.15**).[129,132,336–339] This characteristic would indicate that this family of molecules has an alternative targeting mechanism, possibly via protein or lipid association.

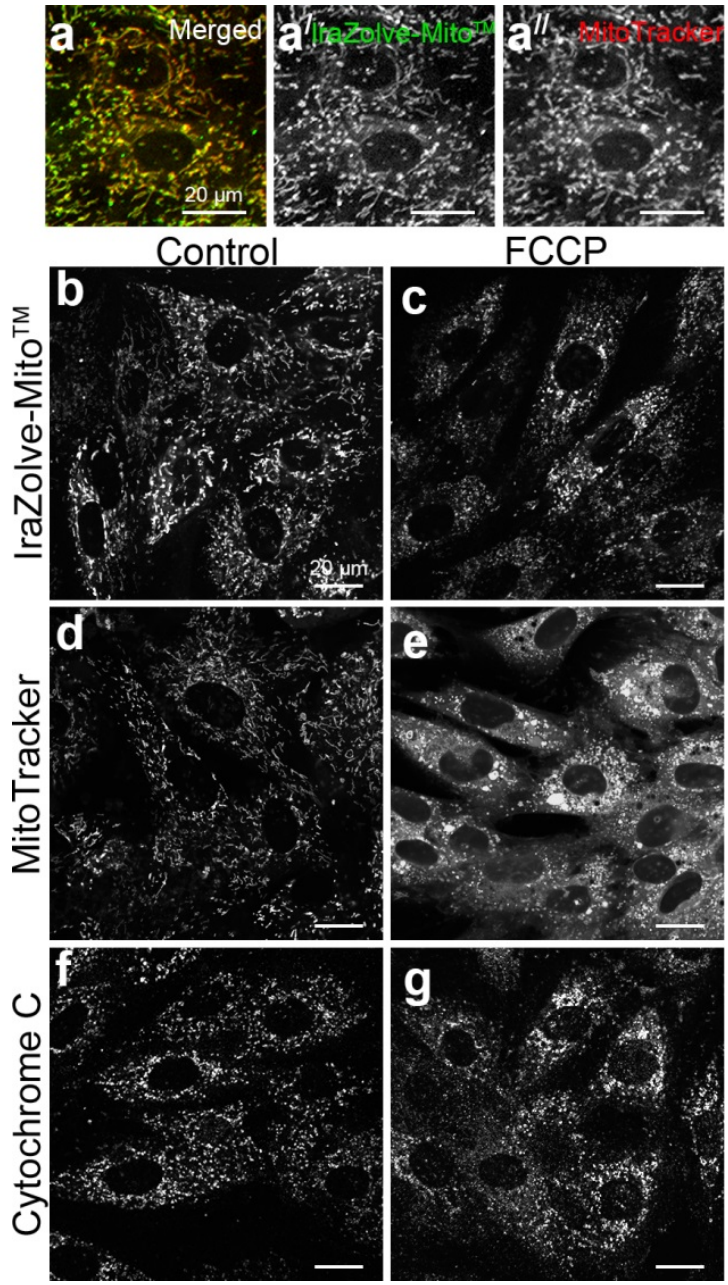

Figure 3.14 Inhibition of mitochondrial membrane potential in H9c2 rat cardiomyoblasts does not disrupt [Ir(**ppy**)$_2$(Me**TzPyPhCN**)]$^+$ (IraZolve-Mito^{TM}) staining. (a - a$^{//}$) Micrographs showing co-staining of [Ir(**ppy**)$_2$(Me**TzPyPhCN**)]$^+$ (green in a; greyscale in a$^{/}$) with MitoTracker® Red CMXRos (red in a; greyscale in a$^{//}$) in H9c2 cells. Scale bars = 20 µm. H9c2 cells were stained with [Ir(**ppy**)$_2$(Me**TzPyPhCN**)]$^+$ (b, c), MitoTracker® Red CMXRos (d, e) or by anti-Cytochrome C antibody (f, g) either under normal conditions (control; b, d, f) or following treatment with FCCP (c, e, g). Scale bars = 20 µm.

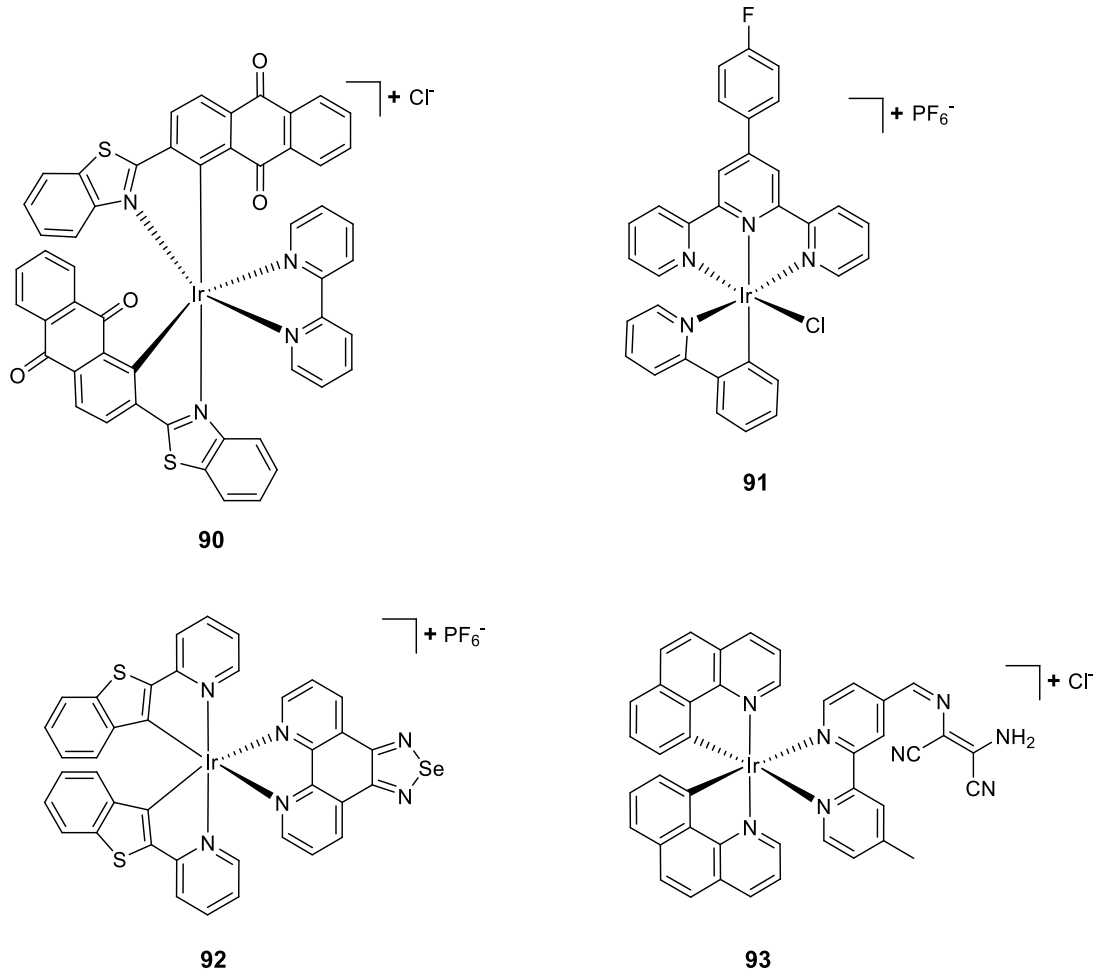

90 91 92 93

Figure 3.15 Example of previously reported iridium(III) probes membrane potential independent localisation into mitochondria.

3.4 Conclusions

In this chapter, the biological investigation of the iridium(III) complexes was performed in live H9c2 rat cardiomyoblast cells.

Quantification of cellular incubation *via* ICP-MS revealed great variability, with trends that cannot be simply correlated to the degree of lipophilicity and charge of the complexes, suggesting different mechanisms of uptake.

The majority of the complexes were internalised into live cells and detection was possible via either one-photon or two-photon imaging modalities. The neutral species were predominantly localised within the endoplasmic reticulum and to various extents within lipid droplets. On the other hand, the cationic species exhibited more specificity for mitochondria.

A noticeable difference between the neutral and cationic probes was found in terms of cytotoxicity. A remarkable low viability of cells during long term experiments for the charged species with respect to the neutral analogues was found. The higher cytotoxicity of the cationic complexes does not seem to be exclusively linked to the amount of complex internalised within the cells, and it is also potentially highly dependent on the localisation.

This study has therefore highlighted that neutral iridium tetrazolato complexes are suitable building blocks for the design of ER and lipid droplets markers for cellular imaging on long timescales. Interestingly, the neutral iridium(III) probes presented in this chapter are one of the few examples of ER-markers, and most importantly, do not shown high cytotoxicity in live cells.[105,137–139,143,305–307] On the other hand, the cationic iridium analogues are good candidates for the design of mitochondrial dyes.[238] However, for their application in live biological imaging their cytotoxicity needs to be carefully considered.

The charged iridium(III) complex [Ir(**ppy**)$_2$(Me**TzPyPhCN**)]$^+$, which has showed a specific mitochondrial accumulation in live H9c2 cells, was also applied for the staining of these organelles in skeletal and cardiac tissues.[283] Interestingly, the probe maintained the same staining pattern in both fresh and fixed tissue samples, suggesting that its localisation mechanism is independent of mitochondrial membrane polarisation. This characteristic, which was previously observed for other cationic iridium(III) complexes,[129,132,336–339] allows [Ir(**ppy**)$_2$(Me**TzPyPhCN**)]$^+$ to be broadly

applicable for the visualisation of mitochondria during stress conditions in both live cell and fresh tissues.

Moreover, this probe can be a useful alternative to immunochemistry commonly applied to fixed tissues, by overcoming the issues of this time consuming process and the risk of adding artefacts to the samples.

Due to its superior properties, $[Ir(\mathbf{ppy})_2(Me\mathbf{TzPyPhCN})]^+$ has been patented (PCT/AU2015/000159 and an Australian Provisional Patent, 2016902815) and commercialised by Rezolve Scientific under the name of IraZolve-Mito™.

3.5 Experimental

3.5.1 Photophysical Measurements

Photophysical measurements have been conducted as outlined in Chapter 2, section 2.6.2, unless otherwise stated.

3.5.2 Lipophilicity Analysis

$LogD_{7.4}$ values were determined by applying the shake-flask method developed by Kunz *et al.*.[308] Equal volumes of phosphate-buffered saline solution (PBS) and *n*-octanol were stirred together for 72 hours prior to use to allow saturation of both the phases. For each experiment, 500 µL of PBS, 530 µL of n-octanol and 30 µL of the complex solution (2 mg of the analysed specie dissolved in 200 µL of DMSO) were combined in an Eppendorf tube and stirred for 30 minutes, follow by centrifugation (5 minutes, 3000 rpm) to separate the two phases. UV/Vis absorption of each phase was recorded at 400 nm. Samples were diluted with the corresponding phase prior to measurement in case the absorption was exciding 1. $LogD_{7.4}$ values were calculated following **Equation 3.1**:

$$logD_{7.4} = log\left[\frac{(A_{octanol(400nm)} \cdot f_{octanol})}{(A_{PBS(400nm)} \cdot f_{PBS})}\right] \quad (\mathbf{3.1})$$

Where $A_{octanol(400nm)}$ and $A_{PBS(400nm)}$ is the absorbance in each phase at 400 nm and $f_{octanol}$ and f_{PBS} are the dilution factors. Given values and standard deviations were derived from three independent experiments.

3.5.3 Cell Culture

The biological investigation was performed in collaboration with Dr Christie A. Bader and Dr Alexandra Sorvina at the School of Pharmacy and Medical Sciences, University of South Australia. H9c2 rat cardiomyoblast cells were maintained in high-glucose (4500 mg/L) DMEM medium (Sigma-Aldrich, USA) containing 10% fetal bovine serum (FBS; In Vitro Technologies, USA) and 2 mM L-glutamine (Sigma-Aldrich, USA) at 37 ºC and 5% CO_2. The H9c2 cells were cultured in 75 mm^2 flasks.

Cells that had been passaged for no more than 18 times, were used for experiments. For ICP-MS, H9c2 cells were seeded at 2.7×10^4 cells/mL and grown in T25 flasks for 72 hours, when 80% confluence was reached. For live cell imaging and MTS assay, the H9c2 cells were seeded at 1×10^5 cells/mL and cultured overnight in either ibidi µ-slide 8 wells in a final volume of 250 µL or 96-well microtiter plate in a final volume of 200 µL.

3.5.4 Cell Staining

H9c2 cells were incubated with the iridium complexes at 20 µM in DMEM full culture medium with 0.2% DMSO (Sigma-Aldrich, St. Louis, USA) for 30 minutes at either 37 ºC or 4 ºC. The cells were washed twice with sterile phosphate-buffered saline solution (PBS; Sigma-Aldrich, St. Louis, USA), before imaging in DMEM. For co-staining experiments, the cells were then incubated with ER-Tracker™ Red, MitoTracker® Red CMXRos, or BODIPY® 500/510 C_1,C_{12} (Life Technologies Australia Pty Ltd, Australia), following manufacturer's instructions.

3.5.5 ICP-MS

The ICP-MS analysis was performed by Todd A. Gillam at the School of Pharmacy and Medical Sciences, University of South Australia. The H9c2 cells were incubated with the iridium complexes at 20 µM (prepared in DMEM full culture medium with 0.2% DMSO) for 30 minutes at 37 ºC and 5% CO_2 . The cells were washed three times with PBS, and then detached with TripLE Express reagent (Gibco, USA) for 2 minutes. The cells were then washed from T25 flasks with 3 mL of DMEM full culture medium, and pelleted by centrifugation (10 minutes, 400 rpm). The medium was removed and the cells were resuspended in 2 mL of PBS for cells counts. The remaining cells were centrifuged (10 minutes, 1000 rpm), the medium removed and the remaining stained cell pellets were desiccated for 3.5 hours at 95 °C. The pellets were reconstituted in 36% HCl (400 µL) and left at 95 °C until dry, in order to digest organic material. The dry samples were then reconstituted in 2% HCl (2.5 mL) and sonicated for 10 minutes before filtering (pore diameter of 0.2 µm). The total iridium determination was

performed with an Agilent 8900x triple quad ICP-MS (Agilent Technologies, USA), using He gas (4 mL/min).

3.5.6 MTS Cell Viability Assay

The cellular NADPH-dependent redox activity was measured using CellTiter 96® AQueous Non-Radioactive Cell Proliferation Assay (MTS), according to the manufacturer's instruction (Promega, USA). The H9c2 cells were stained with the iridium complexes at either 20 μM or 40 μM in DMEM full cell culture medium with 0.2% DMSO, and held at 37 °C and 5% CO_2 for 2 or 24 hours. As a control, H9c2 cells were incubated for the same length of time in DMEM with 0.2% DMSO. Following addition of MTS, the cells were incubated for a further 2 hours in the same conditions. The absorbance of the formazan dye was measured by EnVision multi-label plate reader at 490 nm. The data are reported as the mean ± SEM of three biological replicates for each group.

3.5.7 Live Cell Response to Imaging Conditions

Live H9c2 cells were stained with 20 μM of each iridium complex for 30 minutes. Cells were then imaged for 30 minutes continuously with a frame rate of 2.2 s, with 403 nm excitation and DIC imaging concurrently. Time series were then reviewed for signs of cytotoxicity from the complexes, where cell blebbing was used as an indicator of cells entering apoptosis. The first signs of cell blebbing was recorded in **Table 3.3**. Unstained cells which were imaged using the same protocol and did not show signs of cell blebbing within the 30 minutes experiment. The complex [Ir(**ppy**)(Me**TzPyCN**)]$^+$ was not tested as it is not emissive in cells and hence not suitable as a marker for live cell imaging.

3.5.8 Caspase Assay for the Detection of Apoptosis

The caspase activity was measured using Homogeneous Caspases Assay according to the manufacturer's instruction (Roche, USA). H9c2 cells were incubated with [Ir(**ppy**)$_2$(Me**TziQn**)]$^+$ probe at 20 μM in a complete DMEM media (100 μL) for 30 minutes at 37 ºC and 5% CO_2. Incubation buffer was added into each well and the cells

were left at 37 ºC for 90 minutes. The fluorimetric measurements of released Rhodamine-110 induced by caspases were performed using EnVision multi-label plate reader (PerkinElmer, Beaconsfield, UK) with λ_{ex} = 499 nm and λ_{em} = 521 nm. Data represents the mean ± SEM of four biological replicates for each group.

3.5.9 Photobleaching Analysis

Method in Live Cells

Live H9c2 cells were stained with 20 μM of each complex solution for 30 minutes. Cells were then imaged for 900 seconds, continuously, with a frame rate of 2.2 seconds. The relative intensity emitted from the image was then tracked overtime using NIS Elements V4.50 software (Nikon, Japan). For comparison, H9c2 cells stained with ER-Tracker™ Red were also imaged continuously for 900 seconds and the emission intensity was tracked and plotted against the emission traces for each of the complexes.

Method in Cuvette

3 mL of a diluted (*ca.* 10^{-5} M) PBS solution of each iridium complex was irradiated continuously for 600 seconds with a frame rate of 30 seconds. The irradiation source was a Pen-Ray® Mercury Lamp (λ_{exc} = 365 nm, 5 mW), located 3 cm from the sample. The emission spectra were recorded on an Edinburgh FLSP980-S2S2-stm spectrometer. Only those complexes tested for photostability in cells were tested for photostability in cuvette.

3.5.10 Animal Procedure and Muscle Sample

The experimental procedures were approved by the South Australian Health and Medical Research Institute Animal Ethics Committee and followed the guidelines of the Australian Code of Practice for the Care and Use of Animals for Scientific Purposes developed by the National Health and Medical Research Council. The investigators understood the ethical principles outlined in Grundy *et al*.[340] Animal care and tissue collection was performed by Stacey Holman, Lucy Flynn and Katering Steven at the School of Pharmacy and Medical Sciences, Sansom Institute for Health Research, University of South Australia. Adult pregnant ewes (4 years old; n = 4) were housed in an individual pen in view of other sheep in an indoor housing facility that

was maintained at a constant ambient temperature (20 - 22 °C) and a 12 h light/dark cycle. Sheep were humanely killed via overdose of sodium pentobarbitone (8 g; Vibrac Australia, Peakhurst, Australia). Samples of cardiac muscle tissue were taken from the left ventricle and skeletal muscle was taken from the quadriceps. Collected tissue samples were placed into sterile PBS on ice, protected from light, transported to the imaging facility within 90 minutes and imaged within 7 hours. All experiments were performed on samples from a minimum of 4 animals on 3 separate days.

3.5.11 Preparation of Tissue Sections

Live Tissue Sections

Live tissue samples were cut using a sharp scalpel to allow clean cutting and prevent damage associated with tearing of tissue. Sections were no more than 5 mm in thickness. The sectioning was performed in sterile PBS at room temperature (21 ± 2 °C).

Paraformaldehyde Fixed Tissue Sections

After dissection, cardiac (~ 1 cm^3) and skeletal muscle (~ 1 cm^3) tissues were washed in PBS, and then submerged in 4 % paraformaldehyde (Sigma-Aldrich, St. Louis, USA) for 20 hours at 4 °C. Paraformaldehyde was removed and the fixed tissues were washed in PBS for 30 minutes at room temperature. Samples were then stored in PBS at 4 °C. Fixed tissue sections of ~2 mm thickness were cut by using a sharp scalpel in sterile PBS. Prior to staining, tissue sections were kept in PBS for 2 hours at room temperature.

3.5.12 Tissue Staining

The biological investigation was performed by Dr Christie A. Bader and Dr Alexandra Sorvina at the School of Pharmacy and Medical Sciences, University of South Australia. A staining solution of $[Ir(\mathbf{ppy})_2(Me\mathbf{TzPyPhCN})]^+$ was prepared from a 10 mM stock solution in DMSO, which was diluted in sterile PBS to a final concentration of 20 μM. Fresh and paraformaldehyde fixed tissues were fully submerged in 1 mL of the staining solution in 5 mL tubes and incubated at room temperature with gentle agitation provided by a rocker for 30 minutes. The staining solution was aspirated and

tissues were then washed for 5 minutes in PBS. For mitochondrial staining by MitoTracker® Red CMXRos (diluted at 1:1000 in PBS) tissues were fully immersed in 1 mL of staining solution and incubated on ice for 15 minutes with general agitation. Tissues were then washed in PBS for 5 minutes. For anti-Cytochrome C antibody (Sapphire Bioscience, Redfern, Australia) probing, paraformaldehyde fixed tissues were permeabilised with 0.1% Saponin (Sigma-Aldrich, St. Louis, USA) in PBS for 2 hours at room temperature. To block non-specific binding of the antibodies, tissues were submerged in 5% bovine serum albumin (BSA; Sigma-Aldrich, St. Louis, USA) containing 0.05% Saponin for 2 hours at room temperature. Tissues were then incubated with anti-Cytochrome C antibody (1 µg/mL; prepared in 5% BSA containing 0.05% Saponin) overnight with gentle agitation at 4 ºC. After a washing step, secondary anti-IgG antibody conjugated with Cy5 labels (Jackson ImmunoResearch Laboratories, West Grove, USA) were then added and tissues were incubated for 1 hour at room temperature before a final wash step was performed. These washing steps were performed for 2 hours at room temperature. The Hoechst 33258 DNA stain (1:1000 in PBS; Life Technologies Australia Pty Ltd., Mulgrave, Australia) was performed for 1 minute and followed by a 5 minutes wash in PBS.

3.5.13 Inhibition of Membrane Potential

To investigate if cellular localisation of $[Ir(\mathbf{ppy})_2(Me\mathbf{TzPyPhCN})]^+$ was driven by mitochondrial membrane potential, H9c2 rat cardiomyoblast cells were treated with carbonyl cyanide-p-trifluoromethoxyphenylhydrazone (FCCP; Sigma-Aldrich, St. Louis, USA).[335] The H9c2 cells (1 x 10^5 cells/mL) were plated in ibidi µ-slide 8 wells and cultured overnight at 37 ºC and 5% CO_2 in 250 µL of DMEM medium supplemented with 10% fetal bovine serum and 2 mM L-glutamine. The cells were treated with FCCP, prepared in a complete DMEM media at 100 µM concentration, for 30 minutes at 37 ºC and 5% CO_2. Media was then aspirated and the H9c2 cells were either fixed in 4% PFA for 30 minutes to be used for antibody staining or stained with either $[Ir(\mathbf{ppy})_2(Me\mathbf{TzPyPhCN})]^+$ (20 µM) or MitoTracker (1:1000) for 30 minutes in the presence of FCCP. After staining, the cells were washed and then 300 µL of cell culture media was added for imaging on Nikon A1+ microscope.

3.5.14 Confocal Microscopy

Cells Imaging

Single photon live cell imaging was performed using a Nikon A1+ confocal microscope (Nikon, Japan) with an OKOLab Microscope Incubator (Okolab USA Inc., USA). The iridium complexes were excited at 403 nm and the emission was collected in the 525 - 644 nm region; ER-Tracker™ and MitoTracker® Red were excited at 561 nm and the emission was collected in the region 570 - 620 nm. BODIPY® 500/510 was excited at 488 nm and the emission was collected in the region 500 - 550 nm. Image analysis including co-localisation and emission intensity was measured using NIS elements V4.50 software (Nikon, Japan).

Two-photon microscopy imaging was performed using a Zeiss LSM710 META NLO inverted microscope supplemented with a two-photon Mai-Tai®, tunable Ti:Sapphire femtosecond pulse laser (710 – 920 nm, Spectra-Physics). The emission from the iridium complexes was detected using the following settings: two-photon excitation wavelength at 830 nm, beam splitter MBS 690+, emission interval 520 – 650 nm. The images were acquired using a Plan-APOCHROMAT 63X/ NA1.4 oil immersion objective. The final preparation of the images was conducted with Adobe Photoshop CC (Adobe Systems Inc., USA).

Tissues Imaging

Tissues were mounted with a longitudinal cross-section in contact with the imaging surface of the μ-slide 8 well chambers (DKSH, Hallam, Australia) and kept moist. Good contact between the sample and the surface was achieved by gently pressing the tissue down into the chamber. A dissection microscope was used to place and orientate the tissues.

Once mounted, tissues were immediately imaged with no more than 30 minutes elapsing between mounting and image completion, as imaging beyond this time can lead to excessive drying of tissue samples. Stained tissues were imaged using a Nikon A1+ (Nikon, Japan), fitted with a LU-N4/LU-N4S 4-laser unit (403, 488, 561 and 640 nm), the A1-DUG GaAsP Multi Detector Unit (2 GaAsP PMTs + 2 standard PMTs) and a 32 channel spectral detector (Nikon, Minato, Tokyo, Japan). Images for $[Ir(\mathbf{ppy})_2(Me\mathbf{TzPyPhCN})]^+$ were collected using a 403 nm laser set to 2 power setting and emission between 505 and 625 nm detected by the spectral detector, with gain set

to 180 for cardiac tissue and 170 for skeletal muscle tissue. The pinhole radius was 42.1 μm. For imaging of MitoTracker® Red CMXRos, 561 nm excitation wavelength (0.3 power setting) was used and emission was collected at 595 nm by a GaAsP PMT detector (gain of PMT HV 30). For co-staining experiments the settings above were used in sequence to collect $[Ir(\mathbf{ppy})_2(Me\mathbf{TzPyPhCN})]^+$ and MitoTracker® Red CMXRos respectively, minimising any overlap in spectral profiles.

Anti-Cytochrome C antibody staining was imaged using a 640 nm laser (7 power setting) and emission wavelength at 700 nm by a standard PMT (gain of PMT HV 125). All images were captured using a 40X/WI λS DIC N2 water emersion lens.

For the detection of NAD(P)H in fresh tissues, a Zeiss LSM710 NLO confocal microscope equipped with a two-photon Mai-Tai®, tunable Ti:Sapphire femtosecond pulse laser (Spectra-Physics, USA) was utilised. Images were collected using two-photon excitation at 740 nm and a 474 – 504 nm emission interval.[18] The laser power was 11% and the pinhole set to 600 μm. The pixel dwell time was set to 1.58 μs, and each image was averaged eight times to increase the signal-to-noise ratio. All images were acquired using a LD C-Apochromat 40X/NA 1.1 Water Corr UV-VIS-IR M27 objective (Carl Zeiss, Jena, Germany). The temperature in the imaging facility was set to a constant 19 °C.

Chapter 4

Synthesis and Photophysical Investigation of Amino and Nitro-Functionalised Iridium Tetrazolato Complexes

4.1 Introduction

The intracellular pH plays a central role in numerous biological processes, such as cellular proliferation, endocytosis, apoptosis, autophagy, enzymatic activity and ion transport.[341–345] Abnormal cellular pH values are indicators of inappropriate cellular functions, which are often associated with many common diseases like stroke, cancer and Alzheimer's disease.[346–348] Therefore, sensing and monitoring the pH is essential for understanding the physiological and pathological processes within cells and tissues. For the detection of pH fluctuations, a variety of methods have been employed, including ^{31}P NMR spectroscopy,[349,350] electrochemical techniques using microelectrodes[351,352] and optical microscopy.[45,353,354] Among them, fluorescent and phosphorescent probes have gained much attention due to their high sensitivity and selectivity, combined with relatively low cost, fast response, facilitated detection and non-invasiveness.[45,46,355]

During the design of the sensing system, the presence of protonatable and deprotonatable groups such as amino,[356] carboxylic,[357] hydroxyl[354] or imidazole-functionalised moieties[358] has been employed to regulate the pH-response.

Various luminescent dyes have been explored for the development of optical pH-sensors (refer to **Figure 4.1**), including organic naphthalimide (**94**) and rhodamine (**95**) derivatives, coumarin (**96**) and BODIPY (**97**) probes,[42,43,47,199,359] as well as metal complexes of Ru(II), Re(I), Pt(II) and Ir(III) (**98**-**101**).[354,357,360–365]

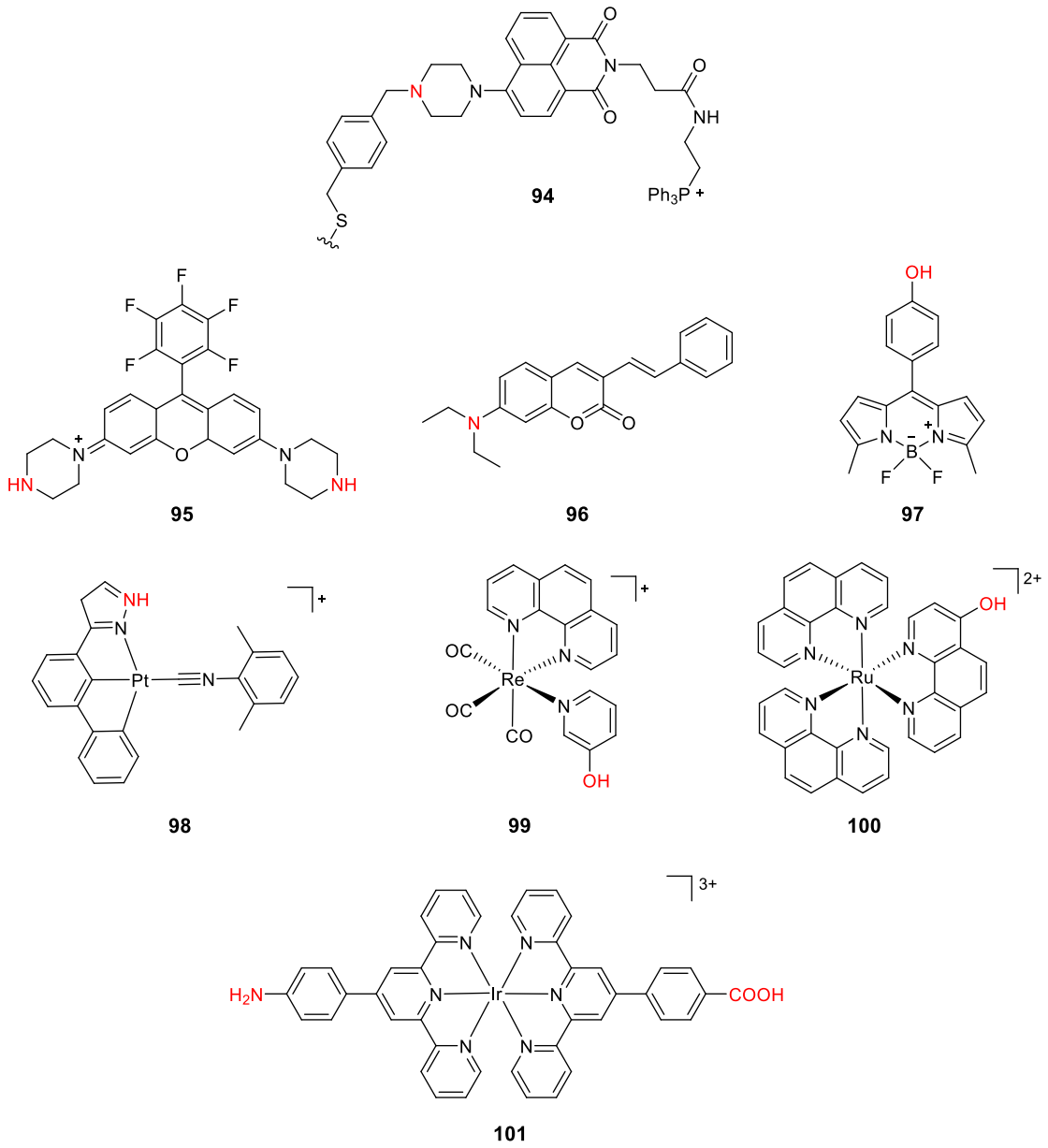

Figure 4.1 Examples of previously reported pH-sensors with the active group(s) highlighted in red.

In this chapter, the synthesis and photophysical investigation of two amino-functionalised iridium(III) tetrazolato complexes, [Ir(**ppy**)$_2$(**TzPyNH$_2$**)] and [Ir(**bzq**)$_2$(**TzPyNH$_2$**)] (**Figure 4.2** - top), will be discussed. Moreover, preliminary protonation and deprotonation reactions have been performed to evaluate the pH-sensing activities of these complexes. Noteworthy, [Ir(**ppy**)$_2$(**TzPyNH$_2$**)] and [Ir(**bzq**)$_2$(**TzPyNH$_2$**)] possess two different sites that can undergo protonation: the amino group and the tetrazolate ring.

For a better understanding of the absorption and emission profile modifications between the neutral and the protonated forms, the synthesis of the cationic analogues [Ir(**ppy**)$_2$(Me**TzPyNH$_2$**)]$^+$ and [Ir(**bzq**)$_2$(Me**TzPyNH$_2$**)]$^+$ was attempted (**Figure 4.2** - top). Unfortunately, the methylated species could not be isolated from the reaction mixture. For this reason, a comparative titration study was performed on [Ir(**ppy**)$_2$(**TzPyCN**)] and [Ir(**bzq**)$_2$(**TzPyCN**)], and their methylated equivalents [Ir(**ppy**)$_2$(Me**TzPyCN**)]$^+$ and [Ir(**bzq**)$_2$(Me**TzPyCN**)]$^+$ (**Figure 4.2** - bottom).

The photophysical performance of [Ir(**ppy**)$_2$(**TzPyNH$_2$**)] is poor in comparison to the emissive properties of [Ir(**ppy**)$_2$(**TzPyCN**)], which is ascribed to the presence of the NH_2 group on the tetrazolate ligand. In particular, the electron-donating NH_2 blue shifts the emission maxima of the complex by increasing the energy of the emitting ^{3}MLCT exciting state, which lays in close proximity with the thermally available and dark ^{3}MC excited state (see section 4.4.3 for details). Moreover, the emission is also quenched by the high energy vibrations due to the stretching of the N-H bonds.

Hence, in order to prove this hypothesis, the amine of [Ir(**ppy**)$_2$(**TzPyNH$_2$**)] was oxidised to an electron-withdrawing NO_2 group. However, the resulting nitro-functionalised complex [Ir(**ppy**)$_2$(**TzPyNO$_2$**)] (**Figure 4.2** - top) has showed a total quenching of the emission even in organic solvent.

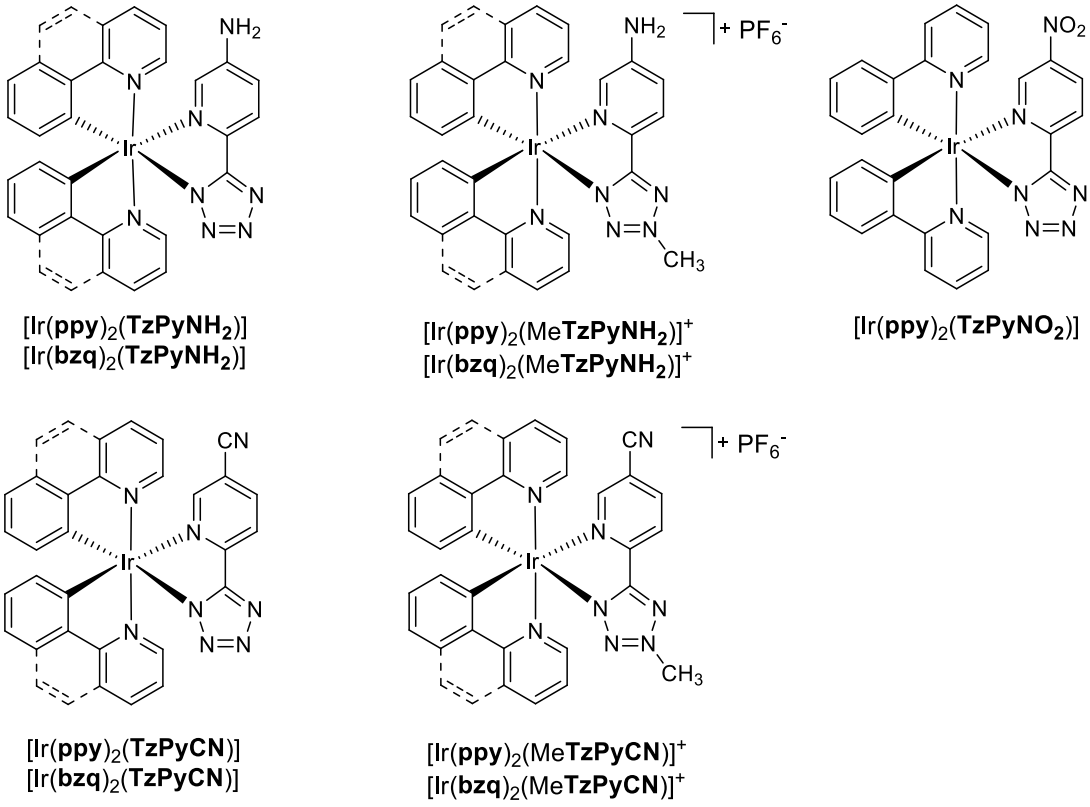

Figure 4.2 Structures of target complexes in this investigation.

4.2 Synthesis of the Tetrazolate Ligand

H**TzPyNH$_2$** was synthesised following a previously reported procedure, showed in **Figure 4.3**, in which the nitrile precursor was reacted with sodium azide and triethylammonium chloride in toluene and heated at reflux for 24 hours.[270]

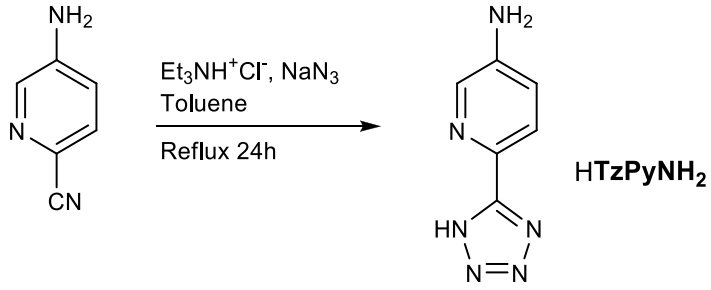

Figure 4.3 Scheme of the synthetic procedure for the preparation of H**TzPyNH$_2$**.

H**TzPyNH$_2$** was isolated as an orange-pink precipitate and was characterised by IR, ^{1}H NMR and ^{13}C NMR spectroscopy.

The IR bands at 3334, 3160 and 1661 cm^{-1} are characteristic of N–H bond stretching and bending of the amino group, whereas the band at 1612 cm^{-1}, associated with C=N stretching, is suggestive of the formation of the tetrazolate ring. Additionally, the lack of the nitrile band at *ca.* 2240 cm^{-1} confirms the conversion of the starting material in the desired product.

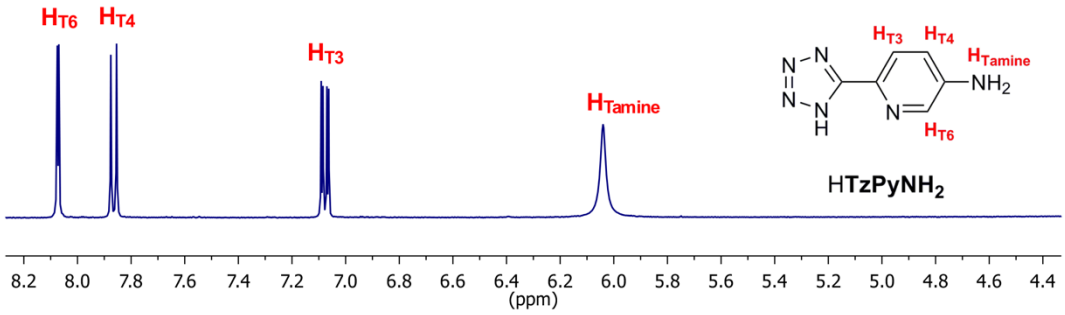

Figure 4.4 ^{1}H NMR in DMSO-d_6 for H**TzPyNH$_2$** with labelling of the proton peaks.

The ^{1}H NMR spectrum of H**TzPyNH$_2$** is shown in **Figure 4.4**. The peaks at 8.07, 7.86 and 7.08 ppm are associated with the pyridinic protons, whereas the broad

singlet peak resonating at 6.04 ppm is assigned to the amino substituent. The ^{13}C NMR spectrum is again in agreement with the proposed structure, displaying the tetrazolic carbon $\mathbf{C_T}$ at 154.9 ppm, which highlights the predominant presence of the N1 tautomeric form of the tetrazolato ring (refer to Chapter 1 – section 1.6).[225,226]

4.3 Synthesis of the Iridium(III) Complexes

4.3.1 Synthesis and Characterisation of Amino-Functionalised Iridium(III) Complexes

The synthesis of the two iridium(III) complexes [Ir(**ppy**)$_2$(**TzPyNH$_2$**)] and [Ir(**bzq**)$_2$(**TzPyNH$_2$**)] was adapted from a published literature method.[236,238] In this case, the use of triethylamine was necessary to deprotonate H**TzPyNH$_2$**, in order to improve its low solubility in the solvent system. Once H**TzPyNH$_2$** was completely dissolved and converted in its anionic form **TzPyNH$_2^-$**, the appropriate dichloro-bridged dimer, [Ir(**ppy**)$_2$(μ-Cl)]$_2$ or [Ir(**bzq**)$_2$(μ-Cl)]$_2$, was added and the reaction mixture stirred at room temperature for 16 hours. (**Figure 4.5** - top).

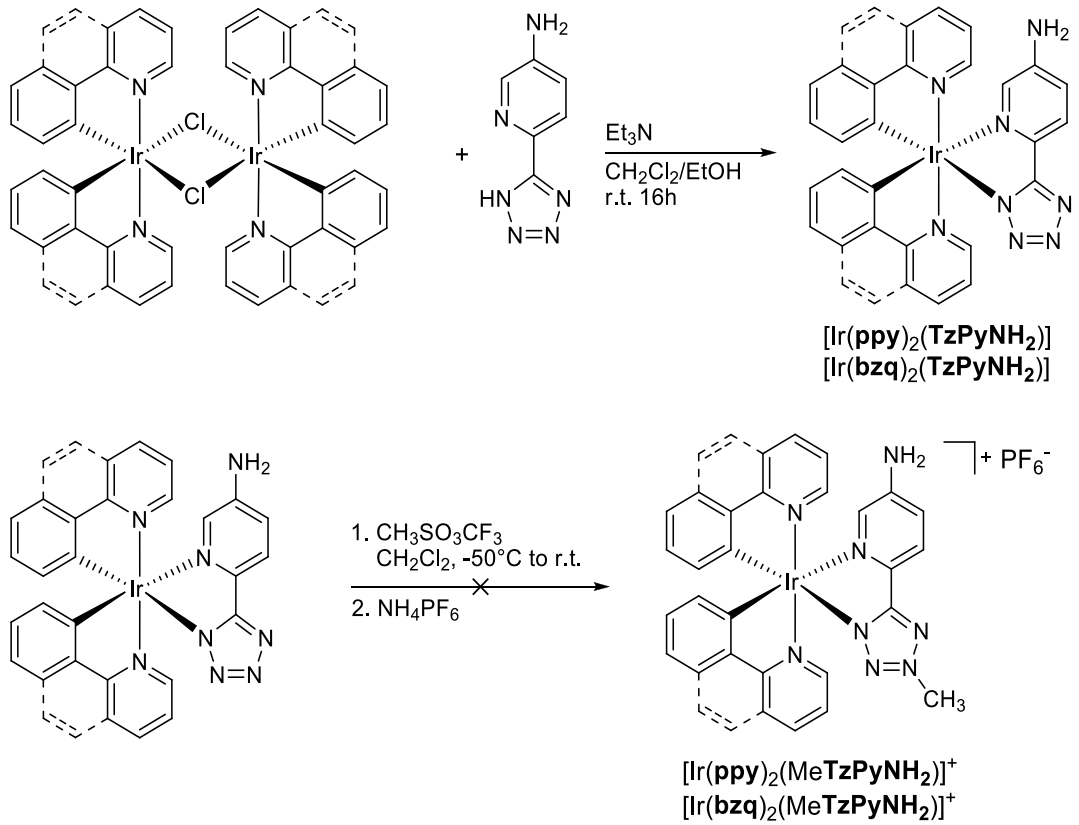

Figure 4.5 Scheme of the synthetic procedure for preparation of neutral [Ir(**ppy**)$_2$(**TzPyNH$_2$**)] and [Ir(**bzq**)$_2$(**TzPyNH$_2$**)] (top) and the attempted reaction scheme for the formation of the cationic [Ir(**ppy**)$_2$(Me**TzPyNH$_2$**)]$^+$ and [Ir(**bzq**)$_2$(Me**TzPyNH$_2$**)]$^+$ (bottom).

The synthesis of the methylated $[Ir(\mathbf{ppy})_2(Me\mathbf{TzPyNH_2})]^+$ and $[Ir(\mathbf{bzq})_2(Me\mathbf{TzPyNH_2})]^+$ (**Figure 4.5** - bottom) was unsuccessful, as an inseparable mixture of products was obtained. The ^{1}H NMR spectrum of the reaction mixture to form $[Ir(\mathbf{ppy})_2(Me\mathbf{TzPyNH_2})]^+$ (**Figure 4.6**) displays three different species, which have been identified as unreacted $[Ir(\mathbf{ppy})_2(\mathbf{TzPyNH_2})]$ and two methylated complexes. The peaks of the unreacted starting material $[Ir(\mathbf{ppy})_2(\mathbf{TzPyNH_2})]$ have been highlighted in the spectrum (black boxes), whereas the presence of two methyl peaks at around 4.45 ppm (red box) is assigned to the two different methylated species.

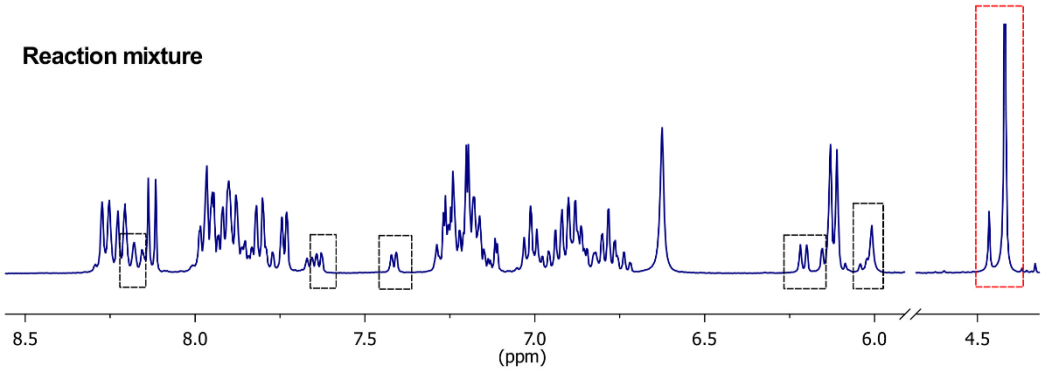

Figure 4.6 ^{1}H NMR spectrum in DMSO-d_6 of the reaction mixture to form $[Ir(\mathbf{ppy})_2(Me\mathbf{TzPyNH_2})]^+$. The signals of the unreacted starting material $[Ir(\mathbf{ppy})_2(\mathbf{TzPyNH_2})]$ and the methyl peaks of two different methylated species have been highlighted in black and red boxes, respectively.

Based on previous reports on iridium(III) tetrazolato complexes,[236,238,239] the electrophilic addition in the N2 or N4 position of the tetrazolate ring is unlikely to happen. For this reason the methylation of the amino group has been investigated, using 5-amino-2-pyridinecarbonitrile as a model molecule and following the same methylation method adopted for $[Ir(\mathbf{ppy})_2(Me\mathbf{TzPyNH_2})]^+$ and $[Ir(\mathbf{bzq})_2(Me\mathbf{TzPyNH_2})]^+$. This substrate was chosen as starting material to simplify the studied system, by avoiding any methylation of the tetrazolato ring. As showed in **Figure 4.7**, two different species were present in the reaction crude, with a ratio of 2:1 (based on NMR integrals). The major compound was identified as the unreacted starting material (green triangle), whereas the second species was represented by the methylated pyridine analogue (red diamond), characterised by the amino broad singlet around 6.40 ppm and a sharp methyl peak at *ca.* 4.30 ppm. On the basis of this result,

the methylation of the amino group using methyl trifluoromethanesulphonate has been discarded as possible explanation for the second methylated byproduct in the reaction to form $[Ir(\mathbf{ppy})_2(Me\mathbf{TzPyNH_2})]^+$.

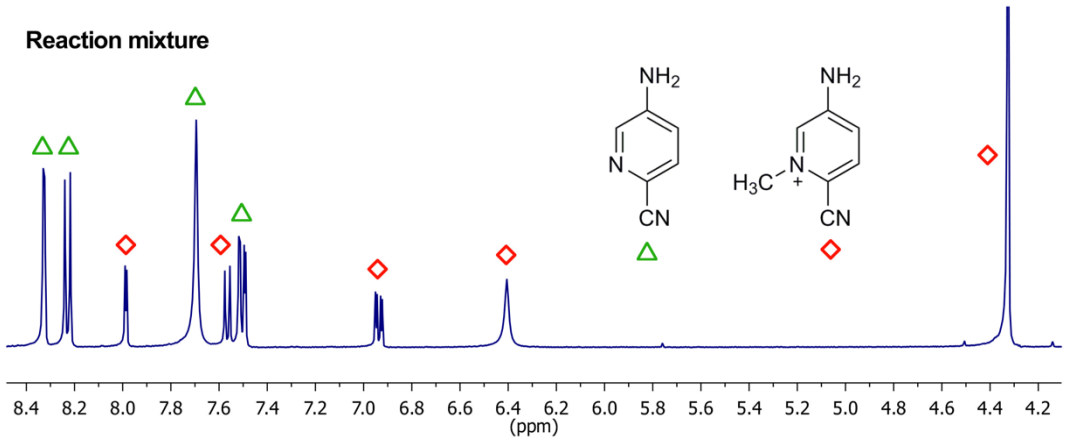

Figure 4.7 ^{1}H NMR spectrum in DMSO-d_6 of the reaction mixture for the methylation of 5-amino-2-pyridinecarbonitrile. In the spectrum, the peaks of the two species are labelled with green triangles and red diamonds for 5-amino-2-pyridinecarbonitrile and the methylated analogous, respectively.

The presence of two methylated species in the reaction mixture showed in **Figure 4.6** can be then attributed only to the methylation in N2 or N4 positions of the tetrazolato ring. In the attempt of proving this hypothesis, a preliminary investigation was firstly performed on H**TzPyNH$_2$**, but the purification and separation of the two isomers *via* column chromatography was not achieved due to cleavage of the amino group and decomposition of the products. The methylation reaction was then carried out on 2-(1*H*-tetrazol-5-yl)pyridine (H**TzPy**) and two isomers were successfully synthesised and purified *via* column chromatography on silica gel and using an ethyl acetate/petroleum spirits 40-60 (9:1 v/v) solvent mixture as eluent. As depicted in **Figure 4.8**, N4-Me**TzPy** showed a marked downfield shift of the aromatic proton peaks in comparison to N3-Me**TzPy**, whereas the methyl groups resonated at similar frequency (4.42 and 4.46 ppm, respectively). Moreover, as previously reported by Butler *et al.*,[226] the different isomers can be distinguished by the chemical shift of the tetrazolic carbon **C$_T$**, which resonates in the range of 162 - 165 ppm for the N3-substituted ring and 152 - 156 ppm for the N4 species (**Figure 4.9**).

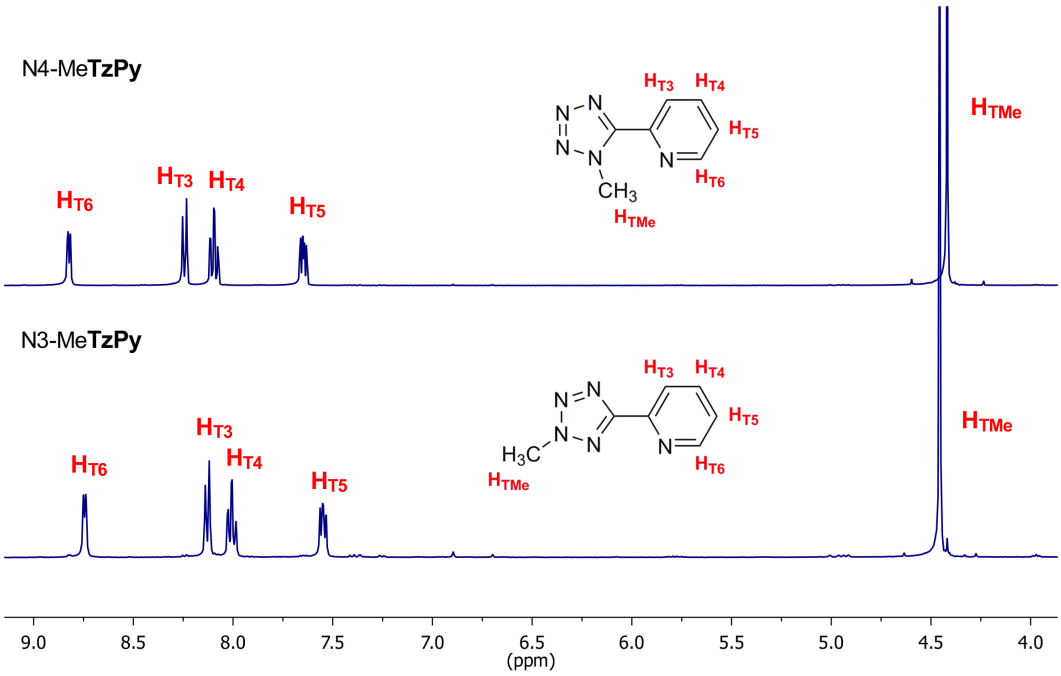

Figure 4.8 ^{1}H NMR in DMSO-d_6 for N4-Me**TzPy** (top) and N3-Me**TzPy** (bottom) with labelling of the proton peaks.

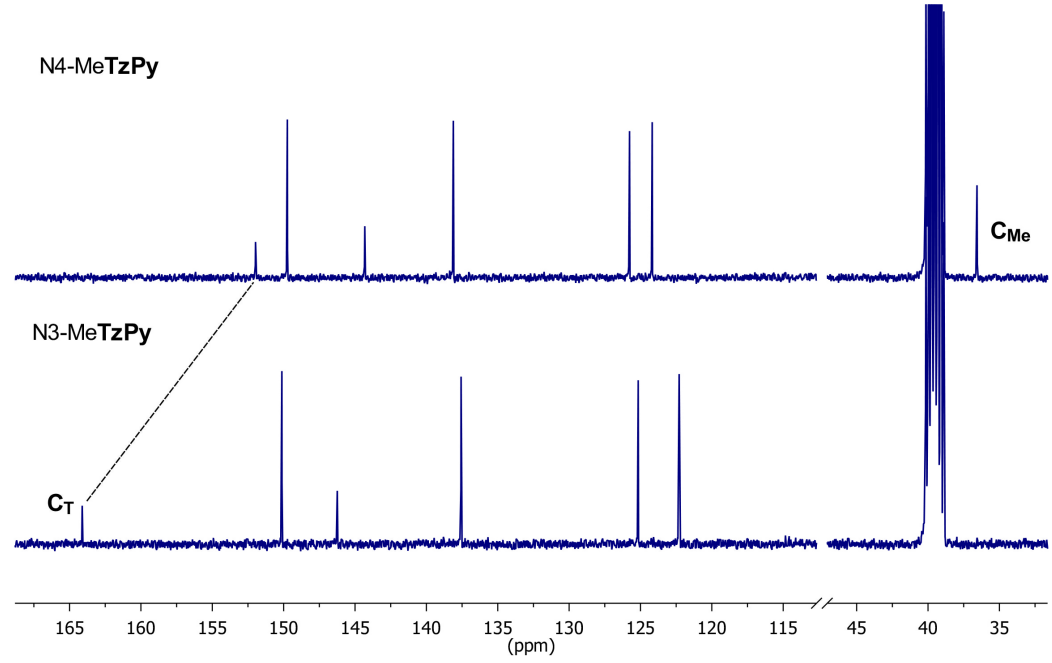

Figure 4.9 ^{13}C NMR in DMSO-d_6 for N4-Me**TzPy** (top) and N3-Me**TzPy** (bottom). In the spectra, the downfield shift of the $\mathbf{C_T}$ is highlighted. The peak of the methyl carbon $\mathbf{C_{Me}}$ is only visible for N4-Me**TzPy**.

Unfortunately, obtaining the ^{13}C NMR spectrum of the reaction mixture to form [Ir(**ppy**)$_2$(Me**TzPyNH$_2$**)]$^+$ was unsuccessful due to the presence of three species. Based on the ^1H NMR spectra, the resonance of the methyl peaks (4.41 – 4.46 ppm) is comparable with the ones exhibits by N3-Me**TzPy** and N4-Me**TzPy** (4.42 -4.46 ppm). Furthermore, the ratio of the two methylated species in the reaction mixture was 5:1, which is again similar to the one obtained for N3-Me**TzPy** and N4-Me**TzPy** (4:1), suggesting that only a small amount of the N4-substituted product was formed. Based on these results, we can identify the two methylated species in **Figure 4.6** as N3 and N4-substituted iridium(III) complexes.

On the other hand, [Ir(**ppy**)$_2$(**TzPyNH$_2$**)] and [Ir(**bzq**)$_2$(**TzPyNH$_2$**)] were isolated with high purity and good yield by precipitation from the crude mixture with addition of diethyl ether and purification *via* column chromatography was not necessary.

The IR spectroscopic characterisation highlights the bands of amino N–H stretching and bending at similar wavenumbers of *ca.* 3305, 3160 and 1640 cm^{-1} and, the tetrazolic C=N stretching at *ca.* 1605 cm^{-1} for both complexes.

The ^1H NMR spectra in DMSO-d_6 showed in **Figure 4.10** confirm the isolation of the desired products. The spectra display the characteristic doublet peaks around 6.5 – 6.0 ppm (black boxes) assigned to cyclometalated iridium species[126,133,273] and, slightly downshifted, the broad singlet peak of the amino substituent (red boxes).
The ^{13}C NMR showed the $\mathbf{C_T}$ signals at 167.5 and 164.2 ppm for [Ir(**ppy**)$_2$(**TzPyNH$_2$**)] and [Ir(**bzq**)$_2$(**TzPyNH$_2$**)], respectively, confirming the coordination of the tetrazolate ligand to the iridium metal centre.

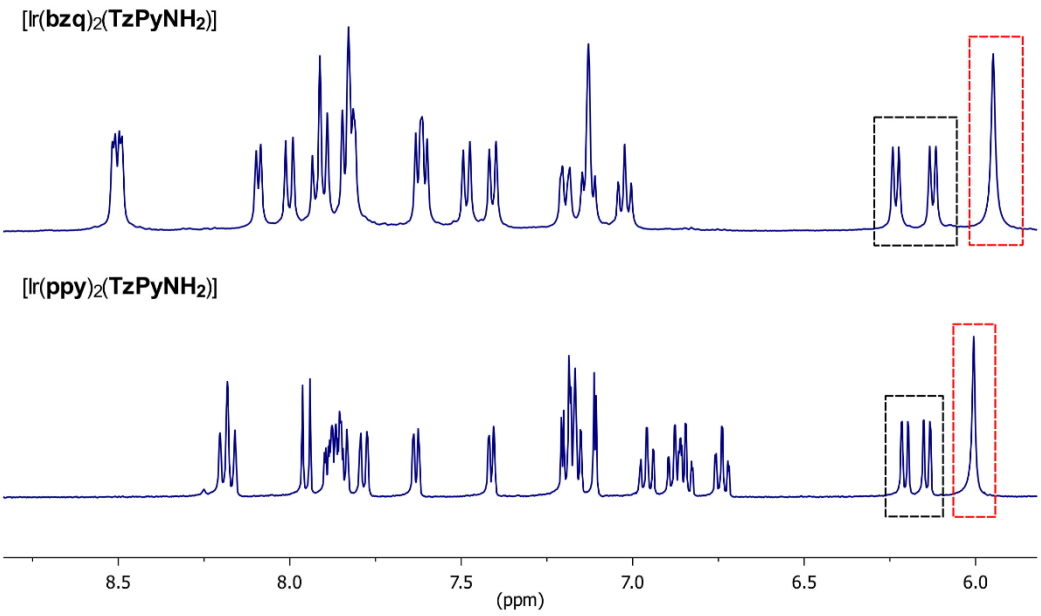

Figure 4.10 ^{1}H NMR in DMSO-*d*$_6$ for [Ir(**bzq**)$_2$(**TzPyNH$_2$**)] (top) and [Ir(**ppy**)$_2$(**TzPyNH$_2$**)] (bottom). In the spectra, the two characteristic doublet peaks of cyclometalated iridium complexes and the singlet peak of the amine have been highlighted in black and red boxes, respectively.

4.3.2 Synthesis and Characterisation of Nitro-Functionalised Iridium(III) Complex

[Ir(**ppy**)$_2$(**TzPyNO$_2$**)] was synthesised by oxidation of [Ir(**ppy**)$_2$(**TzPyNH$_2$**)], using potassium iodide as catalyst and *tert*-butyl hydroperoxide (TBHP) as oxidating agent,[366] as showed in **Figure 4.11**.

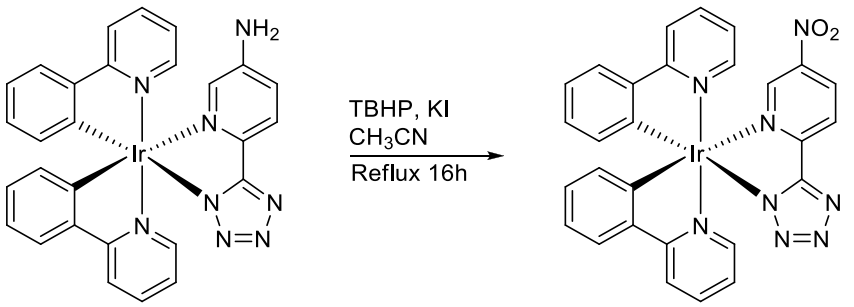

[Ir(**ppy**)$_2$(**TzPyNO$_2$**)]

Figure 4.11 Scheme of the synthetic procedure for the preparation of [Ir(**ppy**)$_2$(**TzPyNO$_2$**)].

Classical methods for the preparation of aromatic nitro compounds involve direct nitration of the aromatic ring under harsh conditions or through the formation of anionic intermediates.[367–369] Interestingly, following the methodology discovered by Reddy *et al.*,[366] direct oxidation of the amino-functionalised iridium(III) complex can be achieved in mild conditions, using acetonitrile as solvent and heating the reaction mixture at reflux for 16 hours.

The unreacted starting material was easily separated by filtration from the crude mixture and recovered, whereas [Ir(**ppy**)$_2$(**TzPyNO$_2$**)] was purified by column chromatography using neutral alumina as stationary phase and isolated in good yield (*ca.* 75%).

The IR spectrum of [Ir(**ppy**)$_2$(**TzPyNO$_2$**)] displays two strong absorption bands at 1478 and 1344 cm^{-1}, which are associated with the asymmetric and symmetric stretching of the nitro group, respectively. In addition to the NO_2 bands, the aromatic stretching of the tetrazolic C=N at 1607 cm^{-1} further supports the formation of the desired product.

The ^{1}H NMR spectrum for this complex matches the proposed structure. Two doublets and a singlet peak at 8.83, 8.55 and 8.37 ppm are associated with the three pyridinic hydrogen atoms of the **TzPyNO$_2^-$** ligand, and resonate at higher chemical shift with respect to [Ir(**ppy**)$_2$(**TzPyNH$_2$**)] due to the oxidation of the electron-donating amine to an electron-withdrawing nitro group (**Figure 4.12**). In the ^{13}C NMR spectrum, the resonance of the **C$_T$** at 167.0 ppm is consistent with other cyclometalated iridium(III) tetrazolato species,[236,238,239,370] and it is indicative of a co-planarity between the pyridyl and tetrazole rings of the ancillary ligand, and therefore chelation to the iridium metal centre.

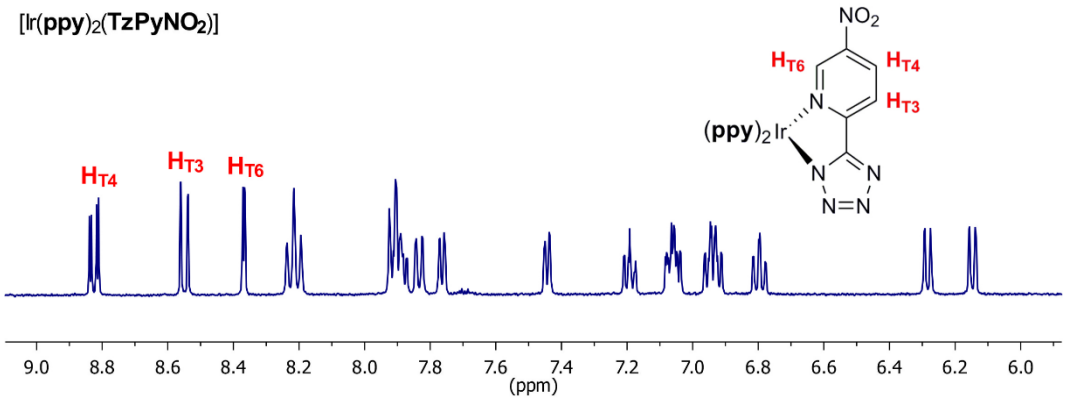

Figure 4.12 ^{1}H NMR in DMSO-*d*$_6$ for [Ir(**ppy**)$_2$(**TzPyNO$_2$**)] with the tetrazolic peaks labelled in the spectrum.

4.3.3 Synthesis and Characterisation of Cyano-Functionalised Iridium(III) Complexes

As discussed in section 4.1 of this chapter, the photophysical behaviour of [Ir(**ppy**)$_2$(**TzPyNH$_2$**)] and [Ir(**bzq**)$_2$(**TzPyNH$_2$**)] in acid/base conditions has been investigated and compared to the one of [Ir(**ppy**)$_2$(**TzPyCN**)] and [Ir(**bzq**)$_2$(**TzPyCN**)]. To minimise the effect of the structural modifications on the photophysical properties, the investigation was carried out on the cyano and amino-functionalised iridium(III) complexes bearing the same cyclometalated ligands (**ppy** or **bzq**).

Based on the synthetic procedure of [Ir(**ppy**)$_2$(**TzPyCN**)] described in Chapter 2 – section 2.3.1, [Ir(**bzq**)$_2$(**TzPyCN**)] was prepared in a similar manner.[236,238]

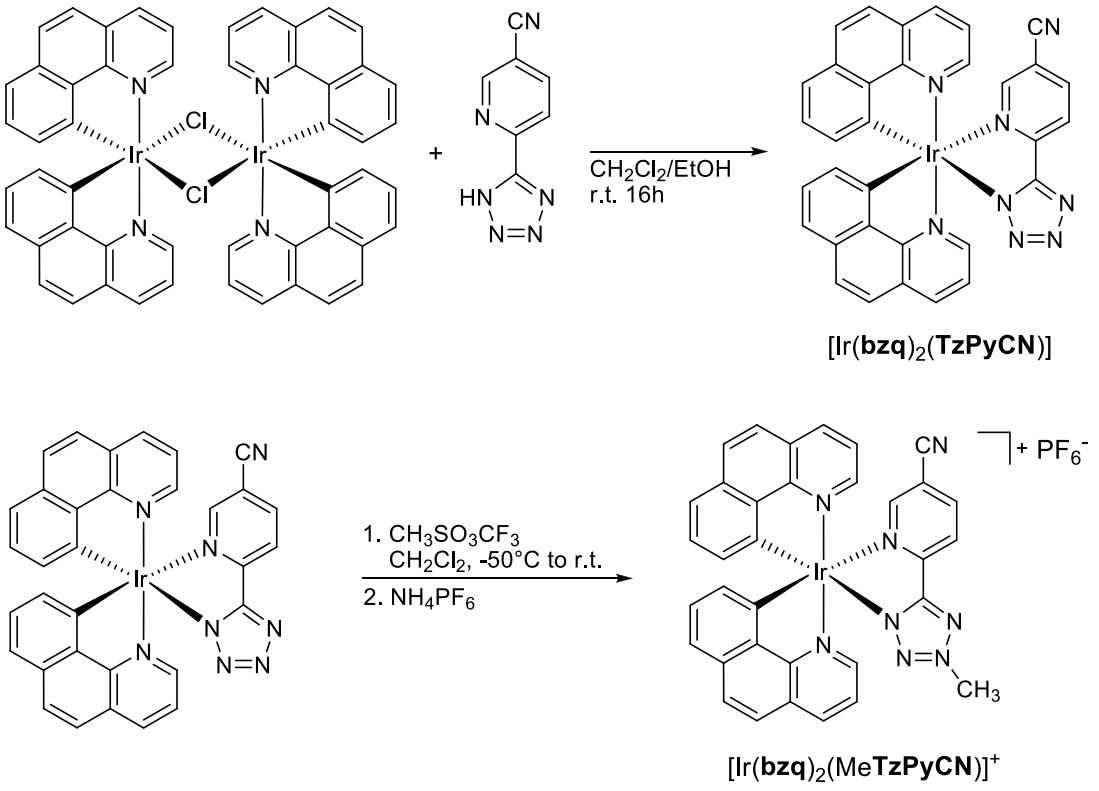

Figure 4.13 Scheme of the synthetic procedures for the preparation of the neutral [Ir(**bzq**)$_2$(**TzPyCN**)] (top) and the methylated [Ir(**bzq**)$_2$(Me**TzPyCN**)]$^+$ (bottom) species.

The reaction is showed in **Figure 4.13** (top), where the dichloro-bridge dimer [Ir(**bzq**)$_2$(μ-Cl)]$_2$ is combined with H**TzPyCN** in dichloromethane/ethanol (10:3 v/v) solvent system and stirred at room temperature for 16 hours to form the crude product. Purification *via* column chromatography using neutral alumina as stationary phase and dichloromethane/acetone (9:1 v/v) solvent system as eluent was required to yield the pure [Ir(**bzq**)$_2$(**TzPyCN**)] (66%).

The reaction of the neutral [Ir(**bzq**)$_2$(**TzPyCN**)] with a slight excess of methyl trifluoromethanesulphonate, followed by metathesis with ammonium hexafluorophosphate led to the formation of the cationic [Ir(**bzq**)$_2$(Me**TzPyCN**)]$^+$ species as a PF_6^- salt (**Figure 4.13** - bottom).

The methylated complex was isolated as a red solid with good yield (*ca.* 75%) and purity by simple extraction from the reaction mixture and without further purification needed.

The neutral and the methylated complexes were characterised by IR spectroscopy, which highlights the sharp C≡N peak around 2238 cm^{-1}, in addition to the tetrazolic C=N stretching at *ca.* 1613 cm^{-1} for both the species.

The ^{1}H NMR spectra for [Ir(**bzq**)$_2$(**TzPyCN**)] and [Ir(**bzq**)$_2$(Me**TzPyCN**)]$^+$ support the achieved isolation of the desired compounds, with the total peak integration being 19 and 22 protons, respectively. The difference in integration is due to the methyl sharp signal resonating at 4.50 ppm and integrating for 3 protons, which highlights the formation of only one methylated species for each complex (**Figure 4.14**).

To further confirm the conversion of the neutral iridium complex in the methylated analogous, the ^{13}C NMR spectra of the two complexes were compared, as shown in **Figure 4.15**. In particular, the methyl peak of [Ir(**bzq**)$_2$(Me**TzPyCN**)]$^+$ is identified at 42.2 ppm and the characteristic $\mathbf{C_T}$ resonance is downshifted from 163.0 for [Ir(**bzq**)$_2$(**TzPyCN**)] to 165.3 ppm for [Ir(**bzq**)$_2$(Me**TzPyCN**)]$^+$. A comparable shift of the $\mathbf{C_T}$ signals was observed for previously published complexes,[236,238,239] supporting the hypothesis of methylation in N3 position of the tetrazolate ligand.

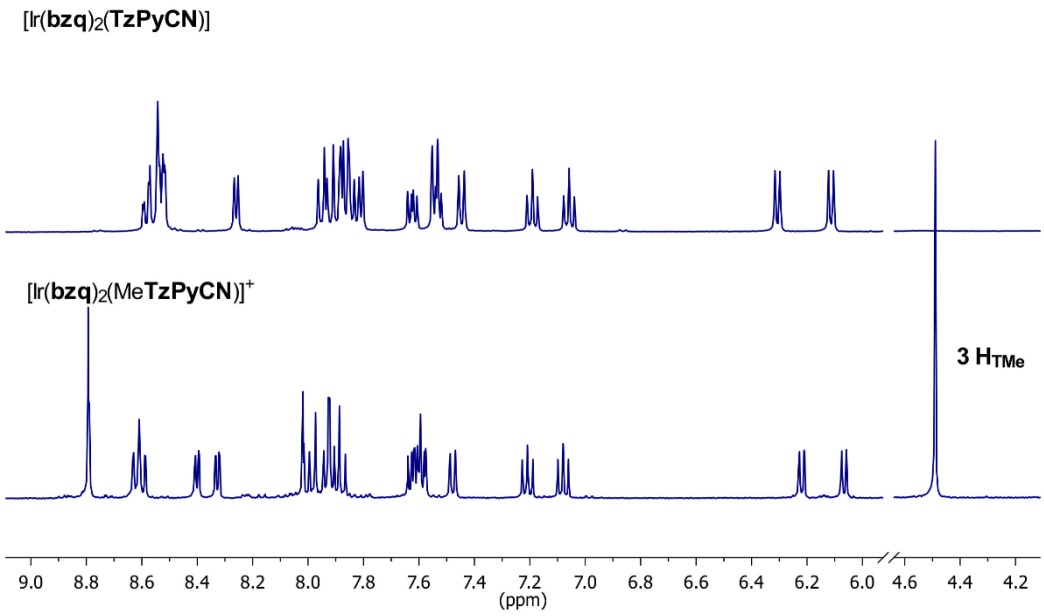

Figure 4.14 ^{1}H NMR in DMSO-*d*$_6$ for the neutral complex [Ir(**bzq**)$_2$(**TzPyCN**)] (top) compared to the methylated analogous [Ir(**bzq**)$_2$(Me**TzPyCN**)]$^+$ (bottom).

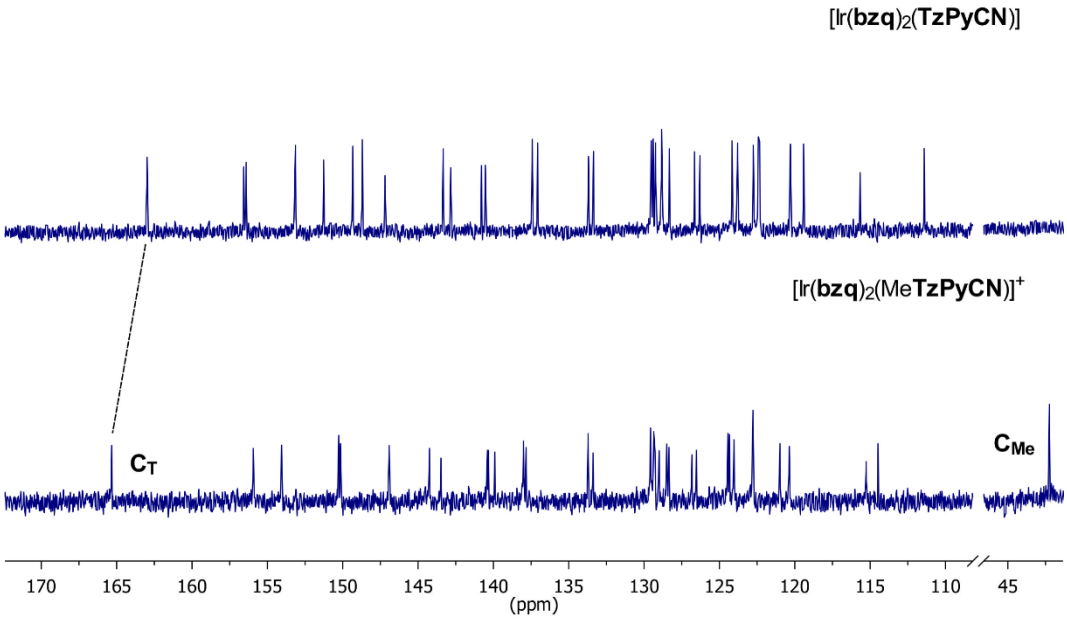

Figure 4.15 ^{13}C NMR in DMSO-*d*$_6$ for the neutral complex [Ir(**bzq**)$_2$(**TzPyCN**)] (top) compared to the methylated analogous [Ir(**bzq**)$_2$(Me**TzPyCN**)]$^+$ (bottom).

4.4 Photophysical Investigation

4.4.1 Absorption in Dichloromethane

The absorption properties of the iridium(III) complexes in air-equilibrated dichloromethane solutions have been summarised in **Table 4.1**.

All the neutral iridium(III) species display comparable absorption profiles (**Figure 4.16** to **Figure 4.18**). With reference to the absorption spectra of similar cyclometalated iridium(III) complexes,[33,260,273,298,311,371] the absorption bands in the 250 – 300 nm region are attributed to spin-allowed ligand-centred (LC) π-π* transitions, localised on the **ppy** and **bzq** ligands. The less intense absorption shoulders in the visible region between 300 and 400 nm are assigned to a mixture of spin-allowed ligand-to-ligand (LLCT) and metal-to-ligand charge transfer (MLCT) transitions. In addition, due to the spin-orbit coupling associated with the iridium metal centre,[76] spin-forbidden MLCT/LLCT transitions are visible as weak absorption tails at *ca.* 400 – 450 nm.[236]

Table 4.1 Absorption data of dichloromethane solutions (10^{-5} M) of the reported complexes.

Complexes	λ_{abs} [nm] (10^4 ε [$M^{-1}cm^{-1}$])
[Ir(**ppy**)$_2$(**TzPyNH$_2$**)]	270 (9.45), 346 (1.79), 387 (0.89), 423 (0.53)
[Ir(**bzq**)$_2$(**TzPyNH$_2$**)]	260 (9.59), 333 (3.63), 375 (1.53), 433 (0.87)
[Ir(**ppy**)$_2$(**TzPyNO$_2$**)]	262 (4.60), 301 (3.40), 384 (0.86), 417 (0.50)
[Ir(**bzq**)$_2$(**TzPyCN**)]	262 (7.83), 290 (4.27), 351 (2.18), 426 (0.80)
[Ir(**bzq**)$_2$(Me**TzPyCN**)]$^+$	284 (3.32), 321 (2.11), 405 (0.78)

A comparison between [Ir(**ppy**)$_2$(**TzPyNH$_2$**)] and [Ir(**bzq**)$_2$(**TzPyNH$_2$**)] highlights a slight blue shift of the absorption bands by changing the cyclometalated ligands from **ppy** to **bzq**, along with higher absorptivity values (**Figure 4.16**). The opposite behaviour was previously observed for Re(I) complexes with formula *fac*-[Re(CO)$_3$(**N^N**)L]$^+$, where **N^N** is either **bpy** (2,2'-bipyridine) or **phen** (1,10-

phenanthroline) and L is a *para*-functionalised 5-aryltetrazolate ligand. In this case, a red shift of the absorption bands and an increase of the molar absorptivity values were recorded between the **phen** and **bpy**-functionalised Re(I) complex.[372]

On the other hand, a more marked red shift of MLCT/LLCT bands was observed in **Figure 4.18** comparing [Ir(**bzq**)$_2$(**TzPyCN**)] and [Ir(**bzq**)$_2$(Me**TzPyCN**)]$^+$ with the less conjugated [Ir(**ppy**)$_2$(**TzPyCN**)] and [Ir(**ppy**)$_2$(Me**TzPyCN**)]$^+$ (absorption data of these complexes are showed in Chapter 2 – section 2.4.1).[115,137,301]

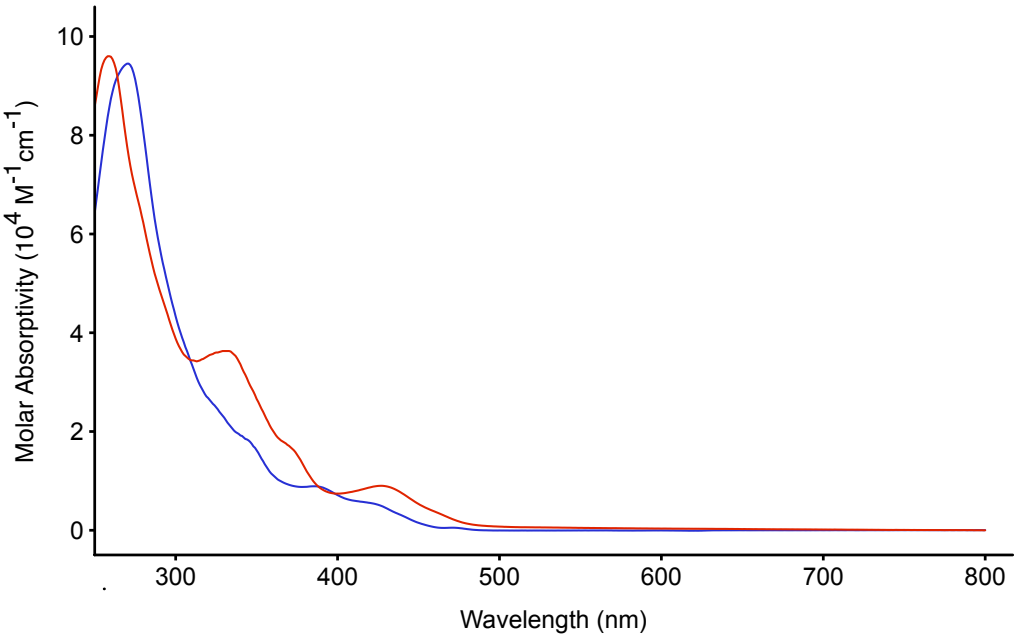

Figure 4.16 Absorption profiles of [Ir(**ppy**)$_2$(**TzPyNH$_2$**)] (blue) and [Ir(**bzq**)$_2$(**TzPyNH$_2$**)] (red) in dichloromethane.

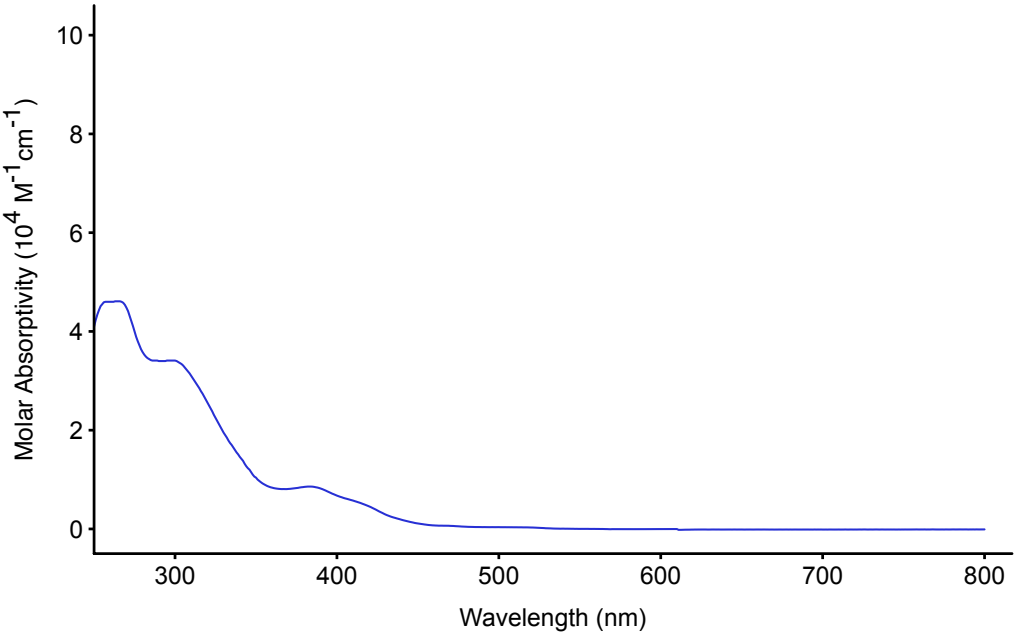

Figure 4.17 Absorption profiles of [Ir(**ppy**)$_2$(**TzPyNO$_2$**)] (blue) in dichloromethane.

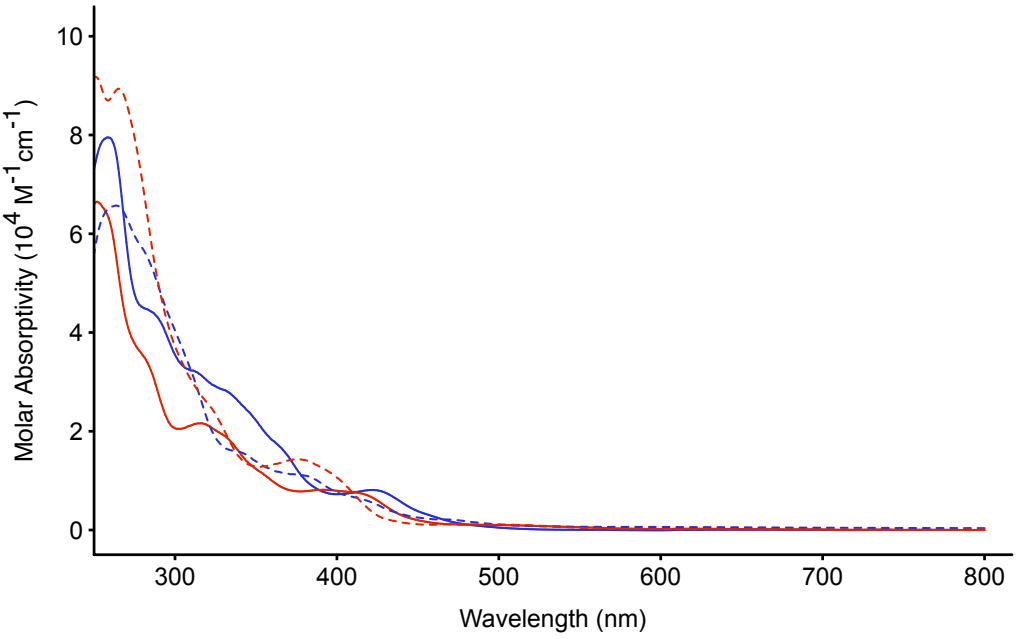

Figure 4.18 Absorption profiles of [Ir(**bzq**)$_2$(**TzPyCN**)] (solid blue), [Ir(**bzq**)$_2$(Me**TzPyCN**)]$^+$ (solid red), [Ir(**ppy**)$_2$(**TzPyCN**)] (dash blue), [Ir(**ppy**)$_2$(Me**TzPyCN**)]$^+$ (dash red) in dichloromethane.

4.4.2 Emission Properties in Dichloromethane

The photophysical properties of the iridium(III) complexes were measured in both air-equilibrated and degassed dichloromethane solutions, and all the data are summarised in **Table 4.2**.

Upon irradiation at 350 nm, all the complexes, with the exception of [Ir(**ppy**)$_2$(**TzPyNO$_2$**)], displayed intense green-yellow to orange-red emission for the amino (**Figure 4.21**) and cyano-functionalised complexes (**Figure 4.22**), respectively.

Table 4.2 Photophysical data of dichloromethane solutions (10^{-5} M) of the reported complexes.

Complex	λ_{em} [nm]	τ_{aer} [ns][a]	τ_{deaer} [ns][a]	Φ_{aer}[b]	Φ_{deaer}[b]
[Ir(**ppy**)$_2$(**TzPyNH$_2$**)]	484, 514	101	1032	0.005	0.028
[Ir(**bzq**)$_2$(**TzPyNH$_2$**)]	524, 555	120	23110	0.005	0.572
[Ir(**ppy**)$_2$(**TzPyNO$_2$**)]	-[c]	-[c]	-[c]	-[c]	-[c]
[Ir(**bzq**)$_2$(**TzPyCN**)]	620	146	508	0.052	0.124
[Ir(**bzq**)$_2$(Me**TzPyCN**)]$^+$	690	24 (54), 152(46)	25 (47), 192 (53)	0.010	0.012

[a] For the biexponential excited state lifetime (τ), the relative weights of the exponential curves are reported in parentheses. [b] Measured versus [Ru(**bpy**)$_3$]$^{2+}$ in H_2O (Φ_r = 0.028).[274] [c] Not emissive.

The emission of [Ir(**ppy**)$_2$(**TzPyNO$_2$**)] was too weak to be distinguishable from the baseline, even in an oxygen-free solution, and has not been reported. Previous studies on rhenium(I) and iridium(III) complexes[373,374] carrying nitro groups showed no emission in solution at 298 K for these species, unlike their non-substituted analogues. In the case of *fac*-[Re(CO)$_3$(5-NO$_2$-**phen**)Cl] (**Figure 4.19**), the lack of emission is due to the quick conversion (*ca.* 10 ps) of the ^{3}MLCT excited state into a close-lying intraligand (IL) $^3n\pi^*$ excited state, whereby the electron density is excited from the NO_2 oxygen lone pairs to the π^* systems of the **phen**. The $^3n\pi^*$state is also short-lived and undergoes rapid non-radiative conversion to the ground state with a lifetime of *ca.* 30 – 70 ps, depending on the solvent.[373] A similar assumption has been

applied to [Ir(**ppy**)$_2$(**TzPyNO$_2$**)], in order to explain why other electron-withdrawing groups, such as nitrile, do not show the same behaviour.

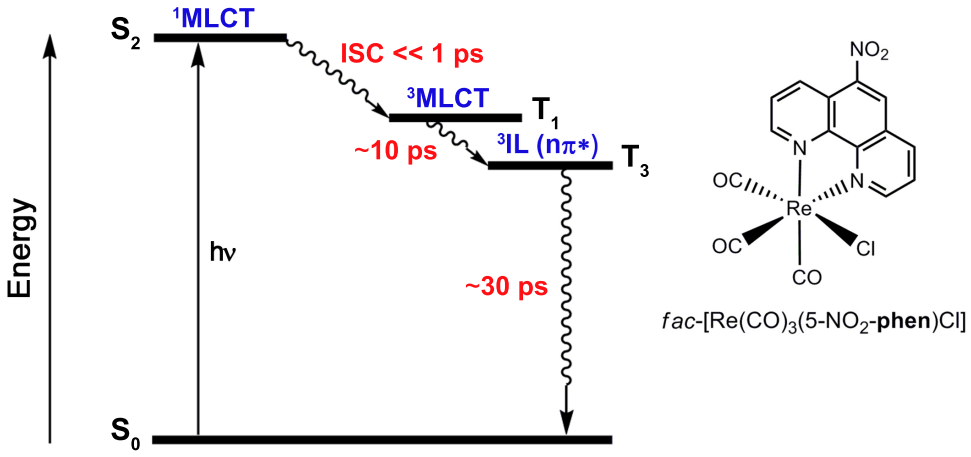

Figure 4.19 Simplified Jablonski diagram (left), illustrating the excited state behaviour of *fac*-[Re(CO)$_3$(5-NO$_2$-**phen**)Cl] (right) in an acetonitrile diluted solution at 298 K.[373]

The emission profiles of [Ir(**ppy**)$_2$(**TzPyNH$_2$**)] and [Ir(**bzq**)$_2$(**TzPyNH$_2$**)] are characterised by structured emission bands with a vibronic progression around 1,200 and 1,060 cm^{-1}, respectively, which indicate that the emissive excited state is derived from a mixing of ligand-centred and charge transfer character. The emission maxima of [Ir(**bzq**)$_2$(**TzPyNH$_2$**)] at 524 and 555 nm is red-shifted in comparison to the ones at 484 and 514 nm for [Ir(**ppy**)$_2$(**TzPyNH$_2$**)], as showed in **Figure 4.21**. The expected red shift is ascribed to the increased conjugation of the cyclometalated **bzq** ligands, which destabilises the HOMO orbitals while stabilising the LUMO, with a resulting smaller HOMO-LUMO energy gap.

In the case of [Ir(**bzq**)$_2$(**TzPyCN**)] (**Figure 4.22**), the substitution of the amino with the electron-withdrawing nitrile group is responsible for the stabilisation of the unoccupied π* orbitals of the tetrazolate ligand, causing a substantial red shift of the emission maximum (λ_{em} = 620 nm). Interestingly, [Ir(**ppy**)$_2$(**TzPyCN**)] (Chapter 2 – section 2.4.2) and [Ir(**bzq**)$_2$(**TzPyCN**)] emits at the same wavelength, suggesting that the HOMO is not homogeneously localised on the cyclometalated ligands. A previous study by Werrett *et al.*[372] had indeed evidenced that **bpy** and **phen** exhibit a similar electronic distribution, which is mainly localised on the pyridyl rings, as depicted in

Figure 4.20. For this reason, the photophysical behaviour of **phen** can be compared to that of a dimethyl-substituted bipyridine Me$_2$**bpy** (**Figure 4.20**).

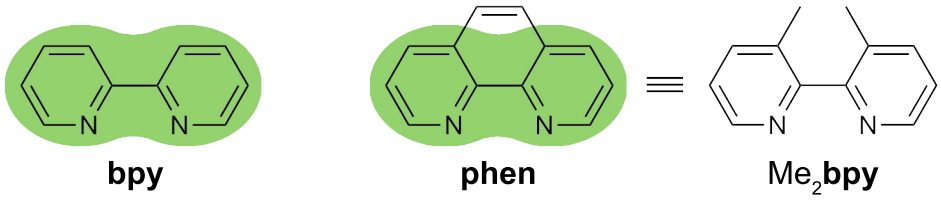

Figure 4.20 Simplified representation of the electronic distribution on **bpy** and **phen** (green). On the right, the structure of Me$_2$**bpy** is reported to highlight the structural similarity with phen.

The methylated complex [Ir(**bzq**)$_2$(Me**TzPyCN**)]$^+$ exhibits a red-shifted emission maximum at 690 nm (**Figure 4.22**), with respect to the neutral [Ir(**bzq**)$_2$(**TzPyCN**)]. As show in Chapter 2, the methylation of the tetrazolate ligand stabilises the π* unoccupied orbitals, demonstrating again the role of these orbitals as electron acceptor in the charge transfer transitions.[236,237] The same trend followed by the neutral complexes can be observed when comparing [Ir(**bzq**)$_2$(Me**TzPyCN**)]$^+$ with [Ir(**ppy**)$_2$(Me**TzPyCN**)]$^+$. In this case, a shift of *ca.* 10 nm in the emission maximum is present upon increasing the conjugation from **ppy** to **bzq**.

At different extent, all the complexes exhibit an elongation of the excited state lifetime decay (τ) and an increase of the photoluminescent quantum yield (Φ) values upon degassing the dichloromethane solution, suggesting phosphorescent decay from excited states of triplet spin multiplicity.[107,201,237]

In particular, [Ir(**ppy**)$_2$(**TzPyNH$_2$**)] and [Ir(**bzq**)$_2$(**TzPyNH$_2$**)] displayed the major increment of excited state lifetime passing from air-equilibrated to degassed solutions, with values of *ca.* 1 and 23 μs. As previously discussed in Chapter 2 – section 2.4.2, the elongation of lifetime can be assigned to a stronger influence of the LC character of the mixed exited state, which results more pronounced for [Ir(**bzq**)$_2$(**TzPyNH$_2$**)].[238] Moreover, the effect of the rigidity of the **bzq** ligands with respect to the **ppy**, may be also responsible for the longer excited state lifetime of [Ir(**bzq**)$_2$(**TzPyNH$_2$**)] in comparison to [Ir(**ppy**)$_2$(**TzPyNH$_2$**)].[372]

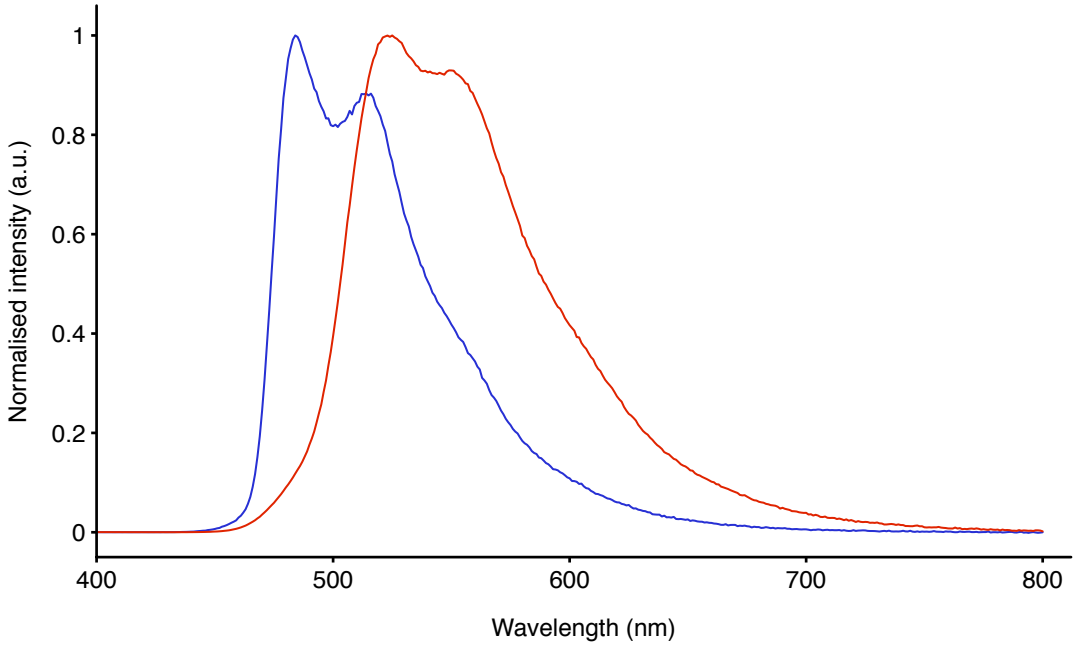

Figure 4.21 Normalised emission profiles of [Ir(**ppy**)$_2$(**TzPyNH$_2$**)] (blue) and [Ir(**bzq**)$_2$(Me**TzPyNH$_2$**)]$^+$ (red) in dichloromethane.

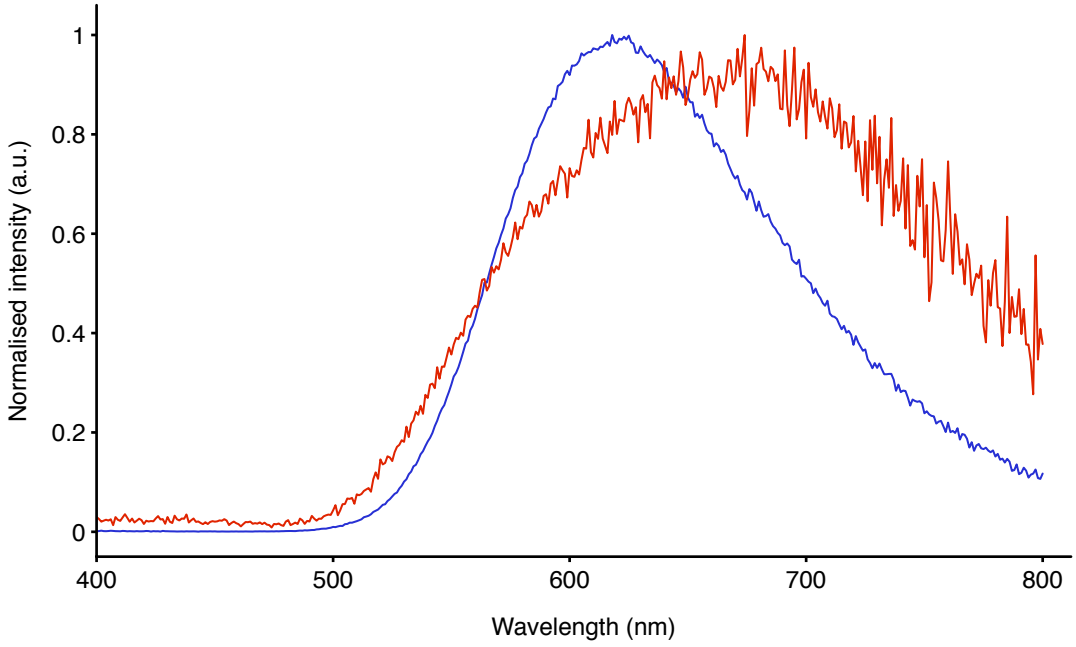

Figure 4.22 Normalised emission profiles of [Ir(**bzq**)$_2$(**TzPyCN**)] (blue) and [Ir(**bzq**)$_2$(Me**TzPyCN**)]$^+$ (red) in dichloromethane.

For a better understanding of the photophysical behaviour of the reported iridium(III) complexes, the radiative (k_r) and non-radiative (k_{nr}) decay constants were calculated for degassed dichloromethane solutions and are summarised in **Table 4.3**. [Ir(**ppy**)$_2$(**TzPyNO$_2$**)] and [Ir(**bzq**)$_2$(Me**TzPyCN**)]$^+$ have been excluded from this evaluation due to the non-emissive nature of the first species and the biexponentiality of the excited state lifetime of the latter.

Table 4.3 Radiative (k_r) and non-radiative (k_{nr}) decay constants in degassed dichloromethane solutions.

Complex	k_r $10^6[s^{-1}]^a$	k_{nr} $10^6[s^{-1}]^b$
[Ir(**ppy**)$_2$(**TzPyNH$_2$**)]	0.027	0.942
[Ir(**bzq**)$_2$(**TzPyNH$_2$**)]	0.025	0.019
[Ir(**ppy**)$_2$(**TzPyNO$_2$**)]	-[c]	-[c]
[Ir(**bzq**)$_2$(**TzPyCN**)]	0.244	1.724
[Ir(**bzq**)$_2$(Me**TzPyCN**)]$^+$	-[c]	-[c]

[a] Calculated as [Φ/τ] using measurements from deaerated dichloromethane solutions. [b] Calculated as [$(1-\Phi)/\tau$] using measurements from deaerated dichloromethane solutions. [c] The lifetime shows a biexponential nature, which did not allowed the calculation of k_r and k_{nr}.

The comparison of the photophysical properties of [Ir(**ppy**)$_2$(**TzPyNH$_2$**)] and [Ir(**bzq**)$_2$(**TzPyNH$_2$**)] highlight comparable radiative decay constants, which are typical of ^{3}LC emission, with $k_r << 2.0 \times 10^5$ s^{-1}.[77] This result is supported by the vibronically structured profile of the luminescent spectra (**Figure 4.21**) recorded for these two complexes, which demonstrates small energy separation of ^{3}MLCT and ^{3}LC levels, with a marked contribution of the ^{3}LC excited state to the emission. On the other hand, a 50 fold increment of the non-radiative constant values was calculated for [Ir(**bzq**)$_2$(**TzPyNH$_2$**)] with respect to [Ir(**ppy**)$_2$(**TzPyNH$_2$**)]. This phenomenon is in agreement with the rigidity of the more conjugated **bzq** with respect to the **ppy** ligand, which would reduce the k_{nr} by minimising the vibrational relaxation (VR).

[Ir(**bzq**)$_2$(**TzPyCN**)] displays k_r and k_{nr} values that are of the same order of magnitude as the radiative ($k_r = 0.751 \times 10^6$ s^{-1}) and non-radiative decay constants ($k_{nr} = 1.140 \times 10^6$ s^{-1}) of [Ir(**ppy**)$_2$(**TzPyCN**)] (Chapter 2 – section 2.4.2). In particular the

k_r values confirm once again the emission from a MLCT excited state.[77] Moreover, in this specific case, the higher conjugation of the cyclometalated ligands does not seem to extremely affect the luminescent properties of the complex.

4.4.3 Temperature-Dependent Luminescence Lifetime Measurements

The difference in the photophysical properties between [Ir(**ppy**)$_2$(**TzPyNH$_2$**)] (section 4.4.2) and [Ir(**ppy**)$_2$(**TzPyCN**)] (Chapter 2 – section 2.4.2) have been rationalised by temperature-dependent luminescence lifetime measurements.

As demonstrated by previous studies, the nature of the lowest-lying excite state in transition metal complexes can be ^{3}LC (ligand-centred), ^{3}MLCT (metal-to-ligand), ^{3}ILCT (intra-ligand), ^{3}MLLCT (metal-ligand-to-ligand) or ^{3}LLCT (ligand-to-ligand) charge transfer in nature.[76,77,375–377] However, in some cases the presence of a dark ^{3}MC excited state in close proximity to the lowest-emissive excited state can lower the emission properties of the complex. In fact, if the energy gap between the emissive and the ^{3}MC excited state is not too high, the latter becomes thermally accessible at room temperature. On the other hand, this thermal activation can be depressed by decreasing the temperature of the system and consequentially populate just the lowest and emissive excited state.[375]

The excited state lifetimes of [Ir(**ppy**)$_2$(**TzPyNH$_2$**)] and [Ir(**ppy**)$_2$(**TzPyCN**)] have been recorded in diluted (*ca.* 10^{-5} M) dichloromethane solutions in a range of temperatures between 198 and 298 K. The data have been plotted as the logarithm of the rate constant (k_{obs}) against the inverse temperature (1/T), as showed in **Figure 4.23**. We can define k_{obs} as in **Equation 4.1**:

$$k_{obs} = k_r + \sum_i k_{nr\,i} \qquad (\mathbf{4.1})$$

where k_r and k_{nr} are the radiative and non-radiative decay constant, respectively. However, the equation can be simplified considering that the radiative transition is essentially governed by spin and symmetry factors,[378] whereas the radiationless rate constant generally increases with decreasing of the excited state energy, as expected on the basis of the energy gap law.[75] The k_{obs} can be then described as k_{nr} by the Arrhenius-type **Equation 4.2**:

$$k_{nr} = A\, e^{\left(\frac{-\Delta E}{RT}\right)} + k_0 \qquad (\mathbf{4.2})$$

where A is the pre-exponent coefficient, k_0 is an independent-temperature factor, ΔE is the difference in energy between the two states, R is the gas constant (8.314 $Jmol^{-1}K^{-1}$) and T is the temperature (K).

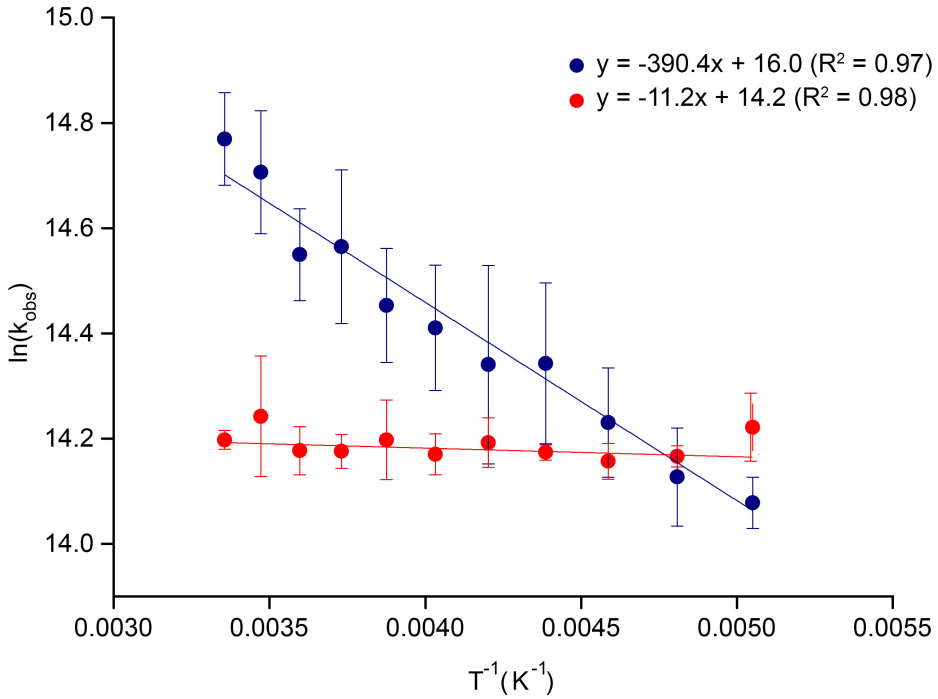

Figure 4.23 Arrhenius plot of the rate constants of [Ir(**ppy**)$_2$(**TzPyNH$_2$**)] (blue) and [Ir(**ppy**)$_2$(**TzPyCN**)] (red). The trendlines and the R^2 values have been reported.

In the case of [Ir(**ppy**)$_2$(**TzPyCN**)], the energy gap ΔE between ^{3}MC and the emissive ^{3}MLCT excited state is high enough that the changing in temperature does not affect the non-radiative constant and the lifetime is maintained constant along the whole range of temperatures.

On the other hand, [Ir(**ppy**)$_2$(**TzPyNH$_2$**)] showed a small ΔE which allowed thermal equilibrium between the ^{3}LC/^{3}MLCT lowest excited states and the ^{3}MC state at room temperature, confirmed by an increase of the non-radiative decay constant. Moreover, lowering the temperature permits to block the thermal population of the ^{3}MC state, which can be verified by the elongation of the excited state lifetimes.

Based on these results, the difference in emissive properties between [Ir(**ppy**)$_2$(**TzPyCN**)] and [Ir(**ppy**)$_2$(**TzPyNH$_2$**)] has been explained by the presence of a thermally accessible and dark ^{3}MC excited state, which lowers the lifetime and the emission intensity of the latter.

4.4.4 Absorption in Aqueous and Lipophilic Solvents

The photophysical behaviour of this series of complexes has been explored in aqueous and lipophilic solvents in order to evaluate their applicability for biological studies. The summary of the absorption data is listed in **Table 4.4**.

Table 4.4 Absorption data of aqueous and lipophilic solutions (10^{-5} M) of the reported iridium(III) complexes.

Complexes	Solvent[a]	λ_{abs} [nm] (10^4 ε [$M^{-1}cm^{-1}$])
[Ir(**ppy**)$_2$ (**TzPyNH$_2$**)]	H_2O	273 (5.30), 388 (0.91), 422 (0.56)
	Lys. Fluid	272 (3.92), 394 (1.03), 435 (0.64)
	PBS	272 (4.56), 349 (1.76), 429 (0.60)
	Ethyl Laurate	276 (1.34), 372 (1.38), 445 (1.04)
[Ir(**bzq**)$_2$ (**TzPyNH$_2$**)]	H_2O	265 (8.08), 339 (4.04), 430 (1.19)
	Lys. Fluid	263 (2.50), 344 (1.80), 432 (0.77)
	PBS	273 (1.92), 361 (1.46), 440 (0.86)
	Ethyl Laurate	262 (2.54), 292 (2.36), 366 (1.88), 455 (0.96)
[Ir(**ppy**)$_2$ (**TzPyNO$_2$**)]	H_2O	270 (1.60), 308 (1.48), 412 (6.43)
	Lys. Fluid	273 (2.11), 306 (2.02), 410 (0.97)
	PBS	271 (2.55), 313 (2.32), 409 (1.17)
	Ethyl Laurate	270 (2.72), 301 (1.98), 388 (0.53), 425 (0.30)
[Ir(**bzq**)$_2$ (**TzPyCN**)]	H_2O	266 (6.96), 294 (4.93), 355 (2.86), 431 (1.21)
	Lys. Fluid	267 (3.63), 298 (2.93), 355 (2.12), 434 (1.06)
	PBS	268 (4.07), 303 (3.34), 365 (2.50), 432 (1.53)
	Ethyl Laurate	258 (5.47), 291 (2.97), 339 (2.09), 433 (0.55)
[Ir(**bzq**)$_2$ (Me**TzPyCN**)]$^+$	H_2O	279 (3.79), 319 (2.25), 403 (0.69)
	Lys. Fluid	279 (3.98), 317 (2.42), 406 (0.77)
	PBS	258 (5.45), 282 (3.23), 324 (1.96), 410 (0.65)
	Ethyl Laurate	262 (2.97), 351 (1.21), 436 (0.65)

[a] Aqueous solvents contain 2% DMSO.

The choice of the solvents was driven by the necessity to establish how the photophysical properties could be modulated in the different cellular-type environments.

A 2% of DMSO was used to dissolve the iridium(III) tetrazolate complexes in the aqueous media to guarantee complete dissolution of the probes.

In general, the absorption profiles in aqueous media and ethyl laurate resemble the ones previously discussed for dichloromethane solutions (section 4.4.1), as showed from **Figure 4.24** to **Figure 4.28**. The complexes exhibit intense spin-allowed ligand-centre (LC) π-π* absorption features in the UV region (250 – 315 nm) and weaker absorption bands at $\lambda \geq 350$ nm, which can be assigned to a mixture of spin-allowed ligand-to-ligand (LLCT) and metal-to-ligand charge transfer (MLCT) transitions. The weak absorption tailing beyond 400 nm has been assigned to spin-forbidden MLCT/LLCT transitions.

Noteworthy, some of the solvents promote a slight aggregation for [Ir(**ppy**)$_2$(**TzPyNH$_2$**)] (**Figure 4.24**) and [Ir(**bzq**)$_2$(**TzPyNH$_2$**)] (**Figure 4.25**), characterised by broad and structureless absorption profiles and lower molar absorptivity coefficients in comparison to the data recorded in dichloromethane solutions.

[Ir(**ppy**)$_2$(**TzPyNO$_2$**)] exhibits relatively low molar absorptivity coefficients for all the solvents, as depicted in **Figure 4.26**. This behaviour was also observed by Gabrielsson *et al.*[373] for the complex *fac*-[Re(CO)$_3$(5-NO$_2$-**phen**)Cl], which was showing molar extinction coefficients of *ca.* 2.0×10^4 and 0.3×10^4 M^{-1} cm^{-1} for the π-π* LC and the MLCT transitions, respectively.

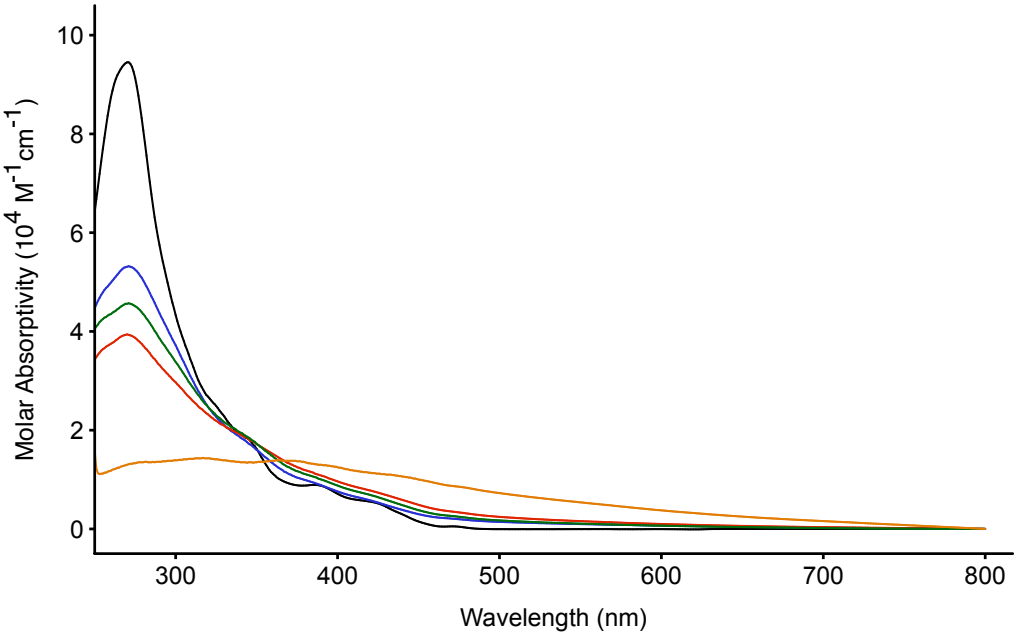

Figure 4.24 Absorption profiles of [Ir(**ppy**)$_2$(**TzPyNH$_2$**)] in dichloromethane (black), H_2O (blue), lys. fluid (red), PBS (green) and ethyl laurate (orange).

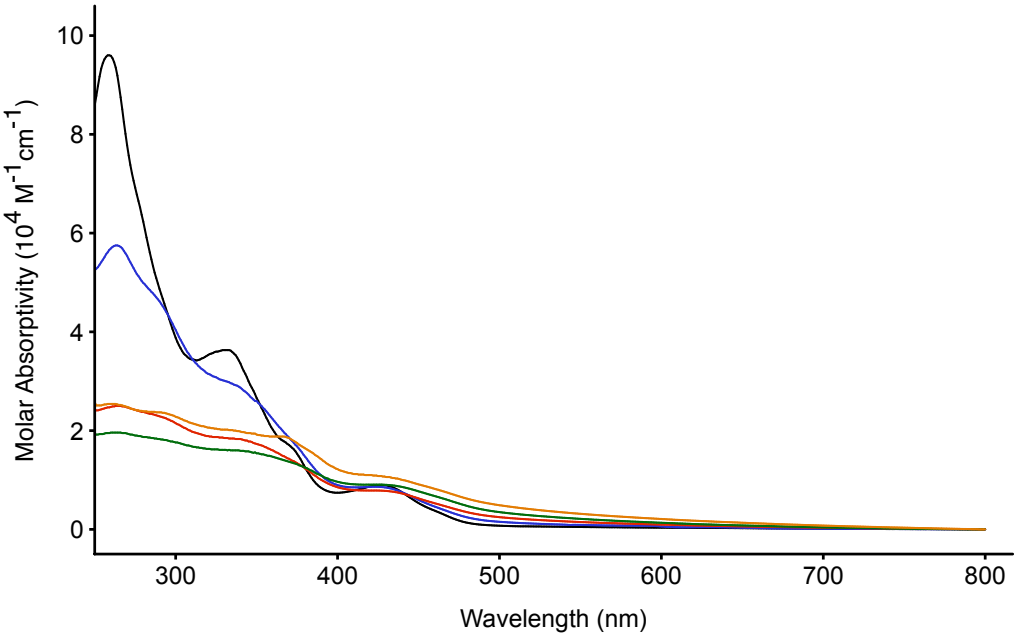

Figure 4.25 Absorption profiles of [Ir(**bzq**)$_2$(**TzPyNH$_2$**)] in dichloromethane (black), H_2O (blue), lys. fluid (red), PBS (green) and ethyl laurate (orange).

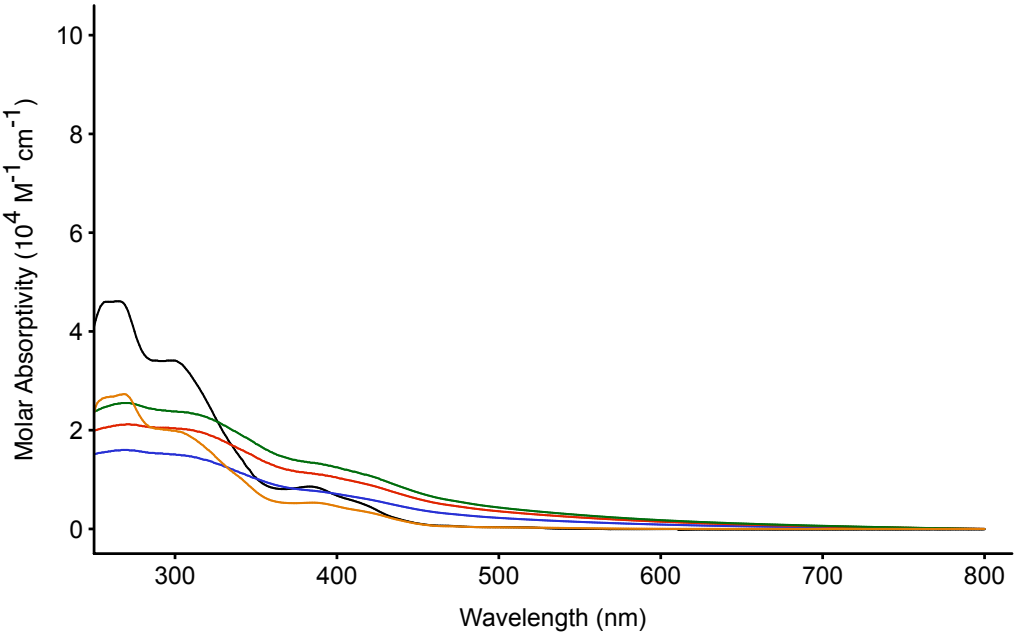

Figure 4.26 Absorption profiles of [Ir(**ppy**)$_2$(**TzPyNO$_2$**)] in dichloromethane (black), H_2O (blue), lys. fluid (red), PBS (green) and ethyl laurate (orange).

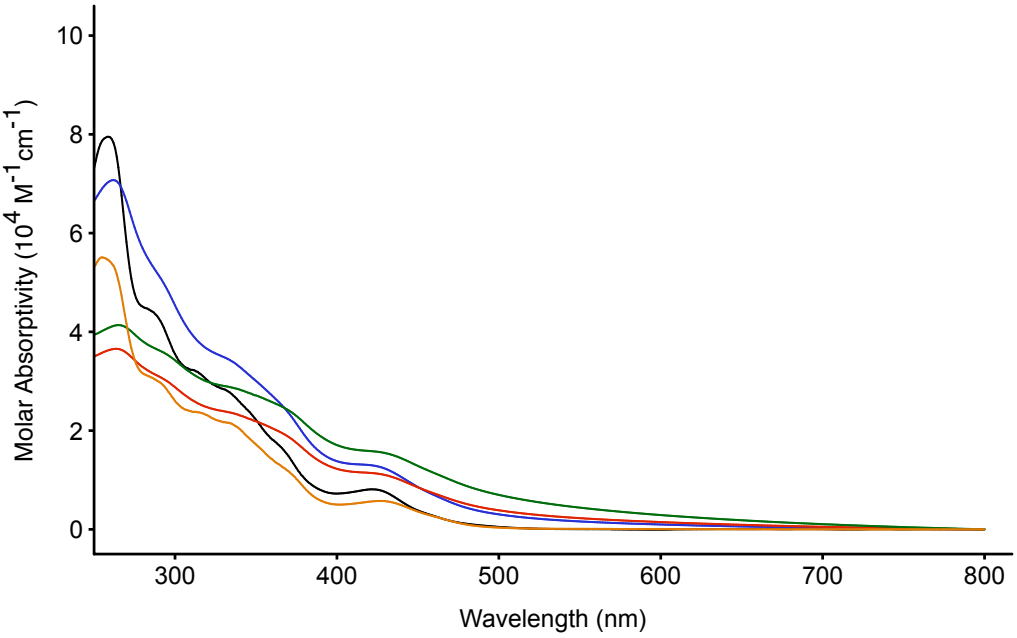

Figure 4.27 Absorption profiles of [Ir(**bzq**)$_2$(**TzPyCN**)] in dichloromethane (black), H_2O (blue), lys. fluid (red), PBS (green) and ethyl laurate (orange).

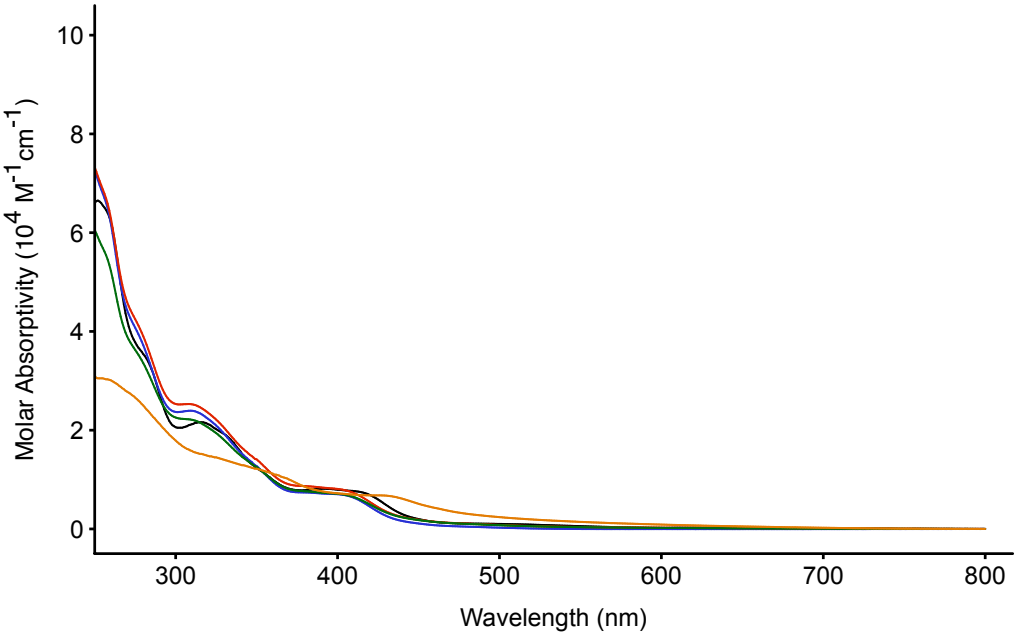

Figure 4.28 Absorption profiles of [Ir(**bzq**)$_2$(Me**TzPyCN**)]$^+$ in dichloromethane (black), H_2O (blue), lys. fluid (red), PBS (green) and ethyl laurate (orange).

4.4.5 Emission Properties in Aqueous Solvents

The photophysical characterisation of the iridium(III) complexes in aqueous and lipophilic solvents has been summarised in **Table 4.5**. The emission properties of [Ir(**ppy**)$_2$(**TzPyNO$_2$**)] and [Ir(**bzq**)$_2$(Me**TzPyCN**)]$^+$ have been excluded due to the non-emissive nature of these species in the solvents used for the photophysical investigation. In particular, the methylated [Ir(**bzq**)$_2$(Me**TzPyCN**)]$^+$ follows the same behaviour as its analogous [Ir(**ppy**)$_2$(Me**TzPyCN**)]$^+$ (Chapter 2 – section 2.4.5), characterised by higher degree of quenching in aqueous media in comparison to dichloromethane solution. In this case, the quenching was so efficient that the emission could not be recorded.

Table 4.5 Photophysical data of aqueous and lipophilic solutions (10^{-5} M) of the reported iridium(III) complexes. [Ir(**ppy**)$_2$(**TzPyNO$_2$**)] and [Ir(**bzq**)$_2$(Me**TzPyCN**)]$^+$ have been excluded due to their non-emissive nature in the investigated solvents.

Complexes	**Solvent**[a]	**λ_{em} [nm]**	**τ_{ear} [ns]**[b]	**Φ_{aer}**[c]
[Ir(**ppy**)$_2$	H_2O	484, 508	30 (3), 466 (97)	0.012
(**TzPyNH$_2$**)]	Lys. Fluid	484, 508	21 (6), 493 (94)	0.018
	PBS	484, 508	22 (6), 474 (94)	0.014
	Ethyl Laurate	484, 520, 555_{sh}	17 (63), 89 (37)	0.010
[Ir(**bzq**)$_2$	H_2O	605	41 (31), 215 (69)	0.001
(**TzPyNH$_2$**)]	Lys. Fluid	606	15 (17), 215 (83)	0.002
	PBS	605	41 (21), 221 (79)	0.001
	Ethyl Laurate	624	22 (14), 294 (86)	0.001
[Ir(**bzq**)$_2$	H_2O	630	102	0.002
(**TzPyCN**)]	Lys. Fluid	630	62	0.001
	PBS	630	71	0.001
	Ethyl Laurate	576	156	0.010

[a] Aqueous solvents contain 2% DMSO. [b] For the biexponential excited state lifetime (τ), the relative weights of the exponential curved are reported in parentheses. [c] Measured versus [Ru(**bpy**)$_3$]$^{2+}$ in H_2O (Φ = 0.028).[274]

The emission profiles of the two amino-functionalised complexes [Ir(**ppy**)$_2$(**TzPyNH$_2$**)] and [Ir(**bzq**)$_2$(**TzPyNH$_2$**)] in different solvent systems do not follow the same trend, implying that the change of the cyclometalated ligands from **ppy** to **bzq** severely affects the photophysical behaviour of these species.

Firstly, the vibronically structured emission profile of [Ir(**ppy**)$_2$(**TzPyNH$_2$**)], shown in dichloromethane (section 4.4.2), is also maintained in the aqueous media, with an additional shoulder present in ethyl laurate at 555 nm (**Figure 4.29**). An increase of the relative intensity of the shoulder appears with increasing concentration of the complex from *ca.* 10^{-7} to 10^{-4} M (Appendix C, **Figure C.1** – **Figure C.2**). Moreover, the excited state lifetime was measured at 484 and 555 nm, with significantly longer decay for the latter (refer to Appendix C – **Table C.1** and **Figure C.3**). Therefore, the appearance of a shoulder at lower energy can be assigned to the formation of aggregates in the lipophilic solvent.[379] On the other hand, [Ir(**bzq**)$_2$(**TzPyNH$_2$**)] displays broad and structureless emissions in both organic and aqueous solvents (**Figure 4.30**), indicating that the emissive excited state lost the LC contribution and consequently the emission originates predominantly from the CT excited state.[136,236,238] In ethyl laurate, two different bands at 606 and 646 nm were visible only at high concentration (10^{-4} M), indicating again some level of aggregation of the complex[379] (Appendix C – **Figure C.6**).

Secondly, the emission profiles of [Ir(**ppy**)$_2$(**TzPyNH$_2$**)] do not reveal any solvatochromic behaviour, whereas [Ir(**bzq**)$_2$(**TzPyNH$_2$**)] shows a red shift of the emission maximum upon increasing the polarity of the solvent from dichloromethane to aqueous media. Interestingly, the emission in ethyl laurate is further red-shifted of *ca.* 20 nm, which is unusual considering the low polarity of the lipophilic solvent. For this reason, the excited state lifetime was recorded at 606 and 646 nm in the more concentrated solution (10^{-4} M), showing higher value for the latter. (Appendix C – **Table C.2**). These data, along with the variations in the excitation profiles in the range of concentrations between 10^{-4} and 10^{-7} M (Appendix C, **Figure C.4** – **Figure C.5**), can be explained as a slight aggregation of [Ir(**bzq**)$_2$(**TzPyNH$_2$**)] in the lipophilic solvent.[379]

The analysis of the excited state lifetimes and luminescent quantum yields for [Ir(**ppy**)$_2$(**TzPyNH$_2$**)] and [Ir(**bzq**)$_2$(**TzPyNH$_2$**)] highlights again the difference in the photophysical properties rising from the increase in the conjugation of the cyclometalated ligands. [Ir(**ppy**)$_2$(**TzPyNH$_2$**)] displays higher lifetime and quantum

yield values in aqueous media with respect to ethyl laurate solution, whereas [Ir(**bzq**)$_2$(**TzPyNH$_2$**)] exhibits comparable values in all the solvents (**Table 4.5**).

The emission spectra of [Ir(**bzq**)$_2$(**TzPyCN**)] in aqueous media and ethyl laurate are depicted in **Figure 4.31**. The broad and featureless profile is maintained in all the solvents, also revealing solvatochromic behaviour as seen for the analogous [Ir(**ppy**)$_2$(**TzPyCN**)] (Chapter 2 – section 2.4.5). Excited state lifetime and quantum yields values are similar in aqueous environment, with average values of *ca.* 80 ns and 0.001, respectively. A slight elongation of the lifetime (156 ns) and increase in quantum yield (0.010) is recorded in ethyl laurate.

The photophysical properties of [Ir(**ppy**)$_2$(**TzPyNH$_2$**)] and [Ir(**bzq**)$_2$(**TzPyCN**)] in aqueous and lipophilic environment make them potential candidates for the application in cellular pH-sensing. On the other hand, [Ir(**bzq**)$_2$(**TzPyNH$_2$**)] has showed lower emission intensity along with some solubility issues, which can interfere during the acid/base investigation. Even if [Ir(**bzq**)$_2$(**TzPyNH$_2$**)] did not exhibit the requirements for the application as cellular pH-sensor, its behaviour will be evaluated as proof of concept. For this reason, the preliminary investigation of the protonation and deprotonation reactions of these complexes will be performed in dichloromethane solution. The use of the organic solvent was also driven by the necessity to compare the emission maxima of the protonated species with the one of [Ir(**ppy**)$_2$(Me**TzPyCN**)]$^+$ and [Ir(**bzq**)$_2$(Me**TzPyCN**)]$^+$, which are virtually not emissive in aqueous media.

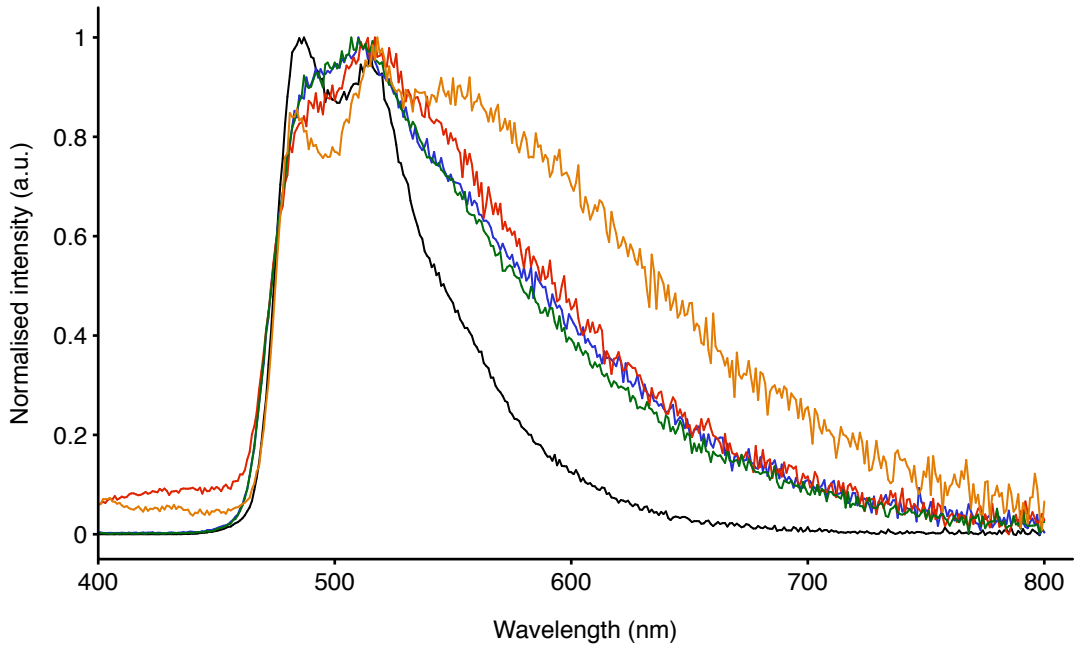

Figure 4.29 Normalised emission profiles of [Ir(**ppy**)$_2$(**TzPyNH$_2$**)] in dichloromethane (black), H_2O (blue), lys. fluid (red), PBS (green) and ethyl laurate (orange).

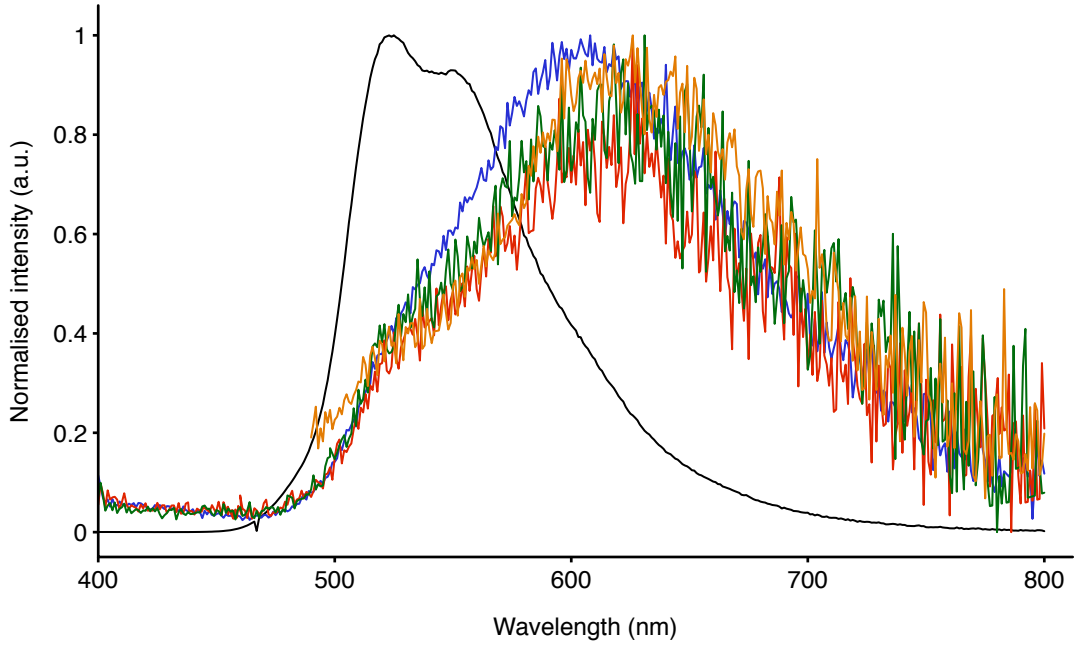

Figure 4.30 Normalised emission profiles of [Ir(**bzq**)$_2$(**TzPyNH$_2$**)] in dichloromethane (black), H_2O (blue), lys. fluid (red), PBS (green) and ethyl laurate (orange).

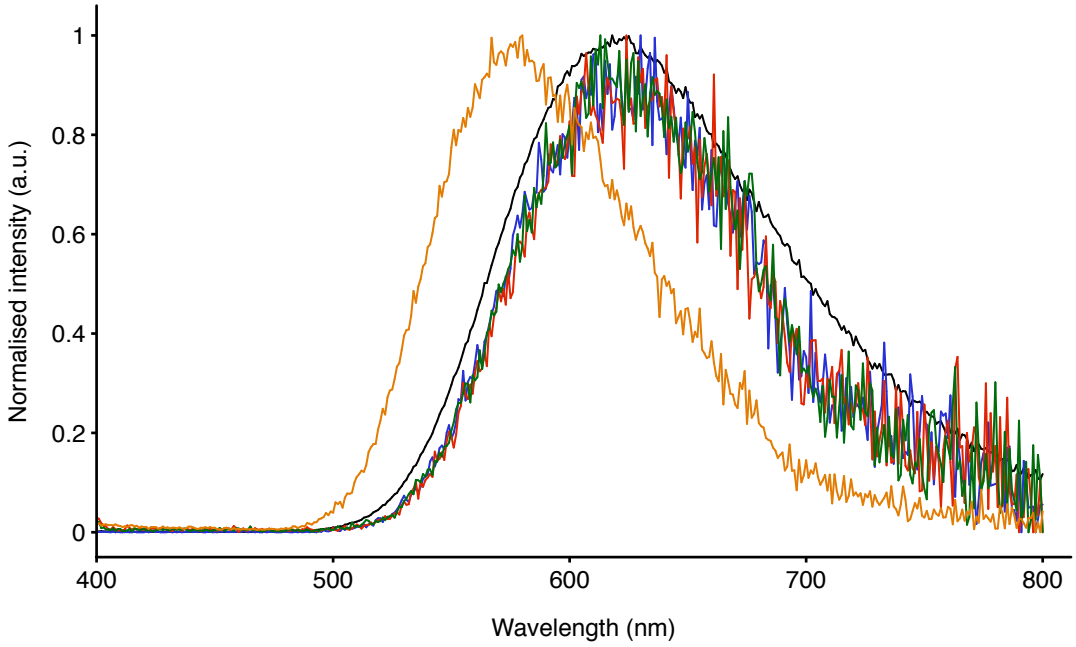

Figure 4.31 Normalised emission profiles of [Ir(**bzq**)$_2$(**TzPyCN**)] in dichloromethane (black), H_2O (blue), lys. fluid (red), PBS (green) and ethyl laurate (orange).

4.5 Protonation and Deprotonation Studies in Dichloromethane Solution

The photophysical properties of octahedral d^6 metal complexes are strongly influenced by the chosen set of coordinated ligands, which are responsible of the wide emission-colour tunability of these species.[65,81,255,380,381] In particular, previously reported tetrazolato-based iridium(III) complexes[231,236,239] and the iridium(III) species discussed in this thesis[238] have demonstrated the participation of the ligand containing the tetrazole in the composition of the emitting MLCT states. Moreover the reactivity of the tetrazolate ring against electrophiles has proved to be an easy method to modulate the photophysical properties by methylation of the neutral complexes in order to obtain cationic analogues.[236,239,265]

Following a previously published study,[231] the protonation and deprotonation reactions of [Ir(**ppy**)$_2$(**TzPyNH$_2$**)] and [Ir(**bzq**)$_2$(**TzPyNH$_2$**)] have been investigated. Noteworthy, the H**TzPyNH$_2$** is bearing an amino group along with a tetrazolate ring, which enables the complexes to have two different nucleophilic sites. In order to determine the protonation mechanism, and considering that the methylated [Ir(**ppy**)$_2$(Me**TzPyNH$_2$**)]$^+$ and [Ir(**bzq**)$_2$(Me**TzPyNH$_2$**)]$^+$ could not be isolated, the same investigation has been performed on [Ir(**ppy**)$_2$(**TzPyCN**)] and [Ir(**bzq**)$_2$(**TzPyCN**)] for comparison purposes.

Absorption and emission spectra have been recorded after each acid or base addition, and for [Ir(**ppy**)$_2$(**TzPyNH$_2$**)] a ^{1}H NMR spectra has been carried out as well. Once again, the photophysical behaviour of [Ir(**ppy**)$_2$(**TzPyNH$_2$**)] and [Ir(**bzq**)$_2$(**TzPyNH$_2$**)] was completely different. It can be anticipated that [Ir(**bzq**)$_2$(**TzPyNH$_2$**)] did not show obvious changes in the absorption (**Figure 4.32**) and emission profiles (**Figure 4.33**), suggesting that the protonation reaction did not take place. Due to the extent cyclometalated ligands, the solubility of the complex in dichloromethane solution results lower than for [Ir(**ppy**)$_2$(**TzPyNH$_2$**)]. The formation of aggregates or partial precipitation of the complex could have protected the amino group and the tetrazolate ring from the electrophilic addition.

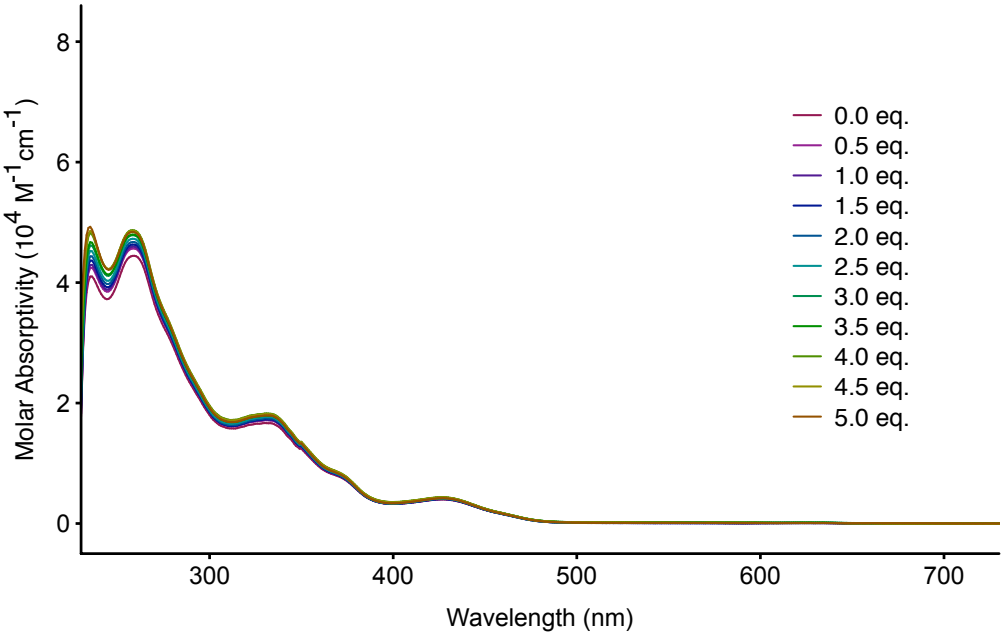

Figure 4.32 Absorption spectra of [Ir(**bzq**)$_2$(**TzPyNH$_2$**)], showing the lack of changes occurring upon the sequential addition of triflic acid to the complex solution.

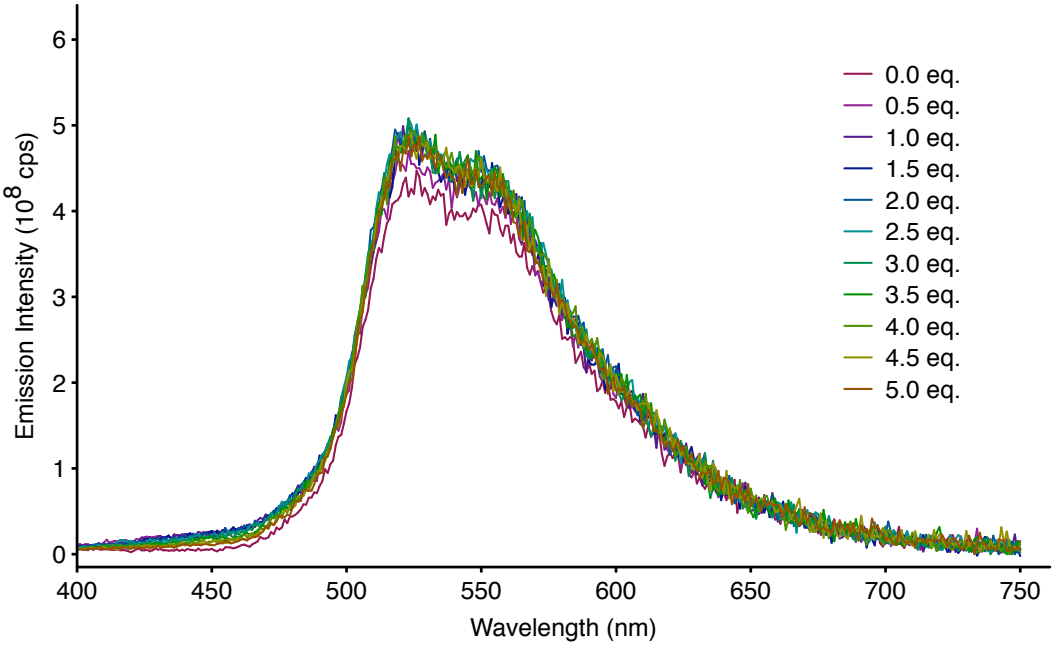

Figure 4.33 Emission spectra of [Ir(**bzq**)$_2$(**TzPyNH$_2$**)], showing the lack of changes occurring upon the sequential addition of triflic acid to the complex solution.

Upon treatment with triflic acid, the absorption profile of [Ir(**ppy**)$_2$(**TzPyNH$_2$**)] showed a decrease of the LC π-π* transitions and the formation of a band around 300 nm (**Figure 4.34**). In the emission profile showed in **Figure 4.35**, a low energy shoulder appeared at *ca.* 555 nm after 2.0 equivalents of acid were added. This shoulder resembled the one discussed in section 4.4.5, in which [Ir(**ppy**)$_2$(**TzPyNH$_2$**)] exhibited the presence of a band at the same emission maximum, which was assigned to some level of aggregation of the complex in ethyl laurate solution.[379] In order to evaluate this hypothesis, the excited state lifetime was measured for the initial solution at 484 nm and after the addition of 5 equivalents of triflic acid at both 484 and 555 nm (**Table 4.6**). As showed in **Table 4.6**, the lifetime decays were comparable, proving that no aggregation was present as a marked elongation of the excited state lifetime at 555 nm would have been observed.[379]

Table 4.6 Excited state lifetimes of [Ir(**ppy**)$_2$(**TzPyNH$_2$**)] in air-equilibrated dichloromethane solution, upon addition of triflic acid aliquots.

Triflic acid aliquots	**λ_{em} [nm]**	**τ_{aer} [ns]**
0.0 eq.	484	82
5.0 eq.	484	85
	555	85

As mentioned before, [Ir(**ppy**)$_2$(**TzPyNH$_2$**)] possesses two different sites for the protonation to occur. Based on the similar basicity of the aromatic amino group with respect to the tetrazolate ring (pka[**PhNH$_3^+$**] = 4.65 ± 0.50, whereas pka[H**Tz**] = 4.70 ± 0.03),[220] it is difficult to predict which of the two protonatable sites will react first.

The ^{1}H NMR of [Ir(**ppy**)$_2$(**TzPyNH$_2$**)] (**Figure 4.36**) suggested that the NH_2 was the first group to be protonated and converted into NH_3^+ due to the lack of the broad singlet peak at 6.01 ppm after the addition of 0.5 equivalents of acid. The presence of the electron-withdrawing NH_3^+ did not shift the emission maxima of the complex, which remained at 484 and 514 nm, but affected the relative intensity of these bands. As showed in **Figure 4.35**, the emission intensity of the band at 484 nm decreased upon

increasing the amount of acid added to the complex solution. After the treatment with 2.0 equivalents of triflic acid, a shoulder at 555 nm started to be visible and the total emission intensity of [Ir(**ppy**)$_2$(**TzPyNH$_2$**)] decreased, which can be ascribed to the protonation of the tetrazolate ring. Unfortunately, a comparison with the methylated [Ir(**ppy**)$_2$(Me**TzPyNH$_2$**)]$^+$ was not possible to perform, but as discussed in Chapter 2 – section 2.4.2 and in section 4.4.2 of this chapter, a decrease of the photophysical properties for cationic species in comparison to their neutral analogues is expected. On the other hand, the ^{1}H NMR spectrum (**Figure 4.36**) did not displayed any major shifts of the peaks to support the protonation of the tetrazolate ring. Based on these data, a final conclusion cannot be drawn but the photophysical study of [Ir(**ppy**)$_2$(**TzPyCN**)] and [Ir(**bzq**)$_2$(**TzPyCN**)] in acid/base conditions can potentially clarify this trend.

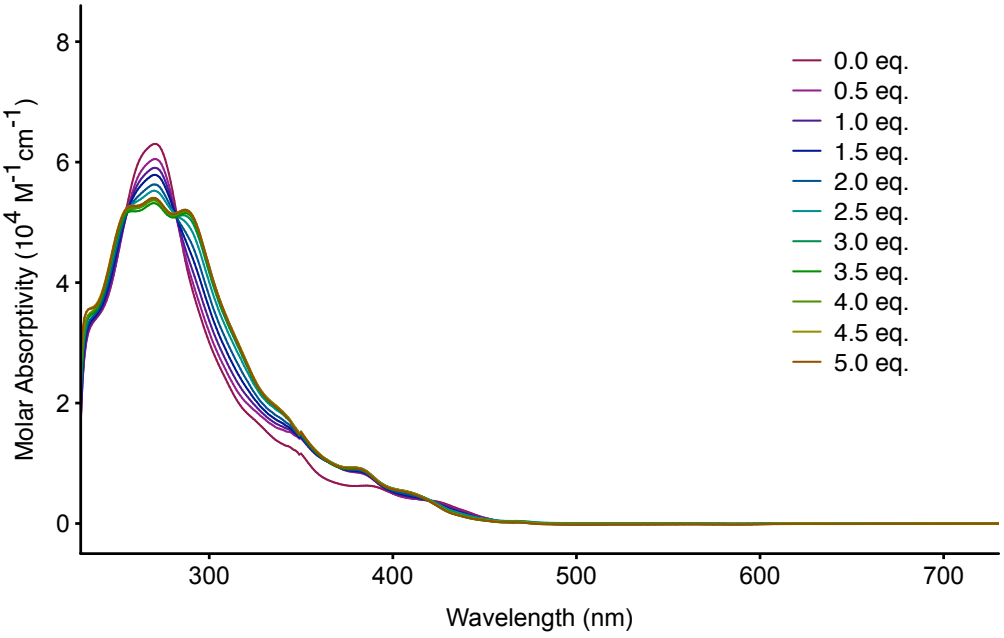

Figure 4.34 Absorption spectra of [Ir(**ppy**)$_2$(**TzPyNH$_2$**)], showing the changes occurring upon the sequential addition of triflic acid to the complex solution.

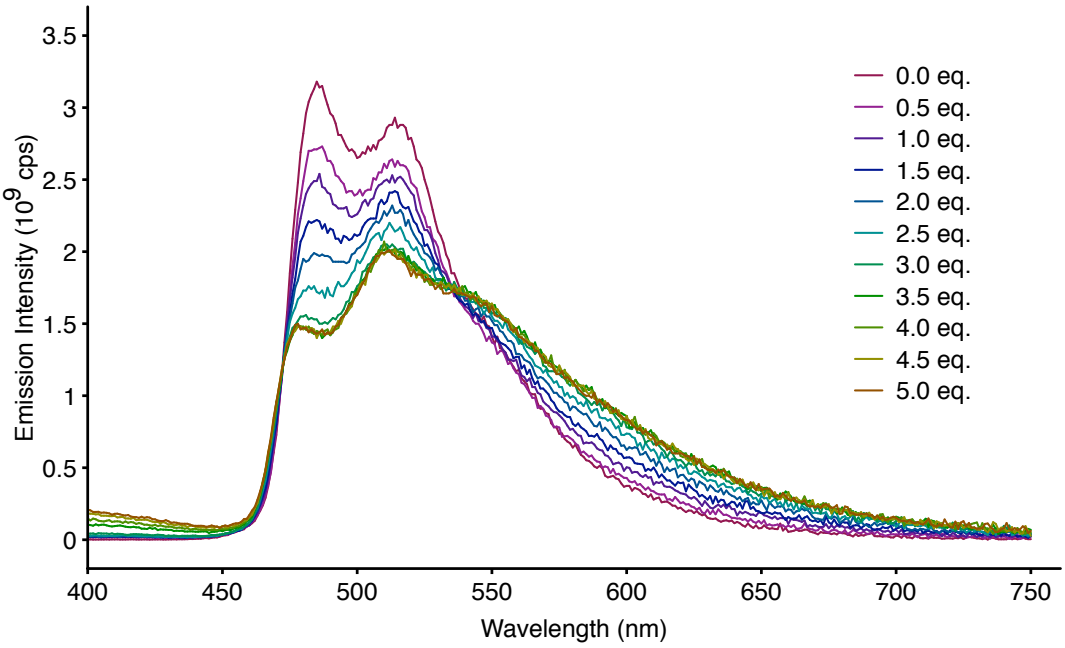

Figure 4.35 Emission spectra of [Ir(**ppy**)$_2$(**TzPyNH$_2$**)], showing the changes occurring upon the sequential addition of triflic acid to the complex solution.

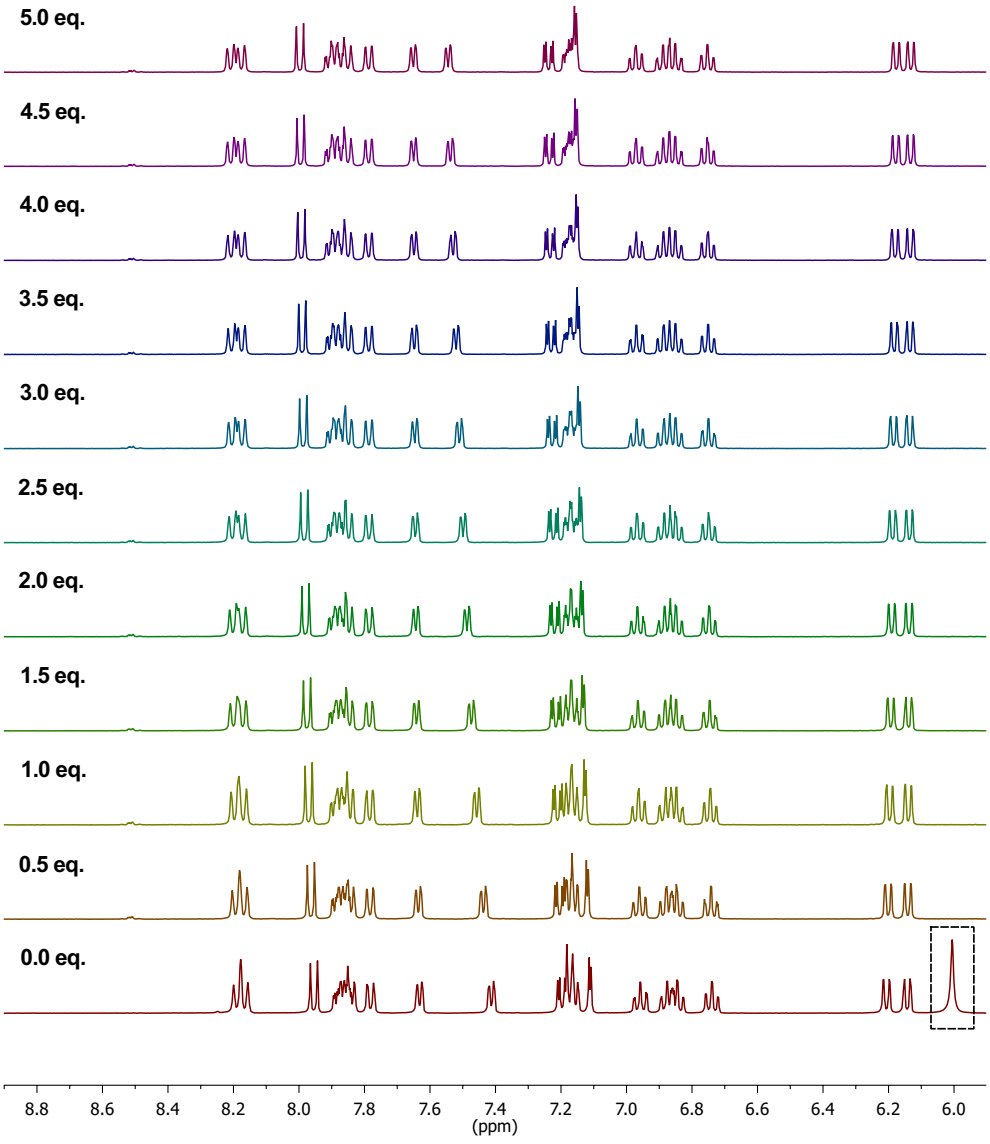

Figure 4.36 ^{1}H NMR spectra in DMSO-*d*$_6$ of [Ir(**ppy**)$_2$(**TzPyNH$_2$**)]. In the black box the amine peak (**2H$_{Tamine}$**) is highlighted. This peak disappears by treatment with triflic acid.

The complexes [Ir(**ppy**)$_2$(**TzPyCN**)] and [Ir(**bzq**)$_2$(**TzPyCN**)] were chosen for the preliminary studies of the effect of acid and base on the photophysical properties, in order to understand the behaviour of [Ir(**ppy**)$_2$(**TzPyNH$_2$**)]. For both the complexes, the methylated analogues [Ir(**ppy**)$_2$(Me**TzPyCN**)]$^+$ and [Ir(**bzq**)$_2$(Me**TzPyCN**)]$^+$ were isolated and their photophysical performance investigated (Chapter 2 – section 2.4.2 and section 4.4.2 of this chapter, respectively).

The absorption spectra of [Ir(**ppy**)$_2$(**TzPyCN**)] and [Ir(**bzq**)$_2$(**TzPyCN**)] have been depicted in **Figure 4.37** and **Figure 4.39**, respectively. Upon sequential addition of triflic acid, the absorption profiles of both the complexes exhibit an increment in the extinction coefficients for the ligand-centred (LC) π-π* transitions. A similar increment along with a slight blue shift is also observed for the LLCT/MLCT transitions at *ca.* 400 nm, in addition to a more structured profile for [Ir(**bzq**)$_2$(**TzPyCN**)] in the wavelengths region between 300 and 400 nm.

Photoexcitation at 350 nm of [Ir(**ppy**)$_2$(**TzPyCN**)] (**Figure 4.38**) and [Ir(**bzq**)$_2$(**TzPyCN**)] (**Figure 4.40**) produced a broad and featureless orange-red emission centred at 620 nm for both the complexes. In this case, the protonation of the tetrazolate ring has showed a complete different behaviour in comparison to the one of [Ir(**ppy**)$_2$(**TzPyNH$_2$**)]. After the addition of 2.0 equivalents of triflic acid, the emission intensity decreased of *ca*. 16-fold and the emission maximum was red-shifted of *ca.* 70 nm, in accordance with the photophysical properties of [Ir(**ppy**)$_2$(Me**TzPyCN**)]$^+$ and [Ir(**bzq**)$_2$(Me**TzPyCN**)]$^+$ (Chapter 2 – section 2.4.2 and section 4.4.2 of this chapter, respectively). This behaviour can be rationalised by considering that the protonation of the tetrazolate ring reduced the electron density on the iridium metal centre, stabilising the *5d* orbitals and consequentially decreasing the HOMO – LUMO gap.[238] To further confirmed the conversion of the neutral species in their cationic analogues, the excited state lifetimes were measured at 620 nm for the initial solution, and 680 – 690 nm after the addition of 5 equivalents of acid. The results have been summarised in **Table 4.7** and, as expected, the lifetime decays decreased for the final solution of the complexes in comparison to the initial ones.

Table 4.7 Excited state lifetimes of [Ir(**ppy**)$_2$(**TzPyCN**)] and [Ir(**bzq**)$_2$(**TzPyCN**)] in air-equilibrated dichloromethane solution, upon addition of triflic acid aliquots.

Complex	Triflic acid aliquots	λ_{em} [nm]	τ_{aer} [ns]
[Ir(**ppy**)$_2$(**TzPyCN**)]	0.0 eq.	620	126
	5.0 eq.	680	45
[Ir(**bzq**)$_2$(**TzPyCN**)]	0.0 eq.	620	128
	5.0 eq.	690	42

The reversibility of the protonation reaction on [Ir(**ppy**)$_2$(**TzPyNH$_2$**)], [Ir(**ppy**)$_2$(**TzPyCN**)] and [Ir(**bzq**)$_2$(**TzPyCN**)] has been investigated by treatment with triethylamine, as depicted in **Figure 4.41**. All the complexes have been reconverted to their corresponding initial neutral species, as previously described by Werrett *et al.*[231] The excited state lifetime was also measured after the addition of 5 equivalents of base and compared to the initial value for all the complexes, in order to evaluate possible variation in the photophysical properties. The lifetime decays are summarised in **Table 4.8** and no major discrepancies are present, confirming that the conversion into the neutral complexes was achieved without any loss in the photophysical performance.

Table 4.8 Excited state lifetimes of [Ir(**ppy**)$_2$(**TzPyNH$_2$**)], [Ir(**ppy**)$_2$(**TzPyCN**)] and [Ir(**bzq**)$_2$(**TzPyCN**)] in air-equilibrated dichloromethane solution at the start of the titration and after the addition of 5 equivalents of triethylamine.

Complex	Solution analysed	λ_{em} [nm]	τ_{aer} [ns]
[Ir(**ppy**)$_2$(**TzPyNH$_2$**)]	Initial	484	82
	Final	484	89
[Ir(**ppy**)$_2$(**TzPyCN**)]	Initial	620	126
	Final	620	118
[Ir(**bzq**)$_2$(**TzPyCN**)]	Initial	620	128
	Final	620	125

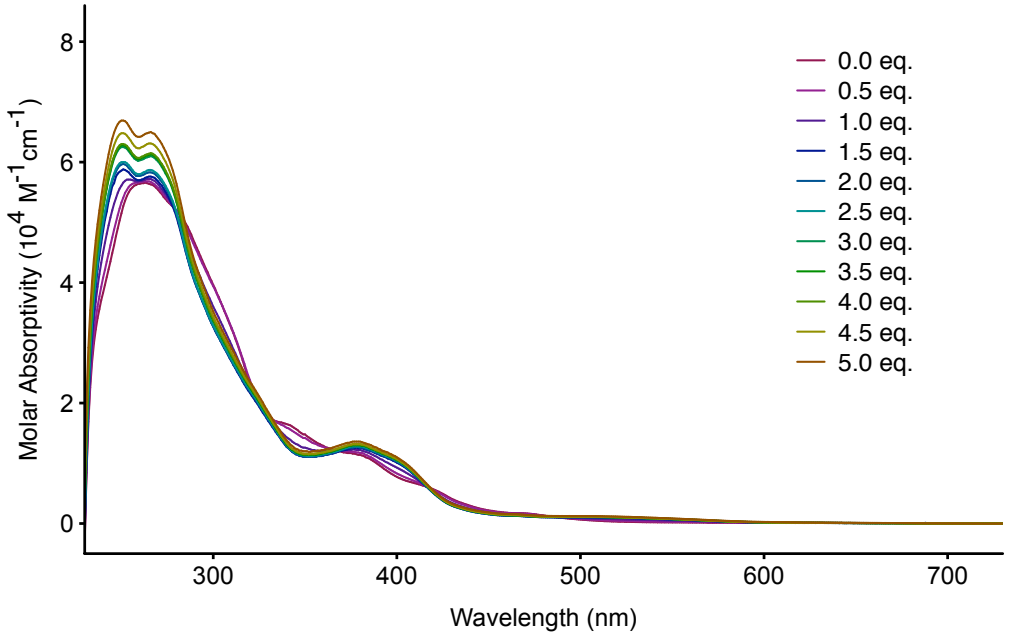

Figure 4.37 Absorption spectra of [Ir(**ppy**)$_2$(**TzPyCN**)], showing the changes occurring upon the sequential addition of triflic acid to the complex solution.

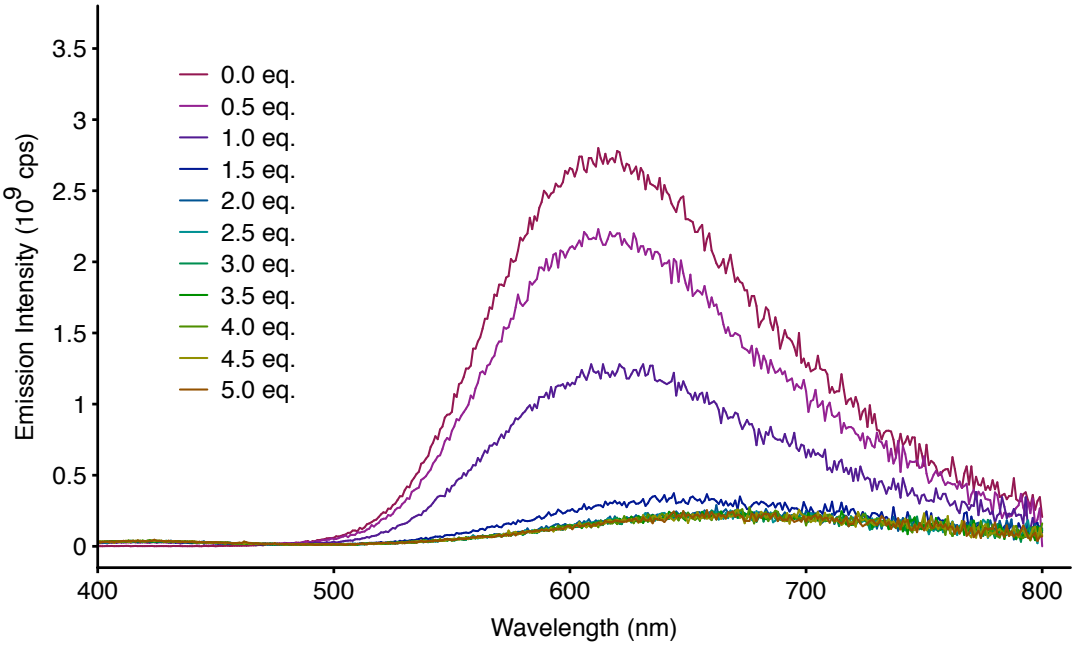

Figure 4.38 Emission spectra of [Ir(**ppy**)$_2$(**TzPyCN**)], showing the changes occurring upon the sequential addition of triflic acid to the complex solution.

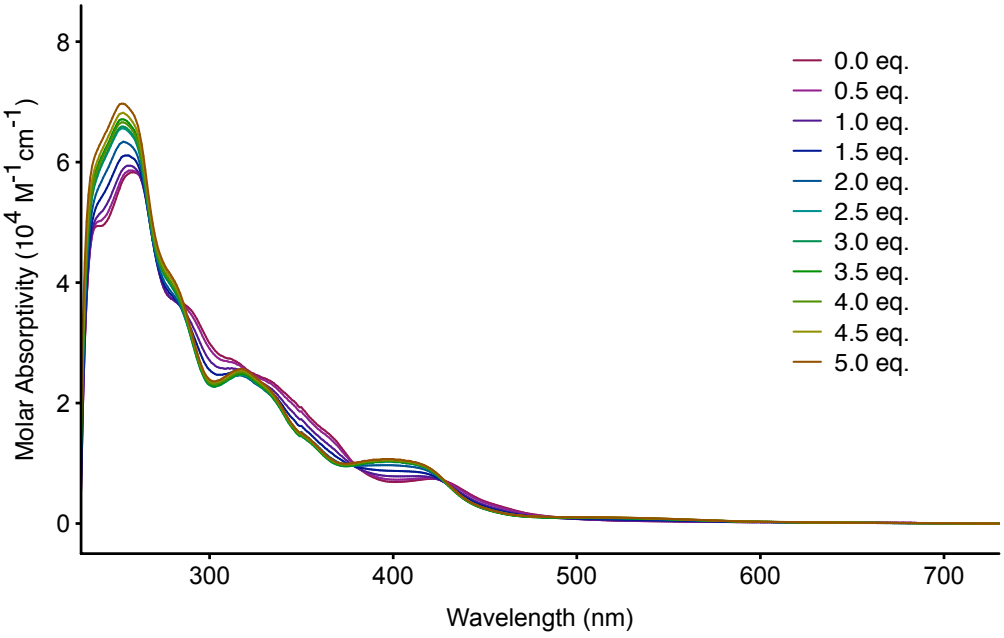

Figure 4.39 Absorption spectra of [Ir(**bzq**)$_2$(**TzPyCN**)], showing the changes occurring upon the sequential addition of triflic acid to the complex solution.

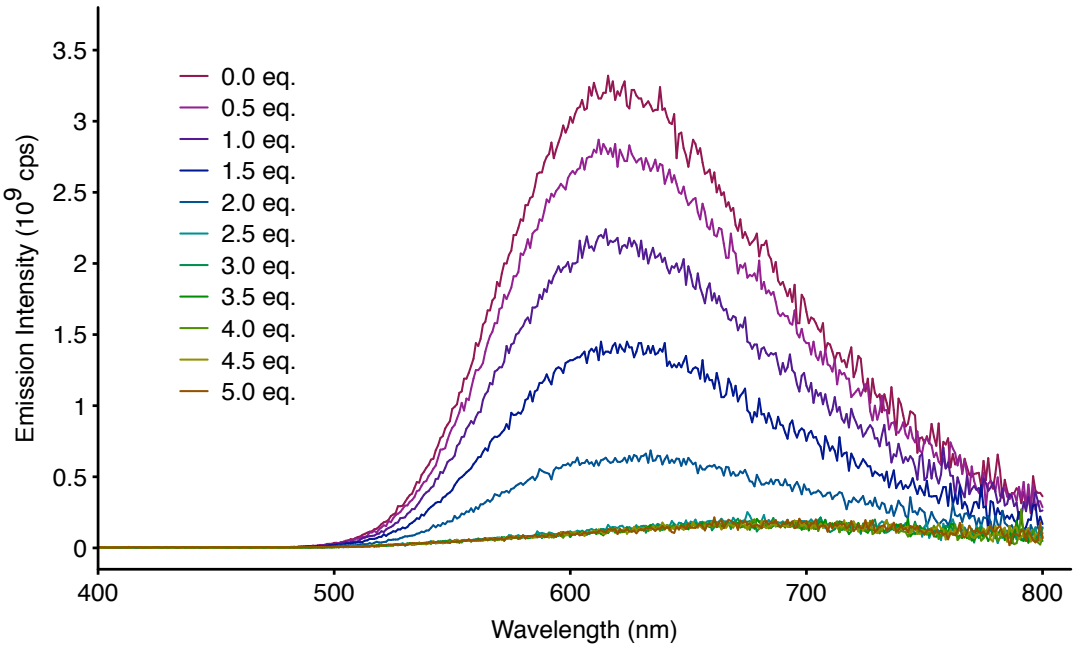

Figure 4.40 Emission spectra of [Ir(**bzq**)$_2$(**TzPyCN**)], showing the changes occurring upon the sequential addition of triflic acid to the complex solution.

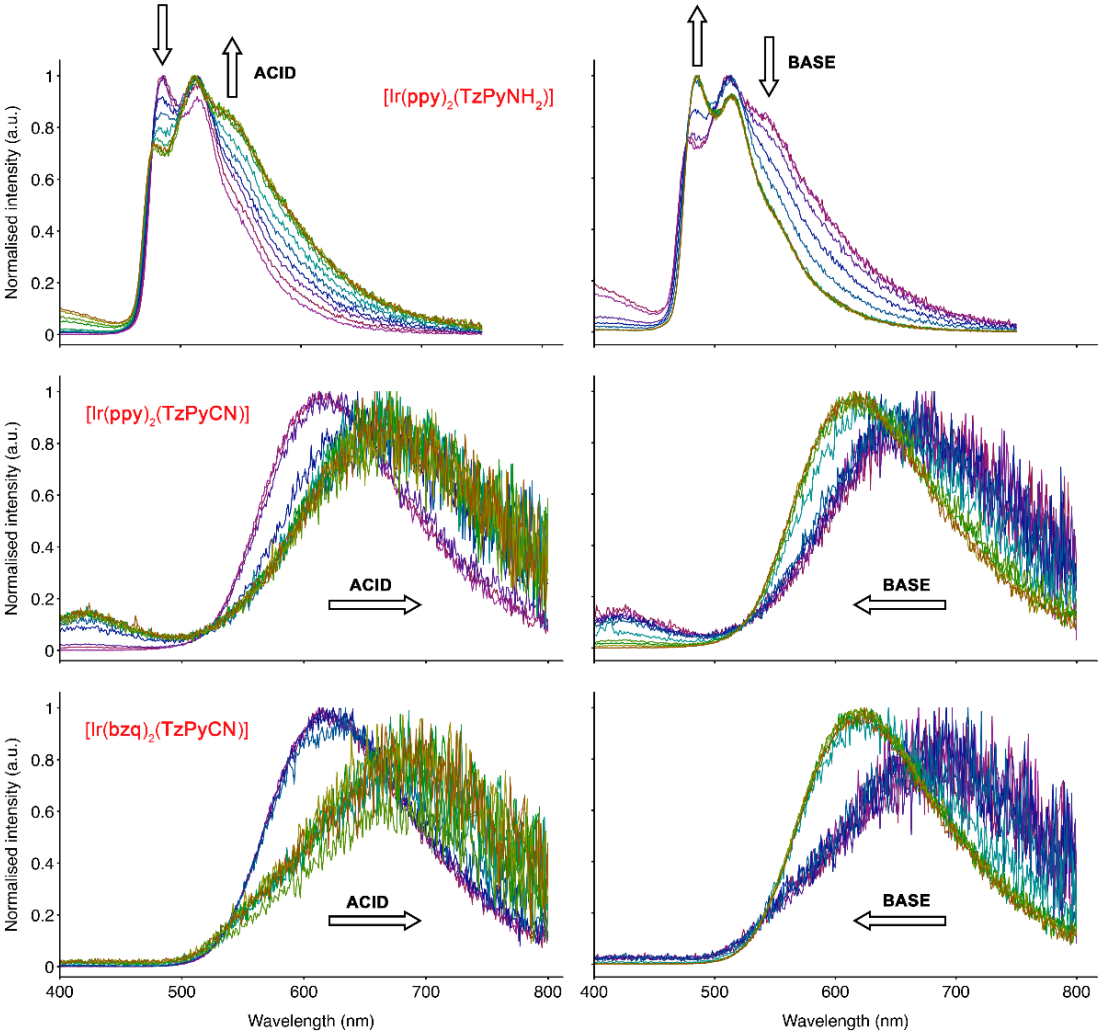

Figure 4.41 Normalised emission spectra of [Ir(**ppy**)$_2$(**TzPyNH$_2$**)] (top), [Ir(**ppy**)$_2$(**TzPyCN**)] (middle) and [Ir(**bzq**)$_2$(**TzPyCN**)] (bottom) highlighting the changes in the emission profiles upon addition of triflic acid (left), followed by addition of triethylamine (right).

4.6 Protonation Studies in Aqueous Medium

Eukaryotic cells contain a large number of organelles with different degrees of acidity.[382] The range of intracellular pH falls in between the slightly alkaline cytoplasm, which exhibits a pH of *ca.* 7.4, and the acidic lysosomes and endosomes, where the pH is around 4.5 – 5.5.[383] For an effective and precise detection of the intracellular H^+, a probe should show changes in the fluorescence intensity, maximum emission wavelength or excited state lifetime in this range of intracellular pH.[46,342,382,384,385]

In the previous paragraph (section 4.5 of this chapter), the protonation and deprotonation properties of [Ir(**ppy**)$_2$(**TzPyNH$_2$**)], [Ir(**bzq**)$_2$(**TzPyNH$_2$**)], [Ir(**ppy**)$_2$(**TzPyCN**)] and [Ir(**bzq**)$_2$(**TzPyCN**)] were investigated in organic solvent. Upon addition of triflic acid, [Ir(**ppy**)$_2$(**TzPyCN**)] and [Ir(**bzq**)$_2$(**TzPyCN**)] exhibit a red shift of the emission maximum of *ca*. 70 nm and a decrease of the emission intensity of *ca.* 16-fold. On the other hand, [Ir(**bzq**)$_2$(**TzPyNH$_2$**)] did not show any changes in the emission profile, probably due to the lower solubility of this complex. Finally, upon protonation, [Ir(**ppy**)$_2$(**TzPyNH$_2$**)] displays a variation in the emission profile, with the appearance of a shoulder at 555 nm and a more reduced decrease of the emission intensity (*ca.* 2-fold) in comparison to [Ir(**ppy**)$_2$(**TzPyCN**)] and [Ir(**bzq**)$_2$(**TzPyCN**)].

The possible application of these probes as cellular pH sensors was explored by measuring the emission spectra (**Figure 4.42**) and excited state lifetimes (**Table 4.9**) of six PBS solutions at different pH values (4.81, 5.44, 5.92, 6.49, 6.90 and 7.45). The ratio between the integral of the emission profile and the maximum integral in the series (I/I_{max}) has been plotted against the pH, as showed in **Figure 4.43**. The pH-titration curves showed that no major changes in the emission intensity are present, indicating that [Ir(**ppy**)$_2$(**TzPyNH$_2$**)], [Ir(**ppy**)$_2$(**TzPyCN**)] and [Ir(**ppy**)$_2$(**TzPyNH$_2$**)] cannot be protonated within the intracellular pH range.

Moreover, the measurement of the lifetimes confirmed that no protonation reaction occurred, as a shorter excited state lifetime values would be expected for the cationic species, as previously demonstrated in section 4.5.

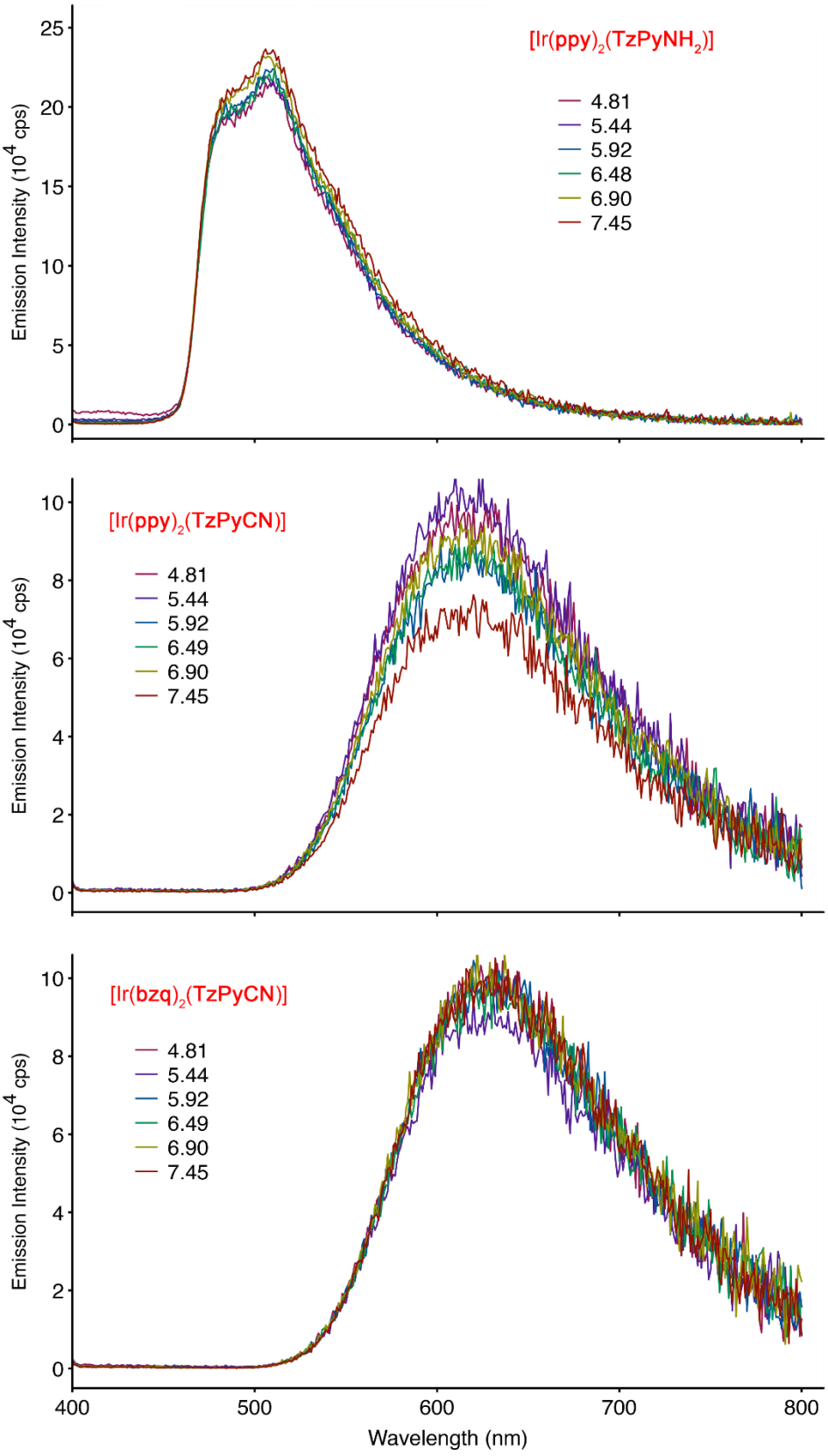

Figure 4.42 Emission spectra of [Ir(**ppy**)$_2$(**TzPyNH$_2$**)] (top), [Ir(**ppy**)$_2$(**TzPyCN**)] (middle) and [Ir(**bzq**)$_2$(**TzPyCN**)] (bottom) in PBS solutions at different pH values.

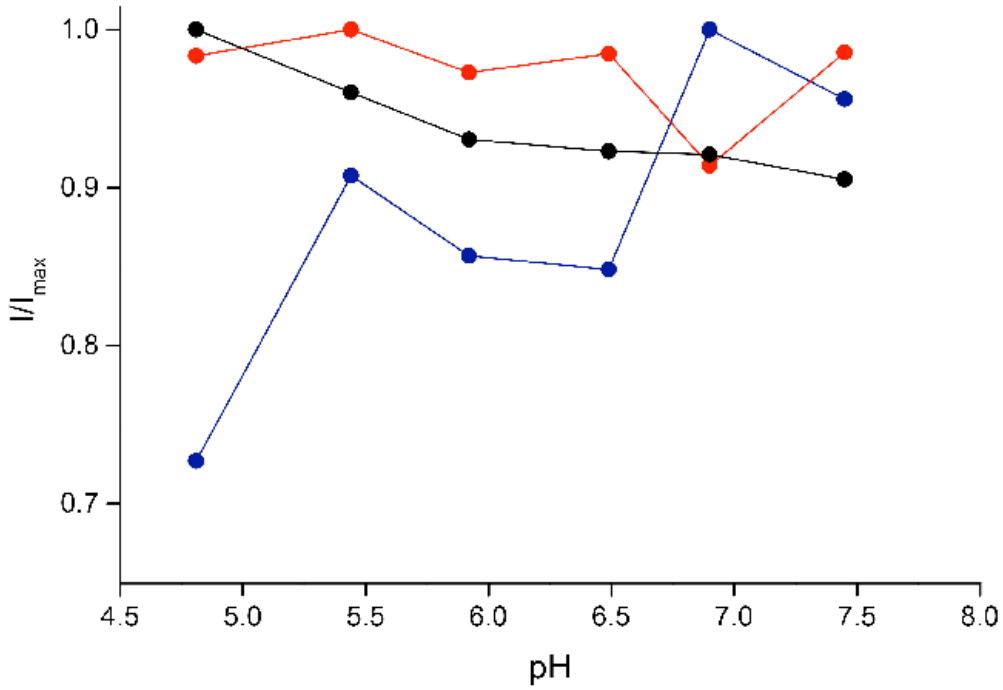

Figure 4.43 pH-titration curves of [Ir(**ppy**)$_2$(**TzPyNH$_2$**)] (black), [Ir(**ppy**)$_2$(**TzPyCN**)] (blue) and [Ir(**bzq**)$_2$(**TzPyCN**)] (red) in PBS solutions.

Table 4.9 Excited state lifetimes of [Ir(**ppy**)$_2$(**TzPyCN**)], [Ir(**bzq**)$_2$(**TzPyCN**)] and [Ir(**ppy**)$_2$(**TzPyNH$_2$**)] in PBS solutions at different pH.

pH	[Ir(**ppy**)$_2$(**TzPyCN**)] **τ [ns]**[a]	[Ir(**bzq**)$_2$(**TzPyCN**)] **τ [ns]**[a]	[Ir(**ppy**)$_2$(**TzPyNH$_2$**)] **τ [ns]**[a]
4.81	26 (10), 175 (90)	23 (15), 113 (85)	32 (10), 440 (90)
5.44	30 (11), 187 (89)	20 (14), 105 (85)	28 (7), 476 (93)
5.92	27 (9), 175 (91)	25 (17), 122 (83)	26 (9), 401 (91)
6.49	30 (11), 188 (89)	28 (18), 120 (82)	21 (7), 462 (93)
6.90	31 (11), 197 (89)	23 (15), 108 (85)	23 (7), 446 (93)
7.45	31 (10), 187 (90)	29 (17), 126 (83)	22 (6), 475 (94)

[a] For the biexponential excited state lifetime (τ), the relative weights of the exponential curves are reported in parentheses.

4.7 Conclusions

In this chapter, two new amino-functionalised iridium(III) complexes, [Ir(**ppy**)$_2$(**TzPyNH$_2$**)] and [Ir(**bzq**)$_2$(**TzPyNH$_2$**)], have been synthesised and characterised by IR and NMR spectroscopy, both of which confirmed the formation of the desired products. Unfortunately, the methylation of these neutral species was unsuccessful, due to the formation of multiple species which could not be separated.

The photophysical investigation in dichloromethane highlighted a typical yellow-green vibronically structured emission from a mixed LC and CT excited state. The LC character of the emissive excited state was more pronounced for the higher conjugated [Ir(**bzq**)$_2$(**TzPyNH$_2$**)], as evidenced by the marked elongation of the lifetime decay in degassed solution.[238,372] Moreover, temperature-dependent luminescence lifetime measurements on diluted dichloromethane solution of [Ir(**ppy**)$_2$(**TzPyNH$_2$**)] have confirmed the presence of a dark and thermally accessible ^{3}MC excited state, which is responsible of the shorter lifetime and the lower emission intensity of this probe in comparison to [Ir(**ppy**)$_2$(**TzPyCN**)].

The applicability of [Ir(**ppy**)$_2$(**TzPyNH$_2$**)] and [Ir(**bzq**)$_2$(**TzPyNH$_2$**)] in biological field was explored by photophysical studies in different aqueous and lipophilic solvents. Even if the emissive performances of the complexes remains comparable to that in dichloromethane, some solubility issues have been encountered.

Protonation and deprotonation reactions to evaluate the pH-sensing activity of [Ir(**ppy**)$_2$(**TzPyNH$_2$**)] and [Ir(**bzq**)$_2$(**TzPyNH$_2$**)] have been performed in dichloromethane and, due to the lack of the methylated analogues [Ir(**ppy**)$_2$(Me**TzPyNH$_2$**)]$^+$ and [Ir(**bzq**)$_2$(Me**TzPyNH$_2$**)]$^+$, compared to the acid/base behaviour of [Ir(**ppy**)$_2$(**TzPyCN**)] and [Ir(**bzq**)$_2$(**TzPyCN**)]. The cyano-functionalised complexes displayed a quenched and red-shifted (*ca.* 70 nm) emission profile upon addition of triflic acid, which could be reversed by treatment with triethylamine. On the other hand, the presence of a new shoulder at 555 nm and a decrease of the emission intensity was recorded for [Ir(**ppy**)$_2$(**TzPyNH$_2$**)], which could not be fully explained. Probably due to the low solubility of [Ir(**bzq**)$_2$(**TzPyNH$_2$**)] in dichloromethane solution, the protonation and deprotonation reactions did not affect the emission profile of this species.

The emission properties of [Ir(**ppy**)$_2$(**TzPyCN**)], [Ir(**bzq**)$_2$(**TzPyCN**)] and [Ir(**ppy**)$_2$(**TzPyNH$_2$**)] were investigated in PBS solutions in the range of pH typical of

the cellular environment, in order to evaluate the applicability of these probes as cellular pH-sensors. Unfortunately, the emission profiles and excited state lifetimes showed no major change in the pH range of 4.8 – 7.5, implying that these probes are not enough sensitive to pH variation in cells, and hence they cannot be used for cellular sensing.

Finally, by oxidation of [Ir(**ppy**)$_2$(**TzPyNH$_2$**)], [Ir(**ppy**)$_2$(**TzPyNO$_2$**)] was successfully synthesised but, due to the presence of the nitro group, the emission of the complex was totally quenched in all the investigated solvents.

4.8 Experimental

4.8.1 General Procedures

General procedures have been conducted as outline in Chapter 2 – section 2.6.2, unless otherwise stated.

The complexes $[Ir(\mathbf{ppy})_2(\mu\text{-}Cl)]_2$[277] and $[Ir(\mathbf{bzq})_2(\mu\text{-}Cl)]_2$[386] were prepared according to previously reported synthetic methods.

For the NMR characterisation, carbon and proton of all the iridium(III) tetrazolato species were labelled as pyridinic (A), phenylic (B), tetrazolic (T) and, benzoquinolynic (bzq), according to **Figure 4.44**.

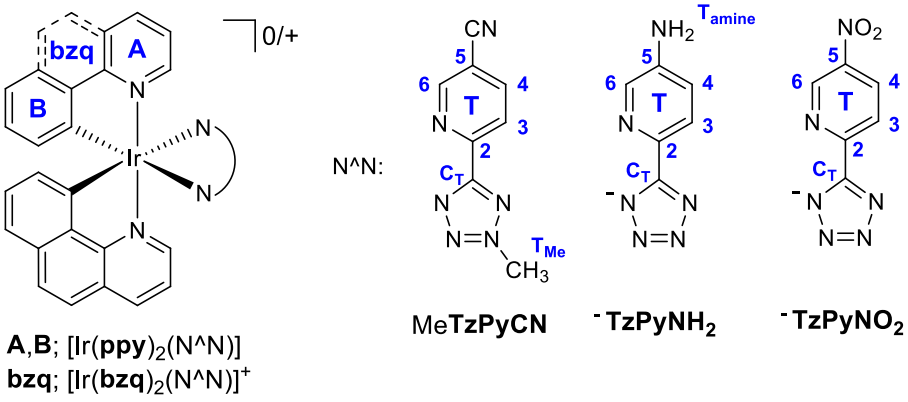

Figure 4.44 NMR referencing layout.

4.8.2 Photophysical Measurements

Photophysical measurements have been carried out as outlined in Chapter 2 – section 2.6.2, unless otherwise stated.

4.8.3 Synthesis

H$\mathbf{TzPyNH_2}$

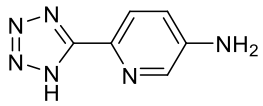

Triethylamine (2.1 mL, 0.015 mol) was added to toluene (15 mL) and the solution was cooled to 0 ºC. HCl 32% (1.3 mL, 0.015 mol) was added to the reaction mixture and stirred until fuming subsided. 5-amino-2-pyridinecarbonitrile (0.500 g, 0.004 mol) and sodium azide (1.090 g, 0.017 mol) were added and heated at reflux overnight. After cooling down to room temperature, the mixture was extracted with water (2 × 15 mL) and the aqueous phase was collected and acidified to pH≈3 with HCl 32%. The formed orange-pink precipitate was then filtered and dried in air. Yield: 0.280 g (41%). M.P. 270 – 272 °C. IR (ν / cm^{-1}): 3334 b (N–H stretch), 3160 br (N–H strech), 1661 w (N–H bend), 1612 w (tetrazole C=N). ^{1}H NMR (δ / ppm, DMSO-d_6): 8.07 (s, 1H, $\mathbf{H_{T6}}$), 7.86 (d, 1H, $\mathbf{H_{T4}}$, J = 8.5 Hz), 7.08 (d, 1H, $\mathbf{H_{T3}}$, J = 8.5 Hz), 6.04 (broad s, 2H, $\mathbf{2H_{Tamine}}$). ^{13}C NMR (δ / ppm, DMSO-d_6): 154.9 ($\mathbf{C_T}$), 147.1 ($\mathbf{C_{T2}}$), 135.9 ($\mathbf{CH_{T6}}$), 130.4 ($\mathbf{C_{T5}}$), 123.4 ($\mathbf{CH_{T4}}$), 119.7 ($\mathbf{CH_{T3}}$). Anal.Calcd for H**TzPyNH**$_2$·0.5(water): C, 42.10; H, 4.12; N, 49.10. Found: C, 42.10; H, 4.07; N, 48.95.

N3-MeTzPy – N4-MeTzPy

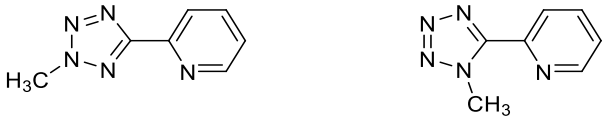

H**TzPy** (0.100 g, 0.680 mmol) was combine with K_2CO_3 (0.376 g, 2.720 mol) and stirred and heated at reflux in 15 mL of acetonitrile for 1 hour. Methyl iodide (0.085 mL, 1.360 mol) was added to the resulting suspension and heated at reflux overnight. The white precipitated was filtered out and discarded, whereas the orange filtrate was collected. The solvents were concentrated and the products were purified *via* column chromatography using silica-filled as stationary phase and an ethyl acetate/petroleum spirits 40 - 60 (9:1 v/v) solvent system as eluent. N3-Me**TzPy** eluted as first fraction (orange) and N4-Me**TzPy** (yellow) as second ones.

N3-Me**TzPy:** Yield: 0.056 g (51%). M.P. 120 – 121 °C. IR (ν / cm^{-1}): 2963, 2852, 2923 w (C–H stretch), 1616 w (tetrazole C=N). ^{1}H NMR (δ / ppm, DMSO-*d*$_6$): 8.74 (s, 1H, $\mathbf{H_{T6}}$), 8.12 (d, 1H, $\mathbf{H_{T3}}$, J = 8.0 Hz), 8.00 (t, 1H, $\mathbf{H_{T4}}$, J = 8.0 Hz), 7.55 (m, 1H, $\mathbf{H_{T5}}$), 4.46 (s, 3H, $\mathbf{H_{TMe}}$). ^{13}C NMR (δ / ppm, DMSO-*d*$_6$): 164.1 ($\mathbf{C_T}$), 150.1 ($\mathbf{C}H_{T6}$), 146.2 ($\mathbf{C_{T2}}$), 137.6 ($\mathbf{C}H_{T4}$), 125.2 ($\mathbf{C}H_{T5}$), 122.3 ($\mathbf{C}H_{T3}$); the methyl C peak was not visible in the spectrum.

N3-Me**TzPy:** Yield: 0.015 g (14%). M.P. 77 – 79 °C. IR (ν / cm^{-1}): 2955, 2852, 2922 w (C–H stretch), 1613 w (tetrazole C=N). ^{1}H NMR (δ / ppm, DMSO-*d*$_6$): 8.81 (s, 1H, $\mathbf{H_{T6}}$), 8.24 (d, 1H, $\mathbf{H_{T3}}$, J = 8.0 Hz), 8.09 (t, 1H, $\mathbf{H_{T4}}$, J = 8.2 Hz), 7.65 (m, 1H, $\mathbf{H_{T5}}$), 4.42 (s, 3H, $\mathbf{H_{TMe}}$). ^{13}C NMR (δ / ppm, DMSO-*d*$_6$): 152.0 ($\mathbf{C_T}$), 149.7 ($\mathbf{C}H_{T6}$), 144.3 ($\mathbf{C_{T2}}$), 138.1 ($\mathbf{C}H_{T4}$), 125.7 ($\mathbf{C}H_{T5}$), 124.2 ($\mathbf{C}H_{T3}$), 36.6 ($\mathbf{C}H_{TMe}$).

[Ir(ppy)$_2$(TzPyNH$_2$)]

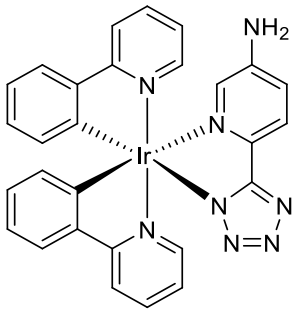

[Ir(**ppy**)$_2$(μ-Cl)]$_2$ (0.285 g, 0.266 mmol) was combined with H**TzPyNH$_2$** (0.108 g, 0.666 mmol) and dissolved in 13 mL of a dichloromethane/ethanol mixture (10:3 v/v). Triethylamine (10 drops) was added and the resulting suspension was stirred at room temperature overnight. The product was precipitated with diethyl ether as a yellow solid, filtered and dried in air. Yield: 0.200 g (57%). M.P. >400°C (dec). IR (ν / cm^{-1}): 3307 b (N–H stretch), 3163 br (N–H stretch), 1641 w (N–H bend), 1605 w (tetrazole C=N). ^{1}H NMR (δ / ppm, DMSO-*d*$_6$): 8.18 (app. t., 2H, **H$_{T4}$**, **H$_{T3}$**, splitting = 8.7 Hz), 7.95 (d, 1H, **H$_{T6}$**, J = 8.6 Hz), 7.90 – 7.86 (m, 3H, **3H$_A$**), 7.78 (d, 1H, **H$_B$**, J = 8.0 Hz), 7.63 (d, 1H, **H$_A$**, J = 5.6 Hz), 7.21 – 7.15 (m, 3H, **3H$_A$**), 7.11 (s, 1H, **H$_B$**), 6.96 (app. t., 1H, **H$_B$**, splitting = 7.5 Hz), 6.90 – 6.83 (m, 2H, **2H$_B$**), 6.74 (app. t., 1H, **H$_B$**, splitting = 7.4 Hz), 6.21 (d, 1H, **H$_B$**, J = 7.5 Hz), 6.15 (d, 1H, **H$_B$**, J = 7.5 Hz), 6.01 (broad s, 2H, **2H$_{Tamine}$**). ^{13}C NMR (δ / ppm, DMSO-*d*$_6$): 167.5 (**C$_T$**), 167.4 (**C$_{T2}$**), 163.9 (**C$_{T5}$**), 152.7 (**C$_A$**), 148.7 (**C**H$_A$), 148.3 (**C**H$_A$), 148.2 (**C**H$_A$), 147.5 (**C$_A$**), 144.3 (**C$_B$**), 144.0 (**C$_B$**), 138.1 (**C**H$_A$), 137.7 (**C**H$_A$), 135.6 (**C$_B$**), 135.2 (**C**H$_B$), 131.4 (**C**H$_B$), 131.2 (**C**H$_B$), 129.9 (**C**H$_B$), 129.0 (**C**H$_B$), 124.7 (**C**H$_A$), 124.2 (**C**H$_B$), 123.3 (**2C**H$_A$), 123.0 (**C**H$_{T6}$), 122.2 (**C$_B$**), 121.6 (**C**H$_B$), 120.9 (**C**H$_B$), 119.5 (**C**H$_{T4}$), 119.3 (**C**H$_{T3}$). Anal.Calcd for [Ir(**ppy**)$_2$(**TzPyNH$_2$**)]·0.2(CH_2Cl_2): C, 49.90; H, 3.18; N, 16.51. Found: C, 49.91; H, 3.21; N, 16.54.

[Ir(bzq)$_2$(TzPyNH$_2$)]

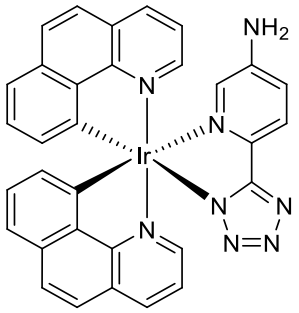

[Ir(**bzq**)$_2$(μ-Cl)]$_2$ (0.325 g, 0.279 mmol) was combined with H**TzPyNH$_2$** (0.120 g, 0.699 mmol) and dissolved in 13 mL of a dichloromethane/ethanol mixture (10:3 v/v). Triethylamine (10 drops) was added and the resulting suspension was stirred at room temperature overnight. The product was precipitated with diethyl ether as a yellow solid, filtered and dried in air. Yield: 0.279 g (69%). M.P. >400 °C (dec). IR (ν / cm^{-1}): 3303 b (N–H stretch), 3158 br (N–H stretch), 1643 w (N–H bend), 1608 w (tetrazole C=N). ^{1}H NMR (δ / ppm, DMSO-*d*$_6$): 8.50 (d, 2H, **H$_{T4}$**, **H$_{T3}$**, J = 7.6 Hz), 8.09 (d, 1H, **H$_{T6}$**, J = 5.2 Hz), 8.00 (d, 1H, **H$_B$**, J = 8.4 Hz), 7.91 (app. t., 2H, **2H$_{bzq}$**, splitting = 8.8 Hz), 7.85 – 7.81 (m, 3H, **3H$_{bzq}$**), 7.62 (d, 2H, **2H$_{bzq}$**, J = 6.8 Hz), 7.49 (d, 1H, **H$_{bzq}$**, J = 7.6 Hz), 7.41 (d, 1H, **H$_{bzq}$**, J = 8.0 Hz), 7.20 (d, 1H, **H$_{bzq}$**, J = 8.8 Hz), 7.13 (app. t., 2H, **2H$_{bzq}$**, splitting = 7.6 Hz), 7.02 (app. t., 1H, **H$_{bzq}$**, splitting = 7.6 Hz), 6.23 (d, 1H, **H$_{bzq}$**, J = 7.2 Hz), 6.13 (d, 1H, **H$_{bzq}$**, J = 7.2 Hz), 5.95 (broad s, 2H, **2H$_{Tamine}$**). ^{13}C NMR (δ / ppm, DMSO-*d*$_6$): 164.2 (**C$_T$**), 157.0 (**C$_{T2}$**), 156.9 (**C$_{bzq}$**), 149.3 (**C$_{bzq}$**), 148.3 (**C**H$_{bzq}$), 147.9 (**C**H$_{T6}$), 147.5 (**C$_{bzq}$**), 144.8 (**C$_{bzq}$**), 140.9 (**C$_{bzq}$**), 140.8 (**C$_{bzq}$**), 137.0 (**C**H$_{T3}$), 136.7 (**C**H$_{T4}$), 135.8 (**C**H$_{bzq}$), 135.7 (**C$_{T5}$**), 133.6 (**C$_{bzq}$**), 133.3 (**C$_{bzq}$**), 129.5 (**C**H$_{bzq}$), 129.4 (**C**H$_{bzq}$), 129.5 (**C**H$_{bzq}$), 128.7 (**C**H$_{bzq}$), 128.6 (**C**H$_{bzq}$), 128.5 (**C**H$_{bzq}$), 126.4 (**C$_{bzq}$**), 126.3 (**C$_{bzq}$**), 123.9 (**C**H$_{bzq}$), 123.6 (**C**H$_{bzq}$), 123.0 (**C**H$_{bzq}$), 122.4 (**C**H$_{bzq}$), 122.3 (**C**H$_{bzq}$), 122.2 (**C**H$_{bzq}$), 119.6 (**C**H$_{bzq}$), 118.9 (**C**H$_{bzq}$). Anal.Calcd for [Ir(**bzq**)$_2$(**TzPyNH$_2$**)]: C, 54.15; H, 2.98; N, 15.79. Found: C, 54.19; H, 3.00; N, 15.75.

[Ir(ppy)$_2$(TzPyNO$_2$)]

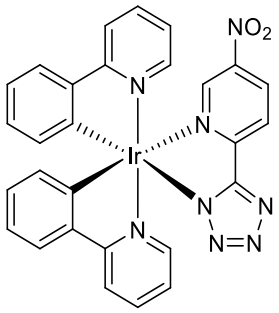

[Ir(**ppy**)$_2$(**TzPyNH$_2$**)] (0.100 g, 0.121 mmol) was dissolved in 5 mL of acetonitrile and KI (0.02 g, 5% mol) was added. An aqueous solution of tert-butyl hydroperoxide (70%, 0.35 mL) was added slowly in 30 minutes. The suspension was heated at the reflux temperature for 24 hours. The solution was then dried and 10 mL of dichloromethane were added. The yellow starting material was filtered and recovered while the filtrated was neutralised with a saturated solution of Na_2SO_3, (20 mL) and washed with water (2 × 15 mL) and brine (15 mL). The organic phase was dried over $MgSO_4$ and filtered. The product was purified *via* alumina-filled column chromatography using Brockmann I grade neutral alumina-filled as stationary phase and ethyl acetate as eluent. The targeted complex eluted as the first fraction (orange). Yield: 0.062 g (74%). M.P. 247 °C (dec). IR (ν / cm^{-1}): 1607 w (tetrazole C=N), 1478 m (NO_2 asym. stretch), 1344 m (NO_2 sym. stretch). ^{1}H NMR (δ / ppm, DMSO-*d$_6$*): 8.83 (d, 1H, **H$_{T4}$**, J = 8.8 Hz), 8.55 (d, 1H, **H$_{T3}$**, J = 9.6 Hz), 8.37 (s, 1H, **H$_{T6}$**), 8.22 (app. t., 2H, **2H$_A$**, splitting = 8.4 Hz), 7.93 – 7.87 (m, 3H, **3H$_A$**), 7.83 (d, 1H, **H$_B$**, J = 8.0 Hz), 7.76 (d, 1H, **H$_B$**, J = 6.4 Hz), 7.44 (d, 1H, **H$_A$**, J = 5.8 Hz), 7.19 (app. t., 1H, **H$_A$**, splitting = 7.2 Hz), 7.08 – 7.04 (m, 2H, **H$_A$**, **H$_B$**), 6.96 – 6.91 (m, 2H, **2H$_B$**), 6.80 (app. t., 1H, **H$_B$**, splitting = 8.8 Hz), 6.28 (d, 1H, **H$_B$**, J = 7.4 Hz), 6.14 (d, 1H, **H$_B$**, J = 7.6 Hz). ^{13}C NMR (δ / ppm, DMSO-*d$_6$*): 167.0 (**C$_T$**), 166.9 (**C$_{T2}$**), 162.0 (**C$_{T5}$**), 152.4 (**C$_A$**), 150.4 (**C$_A$**), 149.5 (**CH$_B$**), 149.1 (**CH$_A$**), 146.1 (**C$_B$**), 145.8 (**C$_B$**), 145.6 (**CH$_{T6}$**), 144.5 (**C$_B$**), 144.0 (**C$_B$**), 138.6 (**CH$_A$**), 138.2 (**CH$_A$**), 135.2 (**CH$_{T4}$**), 131.4 (**CH$_B$**), 131.2 (**CH$_B$**), 130.2 (**CH$_B$**), 129.2 (**CH$_B$**), 125.1 (**CH$_A$**), 124.4 (**CH$_B$**), 123.8 (**CH$_A$**), 123.3 (**CH$_B$**), 122.39 (**CH$_{T3}$**, **CH$_A$**), 121.5 (**CH$_B$**), 119.9 (**CH$_A$**), 119.4 (**CH$_A$**). Anal.Calcd for [Ir(**ppy**)$_2$(**TzPyNO$_2$**)]·0.5(ethyl acetate): C, 48.97; H, 3.15; N, 15.23. Found: C, 48.92; H, 3.17; N, 15.14.

[Ir(bzq)$_2$(TzPyCN)]

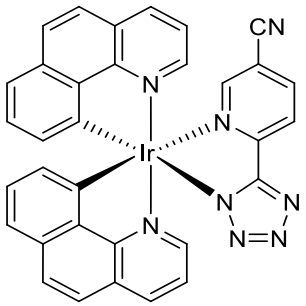

[Ir(**bzq**)$_2$(μ-Cl)]$_2$ (0.250 g, 0.214 mmol) was combined with H**TzPyCN** (0.081 g, 0.471 mmol) and dissolved in 13 mL of a dichloromethane/ethanol mixture (10:3 v/v). The resulting suspension was stirred at room temperature overnight. The solvents were concentrated and the product was purified *via* column chromatography using Brockmann I grade neutral alumina-filled as stationary phase and a dichloromethane/acetone (9:1 v/v) solvent system as eluent. The targeted complex eluted as the second fraction (orange). Yield: 0.202 g (66%). M.P. 309 °C (dec). IR (ν / cm^{-1}): 2235 w (C≡N), 1608 w (tetrazole C=N). ^{1}H NMR (δ / ppm, DMSO-*d*$_6$): 9.01 – 9.34 (m, 4H, **2H$_{bzq}$**, **H$_{T4}$**, **H$_{T3}$**), 8.68 (d, 1H, **H$_{T6}$**, J = 5.2 Hz), 8.38 – 8.22 (m, 6H, **6H$_{bzq}$**), 8.06 – 8.0013 (m, 1H, **H$_{bzq}$**), 7.97 – 7.94 (m, 2H, **2H$_{bzq}$**), 7.62 (d, 1H, **H$_{bzq}$**), 7.48 (app. t., 1H, **H$_{bzq}$**, splitting = 8.0 Hz), 7.03 (app. t., 1H, **H$_{bzq}$**, splitting = 8.0 Hz), 6.72 (d, 1H, **H$_{bzq}$**, J = 7.2 Hz), 6.53 (d, 1H, **H$_{bzq}$**, J = 7.2 Hz). ^{13}C NMR (δ / ppm, DMSO-*d*$_6$): 163.0 (**C$_T$**), 156.6 (**C$_{T2}$**), 156.4 (**C$_{T5}$**), 153.1 (**C**H$_{bzq}$), 151.3 (**C$_{bzq}$**), 149.3 (**C**H$_{T6}$), 148.7 (**C**H$_{bzq}$), 147.2 (**C**N), 143.3 (**C**H$_{bzq}$), 142.8 (**C**H$_{bzq}$), 140.8 (**C**H$_{bzq}$), 140.5 (**C**H$_{bzq}$), 137.4 (**C**H$_{T4}$), 137.1 (**C**H$_{T3}$), 133.7 (**C$_{bzq}$**), 133.4 (**C$_{bzq}$**), 129.5 (**C**H$_{bzq}$), 129.4 (**C**H$_{bzq}$), 129.2 (**C**H$_{bzq}$), 128.8 (**C**H$_{bzq}$), 128.7 (**C**H$_{bzq}$), 128.3 (**C**H$_{bzq}$), 126.7 (**C$_{bzq}$**), 126.3 (**C$_{bzq}$**), 124.2 (**C**H$_{bzq}$), 123.8 (**C**H$_{bzq}$), 122.8 (**C**H$_{bzq}$), 122.4 (**C**H$_{bzq}$), 122.3 (**C**H$_{bzq}$), 120.3 (**C**H$_{bzq}$), 119.4 (**C$_{bzq}$**), 115.7 (**C$_{bzq}$**), 111.4 (**C$_{bzq}$**). Anal.Calcd for [Ir(**bzq**)$_2$(**TzPyCN**)]·0.5(acetone): C, 55.34; H, 2.96; N, 14.96. Found: C, 55.46; H, 2.93; N, 14.89.

[Ir(bzq)$_2$(MeTzPyCN)][PF$_6$]

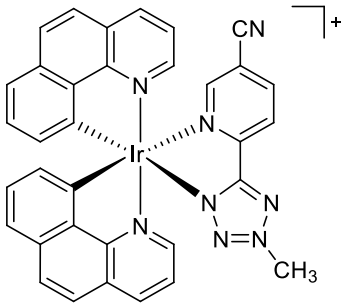

[Ir(**bzq**)$_2$(**TzPyCN**)] (0.050 g, 0.069 mmol) was dissolved in dichloromethane (10 mL) and cooled down to –50 °C using an ethyl acetate/liquid nitrogen cool bath. Thereafter, a 0.1 M methyl trifluoromethanesulfonate solution in dichloromethane (0.017 g, 0.104 mmol) was added dropwise to the vigorously stirred solution. After being maintained at –50°C for 30 minutes, the solution was warmed up at room temperature and left to stirred overnight. An excess of ammonium hexafluorophosphate (0.022 g, 0.140 mmol) was added and stirred for 45 minutes. The crude mixture was washed with water and extracted with dichloromethane (3 × 15 mL) and the combined organic phase was dried on $MgSO_4$. The targeted complex was then collected after filtration and removal of the solvent as a red solid. Yield: 0.051 g (75%). M.P. 308 °C (dec). IR (ν / cm^{-1}): 2239 w (C≡N), 1619 w (tetrazole C=N). ^{1}H NMR (δ / ppm, DMSO-d_6): 8.80 (s, 2H, $\mathbf{H_{T3}}$, $\mathbf{H_{T4}}$), 8.62 (app. t., 2H, $\mathbf{H_{T6}}$, $\mathbf{H_{bzq}}$, splitting = 8.4 Hz), 8.41 (d, 1H, $\mathbf{H_{bzq}}$, J = 5.4 Hz), 8.33 (d, 1H, $\mathbf{H_{bzq}}$, J = 5.4 Hz), 8.03 – 7.87 (m, 5H, $\mathbf{5H_{bzq}}$), 7.65 – 7.56 (m, 3H, $\mathbf{3H_{bzq}}$), 7.49 (d, 1H, $\mathbf{H_{bzq}}$, J = 7.9 Hz), 7.22 (app. t., 1H, $\mathbf{H_{bzq}}$, splitting = 7.6 Hz), 7.09 (app. t., 1H, $\mathbf{H_{bzq}}$, splitting = 7.6 Hz), 6.23 (d, 1H, $\mathbf{H_{bzq}}$, J = 7.2 Hz), 6.08 (d, 1H, $\mathbf{H_{bzq}}$, J = 7.3 Hz), 4.50 (s, 3H, $\mathbf{3H_{TMe}}$). ^{13}C NMR (δ / ppm, DMSO-d_6): 165.3 ($\mathbf{C_T}$), 155.9 ($\mathbf{C_{T2}}$), 155.8 ($\mathbf{C_{T5}}$), 154.1 ($\mathbf{CH_{bzq}}$), 150.3 ($\mathbf{CH_{bzq}}$), 150.2 ($\mathbf{CH_{bzq}}$), 146.9 (**C**N), 144.2 ($\mathbf{CH_{T6}}$), 143.5 ($\mathbf{C_{bzq}}$), 140.4 ($\mathbf{C_{bzq}}$), 140.3 ($\mathbf{C_{bzq}}$), 139.9 ($\mathbf{C_{bzq}}$), 138.0 ($\mathbf{CH_{T4}}$), 137.8 ($\mathbf{CH_{bzq}}$), 133.7 ($\mathbf{C_{bzq}}$), 133.4 ($\mathbf{C_{bzq}}$), 129.6 ($\mathbf{CH_{bzq}}$), 129.4 ($\mathbf{CH_{bzq}}$), 129.3 ($\mathbf{CH_{bzq}}$), 129.0 ($\mathbf{CH_{bzq}}$), 128.5 ($\mathbf{CH_{bzq}}$), 128.4 ($\mathbf{CH_{bzq}}$), 126.8 ($\mathbf{C_{bzq}}$), 126.5 ($\mathbf{C_{bzq}}$), 124.4 ($\mathbf{CH_{bzq}}$), 124.3 ($\mathbf{CH_{bzq}}$), 124.0 ($\mathbf{CH_{T3}}$), 122.8 ($\mathbf{CH_{bzq}}$), 121.0 ($\mathbf{CH_{bzq}}$), 120.4 ($\mathbf{CH_{bzq}}$), 115.3 ($\mathbf{C_{bzq}}$), 114.5 ($\mathbf{C_{bzq}}$), 42.2 ($\mathbf{CH_{Me}}$). Anal.Calcd for [Ir(**bzq**)$_2$(Me**TzPyCN**)][PF$_6$]: C, 46.42; H, 2.52; N, 12.74. Found: C, 46.54; H, 2.53; N, 12.72.

Chapter 5

Synthesis and Photophysical Investigation of Fatty Acid-Functionalised Iridium Tetrazolato Complexes

5.1 Introduction

Fatty acids are found in all known living organisms, in which they play an essential role in membrane formation, energy storage, regulation of protein functions and secondary metabolite production.[248,387–389]

In the case of bacteria, fatty acids are mainly localised in the cell membrane (Gram-positive bacteria) and also cell walls (Gram-negative species) as part of the lipid bylayer.[390,391] On the other hand, in mammalian cells they accumulate in many cellular compartments and their regulation and homeostasis are strongly affected by environmental stress as well as the stage of the cellular life.[392–394]

Most tissues, except for liver and adipose tissue, possess little capacity for *de novo* synthesis of fatty acids and depend on long-chain fatty acid uptake for their biological processes. Therefore, the efficient transport of these molecules through the cellular membrane is of vital importance.[395] Noteworthy, the reduced solubility of fatty acids in aqueous environment (1 - 10 nM) dictates specific requirements for their transport and accumulation within the cells.[396] After decades of studies, researchers have identified two main uptake mechanisms for the transport of fatty acids; a membrane-associated protein, recognised as FAT/CD36, which facilitates the passage of fatty acids through the plasma membrane, and a family of transcription factors, named peroxisome proliferator-activated receptors (PPAR), which can specifically link with fatty acids and their metabolites.[397] Malfunction of FAT/CD36 and PPAR or

general changes in the fatty acid viability can promote the development of obesity-related chronic kidney disease, immune disorders, cancer, type-2 diabetes mellitus, as well as cardiovascular and neurodegenerative diseases.[248,392,393,398,399]

For these reasons, the development of probes for the detection of fatty acids, either in their free form or as more complex lipid, is necessary. The majority of these dyes are organic molecules, such as Nile Red (**102**), Oil Red O (**103**) or Filipin III (**104**), which are available on the market and are routinely used for the staining of cells (**Figure 5.1**). Unfortunately, the staining protocols often require cell fixation, which can cause damage to the cellular ultrastructure. Other organic staining, such as BODIPY™ 503/512 (**105**), LipidTOX (**106**), LD540 (**107**) or the two dyes (**108 - 109**) synthesised by Zhao and co-workers,[400] can be applied for lipid imaging in live cells and overcome some of the issues related to the fixation process. A rhenium(I) tetrazolato complex developed in 2014 by Werrett *et al.*[232,248] and commercialised as ReZolve-L1™ (**110**) was the first example of d^6 transition metal probe for the specific staining of polar lipids. Nevertheless, fluorescent and phosphorescent probes for fatty acids or lipids in general are still somewhat limited.

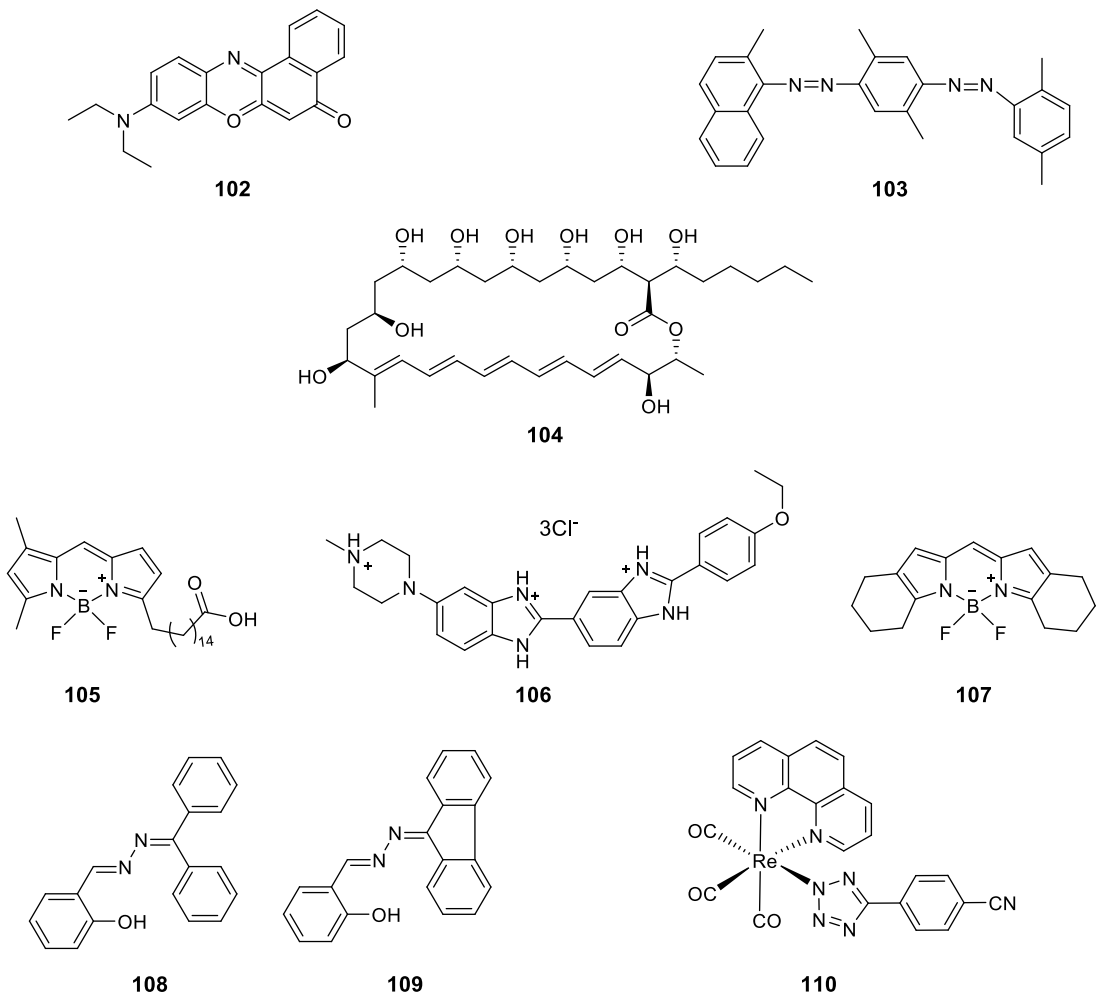

Figure 5.1 Examples of previously reported probes for the detection of lipids in fixed and live cells.

In this chapter, the synthesis and the photophysical investigation of five fatty acid-functionalised iridium(III) complexes (**Figure 5.2**) will be discussed. After the successful uptake and localisation of the cyano-functionalised iridium(III) tetrazolato complexes (described in Chapter 2 and Chapter 3) in the endoplasmic reticulum and lipid droplets, the addition of a fatty acids chain on the tetrazolate ligand was attempted to increase the specificity of these probes for lipids. Five different fatty acids (octanoic, palmitic, stearic, palmitoleic and oleic acid) were employed to evaluate how the chain length and degree of unsaturation could affect the photophysical and biological properties of these complexes.

A variety of synthetic routes for the functionalisation of the tetrazolate moiety were attempted. However, issues with the separation and purification of the desired product from byproducts and unreacted starting materials were encountered. For these reasons, the design of a synthetic procedure using [Ir(**ppy**)$_2$(**TzPyNH$_2$**)] and the acyl chloride of the appropriate fatty acid were performed to successfully isolate [Ir(**ppy**)$_2$(**TzPyNHC$_{8sat}$**)], [Ir(**ppy**)$_2$(**TzPyNHC$_{16sat}$**)], [Ir(**ppy**)$_2$(**TzPyNHC$_{18sat}$**)], [Ir(**ppy**)$_2$(**TzPyNHC$_{16cis}$**)] and [Ir(**ppy**)$_2$(**TzPyNHC$_{18cis}$**)] (**Figure 5.2**).

The photophysical characterisation in diluted dichloromethane solutions highlighted yellow-green emission with relatively low intensity for the whole series, which is consistent with the photophysical properties of the starting material [Ir(**ppy**)$_2$(**TzPyNH$_2$**)]. The temperature-dependent luminescent lifetime measurements on [Ir(**ppy**)$_2$(**TzPyNHC$_{16cis}$**)] confirmed the presence of a dark and low-lying ^{3}MC excited state, which is thermally available at room temperature. These results were again consistent with the ones discussed for [Ir(**ppy**)$_2$(**TzPyNH$_2$**)] in Chapter 4 – section 4.4.3.

Finally, the photophysical features of these family of iridium(III) complexes in aqueous and lipophilic solvents have been used to evaluate their applicability in biological environment and the possibility to discriminate their localisation within the cells based on their emission maxima.

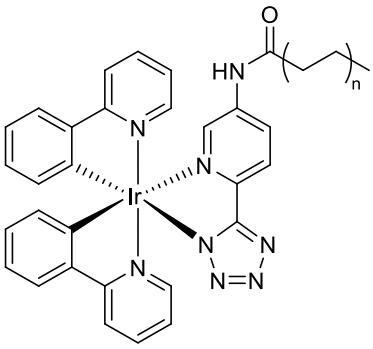

n= 3; [Ir(**ppy**)$_2$(**TzPyNHC$_{8sat}$**)]
n= 7; [Ir(**ppy**)$_2$(**TzPyNHC$_{16sat}$**)]
n= 8; [Ir(**ppy**)$_2$(**TzPyNHC$_{18sat}$**)]

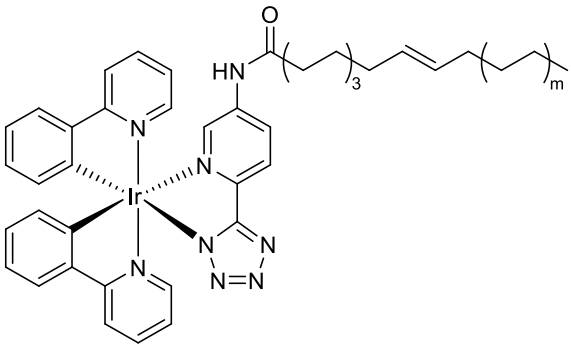

m= 2; [Ir(**ppy**)$_2$(**TzPyNHC$_{16cis}$**)]
m= 3; [Ir(**ppy**)$_2$(**TzPyNHC$_{18cis}$**)]

Figure 5.2 Structure of target complexes in this investigation.

5.2 Synthetic Attempts for the Functionalisation of CN**PyNH$_2$** and H**TzPyNH$_2$**

A variety of synthetic methods was involved in the functionalisation of 5-amino-2-pyridinecarbonitrile (CN**PyNH$_2$**) and H**TzPyNH$_2$**. The first attempt was the reaction of the nitrile and the tetrazolate substrates with a carboxylic acid, using 2-(1*H*-benzotriazol-1-yl)-1,1,3,3-tetramethyluronium hexafluorophosphate (HBTU) as coupling agent in acetonitrile (**Figure 5.3**).[401]

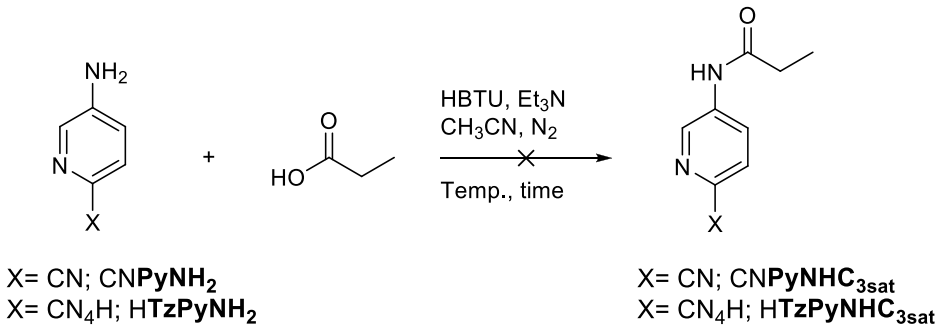

Figure 5.3 Scheme of the attempted synthesis for the formation of CN**PyNHC$_{3sat}$** and H**TzPyNHC$_{3sat}$**. The different reaction conditions are summarised in **Table 5.1**.

In order to find the optimal reaction conditions, propionic acid was utilised as test reaction. The synthesis was performed at different temperatures and reaction times, as showed in **Table 5.1**.

At the start, the reactions were carried out for 24 hours at room temperature or heating at reflux, in order to increase the solubility of the starting materials. In general, the conversion of CN**PyNH$_2$** or H**TzPyNH$_2$** was higher at room temperature, although a byproduct[236] derived from the cleavage of the amino group (H**TzPy**) was formed in all cases and the isolation of the desired products was not possible (**Figure 5.4**). Only for reaction #4 (refer to **Table 5.1**), the product was isolated as a fine precipitate from the reaction mixture in a very low yield (*ca.* 9%). The reaction time was then increased to 72 hours (#5 - #6) in an attempt to enhance the conversion of the amino substrates. Unfortunately, the ratio between product and byproduct (based on the NMR integrals) did not improve in comparison to the 24 hour heated reactions (#3 - #4) and the conversion of CN**PyNH$_2$** or H**TzPyNH$_2$** increased only slightly (**Table 5.1**).

Table 5.1 Summary of the reaction conditions and results for the attempted synthesis of CN**PyNHC**$_{3sat}$ and H**TzPyNHC**$_{3sat}$.

#	Starting Material X**PyNH**$_2$	Temperature (°C)	Time (h)	Conversion (%)	Ratio[a] product:byproduct	Yield (%)
1	CN	25 (r.t.)	24	50	1 : 5	-
2	H**Tz**	25 (r.t)	24	74	1 : 0	9
3	CN	82 (reflux)	24	33	1 : 1	-
4	H**Tz**	82 (reflux)	24	43	2 : 1	-
5	CN	25 (r.t.)	72	40	1 : 1	-
6	H**Tz**	25 (r.t)	72	48	2 : 1	-

[a] The ratio is referred to the peak integration in the ^{1}H NMR spectrum between product and byproduct.

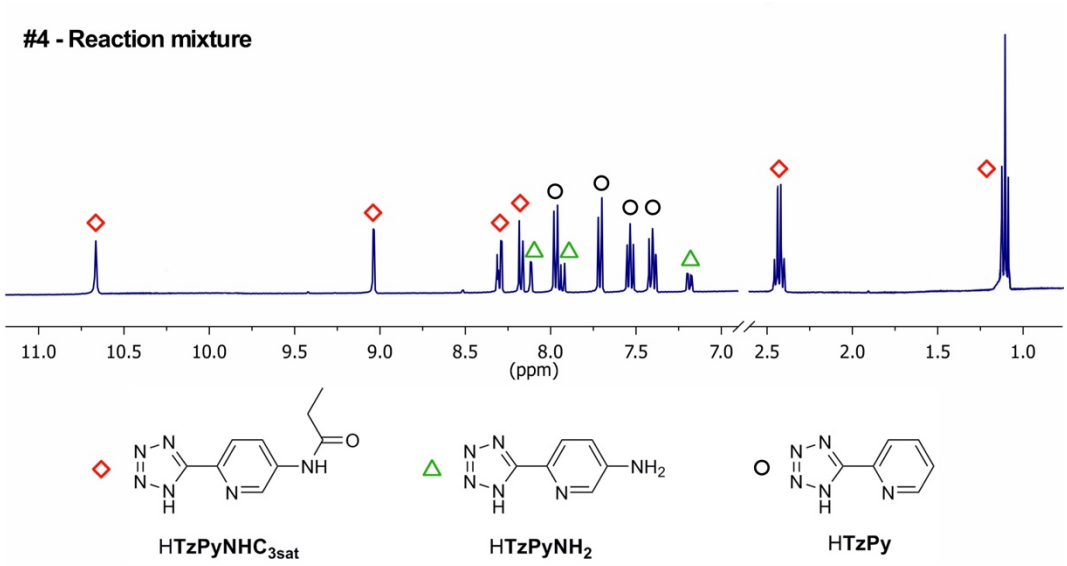

Figure 5.4 ^{1}H NMR spectrum in DMSO-d_6 of the reaction mixture for #4, highlighting the peaks of the desired product H**TzPyNHC**$_{3sat}$ (red diamond), the starting material H**TzPyNH**$_2$ (green triangle) and the byproduct H**TzPy** (black circle).

Based on these results, a different synthetic method was followed. In particular, the reactivity of the carboxylic acid was increased by conversion to the acyl chloride, using oxalyl chloride and dimethylformamide (DMF) as catalyst (**Figure 5.5** - top).[402,403,404] In this case, propionic acid was substituted with the heavier octanoic acid to facilitate the work up of the reaction, which consists in the removal of the solvent and the unreacted oxalyl chloride by evaporation under reduced pressure. Without further purification, octanoyl chloride was reacted with CN**PyNH$_2$** or H**TzPyNH$_2$** in the presence of triethylamine, and stirred in dichloromethane at room temperature for 16 hours (**Figure 5.5** - bottom).[405,406] All the conditions and results are summarised in **Table 5.2**.

Table 5.2 Summary of the reaction conditions and results for the synthesis of CN**PyNHC$_{8sat}$** and H**TzPyNHC$_{8sat}$**.

#	Starting Material X**PyNH$_2$**	Temperature (°C)	Time (h)	Conversion (%)	Ratio[a] product:byproduct	Yield (%)
7	CN	25 (r.t.)	16	75	1 : 0	44
8	H**Tz**	25 (r.t)	16	51	2 : 1	-

[a] The ratio is referred to the peak integration in the ^{1}H NMR spectrum between product and byproduct.

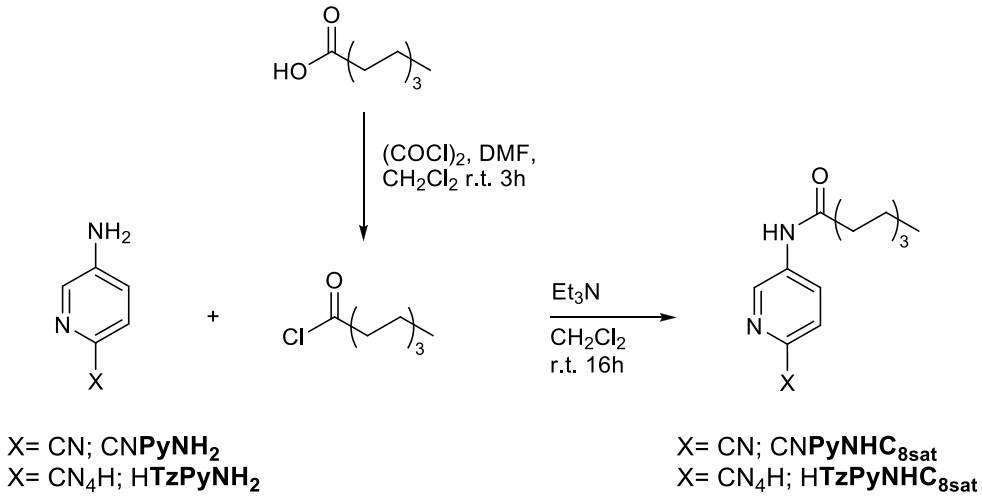

Figure 5.5 Scheme of the synthesis for the preparation of octanoyl chloride (top). On the bottom octanoyl chloride was reacted with CN**PyNH$_2$** or H**TzPyNH$_2$** for the preparation of H**TzPyNHC$_{8sat}$** and CN**PyNHC$_{8sat}$**, respectively.

At the end of the reaction, the crude was extracted with hexane and washed multiple times with a 0.1 M sodium hydroxide solution, before being dried and analysed by ^{1}H NMR.

The ^{1}H NMR spectrum showed the presence of different byproducts along with some unreacted starting material for H**TzPyNHC**$_{8sat}$, whereas CN**PyNHC**$_{8sat}$ was formed and isolated with average yield of *ca.* 45%, as confirmed from the N–H peak resonating at around 10.55 ppm (**Figure 5.6**). On the other hand, a variety of purification techniques, such as extraction, precipitation and column chromatography, were employed without success to isolate the pure H**TzPyNHC**$_{8sat}$.

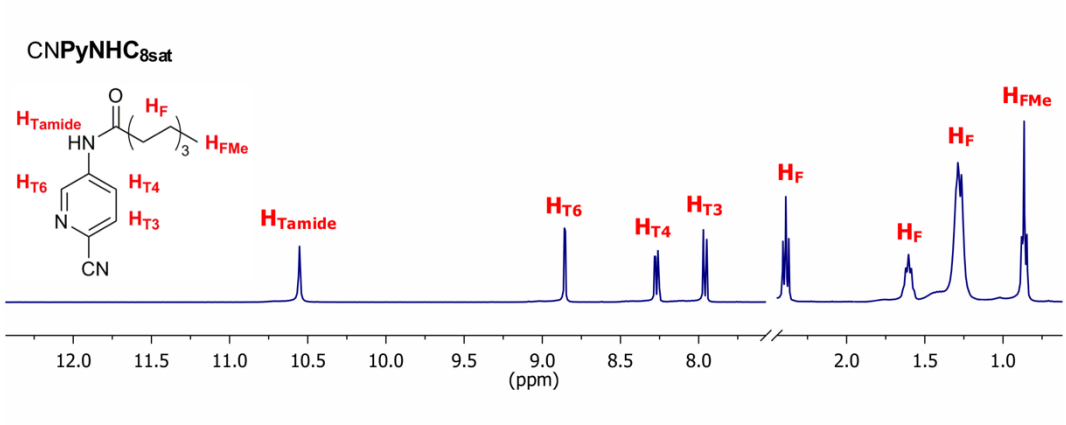

Figure 5.6 ^{1}H NMR in DMSO-d_6 for CN**PyNHC**$_{8sat}$ with labelling of the proton peaks.

For this reason, in order to convert CN**PyNHC**$_{8sat}$ into H**TzPyNHC**$_{8sat}$, the nitrile precursor was reacted with sodium azide in the presence of triethylammonium chloride and heated at the reflux in toluene for 24 hours (**Figure 5.7**).[270]

Once again, the conversion of the starting material was very low (*ca.* 30%) and the product did not precipitate out from the reaction mixture by protonation of the tetrazolate ring. Further attempts to isolate H**TzPyNHC**$_{8sat}$ were unsuccessful, and a different synthetic procedure for the preparation of the fatty acid-functionalised iridium(III) tetrazolato complexes was explored.

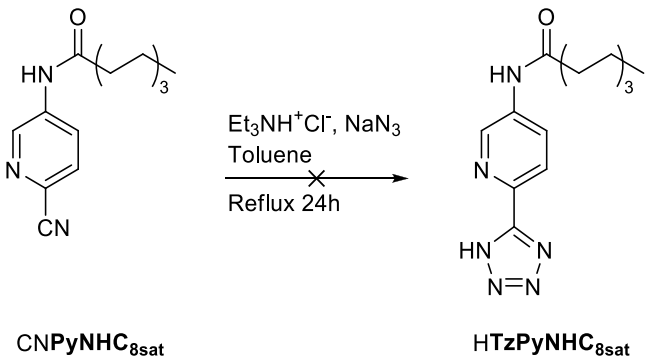

CN**PyNHC**$_{8sat}$ H**TzPyNHC**$_{8sat}$

Figure 5.7 Scheme of the attempted synthetic procedure for the preparation of H**TzPyNHC**$_{8sat}$.

5.3 Synthesis and Characterisation of Fatty Acid-Functionalised Iridium(III) Complexes

The fatty acid-functionalised iridium(III) tetrazolato complexes have been synthesised following the same methodology that was previously applied to CN**PyNH$_2$** and H**TzPyNH$_2$**.[405,406] The advantage of performing the reaction directly on the iridium(III) complex was the enhanced solubility in dichloromethane and the consequently easier work up *via* column chromatography.

Five fatty acids were investigated to evaluate the effect of the aliphatic chain length and the degree of unsaturation on the photophysical and biological properties of these iridium(III) complexes (**Table 5.3**).

Table 5.3 Summary of the fatty acids investigated in this chapter and their structural characteristic.

#	Fatty acid	*C:D*[a]	Chemical structure
1	Octanoic acid	8 : 0	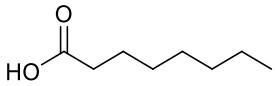
2	Palmitic acid	16 : 0	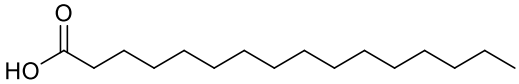
3	Stearic acid	18 : 0	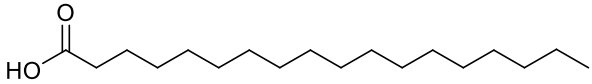
4	Palmitoleic acid	16 : 1	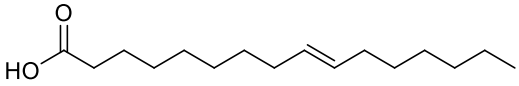
5	Oleic acid	18 : 1	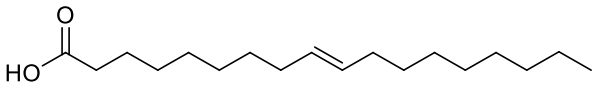

[a] *C:D* is the lipid number, where *C* is the number of carbon atoms in the fatty acid and *D* is the number of double bonds present in the chain.

As showed in **Figure 5.8** (top), five fatty acids were converted in their more reactive acyl chloride analogues by treatment with oxalyl chloride and DMF in an inert atmosphere of nitrogen and dry dichloromethane.[402,403,404] The solvent and any excess of oxalyl chloride were removed by evaporation under reduced pressure and the acyl chloride was used for the following reaction without further purification.

[Ir(**ppy**)$_2$(**TzPyNH$_2$**)] (refer to Chapter 4 – section 4.8.3 for synthesis and characterisation) was combined with the appropriate acyl chloride species and stirred in dry dichloromethane for 16 hours, in the presence of triethylamine (**Figure 5.8** - bottom).

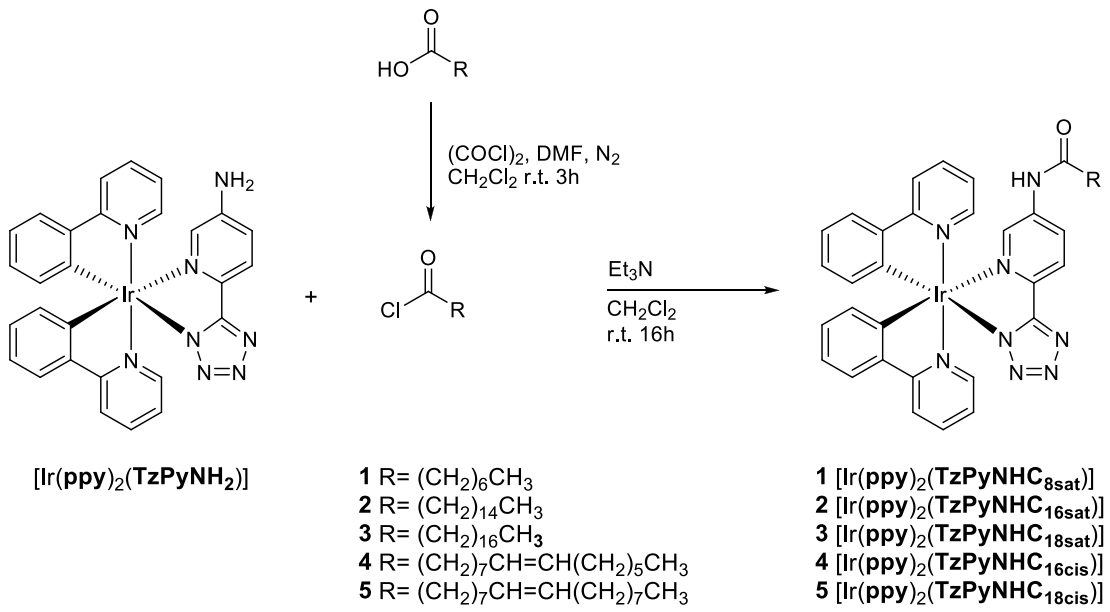

[Ir(**ppy**)$_2$(**TzPyNH$_2$**)]

1 R= $(CH_2)_6CH_3$
2 R= $(CH_2)_{14}CH_3$
3 R= $(CH_2)_{16}CH_3$
4 R= $(CH_2)_7CH{=}CH(CH_2)_5CH_3$
5 R= $(CH_2)_7CH{=}CH(CH_2)_7CH_3$

1 [Ir(**ppy**)$_2$(**TzPyNHC$_{8sat}$**)]
2 [Ir(**ppy**)$_2$(**TzPyNHC$_{16sat}$**)]
3 [Ir(**ppy**)$_2$(**TzPyNHC$_{18sat}$**)]
4 [Ir(**ppy**)$_2$(**TzPyNHC$_{16cis}$**)]
5 [Ir(**ppy**)$_2$(**TzPyNHC$_{18cis}$**)]

Figure 5.8 Scheme of the synthetic procedure for the preparation of different acyl chloride species (top). On the bottom, [Ir(**ppy**)$_2$(**TzPyNH$_2$**)] was reacted with the appropriate acyl chloride to form the corresponding saturated [Ir(**ppy**)$_2$(**TzPyNHC$_{nsat}$**)] (**n** = 8, 16, 18) and unsaturated [Ir(**ppy**)$_2$(**TzPyNHC$_{mcis}$**)] (**m** = 16, 18) iridium(III) complexes.

At the end of the reaction, the formed triethylammonium chloride was removed by precipitation with diethyl ether and the filtrate was washed by a 5% aqueous $NaHCO_3$ solution to eliminate the excess of fatty acids. Finally, the products were purified *via* column chromatography using basic alumina as stationary phase and a dichloromethane/methanol (99.5:0.5 v/v) solvent system mixture as eluent.

The saturated [Ir(**ppy**)$_2$(**TzPyNHC$_{8sat}$**)], [Ir(**ppy**)$_2$(**TzPyNHC$_{16sat}$**)] and [Ir(**ppy**)$_2$(**TzPyNHC$_{18sat}$**)] and the unsaturated [Ir(**ppy**)$_2$(**TzPyNHC$_{16cis}$**)] and [Ir(**ppy**)$_2$(**TzPyNHC$_{18cis}$**)] complexes were characterised by IR, ^{1}H NMR and ^{13}C NMR spectroscopy.

The IR spectra of all the complexes display strong peaks at around 2920 and 2850 cm^{-1} which are assigned to the C–H stretching of the aliphatic chain. Moreover,

the stretching of the C=O group and the tetrazolic C=N are visible at *ca*. 1700 and 1600 cm^{-1}, respectively. In addition to the aforementioned peaks, [Ir(**ppy**)$_2$(**TzPyNHC$_{16cis}$**)] and [Ir(**ppy**)$_2$(**TzPyNHC$_{18cis}$**)] exhibit the stretching of the =C–H, which falls at *ca*. 3040 cm^{-1}, supporting the presence of a double bond in the fatty acid chain.[407]

Spectroscopic characterisation by ^{1}H NMR was employed to further confirm the isolation of the desired products. In particular, the two doublet peaks in the range of 6.5 – 6.0 ppm (**Figure 5.9** – red boxes), which are characteristic of cyclometalated iridium(III) complexes,[126,133,273] have been observed for all the fatty acid-functionalised species. Furthermore, the presence of a singlet peak resonating at *ca.* 10.30 ppm is assigned to the N–H proton, which suggests the conversion of the amino group into an amide one (**Figure 5.9** – black boxes). In the case of [Ir(**ppy**)$_2$(**TzPyNHC$_{16cis}$**)] and [Ir(**ppy**)$_2$(**TzPyNHC$_{18cis}$**)], the unsaturation of the aliphatic chain was supported by the multiplet peak at *ca.* 5.30 ppm, which is not present in the ^{1}H NMR spectra of [Ir(**ppy**)$_2$(**TzPyNHC$_{8sat}$**)], [Ir(**ppy**)$_2$(**TzPyNHC$_{16sat}$**)] and [Ir(**ppy**)$_2$(**TzPyNHC$_{18sat}$**)] (**Figure 5.9** – top – purple box). Finally, all the other aliphatic protons resonate in the range between 2.5 and 1.2 ppm, with the methyl group downshifted at *ca.* 0.5 ppm (**Figure 5.9** – green boxes).

In the ^{13}C NMR spectra showed in **Figure 5.10**, the tetrazolic carbon **C$_T$** (red box) resonates at around 167.5 ppm for both the saturated [Ir(**ppy**)$_2$(**TzPyNHC$_{18sat}$**)] and unsaturated [Ir(**ppy**)$_2$(**TzPyNHC$_{18cis}$**)] complexes, indicating a coplanar arrangement of the pyridyl and tetrazolate ring, as in the case of the precursor [Ir(**ppy**)$_2$(**TzPyNH$_2$**)].[236] Moreover, the **C**O (black box) and the **C**H$_3$ peak (green box) resonating at *ca.* 172.0 and 14.0 ppm, respectively, confirm the coordination of the fatty acids to the iridium complexes.

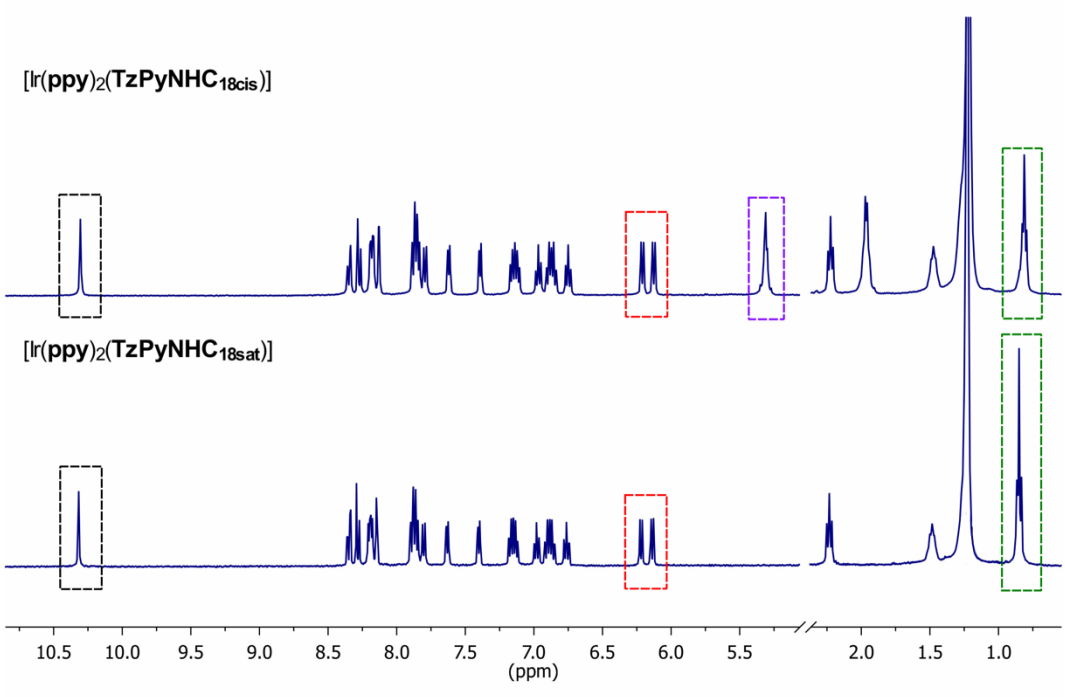

Figure 5.9 ^{1}H NMR in DMSO-d_6 for [Ir(**ppy**)$_2$(**TzPyNHC$_{18cis}$**)] (top) and [Ir(**ppy**)$_2$(**TzPyNHC$_{18sat}$**)] (bottom). In the spectra, the boxes highlight the significant peaks: N–H peak (black), double peaks of cyclometalated iridium species (red), C=C peak of the aliphatic fatty acid chain (purple) and CH_3 peak (green).

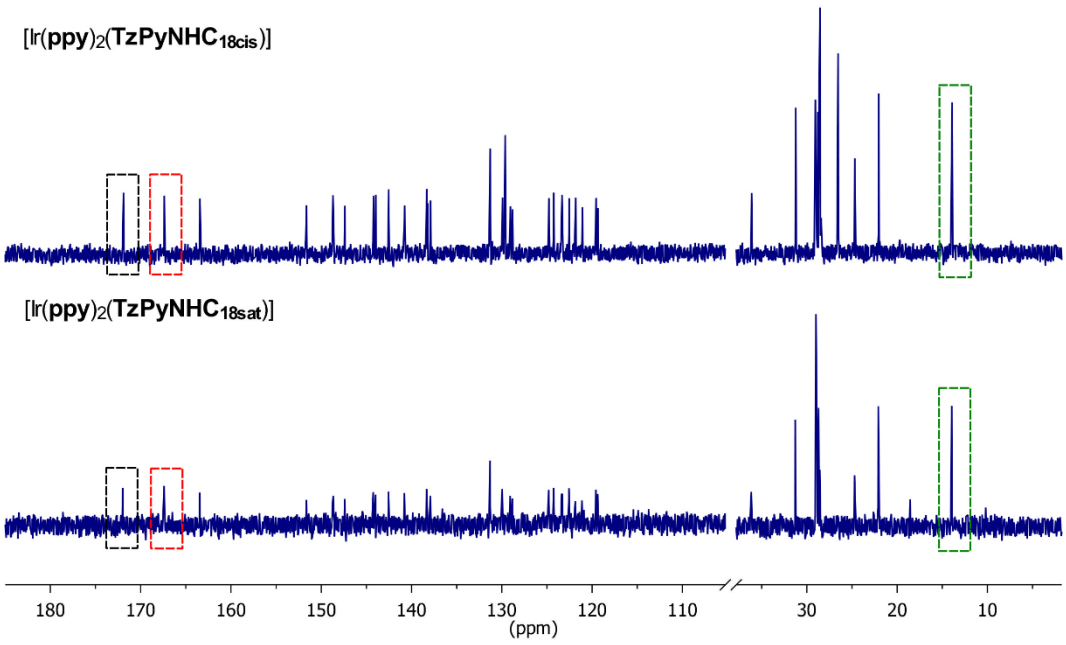

Figure 5.10 ^{13}C NMR in DMSO-d_6 for [Ir(**ppy**)$_2$(**TzPyNHC$_{18cis}$**)] (top) and [Ir(**ppy**)$_2$(**TzPyNHC$_{18sat}$**)] (bottom). In the spectra, the boxes highlight the significant peaks: CO peak (black), C_T peak (red) and CH_3 peak (green).

5.4 Photophysical Investigation

5.4.1 Absorption in Dichloromethane

The UV-Vis absorption spectral data of all the reported iridium(III) complexes in diluted dichloromethane solutions at 298 K have been summarised in **Table 5.4**.

The absorption profiles of [Ir(**ppy**)$_2$(**TzPyNHC$_{8sat}$**)], [Ir(**ppy**)$_2$(**TzPyNHC$_{16sat}$**)], [Ir(**ppy**)$_2$(**TzPyNHC$_{18sat}$**)], [Ir(**ppy**)$_2$(**TzPyNHC$_{16cis}$**)] and [Ir(**ppy**)$_2$(**TzPyNHC$_{18cis}$**)] are comparable, suggesting that the length of the fatty acid chains does not affect the absorption properties of the complexes (**Figure 5.11**), as expected.

Table 5.4 Absorption data of diluted (10^{-5} M) dichloromethane solutions of the reported complexes.

Complexes	**λ_{abs} [nm] (10^4 ε [$M^{-1}cm^{-1}$])**
[Ir(**ppy**)$_2$(**TzPyNHC$_{8sat}$**)]	264 (8.30), 364 (0.46), 420 (0.26)
[Ir(**ppy**)$_2$(**TzPyNHC$_{16sat}$**)]	264 (7.91), 386 (0.29), 423 (0.15)
[Ir(**ppy**)$_2$(**TzPyNHC$_{18sat}$**)]	264 (8.31), 386 (0.36), 422 (0.20)
[Ir(**ppy**)$_2$(**TzPyNHC$_{16cis}$**)]	264 (8.24), 386 (0.36), 421 (0.21)
[Ir(**ppy**)$_2$(**TzPyNHC$_{18cis}$**)]	264 (7.16), 386 (0.26), 418 (0.15)

According to previous spectroscopic studies on related iridium(III) phenylpyridine complexes,[112,124,126,139,231,311] the intense absorption bands in the UV region have been assigned to a spin-allowed ligand-centred (LC) π-π* transitions, localised on the cyclometalated **ppy** ligands. The less intense absorption bands in the visible region of the spectrum at λ > 350 nm are ascribed to spin-allowed and spin-forbidden ligand-to-ligand (LLCT) and metal-to-ligand charge transfer (MLCT) transitions. In particular, the MLCT transitions are associated with transition between the iridium metal centre and both the tetrazolate ligand and the cyclometalated **ppy**, as previously reported in numerous studies on analogous systems.[236–239]

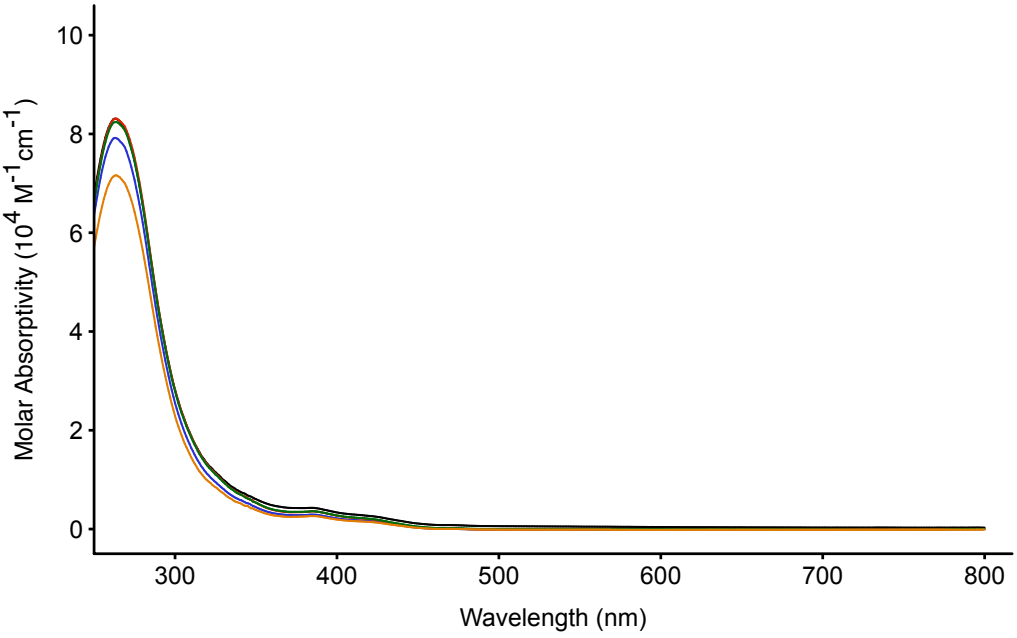

Figure 5.11 Absorption profiles of [Ir(**ppy**)$_2$(**TzPyNHC$_{8sat}$**)] (black), [Ir(**ppy**)$_2$(**TzPyNHC$_{16sat}$**)] (blue), [Ir(**ppy**)$_2$(**TzPyNHC$_{18sat}$**)] (red), [Ir(**ppy**)$_2$(**TzPyNHC$_{16cis}$**)] (green) and [Ir(**ppy**)$_2$(**TzPyNHC$_{18cis}$**)] (orange) in dichloromethane.

5.4.2 Emission in Dichloromethane

The photophysical properties of the fatty acid-functionalised iridium(III) tetrazolato complexes were measured in both air-equilibrated and degassed dichloromethane solutions and the data have been reported in **Table 5.5**.

Table 5.5 Photophysical data of diluted (10^{-5} M) dichloromethane solutions of the reported complexes.

Complex	λ_{em} [nm]	τ_{aer} [ns]	τ_{deaer} [ns]	Φ_{aer}[a]	Φ_{deaer}[a]
[Ir(**ppy**)$_2$(**TzPyNHC$_{8sat}$**)]	484, 514	83	393	0.006	0.071
[Ir(**ppy**)$_2$(**TzPyNHC$_{16sat}$**)]	484, 514	80	374	0.007	0.067
[Ir(**ppy**)$_2$(**TzPyNHC$_{18sat}$**)]	484, 514	83	383	0.007	0.060
[Ir(**ppy**)$_2$(**TzPyNHC$_{16cis}$**)]	484, 514	75	356	0.007	0.054
[Ir(**ppy**)$_2$(**TzPyNHC$_{18cis}$**)]	484, 514	75	360	0.008	0.060

[a] Measured versus [Ru(**bpy**)$_3$]$^{2+}$ in H_2O (Φ_r= 0.028).[274]

Photoexcitation at λ_{ex} = 350 nm of the complexes resulted in a yellow-green emission, consistent with the emission maxima of [Ir(**ppy**)$_2$(**TzPyNH$_2$**)], as described in Chapter 4, section 4.4.2. All the complexes are characterised by a vibronically structured emission bands, with vibronic progression spaced around 1,200 cm^{-1}. Previous studies on transition metal complexes have also demonstrated that featured emission profiles are typical for radiative decays from excited states derived from a mixture of charge transfer and ligand-centred nature (**Figure 5.12**).[77,306,379,386]

The length and degree of unsaturation of the fatty acid chains does not affect the photophysical properties of these complexes when compared to their precursor [Ir(**ppy**)$_2$(**TzPyNH$_2$**)]. Interestingly, these results also suggest that the localisation of the LUMO-type orbitals on the pyridyl ring of the tetrazolate ligand, as shown in previous studies on similar systems,[231,236–238,370] are not perturbed by the presence of the newly formed amide with respect to the amino group of the starting material.

In general, the emission intensity of these complexes is lower compared to the cyano-functionalised iridium(III) probes described in Chapter 2 – section 2.4.2.

Further investigations to describe this behaviour can be found in section 5.4.3 of this chapter.

The emission of [Ir(**ppy**)$_2$(**TzPyNHC$_{8sat}$**)], [Ir(**ppy**)$_2$(**TzPyNHC$_{16sat}$**)], [Ir(**ppy**)$_2$(**TzPyNHC$_{18sat}$**)], [Ir(**ppy**)$_2$(**TzPyNHC$_{16cis}$**)] and [Ir(**ppy**)$_2$(**TzPyNHC$_{18cis}$**)] is sensitive to the presence of molecular oxygen, confirming the assignment of the triplet state phosphorescence.[408,409] In fact, upon deoxygenation of the dichloromethane solutions, an increase of the quantum yield Φ and elongation of the excited state lifetime τ of all the complexes was recorded.

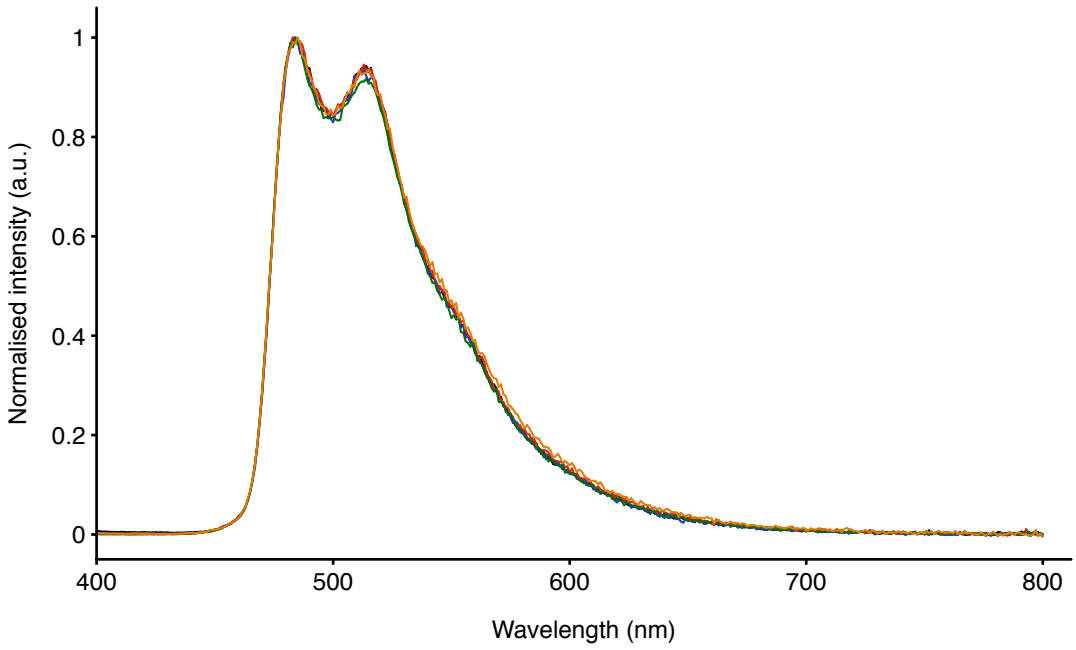

Figure 5.12 Normalised emission profiles of [Ir(**ppy**)$_2$(**TzPyNHC$_{8sat}$**)] (black), [Ir(**ppy**)$_2$(**TzPyNHC$_{16sat}$**)] (blue), [Ir(**ppy**)$_2$(**TzPyNHC$_{18sat}$**)] (red), [Ir(**ppy**)$_2$(**TzPyNHC$_{16cis}$**)] (green) and [Ir(**ppy**)$_2$(**TzPyNHC$_{18cis}$**)] (orange) in dichloromethane.

As expected, the calculation of the radiative (k_r) and non-radiative (k_{nr}) decay constants further confirmed that the fatty acid chains affect the photophysical proprieties of this family of probes in a similar manner, as demonstrated by the comparable values for both k_r and k_{nr} (**Table 5.6**).

On the other hand, some discrepancies can be highlighted when the radiative and non-radiative constants of the fatty acid-functionalised complexes and the precursor [Ir(**ppy**)$_2$(**TzPyNH$_2$**)] ($k_r = 0.027 \times 10^6$ s^{-1}; $k_{nr} = 0.942 \times 10^6$ s^{-1}) are compared. In particular, the radiative decay constant of [Ir(**ppy**)$_2$(**TzPyNH$_2$**)] results one order of magnitude smaller than the ones reported for the fatty acid analogues. A variety of factors affecting the dipole moment can be considered but, in general, the difference in k_r values can be tentatively ascribed to a higher contribution of the LC character in the formation of the emissive excited state, as described in Barigelletti's studies.[77]

Table 5.6 Radiative (k_r) and non-radiative (k_{nr}) decay constants in degassed dichloromethane solutions.

Complexes	k_r 10^6[s^{-1}][a]	k_{nr} 10^6[s^{-1}][b]
[Ir(**ppy**)$_2$(**TzPyNHC$_{8sat}$**)]	0.181	2.364
[Ir(**ppy**)$_2$(**TzPyNHC$_{16sat}$**)]	0.179	2.495
[Ir(**ppy**)$_2$(**TzPyNHC$_{18sat}$**)]	0.157	2.454
[Ir(**ppy**)$_2$(**TzPyNHC$_{16cis}$**)]	0.152	2.657
[Ir(**ppy**)$_2$(**TzPyNHC$_{18cis}$**)]	0.167	2.611

[a] Calculated as [Φ/τ] using measurements from deaerated dichloromethane solutions.
[b] Calculated as [$(1-\Phi)/\tau$] using measurements from the deaerated dichloromethane solutions.

5.4.3 Temperature-Dependent Luminescent Lifetime Measurements

Temperature-dependent luminescence lifetime measurements have been performed in order to rationalise the lower emission properties of the fatty acid-functionalised iridium(III) family in comparison to the cyano-functionalised iridium(III) probes discussed in Chapter 2, section 4.4.2.

[Ir(**ppy**)$_2$(**TzPyCN**)] and [Ir(**ppy**)$_2$(**TzPyNH$_2$**)] have been previously analysed in Chapter 4 - section 4.4.3, and the investigation highlighted the presence of a dark and accessible ^{3}MC excited state, which could be thermally populated at room temperature, increasing the non-radiative decay rate and lowering the emission intensity of the amino complex. On the contrary, the energy gap between the emissive ^{3}MLCT of [Ir(**ppy**)$_2$(**TzPyCN**)] and the ^{3}MC excited state was high enough to avoid any thermal access to the latter, consequentially showing an intense emission from the lowest-lying ^{3}MLCT excited state. Hence, [Ir(**ppy**)$_2$(**TzPyCN**)] and [Ir(**ppy**)$_2$(**TzPyNH$_2$**)] have been considered the extreme cases for this investigation.

The excited state lifetimes of [Ir(**ppy**)$_2$(**TzPyNHC$_{16sat}$**)], [Ir(**ppy**)$_2$(**TzPyNH$_2$**)] and [Ir(**ppy**)$_2$(**TzPyCN**)] have been recorded in air-equilibrated dichloromethane solutions (*ca*. 10^{-5} M) in a range of temperatures between 198 and 298 K. The results have been plotted as the logarithm of the rate constant (k_{obs}) against the inverse temperature (1/T) in an Arrhenius-like plot, depicted in **Figure 5.13** (refer to Chapter 4 – section 4.4.3 for detailed explanation of the equations).

[Ir(**ppy**)$_2$(**TzPyNHC$_{16sat}$**)] and [Ir(**ppy**)$_2$(**TzPyNH$_2$**)] exhibit the same behaviour, characterised by non-radiative decay rate as function of the temperature of the system. Higher k_{nr} have been measured at room temperature (298 K) with respect to the cold dichloromethane solution (198 K), suggesting the presence of a thermally accessible ^{3}MC excited state.[375] On the other hand, [Ir(**ppy**)$_2$(**TzPyCN**)] showed constant non-radiative decay values, which result independent from the changing in the temperature of the system. Thus, the emissive performances of this probe are not affected by the presence of the dark ^{3}MC excited state and are comparable at all temperatures.

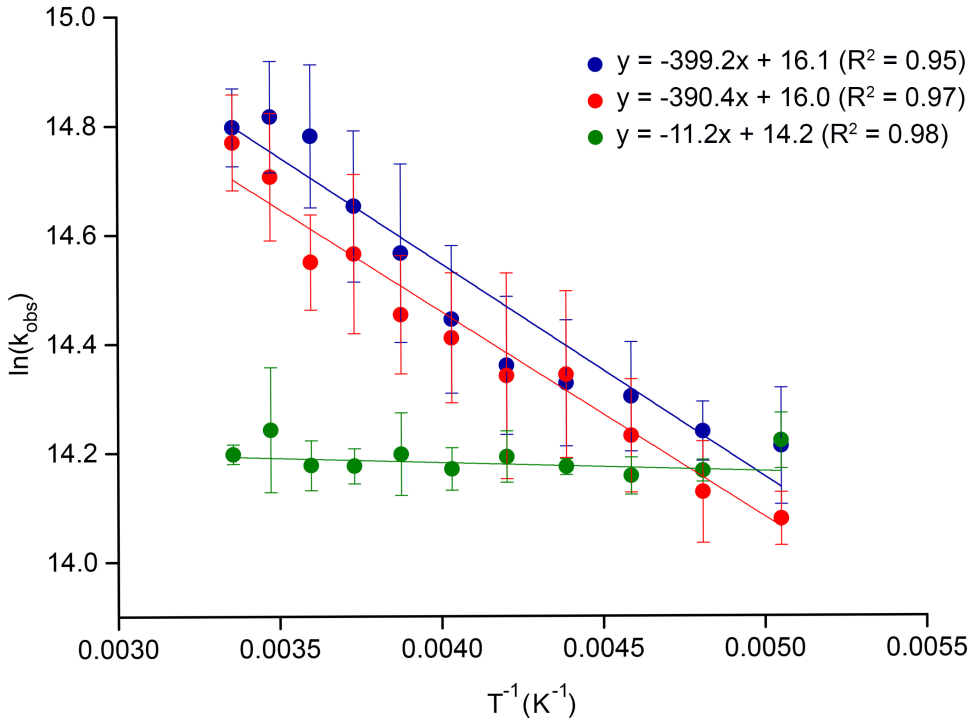

Figure 5.13 Arrhenius plot of the rate constants of [Ir(**ppy**)$_2$(**TzPyNHC$_{16sat}$**)] (blue), [Ir(**ppy**)$_2$(**TzPyNH$_2$**)] (red) and [Ir(**ppy**)(**TzPyCN**)] (green). The trendlines and the R^2 values have been reported.

5.4.4 Absorption in Aqueous and Lipophilic Solvents

The absorption properties of [Ir(**ppy**)$_2$(**TzPyNHC$_{8sat}$**)], [Ir(**ppy**)$_2$(**TzPyNHC$_{16sat}$**)], [Ir(**ppy**)$_2$(**TzPyNHC$_{18sat}$**)], [Ir(**ppy**)$_2$(**TzPyNHC$_{16cis}$**)] and [Ir(**ppy**)$_2$(**TzPyNHC$_{18cis}$**)] have been investigated in lipophilic and aqueous media in order to explore the possible modulation of the probes' behaviour in different cellular compartments.

All the UV-Vis absorption data have been summarised in **Table 5.7** and have been illustrated from **Figure 5.14** to **Figure 5.18**.

A small percentage of DMSO (2%) was employed to increase the solubility of the fatty acid-functionalised iridium(III) complexes in the aqueous media, as previously described in Chapter 4 – section 4.4.4.

In general, for all the complexes the absorption bands in aqueous solvents and ethyl laurate follow the same trend that the ones described for diluted dichloromethane solutions, presented in section 5.4.1 of this chapter. In particular, moderately intense bands are observed at 280 – 300 nm, which can be attributed to the spin-allowed ligand-centred (LC) π-π* transitions of the cyclometalated **ppy** moieties. Moreover, one additional weaker MLCT [dπ(Ir)→π*(**ppy**)] and [dπ(Ir)→π*(**TzPyNHC$_x$**)] absorption band or shoulder with molar extinction coefficient on the order of 0.5 – 1.0 × 10^4 $M^{-1}cm^{-1}$ (depending of the solvents) was also observed at the lower energy between 390 – 400 nm. Finally, the absorption band in the visible region between 410 - 425 nm can be assigned to the spin-forbidden MLCT [dπ(Ir)→π*(**ppy**)] and [dπ(Ir)→π*(**TzPyNHC$_x$**)] transitions, with reference to previous spectroscopic study of related iridium(III) tetrazolato complexes.[231,236–238,370]

Notably, the complexes bearing a saturated fatty acid chain [Ir(**ppy**)$_2$(**TzPyNHC$_{8sat}$**)], [Ir(**ppy**)$_2$(**TzPyNHC$_{16sat}$**)], [Ir(**ppy**)$_2$(**TzPyNHC$_{18sat}$**)] showed higher solubility issues and signs of precipitation in lysosomal fluid solutions in comparison to the unsaturated aliphatic chain - substituted [Ir(**ppy**)$_2$(**TzPyNHC$_{16cis}$**)] and [Ir(**ppy**)$_2$(**TzPyNHC$_{18cis}$**)]. This behaviour has not been observed in the PBS and water, the latter possessing a very similar pH with respect to the lysosomal fluid solution (pH = 7 and 7.4, respectively).

Table 5.7 Absorption data of aqueous and lipophilic solutions (10^{-5} M) of the reported complexes.

Complex	Solvent[a]	λ_{abs} [nm] (10^4 ε [$M^{-1}cm^{-1}$])
[Ir(**ppy**)$_2$ (**TzPyNHC$_{8sat}$**)]	H_2O	287 (4.17), 393 (1.56), 426 (1.20)
	Lys. Fluid	294 (0.43)
	PBS	286 (2.71), 395 (0.87), 431 (0.62)
	Ethyl Laurate	285 (5.90), 413 (0.76), 457 (0.35)
[Ir(**ppy**)$_2$ (**TzPyNHC$_{16sat}$**)]	H_2O	280 (2.63), 392 (0.45), 433 (0.28)
	Lys. Fluid	293 (0.19)
	PBS	289 (0.92), 391 (0.44), 433 (0.40)
	Ethyl Laurate	285 (2.43),412 (0.95), 455 (0.73)
[Ir(**ppy**)$_2$ (**TzPyNHC$_{18sat}$**)]	H_2O	281 (5.27), 393 (2.22), 452 (1.77)
	Lys. Fluid	265 (0.13)
	PBS	281 (0.43)
	Ethyl Laurate	284 (0.89), 416 (0.56), 455 (0.49)
[Ir(**ppy**)$_2$ (**TzPyNHC$_{16cis}$**)]	H_2O	284 (6.38), 397 (1.33), 435 (0.84)
	Lys. Fluid	291 (1.30), 396 (0.63), 433 (0.48)
	PBS	284 (2.57), 395 (0.90), 428 (0.67)
	Ethyl Laurate	277 (2.71), 392 (0.27), 460 (0.17)
[Ir(**ppy**)$_2$ (**TzPyNHC$_{18cis}$**)]	H_2O	282 (6.04), 394 (1.28), 431 (0.85)
	Lys. Fluid	287 (1.19), 395 (0.58), 436 (0.43)
	PBS	285 (2.67), 394 (0.88), 433 (0.60)
	Ethyl Laurate	278 (3.73), 395 (0.45), 436 (0.27)

[a] Aqueous solvents contain 2% DMSO.

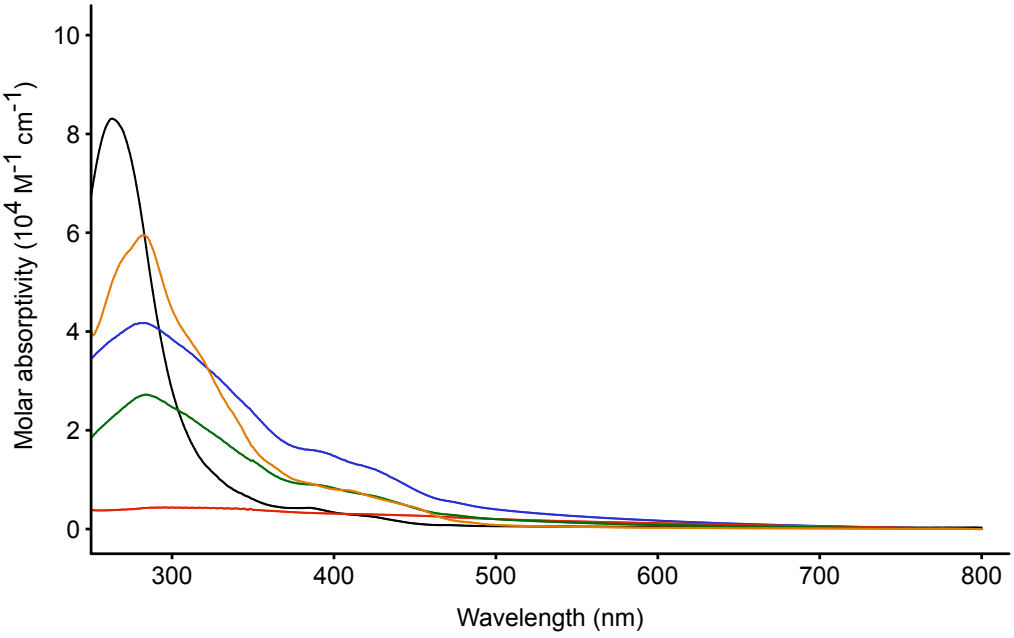

Figure 5.14 Absorption profiles of [Ir(**ppy**)$_2$(**TzPyNHC$_{8sat}$**)] in dichloromethane (black), H_2O (blue), lys. fluid (red), PBS (green) and ethyl laurate (orange).

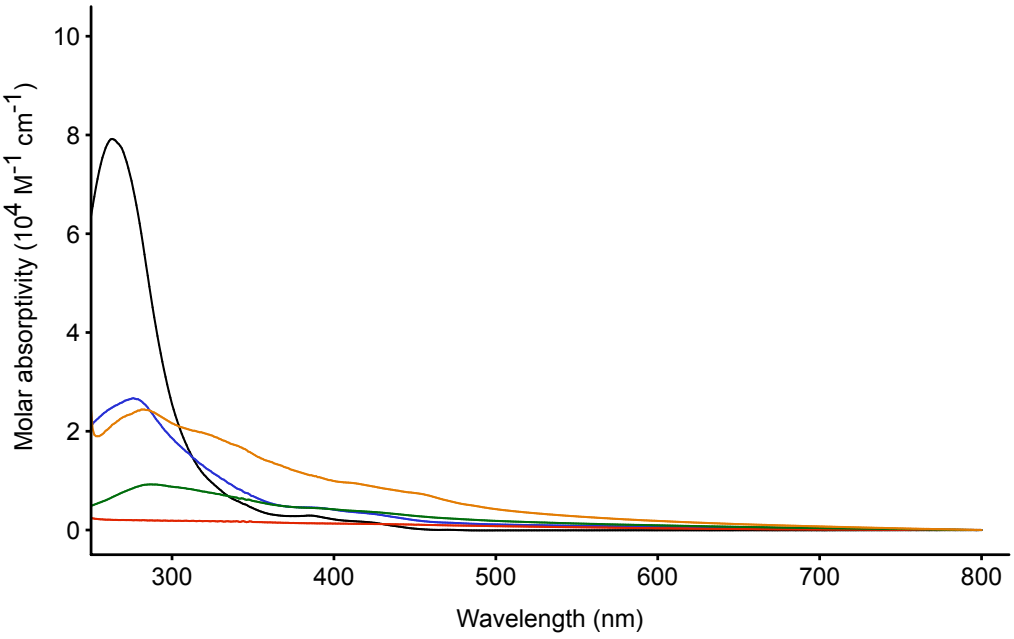

Figure 5.15 Absorption profiles of [Ir(**ppy**)$_2$(**TzPyNHC$_{16sat}$**)] in dichloromethane (black), H_2O (blue), lys. fluid (red), PBS (green) and ethyl laurate (orange).

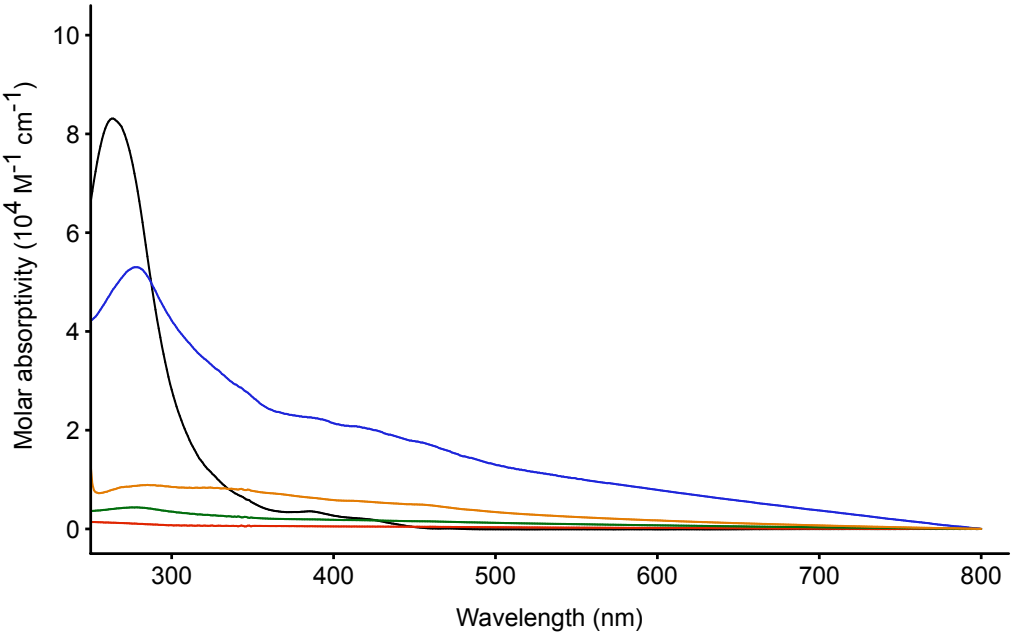

Figure 5.16 Absorption profiles of [Ir(**ppy**)$_2$(**TzPyNHC$_{18sat}$**)] in dichloromethane (black), H_2O (blue), lys. fluid (red), PBS (green) and ethyl laurate (orange).

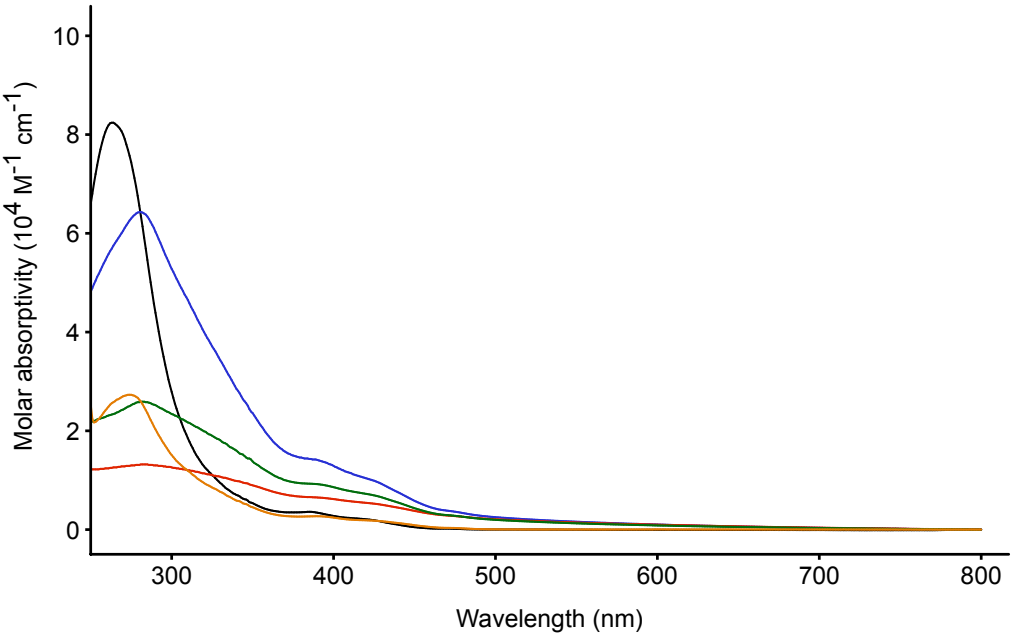

Figure 5.17 Absorption profiles of [Ir(**ppy**)$_2$(**TzPyNHC$_{16cis}$**)] in dichloromethane (black), H_2O (blue), lys. fluid (red), PBS (green) and ethyl laurate (orange).

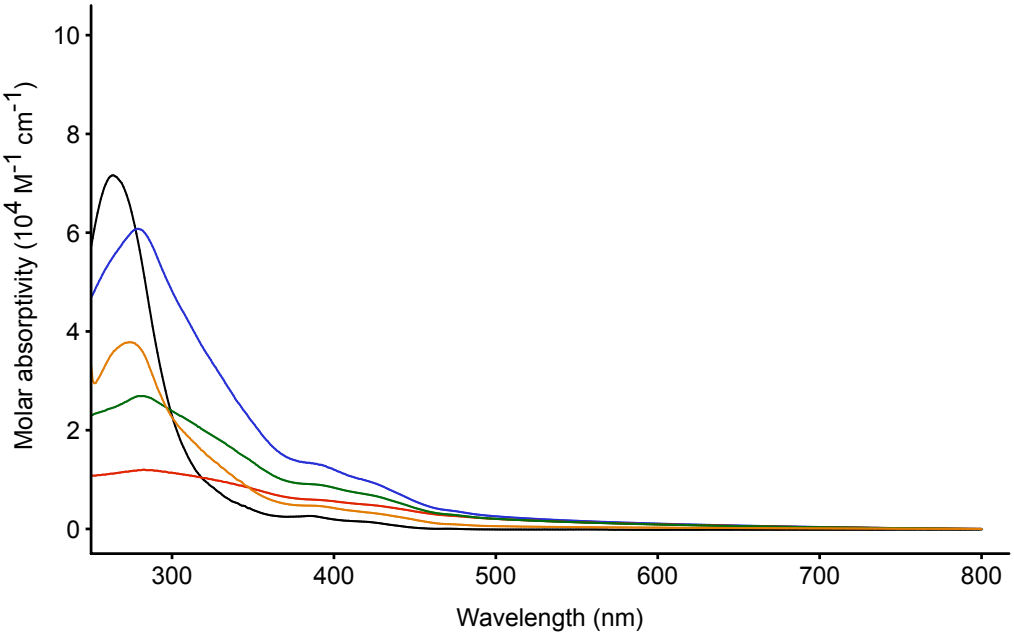

Figure 5.18 Absorption profiles of [Ir(**ppy**)$_2$(**TzPyNHC$_{18cis}$**)] in dichloromethane (black), H_2O (blue), lys. fluid (red), PBS (green) and ethyl laurate (orange).

5.4.5 Emission in Aqueous and Lipophilic Solvents

The photophysical characterisation in aqueous and lipophilic solvents for the reported fatty acid-functionalised iridium(III) tetrazolato complexes has been listed in **Table 5.8**.

Table 5.8 Photophysical data of aqueous and lipophilic solutions (10^{-5} M) of the reported complexes.

Complex	Solvent[a]	λ_{em} [nm]	τ_{aer} [ns][b]	Φ_{aer}[c]
[Ir(**ppy**)$_2$ (**TzPyNHC$_{8sat}$**)]	H_2O	493, 520	55 (81), 277 (19)	0.004
	Lys. Fluid	500, 530	72 (77), 422 (23)	0.042
	PBS	493, 520	52 (79), 321 (21)	0.009
	Ethyl Laurate	493, 523	48 (52), 116 (48)	0.023
[Ir(**ppy**)$_2$ (**TzPyNHC$_{16sat}$**)]	H_2O	495, 526	53 (43), 197 (57)	0.009
	Lys. Fluid	500, 530	45 (50), 214 (50)	0.024
	PBS	495, 526	44 (45), 179 (55)	0.013
	Ethyl Laurate	495, 526	78 (65), 243 (35)	0.015
[Ir(**ppy**)$_2$ (**TzPyNHC$_{18sat}$**)]	H_2O	498, 530	195 (57), 999 (43)	0.024
	Lys. Fluid	502, 526	121 (67), 509 (33)	0.101
	PBS	498, 530	187 (63), 734 (37)	0.082
	Ethyl Laurate	498, 530	173 (70), 873 (30)	0.086
[Ir(**ppy**)$_2$ (**TzPyNHC$_{16cis}$**)]	H_2O	496, 548	70 (25), 946 (75)	0.009
	Lys. Fluid	496, 548	51 (66), 466 (34)	0.013
	PBS	496, 548	59 (55), 462 (45)	0.014
	Ethyl Laurate	489, 521	96	0.059
[Ir(**ppy**)$_2$ (**TzPyNHC$_{18cis}$**)]	H_2O	496, 547	34 (59), 339 (41)	0.005
	Lys. Fluid	493, 537	36 (68), 249 (32)	0.015
	PBS	493, 520	58 (79), 321 (21)	0.011
	Ethyl Laurate	493, 523	48 (52), 116 (48)	0.049

[a] Aqueous solvents contain 2% DMSO. [b] For the biexponential excited state lifetime (τ), the relative weights of the exponential curves are reported in parentheses. [c] Measured versus [Ru(**bpy**)$_3$]$^{2+}$ in H_2O ($\Phi_r = 0.028$).[274]

[Ir(**ppy**)$_2$(**TzPyNHC$_{8sat}$**)], [Ir(**ppy**)$_2$(**TzPyNHC$_{16sat}$**)] and [Ir(**ppy**)$_2$(**TzPyNHC$_{18sat}$**)] (**Figure 5.19 - Figure 5.21**) maintained the same vibronically structured emission profile in aqueous and lipophilic solvents, as previously recorded for the dichloromethane solutions (section 5.4.2 of this chapter), which is typical of emission from a combination of ^{3}MLCT and ^{3}LC excited states.[77,238] The analysis of the emission bands in various solvents highlights a solvatochromic behaviour, characterised by *ca.* 10 – 15 nm bathochromic shift upon increasing the polarity of the system from dichloromethane to the aqueous media. Interestingly, emission in ethyl laurate was red-shifted with respect to the dichloromethane solution, despite the low polarity of the lipophilic medium. In general, no significant differences were recorded between the various solvents, in particular the three aqueous media. Therefore, the emission maxima of these complexes cannot be used to discriminate the different environments within cells.

[Ir(**ppy**)$_2$(**TzPyNHC$_{16cis}$**)] and [Ir(**ppy**)$_2$(**TzPyNHC$_{18cis}$**)] (**Figure 5.22 - Figure 5.23**) displayed a different trend in comparison to [Ir(**ppy**)$_2$(**TzPyNHC$_{8sat}$**)], [Ir(**ppy**)$_2$(**TzPyNHC$_{16sat}$**)] and [Ir(**ppy**)$_2$(**TzPyNHC$_{18sat}$**)], implying that the unsaturation present in the fatty acid chains can play a role in lipophilic and aqueous media, in opposition to what has been observed in dichloromethane solutions.

Firstly, the emission profiles of both [Ir(**ppy**)$_2$(**TzPyNHC$_{16cis}$**)] and [Ir(**ppy**)$_2$(**TzPyNHC$_{18cis}$**)] in aqueous solvents appear different in comparison to the ones in dichloromethane and ethyl laurate, in terms of intensity and shape, as depicted in **Figure 5.22** and **Figure 5.23**. While in the case of saturated species, the intensity and shape of the two bands were relatively similar (refer to **Figure 5.19 - Figure 5.21**), in the case of the unsaturated species the band at longer wavelength shows the double of the intensity and the profile is broader with respect to the band at *ca.* 490 nm. These results suggest that the emission in aqueous environment showed a smaller LC contribution than the one in dichloromethane and ethyl laurate.[256,275]

Secondly, a bathochromic shift is recorded for the aqueous media in comparison to the organic solvent, with a more marked shift of the band at 514 nm (*ca.* 10 – 15 nm) in comparison to the band at 484 nm (*ca.* 15 – 30 nm). Moreover, the emission from ethyl laurate solution is *ca.* 20 nm blue-shifted in comparison to the aqueous media. This characteristic can be potentially used to discriminate the emission of the probes in aqueous and lipophilic compartment, when uptake inside the cells.

The excited state lifetimes are comparable for all the iridium(III) complexes and also for both the aqueous and lipophilic solvents, with values of *ca.* 100 ns for the shorter component and around 400 – 600 ns for the longer one. A simple trend for the luminescent quantum yield values was difficult to rationalise, but in general slightly higher Φ have been recorded for ethyl laurate solutions.

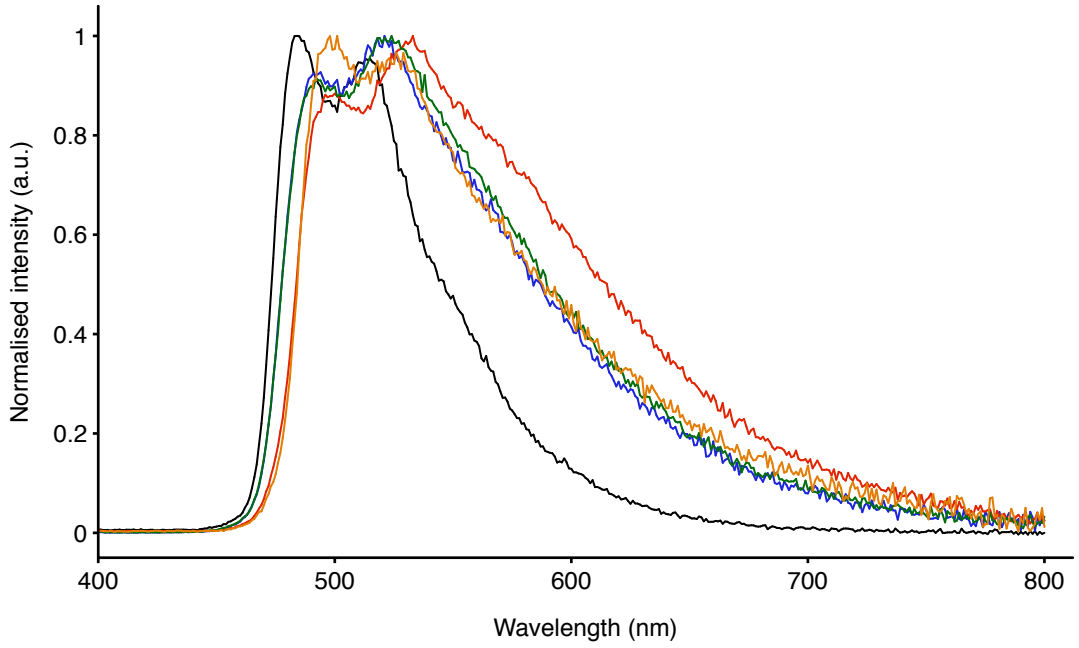

Figure 5.19 Normalised emission profiles of [Ir(**ppy**)$_2$(**TzPyNHC$_{8sat}$**)] in dichloromethane (black), H_2O (blue), lys. fluid (red), PBS (green) and ethyl laurate (orange).

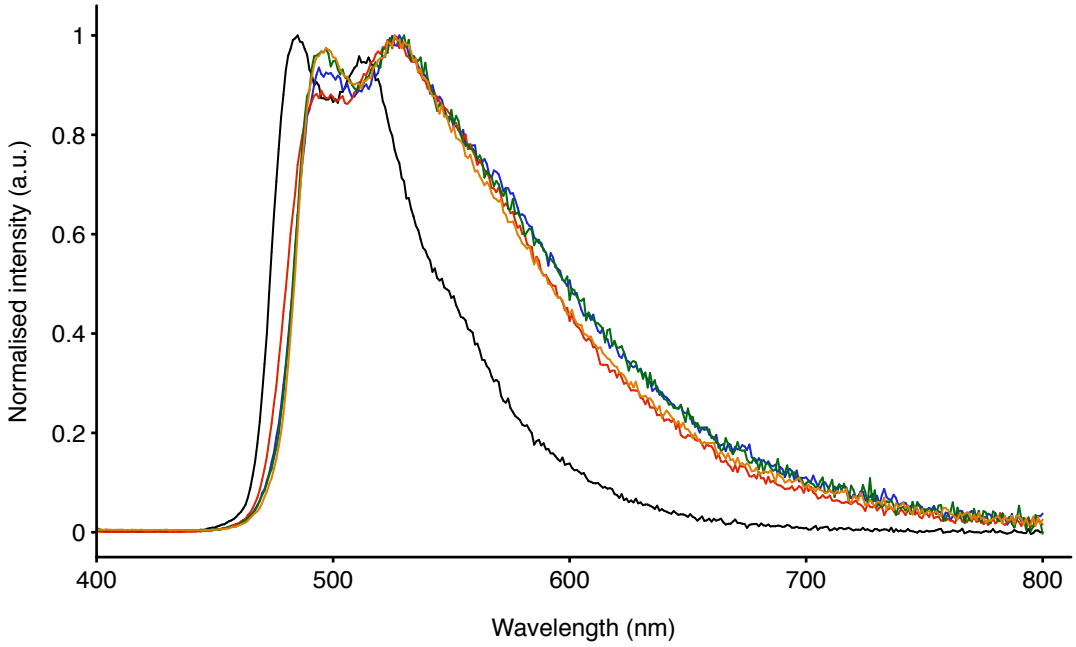

Figure 5.20 Normalised emission profiles of [Ir(**ppy**)$_2$(**TzPyNHC$_{16sat}$**)] in dichloromethane (black), H_2O (blue), lys. fluid (red), PBS (green) and ethyl laurate (orange).

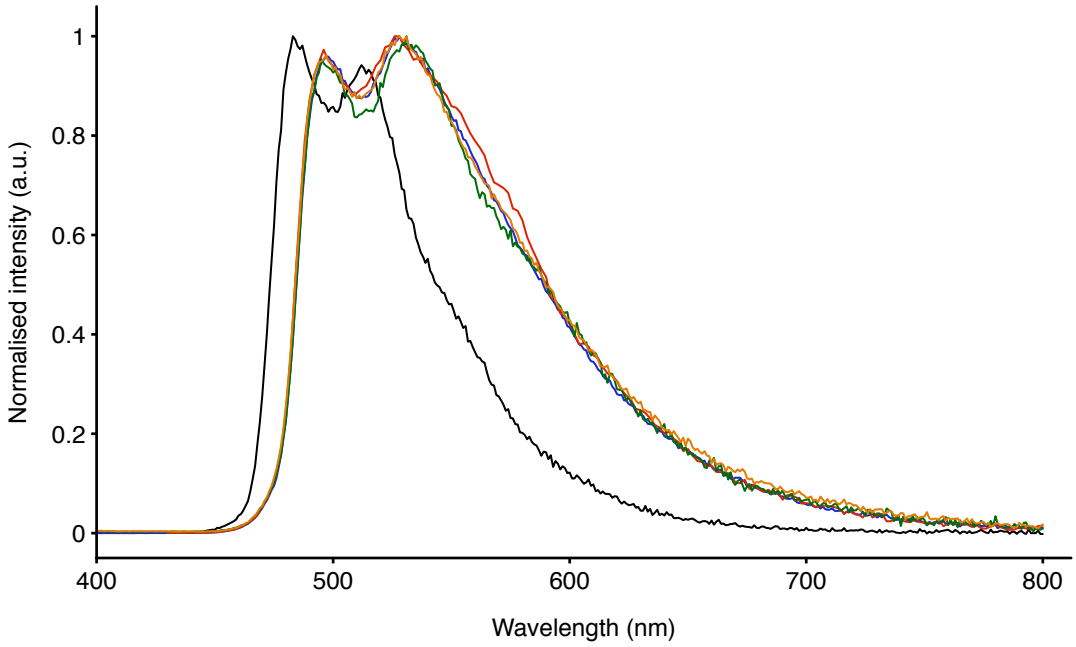

Figure 5.21 Normalised emission profiles of [Ir(**ppy**)$_2$(**TzPyNHC$_{18sat}$**)] in dichloromethane (black), H_2O (blue), lys. fluid (red), PBS (green) and ethyl laurate (orange).

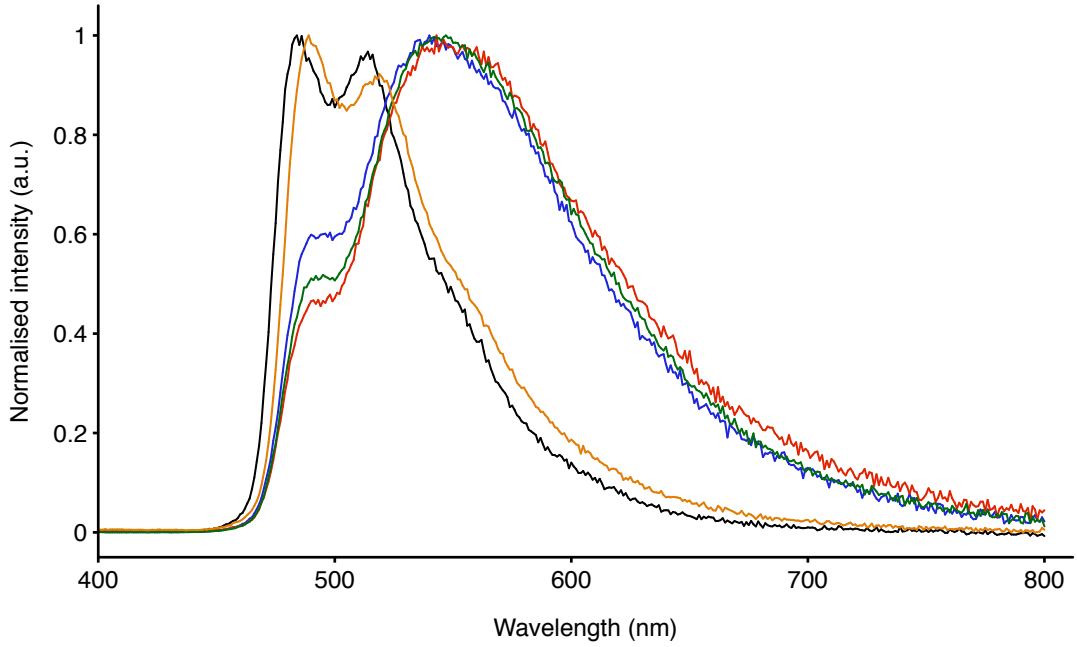

Figure 5.22 Normalised emission profiles of [Ir(**ppy**)$_2$(**TzPyNHC$_{16cis}$**)] in dichloromethane (black), H_2O (blue), lys. fluid (red), PBS (green) and ethyl laurate (orange).

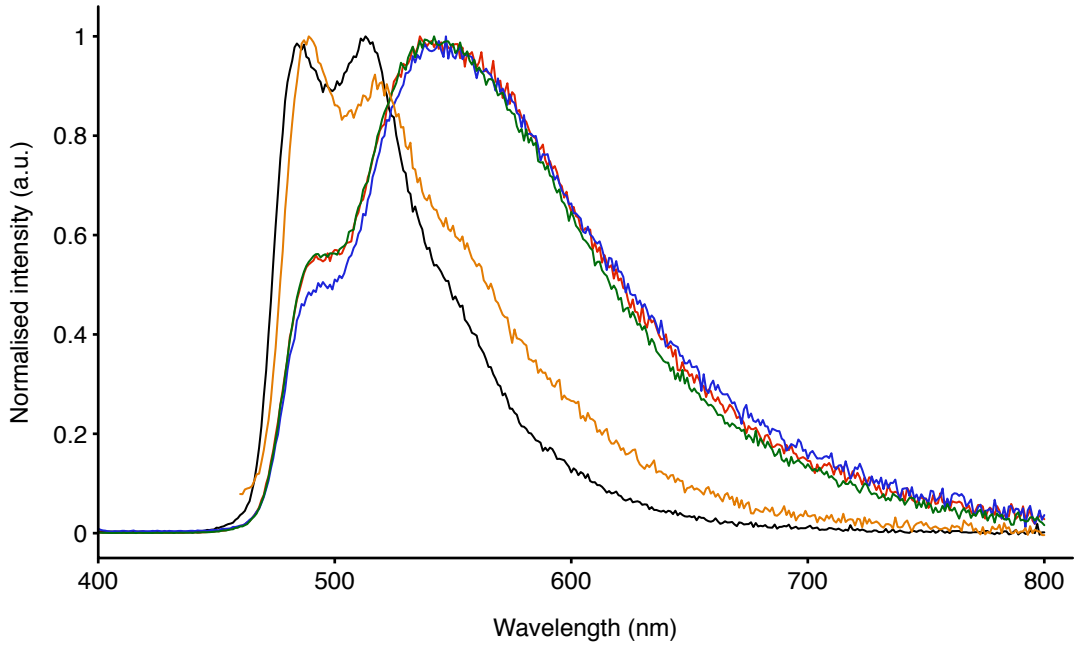

Figure 5.23 Normalised emission profiles of [Ir(**ppy**)$_2$(**TzPyNHC$_{18cis}$**)] in dichloromethane (black), H_2O (blue), lys. fluid (red), PBS (green) and ethyl laurate (orange).

5.5 Conclusions

In this chapter, a family of five fatty acid-functionalised iridium(III) complexes, [Ir(**ppy**)$_2$(**TzPyNHC$_{8sat}$**)], [Ir(**ppy**)$_2$(**TzPyNHC$_{16sat}$**)], [Ir(**ppy**)$_2$(**TzPyNHC$_{18sat}$**)], [Ir(**ppy**)$_2$(**TzPyNHC$_{16cis}$**)] and [Ir(**ppy**)$_2$(**TzPyNHC$_{18cis}$**)], have been discussed.

A variety of synthetic routes has been employed in the attempt of functionalise CN**PyNH$_2$** or H**TzPyNH$_2$** with the appropriate fatty acid chain, but issues during the purification process have made impossible the separation of the desired products from the unreacted starting material and byproducts. However, due to the enhanced solubility of [Ir(**ppy**)$_2$(**TzPyNH$_2$**)] in dichloromethane, the reaction with the different acyl chloride species was successfully achieved and the purification *via* column chromatography allowed the isolation of the final fatty acid-functionalised complexes.

The photophysical investigation in dichloromethane solution showed a yellow-green emission for all the complexes, derived from a mixture of ^{3}MLCT and ^{3}LC excited state and which is comparable with the emission maxima exhibits by the starting material [Ir(**ppy**)$_2$(**TzPyNH$_2$**)]. This result suggests that the LUMO-type orbitals on the pyridyl ring of the tetrazolate ligand are not affected by the substitution of the amino group to an amide one. Moreover, the temperature-dependent lifetime measurements on [Ir(**ppy**)$_2$(**TzPyNHC$_{16cis}$**)] have confirmed the presence of a lower-lying ^{3}MC excited state, which can be thermally populated and is responsible of the reduced emission intensity of the fatty acid-functionalised complexes in comparison to [Ir(**ppy**)$_2$(**TzPyCN**)].

The photophysical properties of this family of complexes have been explored in aqueous and lipophilic solvents to evaluate their applicability in biological environment. In general, the emission was red-shifted upon increase of the medium polarity, with a more marked solvatochromic behaviour for [Ir(**ppy**)$_2$(**TzPyNHC$_{16cis}$**)] and [Ir(**ppy**)$_2$(**TzPyNHC$_{18cis}$**)] in comparison to [Ir(**ppy**)$_2$(**TzPyNHC$_{8sat}$**)], [Ir(**ppy**)$_2$(**TzPyNHC$_{16sat}$**)] and [Ir(**ppy**)$_2$(**TzPyNHC$_{18sat}$**)]. Moreover, the unsaturation of the appended fatty acid chains affects the emission profile in aqueous media for [Ir(**ppy**)$_2$(**TzPyNHC$_{16cis}$**)] and [Ir(**ppy**)$_2$(**TzPyNHC$_{18cis}$**)], which becomes broader, suggesting the smaller contribution from the ^{3}LC excited state to the emission.

Interestingly, this behaviour was not recorded in dichloromethane solution, where the different degree of saturation of the fatty acids did not affect neither the emission maxima nor the profile.

A lack of major variations between water, lysosomial fluid and PBS have been recorded, excluding these probes from the application in cellular pH-sensing field. Nevertheless, due to the emissive nature of these probes in all the assessed solvents for the photophysical investigation, this new family of fatty acid-functionalised iridium(III) probes can be tested for biological imaging applications.

5.6 Experimental

5.6.1 General Procedures

General procedures have been conducted as outline in Chapter 2 – section 2.6.1, unless otherwise stated.

The complex [Ir(**ppy**)$_2$(**TzPyNH$_2$**)] was prepared according to the synthetic method discussed in Chapter 4 – section 2.6.4.

For the NMR characterisation, carbon and proton of all the iridium(III) tetrazolato species were labelled as pyridinic (A), phenylic (B), tetrazolic (T) and, alifatic (F), according to **Figure 5.24**.

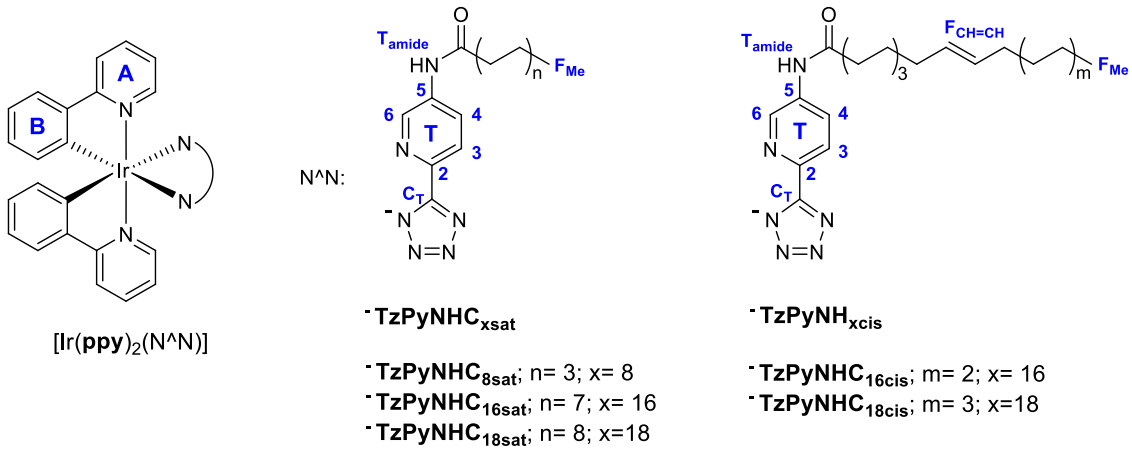

Figure 5.24 NMR referencing layout.

5.6.2 Photophysical Measurements

Photophysical measurements have been carried out as outlined in Chapter 2 – section 2.6.2, unless otherwise stated.

5.6.3 Synthesis

CNPyNHC$_{8sat}$

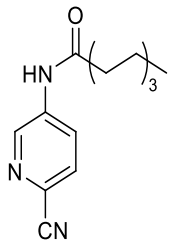

5-Amino-2-pyridinecarbonitrile (0.150 g, 0.126 mmol) and triethylamine (0.26 mL, 1.882 mmol) were combined in 10 mL of dry dichloromethane in inert atmosphere of N_2. Octanoyl chloride (0.22 mL, 1.260 mmol) was dissolved in 3 mL of dry dichloromethane, added dropwise to the reaction mixture and stirred at room temperature overnight. The solution was concentrated and diethyl ether was added. A white precipitate was formed and filtered. The solvent was evaporated under reduce pressure and the solid suspended in hexane (10 mL) and washed with NaOH aqueous solution (0.1 M). The aqueous phase was discarded and the off-white solid collected by vacuum filtration. Yield: 0.138 g (45%). M.P. 100 – 102 °C. IR (ν / cm^{-1}): 2926 s, 2854 s (CH stretch saturated C–C), 2227 w (C≡N), 1680 w (C=O functionalised stretch). ^{1}H NMR (δ / ppm, DMSO-*d*$_6$): 10.55 (s, 1H, **H$_{Tamide}$**), 8.86 (s, 1H, **H$_{T6}$**), 8.27 (d, 1H, **H$_{T4}$**, J = 8.6 Hz), 7.96 (d, 1H, **H$_{T3}$**, J = 8.8 Hz), 1.62 – 1.59 (m, 2H, **2H$_F$**), 1.29 (broad s, 10H, **10H$_F$**), 0.87 (t, 3H, **3H$_{FMe}$**, J = 6.0 Hz). ^{13}C NMR (δ / ppm, DMSO-*d*$_6$): 172.6 (**C**O)**,** 141.7 (**C**H$_{T6}$), 139.1 (**C**N), 129.6 (**C**H$_{T4}$), 125.6 (**C$_{T2}$**), 125.5 (**C**H$_{T3}$), 117.7 (**C$_{T5}$**), 36.3 (**C**H$_F$), 31.1 (**C**H$_F$), 28.5 (**C**H$_F$), 28.4 (**C**H$_F$), 24.7 (**C**H$_F$), 22.0 (**C**H$_F$), 13.9 (**C**H$_{FMe}$). Anal.Calcd for CN**PyNHC$_{8sat}$**·0.3(diethyl ether): C, 68.20; H, 8.34; N, 15.56. Found: C, 67.24; H, 8.48; N, 15.57.

[Ir(ppy)$_2$(TzPyNHC$_{8sat}$)]

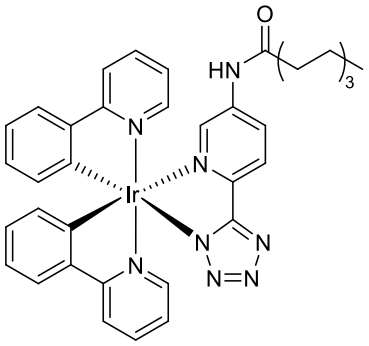

[Ir(**ppy**)$_2$(**TzPyNH$_2$**)] (0.100 g, 0.152 mmol) and triethylamine (0.32 mL, 2.270 mmol) were combined in 10 mL of dry dichloromethane. Octanoyl chloride (0.26 mL, 1.520 mmol) was dissolved in 3 mL of dry dichloromethane, added dropwise to the reaction mixture and stirred at room temperature overnight. The solution was concentrated and diethyl ether was added. A white precipitate was formed and filtered. The filtrate was washed with $NaHCO_3$ 5% solution (3 × 15 mL). The organic phase was dried over $MgSO_4$ anhydrous and the product was purified *via* column chromatography using Brockmann I grade basic alumina-filled as stationary phase and a dichloromethane/methanol (99.5:0.5 v/v) solvent system mixture as eluent. The targeted complex eluted as the second fraction (yellow). Yield: 0.091 g (76%). M.P. 252 – 254 °C. IR (ν / cm^{-1}): 2924 s, 2853 s (CH stretch saturated C–C), 1699 w (C=O functionalised stretch), 1606 w (tetrazole C=N). ^{1}H NMR (δ / ppm, DMSO-*d$_6$*): 10.31 (s, 1H, **H$_{Tamide}$**), 8.34 (d, 1H, **H$_{T4}$**, J = 8.7 Hz), 8.27 (d, 1H, **H$_{T3}$**, J = 8.8 Hz), 8.20 – 8.17 (m, 2H, **2H$_A$**), 8.14 (s, 1H, **H$_{T6}$**), 7.89 – 7.84 (m, 3H, **3H$_A$**), 7.79 (d, 1H, **H$_B$**, J = 7.7 Hz), 7.62 (d, 1H, **H$_B$**, J = 5.6 Hz), 7.39 (d, 1H, **H$_B$**, J = 5.6 Hz), 7.18 – 7.11 (m, 2H, **2H$_A$**), 6.97 (app. t., 1H, **H$_A$**, splitting = 7.4 Hz), 6.91 – 6.84 (m, 2H, **2H$_B$**), 6.75 (app. t., 1H, **H$_A$**, splitting = 7.4 Hz), 6.21 (d, 1H, **H$_B$**, J = 7.5 Hz), 6.13 (d, 1H, **H$_B$**, J = 7.5 Hz), 2.23 (t, 2H, **2H$_F$**, J = 7.5 Hz), 1.52 – 1.45 (m, 2H, **2H$_F$**), 1.22 (broad s, 24H, **24H$_F$**), 0.84 (t, 3H, **3H$_{FMe}$**, J = 7.2 Hz). ^{13}C NMR (δ / ppm, DMSO-*d$_6$*): 172.0 (**C**O)**,** 167.4 (**C$_T$**), 167.3 (**C$_{T2}$**), 163.4 (**C$_A$**), 151.6 (**C$_B$**), 148.7 (**2C**H$_B$), 147.4 (**C$_B$**), 144.2 (**C$_B$**), 144.0 (**C$_B$**), 142.5 (**C$_{T5}$**), 140.8 (**C**H$_{T6}$), 138.3 (**C**H$_A$), 138.2 (**C**H$_A$), 137.9 (**C$_A$**), 131.3 (**2C**H$_B$), 129.9 (**C**H$_B$), 129.1 (**C**H$_B$), 128.8 (**C**H$_{T4}$), 124.8 (**C**H$_A$), 124.2 (**C**H$_B$), 123.4 (**C**H$_A$), 123.3 (**C**H$_A$), 121.8 (**C**H$_A$), 121.1 (**C**H$_B$), 119.6 (**C**H$_A$), 119.4 (**C**H$_A$), 36.1 (**C**H$_F$), 31.1 (**C**H$_F$), 28.5 (**C**H$_F$), 28.4 (**C**H$_F$), 24.7 (**C**H$_F$), 22.0 (**C**H$_F$), 13.9

(**C**H_{FMe}). Anal.Calcd for [Ir(**ppy**)$_2$(**TzPyNHC$_{8sat}$**)]: C, 54.88; H, 4.48; N, 14.22. Found: C, 54.83; H, 4.53; N, 14.18.

[Ir(ppy)$_2$(TzPyNHC$_{16sat}$)]

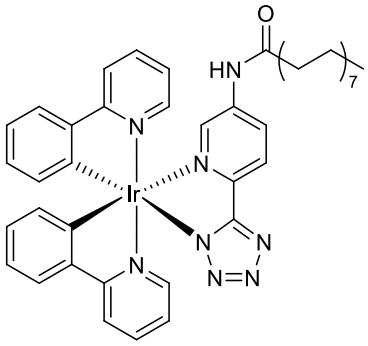

[Ir(**ppy**)$_2$(**TzPyNH$_2$**)] (0.100 g, 0.152 mmol) and triethylamine (0.32 mL, 2.270 mmol) were combined in 10 mL of dry dichloromethane. Palmitoyl chloride (0.46 mL, 1.520 mmol) was dissolved in 3 mL of dry dichloromethane, added dropwise to the reaction mixture and stirred at room temperature overnight. The solution was concentrated and diethyl ether was added. A white precipitate was formed and filtered. The filtrate was washed with $NaHCO_3$ 5% solution (3 × 15 mL). The organic phase was dried over $MgSO_4$ anhydrous and the product was purified *via* column chromatography using Brockmann I grade basic alumina-filled as stationary phase and a dichloromethane/methanol (99.5:0.5 v/v) solvent system mixture as eluent. The targeted complex eluted as the second fraction (yellow). Yield: 0.107 g (78%). M.P. 321 – 314 °C. IR (ν / cm^{-1}): 2923 s, 2849 s (CH stretch saturated C–C), 1703 w (C=O functionalised stretch), 1607 w (tetrazole C=N). ^{1}H NMR (δ / ppm, DMSO-*d$_6$*): 10.31 (s, 1H, **H$_{Tamide}$**), 8.33 (d, 1H, **H$_{T4}$**, J = 8.8 Hz), 8.27 (d, 1H, **H$_{T3}$**, J = 8.7 Hz), 8.20 – 8.17 (m, 2H, **2H$_A$**), 8.14 (s, 1H, **H$_{T6}$**), 7.89 – 7.83 (m, 3H, **3H$_A$**), 7.79 (d, 1H, **H$_B$**, J = 7.9 Hz), 7.62 (d, 1H, **H$_B$**, J = 5.2 Hz), 7.39 (d, 1H, **H$_B$**, J = 5.2 Hz), 7.17 – 7.11 (m, 2H, **2H$_A$**), 6.97 (app. t., 1H, **H$_A$**, splitting = 7.5 Hz), 6.91 – 6.84 (m, 2H, **2H$_B$**), 6.75 (app. t., 1H, **H$_A$**, splitting = 7.4 Hz), 6.21 (d, 1H, **H$_B$**, J = 8.8 Hz), 6.13 (d, 1H, **H$_B$**, J = 8.8 Hz), 2.22 (t, 2H, **2H$_F$**, J = 7.5 Hz), 1.49 – 1.43 (m, 2H, **2H$_F$**), 1.22 (broad s., 24H, **24H$_F$**), 0.84 (t, 3H, **3H$_{FMe}$**, J = 6.8 Hz). ^{13}C NMR (δ / ppm, DMSO-*d$_6$*): 172.0 (**C**O)**,** 167.4 (**C$_T$**), 167.3 (**C$_{T2}$**), 163.5 (**C$_A$**), 151.7 (**C$_B$**), 148.7 (**2C**H$_B$), 147.4 (**C$_B$**), 144.2 (**C$_B$**), 144.0 (**C$_B$**), 142.5 (**C$_{T5}$**), 140.8 (**C**H$_{T6}$), 138.3 (**C**H$_A$), 138.2 (**C**H$_A$), 137.9 (**C$_A$**), 131.3 (**2C**H$_B$), 129.9 (**C**H$_B$), 129.1 (**C**H$_B$), 128.8 (**C**H$_{T4}$), 124.8 (**C**H$_A$), 124.3 (**C**H$_B$),

123.4 (**C**H_A), 123.3 (**C**H_A), 122.6 (**C**H_{T3}), 121.9 (**C**H_A), 121.1 (**C**H_B), 119.6 (**C**H_A), 119.4 (**C**H_A), 36.1 (**C**H_F), 31.3 (**2C**H_F), 29.0 (**2C**H_F), 28.9 (**2C**H_F), 28.8 (**C**H_F), 28.7 (**2C**H_F), 28.6 (**C**H_F), 24.7 (**C**H_F), 22.1 (**2C**H_F), 14.0 (**C**H_{FMe}). Anal.Calcd for [Ir(**ppy**)$_2$(**TzPyNHC$_{16sat}$**)]·0.5(dichloromethane): C, 56.70; H, 5.56; N, 11.89. Found: C, 56.70; H, 5.60; N, 11.87.

[Ir(ppy)$_2$(TzPyNHC$_{18sat}$)]

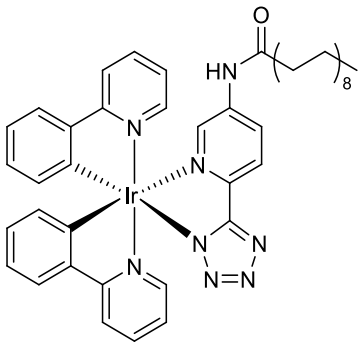

[Ir(**ppy**)$_2$(**TzPyNH$_2$**)] (0.100 g, 0.152 mmol) and triethylamine (0.32 mL, 2.270 mmol) were combined in 10 mL of dry dichloromethane. Stearoyl chloride (0.51 mL, 1.520 mmol) was dissolved in 3 mL of dry dichloromethane, added dropwise to the reaction mixture and stirred at room temperature overnight. The solution was concentrated and diethyl ether was added. A white precipitate was formed and filtered. The filtrate was washed with $NaHCO_3$ 5% solution (3 × 15 mL). The organic phase was dried over $MgSO_4$ anhydrous and the product was purified *via* column chromatography using Brockmann I grade basic alumina-filled as stationary phase and a dichloromethane/methanol (99.5:0.5 v/v) solvent system mixture as eluent. The targeted complex eluted as the second fraction (yellow). Yield: 0.097 g (69%). M.P. 308 – 310 °C. IR (ν / cm^{-1}): 2922 s, 2849 s (CH stretch saturated C–C), 1703 w (C=O functionalised stretch), 1607 w (tetrazole C=N). ^{1}H NMR (δ / ppm, DMSO-d_6): 10.31 (s, 1H, **H$_{Tamide}$**), 8.34 (d, 1H, **H$_{T4}$**, J = 8.7 Hz), 8.27 (d, 1H, **H$_{T3}$**, J = 8.7 Hz), 8.22 – 8.17 (m, 2H, **2H$_A$**), 8.14 (s, 1H, **H$_{T6}$**), 7.91 – 7.82 (m, 3H, **3H$_A$**), 7.79 (d, 1H, **H$_B$**, J = 8.9 Hz), 7.62 (d, 1H, **H$_B$**, J = 7.2 Hz), 7.39 (d, 1H, **H$_B$**, J = 7.2 Hz), 7.18 – 7.10 (m, 2H, **2H$_A$**), 6.97 (app. t., 1H, **H$_A$**, splitting = 8.1 Hz), 6.91 – 6.84 (m, 2H, **2H$_B$**), 6.75 (app. t., 1H, **H$_A$**, splitting = 8.1 Hz), 6.21 (d, 1H, **H$_B$**, J = 7.5 Hz), 6.13 (d, 1H, **H$_B$**, J = 7.5 Hz), 2.22 (t, 2H, **2H$_F$**, J = 7.2 Hz), 1.51 – 1.44 (m, 2H, **2H$_F$**), 1.22 (broad s., 28H, **28H$_F$**), 0.83 (t, 3H, **3H$_{FMe}$**, J = 6.4 Hz). ^{13}C NMR (δ / ppm, DMSO-d_6): 172.0 (**C**O),

167.4 (**C**$_{T}$), 167.3 (**C**$_{T2}$), 163.5 (**C**$_{A}$), 151.7 (**C**$_{A}$), 148.7 (**2C**H$_{B}$), 147.4 (**C**$_{B}$), 144.2 (**C**$_{B}$), 144.0 (**C**$_{B}$), 142.5 (**C**$_{T5}$), 140.8 (**C**H$_{T6}$), 138.3 (**2C**H$_{A}$), 137.9 (**C**$_{B}$), 131.3 (**2C**H$_{B}$), 130.0 (**C**H$_{B}$), 129.1 (**C**H$_{T4}$), 128.8 (**C**H$_{B}$), 124.8 (**2C**H$_{A}$), 124.3 (**C**H$_{B}$), 123.4 (**C**H$_{A}$), 122.6 (**C**H$_{T3}$), 121.9 (**C**H$_{A}$), 121.1 (**C**H$_{B}$), 119.6 (**C**H$_{A}$), 119.4 (**C**H$_{A}$), 36.2 (**C**H$_{F}$), 31.3 (**C**H$_{F}$), 30.7 (**2C**H$_{F}$), 29.0 (**3C**H$_{F}$), 28.9 (**2C**H$_{F}$), 28.8 (**C**H$_{F}$), 28.7 (**2C**H$_{F}$), 28.6 (**C**H$_{F}$), 28.5 (**C**H$_{F}$), 24.7 (**C**H$_{F}$), 22.1 (**C**H$_{F}$), 14.0 (**C**H$_{FMe}$). Anal.Calcd for [Ir(**ppy**)$_2$(**TzPyNHC**$_{18sat}$)]·0.5(methanol): C, 59.15; H, 6.08; N, 11.87. Found: C, 59.16; H, 5.96; N, 11.81.

[Ir(ppy)$_2$(TzPyNHC$_{16cis}$)]

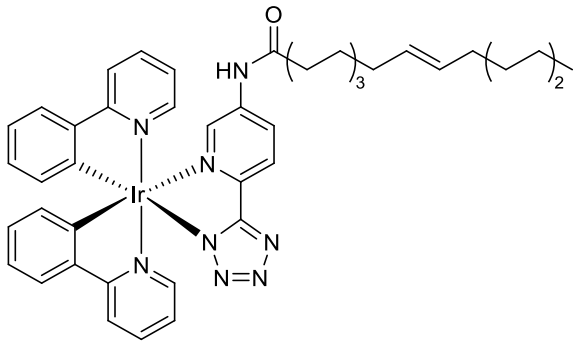

[Ir(**ppy**)$_2$(**TzPyNH$_2$**)] (0.100 g, 0.152 mmol) and triethylamine (0.32 mL, 2.270 mmol) were combined in 10 mL of dry dichloromethane. Palmitoleoyl chloride (0.46 mL, 1.520 mmol) was dissolved in 3 mL of dry dichloromethane, added dropwise to the reaction mixture and stirred at room temperature overnight. The solution was concentrated and diethyl ether was added. A white precipitate was formed and filtered. The filtrate was washed with $NaHCO_3$ 5% solution (3 × 15 mL). The organic phase was dried over $MgSO_4$ anhydrous and the product was purified *via* column chromatography using Brockmann I grade basic alumina-filled as stationary phase and a dichloromethane/methanol (99.5:0.5 v/v) solvent system mixture as eluent. The targeted complex eluted as the second fraction (yellow). Yield: 0.085 g (62%). M.P. 194 – 196 °C. IR (ν / cm^{-1}): 3006 w (=C–H stretch), 2922 s, 2851 s (CH stretch saturated C–C), 1703 w (C=O functionalised stretch), 1607 w (tetrazole C=N). ^{1}H NMR (δ / ppm, DMSO-*d*$_6$): 10.31 (s, 1H, **H$_{Tamide}$**), 8.34 (d, 1H, **H$_{T4}$**, J = 8.8 Hz), 8.27 (d, 1H, **H$_{T3}$**, J = 8.7 Hz), 8.20 – 8.19 (m, 2H, **2H$_A$**), 8.13 (s, 1H, **H$_{T6}$**), 7.89 – 7.83 (m, 3H, **3H$_A$**), 7.79 (d, 1H, **H$_B$**, J = 7.9 Hz), 7.62 (d, 1H, **H$_B$**, J = 5.2 Hz), 7.39 (d, 1H, **H$_B$**, J = 5.2 Hz), 7.18 – 7.10 (m, 2H, **2H$_A$**), 6.97 (app. t., 1H, **H$_A$**, splitting = 7.5 Hz), 6.91 – 6.84 (m, 2H, **2H$_B$**), 6.75 (app. t., 1H, **H$_A$**, splitting = 7.4 Hz), 6.21 (d, 1H, **H$_B$**, J = 8.8 Hz), 6.13 (d, 1H, **H$_B$**, J = 8.8 Hz), 5.32 – 5.30 (m, 2H, **2H$_{FCH=CH}$**), 2.22 (t, 2H, **2H$_F$**, J = 7.5 Hz), 1.99 – 1.94 (m, 3H, **3H$_F$**), 1.51 – 1.46 (m, 2H, **2H$_F$**), 1.23 (broad s., 15H, **15H$_F$**), 0.85 – 0.80 (m, 3H, **3H$_{FMe}$**). ^{13}C NMR (δ / ppm, DMSO-*d*$_6$): 172.0 (**C**O), 167.4 (**C$_T$**), 167.3 (**C$_{T2}$**), 163.5 (**C$_A$**), 151.7 (**C$_B$**), 148.7 (**2C**H$_B$), 147.4 (**C$_B$**), 144.3 (**C$_B$**), 144.0 (**C$_B$**), 142.5 (**C$_{T5}$**), 140.8 (**C**H$_{T6}$), 138.4 (**C**H$_A$), 138.3 (**C**H$_A$), 137.9 (**C$_A$**), 131.3 (**2C**H$_B$), 130.0 (**C**H$_B$), 129.7 (**C**H$_{FCH=CH}$), 129.6 (**C**H$_{FCH=CH}$), 129.1 (**C**H$_B$), 128.9 (**C**H$_{T4}$), 124.8 (**C**H$_A$), 124.3 (**C**H$_B$), 123.4 (**C**H$_A$), 123.3 (**C**H$_A$), 122.6 (**C**H$_{T3}$), 121.9 (**C**H$_A$), 121.1 (**C**H$_B$), 119.6 (**C**H$_A$), 119.4 (**C**H$_A$), 36.2 (**C**H$_F$), 31.1 (**2C**H$_F$), 29.1

(**C**H_F), 28.6 (**2C**H_F), 28.5 (**C**H_F), 28.2 (**C**H_F), 26.6 (**C**H_F), 24.7 (**C**H_F), 22.1 (**2C**H_F), 13.9 (**C**H_{FMe}). Anal.Calcd for [Ir(**ppy**)$_2$(**TzPyNHC$_{16cis}$**)]: C, 58.84; H, 5.50; N, 12.48. Found: C, 59.04; H, 5.55; N, 12.27.

[Ir(ppy)$_2$(TzPyNHC$_{18cis}$)]

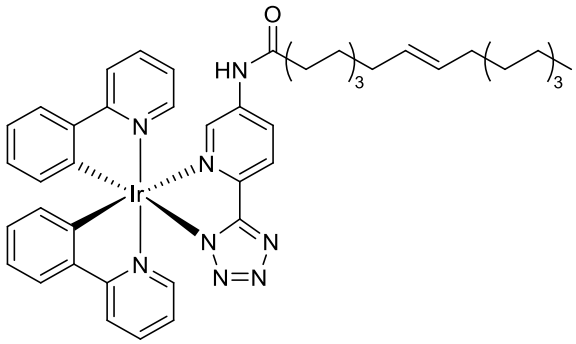

[Ir(**ppy**)$_2$(**TzPyNH$_2$**)] (0.100 g, 0.152 mmol) and triethylamine (0.32 mL, 2.270 mmol) were combined in 10 mL of dry dichloromethane. Oleoyl chloride (0.50 mL, 1.520 mmol) was dissolved in 3 mL of dry dichloromethane, added dropwise to the reaction mixture and stirred at room temperature overnight. The solution was concentrated and diethyl ether was added. A white precipitate was formed and filtered. The filtrate was washed with $NaHCO_3$ 5% solution (3 × 15 mL). The organic phase was dried over $MgSO_4$ anhydrous and the product was purified *via* column chromatography using Brockmann I grade basic alumina-filled as stationary phase and a dichloromethane/methanol (99.5:0.5 v/v) solvent system mixture as eluent. The targeted complex eluted as the second fraction (yellow). Yield: 0.085 g (61%). M.P. 186 – 189 °C. IR (ν / cm^{-1}): 3004 w (=C–H stretch), 2922 s, 2852 s (CH stretch saturated C–C), 1700 w (C=O functionalised stretch), 1606 w (tetrazole C=N). ^{1}H NMR (δ / ppm, DMSO-d_6): 10.31 (s, 1H, **H$_{Tamide}$**), 8.35 (d, 1H, **H$_{T4}$**, J = 8.8 Hz), 8.27 (d, 1H, **H$_{T3}$**, J = 8.7 Hz), 8.19 – 8.17 (m, 2H, **2H$_A$**), 8.13 (s, 1H, **H$_{T6}$**), 7.89 – 7.83 (m, 3H, **3H$_A$**), 7.79 (d, 1H, **H$_B$**, J = 7.9 Hz), 7.62 (d, 1H, **H$_B$**, J = 5.2 Hz), 7.39 (d, 1H, **H$_B$**, J = 5.2 Hz), 7.18 – 7.10 (m, 2H, **2H$_A$**), 6.96 (app. t., 1H, **H$_A$**, splitting = 8.0 Hz), 6.91 – 6.84 (m, 2H, **2H$_B$**), 6.75 (app. t., 1H, **H$_A$**, splitting = 8.0 Hz), 6.21 (d, 1H, **H$_B$**, J = 8.8 Hz), 6.13 (d, 1H, **H$_B$**, J = 8.8 Hz), 5.32 – 5.30 (m, 2H, **2H$_{FCH=CH}$**), 2.22 (t, 2H, **2H$_F$**, J = 7.5 Hz), 1.99 – 1.94 (m, 4H, **4H$_F$**), 1.51 – 1.46 (m, 2H, **2H$_F$**), 1.18 (broad s, 20H, **20H$_F$**), 0.83 – 0.80 (m, 3H, **3H$_{FMe}$**). ^{13}C NMR (δ / ppm, DMSO-d_6): 171.9 (**C**O), 167.4 (**C$_T$**), 167.3 (**C$_{T2}$**), 163.4 (**C$_A$**), 151.6 (**C$_B$**), 148.7 (**C**H$_B$), 148.6 (**C**H$_B$), 147.4 (**C$_B$**),

144.2 (**C**$_{\mathbf{B}}$), 144.0 (**C**$_{\mathbf{B}}$), 142.5 (**C**$_{\mathbf{T5}}$), 140.8 (**C**H$_{\mathbf{T6}}$), 138.3 (**C**H$_{\mathbf{A}}$), 138.2 (**C**H$_{\mathbf{A}}$), 137.9 (**C**$_{\mathbf{A}}$), 131.3 (**2C**H$_{\mathbf{B}}$), 129.9 (**C**H$_{\mathbf{A}}$), 129.6 (**C**H$_{\mathbf{FCH=CH}}$), 129.5 (**C**H$_{\mathbf{FCH=CH}}$), 129.0 (**C**H$_{\mathbf{B}}$), 128.8 (**C**H$_{\mathbf{T4}}$), 124.8 (**C**H$_{\mathbf{B}}$), 124.2 (**C**H$_{\mathbf{B}}$), 123.3 (**C**H$_{\mathbf{A}}$), 123.2 (**C**H$_{\mathbf{A}}$), 122.5 (**C**H$_{\mathbf{T3}}$), 121.8 (**C**H$_{\mathbf{A}}$), 121.1 (**C**H$_{\mathbf{B}}$), 119.6 (**C**H$_{\mathbf{A}}$), 119.4 (**C**H$_{\mathbf{A}}$), 36.1 (**C**H$_{\mathbf{F}}$), 31.2 (**C**H$_{\mathbf{F}}$), 29.1 (**C**H$_{\mathbf{F}}$), 29.0 (**C**H$_{\mathbf{F}}$), 28.8 (**C**H$_{\mathbf{F}}$), 28.6 (**2C**H$_{\mathbf{F}}$), 28.5 (**2C**H$_{\mathbf{F}}$), 28.4 (**C**H$_{\mathbf{F}}$), 26.5 (**2C**H$_{\mathbf{F}}$), 24.7 (**C**H$_{\mathbf{F}}$), 22.0 (**C**H$_{\mathbf{F}}$), 13.9 (**C**H$_{\mathbf{FMe}}$). Anal.Calcd for [Ir(**ppy**)$_2$(**TzPyNHC**$_{\mathbf{18cis}}$)]·0.3(methanol): C, 59.40; H; 5.85; N, 11.96. Found: C, 59.49; H, 5.85; N, 12.00.

Chapter 6

Preliminary Biological Investigation of Amino and Fatty Acid-Functionalised Iridium Tetrazolato Complexes

6.1 Introduction

During the design of organic and transition metal probes, the subcellular localisation or the binding affinity of these luminescent species with specific biological targets are essential properties to be considered.[49,62,291,385] A variety of strategies has been applied to the development of probes with high specificity, which includes the addition of protonatable-deprotonatable groups, cleavage or formation of covalent bonds, complexation and conjugation with biologically relevant vectors.[63,107,114,120,126,263,300,354,356–358,410–413]

Due to the important role of fatty acids and lipids in many aspects of cells biology such as membrane architecture, intracellular trafficking, signalling, hormone regulation, energy storage and secondary metabolite production, the interest in these species has attracted the researchers' attention during the years.[248,393–395,397]

In particular, a plateau of organic fluorophores (**Figure 6.1** – Left and centre – **111**, **112**)[414–417] and few transition metal species of Ir(III), Re(I), Ru(II) and Pt(II)[298,418–423] (**Figure 6.1** – Right – **113**) have been appended with fatty acids or long alkyl chains in order to mimic the biological behaviour of lipids and increase the biospecificity for these targeted moieties. Unfortunately, the investigation of lipid-rich organelles and the monitoring of processes involving fatty acids have been limited by the availability of probes that can specifically visualise lipids in live cells. In fact, as previously mentioned in Chapter 5 – section 5.1, the majority of these dyes can be applied only in fixed cells, due to issues related to membrane permeability or high cytotoxicity against live cells.[232,248]

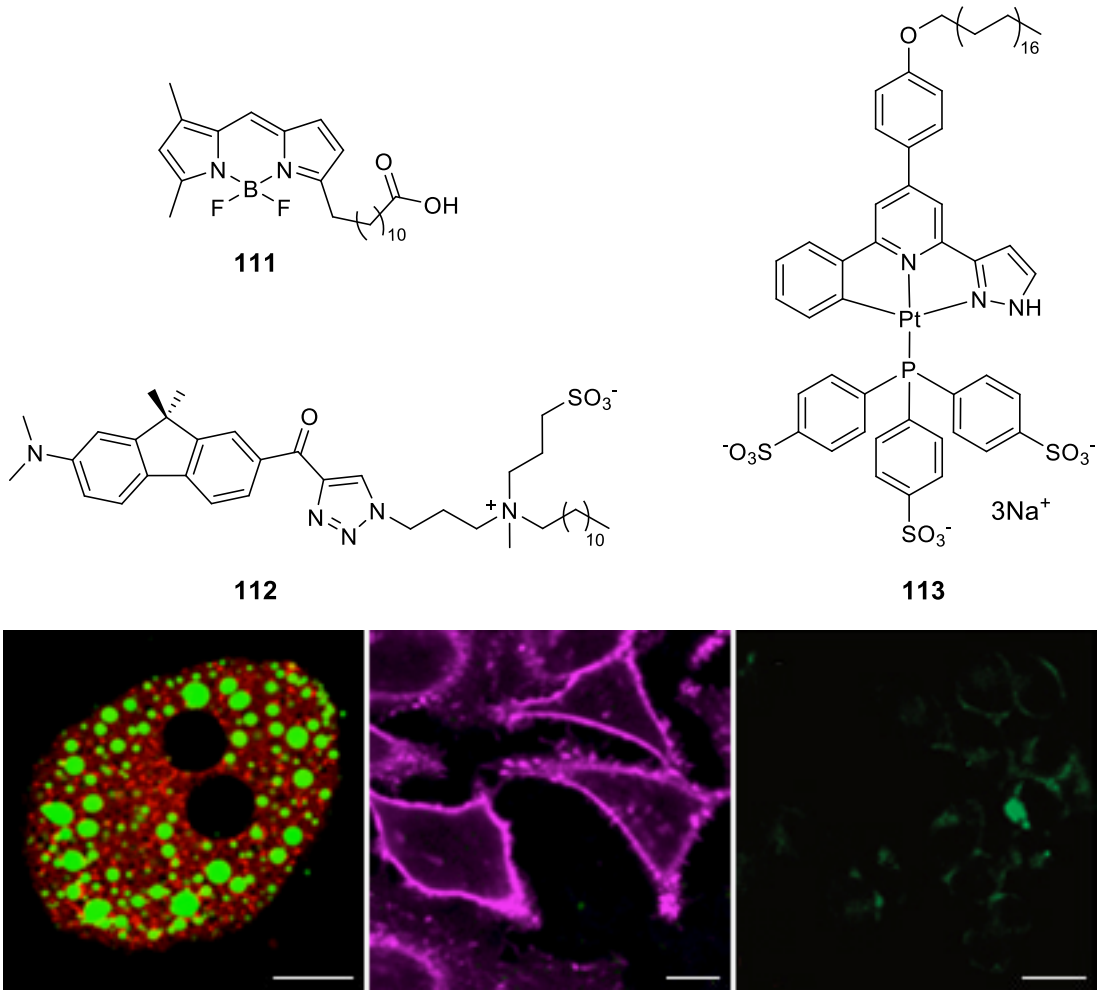

Figure 6.1 Different staining pattern (bottom) of dyes appended with fatty acids or long alkyl chains (top). (Left) Lipid droplets of fixed hepatocytes of wild-types mice stained with **111** (Scale bar = 10 μm). (Centre) Plasma membrane staining of HeLa cells with 0.1 μM of **112** (Scale bar = 20 μm). (Right) Plasma membrane localisation of **113** in HeLa cell (Scale bar = 20 μm). Reproduced with permission from ref[415,416,422].

In this chapter, the preliminary biological investigation on amino and fatty acid-functionalised iridium(III) complexes will be discussed. Normal epithelial prostatic cell line PNT2 were employed instead of H9c2 rat cardiomyoblast cells, due to their bigger size (which allows better visualisation of the probes within the cells) and higher concentration of lipids.

The probes have been successfully internalised in live PNT2 cells and different concentrations of these dyes have been evaluated in order to assess the uptake mechanism and in the attempt to solve solubility issues. It can be anticipated that all the probes have accumulated within the cells, but the detection of few of them was

minimal, probably due to a combination of low emissive properties in aqueous environment and precipitation in the culture medium. The cytotoxicity and photostability of this family of probes has been assessed, highlighting the potential of this class of complexes for the development of lipid probes in live cells.

6.2 Preliminary Biological Investigation

6.2.1 Lipophilicity

Lipophilicity is often closely correlated with the permeability and solubility profile of a compound. In general, the permeability coefficient of a molecule improves with higher values of lipophilicity. On the other hand, an excessive increase of this parameter may contribute to a substantial decrease of the solubility of the compound in biological environment.[86] For this reason, during the design of new imaging and therapeutic agents, the lipophilicity is one of the crucial properties to be considered, along with charge, solubility and bioconjugation to specific biological vectors.[1]

Fatty acids possess amphipathic character due to the presence of an ionisable headgroup and a hydrophobic aliphatic chain, which is responsible for the low solubility in water of these species.[387] Previous works on metallosurfactants have shown remarkable self-assembling features of these complexes in aqueous solutions, with the formation of micellar systems.[379,424–427]

The fatty acid-functionalised iridium(III) complexes, described in Chapter 5, exhibit a similar architecture given the polar iridium(III) core and hydrophobic aliphatic chain, which should increase the lipophilicity value of this family of probes with respect to the amino-functionalised iridium(III) precursor (refer to Chapter 4).

The lipophilicity of [Ir(**ppy**)$_2$(**TzPyNH$_2$**)] , [Ir(**bzq**)$_2$(**TzPyNH$_2$**)] , [Ir(**ppy**)$_2$(**TzPyNHC$_{8sat}$**)], [Ir(**ppy**)$_2$(**TzPyNHC$_{16sat}$**)], [Ir(**ppy**)$_2$(**TzPyNHC$_{18sat}$**)], [Ir(**ppy**)$_2$(**TzPyNHC$_{16cis}$**)] and [Ir(**ppy**)$_2$(**TzPyNHC$_{18cis}$**)] has been measured by the shake-flask method, using a pH= 7.4 buffered PBS solution and *n*-octanol, as outlined in Chapter 3 – section 3.5.2.[308]

All the log$D_{7.4}$ values have been summarised in **Table 6.1**. [Ir(**ppy**)$_2$(**TzPyNH$_2$**)] and [Ir(**bzq**)$_2$(**TzPyNH$_2$**)] possess lipophilicity values (1.99 and 1.87, respectively) which are within the range of previously reported iridium(III) cyclometalated species.[104,115,120,126,134,238] Surprisingly, increasing the conjugation of the cyclometalated ligands from a phenylpyridine (**ppy**) to a benzoquinoline (**bzq**) does not increase the log$D_{7.4}$ values, as observed from other reported data.[126,137]

As expected, by introducing a long and hydrophobic aliphatic chain on the tetrazolate ligand, the lipophilicity of the fatty acid-functionalised iridium(III) probes (log$D_{7.4}$ = 2.26 – 2.84) increase in comparison to their precursor [Ir(**ppy**)$_2$(**TzPyNH$_2$**)]

($logD_{7.4}$ = 1.99).[418,428] Moreover, along the whole series, the lower lipophilicity is observed for [Ir(**ppy**)$_2$(**TzPyNHC$_{16cis}$**)] and [Ir(**ppy**)$_2$(**TzPyNHC$_{18cis}$**)], with values of 2.31 and 2.26, respectively. This behaviour may derive from the presence of the unsaturation on the fatty acid, which increases the rigidity of the chain and modulates the geometry of the whole system in aqueous solution.[426] Interestingly, the length of the fatty acid chain does not affect the lipophilicity of these probes, even when comparing [Ir(**ppy**)$_2$(**TzPyNHC$_{8sat}$**)] ($logD_{7.4}$ = 2.66) with [Ir(**ppy**)$_2$(**TzPyNHC$_{18sat}$**)] ($logD_{7.4}$ = 2.63), bearing 8 and 18-carbon chains, respectively.

Table 6.1 Distribution coefficient values ($logD_{7.4}$) for the amino and fatty acidfunctionalised iridium(III) complexes.

Complexes	**log$D_{7.4}$**
[Ir(**ppy**)$_2$(**TzPyNH$_2$**)]	1.99 ± 0.04
[Ir(**bzq**)$_2$(**TzPyNH$_2$**)]	1.87 ± 0.03
[Ir(**ppy**)$_2$(**TzPyNHC$_{8sat}$**)]	2.66 ± 0.07
[Ir(**ppy**)$_2$(**TzPyNHC$_{16sat}$**)]	2.84 ± 0.08
[Ir(**ppy**)$_2$(**TzPyNHC$_{18sat}$**)]	2.63 ± 0.06
[Ir(**ppy**)$_2$(**TzPyNHC$_{16cis}$**)]	2.31 ± 0.06
[Ir(**ppy**)$_2$(**TzPyNHC$_{18cis}$**)]	2.26 ± 0.06

6.2.2 Localisation and Internalisation

The cellular localisation of the fatty acid (**Figure 6.2**) and amino-functionalised iridium(III) probes (**Figure 6.3**) within PNT2 cells was investigated *via* confocal microscopy, using single photon excitation at 403 nm.

Given the lower solubility in aqueous solutions of these probes in comparison to the cyano and (iso)quinolyl-functionalised complexes described in Chapter 3 – section 3.2.2, the staining protocol was modified. In particular, the amount of DMSO used for the solubilisation of the complexes in the RPMI-1640 culture medium was increased from 0.2 to 2%. Moreover, prolonged sonication of the solutions was required for each dilution step to ensure complete dissolution of the probes.

In general, precipitation issues were encountered with whole series of fatty acid-functionalised iridium(III) probes and with the more conjugated amino-substituted species [Ir(**bzq**)$_2$(**TzPyNH$_2$**)]. The presence of the precipitated probes is evident in **Figure 6.2** and **Figure 6.3**, even after multiple washings with PBS.

Live PNT2 cells were incubated with the iridium complexes at 5 and 10 μM for 20 minutes at 37 °C. Longer incubation time (3 hours) and higher concentrations (20 – 40 μM) were also attempted, showing analogous results. For this reason, only the data derived from the short incubation analysis will be discussed.

The successful uptake of all the probes has been confirmed by recording the emission intensity deriving from the stained cells at different wavelength intervals. As depicted from **Figure 6.4** to **Figure 6.6**, the emission intensity of the probes has been recorded in spectral mode with maximum around 504 – 513 nm, which is consistent with the photophysical data in aqueous solutions discussed in Chapter 4 – section 4.4.5 and Chapter 5 – section 5.4.5 for the amino and fatty acid-functionalised iridium(III) complexes, respectively. In the case of [Ir(**bzq**)$_2$(**TzPyNH$_2$**)], the emission maximum is slightly red-shifted around 524 – 533 nm, which is ascribed to the presence of the more conjugated cyclometalated ligands with respect to the other complexes in the series. Moreover, higher is the intensity in the interval of wavelengths 444 – 453 nm, higher is the contribution of the endogenous species to the recorded emission. The lack of emission in the interval 484 – 493 nm is ascribed to the use of a filter.

The internalisation within cells and detection of [Ir(**ppy**)$_2$(**TzPyNHC$_{8sat}$**)], [Ir(**ppy**)$_2$(**TzPyNHC$_{16cis}$**)], [Ir(**ppy**)$_2$(**TzPyNHC$_{18cis}$**)] (only for 5 μM), [Ir(**ppy**)$_2$(**TzPyNH$_2$**)] and [Ir(**bzq**)$_2$(**TzPyNH$_2$**)] (only for 5 μM) was successfully

achieved. In case of [Ir(**ppy**)$_2$(**TzPyNHC$_{16sat}$**)] and [Ir(**ppy**)$_2$(**TzPyNHC$_{18sat}$**)], a combination of low solubility and low phosphorescence in aqueous environment was probably responsible for the negligible detectability of these species within the cells. The majority of these probes was found to accumulate in the perinuclear area of live PNT2 cells, with staining patterns resembling the endoplasmic reticulum, as previously observed in Chapter 3 – section 3.2.2.[238] To confirm the intracellular localisation of the complexes in this lipid-rich organelle, co-localisation analyses with ER-Tracker™ need to be performed to complete the biological investigation.

Interestingly, the internalisation of this family of probes appeared to occur through two distinctive mechanisms. The accumulation of [Ir(**ppy**)$_2$(**TzPyNH$_2$**)] increases at higher concentration (**Figure 6.3** – column B), suggesting a potential passive diffusion mechanism across the cellular membrane, driven by the concentration gradient. On the other hand, [Ir(**ppy**)$_2$(**TzPyNHC$_{8sat}$**)] and [Ir(**ppy**)$_2$(**TzPyNHC$_{16cis}$**)] (**Figure 6.2**) did not show any significant variations in the cellular uptake upon increase of concentration, which may suggest a mediated transport. Finally, the higher concentration of [Ir(**ppy**)$_2$(**TzPyNHC$_{18cis}$**)] and [Ir(**bzq**)$_2$(**TzPyNH$_2$**)] (**Figure 6.2** and **Figure 6.3**, respectively) inhibited cellular entry. The mechanism of internalisation of [Ir(**ppy**)$_2$(**TzPyNHC$_{16sat}$**)] and [Ir(**ppy**)$_2$(**TzPyNHC$_{18sat}$**)] has not been evaluated due to their poor detectability.

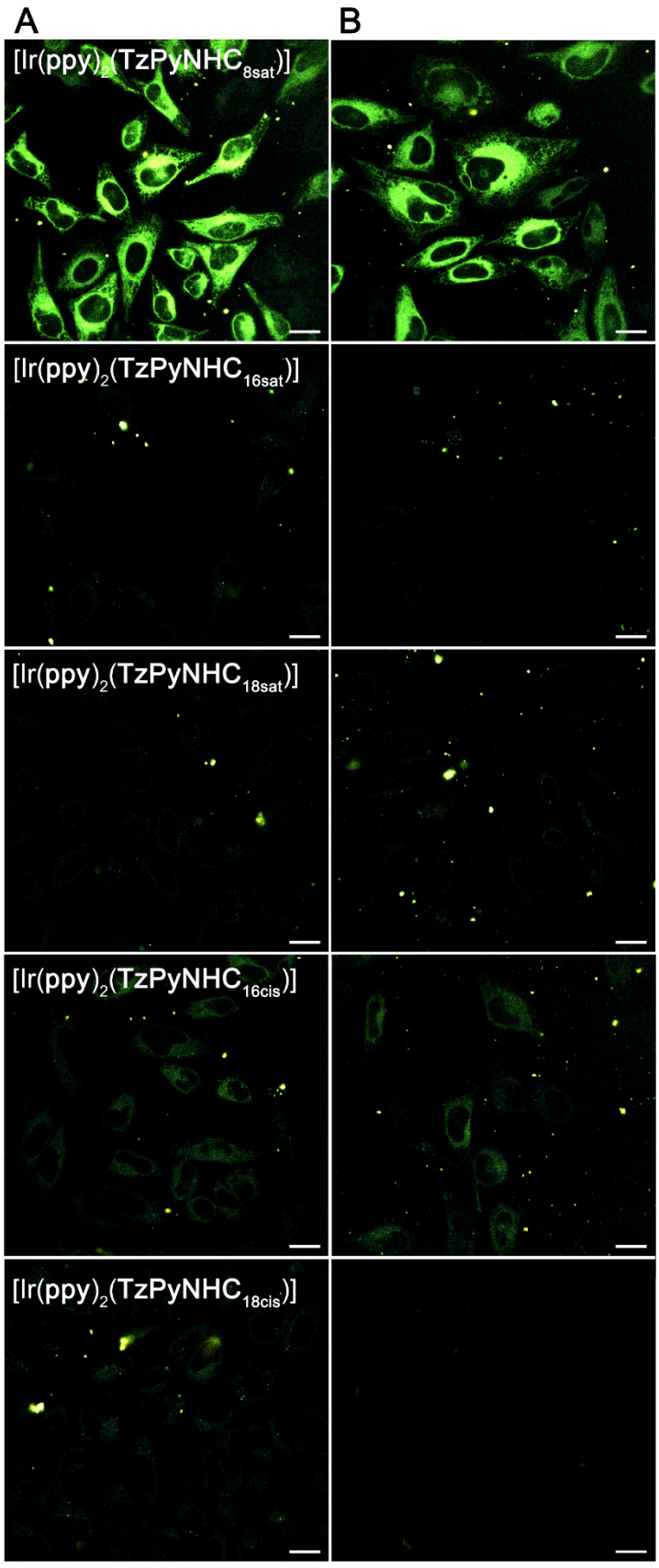

Figure 6.2 Micrographs of live PNT2 cells stained with 5 µM (column A) and 10 µM (column B) of the fatty acid-functionalised iridium(III) complexes. Scale bar = 20 µm.

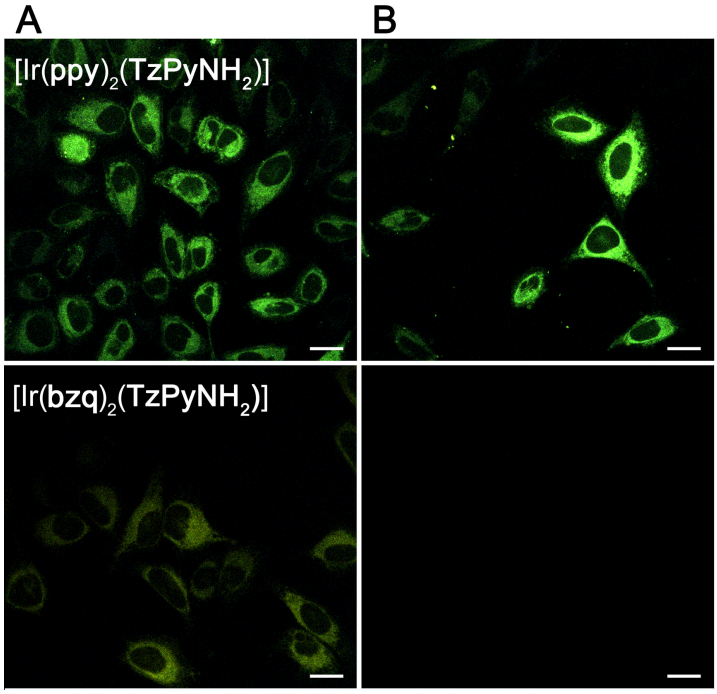

Figure 6.3 Micrographs of live PNT2 cells stained with 5 μM (column A) and 10 μM (column B) of the amino-functionalised iridium(III) complexes. Scale bar = 20 μm.

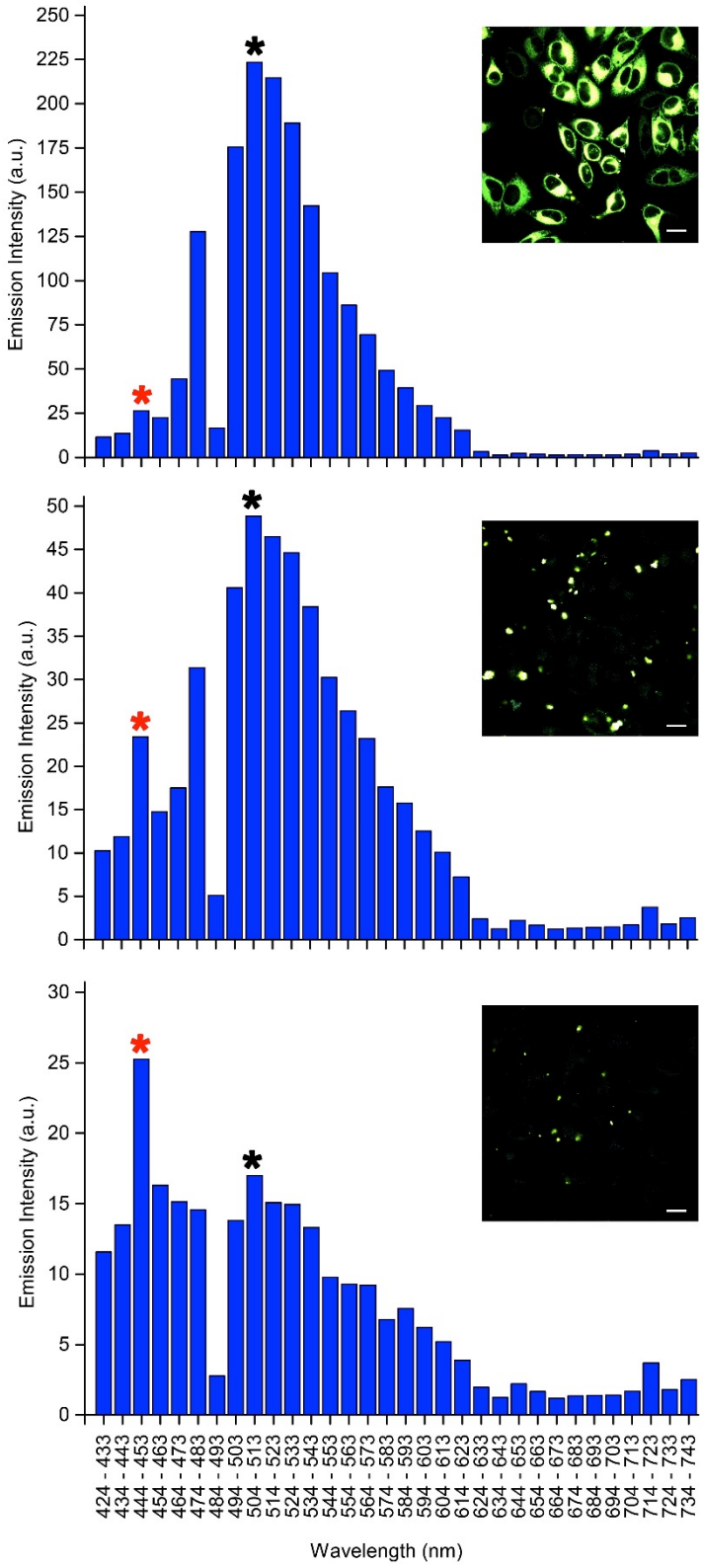

Figure 6.4 Emission profiles of [Ir(**ppy**)$_2$(**TzPyNHC$_{8sat}$**)] (top), [Ir(**ppy**)$_2$(**TzPyNHC$_{16sat}$**)] (middle) and [Ir(**ppy**)$_2$(**TzPyNHC$_{18sat}$**)] (bottom) incubated in live PNT2 cells (5 μM). The maximum emission (black star) and the emission from endogenous species (red star) are highlighted. Scale bar = 20 μm.

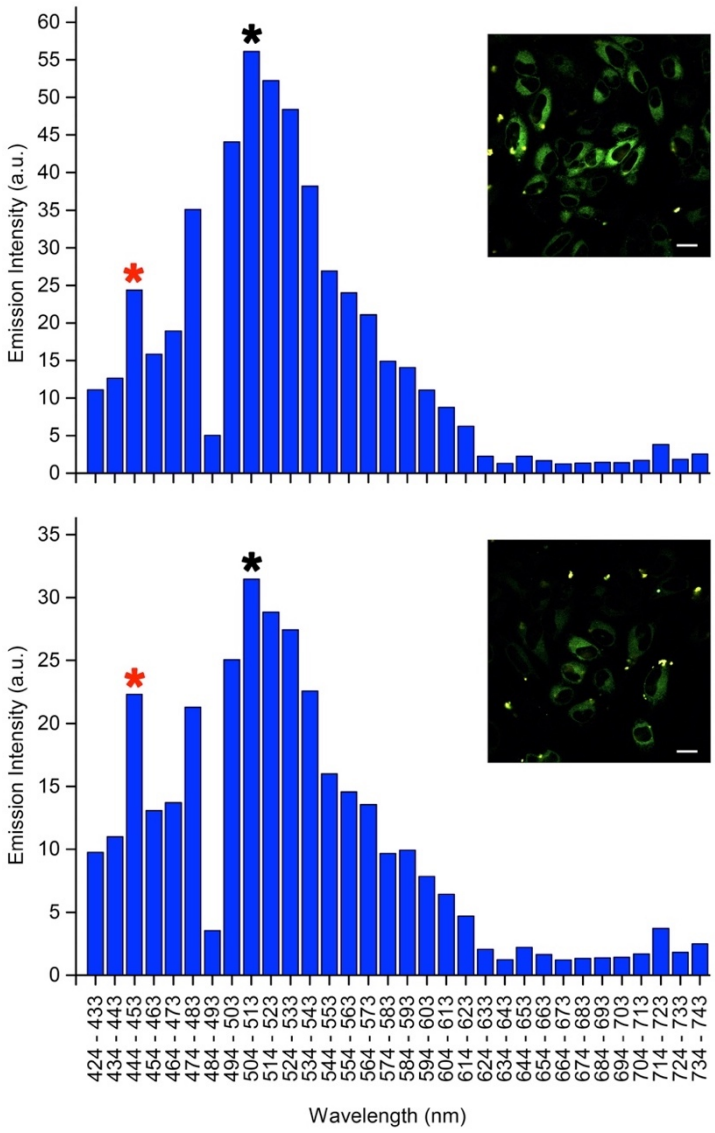

Figure 6.5 Emission profiles of [Ir(**ppy**)$_2$(**TzPyNHC$_{16cis}$**)] (top) and [Ir(**ppy**)$_2$(**TzPyNHC$_{18cis}$**)] (bottom) incubated in live PNT2 cells (5 μM). The maximum emission (black star) and the emission from endogenous species (red star) are highlighted. Scale bar = 20 μm.

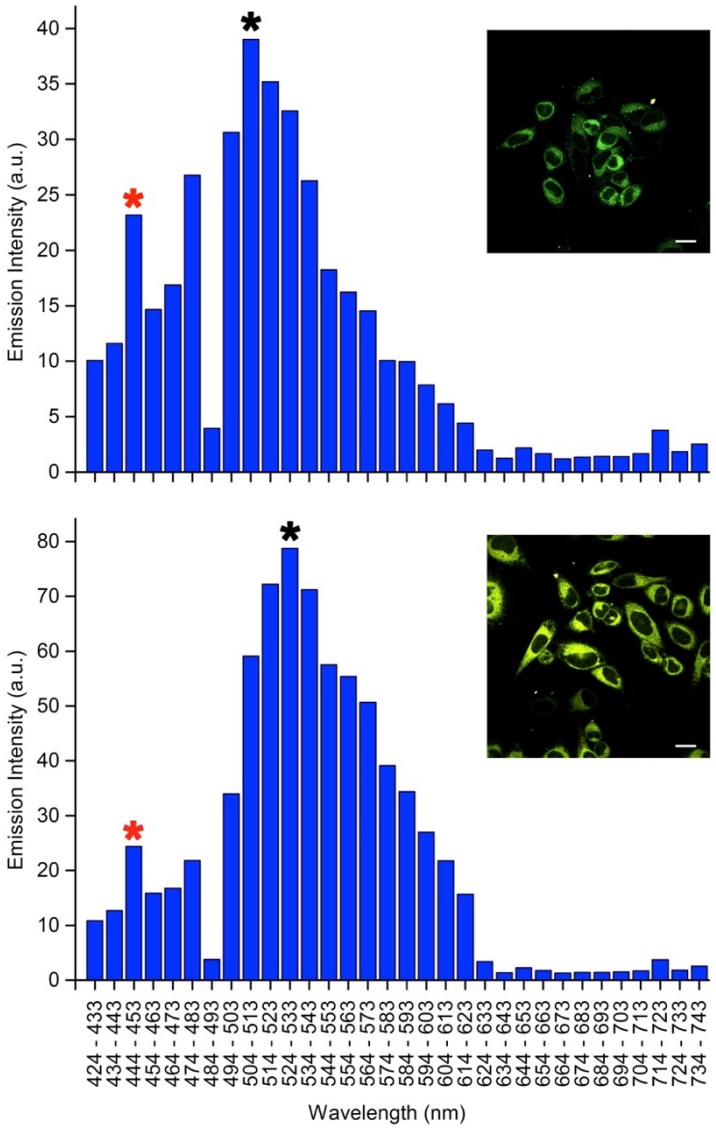

Figure 6.6 Emission profiles of [Ir(**ppy**)$_2$(**TzPyNH$_2$**)] (top) and [Ir(**bzq**)$_2$(**TzPyNH$_2$**)] (bottom) incubated in live PNT2 cells (5 μM). The maximum emission (black star) and the emission from endogenous species (red star) are highlighted. Scale bar = 20 μm.

6.2.3 Cytotoxicity

The cytotoxicity of the fatty acid-functionalised iridium(III) complexes toward PNT2 cells has been evaluated *via* MTS assay, as described in section 6.4.5 of this chapter. Unfortunately, cytotoxicity data of [Ir(**ppy**)$_2$(**TzPyNH$_2$**)] and [Ir(**bzq**)$_2$(**TzPyNH$_2$**)] have not been evaluated due to time constraints.

The cells were incubated for either 2 or 24 hours with concentration of the complexes at 20 or 40 μM. All the complexes exhibited low toxicity even at the longest incubation time and the highest concentration, with viability values ≥85% for [Ir(**ppy**)$_2$(**TzPyNHC$_{8sat}$**)] and [Ir(**ppy**)$_2$(**TzPyNHC$_{18sat}$**)], as depicted in **Figure 6.7**. Even greater cell survival rate was recorded for [Ir(**ppy**)$_2$(**TzPyNHC$_{16sat}$**)], [Ir(**ppy**)$_2$(**TzPyNHC$_{16cis}$**)] and [Ir(**ppy**)$_2$(**TzPyNHC$_{18cis}$**)].

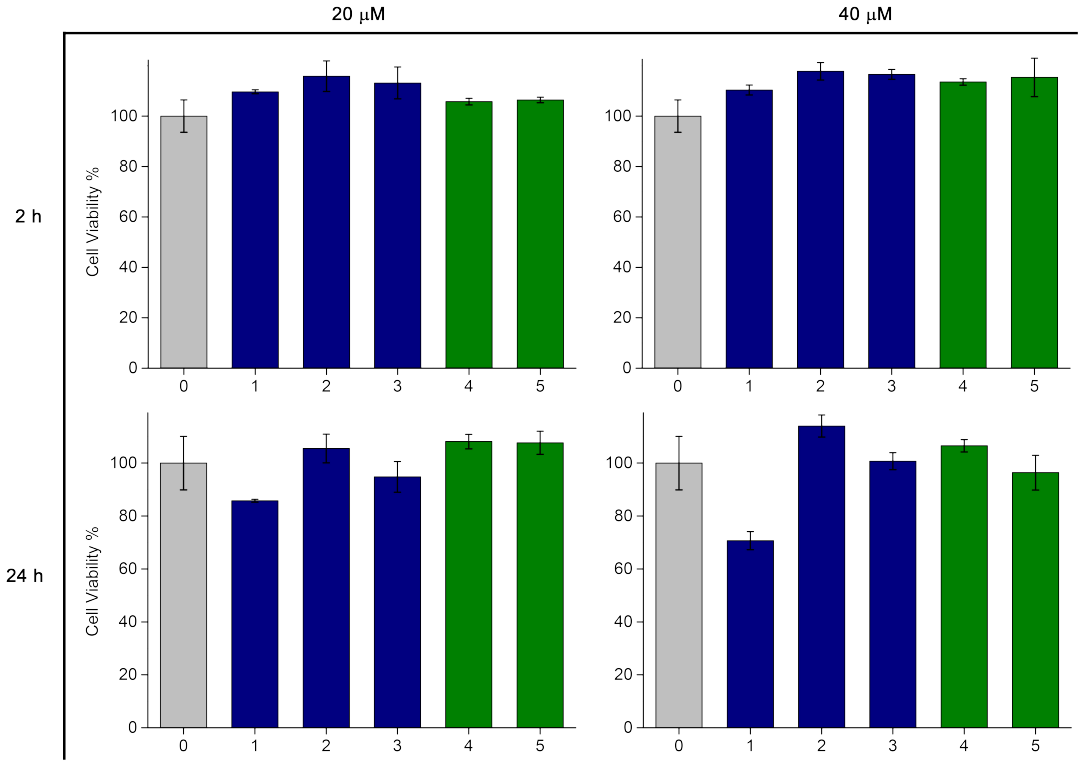

Figure 6.7 Cell viability after 2 and 24 h incubation with iridium complexes at 20 and 40 μM. Saturated fatty acid chain-substituted iridium complexes are represented by blue bars, whereas unsaturated fatty acid chain-substituted iridium complexes are represented by green bars. 0) Control (2% DMSO in serum-free RPMI-1640 medium); 1) [Ir(**ppy**)$_2$(**TzPyNHC$_{8sat}$**)]; 2) [Ir(**ppy**)$_2$(**TzPyNHC$_{16sat}$**)]; 3) [Ir(**ppy**)$_2$(**TzPyNHC$_{18sat}$**)]; 4) [Ir(**ppy**)$_2$(**TzPyNHC$_{16cis}$**)]; 5) [Ir(**ppy**)$_2$(**TzPyNHC$_{18cis}$**)].

Only few examples of metal complexes appended with fatty acid or simple alkyl chains have been investigated for biological applications. When reported, the cytotoxicity studies of related Ir(III), Re(I) and Ru(II) probes (**Figure 6.8**) showed moderate to high cytotoxicity in live cells. [298,418–423] In particular, the two iridium complexes bearing a long alkyl chain in their ancillary bipyridine ligand (**115a-b**) exhibit higher toxicity (IC_{50} = 12.0 and 2.0 μM, respectively) than cisplatin (IC_{50} = 18.1 μM) in the same experimental conditions. Only the Pt(II) complex **113** exhibits low cytotoxicity against live HeLa cells with a viability of *ca.* 90% after 25 hours of incubation.[422]

Based on these results, the low cytotoxicity of the fatty acid-functionalised iridium(III) probes makes them good building block for biological imaging application.

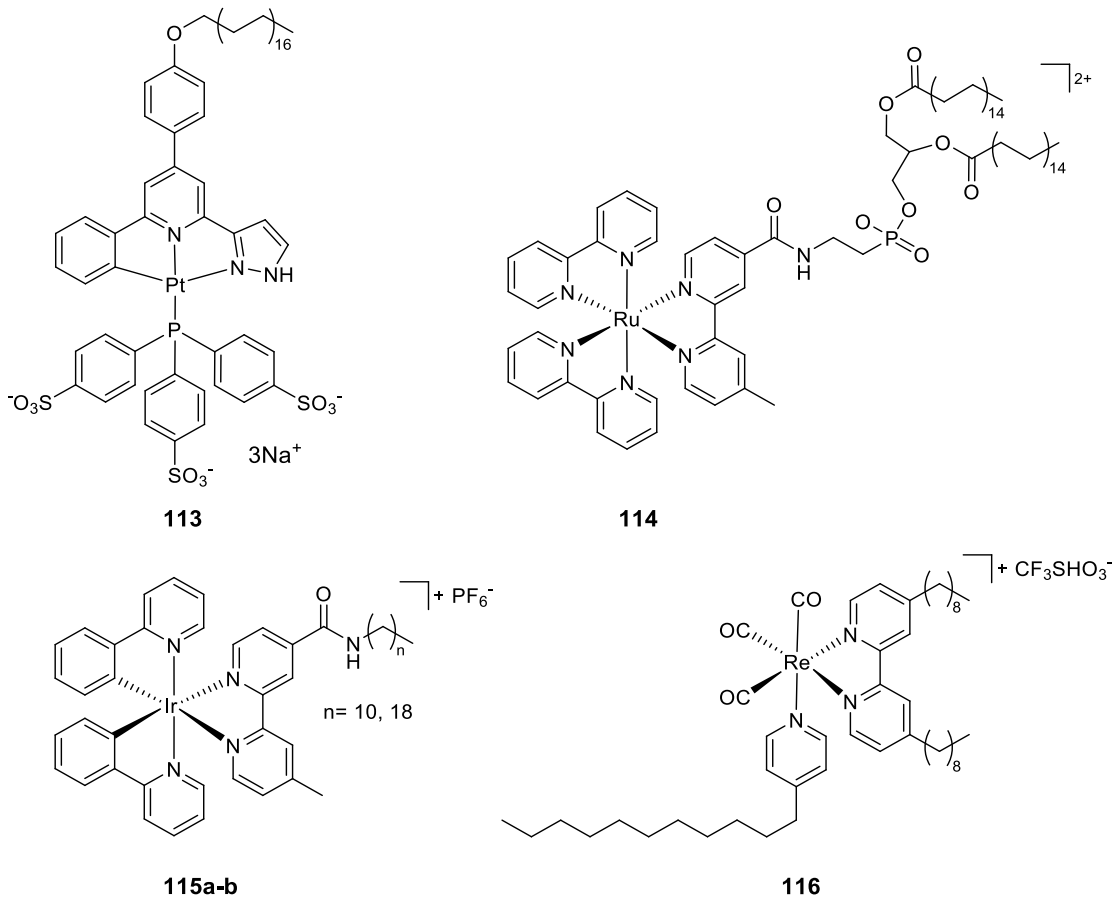

Figure 6.8 Examples of previously reported probes functionalised with fatty acids or long alkyl chains.

6.2.4 Photostability

Transition metal complexes for the application in biological imaging have frequently showed an improved photostability compared to conventional organic fluorophores, which is advantageous when continuous monitoring of biological processes is required or for real-time tracking applications.[113,122,132,336,339] During these analyses, the probe is continuously irradiated and can undergo photodegradation or conversion in species with lower emissive properties. For this reason, the photostability of imaging agents is one of the major requirements, along with low cytotoxicity, high localisation specificity and good solubility in aqueous environment.[1,65,384]

The photostability of amino and fatty acid-functionalised iridium(III) complexes has been assessed, as described in Chapter 3 – section 3.5.9.

The iridium species have been dissolved in PBS solution (2% DMSO) and irradiated using a Pen-Ray Mercury Lamp source at 365 nm for 900 seconds. The variation in emission intensity has been recorded with a time frame of 30 seconds.

Both the amino and fatty acid-appended complexes exhibit high resistance to photobleaching, as reported in **Figure 6.9** and **Figure 6.10**.

From the evaluation of the photostability in cuvette, [Ir(**ppy**)$_2$(**TzPyNHC$_{8sat}$**)], [Ir(**ppy**)$_2$(**TzPyNHC$_{16sat}$**)], [Ir(**ppy**)$_2$(**TzPyNHC$_{18sat}$**)], [Ir(**ppy**)$_2$(**TzPyNHC$_{16cis}$**)], [Ir(**ppy**)$_2$(**TzPyNHC$_{18cis}$**)] and [Ir(**bzq**)$_2$(**TzPyNH$_2$**)] display emission intensity above 60% of the initial values after 900 seconds of continuous irradiation. [Ir(**ppy**)$_2$(**TzPyNH$_2$**)] exhibits greater photostability with respect to the other investigated complexes, with final emission intensity up to 75% the initial value.

As previously mentioned, the photostability of neutral iridium complexes has not been explored in literature and thus the only possible comparison is with the cyano and (iso)quinolyl tetrazolato complexes described in Chapter 3 – section 3.2.5.[238]
The photostability of [Ir(**bzq**)$_2$(**TzPyNH$_2$**)] and the fatty acid-functionalised probes is similar to the one measured for [Ir(**F$_2$ppy**)$_2$(**TzPyCN**)], with a final value of 55% (Chapter 3 – section 3.2.5 - **Figure 3.10**). On the other hand, the more photostable [Ir(**ppy**)$_2$(**TzPyNH$_2$**)] has showed higher resistance to photobleaching, comparable with [Ir(**ppy**)$_2$(**TzPyCN**)] and [Ir(**ppy**)$_2$(**TzQn**)] (Chapter 3 - **Figure 3.10**).

The good photostability in cuvette of these series of probes indicates the need for further testing, in order to assess if this property can also be maintained in cellular environment.

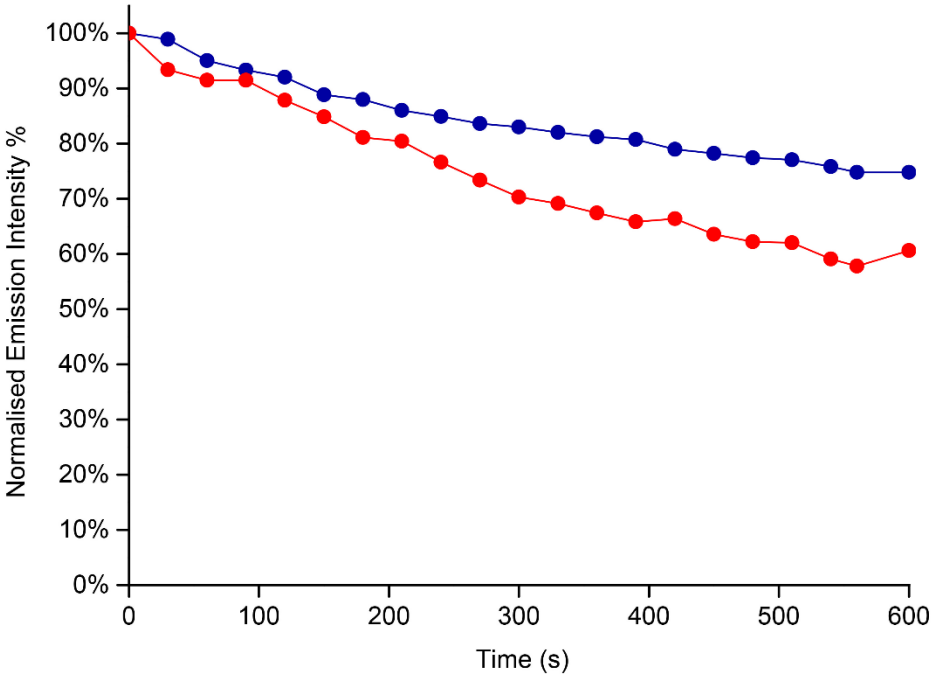

Figure 6.9 Photobleaching analysis in PBS (2% DMSO) of [Ir(**ppy**)$_2$(**TzPyNH$_2$**)] (blue) and [Ir(**bzq**)$_2$(**TzPyNH$_2$**)] (red).

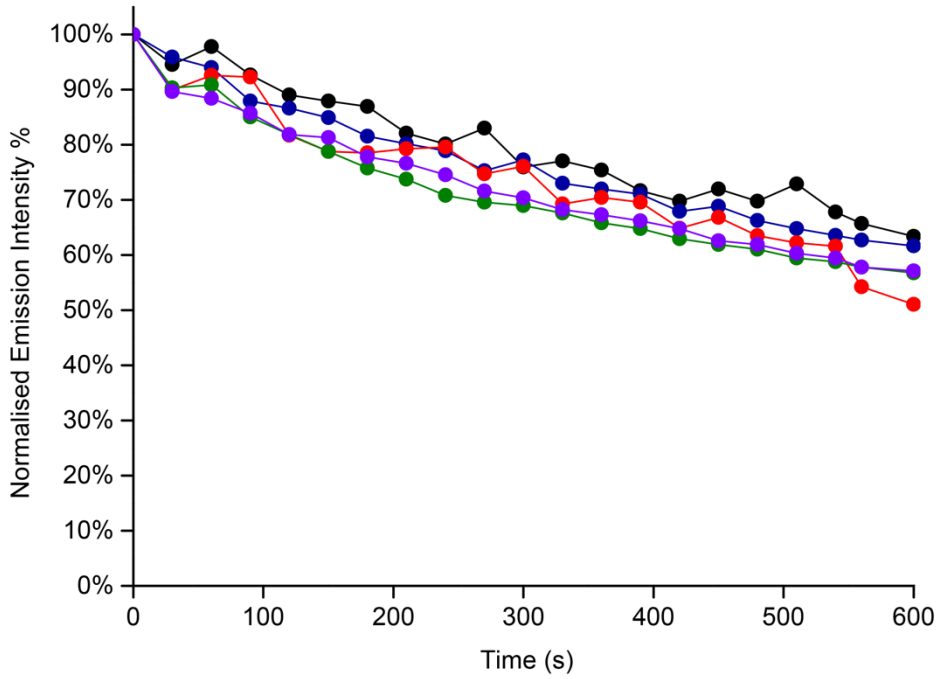

Figure 6.10 Photobleaching analysis in PBS (2% DMSO) of [Ir(**ppy**)$_2$(**TzPyNHC$_{8sat}$**)] (black), [Ir(**ppy**)$_2$(**TzPyNHC$_{16sat}$**)] (blue), [Ir(**ppy**)$_2$(**TzPyNHC$_{18sat}$**)] (red), [Ir(**ppy**)$_2$(**TzPyNHC$_{16cis}$**)] (green) and [Ir(**ppy**)$_2$(**TzPyNHC$_{18cis}$**)] (purple).

6.3 Conclusions

In this chapter, a preliminary biological investigation of the fatty acid and amino-functionalised iridium(III) probes in live PNT2 cell lines has been carried out.

The evaluation of the lipophilicity of this family of compounds has been performed, highlighting higher values for the fatty acid-appended complexes in comparison to the precursor [Ir(**ppy**)$_2$(**TzPyNH$_2$**)]. Interestingly, regardless of the lipophilicity showed by these complexes, solubility issues in aqueous environment have been encountered for the whole series. For this reason, the staining protocol previously applied to the cyano and (iso)quinolyl-functionalised iridium(III) probes (Chapter 3 –section 3.5.4) has been modified.

The majority of the probes has been internalised within PNT2 cells, accumulating in the perinuclear area, with a staining pattern resembling the endoplasmic reticulum. However co-localisation analysis will be required to confirm the accumulation of the probes in this organelle. [Ir(**ppy**)$_2$(**TzPyNHC$_{16sat}$**)] and [Ir(**ppy**)$_2$(**TzPyNHC$_{18sat}$**)] have showed low detectability within the cells, probably due to poor solubility, which decreases the uptake, and also low emission in aqueous media.

Interestingly, internalisation tests varying the concentration of the probes have suggested different mechanism of uptake. In particular [Ir(**ppy**)$_2$(**TzPyNH$_2$**)] seems to be internalised through a potential passive diffusion mechanism, whereas [Ir(**ppy**)$_2$(**TzPyNHC$_{8sat}$**)] and [Ir(**ppy**)$_2$(**TzPyNHC$_{16cis}$**)] undergo a mediated transport. Finally, the cellular entry of [Ir(**ppy**)$_2$(**TzPyNHC$_{18cis}$**)] and [Ir(**bzq**)$_2$(**TzPyNH$_2$**)] at higher concentration is inhibited, possibly due to precipitation of the probes.

The cytotoxicity assay showed good cellular viability (≥ 85%) at high concentration and long incubation time. Moreover, the length of the chains or the degree of unsaturation of the appended fatty acids does not affect the toxicity of the complexes. These derivatives, along with few Pt(II) species,[421,422] are also ones of the few examples in literature of low toxic probes functionalised with fatty acids or long alkyl chains.

Finally, high photostability in cuvette has been recorded for the whole series of iridium(III) complexes.

Based on these results, upon minor modifications on the chemical structure to overcome the solubility issues, these series of probes can be used as scaffold for the synthesis of other fatty acids-functionalised analogues. In particular, as showed in previous works, the introduction of a PEG moieties could potentially increase the water-solubility of the complexes, without major effects on the localisation within the cells.[429]

6.4 Experimental

6.4.1 Photophysical Measurements

Photophysical measurements have been conducted as outlined in Chapter 2, section 2.6.2, unless otherwise stated.

6.4.2 Lipophilicity Analysis

$LogD_{7.4}$ values were determined by applying the shake-flask method developed by Kunz *et al.*.[308] The analysis has been described in detailed in Chapter 3, section 3.5.2.

6.4.3 Cell Culture

The biological investigation was performed in collaboration with Dr Christie A. Bader and Dr Alexandra Sorvina at the School of Pharmacy and Medical Sciences, University of South Australia. Normal epithelial prostatic cell line PNT2 were maintained in FBS-free (fetal bovine serum) RPMI-1640 culture medium (Sigma-Aldrich, USA) at 37 ºC and 5% CO_2. The PNT2 cells were cultured in 75 mm^2 flasks. Cells that had been passaged for no more than 18 times, were used for experiments. For live cell imaging and MTS assay, the PNT2 cells were seeded at 1×10^5 cells/mL and cultured overnight in either ibidi µ-slide 8 wells in a final volume of 250 µL or 96-well microtiter plate in a final volume of 200 µL.

6.4.4 Cell Staining

PNT2 cells were incubated with the iridium complexes at 5, 10, 20 and 40 µM in FBS-free RPMI-1640 culture medium with 2% DMSO (Sigma-Aldrich, St. Louis, USA) for 20 minutes at 37 ºC and 5% CO_2. The cells were washed twice with sterile phosphate-buffered saline solution (PBS; Sigma-Aldrich, St. Louis, USA), before imaging in RPMI-1640.

6.4.5 MTS Cell Viability Assay

The cellular NADPH-dependent redox activity was measured using CellTiter 96® AQueous Non-Radioactive Cell Proliferation Assay (MTS), according to the manufacturer's instruction (Promega, USA). The PNT2 cells were stained with the iridium complexes at either 20 μM or 40 μM in FBS-free RPMI-1640 culture medium with 2% DMSO, and held at 37 °C and 5% CO_2 for 2 or 24 hours. As a control, PNT2 cells were incubated for the same length of time in FBS-free RPMI-1640 with 2% DMSO. Following addition of MTS, the cells were incubated for a further 2 hours in the same conditions. The absorbance of the formazan dye was measured by EnVision multi-label plate reader at 490 nm. The data are reported as the mean ± SEM of three biological replicates for each group.

6.4.6 Photobleaching Analysis

The photobleaching analysis has been performed following the method in cuvette delineated in Chapter 3, section 3.5.9.

6.4.7 Confocal Microscopy

Single photon live cell imaging was performed using a Nikon A1+ confocal microscope (Nikon, Japan) with an OKOLab Microscope Incubator (Okolab USA Inc., USA). The iridium complexes were excited at 403 nm and the emission was collected in the 400 - 750 nm region. Image analysis was measured using NIS elements V4.50 software (Nikon, Japan). The final preparation of the images was conducted with Adobe Photoshop CC (Adobe Systems Inc., USA).

Chapter 7

Conclusions and Future Work

The research presented in this thesis was intended to explore the structure-activity relationship of a series of iridium tetrazolato complexes. Modifications on the chemical structure of both the cyclometalated and the tetrazolate ancillary ligands were systematically made in order to assess how the photophysical and biological properties of the complexes would be affected.

This aim was dictated by the lack of literature regarding a methodical rationalisation between the chemical structure of complexes and their photophysical and biological behaviour, which would be extremely beneficial for the design of a new advanced generation of iridium probes for applications in life science. Moreover, due to their favourable emissive properties and easy tunability, iridium(III) tetrazolato complexes have been previously studied and applied in light emitting devices but their use in biological imaging was still unexplored.

The first series of iridium(III) complexes (**Figure 7.1**) discussed in this thesis[238] followed the interesting discovery of a rhenium tetrazolato complex with formula *fac*-[Re(CO)$_3$(**phen**)(**TzPhCN**)], which represented the first metal probe to localise in lipid droplets.[232,248] The functionalisation of the tetrazolate ligand with a nitrile group was then apply to the iridium(III) series in order to investigate the possibility of a similar internalisation within live cells. Small chemical modifications in the structure of the complexes were made in order to modulate emission maxima, lipophilicity and charge. In fact, to evaluate the role played by the charge, all the neutral complexes have been methylated to obtain the cationic analogues for a systematic comparison. Interestingly, only few examples of neutral iridium(III) probes have been reported in literature.[82,103,109–112,120–122,125,128,133] Quinolyl (H**TzQn**) and isoquinolyl-tetrazolate (H**TziQn**) ligands were also studied in the place of the nitrile pyridyl-tetrazolato ligand (H**TzPyCN)**, to evaluate the effect of the increased conjugation on the lipophilicity of the complexes. Photophysical measurements in

organic, lipophilica and aqueous media showed a solvatochromic emission of MLCT nature, with a red shift of the cationic species with respect to their neutral analogues. The internalisation within live H9c2 cells highlighted endoplasmic reticulum accumulation, in addition to the staining of lipid droplets, for the neutral complexes and $[Ir(\mathbf{ppy})_2(Me\mathbf{TzQn})]^+$, whereas the two charged probes $[Ir(\mathbf{F}_2\mathbf{ppy})_2(Me\mathbf{TzPyCN})]^+$ and $[Ir(\mathbf{ppy})_2(Me\mathbf{TzPyPhCN})]^+$ localised in mitochondria. Moreover, the cytotoxicity assay revealed high toxicity of the charged complexes in comparison to the neutral species, probably due to a combination of cellular uptake and intracellular localisation. In fact, the high cytotoxicity of iridium(III) complexes for the staining of mitochondrial is a common trend in previously reported publications.[124,126,130,132,134–136] On the other hand, the neutral cyano and (iso)quinolyl-functionalised iridium(III) probes represent the first example of non-toxic metal complexes for the staining of endoplasmic reticulum.[238]

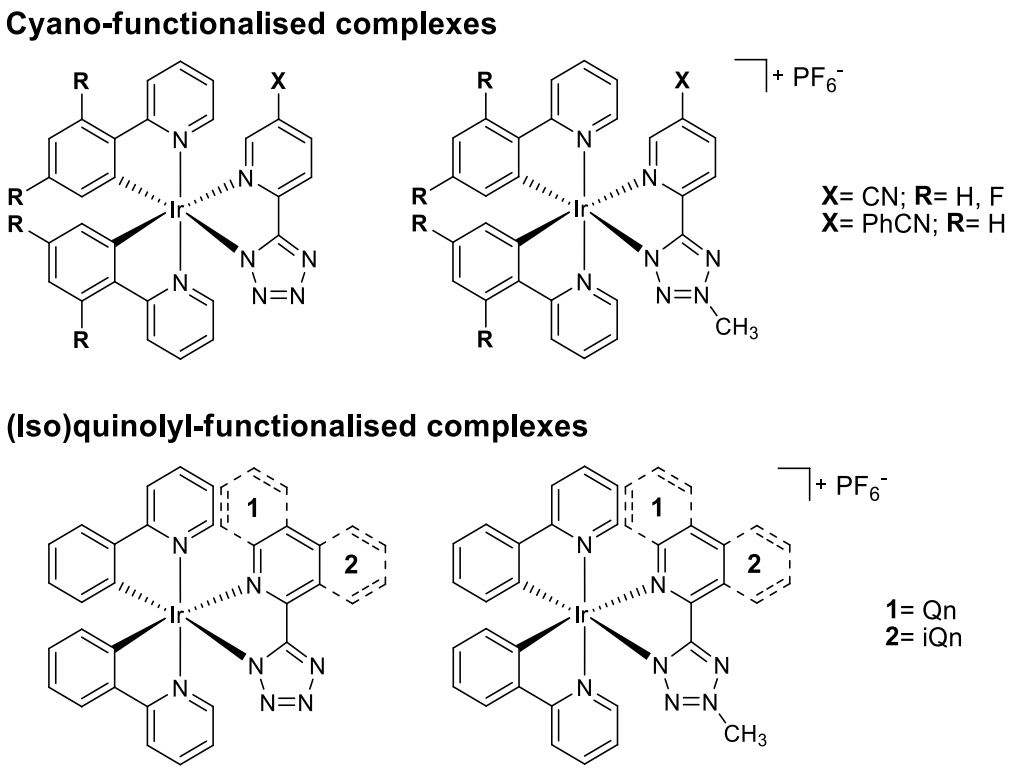

Figure 7.1 Structures of the investigated cyano (top) and (iso)quinolyl-functionalised iridium(III) complexes (bottom).

[Ir(**ppy**)$_2$(Me**TzPyPhCN**)]$^+$, which exhibits mitochondrial accumulation in live cells, was also tested in fresh and frozen tissues.[283] Interestingly, the imaging of fixed tissue samples mostly relies on immunochemistry, which is time-consuming and can produce artefacts, due to fixation processes. Remarkably, [Ir(**ppy**)$_2$(Me**TzPyPhCN**)]$^+$ could accumulate within the mitochondria of both the fresh and fixed muscle tissues, suggesting an internalisation mechanism which is independent of mitochondrial membrane polarisation.

In the second family of iridium complexes the nitrile group on the tetrazolato ligand was substituted with an amino group (**Figure 7.2**) for the investigation of protonation/deprotonation reactions. Variation on the cyclometalated ligands were achieved by replacing **ppy** with the more conjugated **bzq**. [Ir(**ppy**)$_2$(**TzPyNH$_2$**)] and [Ir(**bzq**)$_2$(**TzPyNH$_2$**)] showed lower emission properties in all the investigated solvents in comparison to the previously discussed family of complexes. Temperature-dependent luminescent lifetime measurements highlighted the presence of a thermally available and dark ^{3}MC excited state, which is responsible of the increase of non-radiative decay pathways and hence the poor emission of these species. The NH_2 group was also oxidised to a NO_2 group, but the emission of [Ir(**ppy**)$_2$(**TzPyNO$_2$**)] was completely quenched even in oxygen-free dichloromethane solution. Nevertheless, the pH-sensing activity of [Ir(**ppy**)$_2$(**TzPyNH$_2$**)] and [Ir(**bzq**)$_2$(**TzPyNH$_2$**)] was tested in organic solution, showing decrease of the emission intensity and appearance of a shoulder at *ca.* 555 nm upon protonation for [Ir(**ppy**)$_2$(**TzPyNH$_2$**)]. On the other hand, probably due to the low solubility of [Ir(**bzq**)$_2$(**TzPyNH$_2$**)] in dichloromethane solution, the acid-base titration did not affect the emission profile of this species. The applicability as cellular pH-sensor of [Ir(**ppy**)$_2$(**TzPyNH$_2$**)] was evaluated by performing the titration in aqueous environment in a pH range of 4.8 – 7.5. Unfortunately, no changes were recorded, implying that the emission of the probes is not sensitive enough to small cellular pH variations.

Amino-functionalised complexes

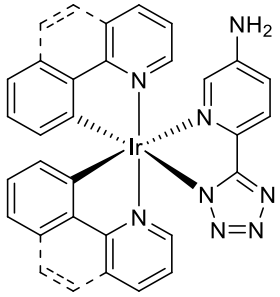

Figure 7.2 Structures of the investigated amino-functionalised iridium(III) complexes.

Finally, [Ir(**ppy**)$_2$(**TzPyNH$_2$**)] was reacted with different fatty acid chains to form the fatty acid-functionalised iridium(III) series (**Figure 7.3**). The photophysical properties of this family of complexes were not affected by the degree of unsaturation and the length of the aliphatic chains, resulting in a yellow-green emission and low quantum yield ($\Phi_{aer} < 1$), as displayed by the starting material [Ir(**ppy**)$_2$(**TzPyNH$_2$**)]. Temperature-dependent luminescent lifetime measurement on [Ir(**ppy**)$_2$(**TzPyNHC$_{16cis}$**)] confirmed the presence of a low-lying ^{3}MC excited state, which can be easily populated at room temperature, reducing the emission intensity of the probe. The emission in aqueous and lipophilic solvents was recorded, highlighting a solvatochromic red shift (*ca.* 10 – 15 nm) of the emission maxima upon increase of the medium polarity. Interestingly, the emission profiles of the unsaturated species [Ir(**ppy**)$_2$(**TzPyNHC$_{16cis}$**)] and [Ir(**ppy**)$_2$(**TzPyNHC$_{16cis}$**)] become broader, suggesting the smaller contribution of the ^{3}LC excited state to the emission.

A preliminary biological investigation for the amino and fatty acid-functionalised iridium(III) complexes was performed using live PNT2 cells. As expected, upon addition of long hydrophobic chains, the lipophilicity of the fatty acid-functionalised family was higher than the amino-functionalised complexes. Moreover, solubility issues in aqueous media were encountered for the whole series, requiring modifications in the protocol with respect to the one used for the previously discussed cyano and (iso)quinolyl-functionalised probes. All the complexes were internalised in live cells, showing different mechanisms of uptake, such as passive diffusion or mediated transport. [Ir(**ppy**)$_2$(**TzPyNHC$_{16sat}$**)] and [Ir(**ppy**)$_2$(**TzPyNHC$_{18sat}$**)] showed low detectability within the cells, probably due to a combination of low emissive properties in aqueous media and precipitation issues. The cytotoxicity analyses

showed cellular viability higher than 85% at 40 μM and 24 hour incubation time, which was independent of the length and unsaturation of the appended fatty acid chains. Interestingly, these fatty acid complexes represent a rare examples of non-toxic probes bearing long aliphatic chains, along with few Pt(II) species.[421,422]

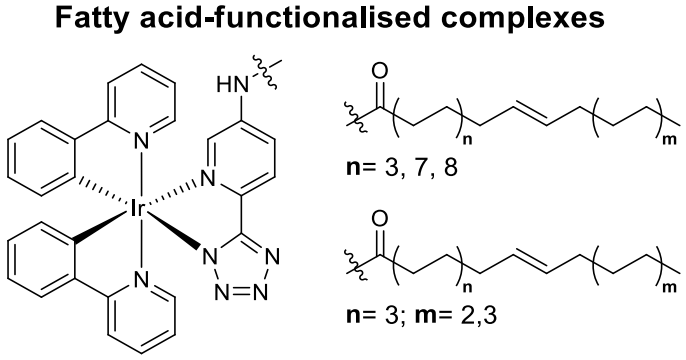

Figure 7.3 Structures of the investigated fatty acid-functionalised iridium(III) complexes.

The data presented in this thesis have showed the relationship between charge and cytotoxicity of the investigated iridium(III) complexes, highlighting the low toxicity of neutral species in comparison with their cationic analogues. Further research on neutral complexes for applications in biological imaging may be of interest, especially due to presence of only few examples of neutral complexes in the field. [82,103,109–112,120–122,125,128,133] In addition, the role of the positive charge may be further investigated by modifying the tetrazolate ligand with an aliphatic chain appended with a phosphonium moiety, in the proposed structures presented in **Figure 7.4**. This study is currently undergoing in Massi's research group.

The results in this thesis also suggest that further research efforts in the systematic study of the structure-activity relationship on iridium(III) complexes may be beneficial for the development of a superior generation of imaging and therapeutic agents.

The biological investigation of amino and fatty acid-functionalised iridium(III) probes needs to be completed. Co-localisation analyses with organic dyes may provide more evidence about the specific accumulation of the complexes within the cells. Another useful technique would be ICP-MS, which may determine the amount of complex present in the different organelles.

Finally, further studies to enhance the poor solubility of the amino and fatty acid-functionalised iridium(III) complexes may be of interested. In particular, the conjugation of these complexes with water-soluble moieties, such as PEG, may increase their solubility in aqueous media, without affecting their cytotoxicity and localisation within the cells.

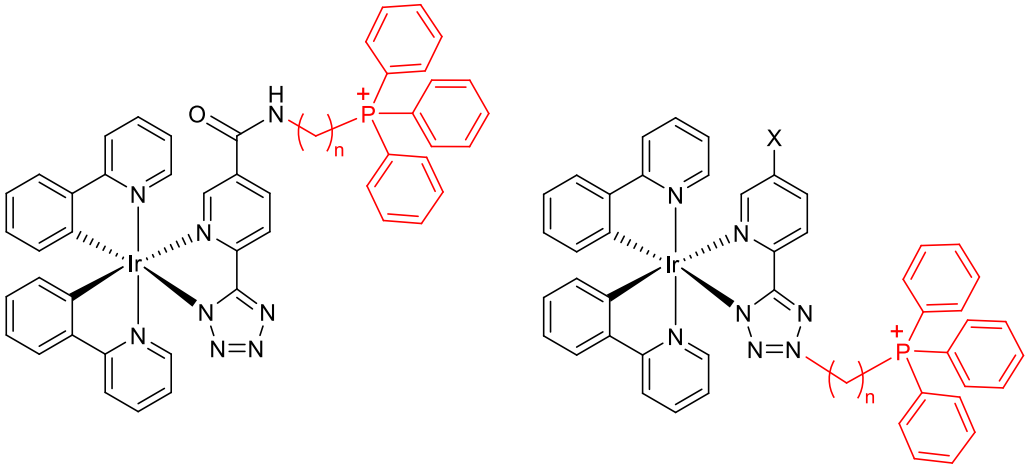

Figure 7.4 Proposed structures of iridium(III) complexes appended with a positively charged phosphonium moiety.

References

1 C. Caporale and M. Massi, *Coord. Chem. Rev.*, 2018, **363**, 71–91.

2 C. W. Schmidt, *Environ. Heal. Prospect.*, 2012, **120**, 118–121.

3 A. Fenster and D. B. Downey, *IEEE Eng. Med. Biol. Mag.*, 1996, **15**, 41–51.

4 D. Hao, T. Ai, F. Goerner, X. Hu, V. M. Runge and M. Tweedle, *J. Magn. Reson. Imaging*, 2012, **36**, 1060–1071.

5 M. Bottrill, L. Kwok and N. J. Long, *Chem. Soc. Rev.*, 2006, **35**, 557–571.

6 S. Maniam and J. Szklaruk, *World J. Radiol.*, 2010, **2**, 309–322.

7 M. A. Klenner, G. Pascali, B. Zhang, T. R. Sia, L. K. Spare, A. M. Krause-Heuer, J. R. Aldrich-Wright, I. Greguric, A. J. Guastella, M. Massi and B. H. Fraser, *Chem. - A Eur. J.*, 2017, **23**, 6499–6503.

8 R. E. Jacobs and S. R. Cherry, *Curr. Opin. Neurobiol.*, 2001, **11**, 621–629.

9 D. J. Brooks, *NeuroRx*, 2005, **2**, 226–236.

10 M. M. Khalil, J. L. Tremoleda, T. B. Bayomy and W. Gsell, *Int. J. Mol. Imaging*, 2011, 1–15.

11 K. Licha and C. Olbrich, *Adv. Drug Deliv. Rev.*, 2005, **57**, 1087–1108.

12 C. Balas, *Meas. Sci. Technol.*, 2009, **20**, 1–12.

13 H. Cho, *MATEC Web Conf.*, 2015, **32**, 1–6.

14 C. Stringari, R. Sierra, P. J. Donovan and E. Gratton, *J. Biomed. Opt.*, 2012, **17**, 1–11.

15 C. Ma, K. Wu, K. Wang, H. He, F. Ning and J. Wang, *Anal. Methods*, 2016, **8**, 7453–7459.

16 Y. Wang, C. Song, M. Wang, Y. Xie, L. Mi and G. Wang, *IEEE J. Sel. Top. Quantum Electron.*, 2016, **22**, 1–7.

17 Q. Li and S. Seeger, *Appl. Spectrosc. Rev.*, 2010, **45**, 12–43.

18 A. Sorvina, C. A. Bader, M. C. Lock, D. A. Brooks, J. L. Morrison and S. E.

Plush, *J. Biophotonics*, 2017, 1–8.

19 M. Lukies, *Radiopaedia.org*, 2017, https://radiopaedia.org/cases/normal-pelvis-and-bo.

20 J. Jones, *Radiopaedia.org*, 2006, https://rahttps://radiopaedia.org/images/24804.

21 A. Mehta, *Brainfacts.org*, 2014, http://www.brainfacts.org/in-the-lab/tools-and-tec.

22 Cecilia Schubert, *Neurosci. News*, 2016, http://neurosciencenews.com/amyloid-beta-versatili.

23 R. L. Mosley and K. Estes, *Unmc.edu*, https://www.unmc.edu/pharmacology/research/cores/s.

24 M. W. Davidson, *Micro.magnet.fsu.edu*, 2004, https://micro.magnet.fsu.edu/primer/techniques/flu.

25 A. H. Gandjbakhche, V. Chernomordik, D. Hattery, M. Hassan and I. Gannot, *Technol. Cancer Res. Treat.*, 2003, **2**, 537.

26 J.-Y. Scoazec, *Gut*, 2003, **52 Suppl 4**, iv1-v6.

27 V. Ntziachristos, *Nat. Methods*, 2010, **7**, 603–614.

28 W. R. Zipfel, R. M. Williams and W. W. Webb, *Nat. Biotechnol.*, 2003, **21**, 1369–1377.

29 M. R. Hamblin and T. N. Demidova, *Proc. SPIE*, 2006, **6140**, 614001–12.

30 M. D. Cahalan, I. Parker, S. H. Wei and M. J. Miller, *Nat. Rev. Immunol.*, 2002, **2**, 872–880.

31 Y. Liu, P. Zhang, X. Fang, G. Wu, S. Chen, Z. Zhang, H. Chao, W. Tan and L. Xu, *Dalt. Trans.*, 2017, **46**, 4777–4785.

32 K. Kiyose, H. Kojima and T. Nagano, *Chem. - An Asian J.*, 2008, **3**, 506–515.

33 G. Zhang, H. Zhang, Y. Gao, R. Tao, L. Xin, J. Yi, F. Li, W. Liu and J. Qiao, *Organometallics*, 2014, **33**, 61–68.

34 W. Tan, Q. Zhang, J. Zhang and H. Tian, *Org. Lett.*, 2009, **11**, 161–164.

35 Z. Guo, S. Park, J. Yoon and I. Shin, *Chem. Soc. Rev.*, 2014, **43**, 16–29.

36 J. Liu, Y. Q. Sun, H. Zhang, H. Shi, Y. Shi and W. Guo, *ACS Appl. Mater. Interfaces*, 2016, **8**, 22953–22962.

37 H. Ganjali and M. Ganjali, *Int. J. Farming Allied Sci.*, 2013, **2**, 686–689.

38 N. W. Troiano, W. A. Ciovacco and M. A. Kacena, *J. Histotechnol.*, 2009, **32**, 27–31.

39 J. H. Williams, B. L. Mepham and D. H. Wright, *J. Clin. Pathol.*, 1997, **50**, 422–428.

40 C. Cottet-Rousselle, X. Ronot, X. Leverve and J. F. Mayol, *Cytom. Part A*, 2011, **79 A**, 405–425.

41 W. Yang and R. Yuste, *Nat. Methods*, 2017, **14**, 349–359.

42 D. Aigner, S. M. Borisov, F. J. Orriach Fernández, J. F. Fernández Sánchez, R. Saf and I. Klimant, *Talanta*, 2012, **99**, 194–201.

43 L. Long, X. Li, D. Zhang, S. Meng, J. Zhang, X. Sun, C. Zhang, L. Zhou and L. Wang, *RSC Adv.*, 2013, **3**, 12204–12209.

44 N. Panchuk-Voloshina, R. P. Haugland, J. Bishop-Stewart, M. K. Bhalgat, P. J. Millard, F. Mao, W. Y. Leung and R. P. Haugland, *J. Histochem. Cytochem.*, 1999, **47**, 1179–1188.

45 X.-F. Zhang, T. Zhang, S.-L. Shen, J.-Y. Miao and B.-X. Zhao, *RSC Adv.*, 2015, **3**, 3260–3266.

46 H. Zhu, J. Fan, J. Du and X. Peng, *Acc. Chem. Res.*, 2016, **49**, 2115–2126.

47 H. N. Kim, M. H. Lee, H. J. Kim, J. S. Kim and J. Yoon, *Chem. Soc. Rev.*, 2008, **37**, 1465–1472.

48 T. Terai and T. Nagano, *Pflugers Arch. Eur. J. Physiol.*, 2013, **465**, 347–359.

49 L. D. Lavis and R. T. Raines, *ACS Chem. Biol.*, 2008, **3**, 142–155.

50 M. Sameiro and T. Gonçalves, *Chem. Rev.*, 2009, **109**, 190–212.

51 P. L. Choyke, R. Alford, H. M. Simpson, J. Duberman, G. Craig Hill, M. Ogawa, C. Regino and H. Kobayashi, *Mol. Imaging*, 2009, **8**, 341–354.

52 K. P. Quinn, G. V. Sridharan, R. S. Hayden, D. L. Kaplan, K. Lee and I. Georgakoudi, *Sci. Rep.*, 2013, **3**, 1–10.

53 M. C. Skala, K. M. Riching, A. Gendron-Fitzpatrick, J. Eickhoff, K. W. Eliceiri, J. G. White and N. Ramanujam, *Proc. Natl. Acad. Sci.*, 2007, **104**, 19494–19499.

54 T. S. Blacker, Z. F. Mann, J. E. Gale, M. Ziegler, A. J. Bain, G. Szabadkai and M. R. Duchen, *Nat. Commun.*, 2014, **5**, 1–9.

55 C. W. Shuttleworth, *Neurochem Int.*, 2010, **56**, 379–386.

56 A. Ghisaidoobe and S. Chung, *Int. J. Mol. Sci.*, 2014, **15**, 22518–22538.

57 N. Tayeh, T. Rungassamy and J. R. Albani, *J. Pharm. Biomed. Anal.*, 2009, **50**, 107–116.

58 E. P. Ippen, C. V. Shank and A. Dienes, *IEEE J. Quantum Electron.*, 1971, 178–

179.

59 D. Beer and J. Weber, *IEEE J. Quantum Electron.*, 1972, **5**, 307–309.

60 C. Eggeling, J. Widengren, R. Rigler and C. A. M. Seidel, *Anal. Chem.*, 1998, **70**, 2651–2659.

61 L. E. Wedlock and S. J. Berners-Price, *Aust. J. Chem.*, 2011, **64**, 692–704.

62 M. P. Coogan and V. Fernandez-Moreira, *Chem. Commun.*, 2013, **50**, 384–399.

63 H.-W. Liu, K. Y. Zhang, W. H.-T. Law and K. K.-W. Lo, *Organometallics*, 2010, **29**, 3474–3476.

64 M. Mauro, A. Aliprandi, D. Septiadi, N. S. Kehr and L. De Cola, *Chem. Soc. Rev.*, 2014, **43**, 4144–4166.

65 K. K.-W. Lo, *Acc. Chem. Res.*, 2015, **48**, 2985–2995.

66 D. Sun, Y. Liu, Q. Yu, D. Liu, Y. Zhou and J. Liu, *J. Inorg. Biochem.*, 2015, **150**, 90–99.

67 T. S.-M. Tang, H.-W. Liu and K. K.-W. Lo, *Chem. Commun.*, 2017, **53**, 3299–3302.

68 K. Yin Zhang, K. Ka-Shun Tso, M. W. Louie, H. W. Liu and K. Kam-Wing Lo, *Organometallics*, 2013, **32**, 5098–5102.

69 T. Zou, C. T. Lum, S. S. Y. Chui and C. M. Che, *Angew. Chemie - Int. Ed.*, 2013, **52**, 2930–2933.

70 X. S. Xiao, W. L. Kwong, X. Guan, C. Yang, W. Lu and C. M. Che, *Chem. - A Eur. J.*, 2013, **19**, 9457–9462.

71 V. Balzani, B. Sebastiano, C. G. Ciamician, U. Bologna, C. Inorganica, C. Analitica, C. Fisica and U. Messina, *Top. Curr. Chem.*, 2007, **280**, 1–36.

72 J. R. Lakowicz, *Principles of Fluorescence Spectroscopy*, 2006.

73 D. Beljonne, Z. Shuai, G. Pourtois and J. L. Bredas, *J. Phys. Chem. A*, 2001, **105**, 3899–3907.

74 S. Lamansky, P. Djurovich, D. Murphy, F. Abdel-Razzaq, R. Kwong, I. Tsyba, M. Bortz, B. Mui, R. Bau and M. E. Thompson, *Inorg. Chem.*, 2001, **40**, 1704–1711.

75 J. V. Caspar and T. J. Meyer, *J. Phys. Chem.*, 1983, **87**, 952–957.

76 R. A. Kirgan, P. B. Sullican and D. P. Rillema, *Top. Curr. Chem.*, 2007, **281**, 45–100.

77 L. Flamigni, A. Barbieri, C. Sabatini, B. Ventura and F. Barigelletti, *Top. Curr. Chem.*, 2007, **171**, 143–203.

78 D. L. Dexter and J. H. Schulman, *J. Chem. Phys.*, 1954, **22**, 1063–1070.

79 K. D. Chaudhuri, *Zeitschrift fur Phys.*, 1959, **154**, 34–42.

80 V. Fernandez-Moreira, F. L. Thorp-Greenwood and M. P. Coogan, *Chem. Commun.*, 2010, **46**, 186–202.

81 F. L. Thorp-Greenwood, R. G. Balasingham and M. P. Coogan, *J. Organomet. Chem.*, 2012, **714**, 12–21.

82 S. W. Botchway, M. Charnley, J. W. Haycock, A. W. Parker, D. L. Rochester, J. A. Weinstein and J. A. G. Williams, *Proc. Natl. Acad. Sci.*, 2008, **105**, 16071–16076.

83 E. Baggaley, S. W. Botchway, J. W. Haycock, H. Morris, I. V. Sazanovich, J. A. G. Williams and J. A. Weinstein, *Chem. Sci.*, 2014, **5**, 879–886.

84 J.-C. G. Bünzli, *Interface Focus*, 2013, **3**, 1–17.

85 M. W. Louie, H. W. Liu, M. H. C. Lam, Y. W. Lam and K. K.-W. Lo, *Chem. - A Eur. J.*, 2011, **17**, 8304–8308.

86 E. Rutkowska, K. Pająk and K. Jóźwiak, *Acta Pol. Pharm. - Drug Res.*, 2013, **70**, 3–18.

87 A. M. Smith, M. C. Mancini and S. Nie, *Nat. Nanotechnol.*, 2009, **4**, 710–711.

88 H.-Y. Youn, D. J. McCanna, J. G. Sivak and L. W. Jones, *Mol. Vis.*, 2011, **17**, 237–246.

89 Y.-J. Gong, X.-B. Zhang, G.-J. Mao, L. Su, H.-M. Meng, W. Tan, S. Feng and G. Zhang, *Chem. Sci.*, 2016, **7**, 2275–2285.

90 L. A. Sordillo, Y. Pu, S. Pratavieira, Y. Budansky and R. R. Alfano, *J. Biomed. Opt.*, 2014, **19**, 56004.

91 U. Jungwirth, C. R. Kowol, B. K. Keppler, C. G. Hartinger, W. Berger and P. Heffeter, *Antioxid Redox Signal.*, 2011, **15**, 1085–1127.

92 D. Ashen-Garry and M. Selke, *Photochem. Photobiol.*, 2014, **90**, 257–274.

93 P. R. Ogilby, *Chem. Soc. Rev.*, 2010, **39**, 3181–3209.

94 M. C. DeRosa and R. J. Crutchley, *Coord. Chem. Rev.*, 2002, **233–234**, 351–371.

95 G. Boso, D. Ke, B. Korzh, J. Bouilloux, N. Lange and H. Zbinden, *Biomed. Opt. Express*, 2016, **7**, 944–950.

96 R. E. Doherty, I. V. Sazanovich, L. K. McKenzie, A. S. Stasheuski, R. Coyle, E. Baggaley, S. Bottomley, J. A. Weinstein and H. E. Bryant, *Sci. Rep.*, 2016, **6**, 1–9.

97 A. Kastl, S. Dieckmann, K. Wähler, T. Völker, L. Kastl, A. L. Merkel, A. Vultur, B. Shannan, K. Harms, M. Ocker, W. J. Parak, M. Herlyn and E. Meggers, *ChemMedChem*, 2013, **8**, 924–927.

98 L. K. McKenzie, I. V. Sazanovich, E. Baggaley, M. Bonneau, V. Guerchais, J. A. G. Williams, J. A. Weinstein and H. E. Bryant, *Chem. - A Eur. J.*, 2017, **23**, 234–238.

99 B. S. Howerton, D. K. Heidary and E. C. Glazer, *J. Am. Chem. Soc.*, 2012, **134**, 8324–8327.

100 J. Liu, C. Jin, B. Yuan, Y. Chen, X. Liu, L. Ji and H. Chao, *Chem. Commun.*, 2017, **53**, 9878–9881.

101 Q. Zhao, M. Yu, L. Shi, S. Liu, C. Li, M. Shi, Z. Zhou, C. Huang and F. Li, *Organometallics*, 2010, **29**, 1085–1091.

102 C. Jin, J. Liu, Y. Chen, R. Guan, C. Ouyang, Y. Zhu, L. Ji and H. Chao, *Sci. Rep.*, 2016, 1–13.

103 L. Murphy, A. Congreve, L.-O. Pålsson and J. A. G. Williams, *Chem. Commun.*, 2010, **46**, 8743–8745.

104 L. He, Y. Li, C.-P. Tan, R.-R. Ye, M.-H. Chen, J.-J. Cao, L.-N. Ji and Z.-W. Mao, *Chem. Sci.*, 2015, **6**, 5409–5418.

105 T. F. Anjong, G. Kim, H. Y. Jang, J. Yoon and J. Kim, *New J. Chem.*, 2017, **41**, 377–386.

106 K. K.-S. Tso and K. K.-W. Lo, *Iridium(III) Optoelectron. Photonics Appl.*, 2017, 415–477.

107 A. Baschieri, S. Muzzioli, V. Fiorini, E. Matteucci, M. Massi, L. Sambri and S. Stagni, *Organometallics*, 2014, **33**, 6154–6164.

108 M. Yu, Q. Zhao, L. Shi, F. Li, Z. Zhou, H. Yang, T. Yi and C. Huang, *Chem. Commun.*, 2008, 2115–2117.

109 Y. Wu, H. Jing, Z. Dong, Q. Zhao, H. Wu and F. Li, *Inorg. Chem.*, 2011, **50**, 7412–7420.

110 W. Tan, J. Zhou, F. Li, T. Yi and H. Tian, *Chem. - An Asian J.*, 2011, **6**, 1263–1268.

111 H. Wu, T. Yang, Q. Zhao, J. Zhou, C. Li and F. Li, *Dalt. Trans.*, 2011, **40**, 1969–1976.

112 Y. Zhou, J. Jia, W. Li, H. Fei and M. Zhou, *Chem Commun*, 2013, **49**, 3230–3232.

113 W. Lv, T. Yang, Q. Yu, Q. Zhao, K. Y. Zhang, H. Liang, S. Liu, F. Li and W. Huang, *Adv. Sci.*, 2015, **2**, 1500107.

114 L. C.-C. Lee, J. C.-W. Lau, H.-W. Liu and K. K.-W. Lo, *Angew. Chem. Int. Ed.*, 2016, **55**, 1046–1049.

115 K. Y. Zhang, S. P.-Y. Li, N. Zhu, L. W.-S. Or, M. S.-H. Cheung, Y.-W. Lam and K. K.-W. Lo, *Inorg. Chem.*, 2010, **49**, 2530–2540.

116 C. Li, M. Yu, Y. Sun, Y. Wu, C. Huang and F. Li, *J. Am. Chem. Soc.*, 2011, **133**, 11231–11239.

117 C. Li, Y. Liu, Y. Wu, Y. Sun and F. Li, *Biomaterials*, 2013, **34**, 1223–1234.

118 A. Wragg, M. R. Gill, D. Turton, H. Adams, T. M. Roseveare, C. Smythe, X. Su and J. A. Thomas, *Chem. - A Eur. J.*, 2014, **20**, 14004–14011.

119 A. Wragg, M. R. Gill, L. McKenzie, C. Glover, R. Mowll, J. a. Weinstein, X. Su, C. Smythe and J. A. Thomas, *Chem. - A Eur. J.*, 2015, **21**, 11865–11871.

120 P. Steunenberg, A. Ruggi, N. S. Van Den Berg, T. Buckle, J. Kuil, F. W. B. Van Leeuwen and A. H. Velders, *Inorg. Chem.*, 2012, **51**, 2105–2114.

121 S. Moromizato, Y. Hisamatsu, T. Suzuki, Y. Matsuo, R. Abe and S. Aoki, *Inorg. Chem.*, 2012, **51**, 12697–12706.

122 K. Qiu, H. Huang, B. Liu, Y. Liu, Z. Huang, Y. Chen, L. Ji and H. Chao, *ACS Appl. Mater. Interfaces*, 2016, **8**, 12702–12710.

123 S. P.-Y. Li, T. S.-M. Tang, K. S.-M. Yiu and K. K.-W. Lo, *Chem. - A Eur. J.*, 2012, **18**, 13342–13354.

124 T. S.-M. Tang, K.-K. Leung, M.-W. Louie, H.-W. Liu, S. H. Cheng and K. K.-W. Lo, *Dalt. Trans.*, 2015, **44**, 4945–4956.

125 B. Wang, Y. Liang, H. Dong, T. Tan, B. Zhan, J. Cheng, K. K.-W. Lo, Y. W. Lam and S. H. Cheng, *ChemBioChem*, 2012, **13**, 2729–2737.

126 W. H.-T. Law, L. C.-C. Lee, M.-W. Louie, H.-W. Liu, T. W.-H. Ang and K. K.-W. Lo, *Inorg. Chem.*, 2013, **52**, 13029–13041.

127 K. K.-W. Lo, B. T.-N. Chan, H.-W. Liu, K. Y. Zhang, S. P.-Y. Li and T. S.-M. Tang, *Chem. Commun.*, 2013, **49**, 4271–4273.

128 A. Nakagawa, Y. Hisamatsu, S. Moromizato, M. Kohno and S. Aoki, *Inorg. Chem.*, 2014, **53**, 409–422.

129 L. Sun, Y. Chen, S. Kuang, G. Li, R. Guan, J. Liu, L. Ji and H. Chao, *Chem. - A Eur. J.*, 2016, **22**, 8955–8965.

130 K. K.-S. Tso, K.-K. Leung, H.-W. Liu and K. K.-W. Lo, *Chem. Commun.*, 2016,

52, 4557–4560.

131 J. Liu, C. Jin, B. Yuan, X. Liu, Y. Chen, L. Ji and H. Chao, *Chem. Commun.*, 2017, **53**, 2052–2055.

132 H. Huang, P. Zhang, K. Qiu, J. Huang, Y. Chen, L. Ji and H. Chao, *Sci. Rep.*, 2016, **6**, 1–12.

133 P. Alam, S. Dash, C. Climent, G. Kaur, A. R. Choudhury, D. Casanova, P. Alemany, R. Chowdhury and I. R. Laskar, *RSC Adv.*, 2017, **7**, 5642–5648.

134 J.-J. Cao, C.-P. Tan, M.-H. Chen, N. Wu, D.-Y. Yao, X.-G. Liu, L.-N. Ji and Z.-W. Mao, *Chem. Sci.*, 2017, **8**, 631–640.

135 M. Ouyang, L. Zeng, H. Huang, C. Jin, J. Liu, Y. Chen, L. Ji and H. Chao, *Dalt. Trans.*, 2017, **46**, 6734–6744.

136 S. P.-Y. Li, C. T.-S. Lau, M.-W. Louie, Y.-W. Lam, S. H. Cheng and K. K.-W. Lo, *Biomaterials*, 2013, **34**, 7519–7532.

137 J. S. Y. Lau, P. K. Lee, K. H. K. Tsang, C. H. C. Ng, Y. W. Lam, S. H. Cheng and K. K. W. Lo, *Inorg. Chem.*, 2009, **48**, 708–718.

138 K. K.-W. Lo, S.-K. Leung and C.-Y. Pan, *Inorganica Chim. Acta*, 2012, **380**, 343–349.

139 R. Cao, J. Jia, X. Ma, M. Zhou and H. Fei, *J. Med. Chem.*, 2013, **56**, 3636–3644.

140 S. Liu, W. Qiao, G. Cao, Y. Chen, Y. Ma and Y. Huang, *Macromol. Rapid Commun.*, 2013, **34**, 81–86.

141 K. Y. Zhang, H.-W. Liu, T. T.-H. Fong, X.-G. Chen and K. K.-W. Lo, *Inorg. Chem.*, 2010, **49**, 5432–5443.

142 S. P.-Y. Li, A. M.-H. Yip, H.-W. Liu and K. K.-W. Lo, *Biomaterials*, 2016, **103**, 305–313.

143 J. S. Nam, M. G. Kang, J. Kang, S. Y. Park, S. J. C. Lee, H. T. Kim, J. K. Seo, O. H. Kwon, M. H. Lim, H. W. Rhee and T. H. Kwon, *J. Am. Chem. Soc.*, 2016, **138**, 10968–10977.

144 S. P.-Y. Li, H.-W. Liu, K. Y. Zhang and K. K.-W. Lo, *Chem. - A Eur. J.*, 2010, **16**, 8329–8339.

145 K. Luby-Phelps, *Mol. Biol. Cell*, 2013, **24**, 2593–2596.

146 R. E. Goldstein and J.-W. van de Meent, *Interface Focus*, 2015, **5**, 1–15.

147 G. Dirk and U. Kutay, *Annu. Rev. Cell Dev. Biol.*, 1999, **15**, 607–660.

148 Q. Zhao, S. Liu, M. Shi, C. Wang, M. Yu, L. Li, F. Li, T. Yi and C. Huang, *Inorg. Chem.*, 2006, **45**, 6152–6160.

149 J. Liu, W. Bu, L. Pan and J. Shi, *Angew. Chem. Int. Ed.*, 2013, **52**, 4375–4379.

150 W. Zhu, X. Meng, Y. Yang, Q. Zhang, Y. Xie and H. Tian, *Chem. - A Eur. J.*, 2010, **16**, 899–906.

151 F. J. Giordano, *J. Clin. Invest.*, 2005, **115**, 500–508.

152 J. Biddlestone, D. Bandarra and S. Rocha, *Int. J. Mol. Med.*, 2015, **35**, 859–869.

153 B. Muz, P. de la Puente, F. Azab and A. K. Azab, *Hypoxia*, 2015, **3**, 83–92.

154 D. A. MacKenzie, A. R. Sherratt, M. Chigrinova, L. L. W. Cheung and J. P. Pezacki, *Curr. Opin. Chem. Biol.*, 2014, **21**, 81–88.

155 G. Li, Q. Lin, L. Ji and H. Chao, *J. Mater. Chem. B Mater. Biol. Med.*, 2014, **2**, 7918–7926.

156 M. Li, Y. Wang, Y. Yang, Y. Gao, M. Zhao, M. Zheng and S. Peng, *Dalt. Trans.*, 2015, **44**, 14071–14076.

157 T. Pederson, *Cold Spring Harb. Lab. Press*, 2015, 1–17.

158 S. Gorski and T. Misteli, *J. Cell Sci.*, 2005, **118**, 4083–4092.

159 W. Jiang, Y. Gao, Y. Sun, F. Ding, Y. Xu, Z. Bian, F. Li, J. Bian and C. Huango, *Inorg. Chem.*, 2010, **49**, 3252–3260.

160 M. Dundr and T. Misteli, *Biochem. J.*, 2001, **356**, 297–310.

161 D. Hernandez-Verdun, P. Roussel, M. Thiry, V. Sirri and D. L. J. Lafontaine, *Wiley Interdiscip. Rev. RNA*, 2010, **1**, 415–431.

162 H. Ahmad, A. Wragg, W. Cullen, C. Wombwell, A. J. H. M. Meijer and J. A. Thomas, *Chem. - A Eur. J.*, 2014, **20**, 3089–3096.

163 D. J. Klionsky and S. D. Emr, *Science*, 2000, **290**, 1717–1721.

164 J. P. Luzio, P. R. Pryor and N. A. Bright, *Nat. Rev. Mol. Cell Biol.*, 2007, **8**, 622–632.

165 M. Ghosh, F. Carlsson, A. Laskar, X.-M. Yuan and W. Li, *FEBS Lett.*, 2011, **585**, 623–629.

166 M. E. Guicciardi, M. Leist and G. J. Gores, *Oncogene*, 2004, **23**, 2881–2890.

167 U. Repnik and B. Turk, *Mitochondrion*, 2010, **10**, 662–669.

168 L. Zhang, R. Sheng and Z. Qin, *Acta Biochim. Biophys. Sin.*, 2009, **41**, 437–445.

169 R. P. Hesselink, A. J. M. Wagenmakers, M. R. Drost and G. J. Van der Vusse, *Biochim. Biophys. Acta*, 2003, **1637**, 164–170.

170 E. F. Neufeld, *Annu. Rev. Biochem.*, 1991, **60**, 257–280.

171 C. C. Scott, F. Vacca and J. Gruenberg, *Semin. Cell Dev. Biol.*, 2014, **31**, 2–10.

172 J. P. Luzio, B. M. Mullock, P. R. Pryor, M. R. Lindsay, D. E. James and R. C. Piper, *Biochem. Soc. Trans.*, 2001, **29**, 476–480.

173 F. R. Maxfield, *Cold Spring Harb. Perspect. Biol.*, 2014, **6**, 1–16.

174 R. A. Nixon, *Neurobiol. Aging*, 2005, **26**, 373–382.

175 L. Zhu, W. Lv, S. Liu, H. Yan, Q. Zhao and W. Huang, *Chem. Commun.*, 2013, **49**, 10638–10640.

176 C. R. Berkers, F. W. B. van Leeuwen, T. a Groothuis, V. Peperzak, E. W. van Tilburg, J. Borst, J. J. Neefjes and H. Ovaa, *Mol. Pharm.*, 2007, **4**, 739–748.

177 X. Zhu, W. Lu, Y. Zhang, A. Reed, B. Newton, Z. Fan, H. Yu, P. C. Ray and R. Gao, *Chem. Commun.*, 2011, **47**, 10311–10313.

178 Y.-M. Ho, N.-P. B. Au, K.-L. Wong, C. T.-L. Chan, W.-M. Kwok, G.-L. Law, K.-K. Tang, W.-Y. Wong, C.-H. E. Ma and M. H.-W. Lam, *Chem. Commun.*, 2014, **50**, 4161–4163.

179 L. He, S.-Y. Liao, C.-P. Tan, Y.-Y. Lu, C.-X. Xu, L.-N. Ji and Z.-W. Mao, *Chem. Commun.*, 2014, **50**, 5611–5614.

180 H. Yu, Y. Xiao and L. Jin, *J. Am. Chem. Soc.*, 2012, **134**, 17486–17489.

181 S. Di Gioia and M. Conese, *Drug Des. Devel. Ther.*, 2008, **2**, 163–188.

182 A. Akinc, M. Thomas, A. M. Klibanov and R. Langer, *J. Gene Med.*, 2005, **7**, 657–663.

183 K.-M. Lee, Y.-B. Lee and O. I.-J., *J. Nanosci. Nanotechnol.*, 2011, **11**, 7078–7081.

184 A. C. Hunter, *Adv. Drug Deliv. Rev.*, 2006, **58**, 1523–1531.

185 J. Rejman, M. Conese and A. Bragonzi, *Mol. Ther.*, 2005, **12**, 237–247.

186 J. R. Friedman and J. Nunnari, *Nature*, 2014, **505**, 335–343.

187 S. A. Detmer and D. C. Chan, *Nat. Rev. Mol. Cell Biol.*, 2007, **8**, 870–879.

188 J. Nunnari and A. Suomalainen, *Cell*, 2012, **148**, 1145–1159.

189 S. Vyas, E. Zaganjor and M. C. Haigis, *Cell*, 2016, **166**, 555–566.

190 R. J. Gillies, I. Robey and R. a Gatenby, *J Nucl Med*, 2008, **49**, 24S–42S.

191 S. Rodríguez-Enríquez, A. Marín-Hernández, J. C. Gallardo-Pérez, L. Carreño-Fuentes and R. Moreno-Sánchez, *Mol. Nutr. Food Res.*, 2009, **53**, 29–48.

192 X. Ning, J. Guo, M. a. Wolfert and G. J. Boons, *Angew. Chem. Int. Ed.*, 2008, **47**, 2253–2255.

193 A. E. Wendlandt and S. S. Stahl, *Angew. Chem. Int. Ed.*, 2015, **54**, 14638–14658.

194 Z. Liu, R. J. Deeth, J. S. Butler, A. Habtemariam, M. E. Newton and P. J. Sadler, *Angew. Chem. Int. Ed.*, 2013, **52**, 4194–4197.
195 F. M. Veronese, *Biomaterials*, 2001, **22**, 405–417.
196 Y. Hong, J. W. Y. Lam and B. Z. Tang, *Chem. Commun.*, 2009, 4332–4353.
197 D. P. Narendra and R. J. Youle, *Nat. Rev. Mol. Cell Biol.*, 2011, **12**, 9–14.
198 M. Zanoni, F. Piccinini, C. Arienti, A. Zamagni, S. Santi, R. Polico, A. Bevilacqua and A. Tesei, *Sci. Rep.*, 2016, **6**, 1–11.
199 M. H. Lee, N. Park, C. Yi, J. H. Han, J. H. Hong, K. P. Kim, D. H. Kang, J. L. Sessler, C. Kang and J. S. Kim, *J. Am. Chem. Soc.*, 2014, **136**, 14136–14142.
200 S. J. Riedl and Y. Shi, *Nat. Rev. Mol. Cell Biol.*, 2004, **5**, 897–907.
201 C. Jin, J. Liu, Y. Chen, L. Zeng, R. Guan, C. Ouyang, L. Ji and H. Chao, *Chem. - A Eur. J.*, 2015, **21**, 12000–12010.
202 J. V Jokerst, T. Lobovkina, R. N. Zare and S. S. Gambhir, *Nanomedicine*, 2011, **6**, 715–728.
203 M. J. Phillips and G. K. Voeltz, *Nat. Rev. Mol. Cell Biol.*, 2016, **17**, 69–82.
204 D. S. Schwarz and M. D. Blower, *Cell. Mol. Life Sci.*, 2016, **73**, 79–94.
205 C. Xu, B. Bailly-Maitre and J. C. Reed, *J. Clin. Invest.*, 2005, **115**, 2656–2664.
206 A. H. Schönthal, *Scientifica (Cairo).*, 2012, **2012**, 1–26.
207 C. Wilson, R. Venditti, L. R. Rega, A. Colanzi, G. D'Angelo and M. A. De Matteis, *Biochem. J.*, 2011, **433**, 1–9.
208 C. Rabouille and G. Haase, *Front. Neurosci.*, 2016, **9**, 489.
209 M. G. Bexiga and J. C. Simpson, *Int. J. Mol. Sci.*, 2013, **14**, 18670–18681.
210 J. Fan, Z. Hu, L. Zeng, W. Lu, X. Tang, J. Zhang and T. Li, *Int. J. Dev. Neurosci.*, 2008, **26**, 523–534.
211 R. H. McMenamy, *J. Biol. Chem.*, 1965, **240**, 4235–4243.
212 A. Bertuzzi, G. Mlngrone, A. Gandolfi, A. V Greco, S. Ringoir and R. Vanholder, *Clin. Chim. Acta*, 1997, **265**, 183–192.
213 X. Wang, J. Jia, Z. Huang, M. Zhou and H. Fei, *Chem. - A Eur. J.*, 2011, **17**, 8028–8032.
214 J. Wang, Y. Liu, M. Jiang, Y. Li, L. Xia and P. Wu, *Chem. Commun.*, 2018, **54**, 1004–1007.
215 M.-J. Li, C.-Q. Zhan, M.-J. Nie, G.-N. Chen and X. Chen, *J. Inorg. Biochem.*, 2011, **105**, 420–425.
216 A. R. English and G. K. Voeltz, *Cold Spring Harb. Perspect. Biol.*, 2013, **5**, 1–

16.

217 L. M. Kaminskas, B. J. Boyd, P. Karellas, G. Y. Krippner, R. Lessene, B. Kelly and C. J. H. Porter, *Mol. Pharm.*, 2008, **5**, 449–463.

218 C. Yang, S. Gao, F. Dagnæs-Hansen, M. Jakobsen and J. Kjems, *ACS Appl. Mater. Interfaces*, 2017, **9**, 12203–12216.

219 D. Pozzi, V. Colapicchioni, G. Caracciolo, S. Piovesana, A. L. Capriotti, S. Palchetti, S. De Grossi, A. Riccioli, H. Amenitsch and A. Laganà, *Nanoscale*, 2014, **6**, 2782–2792.

220 A. A. A. Boraei, *J. Chem. Eng. Data*, 2001, **46**, 939–943.

221 M. Asif, *Pharm. Methods*, 2014, **5**, 1–9.

222 M. A. Malik, M. Y. Wani, S. A. Al-Thabaiti and R. A. Shiekh, *J. Incl. Phenom. Macrocycl. Chem.*, 2014, **78**, 15–37.

223 C. N. S. S. P. Kumar, D. K. Parida, A. Santhoshi, A. K. Kota, B. Sridhar and V. J. Rao, *Med. Chem. Commun.*, 2011, **2**, 486–492.

224 R. N. Butler and F. L. Scott, *J. Org. Chem.*, 1966, **31**, 3182–3187.

225 R. N. Butler and V. C. Garvin, *J. Chem. Soc. Perkin Trans. 1*, 1981, 390–393.

226 R. N. Butler, V. C. Garvin, H. Lumbroso, C. Liegeois, L. D. C. Gbnbrale, U. Pierre, P. Jussieu and P. Cedex, *J. Chem. Soc. Perkin Trans. 2*, 1984, 721–725.

227 S. Stagni, E. Orselli, A. Palazzi, L. De Cola, S. Zacchini, C. Femoni, M. Marcaccio, F. Paolucci and S. Zanarini, *Inorg. Chem.*, 2007, **46**, 9126–9138.

228 H. Shahroosvand, S. Abaspour, B. Pashaei, E. Radicchi, F. De Angelis and F. Bonaccorso, *Chem. Commun.*, 2017, **53**, 6211–6214.

229 S. Zanarini, A. J. Bard, M. Marcaccio, A. Palazzi, F. Paolucci and S. Stagni, *J. Phys. Chem. B*, 2006, **110**, 22551–22556.

230 M. V. Werrett, P. J. Wright, P. V Simpson, P. Raiteri, B. W. Skelton, S. Stagni, A. G. Buckley, J. Rigby and M. Massi, *Dalt. Trans.*, 2015, 20636–20647.

231 M. V. Werrett, S. Muzzioli, P. J. Wright, A. Palazzi, P. Raiteri, S. Zacchini, M. Massi and S. Stagni, *Inorg. Chem.*, 2014, **53**, 229–243.

232 C. a. Bader, R. D. Brooks, Y. S. Ng, A. Sorvina, M. V. Werrett, P. J. Wright, A. G. Anwer, D. a. Brooks, S. Stagni, S. Muzzioli, M. Silberstein, B. W. Skelton, E. M. Goldys, S. E. Plush, T. Shandala and M. Massi, *RSC Adv.*, 2014, **4**, 16345–16351.

233 P. J. Wright, M. G. Affleck, S. Muzzioli, B. W. Skelton, P. Raiteri, D. S. Silvester, S. Stagni and M. Massi, *Organometallics*, 2013, **32**, 3728–3737.

234 V. Fiorini, A. M. Ranieri, S. Muzzioli, K. D. M. Magee, S. Zacchini, N. Akabar, A. Stefan, M. I. Ogden, M. Massi and S. Stagni, *Dalt. Trans.*, 2015, **44**, 20597–20608.

235 F. Monti, A. Baschieri, I. Gualandi, J. J. Serrano-Pérez, J. M. Junquera-Hernández, D. Tonelli, A. Mazzanti, S. Muzzioli, S. Stagni, C. Roldan-Carmona, A. Pertegás, H. J. Bolink, E. Ortí, L. Sambri and N. Armaroli, *Inorg. Chem.*, 2014, **53**, 7709–7721.

236 S. Stagni, S. Colella, A. Palazzi, G. Valenti, S. Zacchini, F. Paolucci, M. Marcaccio, R. Q. Albuquerque and L. De Cola, *Inorg. Chem.*, 2008, **47**, 10509–10521.

237 V. Fiorini, S. Zacchini, P. Raiteri, R. Mazzoni, V. Zanotti, M. Massi and S. Stagni, *Dalt. Trans.*, 2016, **45**, 12884–12896.

238 C. Caporale, C. A. Bader, A. Sorvina, K. D. M. MaGee, B. W. Skelton, T. A. Gillam, P. J. Wright, P. Raiteri, S. Stagni, J. L. Morrison, S. E. Plush, D. A. Brooks and M. Massi, *Chem. - A Eur. J.*, 2017, **23**, 15666–15679.

239 V. Fiorini, I. Zanoni, S. Zacchini, A. L. Costa, A. Hochkoeppler, V. Zanotti, A. M. Ranieri, M. Massi, A. Stefan and S. Stagni, *Dalt. Trans.*, 2017, **46**, 12328–12338.

240 V. Fiorini, A. D'Ignazio, K. D. M. Magee, M. I. Ogden, M. Massi and S. Stagni, *Dalt. Trans.*, 2016, **45**, 3256–3259.

241 W. Ouellette, H. Liu, C. J. O'Connor and J. Zubieta, *Inorg. Chem.*, 2009, **48**, 4655–4657.

242 L. Bergmann, C. Braun, M. Nieger and S. Bräse, *Dalt. Trans.*, 2018, **47**, 608–621.

243 C. Femoni, S. Muzzioli, A. Palazzi, S. Stagni, S. Zacchini, F. Monti, G. Accorsi, M. Bolognesi, N. Armaroli, M. Massi, G. Valenti and M. Marcaccio, *Dalt. Trans.*, 2013, **42**, 997–1010.

244 J. H. Nelson, D. L. Schmitt, R. A. Henry, D. W. Moore, H. B. Jonassen, J. H. Nelson, D. L. Schmitt, R. A. Henry, D. W. Moore and H. B. Jonassen, *Inorg. Chem.*, 1970, **9**, 2678–2681.

245 K. D. M. MaGee, P. J. Wright, S. Muzzioli, C. M. Siedlovskas, P. Raiteri, M. V Baker, D. H. Brown, S. Stagni and M. Massi, *Dalton Trans.*, 2013, **42**, 4233–6.

246 T. V. Serebryanskaya, T. Yung, A. A. Bogdanov, A. Shchebet, S. A. Johnsen,

A. S. Lyakhov, L. S. Ivashkevich, Z. A. Ibrahimava, T. S. Garbuzenco, T. S. Kolesnikova, N. I. Melnova, P. N. Gaponik and O. A. Ivashkevich, *J. Inorg. Biochem.*, 2013, **120**, 44–53.

247 C. A. Strassert, C. H. Chien, M. D. Galvez Lopez, D. Kourkoulos, D. Hertel, K. Meerholz and L. De Cola, *Angew. Chemie - Int. Ed.*, 2011, **50**, 946–950.

248 C. A. Bader, T. Shandala, E. A. Carter, A. Ivask, T. Guinan, S. M. Hickey, M. V. Werrett, P. J. Wright, P. V. Simpson, S. Stagni, N. H. Voelcker, P. A. Lay, M. Massi, S. E. Plush and D. A. Brooks, *PLoS One*, 2016, **11**, 1–24.

249 R. Palreddy, J. Mohmed, N. Nagula, B. Srinivas and C. S. Devi, *IOSR J. Pharm.*, 2014, **4**, 21–33.

250 K. A. King, P. J. Spellane and R. J. Watts, *J. Am. Chem. Soc.*, 1985, **107**, 1431–1432.

251 M. Baldo, S. Lamansky, P. E. Burrows, M. E. Thompson and S. R. Forrest, *Appl. Phys. Lett.*, 1999, **75**, 4.

252 C. Adachi, M. Baldo, S. R. Forrest and M. E. Thompson, *Appl. Phys. Lett.*, 2000, **77**, 904.

253 K. K.-W. Lo, S. P.-Y. Li and K. Y. Zhang, *New J. Chem.*, 2011, **35**, 265–287.

254 K. K.-W. Lo and K. Y. Zhang, *RSC Adv.*, 2012, 12069–12083.

255 K. K.-W. Lo and K. K.-S. Tso, *Inorg. Chem. Front.*, 2015, **2**, 510–524.

256 C. D. Ertl, L. Gil-Escrig, J. Cerdá, A. Pertegás, H. J. Bolink, J. M. Junquera-Hernández, A. Prescimone, M. Neuburger, E. C. Constable, E. Ortí and C. E. Housecroft, *Dalt. Trans.*, 2016, **45**, 11668–11681.

257 A. F. Henwood, A. K. Bansal, D. B. Cordes, A. M. Z. Slawin, I. D. W. Samuel and E. Zysman-Colman, *J. Mater. Chem. C*, 2016, **4**, 3726–3737.

258 A. F. Henwood and E. Zysman-Colman, *Top. Curr. Chem.*, 2016, **374**, 1–41.

259 D. Wang, Y. Wu, H. Dong, Z. Qin, D. Zhao, Y. Yu, G. Zhou, B. Jiao, Z. Wu, M. Gao and G. Wang, *Org. Electron. physics, Mater. Appl.*, 2013, **14**, 3297–3305.

260 A. Sinopoli, C. J. Wood, E. A. Gibson and P. I. P. Elliott, *Inorg. Chim. Acta*, 2017, **457**, 81–89.

261 A. Telleria, B. S. E. C. Kohlrausch, C. Duarte, S. Rodembusch, J. Dupont, Z. Freixa and M. J. L. Santos, *ChemistrySelect*, 2016, **1**, 2842–2848.

262 M. Wang, W. Wang, T. S. Kang, C. H. Leung and D. L. Ma, *Anal. Chem.*, 2016, **88**, 981–987.

263 D. Ma, S. Lin, W. Wang, C. Yang and C. Leung, *Chem. Sci.*, 2017, **8**, 878–889.

264 W. Wang, Z. Mao, M. Wang, L.-J. Liu, D. W. J. Kwong, C.-H. Leung and D.-L. Ma, *Chem. Commun.*, 2016, **52**, 3611–3614.

265 M. V. Werrett, G. S. Huff, S. Muzzioli, V. Fiorini, S. Zacchini, B. W. Skelton, A. Maggiore, J. M. Malicka, M. Cocchi, K. C. Gordon, S. Stagni and M. Massi, *Dalt. Trans.*, 2015, **44**, 8379–8393.

266 W. Q. Ong, H. Zhao, X. Fang, S. Woen, F. Zhou, W. Yap, H. Su, S. F. Y. Li and H. Zeng, *Org. Lett.*, 2011, **13**, 3194–3197.

267 A. M. Tondreau, J. M. Darmon, B. M. Wile, S. K. Floyd, E. Lobkovsky and P. J. Chirik, *Organometallics*, 2009, **28**, 3928–3940.

268 N. G. R. Hearns, R. Clérac, M. Jennings and K. E. Preuss, *Dalton Trans.*, 2009, 3193–3203.

269 Z. P. Demko and K. B. Sharpless, *J. Org. Chem.*, 2001, **66**, 7945–7950.

270 K. Koguro, T. Oga, S. Mitsui and R. Orita, *Synthesis (Stuttg).*, 1998, **1998**, 910–914.

271 N. M. La, R. Burgard and C. Wentrup, *J. Org. Chem.*, 2004, **69**, 2033–2036.

272 A. Suzuki, *J. Organomet. Chem.*, 1999, **576**, 147–168.

273 W. H. T. Law, K. K. Leung, L. C. C. Lee, C. S. Poon, H. W. Liu and K. K. W. Lo, *ChemMedChem*, 2014, **9**, 1316–1329.

274 K. Nakamaru, *Bull. Chem. Soc. Jpn.*, 1982, 55, 2697–2705.

275 H. Braunschweig, T. Dellermann, R. D. Dewhurst, B. Hupp, T. Kramer, J. D. Mattock, J. Mies, A. K. Phukan, A. Steffen and A. Vargas, *J. Am. Chem. Soc.*, 2017, **139**, 4887–4893.

276 P. T. Chou, Y. Chi, M. W. Chung and C. C. Lin, *Coord. Chem. Rev.*, 2011, **255**, 2653–2665.

277 S. Sprouse, K. a. King, P. . Spellane and R. J. Watts, *J. Am. Chem. Soc.*, 1984, **106**, 6647–6653.

278 J. N. Demas and G. A. Crosby, *J. Phys. Chem.*, 1971, **75**, 991–1024.

279 et al. M. J. Frisch, G. W. Trucks, H. B. Schlegel, G. E. Scuseria, M. A. Robb, J. R. Cheeseman, G. Scalmani, V. Barone, B. Mennucci, G. A. Petersson, *Gaussian09, Revis. B.01*, 2009.

280 C. Lee, W. Yang and R. G. Parr, *Phys. Rev. B*, 1988, **37**, 785–789.

281 A. D. Becke, *J. Chem. Phys.*, 1993, **98**, 1372.

282 J. Tomasi, B. Mennucci and R. Cammi, *Chem. Rev.*, 2005, **105**, 2999–3093.

283 A. Sorvina, C. A. Bader, J. R. T. Darby, M. C. Lock, J. Y. Soo, I. R. D. Johnson, C. Caporale, N. H. Voelcker, S. Stagni, M. Massi, J. L. Morrison, S. E. Plush and D. A. Brooks, *Sci. Rep.*, 2018, **8**, 8191.

284 J. a Thomas, *Chem. Soc. Rev.*, 2015, **44**, 4494–4500.

285 T. Beveridge, *Biotech. Histochem.*, 2001, **76**, 111–118.

286 A. H. Fischer, K. A. Jacobson, J. Rose and R. Zeller, *Cold Spring Harb. Protoc.*, 2008, **3**, 4986–4988.

287 R. Y. Tsien, *Angew. Chem. Int. Ed. Engl.*, 2009, **48**, 5612–5626.

288 S. J. Remington, *Protein Sci.*, 2011, **20**, 1509–1519.

289 D. Bera, L. Qian, T. K. Tseng and P. H. Holloway, *Materials (Basel).*, 2010, **3**, 2260–2345.

290 A. Foubert, N. V. Beloglazova, A. Rajkovic, B. Sas, A. Madder, I. Y. Goryacheva and S. De Saeger, *TrAC - Trends Anal. Chem.*, 2016, **83**, 31–48.

291 D. Parker, *Aust. J. Chem.*, 2011, **64**, 239–243.

292 Q. Zhao, C. Huang and F. Li, *Chem. Soc. Rev.*, 2011, **40**, 2508–2524.

293 Y. Chen, R. Guan, C. Zhang, J. Huang, L. Ji and H. Chao, *Coord. Chem. Rev.*, 2016, **310**, 16–40.

294 A. J. Amoroso and S. J. A. Pope, *Chem. Soc. Rev.*, 2015, **44**, 4723–4742.

295 A. Mohamadi and L. W. Miller, *Bioconjugate Chem.*, 2016, **27**, 2540–2548.

296 G. Li, Q. Lin, L. Ji and H. Chao, *J. Mater. Chem. B*, 2014, **2**, 7918–7926.

297 S. Stimpson, D. R. Jenkinson, A. Sadler, M. Latham, A. Wragg, A. J. H. M. Meijer and J. a. Thomas, *Angew. Chemie - Int. Ed.*, 2015, **54**, 3000–3003.

298 K. K.-W. Lo, W. H.-T. Law, J. C.-Y. Chan, H.-W. Liu and K. Y. Zhang, *Metallomics*, 2013, **5**, 808–812.

299 S. K. Leung, K. Y. Kwok, K. Y. Zhang and K. K. W. Lo, *Inorg. Chem.*, 2010, **49**, 4984–4995.

300 K. K. W. Lo and J. S. Y. Lau, *Inorg. Chem.*, 2007, **46**, 700–709.

301 K. K. Lo, J. S. Chan, L. Lui and C. Chung, *Organometallics*, 2004, **23**, 3108–3116.

302 T. U. Connell, J. L. James, A. R. White and P. S. Donnelly, *Chem. - A Eur. J.*, 2015, **21**, 14146–14155.

303 J. M. Nicholls, L. L. Poon, K. C. Lee, W. F. Ng, S. T. Lai, C. Y. Leung, C. M. Chu, P. K. Hui, K. L. Mak, W. Lim, K. W. Yan, K. H. Chan, N. C. Tsang, Y. Guan, K. Y. Yue and J. S. Peiris, *Lancet*, 2003, **361**, 1773–1778.

304 Y. Li, B. Liu, X.-R. Lu, M.-F. Li, L.-N. Ji and Z.-W. Mao, *Dalt. Trans.*, 2017, **46**, 11363–11371.

305 S. Zhang, M. Hosaka, T. Yoshihara, K. Negishi, Y. Iida, S. Tobita and T. Takeuchi, *Cancer Res.*, 2010, **70**, 4490–4498.

306 S.-K. Leung, H.-W. Liu and K. K.-W. Lo, *Chem. Commun. (Camb).*, 2011, **47**, 10548–10550.

307 S. Mandal, D. K. Poria, R. Ghosh, P. S. Ray and P. Gupta, *Dalt. Trans.*, 2014, **43**, 17463–17474.

308 W. Huber, R. Linder, J. Niesel, U. Schatzschneider, B. Spingler and P. C. Kunz, *Eur. J. Inorg. Chem.*, 2012, 3140–3146.

309 A. M. Courtis, S. A. Santos, Y. Guan, J. A. Hendricks, B. Ghosh, D. M. Szantai-Kis, S. A. Reis, J. V. Shah and R. Mazitschek, *Bioconjugate Chem.*, 2014, **25**, 1043–1051.

310 S. Purser, P. R. Moore, S. Swallow and V. Gouverneur, *Prog. Med. Chem.*, 2015, **54**, 65–133.

311 F.-X. Wang, M.-H. Chen, X.-Y. Hu, R.-R. Ye, C.-P. Tan, L.-N. Ji and Z.-W. Mao, *Sci. Rep.*, 2016, **6**, 1–15.

312 K. E. Merten, Y. Jiang, W. Feng and Y. J. Kang, *J. Pharm. Exp. Ther.*, 2006, **319**, 934–940.

313 Y. Han and H. V. Huynh, *Dalt. Trans.*, 2011, **40**, 2141–2147.

314 J. Adler and I. Parmryd, *Cytometry*, 2010, **77**, 733–742.

315 Q. Gao and J. M. Goodman, *Front. Cell Dev. Biol.*, 2015, **3**, 49.

316 N. Jacquier, V. Choudhary, M. Mari, A. Toulmay, F. Reggiori and R. Schneiter, *J. Cell Sci.*, 2011, **124**, 2424–2437.

317 J. S. Modica-Napolitano and J. R. Aprille, *Adv. Drug Deliv. Rev.*, 2001, **49**, 63–70.

318 S. H. Kaufmann, S. H. Lee, X. W. Meng, D. A. Loegering, T. J. Kottke, A. J. Henzing, S. Ruchaud, K. Samejima and W. C. Earnshaw, *Methods*, 2008, **44**, 262–272.

319 Y. You, S. Cho and W. Nam, *Inorg. Chem.*, 2014, **53**, 1804–1815.

320 C. Köhler, S. Orrenius and B. Zhivotovsky, *J. Immunol. Methods*, 2002, **265**, 97–110.

321 D. R. McIlwain, T. Berger and T. W. Mak, *Cold Spring Harb. Perspect. Biol.*, 2013, 1–28.

322 R. Zondervan, F. Kulzer, M. a. Kol'chenko and M. Orrit, *J. Phys. Chem. A*, 2004, **108**, 1657–1665.

323 L. He, C. P. Tan, R. R. Ye, Y. Z. Zhao, Y. H. Liu, Q. Zhao, L. N. Ji and Z.-W. Mao, *Angew. Chemie - Int. Ed.*, 2014, **53**, 12137–12141.

324 R. Rizzuto, D. De Stefani, A. Raffaello and C. Mammucari, *Nat. Rev. Mol. Cell Biol.*, 2012, **13**, 566–578.

325 A. A. Starkov, *Ann. NY Acad. Sci.*, 2008, **1147**, 37–52.

326 M. Liesa and O. S. Shirihai, *Cell Metab.*, 2013, **17**, 491–506.

327 G. W. Dorn, *EMBO Mol. Med.*, 2015, **7**, 865–877.

328 N. Miller, H. Shi, A. S. Zelikovich and Y.-C. Ma, *Hum. Mol. Genet.*, 2016, **25**, 3395–3406.

329 C. Lopez-Crisosto, C. Pennanen, C. Vasquez-Trincado, P. E. Morales, R. Bravo-Sagua, A. F. G. Quest, M. Chiong and S. Lavandero, *Nat. Rev. Cardiol.*, 2017, **14**, 342–360.

330 C. S. Chen and K. R. Gee, *Free Radic. Biol. Med.*, 2000, **28**, 1266–1278.

331 A. Cossarizza, M. Baccarani-Contri, G. Kalashnikova and C. Franceschi, *Biochem. Biophys. Res. Commun.*, 1993, 197, 40–45.

332 B. Glancy, L. M. Hartnell, D. Malide, Z. X. Yu, C. A. Combs, P. S. Connelly, S. Subramaniam and R. S. Balaban, *Nature*, 2015, **523**, 617–620.

333 M. Vendelin, N. Béraud, K. Guerrero, T. Andrienko, A. V. Kuznetsov, J. Olivares, L. Kay and V. A. Saks, *Am J Physiol Cell Physiol*, 2005, **288**, C757-767.

334 C. A. Lewis, S. J. Parker, B. P. Fiske, D. McCloskey, D. Y. Gui, C. R. Green, N. I. Vokes, A. M. Feist, M. G. Vander Heiden and C. M. Metallo, *Mol. Cell*, 2014, **55**, 253–263.

335 M. Kalbáčová, M. Vrbacký, Z. Drahota and Z. Mělková, *Cytom. Part A*, 2003, **52A**, 110–116.

336 H. Huang, L. Yang, P. Zhang, K. Qiu, J. Huang, Y. Chen, J. J. Diao, J. Liu, L. Ji, J. Long and H. Chao, *Biomaterials*, 2016, **83**, 321–331.

337 Y. Chen, L. Qiao, L. Ji and H. Chao, *Biomaterials*, 2014, **35**, 2–13.

338 Y. Chen, L. Qiao, B. Yu, G. Li, C. Liu, L. Ji and H. Chao, *Chem. Commun.*, 2013, **49**, 11095–11097.

339 Y. Chen, W. Xu, J. Zuo, L. Ji and H. Chao, *J. Mater. Chem. B*, 2015, **3**, 3306–3314.

340 D. Grundy, *J. Physiol.*, 2015, **593**, 2547–2549.

341 J. Srivastava, D. L. Barber and M. P. Jacobson, *Physiology*, 2007, **22**, 30–39.

342 Y. Xu, Z. Jiang, Y. Xiao, F. Z. Bi, J. Y. Miao and B. X. Zhao, *Anal. Chim. Acta*, 2014, **820**, 146–151.

343 P. Swietach, R. D. Vaughan-Jones, A. L. Harris and A. Hulikova, *Philos. Trans. R. Soc.*, 2014, **369**, 1–9.

344 D. Lagadic-Gossmann, L. Huc and V. Lecureur, *Cell Death Differ.*, 2004, **11**, 953–961.

345 H. Sakai, G. Li, Y. Hino, Y. Moriura, J. Kawawaki, M. Sawada and M. Kuno, *J Physiol*, 2013, **23**, 5851–5866.

346 H. Izumi, T. Torigoe, H. Ishiguchi, H. Uramoto, Y. Yoshida, M. Tanabe, T. Ise, T. Murakami, T. Yoshida, M. Nomoto and K. Kohno, *Cancer Treat. Rev.*, 2003, **29**, 541–549.

347 M. Schindler, S. Grabski, E. Hoff and S. M. Simon, *Biochemistry*, 1996, **35**, 2811–2817.

348 T. A. Davies, R. E. Fine, R. J. Johnson, C. A. Levesque, W. H. Rathbun, K. F. Seetoo, S. J. Smith, G. Strohmeier, L. Volicer, L. Delva and ., *Biochem.Biophys.Res.Commun.*, 1993, 194, 537–543.

349 G. G. Fox and G. Ratcliffe, *Plant Physiol.*, 1990, **93**, 512–521.

350 A. C. Kuesel, G. Graschew, S. W. E. Hull, W. Lorenz and H. W. Thielmanns, *NMR Biomed.*, 1990, **3**, 78–89.

351 B. Y. C. C. Aickin and R. C. Thomas, *J. Physiol.*, 1977, **267**, 791–810.

352 E. Bitziou, O. Hare and B. Anil, 2010, 482–487.

353 H. Hou, Y. Zhao, C. Li, M. Wang, X. Xu and Y. Jin, *Sci. Rep.*, 2017, **7**, 1759.

354 Z. Wu, J. Mu, Q. Wang, X. Chen, L. Jensen, C. Yi and M. J. Li, *J. Organomet. Chem.*, 2015, **791**, 175–182.

355 D. Wencel, T. Abel and C. McDonagh, *Anal. Chem.*, 2014, **86**, 15–29.

356 D. Hara, H. Komatsu, A. Son, S. Nishimoto and K. Tanabe, *Bioconjugate Chem.*, 2015, **26**, 645–649.

357 S. Pizarro, M. Gallardo, C. Leyton, E. Castro, F. Gajardo and A. Delgadillo, *Spectrochim. Acta - Part A Mol. Biomol. Spectrosc.*, 2015, **146**, 61–65.

358 H. Chao, B.-H. Ye, Q.-L. Zhang and L.-N. Ji, *Inorg. Chem. Commun.*, 1999, **2**, 338–340.

359 R. Wang, C. Yu, F. Yu, L. Chen and C. Yu, *TrAC - Trends Anal. Chem.*, 2010,

29, 1004–1013.

360 H. J. Kim, Y. C. Jeong, J. Heo, J. Il Rhee and K. Hwang, *Bull. Korean Chem. Soc.*, 2009, **30**, 539–540.

361 G.-Y. Bai, K.-Z. Wang, Z.-M. Duan and L.-H. Gao, *J. Inorg. Biochem.*, 2004, **98**, 1017–1022.

362 S. San Tan, S. Yanagisawa, K. Inagaki, Y. Morikawa and M. B. Kassim, *Phys. Chem. Chem. Phys.*, 2017, **19**, 25734–25745.

363 W. D. Bare, N. H. Mack, J. N. Demas and B. A. DeGraff, *Appl. Spectrosc.*, 2004, **58**, 1093–1100.

364 J. L.-L. Tsai, T. Zou, J. Liu, T. Chen, A. O.-Y. Chan, C. Yang, C.-N. Lok and C.-M. Che, *Chem. Sci.*, 2015, **6**, 3823–3830.

365 D. C. Goldstein, Y. Y. Cheng, T. W. Schmidt, M. Bhadbhade and P. Thordarson, *Dalt. Trans.*, 2011, **40**, 2053.

366 K. R. Reddy, C. U. Maheswari, M. Venkateshwar and M. L. Kantam, *Adv. Synth. Catal.*, 2009, **351**, 93–96.

367 G. a Olah, P. Ramaiah and G. K. Prakash, *Proc. Natl. Acad. Sci. U. S. A.*, 1997, **94**, 11783–11785.

368 J. Freire De Queiroz, J. W. D. M. Carneiro, A. A. Sabino, R. Sparrapan, M. N. Eberlin and P. M. Esteves, *J. Org. Chem.*, 2006, **71**, 6192–6203.

369 A. P. Koskin, I. V. Mishakov and A. A. Vedyagin, *Resour. Technol.*, 2016, **2**, 118–125.

370 B. Umamahesh, N. S. Karthikeyan, K. I. Sathiyanarayanan, J. M. Malicka and M. Cocchi, *J. Mater. Chem. C*, 2016, **4**, 10053–10060.

371 F. Zhang, C. Si, X. Dong, D. Wei, X. Yang, K. Guo, B. Wei, Z. Li, C. Zhang, S. Li, B. Zhai and G. Cao, *J. Mater. Chem. C*, 2017, **5**, 9146–9156.

372 M. V. Werrett, D. Chartrand, J. D. Gale, G. S. Hanan, J. G. MacLellan, M. Massi, S. Muzzioli, P. Raiteri, B. W. Skelton, M. Silberstein and S. Stagni, *Inorg. Chem.*, 2011, **50**, 1229–1241.

373 A. Gabrielsson, P. Matousek, M. Towrie, F. Hartl, S. Záliš and A. Vlček, *J. Phys. Chem. A*, 2005, **109**, 6147–6153.

374 X. Shen, F. L. Wang, F. Sun, R. Zhao, X. Wang, S. Jing, Y. Xu and D. R. Zhu, *Inorg. Chem. Commun.*, 2011, **14**, 1511–1515.

375 V. Balzani, A. Juris, F. Barigelletti, S. Campagna, P. Belser and V. Von Zelewsky, *Coord. Chem. Rev.*, 1988, **84**, 85–277.

376 D. Felder, J. F. Nierengarten, F. Barigelletti, B. Ventura and N. Armaroli, *J. Am. Chem. Soc.*, 2001, **123**, 6291–6299.

377 J. R. Kirchhoff, R. E. Gamache, M. W. Blaskie, A. A. D. Paggio, R. K. Lengel and D. R. Mcmillin, *Inorg. Chem.*, 1983, **22**, 2380–2384.

378 G. A. Crosby, *Acc. Chem. Res.*, 1975, **8**, 231–238.

379 M. Mauro, G. De Paoli, M. Otter, D. Donghi, G. D'Alfonso and L. De Cola, *Dalt. Trans.*, 2011, **40**, 12106–12116.

380 D.-L. Ma, S. Lin, W. Wang, C. Yang and C.-H. Leung, *Chem. Sci.*, 2017, **8**, 878–889.

381 E. Baggaley, J. A. Weinstein and J. A. G. Williams, *Coord. Chem. Rev.*, 2012, **256**, 1762–1785.

382 H. Zhu, J. Fan, Q. Xu, H. Li, J. Wang, P. Gao and X. Peng, *Chem. Commun.*, 2012, **48**, 11766.

383 J. R. Casey, S. Grinstein and J. Orlowski, *Nat. Rev. Mol. Cell Biol.*, 2010, **11**, 50–61.

384 K. Qiu, Y. Chen, T. W. Rees, L. Ji and H. Chao, *Coord. Chem. Rev.*, 2017.

385 E. J. New, D. Parker, D. G. Smith and J. W. Walton, *Curr. Opin. Chem. Biol.*, 2010, **14**, 238–246.

386 S. Lamansky, P. Djurovich, D. Murphy, F. Abdel-Razzaq, H. E. Lee, C. Adachi, P. E. Burrows, S. R. Forrest and M. E. Thompson, *J. Am. Chem. Soc.*, 2001, **123**, 4304–4312.

387 J. R. Simard, F. Kamp and J. A. Hamilton, *Biophys. J.*, 2008, **94**, 4493–4503.

388 A. J. Pérez and H. B. Bode, *J. Lipid Res.*, 2014, **55**, 1897–1901.

389 A. C. Rustan and C. A. Drevon, *Encycl. Life Sci.*, 2005, 1–7.

390 K. Y. Cho and M. R. J. Salton, *Biochim. Biophys. Acta*, 1966, **116**, 73–79.

391 J. E. Cronan and J. Thomas, *Methods Enzym.*, 2009, **459**, 395–433.

392 R. N.M. Weijers, *Curr. Diabetes Rev.*, 2012, **8**, 390–400.

393 E. Currie, A. Schulze, R. Zechner, T. C. Walther and R. V. Farese, *Cell Metab.*, 2013, **18**, 153–161.

394 M. S. Wicha, L. A. Liotta and W. R. Kidwell, *Cancer Res.*, 1979, **39**, 426–435.

395 X. Su and N. A. Abumrad, *Trends Endocrinol. Metab.*, 2009, **20**, 72–77.

396 H. Vorum, R. Brodersen, U. Kragh-Hansen and A. O. Pedersen, *Biochim. Biophys. Acta*, 1992, **1126**, 135–142.

397 J. F. C. Glatz and J. Luiken, *Biochimie*, 2017, **136**, 21–26.

398 T. K. Motawi, O. G. Shaker, M. F. Ismail and N. H. Sayed, *Sci. Rep.*, 2017, **7**, 1–8.

399 P. Yang, Y. Xiao, X. Luo, Y. Zhao, L. Zhao, Y. Wang, T. Wu, L. Wei and Y. Chen, *J. Lipid Res.*, 2017, **58**, 1417–1427.

400 Z. Wang, C. Gui, E. Zhao, J. Wang, X. Li, A. Qin, Z. Zhao, Z. Yu and B. Z. Tang, *ACS Appl. Mater. Interfaces*, 2016, **8**, 10193–10200.

401 C. A. G. N. Montalbetti and V. Falque, *Tetrahedron*, 2005, **61**, 10827–10852.

402 A. Wissner and C. V. Grudzinskas, *J. Org. Chem.*, 1978, **43**, 3972–3974.

403 N. J. Meenu Beniwal, *Eur. J. Biomed. Pharm. Sci.*, 2015, **2**, 1340–1374.

404 A. H. Cherney, N. T. Kadunce and S. E. Reisman, *J. Am. Chem. Soc.*, 2013, **135**, 7442–7445.

405 M. Wong, *Epilepsia*, 2010, **51**, 27–36.

406 K. Ghosh, S. S. Ali, A. R. Sarkar, A. Samadder, A. R. Khuda-Bukhsh, I. D. Petsalakis and G. Theodorakopoulos, *Org. Biomol. Chem.*, 2013, **11**, 5666–5672.

407 N. A. Gomez, R. Abonia, H. Cadavid and I. H. Vargas, *J. Braz. Chem. Soc.*, 2011, **22**, 2292–2303.

408 C. Schweitzer and R. Schmidt, *Chem. Rev.*, 2003, **103**, 1685–1757.

409 A. A. Abdel-shafi and D. R. Worrall, *J. Photochem. Photobiol.*, 2005, **172**, 170–179.

410 K. K. W. Lo and T. K. M. Lee, *Inorg. Chim. Acta*, 2007, **360**, 293–302.

411 Q. Zhao, F. Li and C. Huang, *Chem. Soc. Rev.*, 2010, **39**, 3007–3030.

412 Q. Gong, L. Li, X. Wu and H. Ma, *Chem. Sci.*, 2016, **7**, 4694–4697.

413 L. Li and Z. Zhang, *Molecules*, 2016, **21**, 1–22.

414 G. C. Atella and M. Shahabuddin, *J. Exp. Biol.*, 2002, **205**, 3623–3630.

415 J. Shaya, M. Collot, F. Bénailly, N. Mahmoud, Y. Mély, B. Y. Michel, A. S. Klymchenko and A. Burger, *ACS Chem. Biol.*, 2017, **12**, 3022–3030.

416 H. Wang, E. Wei, A. D. Quiroga, X. Sun, N. Touret and R. Lehner, *Mol. Biol. Cell*, 2010, **21**, 1991–2000.

417 Y. Xia and L. Peng, *Chem. Rev.*, 2013, **113**, 7880–7929.

418 K. K. W. Lo, P. K. Lee and J. S. Y. Lau, *Organometallics*, 2008, **27**, 2998–3006.

419 L. Li, H. Szmacinski and J. R. Lakowicz, *Biospectroscopy*, 1997, **3**, 155–159.

420 L. Li, H. Szmacinski and J. R. Lakowicz, *Anal. Biochem.*, 1997, **244**, 80–85.

421 T. Zou, C.-N. Lok, Y. M. E. Fung and C.-M. Che, *Chem. Commun.*, 2013, **49**, 5423–5425.

422 C. K. Koo, K. L. Wong, C. W. Y. Man, H. L. Tam, S. W. Tsao, K. W. Cheah and M. H. W. Lam, *Inorg. Chem.*, 2009, **48**, 7501–7503.

423 G. Balakrishnan, T. Rajendran, K. Senthil Murugan, M. Sathish Kumar, V. K. Sivasubramanian, M. Ganesan, A. Mahesh, T. Thirunalasundari and S. Rajagopal, *Inorg. Chim. Acta*, 2015, **434**, 51–59.

424 D. Domínguez-gutiérrez, M. Surtchev, E. Eiser and C. J. Elsevier, *Nano Lett.*, 2006, **6**, 145–147.

425 P. C. Griffiths, I. A. Fallis, T. Chuenpratoom and R. Watanesk, *Adv. Colloid Interface Sci.*, 2006, **122**, 107–117.

426 T. Owen and A. Butler, *Coord. Chem. Rev.*, 2011, **225**, 678–687.

427 L. Zhao, K. M. C. Wong, B. Li, W. Li, N. Zhu, L. Wu and V. W. W. Yam, *Chem. - A Eur. J.*, 2010, **16**, 6797–6809.

428 A. Sansee, S. Meksawangwong, K. Chainok, K. J. Franz, M. Gál, L.-O. Pålsson, W. Puniyan, R. Traiphol, R. Pal and F. Kielar, *Dalt. Trans.*, 2016, **45**, 17420–17430.

429 A. M.-H. Yip and K. K.-W. Lo, *Coord. Chem. Rev.*, 2018, **361**, 138–163.

Appendix A

Table A.1 Crystal data and structure refinement for [Ir(**F$_2$ppy**)$_2$(**TzPyCN**)].

Identification code	[Ir(**F$_2$ppy**)$_2$(**TzPyCN**)]
Empirical formula	$C_{30.50}H_{18}Cl_3F_4IrN_8$
Formula weight	871.08
Temperature	100(2) K
Wavelength	0.71073 Å
Crystal system	Monoclinic
Space group	*I*2/*a*
Unit cell dimensions	*a* = 19.3193(4) Å
	b = 10.42280(10) Å
	c = 31.7649(6) Å
	β = 106.177(2)°
Volume	6142.96(19) Å^3
Z	8
Density (calculated)	1.884 Mg/m^3
	4.670 mm^{-1}
Crystal size	0.30 x 0.19 x 0.055 mm^3
θ range for data collection	2.065 to 33.049°.
Index ranges	-25<=h<=28, -15<=k<=12, -47<=l<=46
Reflections collected	38758
Independent reflections	10992 [*R*(int) = 0.0507]
Completeness to θ = 31.00°	100.0 %
Absorption correction	Semi-empirical from equivalents
Max./min. transmission	1.000/0.873
Refinement method	Full-matrix least-squares on F^2
Data / restraints / parameters	10992 / 672 / 598
Goodness-of-fit on F^2	1.038
Final *R* indices [$I>2\sigma(I)$]	*R*1 = 0.0421, *wR*2 = 0.0857
R indices (all data)	*R*1 = 0.0648, *wR*2 = 0.0948
Largest diff. peak and hole	2.125 and -1.357 e.Å^{-3}

Table A.2 Selected Bond lengths [Å] and angles [°] for [Ir(**F$_2$ppy**)$_2$(**TzPyCN**)].

Ir(1)-C(21)	2.000(4)
Ir(1)-N(11)	2.034(3)
Ir(1)-N(31)	2.042(3)
Ir(1)-C(41)	2.066(17)
Ir(1)-N(51)	2.107(3)
Ir(1)-N(61)	2.22(3)
C(21)-Ir(1)-N(11)	80.51(14)
C(21)-Ir(1)-N(31)	95.27(14)
N(11)-Ir(1)-N(31)	172.93(12)
C(21)-Ir(1)-C(41)	92.4(6)
N(11)-Ir(1)-C(41)	97.7(5)
N(31)-Ir(1)-C(41)	76.8(5)
C(21)-Ir(1)-N(51)	96.84(13)
N(11)-Ir(1)-N(51)	91.50(12)
N(31)-Ir(1)-N(51)	94.65(12)
C(41)-Ir(1)-N(51)	168.0(6)
C(21)-Ir(1)-N(61)	173.4(7)
N(11)-Ir(1)-N(61)	98.3(9)
N(31)-Ir(1)-N(61)	86.5(9)
C(41)-Ir(1)-N(61)	94.2(9)
N(51)-Ir(1)-N(61)	76.7(7)

Table A.3 Crystal data and structure refinement for [Ir(**ppy**)$_2$(Me**TzPyPhCN**)]$^+$.

Identification code	[Ir(**ppy**)$_2$(Me**TzPyPhCN**)]$^+$
Empirical formula	$C_{37.38}H_{28.75}Cl_{2.75}F_6IrN_8P$
Formula weight	1024.59
Temperature	100(2) K
Wavelength	1.54178 Å
Crystal system	Monoclinic
Space group	*P*2/*n*
Unit cell dimensions	*a* = 22.1244(4) Å
	b = 12.7352(2) Å
	c = 30.7626(4) Å
	β = 108.760(2)°
Volume	8207.2(2) Å^3
Z	8
Density (calculated)	1.658 Mg/m^3
	8.889 mm^{-1}
Crystal size	0.250 x 0.151 x 0.029 mm^3
θ range for data collection	2.968 to 67.348°.
Index ranges	-19<=h<=26, -15<=k<=15, -36<=l<=35
Reflections collected	51875
Independent reflections	14634 [*R*(int) = 0.0509]
Completeness to θ = 67.348°	99.2 %
Absorption correction	Analytical
Max. and min. transmission	0.731 and 0.195
Refinement method	Full-matrix least-squares on F^2
Data / restraints / parameters	14634 / 197 / 1057
Goodness-of-fit on F^2	1.052
Final *R* indices [$I>2\sigma(I)$]	*R*1 = 0.0541, *wR*2 = 0.1480
R indices (all data)	*R*1 = 0.0717, *wR*2 = 0.1637
Largest diff. peak and hole	1.581 and -1.016 e.Å^{-3}

Table A.4 Selected Bond lengths [Å] and angles [°] for [Ir(**ppy**)$_2$(Me**TzPyPhCN**)]$^+$.

Ir(1)-C(121)	1.994(6)
Ir(1)-C(141)	2.005(7)
Ir(1)-N(111)	2.022(7)
Ir(1)-N(131)	2.031(7)
Ir(1)-N(151)	2.147(6)
Ir(1)-N(161)	2.175(5)
C(121)-Ir(1)-C(141)	90.3(3)
C(121)-Ir(1)-N(111)	80.8(3)
C(141)-Ir(1)-N(111)	95.0(3)
C(121)-Ir(1)-N(131)	95.2(3)
C(141)-Ir(1)-N(131)	81.1(3)
N(111)-Ir(1)-N(131)	174.4(3)
C(121)-Ir(1)-N(151)	99.8(2)
C(141)-Ir(1)-N(151)	169.9(2)
N(111)-Ir(1)-N(151)	87.1(3)
N(131)-Ir(1)-N(151)	97.5(2)
C(121)-Ir(1)-N(161)	175.1(2)
C(141)-Ir(1)-N(161)	94.6(2)
N(111)-Ir(1)-N(161)	98.3(2)
N(131)-Ir(1)-N(161)	86.0(2)
N(151)-Ir(1)-N(161)	75.4(2)

Table A.5 Calculated low energy transitions for [Ir(**ppy**)$_2$(**TzQn**)].

Wavelength	Intensity	Levels	Character
405.42 nm	0.0806	HOMO → LUMO+1	96.7%
379.99 nm	0.0366	HOMO-1 → LUMO	91.9%
359.83 nm	0.0879	HOMO-3 → LUMO	51.5%
		HOMO-2 → LUMO	40.4%
351.48 nm	0.0335	HOMO-3 → LUMO	42.0%
		HOMO-2 → LUMO	53.3%
343.21 nm	0.0270	HOMO-1 → LUMO+1	85.8%
341.68 nm	0.0390	HOMO → LUMO+3	89.2%
328.98 nm	0.0665	HOMO-1 → LUMO+2	51.5%
		HOMO → LUMO+5	18.1%
327.97 nm	0.0275	HOMO-3 → LUMO+1	19.4%
		HOMO-2 → LUMO+1	12.1%
		HOMO → LUMO+5	60.3%
326.62 nm	0.0416	HOMO-4 → LUMO	94.1%
322.77 nm	0.0443	HOMO-2 → LUMO+1	44.9%
		HOMO-1 → LUMO+2	25.8%
		HOMO → LUMO+5	12.4%
321.34 nm	0.0333	HOMO-3 → LUMO+2	51.6%
		HOMO-2 → LUMO+2	29.5%
316.56 nm	0.0152	HOMO-5 → LUMO	15.8%
		HOMO-3 → LUMO+1	45.0%
		HOMO-2 → LUMO+1	13.5%
314.95 nm	0.1188	HOMO-6 → LUMO	26.5%
		HOMO-5 → LUMO	45.0%
312.65 nm	0.1398	HOMO-6 → LUMO	47.6%
		HOMO-5 → LUMO	24.9%
		HOMO-2 → LUMO+2	11.3%
311.27 nm	0.2456	HOMO-6 → LUMO	10.1%
		HOMO-3 → LUMO+2	28.4%
		HOMO-2 → LUMO+2	44.0%
304.99 nm	0.0513	HOMO-7 → LUMO	80.4%
297.72 nm	0.0689	HOMO-4 → LUMO+1	62.5%

Table A.6 Calculated low energy transitions for [Ir(**ppy**)$_2$(**TziQn**)].

Wavelength	Intensity	Levels	Character
408.40 nm	0.0896	HOMO → LUMO+1	96.8%
384.25 nm	0.0453	HOMO-1 → LUMO	90.8%
364.16 nm	0.1632	HOMO-3 → LUMO	22.9%
		HOMO-2 → LUMO	65.9%
335.49 nm	0.1799	HOMO-5 → LUMO	13.3%
		HOMO-4 → LUMO	74.7%
328.51 nm	0.0879	HOMO-3 → LUMO+1	12.4%
		HOMO-2 → LUMO+1	29.9%
		HOMO-1 → LUMO+1	42.6%
322.39 nm	0.0583	HOMO-3 → LUMO+2	25.9%
		HOMO-2 → LUMO+2	39.8%
		HOMO-1 → LUMO+2	19.4%
321.40 nm	0.0410	HOMO-2 → LUMO+1	45.3%
		HOMO-2 → LUMO+2	17.1%
		HOMO-1 → LUMO+2	15.2%
311.83 nm	0.0526	HOMO-3 → LUMO+1	73.2%
		HOMO-2 → LUMO+1	7.3%
		HOMO-1 → LUMO+2	4.0%
307.34 nm	0.1940	HOMO-3 → LUMO+2	58.7%
		HOMO-2 → LUMO+2	28.1%
		HOMO-1 → LUMO+2	2.0%
		HOMO-1 → LUMO+3	4.0%

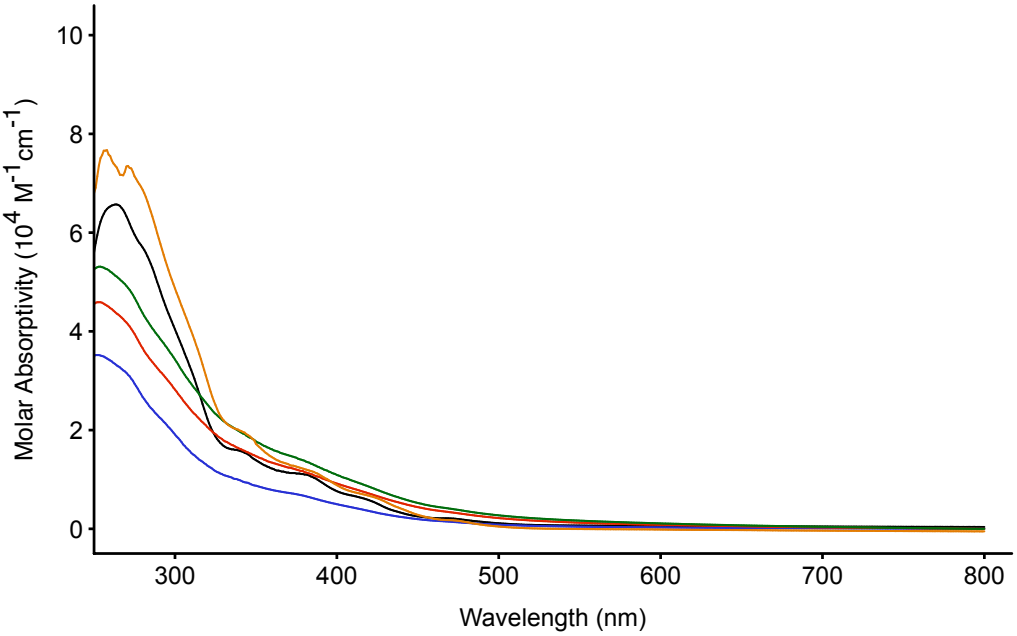

Figure A.1 Absorption profiles of [Ir(**ppy**)$_2$(**TzPyCN**)] in dichloromethane (black), H_2O (blue), lys. fluid (red), PBS (green) and ethyl laurate (orange).

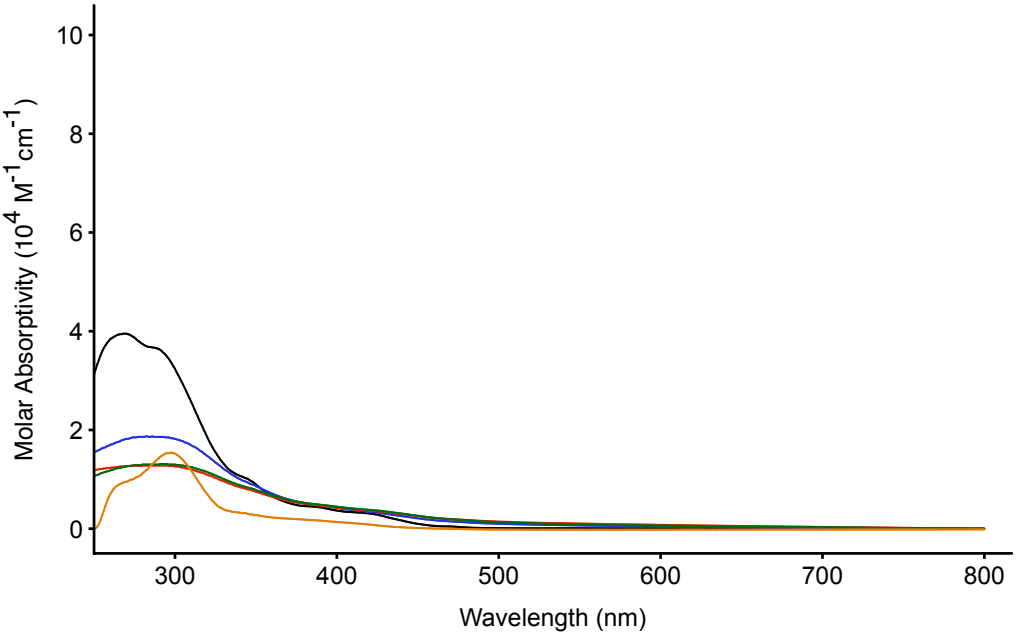

Figure A.2 Absorption profiles of [Ir(**ppy**)$_2$(**TzPyPhCN**)] in dichloromethane (black), H_2O (blue), lys. fluid (red), PBS (green) and ethyl laurate (orange).

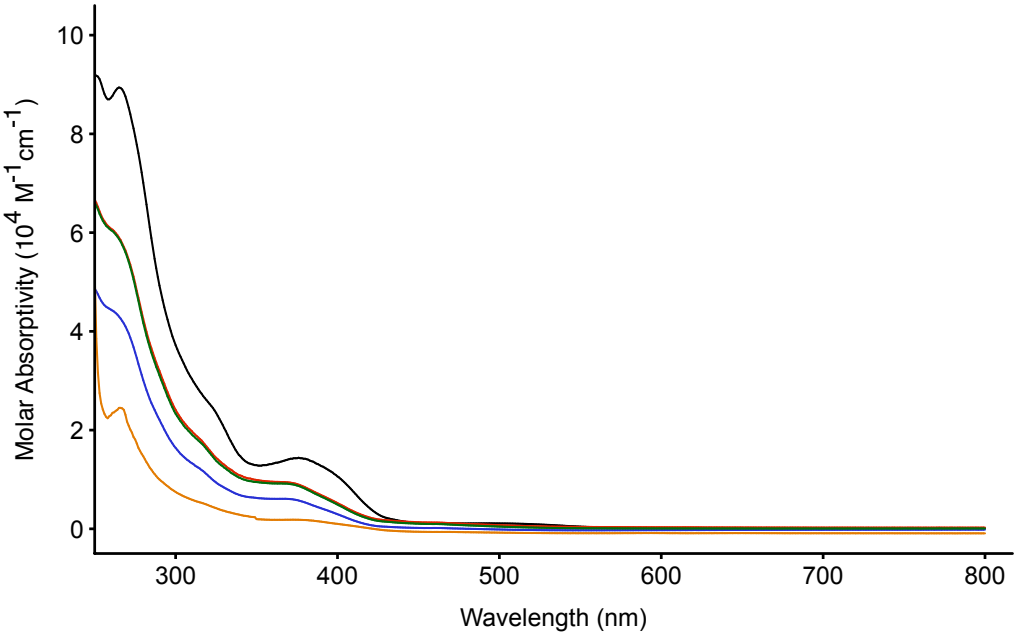

Figure A.3 Absorption profiles of [Ir(**ppy**)$_2$(Me**TzPyCN**)]$^+$ in dichloromethane (black), H_2O (blue), lys. fluid (red), PBS (green) and ethyl laurate (orange).

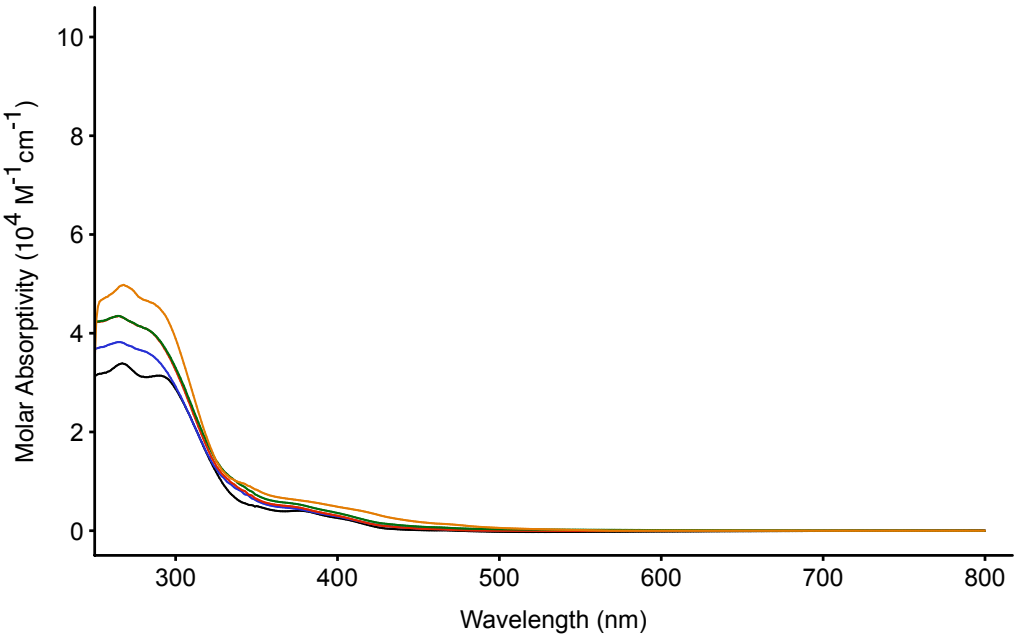

Figure A.4 Absorption profiles of [Ir(**ppy**)$_2$(Me**TzPyPhCN**)]$^+$ in dichloromethane (black), H_2O (blue), lys. fluid (red), PBS (green) and ethyl laurate (orange).

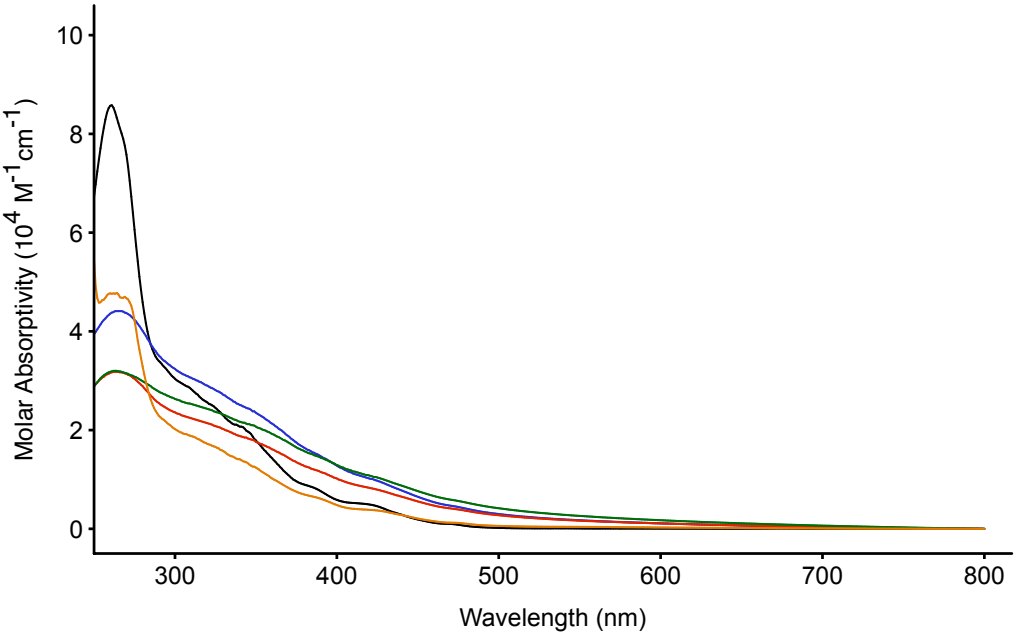

Figure A.5 Absorption profiles of [Ir(**ppy**)$_2$(**TzQn**)] in dichloromethane (black), H_2O (blue), lys. fluid (red), PBS (green) and ethyl laurate (orange).

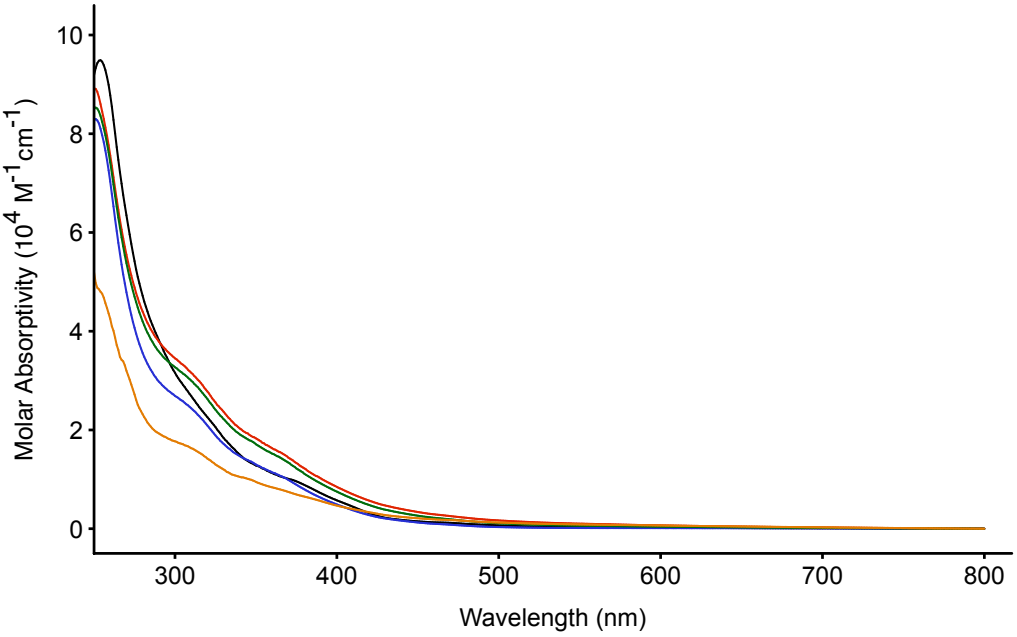

Figure A.6 Absorption profiles of [Ir(**ppy**)$_2$(Me**TzQn**)]$^+$ in dichloromethane (black), H_2O (blue), lys. fluid (red), PBS (green) and ethyl laurate (orange).

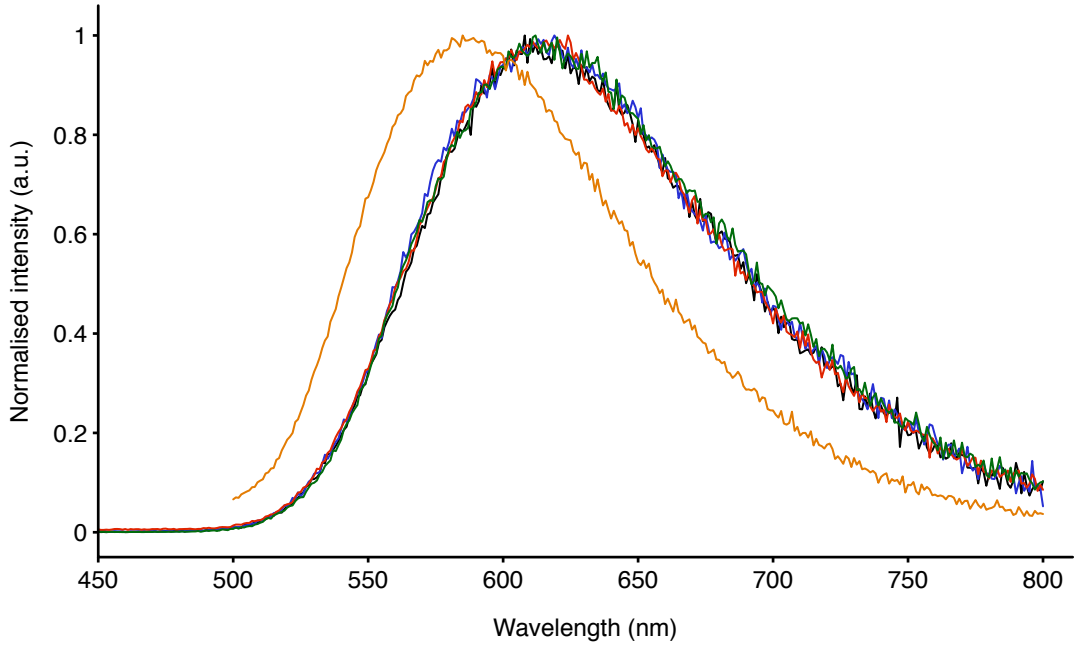

Figure A.7 Emission profiles of [Ir(**ppy**)$_2$(**TzPyCN**)] in dichloromethane (black), H_2O (blue), lys. fluid (red), PBS (green) and ethyl laurate (orange).

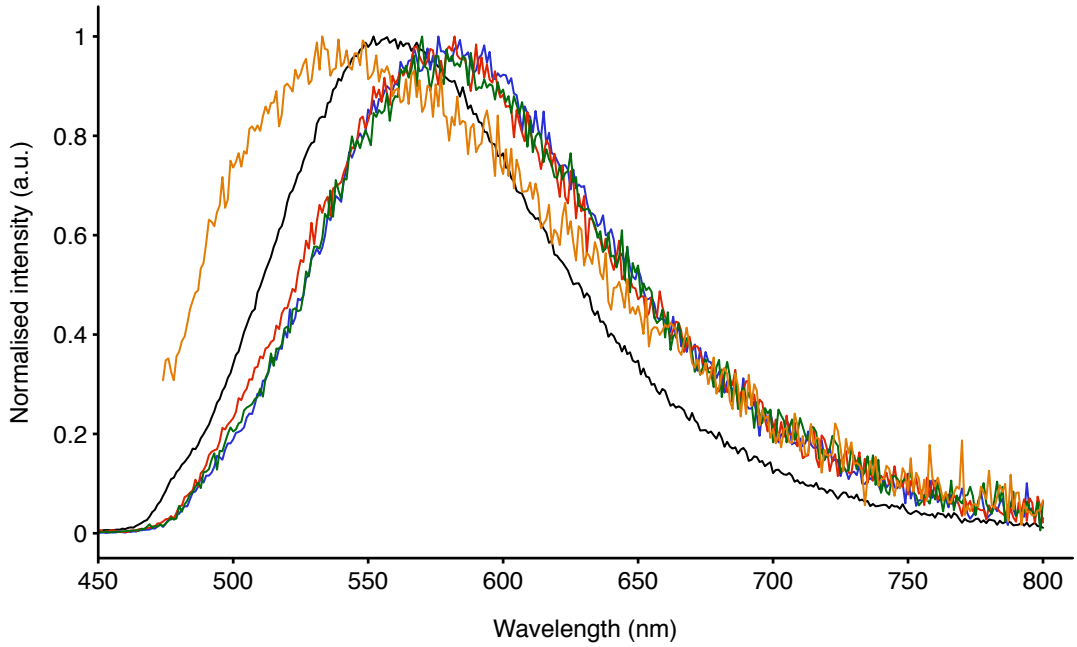

Figure A.8 Emission profiles of [Ir(**ppy**)$_2$(**TzPyPhCN**)] in dichloromethane (black), H_2O (blue), lys. fluid (red), PBS (green) and ethyl laurate (orange).

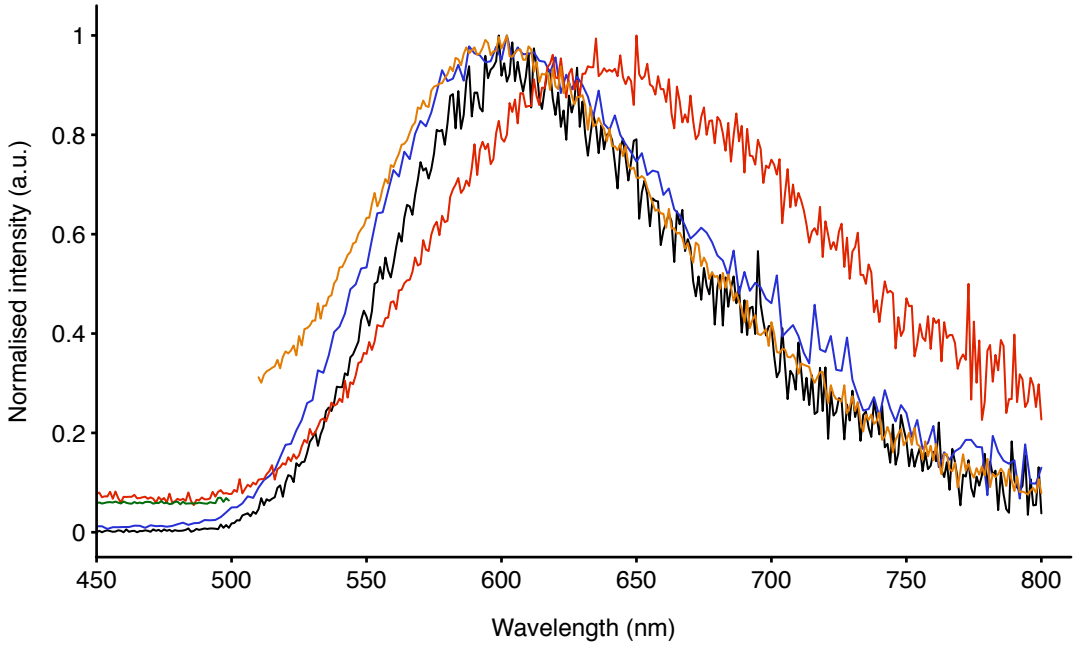

Figure A.9 Emission profiles of [Ir(**ppy**)$_2$(Me**TzPyPhCN**)]$^+$ in dichloromethane (black), H_2O (blue), lys. fluid (red), PBS (green) and ethyl laurate (orange).

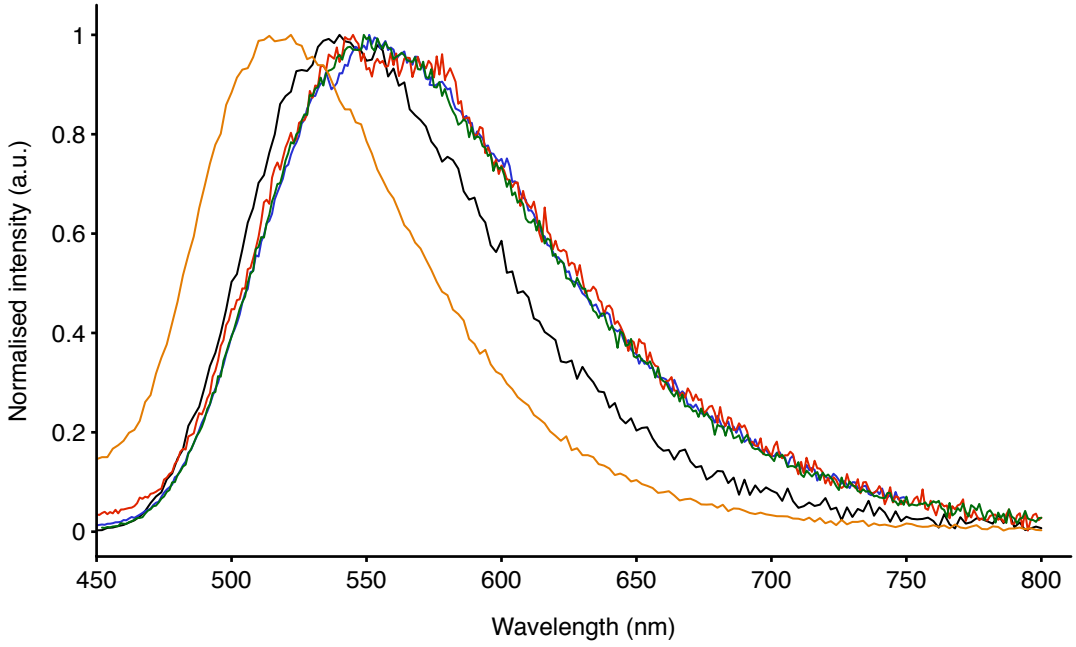

Figure A.10 Emission profiles of [Ir(**ppy**)$_2$(**TzQn**)] in dichloromethane (black), H_2O (blue), lys. fluid (red), PBS (green) and ethyl laurate (orange).

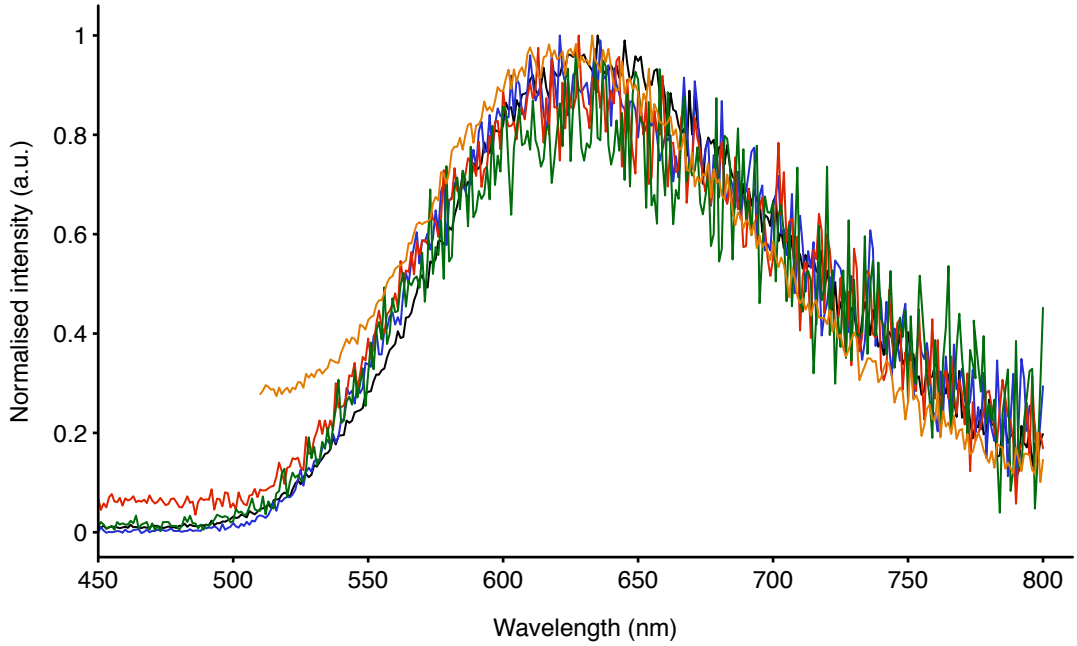

Figure A.11 Emission profiles of [Ir(**ppy**)$_2$(Me**TzQn**)]$^+$ in dichloromethane (black), H_2O (blue), lys. fluid (red), PBS (green) and ethyl laurate (orange).

Appendix B

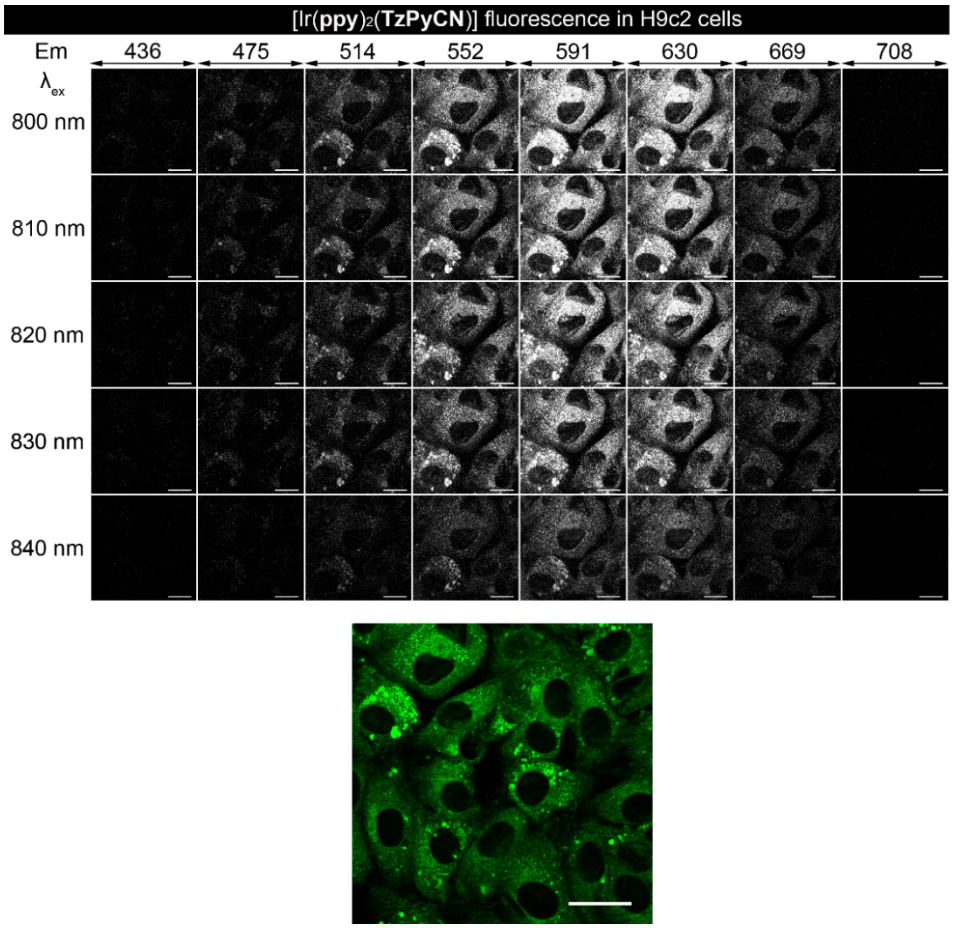

Figure B.1 (Top) Representative lambda stack micrographs of live H9c2 cells using META detection module, sampling emission over the visible spectrum with 38.9 nm wavelength intervals. The complexes were excited with two-photon laser. Scale bar = 15 μm. (Bottom) Two-photon microscopy image (λ_{ex} = 830 nm) of live H9c2 cells stained with [Ir(**ppy**)$_2$(**TzPyCN**)] (20 μM, 30 mins). Scale bar = 30 μm.

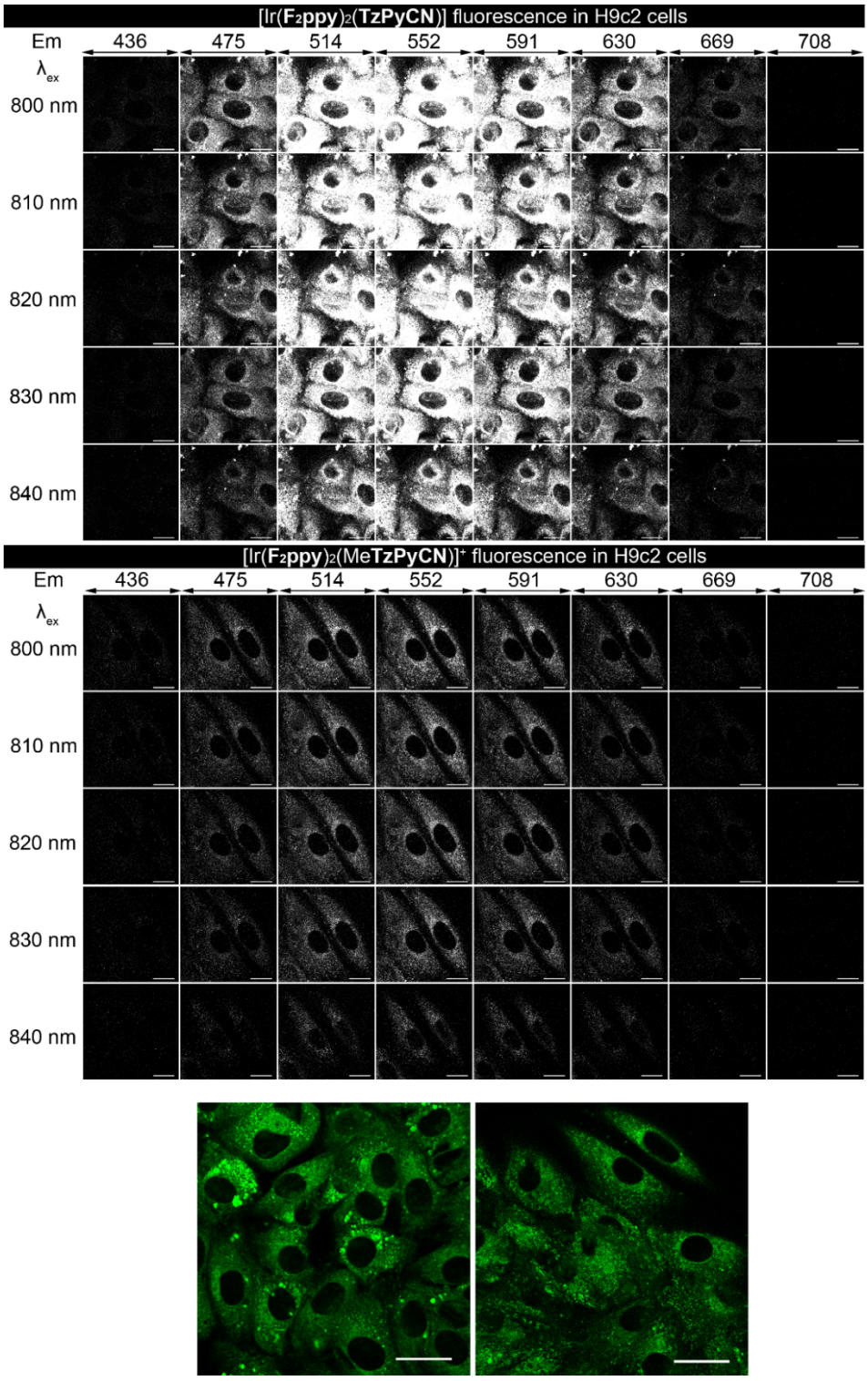

Figure B.2 (Top) Representative lambda stack micrographs of live H9c2 cells using META detection module, sampling emission over the visible spectrum with 38.9 nm wavelength intervals. The complexes were excited with two-photon laser. Scale bar = 15 μm. (Bottom) Two-photon microscopy images (λ_{ex} = 830 nm) of live H9c2 cells stained with [Ir(**F$_2$ppy**)$_2$(**TzPyCN**)] (left) and [Ir(**F$_2$ppy**)$_2$(Me**TzPyCN**)]$^+$ (right) (20 μM, 30 mins). Scale bar = 30 μm.

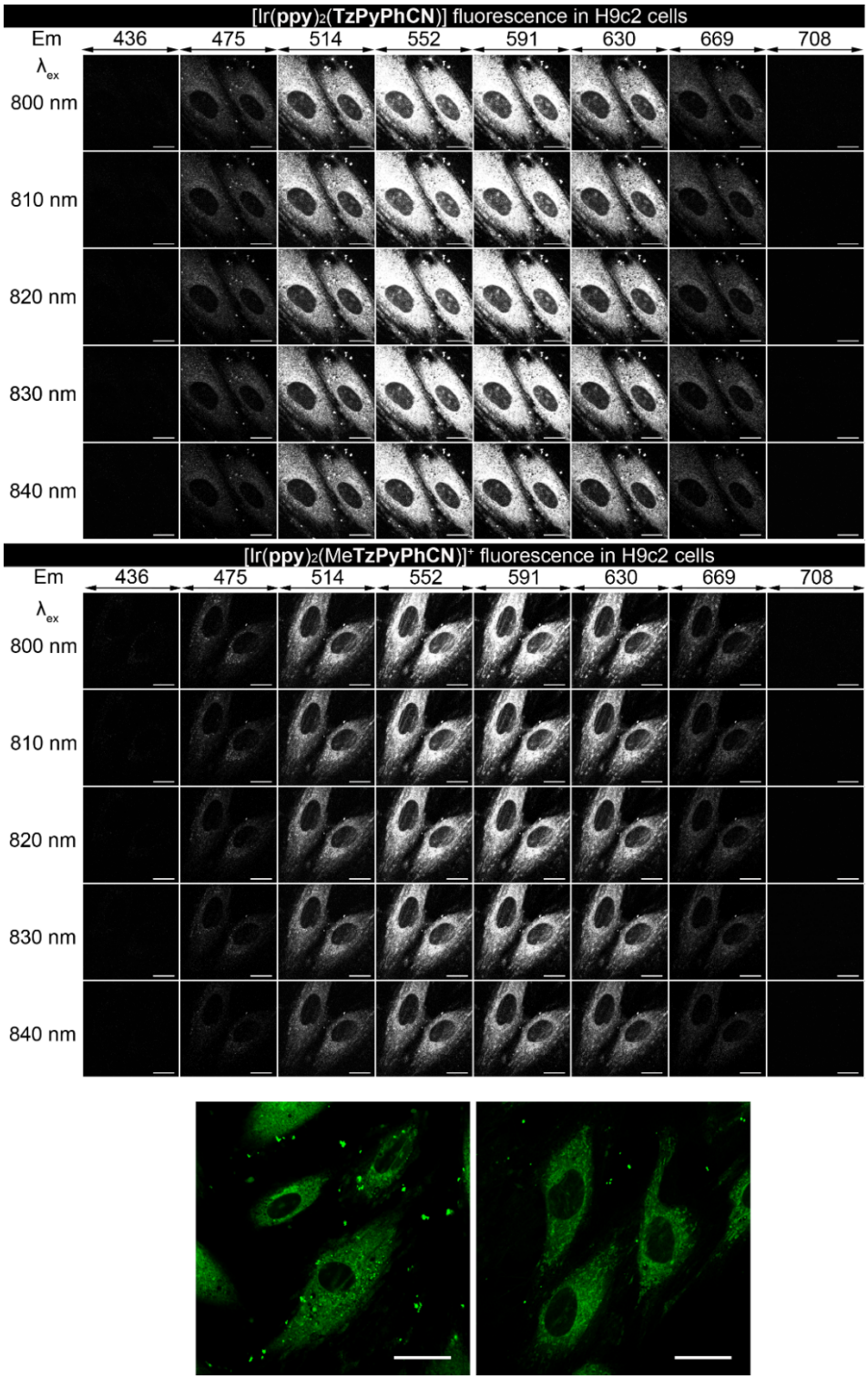

Figure B.3 (Top) Representative lambda stack micrographs of live H9c2 cells using META detection module, sampling emission over the visible spectrum with 38.9 nm wavelength intervals. The complexes were excited with two-photon laser. Scale bar = 15 μm. (Bottom) Two-photon microscopy images (λ_{ex} = 820 nm) of live H9c2 cells stained with [Ir(**ppy**)$_2$(**TzPyPhCN**)] (left) and [Ir(**ppy**)$_2$(Me**TzPyPhCN**)]$^+$ (right) (20 μM, 30 mins). Scale bar = 30 μm.

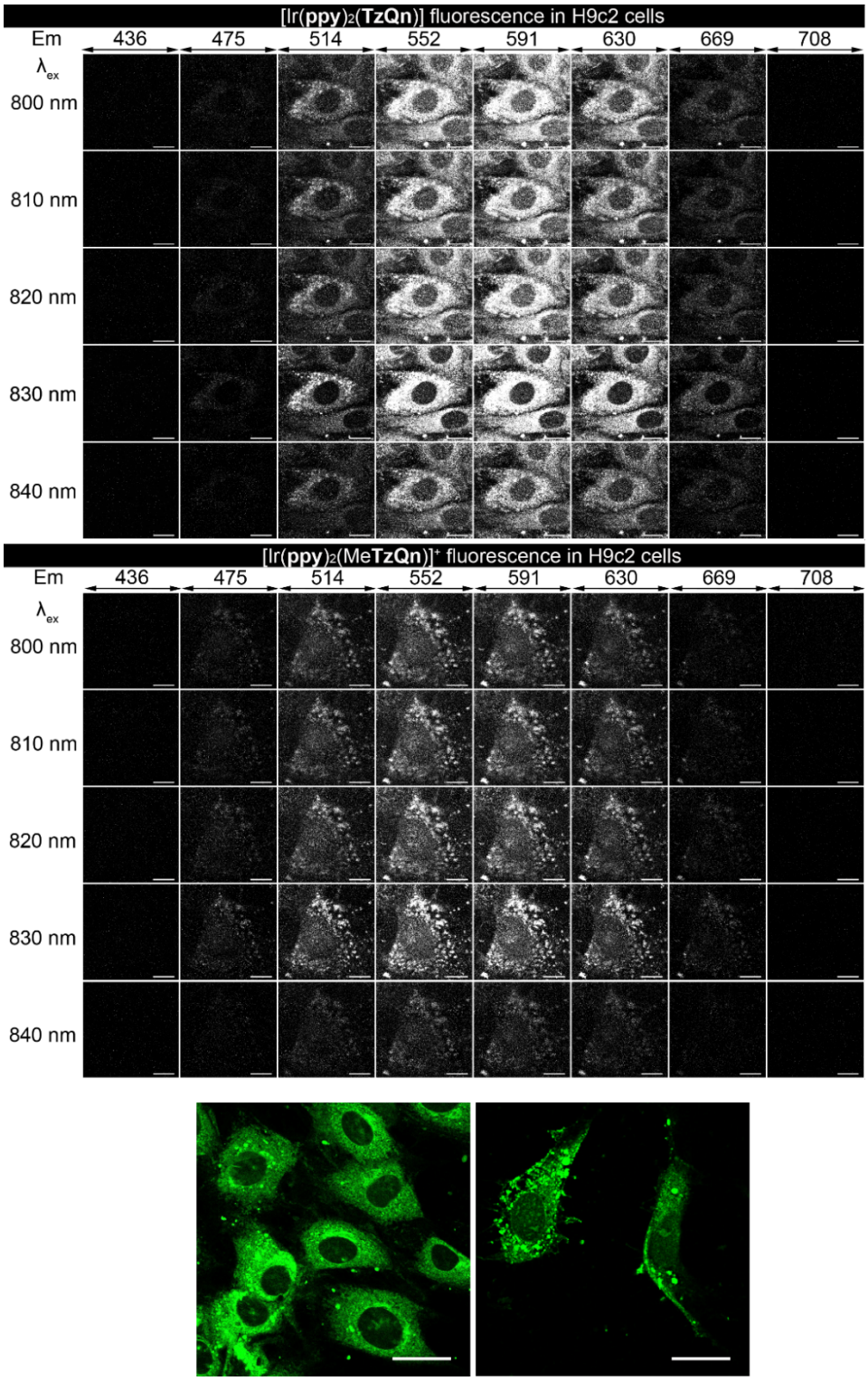

Figure B.4 (Top) Representative lambda stack micrographs of live H9c2 cells using META detection module, sampling emission over the visible spectrum with 38.9 nm wavelength intervals. The complexes were excited with two-photon laser. Scale bar = 15 μm. (Bottom) Two-photon microscopy images (λ_{ex} = 830 nm) of live H9c2 cells stained with [Ir(**ppy**)$_2$(**TzQn**)] (left) and [Ir(**ppy**)$_2$(Me**TzQn**)]$^+$ (right) (20 μM, 30 mins). Scale bar = 30 μm.

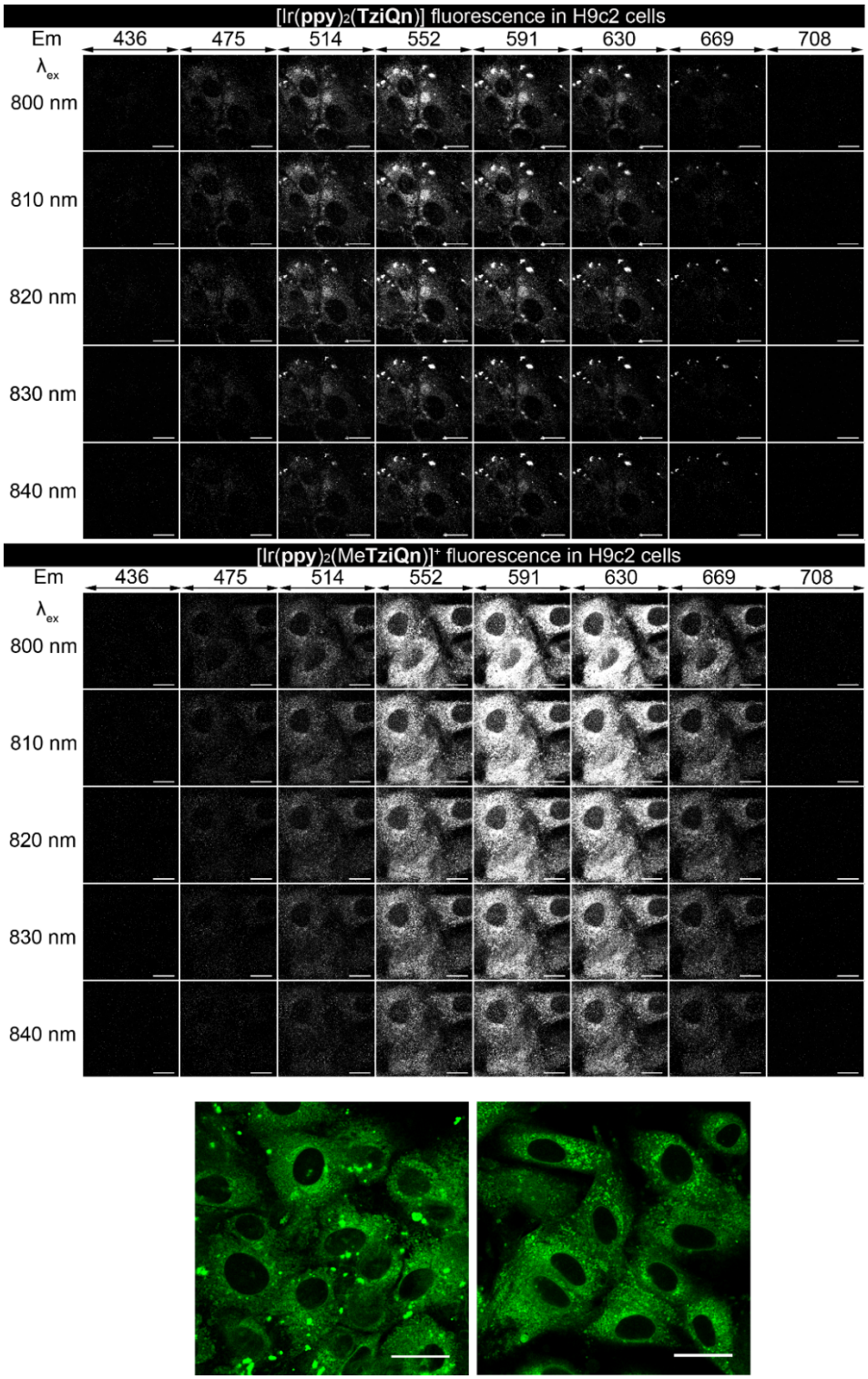

Figure B.5 (Top) Representative lambda stack micrographs of live H9c2 cells using META detection module, sampling emission over the visible spectrum with 38.9 nm wavelength intervals. The complexes were excited with two-photon laser. Scale bar = 15 μm. (Bottom) Two-photon microscopy images (λ_{ex} = 810 nm) of live H9c2 cells stained with [Ir(**ppy**)$_2$(**TziQn**)] (left) and [Ir(**F$_2$ppy**)$_2$(Me**TziQn**)]$^+$ (right) (20 μM, 30 mins). Scale bar = 30 μm.

Appendix C

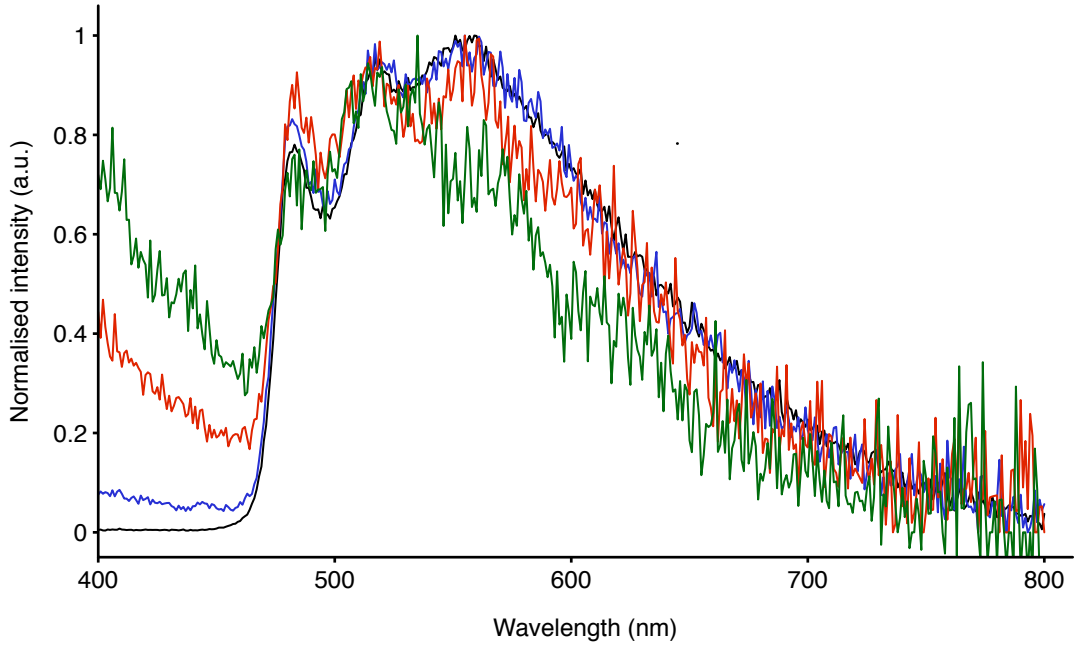

Figure C.1 Normalised emission profile of [Ir(**ppy**)$_2$(**TzPyNH$_2$**)] in ethyl laurate at different concentration: 10^{-4} M (black), 10^{-5} M (blue), 10^{-6} M (red) and 10^{-7} M (green).

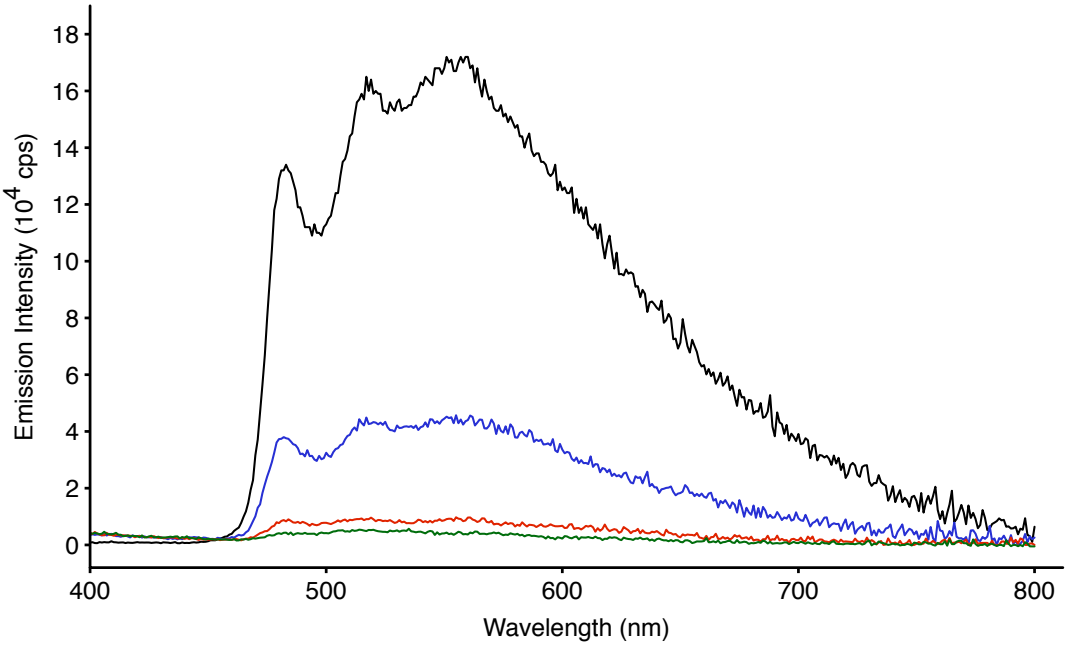

Figure C.2 Emission profile of [Ir(**ppy**)$_2$(**TzPyNH$_2$**)] in ethyl laurate at different concentration: 10^{-4} M (black), 10^{-5} M (blue), 10^{-6} M (red) and 10^{-7} M (green).

Table C.1 Excited state lifetimes of [Ir(**ppy**)$_2$(**TzPyNH$_2$**)] in diluted (10^{-4} M) ethyl laurate solution, measured at different maxima emission wavelengths.

λ_{em} [nm][a]	τ [ns][b]
484	17 (63), 89 (37)
555	41 (32), 258 (68)

[a] Maximum emission wavelength (λ_{em}) at which the excited state lifetime (τ) was measured. [b] For the biexponential excited state lifetime (τ), the relative weights of the exponential curves are reported in parentheses.

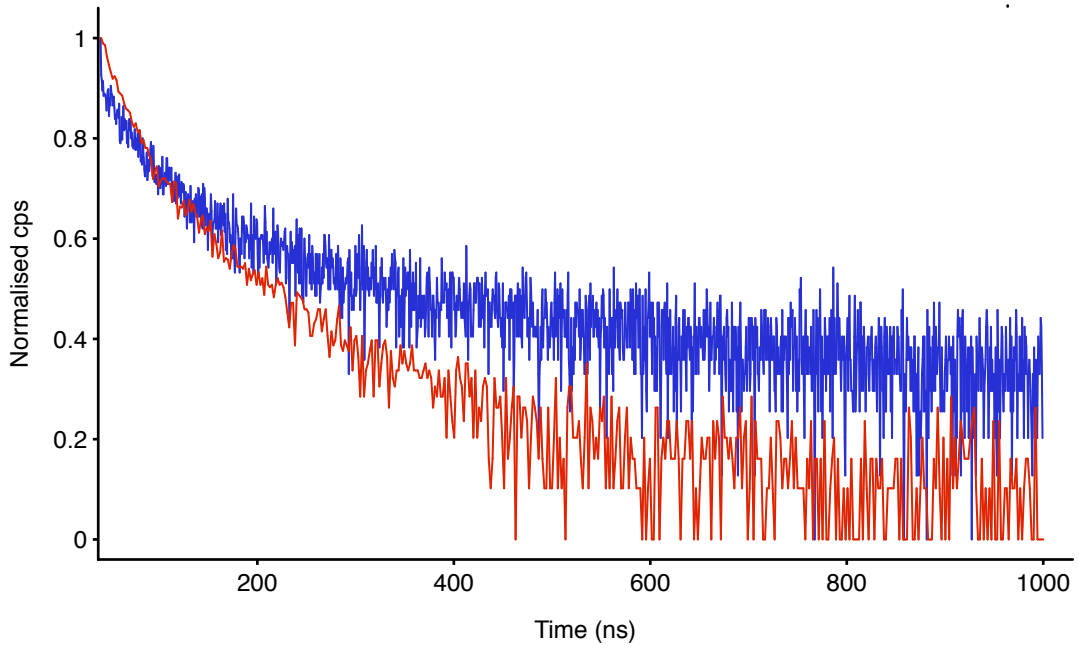

Figure C.3 Excited state lifetime profiles of [Ir(**ppy**)$_2$(**TzPyNH$_2$**)] in ethyl laurate, measured at λ_{em} = 484 nm (blue) and λ_{em} = 555 nm (red).

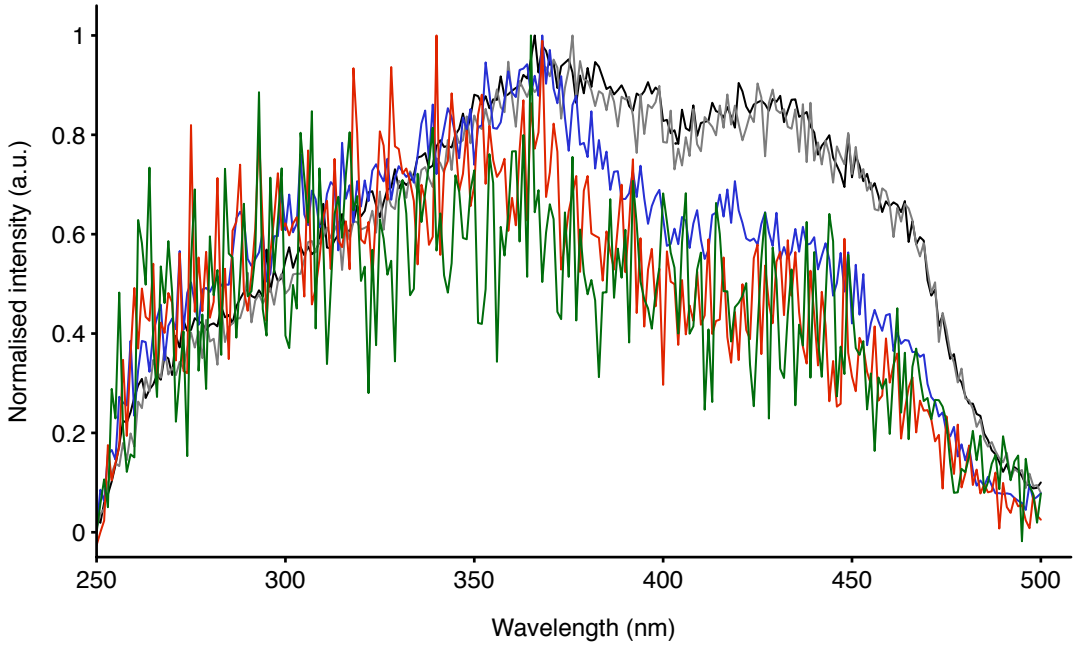

Figure C.4 Normalised excitation profile of [Ir(**bzq**)$_2$(**TzPyNH$_2$**)] in ethyl laurate at different concentration: 10^{-4} M at λ_{emi} = 606 nm (black), 10^{-4} M at λ_{emi} = 646 nm (grey), 10^{-5} M (blue), 10^{-6} M (red) and 10^{-7} M (green).

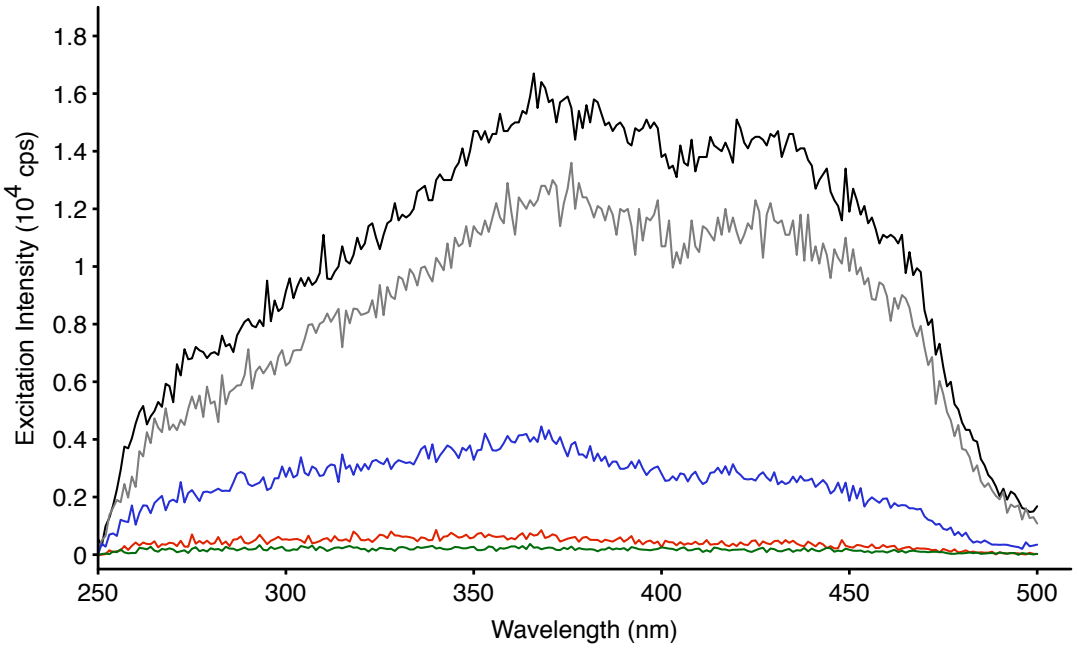

Figure C.5 Excitation profile of [Ir(**bzq**)$_2$(**TzPyNH$_2$**)] in ethyl laurate at different concentration: 10^{-4} M at λ_{emi} = 606 nm (black), 10^{-4} M at λ_{emi} = 646 nm (grey), 10^{-5} M (blue), 10^{-6} M (red) and 10^{-7} M (green).

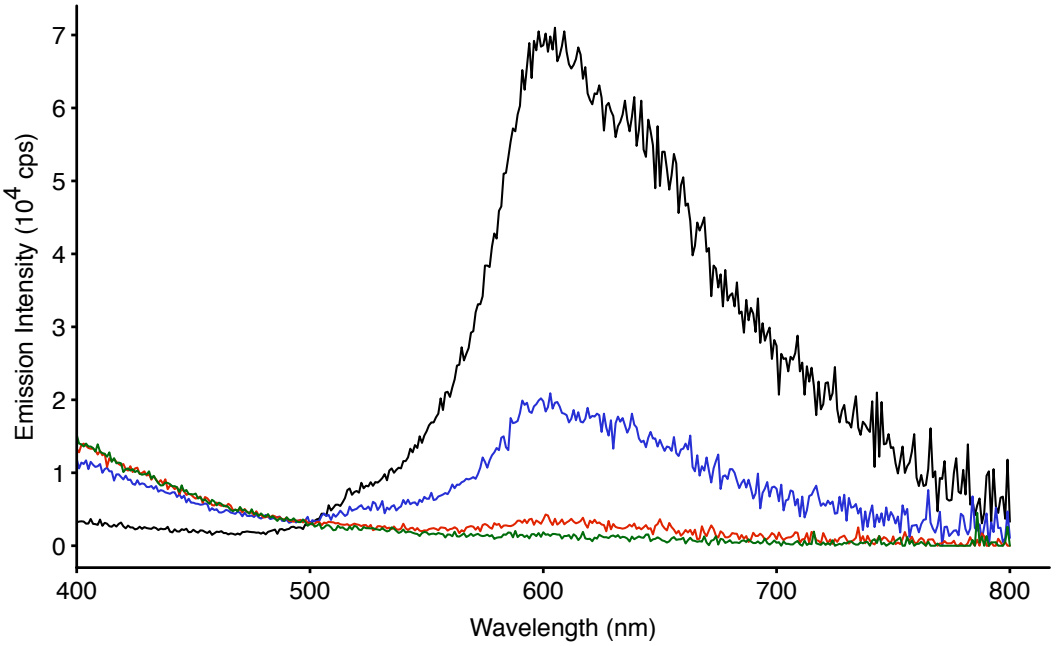

Figure C.6 Emission profile of [Ir(**bzq**)$_2$(**TzPyNH$_2$**)] in ethyl laurate at different concentration: 10^{-4} M (black), 10^{-5} M (blue), 10^{-6} M (red) and 10^{-7} M (green).

Table C.2 Excited state lifetimes of [Ir(**bzq**)$_2$(**TzPyNH$_2$**)] in diluted (10^{-4} M) ethyl laurate solution, measured at different maxima emission wavelengths.

λ_{em} **[nm]**[a]	τ **[ns]**[b]
606	83
646	169

[a] Maximum emission wavelength (λ_{em}) at which the excited state lifetime (τ) was measured.